

# **RIKEN Accelerator Progress Report**

1982

vol. 16

理化学研究所  
*the Institute of Physical and Chemical Research*

**RIKEN Accelerator Progress Report** 1982  
**January-December**

理化学研究所  
**the Institute of Physical and Chemical Research**  
**Wako-shi, Saitama, 351 JAPAN**

## Editors

Y. Gono	A. Hashizume
T. Inamura	H. Kamitsubo
M. Odera	N. Shiotani

This volume contains recent information of the accelerators at RIKEN (IPCR), informal reports and abstracts of papers which will be published at scientific meetings or in publications by staff members, guests, and visitors.

All rights reserved. This report or any part thereof may not be reproduced in any form (including photostatic or microfilm form) without written permission from the publisher.

## P R E F A C E

This is the sixteenth issue of the RIKEN Accelerator Progress Report and summarizes research activities and technical developments carried out at the Institute of Physical and Chemical Research (RIKEN) using accelerators during the period from January to December in 1982.

Nuclear science is one of the principal research activities at RIKEN and about one hundred scientists from inside as well as outside of the institute take part in the collaborative studies which cover the research fields of nuclear physics, atomic and solid state physics, nuclear and radiation chemistry, material engineering and radiation biology. It should also be emphasized that the accelerators at RIKEN are open for the trials and tests to the application of accelerators to the industrial uses. In the past one year the cyclotron provided protons, deuterons and alpha particles for these purposes.

In order to extend the research area in the nuclear science and to develop the research activities using the accelerators at RIKEN a new separated sector cyclotron with  $k = 540$  is under construction. We expect we can get the first beam in the middle of 1986.

We would like to acknowledge to Prof. K. Shinohara for his critical reading of the manuscripts and valuable comments. We also thank to Mrs. H. Masamoto and H. Takada for their editorial works.

*Hirotsugu Kamitsubo*

---

H. Kamitsubo  
Editor



# CONTENTS

Page

PREFACE	
I. INTRODUCTION .....	1
II. OPERATION OF ACCELERATORS	
1. Cyclotron Operation .....	2
2. Operation Statistics of RILAC .....	5
3. TANDETRON-Operation .....	8
III. RESEARCH ACTIVITIES	
1. Nuclear Physics	
1. Excitation Functions for $^{14}\text{N}$ -Induced Reactions on $^{62}\text{Ni}$ .....	9
2. Strongly Damped Components in the Reactions of $^{20}\text{Ne} + ^{92}\text{Mo}$ and $^{20}\text{Ne} + ^{100}\text{Mo}$ Systems .....	12
3. High-lying Proton Strengths Observed in ( $^{12}\text{C}$ , $^{11}\text{B}$ ) Reactions .....	15
4. Polarization Measurement for Continuous Protons Emitted in the ( $\alpha$ , p) and ( $^{14}\text{N}$ , p) Reactions .....	18
5. Angular-Momentum Transfer and Alignment Following Preequilibrium $\alpha$ -Particle Emission in $^{16}\text{O}$ - and $^{20}\text{Ne}$ -Induced Reactions .....	19
6. Light-Particle Emission in $^7\text{Li}$ -Induced Reactions .....	22
7. Momentum Transfer Light-Particle Emission Following 210 MeV $^{14}\text{N}$ -Bombardment on $^{232}\text{Th}$ .....	26
8. Spin Polarization of Residual Nucleus in Heavy Ion Reaction .....	28
9. Vector Analyzing Power Measurements for (d, p) and (p, d) Reactions on Sn Isotopes and Deuteron D-state Effects .....	31
10. Excitation Modes of the $\gamma$ -band in $^{24}\text{Mg}$ through the $^{24}\text{Mg}(\vec{p}, p')$ Reaction .....	35
11. Multiple Coulomb Excitation of $^{167}\text{Er}$ .....	38
12. Excited States in $^{157}\text{Yb}$ and $^{158}\text{Yb}$ .....	41
13. Analysis of Gamma-Ray Multiplicity Distributions for the $^{159}\text{Tb}(^{14}\text{N}, \alpha xn)$ Reaction at 115 MeV .....	43

	Page
14. Level Scheme of $^{217}\text{Ra}$ .....	46
15. Level Schemes of $^{216,218}\text{Ra}$ .....	48
16. In-Beam $\alpha$ - and $\gamma$ -Ray Study on $^{215}\text{Fr}$ and $^{217}\text{Ac}$ .....	51
17. Numerical Analysis of 1280 MeV $^{208}\text{Pb}$ Reactions on $^{94}\text{Zr}$ , $^{110}\text{Pd}$ , $^{148}\text{Sm}$ , and $^{170}\text{Er}$ Based on the Linear Response Theory .....	54
18. Effects of the Mass Fragmentation Potential on the Mass Diffusion Phenomena .....	58
19. Exact Finite-range Coupled-channel Born Approximation Calculations with Spin-orbit Interactions .....	61
20. Effects of Two Particle-Two Hole Excitations on the Mass Distributions in Ion-Ion Collisions .....	63
2. Atomic and Solid-State Physics	
1. Target Gas Pressure Dependence of REC X-Rays from Ne-Ion Bombardment .....	66
2. Target Gas Pressure Dependence of K-X Rays from 110 MeV Ne Ions .....	69
3. High Resolution Measurements of K X-Rays from Argon Ions Impinging on Foils .....	72
4. Argon L-MM Auger Spectra in $\text{Ar}^{n+} + \text{Ar}$ Collisions (I) Identification of Auger Lines .....	75
5. Argon L-MM Auger Spectra in $\text{Ar}^{n+} + \text{Ar}$ Collisions (II) Energy Dependence of the Auger Spectra .....	77
6. Argon L-MM Auger Spectra in $\text{Ar}^{n+} + \text{Ar}$ Collisions (III) Structure of Argon L-MM Auger Spectra in 21 MeV $\text{Ar}^{4+}$ Impact on Ar .....	79
7. Angular Distribution of Sn L X-Rays .....	82
8. Production of Highly Charged Ions by Heavy-Ion Bombardment of Rare-Gas Targets .....	85
9. Mechanical Design of Apparatus to Measure Secondary Ions .....	87

	Page
10. Scan Controller for Secondary Ion Experiment .....	88
11. Analysis of F K $\alpha$ -Emission Satellite Spectra from Fluorine Compounds by the DV-X $\alpha$ Method .....	89
12. Determination of Electron Contact Densities for Outermost Electrons in Tin Compounds .....	91
13. Optical Detection of Atomic and Nuclear Spin Polarization Produced by Beam-Foil Interaction .....	94
14. Effects of Chemical Bond on O K $\alpha$ Spectra from Multiply Ionized States .....	96
15. Supertransferred Hyperfine Magnetic Field at $^{119}\text{Sn}^{4+}(\leftarrow^{119}\text{Sb}^{5+})$ on $\text{Cr}_2\text{O}_3$ Surfaces .....	98
16. Emission Mössbauer Studies of Dilute $^{119}\text{Sb}$ Ions Adsorbed on Ferrimagnetic Spinel Oxide Surfaces .....	101
17. Perturbed Angular Correlation of $\gamma$ -Rays Emitted from $^{111}\text{Cd}$ ( $\leftarrow^{111}\text{In}$ ) on $\alpha\text{-Fe}_2\text{O}_3$ , $\text{Cr}_2\text{O}_3$ , and $\alpha\text{-Al}_2\text{O}_3$ Surfaces .....	103
18. Dependence of Secondary Electron Emission Coefficients on Metal Targets under Bombardment with Bare Projectiles .....	105
19. Lattice Location of Sn Atoms Implanted into Al Crystals as Investigated by Means of Channeling Method .....	108
20. Amorphization of Diamond Surface Layer by Zn-implantation .....	109
21. Pulsed Laser Annealing of Cd-implanted GaP .....	111
22. Radiation Damages in Amorphous Alloys Irradiated with $\text{C}^{4+}$ and $\text{N}^{4+}$ Ions .....	113
23. Positron Angular Correlation Measurements on Oxygen Implanted Molybdenum Containing Voids .....	114
24. Effect of an Injected Helium Layer near Surface on the Tensile Properties of Fe-Ni-Cr Alloys .....	115
25. Effects of Fast Neutron Irradiation on Insulating Materials .....	118
 3. Radiochemistry and Nuclear Chemistry	

	Page
1. Radioisotope Production and Labelled Compound Synthesis . . . . .	120
2. Charged Particle Activation Analysis of Semiconductor Materials . . . . .	122
3. Rutherford Forward Scattering Applied to the Study of Hydrogen in Amorphous Silicon for Solar Cell . . . . .	125
4. Separation of $^{119}\text{Sb(V)}$ , $^{119\text{m}}\text{Te(IV)}$ and $\text{Sn(IV)}$ by Adsorption on Activated Carbon . . . . .	128
5. Mössbauer Emission Study of Defect $^{119}\text{Sn}$ Atoms in Solids . . . . .	130
6. Research Project on Coulomb-Excitation Mössbauer Spectroscopy Using Heavy Ions Accelerated by RILAC . . . . .	132
 4. Radiation Chemistry and Radiation Biology	
1. Spectroscopic Studies on the Electronic Excited States Formed at High Density in Heavy-Ion Track . . . . .	134
2. Application of Thermoluminescence Dosimeter for Dose Measurement of High-LET Radiation . . . . .	137
3. Track Structure Theories and Inactivation Cross Sections of Bacterial Spores for Heavy Ions . . . . .	139
4. Mutagenesis of Chinese Hamster V79 Cells by Nitrogen Ion Beam . . . . .	142
5. Recovery from Potentially Lethal Damage of Human Cultured Cells after Irradiation of Nitrogen Ion Beams . . . . .	144
 5. Miscellaneous	
1. Quantitative Trace Analysis by Particle Induced X-Ray Emission . . . . .	145
 IV. ACCELERATOR DEVELOPMENT	
1. Beam Attenuation Method Using Charge Transfer Reactions . . . . .	147
2. Design of Axial Extraction PIG-Source . . . . .	149
3. ECR Ion Source . . . . .	153
4. Identification Method of Ions in the Beam from the RILAC Injector . . . . .	155

	Page
5. Bunch Signal Sensitization by Use of Secondary Electron Emission .....	158
6. Bunch Phase Monitor .....	160
7. Linac Energy Tuning by Phase Control .....	162
8. Suppression of Secondary Electron from Beam Stopper .....	164
9. Status of RILAC RF System .....	166
10. Investigation of Frequency Characteristics of the Screen Grid Bypass Capacitor at the Final Stage of RF Power Amplifier for RILAC .....	169
11. Basic Study on the RF High Power Amplifier for RIKEN SSC Study of the Screen Bypass Capacitor for the Final Stage .....	171
12. Grid Tuning Circuit of $\lambda$ Type for the RF Power Amplifier for RIKEN SSC .....	173
13. Control System of the Linac .....	176
14. On a Possible Medium- $\beta$ RFQ Structure .....	178
15. Present Status of the RIKEN SSC Project .....	181
16. Construction of the Sector Magnets for the RIKEN SSC .....	183
17. Measurement of the Magnetic Fields of the RIKEN SSC .....	186
18. Magnetic Field Measuring System for the RIKEN SSC Sector Magnet .....	188
19. Structural Analysis of Sector Magnet by Finite Element Method .....	193
20. Measurement of the Trim Coil Fields and Determination of Trim Coils Power Supplies for the RIKEN SSC .....	197
21. Beam Extraction System for the RIKEN SSC (II) Design Calculation of Magnetic Deflection Channel .....	201
22. Vacuum System of the SSC .....	205
23. Test of Model Pneumatic Expansion Seal .....	207

	Page
24. Preliminary Experiment on the Surface Cleaning of the Vacuum Chamber for the RIKEN SSC .....	210
25. Preliminary Experiment on Discharge Cleaning of a Sector Magnet Vacuum Chamber for the SSC .....	212
26. Beam Diagnostic System for the RIKEN SSC .....	215
27. Model Test of 1/5 Scale Movable Box Type RF Resonator for the RIKEN SSC .....	217
28. Effect of a Resonance on the Beam in the RIKEN SSC .....	219
29. SSC Beam Handling System .....	222
30. Biological and Physical Irradiation Beam Channel for the RIKEN SSC .....	224
31. Calculation of RF Electromagnetic Field by Finite Element Method (II) .....	227
32. Status Report of the Prototype Baby Cyclotron .....	230
 V. RADIATION MONITORING	
1. Routine Monitoring of the Cyclotron .....	233
2. Leakage-Radiation Measurement at the Underground Passage of the Cyclotron Building .....	235
3. Leakage X-Ray Measurement on TANDETRON .....	237
4. Radiation Levels Due to Neutrons from the Cyclotron outside the Cyclotron Building .....	239
5. Radiation Shielding for the RIKEN SSC Facility .....	243
VI. LIST OF PUBLICATIONS .....	247
VII. LIST OF OUTSIDE USERS AND THEIR THEMES .....	257
VIII. LIST OF SEMINARS .....	259
IX. LIST OF PERSONNEL .....	261
 AUTHOR INDEX	

## I. INTRODUCTION

H. Kamitsubo

Since the collaborative research works started in 1967 using the 160 cm cyclotron at this institute, the experimental studies of nuclear and atomic physics, solid state physics, nuclear and radiation chemistry, material engineering and radiation biology as well as the developments of the instrumentation have been carried out. The main facilities now devoted for these research works are the 160 cm cyclotron, the variable-frequency heavy-ion linac (RILAC) and the tandem van de Graaf accelerator (TANDETRON).

During the past one year the cyclotron was in good condition as before and  $^{13}\text{C}$  and  $^{18}\text{O}$  ions were newly added to the ion group which can be provided steadily for the users. The RILAC has been in steady operation in this period and ions of gaseous elements as well as metallic ones such as aluminum and nickel were used for studies in various research fields. The TANDETRON was also in steady operation and ions of helium and boron were mainly used for the studies of solid state physics and chemical analysis.

A majority of research works have been carried out with heavy ions. In the field of nuclear physics, studies of strongly damped components in heavy ion reactions, spin-polarization of residual nuclei in heavy-ion collisions and in beam  $\alpha$ - and  $\gamma$ -ray spectroscopy on actinide nuclei have been continued. X-rays, Auger electrons and recoil ions were measured in atomic collisions to get the information on the spectroscopy of highly ionized atoms as well as on the collision mechanism.

Activation analysis of impurity oxygen has been continued to get the calibration curve for infra-red spectrophotometry of oxygen in semiconductors. Resonance reaction of  $^{11}\text{B} + \text{p}$  and forward-angle Rutherford scattering of argon were applied to measure the hydrogen distribution in the amorphous silicon and other materials.

Measurements of perturbed angular correlation and Mössbauer effect were applied to study the solid state physics and chemistry. This technique will be developed to the on-beam measurements. Spectroscopic study on the excitation of noble gas atoms at the primary stage of the collision was continued. Application of the cyclotron to the industrial and engineering problems has been developed.

Construction of the separated sector cyclotron is in progress. During the past one year, two among four sector magnets were finished at the factory and their field distribution were measured. Design of the remaining parts is now under way.

## II. OPERATION OF ACCELERATORS

### 1. Cyclotron Operation

K. Ogiwara, S. Fujita, H. Takebe, S. Kohara,  
K. Ikegami, T. Kageyama, and I. Kohno

The cyclotron was operated on the 24 h a day basis during the period from Oct. 23, 1981 to Oct. 22, 1982. The total operation time of 4365.3 h is 3 % (266.8 h) longer than that of the last year. This increase in operation time is due to increased beam time shown in Table 1.

Table 1. Cyclotron operation.

	Oscillator	Ion-source	Beam
Reading of time meter on Oct. 23, 1981	71424.4	75610.8	41327.2
Reading of time meter on Oct. 22, 1982	76325.3	80614.2	45692.5
Difference	4900.9	5003.4	4365.3
Percentage of 365 days	55.9%	57.1%	49.8%
Schedule in this period			
Beam time	235 (days)		
Overhaul and installation work	58		
Periodical inspection and repair	22		
Vacation and holidays	50		

Figure 1 shows the net beam time from the difference of reading of time meter over the past 10 years. The average of the net beam time is about 4400 h, and the net beam time indicates constant operation of the cyclotron in the last few years. Table 2 shows the beam time allotment to various activities in this period. The scheduled beam time was decreased by 24 h compared with that of the last year: requirement for heavy ion beams decreased; its decrease was 359 h.

Table 3 shows the distribution of the scheduled beam time among particles accelerated. Newly accelerated ions such as  $^{13}\text{C}^{4+}$   $^{18}\text{O}^{5+}$  were accelerated up to 100 MeV and several experiments were performed. In this period, the beam times for protons and newly accelerated ions were increased in contrast to the decrease for  $^{20}\text{Ne}^{6+}$  and  $^{14}\text{N}^{4+}$ .

Figure 2 shows the beam time of heavy and light ions over the past 8 years. Request for heavy ion beam continued to decrease, still the cyclotron was operated to accelerate heavy ions for more than 72 % of the total scheduled beam time in the past 3 years.

Table 2. Scheduled beam time and subjects of activity in the period XVII .

Subject		Heavy ion	Light particles	Total
Nucl. Phys.	Nuclear reaction	2573 (h)	302 (h)	2875 (h)
	In-beam spectroscopy	449	0	449
	RI production	24	80	104
Fields others than Nucl. Phys.	Nuclear chemistry	4	320	324
	Radiation biology	147	5	152
	Radiation chemistry	234	0	234
	Solid state physics	190	291	481
	Inner atomic shell excitation study	116	48	164
Outside users	Study of radiation damage	0	133	133
	Nuclear fuel study	0	164	164
	RI Production	0	90	90
Total		3737	1433	5170
Percent in total		72.3 %	27.7 %	100 %
-----				
Maintenance, operation and engineering				
Exchange of ion sources			96 (h)	
Machine inspection and repair			560	
Total			656	

Table 3. Distribution of beam time among particles accelerated.

Particle	(h)	(%)	Particle	(h)	(%)
P	546	10.6	N <sup>5+</sup>	765	14.8
d	24	0.5	O <sup>5+</sup>	574	11.1
<sup>3</sup> He <sup>++</sup>	223	4.3	<sup>20</sup> Ne <sup>6+</sup>	500	9.7
<sup>4</sup> He <sup>++</sup>	592	11.5	<sup>13</sup> C <sup>4+ a)</sup>	592	11.4
<sup>7</sup> Li <sup>++</sup>	70	1.4	<sup>18</sup> O <sup>5+ a)</sup>	70	1.3
<sup>12</sup> C <sup>4+</sup>	521	10.0			
N <sup>4+</sup>	693	13.4	Total	5170	100

a) Newly accelerated ions.

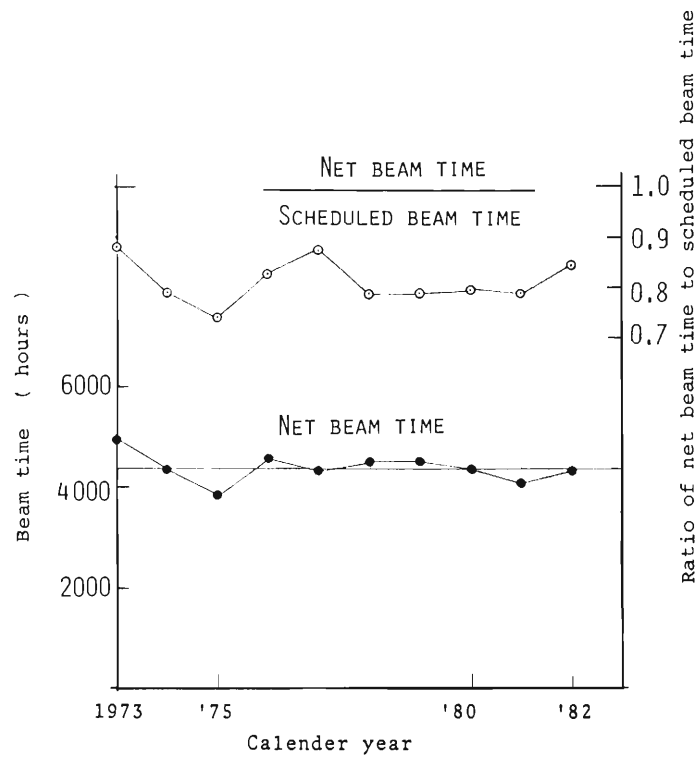


Fig. 1. Net beam time and the ratio of net beam time to scheduled beam time.

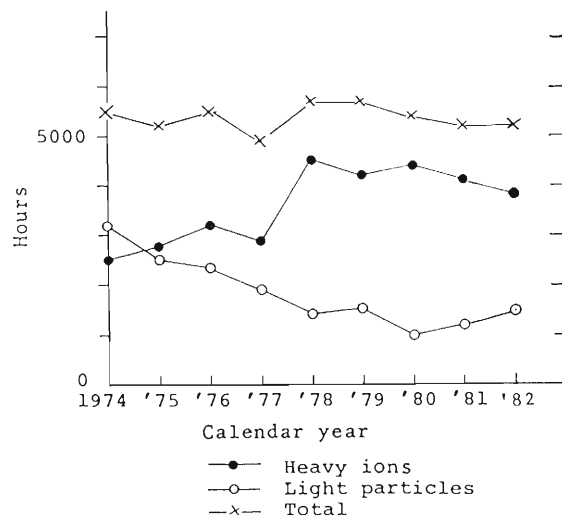


Fig. 2. The cyclotron beam time history.

## II-2. Operation Statistics of RILAC

Y. Miyazawa, M. Hemmi, T. Inoue, T. Kambara, T. Kubo, Y. Chiba,  
M. Yanokura, E. Ikezawa, T. Tonuma, M. Kase, and Y. Gono

The Riken heavy-ion linear accelerator, RILAC, started to supply beams of heavy ions in the fall of 1981 for various experiments. Regular allocation of machine time to the proposed experiments has begun since Feb. 8th, 1982. Initially, the ratio of time used for machine development and maintenance, experiments, and unscheduled shut-down by machine failure was roughly 1 : 1 : 0.05. Percentage of beam time for experiments grew rapidly, especially after the summer overhauling. In October, loss of time by machine failure became negligible when compared to the time for the experiments and machine development. Though it is still necessary to develop and improve the high power amplifiers to cover the whole intended frequency range, the machine is stable enough for over-night operation. Table 1 gives statistics of operation from February to October in this year. Figure 1 shows the ion species accelerated in this period, and Fig. 2 shows the area covered in the specification map of energy and frequency. Figures attached to each line are the ratios of mass to charge of ions.

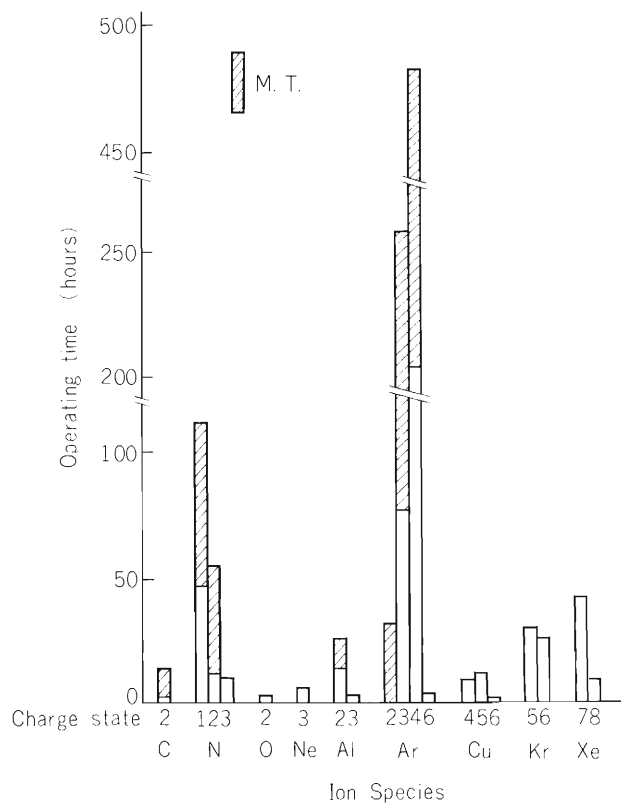


Fig. 1. Statistics of ions used in the period Feb. 8 - Oct. 23. Figures below abscissa give number of charge of each ion.

Table 1. Statistics of operation in the period Feb. 8 – Oct. 31, 1982.

Schedule in this period		
Beam time	144 days	(54%)
Overhaul and improvement work	43	(16%)
Periodical inspection and repair	24	( 9%)
Vacations and holidays	55	(21%)
Total	266 days	

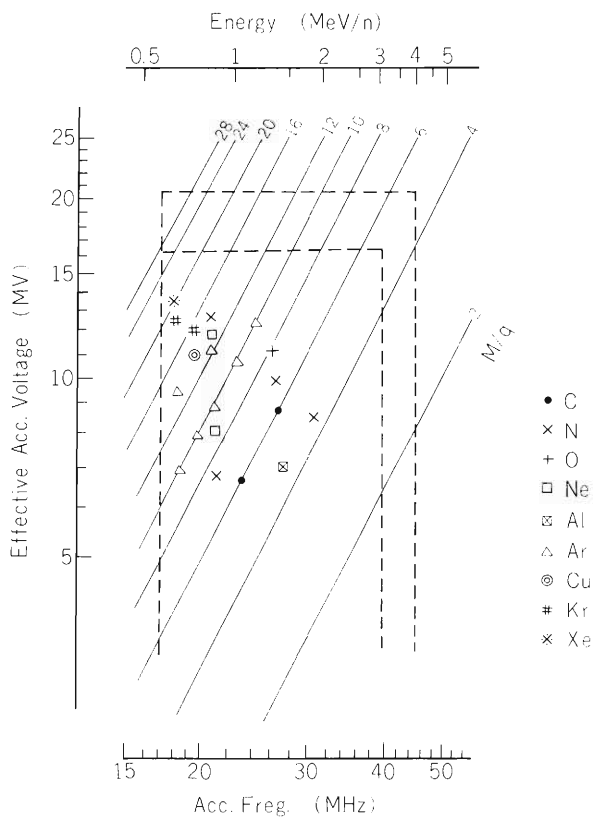


Fig. 2. Specification map and area covered in the period of Fig. 1. The area enclosed by broken lines gives the specification of the linac. Smaller square is the area intended to be covered in a few years, and the larger one later, after the voltage holding capacity of the cavity and the higher frequency characteristics of the power amplifiers are improved. Figures at each line give mass to charge ratios of ions to be accelerated.

Heat exchangers of the water cooling system were found not functioning properly in June. Temperature difference between the primary and the secondary coolant was much larger than the specified value, suggesting something wrong has occurred which hindered heat conduction through plate separating the two coolant circuits. Also the mesh filter made of stainless steel in a liquid Freon circuit was discovered broken in small pieces. It was worried that the metallic fragments might have flown into the cooling channel of the insulating liquid to destroy insulation. Therefore, the regular summer overhaul interval was extended by a week and cleaning of the heat exchangers and inspection of the insulating liquid channel were done. A lot of remnant pieces of the stainless steel filter was recovered from the Freon 123 channel. Black coloured mud or slime was found sticking thick on the side of plate on which water from the cooling tower flows. Table 2 shows temperature at the inlet and outlet of the heat exchangers. Note that the temperature difference between the primary and the secondary channels decreased considerably after the overhaul. Also the pressure drop in the cooling tower water channel became small.

Table 3 gives the major machine troubles which caused the unscheduled shut-down of the linac for more than a half day.

Table 2. Temperature and pressure at the inlets and outlets of heat exchangers of cooling system.

Channel	Part		July 9			Sept. 9		
			Inlet	Outlet	Diff.	Inlet	Outlet	Diff.
Deionized water channel (Hex-3)	Cooling tower water side	{ Temp. ( $^{\circ}$ C)	32	33.5	1.5	35	36	1.0
		{ Pressure (kg/cm $^2$ )	3.7	1.5	2.2	2.6	1.7	0.9
	Deionized water side	{ Temp. ( $^{\circ}$ C)	45	41.5	3.5	40	37	3.0
		{ Pressure (kg/cm $^2$ )	9.7	9.0	0.7	9.6	9.0	0.6
Cavity channel (Hex-4)	Cooling tower water side	{ Temp. ( $^{\circ}$ C)	32	33.5	1.5	35	36	1.0
		{ Pressure (kg/cm $^2$ )	3.2	1.5	1.7	2.6	1.9	0.7
	Cavity side	{ Temp. ( $^{\circ}$ C)	37	36.8	0.2	36.2	36	0.2
		{ Pressure (kg/cm $^2$ )	0.95	0.55	0.4	0.9	0.5	0.4

Table 3. Major troubles in the period Nov. 1, 1981 – Oct. 31, 1982.

Equipment	Trouble	Time required for repair
RF power amplifiers	Power tube failure due to vacuum degradation	1 day
	Destruction of resistor in screen grids power supply	1.5 days
	Insulation failure of by-pass condenser of screen grids by water spray from a cooling pipe	1 days
Cavity	Leakage of water from a cooling pipe in the vacuum chamber	10 days

### II-3. TANDETRON-Operation

H. Sakairi, E. Yagi, T. Kobayashi, and T. Urai

During one year from the November in 1981 the machine was operated for 134 days in total: 88 days for experiments and 46 days for tests.

Subjects of the experimental studies were as follows:

- (1) Application of backscattering spectroscopy,
  - (a) Effects of ion implantation on properties of electrodes,
  - (b) Improvement of corrosion-resistance of steels by ion implantation,
  - (c) Electrical conductivity of an ion implanted diamond,
  - (d) Laser annealing effects on ion implanted GaP,
  - (e) Lattice location of Sn atoms implanted into Al crystals,
- (2) Application to the fields other than backscattering spectroscopy,
  - (f) Ion induced X-ray spectroscopy of chemical effects,
  - (g) PIXE analysis of dried bloods,
  - (h) Heavy ion radiation damage of metals.

Species of ions which were newly utilized to the experiments this year were boron and carbon. The condition of operation and resulted beam intensity for them are shown in Table 1.

In the first half of this year troubles occurred frequently in the lithium vapour canal; lithium vapour liquidified to make a membrane at the beam path in the canal. This situation was improved greatly in the last half of the year.

Table 1. Operating conditions and beam intensity .

Ion	Negative ion beam intensity ( $\mu\text{A}$ )	Terminal voltage (MV)	Acceleration energy (MeV)	Beam intensity ( $\mu\text{A}$ )
$\text{B}^{2+}$	1.0	1.0	2.4	0.34
$\text{C}^+$	7	0.7	1.4	0.6
$\text{C}^{3+}$	10	0.7	2.8	0.9

### III. RESEARCH ACTIVITIES

#### 1. Nuclear Physics

##### 1. Excitation Functions for $^{14}\text{N}$ -Induced Reactions on $^{62}\text{Ni}$

K. Sueki, Y. Hamajima,\* M. Takahashi,\*  
Y. Nagame,\*\* H. Nakahara, and I. Kohno

$\left[ \begin{array}{l} \text{NUCLEAR REACTIONS } ^{62}\text{Ni}(^{14}\text{N}, \text{X}), E_{\text{Lab}} = 40 - 120 \text{ MeV, measured cross} \\ \text{sections, excitation functions; calculation statistical models.} \end{array} \right]$

The aim of the present work is to measure the excitation functions of evaporation-like residues in the  $^{14}\text{N} + ^{62}\text{Ni}$  reaction and to see if the reaction mechanism leading to those products can be understood in terms of the ordinary model of compound formation and evaporation.

Self-supporting  $^{62}\text{Ni}$  target foils of  $1 - 2 \text{ mg/cm}^2$  (isotopic abundance 98.5%) were prepared by electrodeposition. They were assembled into a stack together with Al foils ( $5 - 6 \text{ mg/cm}^2$ ) of 99.997 % purity which served as collectors of recoiling products and beam energy degraders. Irradiations were performed at the cyclotron with initial beam energies of 95 MeV and 120 MeV for  $1 - 2 \text{ h}$  with beam intensities of  $100 - 200 \text{ nA}$ . The beam energy incident on each target was estimated from the range-energy table of Northcliffe and Schilling,<sup>1)</sup> and the energy range covered was from 40 to 120 MeV. The cross sections were determined by directly observing the  $\gamma$ -rays of the reaction products with a Ge(Li) detector.

The excitation functions obtained in this work are shown in Fig. 1(a), 1(b), and 1(c). The cross sections of  $^{73}\text{Se}$ ,  $^{71}\text{As}$ ,  $^{69}\text{Ge}$ ,  $^{67}\text{As}$ , and  $^{65}\text{Ga}$  are corrected for the contributions from the respective parent nuclides in the  $\beta$ -decay chain, and thus they are the so called independent yields. The cross sections of the parent nuclides of  $^{70}\text{As}$  and  $^{66}\text{Ga}$  were found below 10 mb, which is the detection limit in this work. Therefore, yields of  $^{70}\text{As}$  and  $^{66}\text{Ga}$  can approximately be considered as independent ones. The nuclides,  $^{74\text{m}}\text{Br}$ ,  $^{72}\text{As}$ , and  $^{68}\text{Ga}$ , are shielded nuclides in the respective  $\beta$ -decay chain and their observed yields are also independent yields.

The excitation functions in the present energy region can be classified into two groups: (1)  $^{74\text{m}}\text{Br}$ ,  $^{73}\text{Se}$ , and  $^{72}\text{As}$  which exhibit simple peaks revealing that they have simple reaction channels; and (2) the products with the mass number smaller than 71 which show two peaks, suggesting that they are produced by various evaporation channels.

The experimental results are compared with predictions of the statistical evaporation model by using the codes, ALICE<sup>2)</sup> and GROG12.<sup>3)</sup> The decay rate of the compound nucleus,  $R(E_\alpha, J : E_f, i, s)$  are given by

$$R(E_c, J : E_f, j, s)dE_f = \frac{dE_f}{h} \frac{\Omega(E_f, j)}{\Omega(E_c, J)} \sum_{s=|j-s|}^{j+s} \sum_{\ell=|J-s|}^{J+s} T_\ell, \quad (1)$$

\* Faculty of Science, Tokyo Metropolitan University.

\*\* Present address: Japan Atomic Energy Research Institute, Tokai.

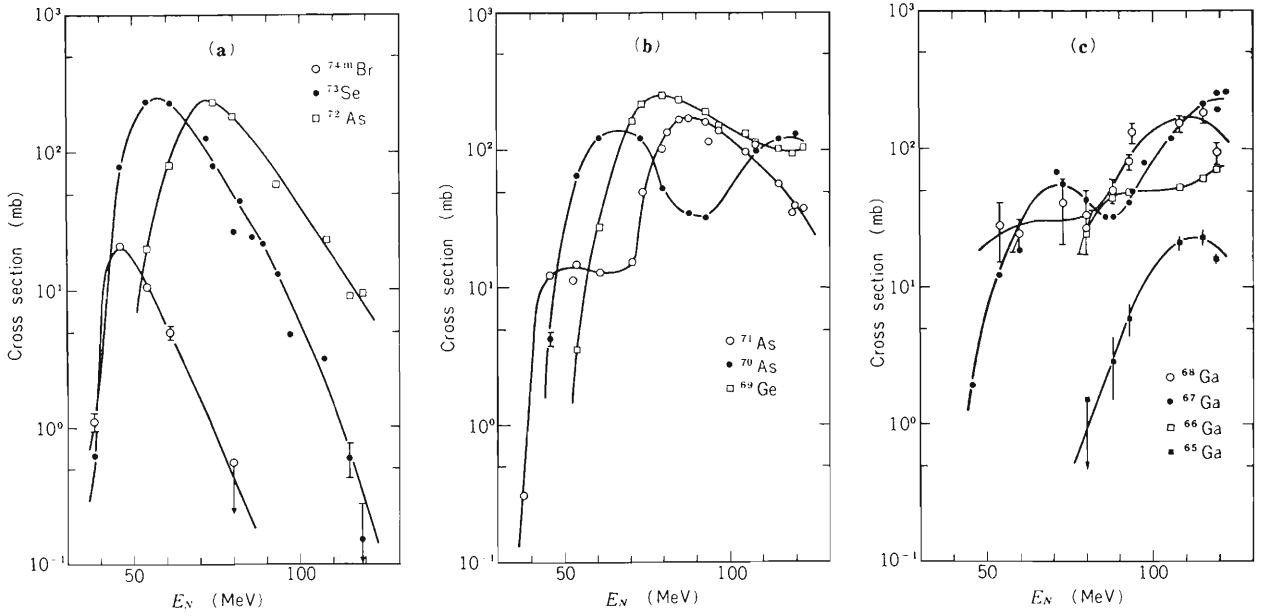


Fig. 1. Excitation functions of evaporation-like residues: (a)  $^{74m}\text{Br}$ ,  $^{73}\text{Se}$ , and  $^{72}\text{As}$ ; (b)  $^{71}\text{As}$ ,  $^{70}\text{As}$ ,  $^{69}\text{Ge}$ ; (c)  $^{68}\text{Ga}$ ,  $^{67}\text{Ga}$ ,  $^{66}\text{Ga}$ , and  $^{65}\text{Ga}$ . The lines are drawn through experimental points to guide the eye.

where  $E_c$  denotes the excitation energy of the compound nucleus, and  $E_f$  denotes the energy of the residual nucleus.  $J$ ,  $j$ , and  $s$  are the angular momentum of the compound, residue, and the particle emitted from the compound nucleus, respectively.  $\Omega$  is the level density, and  $T_\ell$  is the transmission coefficient for the orbital angular momentum  $\ell$ . In the ALICE code it is assumed that  $d\Omega(E, J) \propto (2J + 1)d\Omega(E)$ , and thus, Eqn.(1) can be written as

$$R(E_f)dE_f = \frac{dE_f}{h} (2s + 1) \frac{\Omega(E_f)}{\Omega(E_c)} \sum_{\ell=0}^{\infty} (2\ell + 1)T_\ell. \quad (2)$$

In the GROGI2 code the calculation is made using Eqn.(1) which rigorously takes into account the angular momentum conservation. In both of the codes almost identical level densities and transmission coefficients are employed. The GROGI2 calculation is now still in progress, and only a part of the results are given here.

In Fig. 2 are shown the excitation functions of experimental and calculated results for  $^{73}\text{Se}$ ,  $^{72}\text{As}$ ,  $^{71}\text{As}$ , and  $^{70}\text{As}$ . In the calculation, the critical angular momenta which were estimated from the empirical data reported for  $(^{14}\text{N} + ^{58}\text{Ni})$  and  $(^{14}\text{N} + ^{62}\text{Ni})$  reaction systems<sup>4)</sup> with the aid of the Bass model<sup>5)</sup> were supplied as inputs. The figures show that (1) the predictions by ALICE are in all cases shifted in energy by about 20 MeV to the lower energy side of the experimental points, and that (2) the GROGI2 code gives better overall agreements, but for  $^{73}\text{Se}$  and  $^{72}\text{As}$  the experimental results are larger than those expected at the high energy region of excitation functions. These observations indicate that the observed excitation functions can be understood fairly well by the evaporation model if the effect of the angular momenta of emitted particles are taken into account rigorously. However, the observed discrepancy for  $^{73}\text{Se}$  and  $^{72}\text{As}$  may indicate the possibility of incomplete fusion processes at higher incident energies. This conclusion is also supported by the results on the differential projected ranges of  $^{73}\text{Se}$  observed in the 115 MeV  $^{14}\text{N} + ^{62}\text{Ni}$ <sup>6)</sup> which could only be explained on the assumption of higher energy  $^3\text{H}$  particle emissions.

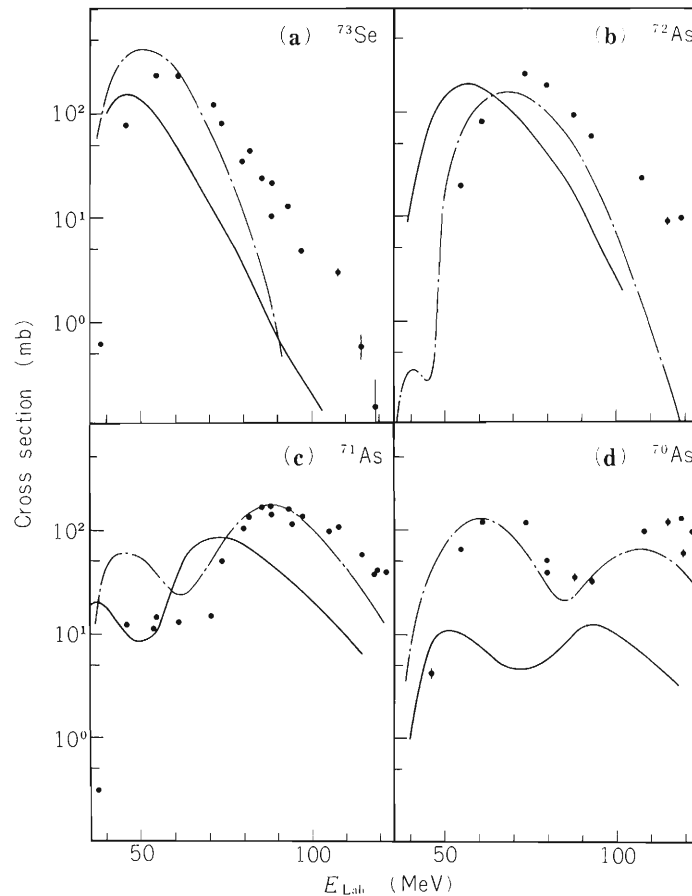


Fig. 2. Comparison between experimental excitation functions (closed points) and the predictions by the codes ALICE (solid line) and GROG12 (dot-dashed line): (a) <sup>73</sup>Se, (b) <sup>72</sup>As, (c) <sup>71</sup>As, and (d) <sup>70</sup>As.

## References

- 1) L.C. Northcliffe and R.F. Schilling: Nucl. Data Tables, A7, 233 (1970).
- 2) M. Blann and F. Plasil: U.S. Atomic Energy Commission Report N° C00-3494-10 (1973) (unpublished).
- 3) J.R. Grover and J. Gilat: Phys. Rev., 157, 802 (1967).
- 4) M. Yanokura, H. Nakahara, and I. Kohno: J. Phys. Soc. Japan, 50, 369 (1981).
- 5) R. Bass: Nucl. Phys., A231, 45 (1974).
- 6) Y. Nagame, M. Watanabe, H. Kudo, K. Sueki, and H. Nakahara: Accepted in Radiochim. Acta.

### III-1-2. Strongly Damped Components in the Reactions of $^{20}\text{Ne} + ^{92}\text{Mo}$ and $^{20}\text{Ne} + ^{100}\text{Mo}$ Systems

I. Kohno, Y. Nagame, K. Sueki, M. Takahashi,\* and H. Nakahara

NUCLEAR REACTIONS  $^{20}\text{Ne} + ^{92}\text{Mo}$ ,  $^{20}\text{Ne} + ^{100}\text{Mo}$ ; strongly damped components, Z(atomic number) distribution, target isotope dependence, diffusion model, rotating liquid drop model.

The reactions of  $^{20}\text{Ne} + ^{92}\text{Mo}$  and  $^{20}\text{Ne} + ^{100}\text{Mo}$  systems were investigated experimentally. The strongly damped components, especially, symmetric mass fragmentation products were analyzed in terms of the diffusion model<sup>1)</sup> as well as the rotating liquid drop model<sup>2)</sup> for fission. The systems studied in this work, the conditions for compound nucleus formation and its decay by fission are summarized in Table 1.

The details of the experimental procedure are similar to those for the reaction of  $^{20}\text{Ne} + ^{50}\text{Cr}$  reported in a previous report.<sup>4)</sup> The experimental results such as grazing angle( $\theta_{\text{gr}}$ ), reaction cross section ( $\sigma_r$ ) and critical angular momentum ( $\ell_{\text{cr}}$ ) obtained from elastic scattering and evaporation residue cross section data are summarized in Table 2. The trends of the energy spectra obtained in the 146 MeV  $^{20}\text{Ne} + ^{92}\text{Mo}$  and  $^{20}\text{Ne} + ^{100}\text{Mo}$  systems are similar to those observed in the 146 MeV  $^{20}\text{Ne} + ^{50}\text{Cr}$  reaction.<sup>4)</sup>

Table 1. Summary of the conditions for compound nucleus formation and its decay by fission.

Reaction	Compound nucleus	Fissility parameter	$E_{\text{lab}}$ (MeV)	$E_{\text{X}}^{\text{CN}}$ (MeV) <sup>a)</sup>	$\ell_{\text{crit}}$ (h) <sup>b)</sup>	$\ell_{\text{Bf=Bn}}$ (h) <sup>c)</sup>	Bf at $\ell_{\text{crit}}$ (MeV)
$^{20}\text{Ne} + ^{92}\text{Mo}$	$^{112}\text{Te}$	0.479	146	103.7	61	60	10.9
$^{20}\text{Ne} + ^{100}\text{Mo}$	$^{120}\text{Te}$	0.453	146	118.2	64	70	15.3

a) compound nucleus excitation energies.

b) Bass model.<sup>3)</sup>

c)  $\ell_{\text{Bf=Bn}}$  characterizes the  $\ell$  value at which the fission barrier Bf coincides with neutron binding energy.

Table 2. Experimental results obtained from elastic scattering and evaporation residue cross section data.

Reaction	$\theta_{\text{gr}}^{\text{cm}}$ (deg)	$\ell_{\text{gr}}$ (h)	$\sigma_r$ (mb)	$\sigma_{\text{ER}}$ (mb)	$\ell_{\text{crit}}$ (h)	$E_{\text{CM}}$ (MeV)	$V_c$ (MeV)
$^{20}\text{Ne} + ^{92}\text{Mo}$	$37.7 \pm 0.5$	$72 \pm 1$	$1780 \pm 24$	$1001 \pm 50$	$54 \pm 3$	120	59.5
$^{20}\text{Ne} + ^{100}\text{Mo}$	$36.4 \pm 0.5$	$74 \pm 2$	$1844 \pm 25$	$1021 \pm 53$	$56 \pm 3$	122	58.7

\* Department of Chemistry, Tokyo Metropolitan University.

The charge distributions observed in the 146 MeV  $^{20}\text{Ne} + ^{92}\text{Mo}$  and  $^{20}\text{Ne} + ^{100}\text{Mo}$  reactions are shown in Fig. 1. The cross sections of particle emission decrease towards larger  $Z$  value from the projectile  $Z = 10$  and have minimum values at the  $Z$  value of 16. Above the  $Z$  value of 16 broad peakings at around  $Z = 26$ , corresponding to a half value of compound systems are seen. Furthermore, the yields above  $Z = 15$  were found

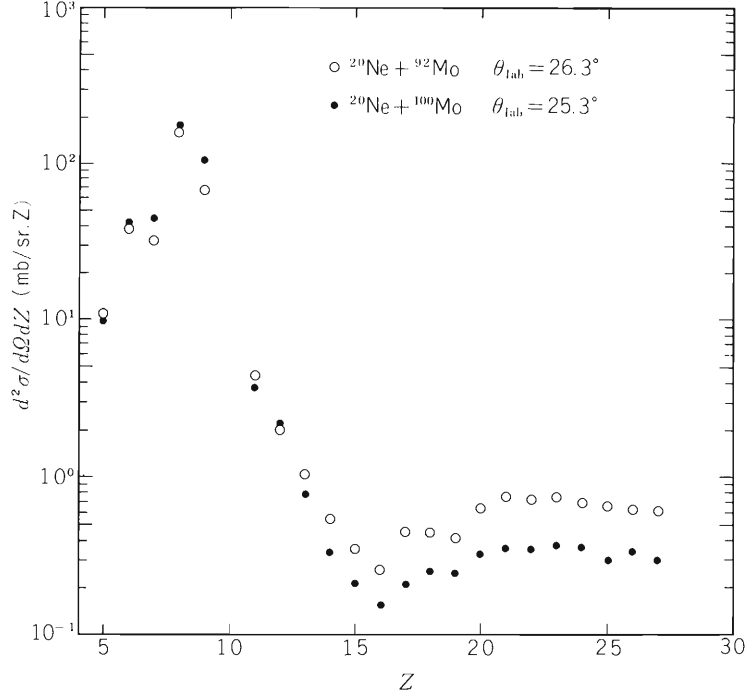


Fig. 1. Experimental charge ( $Z$ ) distributions obtained from the reactions 146 MeV  $^{20}\text{Ne} + ^{92}\text{Mo}$  and  $^{20}\text{Ne} + ^{100}\text{Mo}$ .

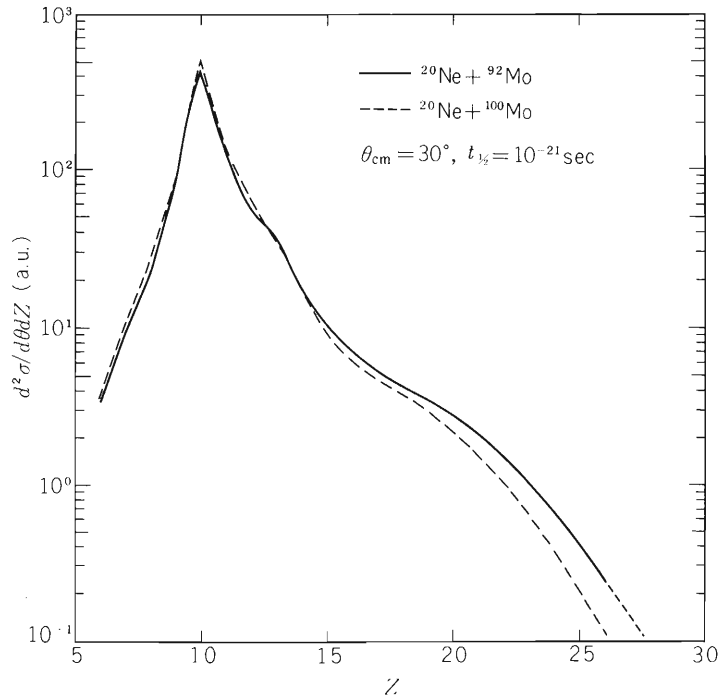


Fig. 2. Charge distributions calculated by the diffusion model. The solid line shows the distribution of  $^{20}\text{Ne} + ^{92}\text{Mo}$  and the dashed for the  $^{20}\text{Ne} + ^{100}\text{Mo}$ .

to be about two times larger for the  $^{20}\text{Ne} + ^{92}\text{Mo}$  system than for the  $^{20}\text{Ne} + ^{100}\text{Mo}$  system, while the difference was not observed in the products lighter than  $Z = 13$ .

If it is assumed that the transfer of charge  $Z$  or mass  $A$  conforms to the diffusion phenomena, the charge distribution is calculated by the same method as in the previous report.<sup>5)</sup> Figure 2 shows the calculated charge distributions for  $^{20}\text{Ne} + ^{92}\text{Mo}$  and  $^{20}\text{Ne} + ^{100}\text{Mo}$  systems. In this figure the cross sections below  $Z = 15$  which are decreasing towards larger  $Z$  agree with the experimental results, while the broad peakings above  $Z = 16$  are not found and also the isotopic dependence of the cross sections above  $Z = 15$  is not found.

In order to explain the cross sections above  $Z = 16$  the statistical analysis of the fission cross section  $\sigma_{\text{Fiss}}$  was carried out by the computer code OVERLAID ALICE.<sup>6)</sup> The comparison of calculated fission cross sections with the experimental cross sections of symmetrically split products obtained by summing up the cross sections above  $Z = 16$  is shown in Table 3. The ratio of the calculated cross section for  $^{20}\text{Ne} + ^{92}\text{Mo}$  to that for  $^{20}\text{Ne} + ^{100}\text{Mo}$  is nearly equal to the ratio of experimental results.

From the above experimental results and analysis of these results, it is suggested that, in the strongly damped components of the reactions 146 MeV  $^{20}\text{Ne} + ^{92}\text{Mo}$  and  $^{20}\text{Ne} + ^{100}\text{Mo}$ , the particles with the  $Z$  value below 15 are emitted by the deep-inelastic collision, while the particles with the  $Z$  value above 16 are mainly fission products of the compound nuclei.

Table 3. A comparison of calculated fission cross sections with the ones extracted from the experimental charge distributions.

Reaction	$\sigma_{\text{Fiss}}$ (exp) (mb)	$\sigma_{\text{Fiss}}$ (cal) (mb)
$^{20}\text{Ne} + ^{92}\text{Mo}$	$22 \pm 5$	17.3
$^{20}\text{Ne} + ^{100}\text{Mo}$	$12 \pm 4$	7.66

## References

- 1) W. Norenberg: J. Phys. C5, 37, 141 (1976); S. Agarwal, J. Galin, B. Gatty, D. Guerreau, M. Lefort, and X. Tarrago: Z. Phys., A296, 287 (1980).
- 2) S. Cohen, F. Plasil, and W.J. Swiatecki: Ann. Phys., 82, 557 (1974).
- 3) R. Bass: Nucl. Phys., A231, 45 (1974).
- 4) Y. Nagame, I. Kohno, M. Yanokura, H. Kudo, and H. Nakahara: IPCR Cyclotron Progr. Rep., 14, 34 (1980).
- 5) Y. Nagame, I. Kohno, H. Nakahara, H. Kudo, K. Sueki, M. Takahashi, and M. Yanokura: RIKEN Accel. Progr. Rep., 15, 33 (1981).
- 6) Blann, M.: U.S. ERDA No. COO-3494-29, Rochester (1976). (unpublished), "OVERLAID ALICE: A Statistical Model Computer Code Including Fission and Preequilibrium".

### III-1-3. High-lying Proton Strengths Observed in ( $^{12}\text{C}$ , $^{11}\text{B}$ ) Reactions\*

M. Ishihara, E. Takada,\*\* T. Murakami,\*\*\*  
E. Ungricht,\*\*\* Y. -W. Lui,\*\*\* R. Tribble,\*\*\*  
Y. Toba,\*\*\* and Y. Mihara\*\*\*

$\left\{ \begin{array}{l} \text{NUCLEAR REACTION } (^{12}\text{C}, ^{11}\text{B}) \text{ and } (^{12}\text{C}, ^{11}\text{C}) \text{ on} \\ ^{144}\text{Sm} \text{ etc. } E = 180 \text{ MeV; population of single-particle} \\ \text{states.} \end{array} \right.$

In this work, we have investigated heavy-ion one-nucleon transfer reactions, ( $^{12}\text{C}$ ,  $^{11}\text{B}$ ) and ( $^{12}\text{C}$ ,  $^{11}\text{C}$ ) on various heavy target nuclei. The primary aim of the investigation is to test the capability of those reactions in populating high-lying single-particle states relevant to the major shell  $1 \hbar\omega$  above the Fermi level. Such possibility for the stripping reactions may be inferred in view of the situations for one-nucleon pickup reactions, which have been known<sup>1)</sup> to be useful in locating single-particle hole strengths for deeply bound states as well as state close to the Fermi level. We have used the heavy-ion projectile  $^{12}\text{C}$ , anticipating that the selectivity due to matching conditions of the heavy-ion reactions may help to obtain simplified energy spectra in favour of high-spin-state population. Indeed we have found the reactions to be quite useful in exciting high-lying single-particle states.

The experiment was performed using 180 MeV  $^{12}\text{C}$  ions from Texas A & M AVF Cyclotron. A variety of target nuclei, such as  $^{90}\text{Zr}$ ,  $^{118}\text{Sn}$ ,  $^{144, 148, 154}\text{Sm}$ ,  $^{208}\text{Pb}$  were bombarded. Energy spectra and angular distributions were observed by detecting and identifying ejectiles with sets of Si-detector telescopes.

A typical result is illustrated in Fig. 1, where the  $^{11}\text{B}$  energy spectrum at  $17^\circ$  for the  $^{144}\text{Sm}(^{12}\text{C}, ^{11}\text{B})$  reaction is shown. Besides the low-lying peaks (denoted by  $2d_{5/2}$  and  $1h_{11/2}$ ), two strong broad peaks are seen at higher excitation energies as indicated by "a" (at  $\sim 6.0$  MeV) and "b" (at  $\sim 7.5$  MeV). These peaks are well distinguished from the underlying continuum (dashed line), which is typical of quasi-elastic reactions with Gaussian-like shape peaked at energy corresponding to the incident beam velocity. The  $^{11}\text{B}$  spectra for other targets showed similar structures at high energies, though they are less distinguished than those for  $^{144}\text{Sm}$  target. The spectra for the ( $^{12}\text{C}$ ,  $^{11}\text{C}$ ) reactions also showed selectively populated peaks. However the excitation energies for those states are relatively low as compared to the cases of ( $^{12}\text{C}$ ,  $^{11}\text{B}$ ) reactions, probably reflecting the difference in matching conditions associated with the Coulomb energy difference between incident and outgoing channels.

\* This work is made under the auspice of the US-Japan research collaboration program funded by Science and Technology Agency of Japan.

\*\* Department of Physics, Osaka University.

\*\*\* Texas A & M University, Cyclotron Institute.

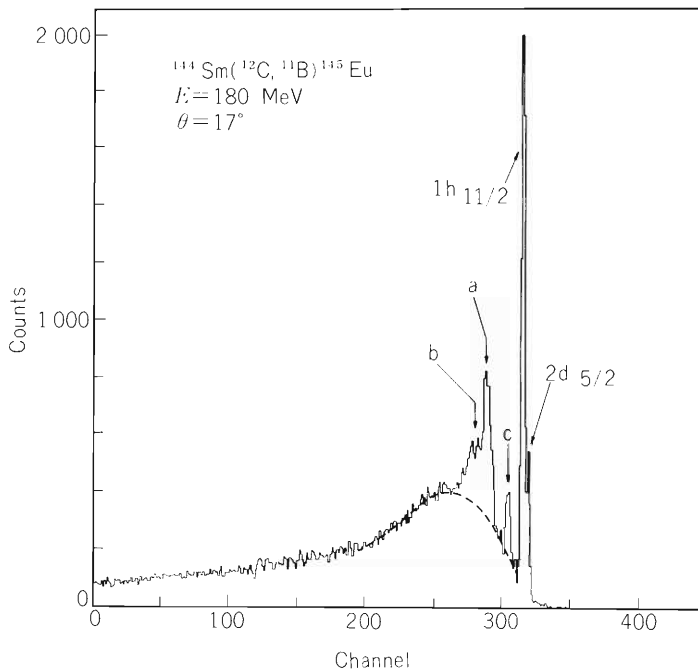


Fig. 1. Energy spectrum of  $^{11}\text{B}$  observed at  $17^\circ$  in the  $^{144}\text{Sm}(^{12}\text{C}, ^{11}\text{B})^{145}\text{Eu}$  reaction at 180 MeV. Two broad lines denoted by a and b, respectively, correspond to excitation energies of  $\sim 6.0$  and  $\sim 7.5$  MeV. The peak c is partly due to excitation of  $^{11}\text{B}$  at the 2.14 MeV  $1/2^-$  state. The dashed line indicates the shape of continuum background.

On the basis of excitation energies, the broad peaks in Fig. 1 are supposed to be associated with excited states in the next upper major shell. Inspection of matching conditions may then suggest that two highest-spin states,  $1i_{13/2}^+$  and  $1h_{9/2}^-$ , are plausible candidates for those peaks. Quite recently, study of one-proton transfer on the same target in  $(d, t)$  and  $(^3\text{He}, d)$  reactions has been reported.<sup>2)</sup> The spectra observed in those reactions are very similar to those for the  $(^{12}\text{C}, ^{11}\text{B})$  reaction. Analysis of the  $(\alpha, t)$  angular distributions indicated that the peaks “a” and “b” are, respectively, ascribed to  $\ell = 5$  and 6 transitions.

In earlier experiments with heavy ions, such high-lying single-particle strengths have never been identified. In some cases, the failure may be attributed to use of ions with insufficient energies: Indeed the comparison of the data for  $^{90}\text{Zr}(^{12}\text{C}, ^{11}\text{B})$  reactions at 180 MeV (present study) and at 98 MeV (Ref. 3) shows that population of high-energy high-spin states are more enhanced for the higher-energy bombardment. There have also been studies<sup>4)</sup> using high-energy heavy ions. However use of inappropriate projectiles seems to have hampered to obtain clean spectra. For instance,  $^{15}\text{N}$  ejectile from  $(^{16}\text{O}, ^{15}\text{N})$  can be strongly excited particularly at 6.4 MeV  $1p_{3/2}$  hole state, yielding kinematically broadened structure which disturbs the energy spectrum in the high-energy region of interest. For the case of  $(^{12}\text{C}, ^{11}\text{B})$ , such ejectile excitation was found to occur only weakly as represented by the peak labelled with “c”.

The present study has revealed that heavy-ion reactions can be useful for the study of single-particle strengths ranging to high energy regions. Angular distributions observed, however, show very similar bell-shaped patterns for different peaks, demonstrating little capability of heavy-ion reactions in distinguishing transferred  $\ell$  values. This deficiency of heavy-ion reactions as compared to light-ion reactions may possibly be compensated by the advantages such as follows: (1) Population of observed high-lying states relative to that of low-lying states appears to be stronger in the heavy-ion reactions than in the light-ion reactions. (2) It is probable that strong  $j$  dependence<sup>5)</sup> of population arising from matching conditions may be exploited in heavy-ion reactions to easily distinguish between  $j >$  and  $j <$  states. Such aspects are presently under systematical investigation using different heavy-ion projectiles with varied energies and also comparing with data from  $(\alpha, t)$  reactions.

## References

- 1) e.g., S. Gales: Nucl. Phys., A354, 193C (1981).
- 2) S. Gales, C.P. Massolo, S. Fortier, E. Gerlic, J. Guillot, E. Hourani, J.M. Maison, J.P. Schappira, B. Zwieglinski, P. Martin, and V. Comparat: Phys. Rev. Lett., 48, 1593 (1982).
- 3) S.T. Thornton, D.E. Gustafson, J.L.C. Ford Jr., K.S. Toth, and D.C. Hensley: Phys. Rev. C, 13, 1502 (1976).
- 4) e.g., C. Olmer, M. Mermaz, M. Buenerd, C.K. Gelbke, O.L. Hendrie, J. Mahoney, D.K. Scott, M.H. Macfarlane, and S.C. Pieper: *ibid.*, 18, 205 (1978).
- 5) P.D. Bond, J. Barette, C. Baktash, C.E. Thorn, and A.J. Kreiner: Phys. Rev. Lett., 46, 1595 (1981).

### III-1-4. Polarization Measurement for Continuous Protons Emitted in the ( $\alpha$ , p) and ( $^{14}\text{N}$ , p) Reactions

T. Nomura, S. Kohmoto, K. Sueki, T. Kubo,  
H. Kudo, and H. Utsunomiya

$\left[ \begin{array}{l} \text{NUCLEAR REACTIONS } ^{27}\text{Al}(^{14}\text{N}, \text{p}), ^{59}\text{Co}(^{14}\text{N}, \text{p}), E = 95 \text{ MeV}, ^{181}\text{Ta}(\alpha, \text{p}), \\ E = 40 \text{ MeV}; \text{ measured spin polarization of protons } (\theta = 45^\circ, 120^\circ). \\ \text{Double scattering method.} \end{array} \right]$

Spin polarization of protons having continuous energy distributions emitted in the ( $^{14}\text{N}$ , p) and ( $\alpha$ , p) reactions have been measured by the double scattering method using a new polarimeter with large efficiency. The present polarimeter uses a carbon plate of about  $34 \text{ mg/cm}^2$  in thickness as an analyzer (the second target), and is very similar to that used for the previous measurement in the  $^{93}\text{Nb}(^{14}\text{N}, \text{p})$  reaction at  $95 \text{ MeV}$ <sup>1)</sup> except for the following points:

- (1) An average second scattering angle is chosen to be  $50^\circ$ .
- (2) Large ( $200 \text{ mm}^2$ ) counter telescopes consisting of Si  $\Delta E$  ( $50 \mu\text{m}$ ) – E ( $2 \text{ mm}$ ) detectors are used to measure protons scattered by the analyzer. Rectangular slits of  $8 \text{ mm}$  in width and  $13 \text{ mm}$  in height are inserted in front of these asymmetry counters. This makes it possible to use large solid angles without decreasing analyzing powers very much.
- (3) A  $100 \mu\text{m}$  Si detector is used as an  $\Delta E_1$  counter. A rectangular slit of  $3 \text{ mm}$  in width and  $8 \text{ mm}$  in height is placed  $12 \text{ mm}$  before the analyzer.

The solid angle of the carbon analyzer looking at the beam spot is  $17.3 \text{ msr}$ , while both the asymmetry counters have solid angles of  $170 \text{ msr}$ . These values are about three times as large as those of the old polarimeter.<sup>1)</sup>

The spin polarization was measured at  $45^\circ$  with respect to the beam direction by bombarding  $^{27}\text{Al}$  and  $^{59}\text{Co}$  targets with  $95 \text{ MeV } ^{14}\text{N}$  beam as well as by irradiating a  $^{181}\text{Ta}$  target with  $40 \text{ MeV}$  alpha beam. The measurement was also made at  $120^\circ$  in the case of the  $^{59}\text{Co}(^{14}\text{N}, \text{p})$  reaction. A preliminary analysis of the data has yielded the following features:

- (1) The polarization is close to zero in the case of the  $^{27}\text{Al}(^{14}\text{N}, \text{p})$  reaction at  $45^\circ$ .
- (2) In the  $^{59}\text{Co}(^{14}\text{N}, \text{p})$  and  $^{181}\text{Ta}(\alpha, \text{p})$  reactions at  $45^\circ$ , the polarization is positive for high energy protons ( $E_p > 12 \text{ MeV}$ ), but is smaller than the values obtained in the  $^{93}\text{Nb}(^{14}\text{N}, \text{p})$  reaction at  $40^\circ$  described previously.<sup>1)</sup>
- (3) The polarization is likely to be negative in the case of the  $^{59}\text{Co}(^{14}\text{N}, \text{p})$  reaction at  $120^\circ$ . A more detailed analysis is now in progress.

#### Reference

- 1) T. Sugitate, T. Nomura, M. Ishihara, Y. Gono, H. Utsunomiya, K. Ieki, and S. Kohmoto: Nucl. Phys., A388, 402 (1982).

### III-1-5. Angular-Momentum Transfer and Alignment Following Preequilibrium $\alpha$ -Particle Emission in $^{16}\text{O}$ - and $^{20}\text{Ne}$ -Induced Reactions

T. Nomura, H. Utsunomiya, S. Kohmoto, and M. Sasagase\*

$\left\{ \begin{array}{l} \text{NUCLEAR REACTIONS } ^{209}\text{Bi}(^{16}\text{O}, \alpha\text{f}), E = 120 \text{ MeV}, ^{209}\text{Bi}(^{20}\text{Ne}, \alpha\text{f}), \\ E = 146 \text{ MeV}; \text{ measured angular correlations; deduced } I \text{ and } P_{zz}. \end{array} \right.$

The average magnitude and alignment of angular momenta transferred to fusion-like products resulting from preequilibrium  $\alpha$ -particle emission have been determined by  $\alpha$ -f angular correlation measurements in the reactions of  $^{209}\text{Bi}(^{16}\text{O}, \alpha\text{f})$  and  $^{209}\text{Bi}(^{20}\text{Ne}, \alpha\text{f})$ , in which the residual nuclei following the  $\alpha$ -particle emission partly decay via fission.

A self-supporting  $^{209}\text{Bi}$  target of  $0.8 \text{ mg/cm}^2$  thickness was bombarded with  $120 \text{ MeV } ^{16}\text{O}$ - and  $146 \text{ MeV } ^{20}\text{Ne}$ -ions from the cyclotron. Alpha particles were detected with  $\text{Si } \Delta E(50 \mu\text{m}) - E(2 \text{ mm})$  counter telescopes, while fission fragments were measured in a  $30 \mu\text{m}$  Si detector. The experimental arrangement for the present measurement was the same as described in our previous work.<sup>1)</sup>

Figure 1 shows the measured in-plane and out-of-plane angular correlations, in which the  $\alpha$ -particles were detected at  $20^\circ$  and  $50^\circ$  with respect to the beam direction. The analysis of the experimental data has been made in the same way as described in Ref. 1. The K-distribution of a fissile nucleus is assumed to be gaussian, in which the width parameter  $\bar{K}_0$  has been estimated from the temperature and the moment of inertia at the saddle point following the procedure given in Ref. 2. Then, the angular correlations depend on the average magnitude  $I$  of angular momenta of a fissile nucleus and their alignment along the normal (z-axis) to the reaction plane. We fitted the data by assuming one-dimensional dealignment of the spin vector  $I$ , which is expressed by either (A) or (B) given below:

(A)  $I$  is composed of random coupling of a component  $I_1$  completely aligned along the z-axis and a component  $I_2$  uniformly distributed in a plane perpendicular to the recoil direction (x-axis) of the fissile nucleus, i.e.,  $I = I_1 + I_2$ ; adjustable parameters in the fit were taken to be the magnitude of  $I$  and  $I_2$ .

(B) The polar angle  $\beta$  of  $I$  is distributed by  $\exp(-\beta^2/2\beta_0^2)$ , where the magnitude of  $I$  and  $\beta_0$  were taken as the fitting parameters.

The results are given in Table 1, where the average entrance angular momentum  $\ell_i$  for preequilibrium  $\alpha$ -particle emission calculated from  $\ell_i = AI/(A - 4)$  ( $A$  is the mass number of projectile) and the critical angular momentum  $\ell_{cr}$  for complete fusion estimated from a model of Wilczynski<sup>3)</sup> are also given for comparison. It is clear that  $\ell_i$  is considerably smaller than  $\ell_{cr}$  in both reactions. Note that the value of  $I$  presently deduced generally gives the upper limit of angular momenta transferred to a residual nucleus produced via  $\alpha$ -particle emission, because higher spin states of the residual nucleus decay by fission more preferentially.<sup>1)</sup>

\* Hitachi Computer Engineering.

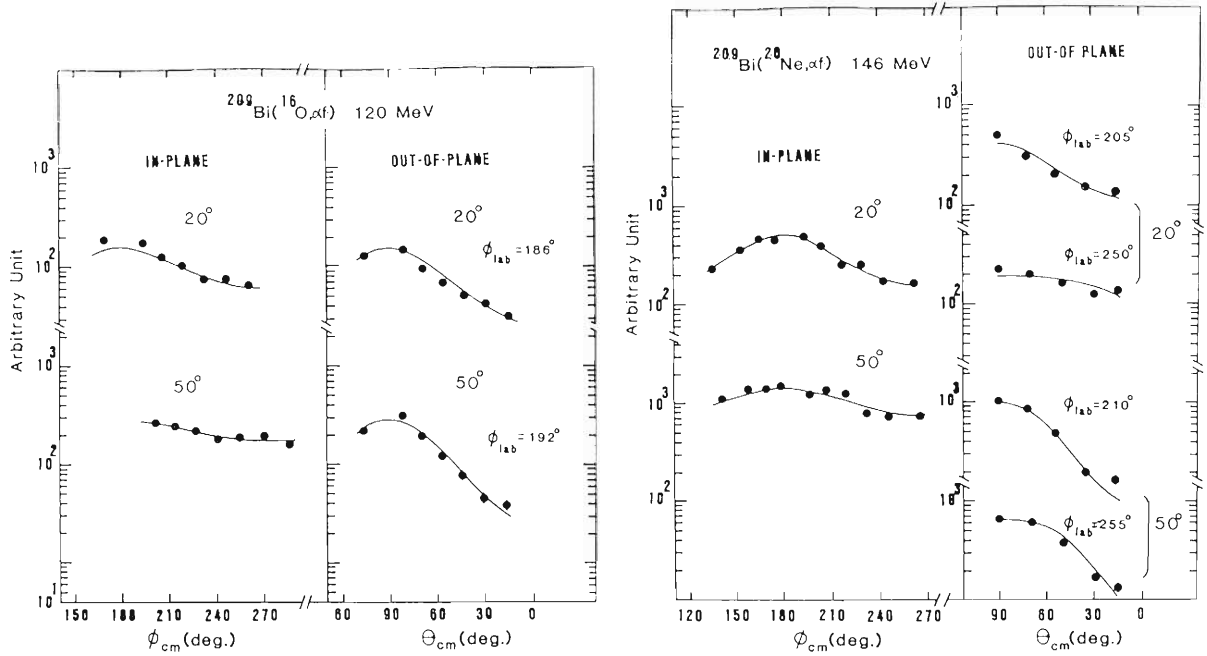


Fig. 1. The experimental  $\alpha$ -f angular correlations taken in the reactions of  $^{209}\text{Bi}(^{16}\text{O}, \alpha f)$  at 120 MeV and  $^{209}\text{Bi}(^{20}\text{Ne}, \alpha f)$  at 146 MeV, where  $\alpha$  particles were detected at  $20^\circ$  and  $50^\circ$  with respect to the beam direction. The polar angle  $\theta$  is taken from the normal to the reaction plane defined by the direction of the measured  $\alpha$  particles and the beam, while the azimuthal angle  $\phi$  is taken from the recoil direction of the fissile nucleus. The solid curves show the best fits by method A.

Table 1. Results of the analysis.

Beam	$\psi_\alpha$	Method	I	$I_2$	$\beta$	$P_{zz}$	$\ell_i$	$\ell_{cr}$
$^{16}\text{O}$	$20^\circ$	A	$30 \pm 4$	26	—	0.46	$40 \pm 5$	53
		B	$35 \pm 5$	—	$53^\circ$	0.39	$47 \pm 7$	
	$50^\circ$	A	$28 \pm 2$	17	—	0.74	$37 \pm 3$	53
		B	$32 \pm 4$	—	$31^\circ$	0.66	$43 \pm 5$	
$^{20}\text{Ne}$	$20^\circ$	A	$40 \pm 4$	38	—	0.31	$50 \pm 5$	60
		B	$44 \pm 4$	—	$72^\circ$	0.28	$55 \pm 5$	
	$50^\circ$	A	$36 \pm 2$	25	—	0.63	$45 \pm 3$	60
		B	$41 \pm 4$	—	$39^\circ$	0.55	$51 \pm 5$	

All angular momenta are given in unit of  $\hbar$  and  $P_{zz} = \frac{3}{2} \langle I_z^2 \rangle / \langle I^2 \rangle - 0.5$ .

The analysis based on two-dimensional dealignment of  $I$  (non-zero  $x$ -component of  $I$ ) made in the same way as in Ref. 1 has resulted in an increase of  $I$  only by  $1-2 \hbar$  and does not affect the above conclusion ( $\ell_i < \ell_\alpha$ ) seriously. The present result therefore indicates that the preequilibrium  $\alpha$ -particle emission in the present reactions mainly originates from impact parameters ensuring enough overlap of projectile and target nuclei. This supports an interpretation that the  $\alpha$ -particles of interest are emitted as the precompound decay during the fusion process.

#### References

- 1) H. Utsunomiya, T. Nomura, M. Ishihara, T. Sugitate, K. Ieki, and S. Kohmoto: Phys. Lett., 105B, 135 (1981).
- 2) B.B. Back and S. Bjørnholm: Nucl. Phys., A302, 343 (1978).
- 3) J. Wilczyski: *ibid.*, A216, 386 (1973).

III-1-6. Light-Particle Emission in  ${}^7\text{Li}$ -Induced Reactions

H. Utsunomiya, S. Kubono,\* M. Tanaka,\*  
M. Sugitani,\* K. Morita,\* T. Nomura, and Y. Hamajima\*\*

NUCLEAR REACTION  ${}^{159}\text{Tb}({}^7\text{Li}, x\gamma)$ ,  ${}^{232}\text{Th}({}^7\text{Li}, xf)$ ,  $E = 77\text{ MeV}$ ,  
 $x = p, d, t, \alpha$ ; measured  $\sigma(E, \theta)$ , angular correlations; deduced spin  
 alignment, transferred angular momenta.

The light-particle emission has been studied in coincidence with  $\gamma$ -rays or fission fragments resulting from fusionlike residual nuclei following  ${}^7\text{Li}$ -induced reactions on  ${}^{159}\text{Tb}$  and  ${}^{232}\text{Th}$  in order to deduce the magnitude and alignment of the transferred angular momenta in the relevant emission.

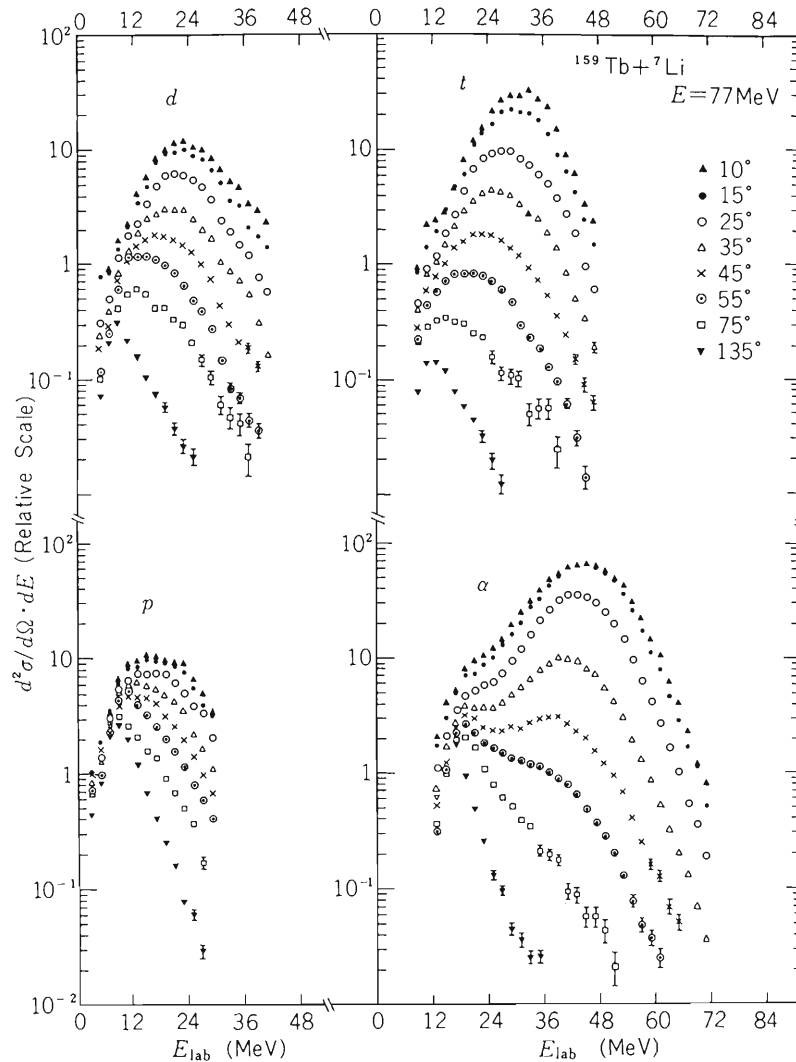


Fig. 1. Some energy spectra of protons, deuterons, tritons and  $\alpha$  particles observed at various angles in the  ${}^{159}\text{Tb} + {}^7\text{Li}$  reaction at 77 MeV. The laboratory angles are indicated.

\* Institute for Nuclear Study, University of Tokyo.

\*\* Faculty of Science, Tokyo Metropolitan University.

The experiment was performed with 77 MeV  ${}^7\text{Li}$  ions from an INS cyclotron. A self-supporting  ${}^{159}\text{Tb}$  target of  $3.2 \text{ mg/cm}^2$  thickness and a  ${}^{232}\text{Th}$  target of about  $0.5 \text{ mg/cm}^2$  thickness electrodeposited onto an Al backing was used. Some energy spectra for p, d, t, and  $\alpha$  measured in singles in the  ${}^{159}\text{Tb} + {}^7\text{Li}$  reaction are shown in Fig. 1. At very forward angles the spectra exhibit a bump at around an energy corresponding to the beam velocity, suggesting the breakup mechanism as a dominant origin of the light-particle emission. This feature is very clear for the case of tritons and  $\alpha$ -particles, while it is less visible for protons and deuterons, presumably due to the cluster structure of  ${}^7\text{Li}$ . The  $\alpha$ -particle spectra were also taken in coincidence with  $\gamma$ -rays from the  ${}^{159}\text{Tb}({}^7\text{Li}, \alpha xn){}^{162-x}\text{Dy}$  reactions. The spectra obtained after the summation over those from all  $\alpha xn$  channels are similar to singles spectra, although the bump around the beam velocity are less pronounced, suggesting that the breakup-fusion process takes place to a considerable extent.

Figure 2 shows out-of-plane angular distributions of  $\gamma$ -rays characteristic of various  $\alpha xn$  channels, which were measured in coincidence with  $\alpha$ -particles at  $30^\circ$ . The same measurement was also made at  $\psi_\alpha = 60^\circ$ . They were fitted by assuming that the population parameter of each initial state is given by

$$w(m) \propto \exp\left\{-\frac{(J-m)^2}{2\sigma^2}\right\}, \quad (1)$$

where  $J$  is a spin of the initial state which emits  $\gamma$ -rays of interest and  $m$  is its component along the normal to the reaction plane. The result is given in Table 1.

In-plane and out-of-plane angular distributions of fission fragments measured in coincidence with light particles emitted at  $20^\circ$  in the  ${}^{232}\text{Th} + {}^7\text{Li}$  reaction are shown in Fig. 3. They were analyzed in the same way as described in a preceding paper.<sup>1)</sup> The result is given in Table 2. The following points should be noted:

(1) The alignment ( $\mathbf{P}_{zz}$ ) of the transferred angular momenta ( $J$ ) for the case of  $\alpha$ -particle emission is close to that obtained from the analysis of the  $\gamma$ -ray angular distributions (see Table 1), except for the  $\alpha 5n$  channel, where the  $\alpha$ -particle energy is very low and thus the evaporation process must be dominant.

(2) The sum of  $J$  for triton and  $\alpha$ -particle emission is almost equal to the grazing angular momentum in the  ${}^{232}\text{Th} + {}^7\text{Li}$  reaction at the present energy. Note that this sum corresponds to the entrance angular momentum if tritons and  $\alpha$ -particles originate from  ${}^7\text{Li}$  breakup and one of them can be considered as a spectator while the other is captured by a target nucleus.

The second feature is in sharp contrast with conclusions of Refs. 1, 2, where the average entrance angular momentum for preequilibrium  $\alpha$ -particle emission in  ${}^{14}\text{N}$ -,  ${}^{16}\text{O}$ -, and  ${}^{20}\text{Ne}$ -induced reactions is considerably smaller than critical angular momentum for complete fusion at each reaction, which is of course even smaller than the grazing angular momentum. It is also interesting to note that the value of  $\mathbf{P}_{zz}$  for triton and  $\alpha$ -particle emission in the  ${}^7\text{Li}$ -induced reaction is much larger than that obtained in Refs. 1, 2 at the same emission angle.

The above facts can therefore be considered as characteristic features of the breakup-fusion process.

Table 1. The best fit parameters in the analysis of the  $\gamma$ -ray angular distributions.  $\mathbf{P}_{zz}$  is calculated from  $\mathbf{P}_{zz} = \left\{ 3\langle m^2 \rangle - J(J+1) \right\} / J(2J-1)$ .

Emission angle of $\alpha$	Reaction channel	Transition $J \rightarrow J'$	$\sigma/J$	$\mathbf{P}_{zz}$
$30^\circ$	$\alpha 2n$	$6^+ \rightarrow 4^+$	$0.23 \pm 0.02$	$0.62 \pm 0.04$
	$\alpha 3n$	$17^{+}/2 \rightarrow 13^{+}/2$	$0.23 \pm 0.01$	$0.60 \pm 0.02$
	$\alpha 4n$	$4^+ \rightarrow 2^+$	$0.26 \pm 0.01$	$0.61 \pm 0.02$
	$\alpha 5n$	$21^{+}/2 \rightarrow 17^{+}/2$	$0.37 \pm 0.04$	$0.33 \pm 0.05$
$60^\circ$	$\alpha 4n$	$4^+ \rightarrow 2^+$	$0.29 \pm 0.02$	$0.56 \pm 0.04$
	$\alpha 5n$	$17^{+}/2 \rightarrow 13^{+}/2$	$0.50 \pm 0.06$	$0.24 \pm 0.05$
	$\alpha 6n$	$4^+ \rightarrow 2^+$	$0.71 \pm 0.22$	$0.15 \pm 0.10$

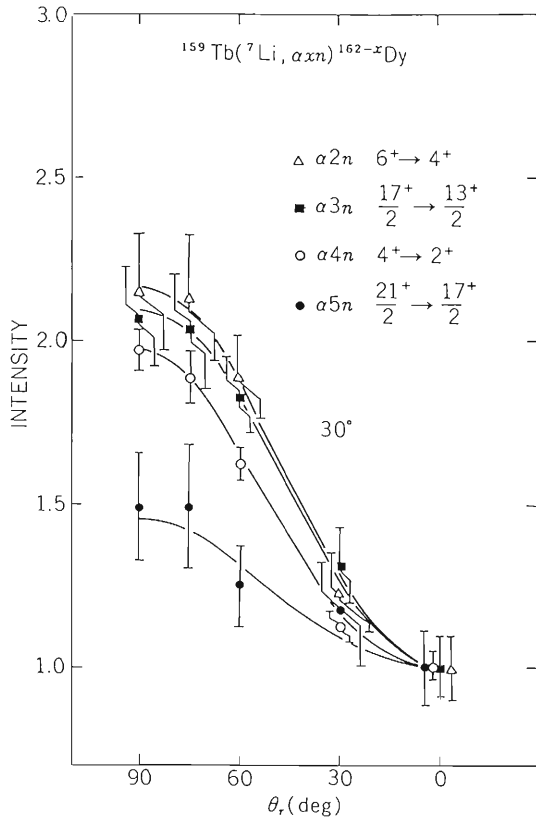


Fig. 2. Out-of-plane angular distributions of discrete  $\gamma$ -rays from  $^{162-x}\text{Dy}$  measured in coincidence with  $\alpha$  particles at  $30^\circ$  in the  $^{159}\text{Tb} + ^7\text{Li}$  reaction at 77 MeV. The solid curves show the best fits.

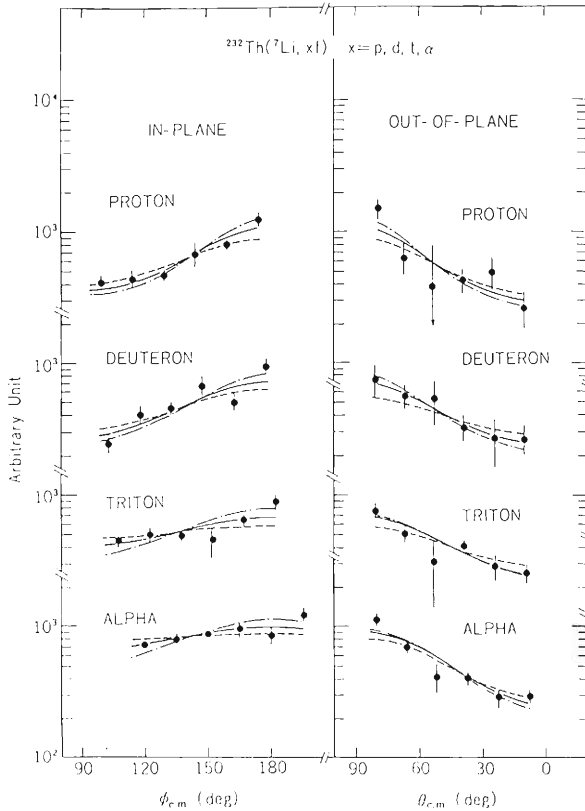


Fig. 3. In-plane and out-of-plane angular distributions of fission fragments measured in coincidence with protons, deuterons, tritons and  $\alpha$  particles emitted at  $20^\circ$  in the  $^{232}\text{Th}(^7\text{Li}, xf)$  ( $x = p, d, t, \alpha$ ) reaction at 77 MeV. The best fits are given by solid curves. The dashed and dotted-dashed curves correspond to the fit with the lower and upper limit of  $J$  within one standard deviation, respectively, showing the sensitivity of the fit on  $J$ .

Table 2. The best fit parameters obtained for the reaction  $^{232}\text{Th}(^7\text{Li}, \text{xf})$  ( $x = \text{p}, \text{d}, \text{t}, \alpha$ ) at 77 MeV.  
All symbols refer to Ref. 1. The angular momenta are given in unit of  $\hbar$  and  $\beta_0$  in degrees.

Emitted particles	Method	J	$J_2$	$\beta_0$	$P_{zz}$
p	A	$32 \pm 7$	31	—	$0.30 \pm \begin{smallmatrix} 0.02 \\ 0.01 \end{smallmatrix}$
	B	$36 \pm 8$	—	69	$0.39 \pm < 0.01$
d	A	$27 \pm 6$	26	—	$0.31 \pm \begin{smallmatrix} < 0.01 \\ 0.06 \end{smallmatrix}$
	B	$29 \pm 7$	—	71	$0.38 \pm 0.01$
t	A	$21 \pm 5$	17	—	$0.51 \pm \begin{smallmatrix} 0.10 \\ 0.16 \end{smallmatrix}$
	B	$21 \pm 6$	—	41	$0.56 \pm \begin{smallmatrix} 0.03 \\ 0.09 \end{smallmatrix}$
$\alpha$	A	$20 \pm 4$	14	—	$0.63 \pm \begin{smallmatrix} 0.16 \\ 0.14 \end{smallmatrix}$
	B	$22 \pm 4$	—	35	$0.63 \pm \begin{smallmatrix} 0.03 \\ 0.08 \end{smallmatrix}$

#### References

- 1) T. Nomura, H. Utsunomiya, S. Kohmoto, and M. Sasagase: p. 19 in this report.
- 2) H. Utsunomiya, T. Nomura, M. Ishihara, T. Sugitate, K. Ieki, and S. Kohmoto: *Phys. Lett.*, **105B**, 135 (1981).

### III-1-7. Momentum Transfer Light-Particle Emission Following 210 MeV $^{14}\text{N}$ -Bombardment on $^{232}\text{Th}$

T. Nomura, T. Fukuda,\* H. Ogata,\*\* I. Miura,\*\*  
K. Katori,\* T. Shimoda, and S. Shimoura\*\*\*

NUCLEAR REACTION  $^{232}\text{Th}(^{14}\text{N}, \text{xf})$ ,  $x = \text{p, d, t, } \alpha$ ,  $E = 210 \text{ MeV}$ ; measured  
 $\sigma_x(\theta, E)$ , x-f-f angular correlations; deduced momentum transfer.

The laboratory angle ( $\theta_{\text{ff}}$ ) between two fission fragments in a binary fission depends on the magnitude and the direction of linear momentum carried by a fissioning nucleus in the laboratory system. The distribution of  $\theta_{\text{ff}}$  in a nuclear reaction using a target nucleus with large fissionability

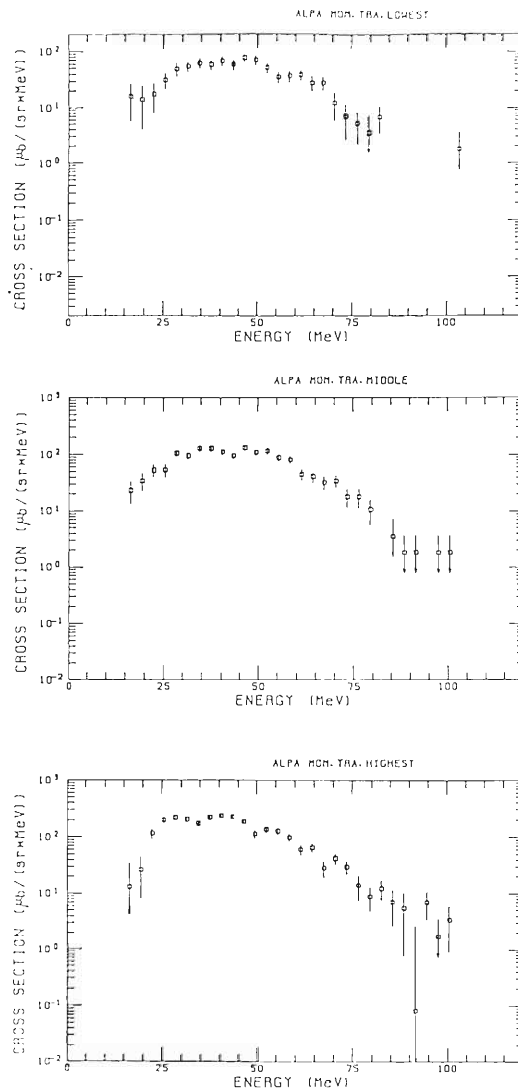


Fig. 1. Energy spectra of  $\alpha$  particles observed at  $33^\circ$  in coincidence with two fission fragments; the three spectra correspond to those of low, middle and high momentum transfer to the fissioning nuclei (see text).

\* Department of Physics, Osaka University.

\*\* Research Center for Nuclear Study, Osaka University.

\*\*\* Department of Physics, Kyoto University.

therefore determines the distribution of momentum transferred from the projectile to the target. In this work we have measured the  $\theta_{\text{ff}}$  distribution in coincidence with light particles emitted in the  $^{232}\text{Th} + ^{14}\text{N}$  reaction to deduce possible missing momentum carried by unobserved particles.

A  $^{232}\text{Th}$  target was bombarded with 210 MeV  $^{14}\text{N}$  ions from a cyclotron at RCNP (Research Center for Nuclear Study, Osaka University). Fission fragments were measured with two position sensitive detectors placed near  $90^\circ$  and  $270^\circ$  with respect to the beam direction, while light particles (p, d, t, and  $\alpha$ ) were measured at the emission angles ( $\theta_x$ ) of  $10^\circ$ ,  $20^\circ$ ,  $33^\circ$ ,  $44^\circ$ , and  $55^\circ$  with counter telescopes consisting of Si and Ge detectors. The  $\theta_{\text{ff}}$  distribution in this set-up is sensitive to the momentum component ( $\Delta p$ ) of the fissioning nucleus along the beam direction. Figure 1 shows energy spectra of  $\alpha$  particles observed at  $\theta_x = 33^\circ$  as examples; the three spectra shown correspond to those yielding low ( $\Delta p < 0.25p_{\text{max}}$ ), middle ( $0.25p_{\text{max}} < \Delta p < 0.5p_{\text{max}}$ ) and high momentum transfer ( $\Delta p > 0.5p_{\text{max}}$ ), where  $p_{\text{max}}$  is a value of  $\Delta p$  corresponding to the full momentum transfer obtained under the assumption that even the observed particle carries no momentum.

The preliminary analysis has yielded the following features for the ratio of  $\Delta p_{\text{av}}/\Delta p_{\text{max}}$ , where  $\Delta p_{\text{av}}$  is the average value of  $\Delta p$ , and  $\Delta p_{\text{max}}$  is the maximum magnitude of available momentum transfer, i.e., a value of  $\Delta p$  when no missing momentum exists. Note that the momentum of the observed light particle is taken into account to estimate  $\Delta p_{\text{max}}$ , so that  $\Delta p_{\text{max}}$  is different from  $p_{\text{max}}$ .

(1) The ratio of  $\Delta p_{\text{av}}/\Delta p_{\text{max}}$  is nearly independent of kinetic energy ( $E_x$ ) of observed light particles over the wide range of  $E_x$ . The energy averaged values of this ratio at  $\theta_x = 20^\circ$  are around 0.75 for proton, 0.68 for deuteron, 0.65 for triton and 0.55 for  $\alpha$  particle.

(2) The above ratio is smallest at  $\theta_x = 10^\circ$ , and increases monotonically with increasing  $\theta_x$ .

A detailed analysis of the data is now in progress.

### III-1-8. Spin Polarization of Residual Nucleus in Heavy Ion Reaction

K. Ieki, M. Ishihara, T. Inamura, S. Kohmoto,  
H. Utsunomiya, K. Sueki, and H. Kudo

NUCLEAR REACTION  $^{159}\text{Tb}(^{14}\text{N}, \alpha\gamma)$ ,  $E = 115 \text{ MeV}$ ,  $^{159}\text{Tb}(^7\text{Li}, \alpha\gamma)$   
 $E = 49 \text{ MeV}$ ; measured  $\gamma$ -ray circular polarization; deduced spin  
 polarization.

In the study of heavy-ion reaction mechanism, it is important to have information on the angular momentum transfer to the residual nucleus and its spin orientation. Gamma rays emitted from such an oriented nucleus are circularly polarized. The measurement of  $\gamma$ -ray circular polarization will, therefore, provide a useful probe into the reaction mechanism. This method was first used for some few nucleon transfer reactions by Trautmann et al.<sup>1)</sup> We applied this method for fast light particle emission phenomena in  $^7\text{Li}$ -induced and  $^{14}\text{N}$ -induced reactions.

A  $3.4 \text{ mg/cm}^2$  thick  $^{159}\text{Tb}$  foil was bombarded with a  $115 \text{ MeV}$   $^{14}\text{N}$  beam and with a  $49 \text{ MeV}$   $^7\text{Li}$  beam from the cyclotron. Alpha particles were measured with counter telescopes consisting of  $50 \mu\text{m}$  –  $1500 \mu\text{m}$  Si detectors. Measurements were performed at four angles ( $20^\circ$ ,  $30^\circ$ ,  $40^\circ$ ,  $50^\circ$ ) for  $^{159}\text{Tb} + ^{14}\text{N}$  and at  $40^\circ$  for  $^{159}\text{Tb} + ^7\text{Li}$  with respect to the beam axis. At forward angles an aluminum absorber of  $140 \mu\text{m}$  thickness was used to avoid intense elastic particles. Gamma-ray circular polarization was measured with two forward-scattering type Compton polarimeters<sup>2)</sup> placed perpendicularly to the reaction plane. A pair of telescopes and a pair of polarimeters were set symmetrically to the beam axis so that geometrical asymmetry can be cancelled out using four coincidence pairs.<sup>3)</sup> The magnetization direction of the polarimeter

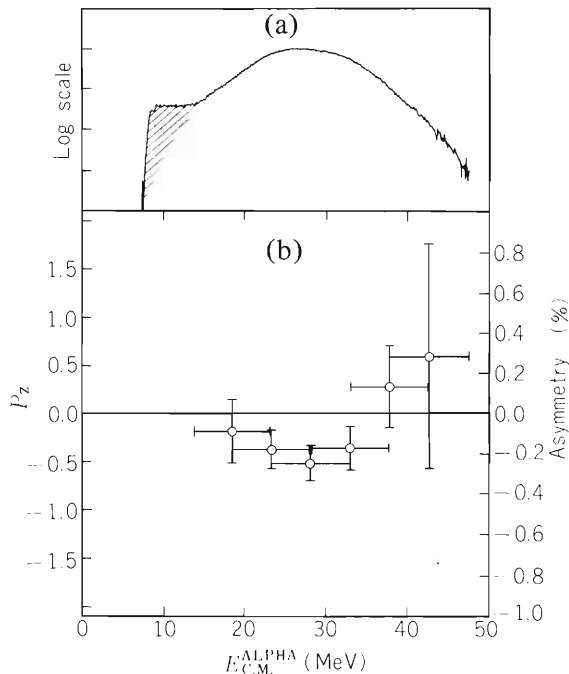


Fig. 1. (a) The energy spectrum and (b) the  $\gamma$ -ray circular polarization for the  $^{159}\text{Tb}(^7\text{Li}, \alpha)$  reaction. Emitted  $\alpha$  particle were measured at  $40^\circ$  to the beam. Shaded area indicates  $\alpha$  component from target contamination.

was changed for each run to cancel out the spurious asymmetry which originated from an unequal treatment of four coincidence pairs in electronic circuit. The spin polarization was deduced from the  $\gamma$ -ray circular polarization by assuming three statistical dipole  $\gamma$  transitions and a stretched E2  $\gamma$  cascade. The sign of the spin polarization was defined by referring to the scattering normal  $\mathbf{k}_i \times \mathbf{k}_f$ .

In Fig. 1, we show the results for the  $^{159}\text{Tb}(^7\text{Li}, \alpha)$  reaction. The energy spectrum (a) is well characterized by a Gaussian distribution of  $\alpha$ -particle velocity centered at the beam velocity. The

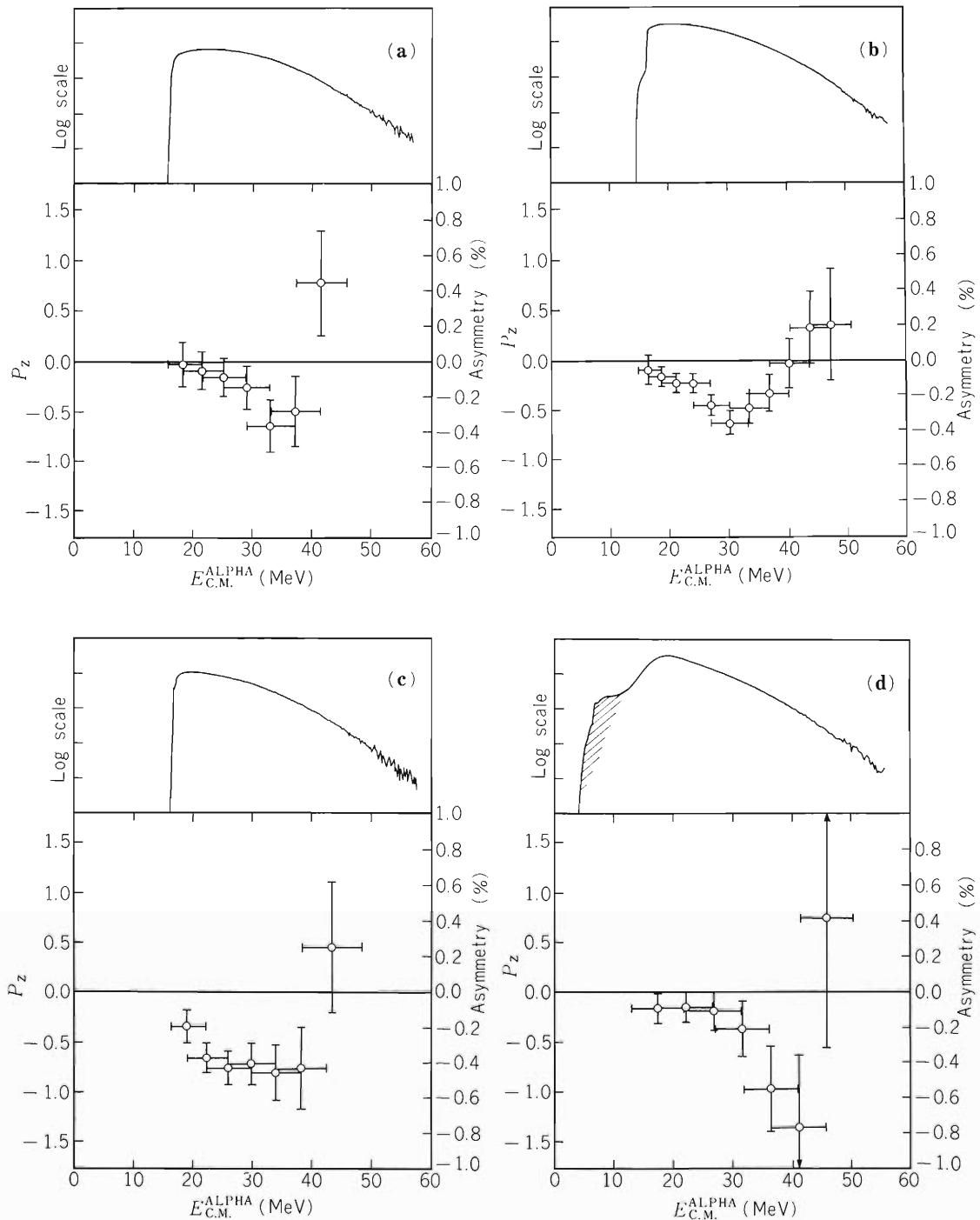


Fig. 2. The energy spectrum and  $\gamma$ -ray circular polarization for the  $^{159}\text{Tb}(^{14}\text{N}, \alpha)$  reaction at (a)  $20^\circ$ , (b)  $30^\circ$ ; (c)  $40^\circ$ , (d)  $50^\circ$  (in laboratory angles). Shaded area indicates  $\alpha$  component from target contamination.

sign of the spin polarization (b) is negative for the beam velocity region and becomes positive at higher energy region. The negative value of the polarization means that  $\alpha$  particles are emitted in the positive deflection angle. This can be interpreted as the result of a simple transfer reaction.

The positive polarization at the higher energy region is explained as a recoil effect in the massive transfer process. When energetic  $\alpha$  particles are emitted, the residual nucleus receives the tangential momentum whose direction is opposite to that of the emitted particle. The tendency of the measured polarization is well explained by taking into account the internal motion of triton and  $\alpha$  and the tangential velocity of the momentum at the nuclear surface.

In Fig. 2, we show the results for  $\alpha$  particles from the  $^{159}\text{Tb} + ^{14}\text{N}$  reaction. At the detection angle of  $40^\circ$  the spin polarization is very similar to that of the  $^{159}\text{Tb} + ^7\text{Li}$  reaction. But the same explanation of energy dependence of spin polarization as was made in the Li case is not applicable to this case. Since the transferred mass is larger, the needed internal energy becomes larger, and the sign change must occur at 98 MeV of  $\alpha$  particle energy. In the case of  $^{14}\text{N}$  induced reaction, contributions from other reaction mechanisms must be considered. The sequential decay of emitted  $^8\text{Be}$  is known to contribute to the  $\alpha$ -emission channel considerably<sup>4)</sup>: the proportion of  $\alpha$  particle cross section due to the sequential decay of  $^8\text{Be}$  is less than 30 % at  $E_\alpha \leq 40$  MeV, and becomes larger at higher energy. The recoil-effect calculation of ( $^{14}\text{N}$ ,  $^8\text{Be}$ ) shows that the spin polarization changes its sign at  $E_{8\text{Be}} \cong 80$  MeV, i.e.  $E_\alpha \cong 40$  MeV for the  $^8\text{Be}$  sequential decay process. The spin polarization is negative for two processes for  $E_\alpha < 40$  MeV. At about  $E_\alpha = 40$  MeV, two processes cancel out to result in zero polarization. At higher energy, the positive component becomes predominant. Thus the observed spin polarization can be understood by considering  $^{10}\text{B}$  and  $^6\text{Li}$  massive transfer processes.

At  $\theta_{\text{lab.}} = 50^\circ$  (Fig. 2 (d)), the competition with the evaporation from the compound nucleus occurs, reducing the spin polarization at lower energy region. At more forward angles (Fig. 2 (a),(b)), the spin polarization also has smaller values for smaller  $\alpha$  particle energy. This fact may be explained by the hot-spot picture as was proposed in the case of the proton polarization,<sup>5)</sup> which shows positive polarization.

It may be possible to apply the hot spot picture to the positive polarization at the high energy region. But it is difficult to explain the observed spin polarization and  $\alpha$ -energy spectra simultaneously in terms of the hot-spot only.

## References

- 1) W. Trautmann, J. de Boer, W. Dünneweber, G. Graw, R. Kopp, C. Lauterbach, H. Puchta, and U. Lynen: Phys. Rev. Lett., 39, 1062 (1977).
- 2) K. Ieki and M. Ishihara: RIKEN Accel. Progr. Rep., 15, 119 (1981).
- 3) W. Trautmann, C. Lauterbach, J. de Boer, W. Dünneweber, G. Graw, W. Hamann, W. Hering, and H. Puchta: Nucl. Instr. and Method, 184, 449 (1981).
- 4) H. Utsunomiya, T. Nomura, M. Ishihara, Y. Gono, T. Sugitate, K. Ieki, and S. Kohmoto: IPCR Cyclotron Progr. Rep., 14, 19 (1980).
- 5) T. Sugitate, T. Nomura, M. Ishihara, Y. Gono, H. Utsunomiya, K. Ieki, and S. Kohmoto: Nucl. Phys., A388, 402 (1982).

### III-1-9. Vector Analyzing Power Measurements for (d, p) and (p, d) Reactions on Sn Isotopes and Deuteron D-state Effects

T. Kubo, H. Ohnuma,\* T. Kishimoto,\*  
M. Sugitani,\*\* and T. Suehiro\*\*\*

NUCLEAR REACTIONS  $^{116}\text{Sn}(d, p)$   $E_d = 55.4$  MeV,  $^{118}\text{Sn}(p, d)$   
 $E_p = 60.8$  MeV; vector-polarized beams, measured  $d\sigma/d\Omega(\theta)$ ,  $A_y(\theta)$ ,  
DWBA analysis, deuteron D-state, enriched targets.

We have measured vector analyzing powers( $A_y$ ) and differential cross sections ( $d\sigma/d\Omega$ ) for  $^{116}\text{Sn}(d, p)^{117}\text{Sn}$  reaction at  $E_d = 55.4$  MeV and  $^{118}\text{Sn}(p, d)^{117}\text{Sn}$  reaction at  $E_p = 60.8$  MeV, using vector-polarized deuteron and proton beams. It was expected to observe deuteron D-state effects on the vector analyzing powers in direct (d, p) and (p, d) reactions at relatively high incident energies.

The polarized beams were provided by an atomic-beam-type polarized ion source and accelerated by the AVF cyclotron at RCNP (Research Center for Nuclear Physics, Osaka University). The beam polarization was periodically reversed during data taking runs to reduce systematic errors, and was monitored by using a carbon polarimeter placed before targets. The absolute value of the polarization was about 44 % for deuterons and 82 % for protons. The targets used were self-supporting foils of enriched isotopes. Scattered particles were analyzed by spectrograph RAIDEN and detected in a proportional counter system. Figure 1 shows examples of proton spectrum from the (d, p) reaction and of deuteron spectrum from the (p, d) reaction. The overall energy resolution was about 55 keV full width at half maximum. Experimental analyses were carried out for final states in  $^{117}\text{Sn}$  that were strongly excited and well resolved as seen in the spectra. The experimental results for the  $1/2^+$  ground

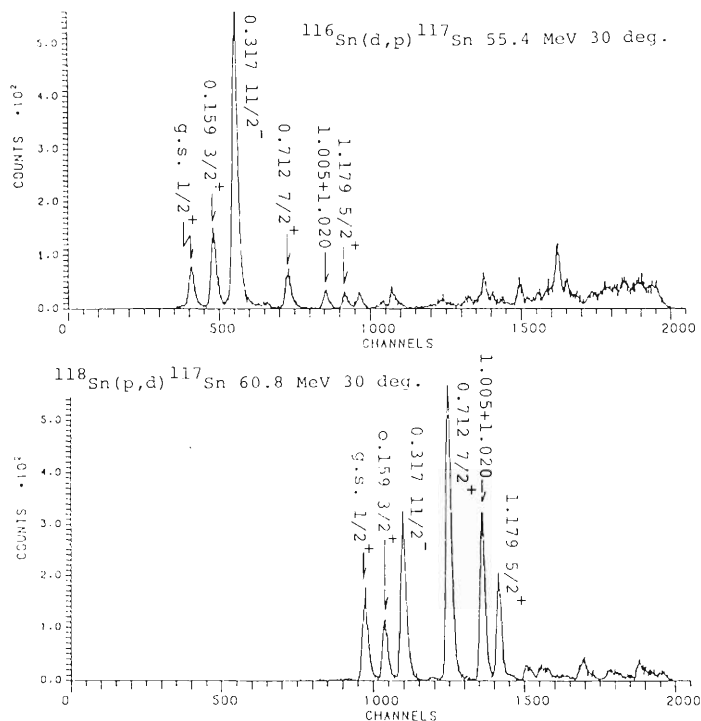


Fig. 1. Proton spectrum(upper) from the  $^{116}\text{Sn}(d, p)^{117}\text{Sn}$  reaction at 55.4 MeV and deuteron spectrum(lower) from the  $^{118}\text{Sn}(p, d)^{117}\text{Sn}$  reaction at 60.8 MeV.

\* Department of Physics, Tokyo Institute of Technology.

\*\* Institute for Nuclear Study, University of Tokyo.

\*\*\* Department of Physics, Tohoku Institute of Technology.

state( $3s_{1/2}$ ),  $3/2^+$ -state at 0.159 MeV( $2d_{3/2}$ ),  $11/2^-$ -state at 0.317 MeV( $1h_{11/2}$ ),  $7/2^+$ -state at 0.712 MeV( $1g_{7/2}$ ) and  $5/2^+$ -state at 1.179 MeV( $2d_{5/2}$ ) are shown in Figs. 2 and 3 together with those of calculations.

Exact-finite-range DWBA calculations were carried out by using the code DWUCK5 in which the deuteron D-state effects could be included. Distorting potential parameters used in the calculations are given in Table 1. The proton parameters are those taken from reference 1 that reproduce the cross sections of elastic scattering of 61.4 MeV proton on  $^{116}\text{Sn}$ . The deuteron parameters are of so-called adiabatic potential with which contributions from deuteron break-up channel to (d, p) and (p, d) reactions can be approximately involved. Following the formula of Harvey & Johnson,<sup>2)</sup> we constructed the adiabatic potential from the neutron and proton potentials of Becchetti & Greenlees.<sup>3)</sup> Non-locality corrections for these distorting potentials were included in local energy approximation. The Reid soft core potential<sup>4)</sup> was used for the n-p interaction( $V_{n-p}$ ) to describe the transfer of neutron as well as to generate the deuteron internal wave functions. The form factor of the transferred neutron was made with usual separation energy method. The results of the calculations with and without the D-state effects are shown in Fig. 2 for the cross sections and in Fig. 3 for the analyzing powers. The cross sections calculated were normalized to those measured at forward angles.

The cross sections are, on the whole, well reproduced by the calculation except for the  $2d_{5/2}$ -state in the (d, p) reaction and the  $1h_{11/2}$ - and  $1g_{7/2}$ -states in the (p, d) reaction which are somewhat poorly reproduced at backward angles. On the other hand, the analyzing powers are very poorly reproduced except for  $1_n = 0$  transitions to the  $3s_{1/2}$ -state(ground state). The reproduction of the  $1_n = 0$  transitions is fair to examine the D-state effects, although it is a little poor at forward angles where calculated curves are slightly shifted in the forward direction in comparison to the experimental data.

The calculations of the cross sections are found not much affected by the inclusion of the deuteron D-state effects. The D-state effects only slightly increase the intensity around minima. However, large D-state effects can be seen in the results of the analyzing powers in comparison with those of the cross sections. The reproduction

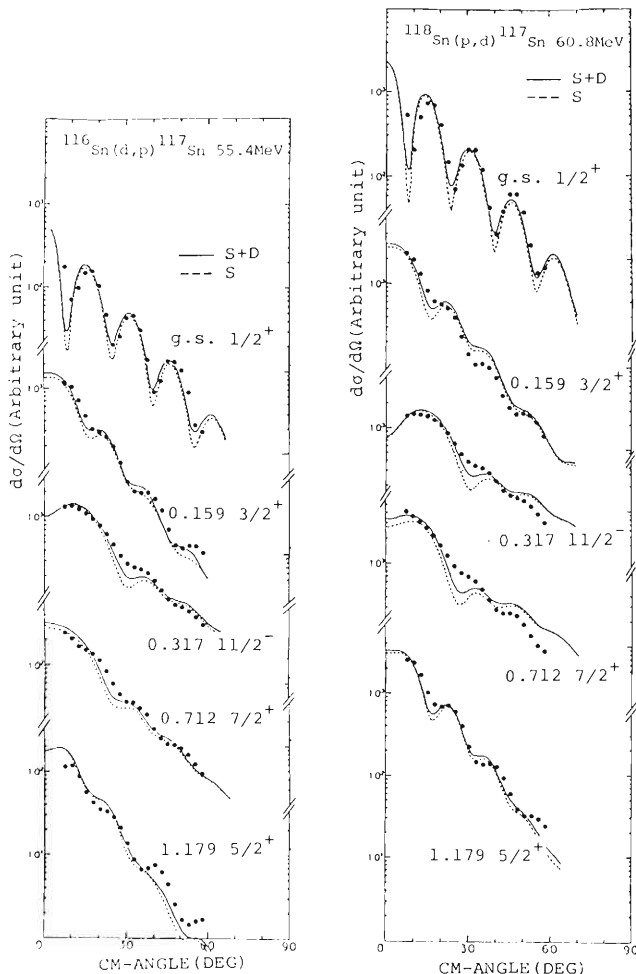


Fig. 2. Cross sections for the  $^{116}\text{Sn}(d, p)$   $^{117}\text{Sn}$ (left) and  $^{118}\text{Sn}(p, d)$   $^{117}\text{Sn}$ (right) reactions compared with the calculations with(solid line) and without(dashed line) the D-state effects.

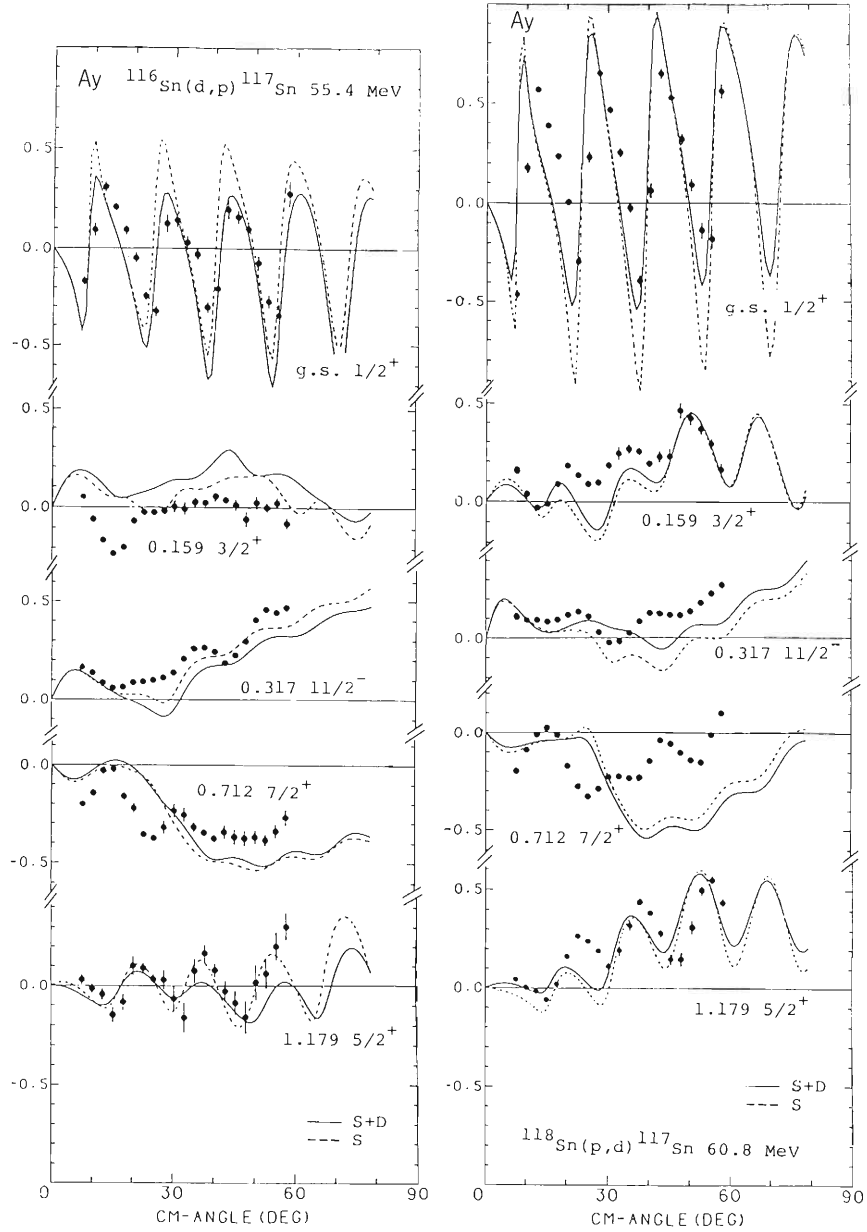


Fig. 3. Vector analyzing powers for the  $^{116}\text{Sn}(d, p)^{117}\text{Sn}$ (left) and  $^{118}\text{Sn}(p, d)^{117}\text{Sn}$ (right) reactions compared with the calculations with (solid line) and without (dashed line) the D-state effects.

Table 1. Distorting potential parameters.

	$V_0$	$r_0$	$a_0$	$W$	$W_D$	$r_i$	$a_i$	$V_{so}$	$r_{so}$	$a_{sc}$	$r_c$
Deuteron	95.18	1.17	0.75	8.94	9.80	1.29	0.60	6.20	1.01	0.75	1.25
Proton	41.93	1.179	0.687	3.80	5.10	1.24	0.808	6.11	1.057	0.80	1.25

of the  $I_n = 0$  transitions is found much improved around positive peaks for the (d, p) reactions and around negative peaks for the (p, d) reaction with the inclusion of the D-state effects. It may not be adequate to examine the D-state effects on the analyzing powers of the other transitions, since they are very poorly reproduced and the D-state effects do not necessarily improve their reproduction. However, if we see only the results of the calculations, we can see the large D-state effects. The calculations on the  $2d_{3/2^-}$ ,  $1h_{11/2^-}$ , and  $2d_{5/2^-}$ -states in the (d, p) reaction and the  $1h_{11/2^-}$ -state in the (p, d) reaction are much affected.

For comparison, we tried DWBA calculation using a deuteron distorting potential that reproduces the elastic scattering. This calculation gave very poor results for the cross sections as well as the analyzing powers.

We failed to reproduce consistently the experimental data by the calculations including the deuteron D-state effects. However, the large D-state effects were observed for the analyzing powers. Especially, the fit of the  $I_n = 0$  transitions were much improved. More detailed analyses are in progress.

#### References

- 1) G. B. Fulmer, J. B. Ball, A. Scott, and M. L. Whiten: Phys. Rev., 181, 1565 (1969).
- 2) J. D. Harvey and R. C. Johnson: *ibid.*, C3, 636 (1971).
- 3) F. D. Becchetti and G. W. Greenlees: *ibid.*, 182, 1190 (1969).
- 4) R. V. Reid: Ann. Phys. (NY), 50, 411 (1968).

### III-1-10. Excitation Modes of the $\gamma$ -band in $^{24}\text{Mg}$ through the $^{24}\text{Mg}(\vec{p}, p')$ Reaction

M. Sugitaru,\* T. Hasegawa,\* S. Kubono,\* Y. Ishizaki,\*  
K. Iwatani,\*\* and T. Fujisawa

(NUCLEAR REACTIONS,  $^{24}\text{Mg}(\vec{p}, p')$  E = 29.3 and  
40.3 MeV; measured cross section and analyzing power.)

Coupled channel analyses with the symmetric rotator model gave a great success in the study of inelastic excitation of ground rotational bands (GRB) of deformed nuclei. On the other hand, excitation modes of side bands had been scarcely investigated. In recent years, the  $\gamma$ -band of  $^{24}\text{Mg}$ , the band head of which is the  $2_2^+$  state at 4.24 MeV, was investigated by proton inelastic scattering at various energies.<sup>1),2)</sup> As a result, excitation modes of the GRB could be explained by ordinary coupled channel analyses (CC) using the symmetric rotator model. However, the cross sections of the members of the  $\gamma$ -band could not be reproduced by the CC calculations using the asymmetric rotator model, mainly the Davydov-Filipov model<sup>3)</sup> (D-F model). In this reaction, it is expected that polarization phenomena reflect delicate shades of the nuclear structure and the reaction mechanisms. We measured analyzing powers and cross sections of the  $^{24}\text{Mg}(\vec{p}, p')$  reaction and performed the second-order distorted wave Born approximation (DWBA) analyses with the shell model description, which improves the defects of the D-F model.

The experiment was performed with 29.3 and 40.3 MeV polarized proton beams obtained from the SF cyclotron with a polarized ion source<sup>4)</sup> made by the RIKEN staff at INS, University of Tokyo. A self-supporting enriched (> 98 %) metallic  $^{24}\text{Mg}$  target was used. The thickness of the target was 0.34 mg/cm<sup>2</sup> and contamination of oxygen was less than 2 % in weight. The beam intensity on the target was about 30 nA and the polarization was about 50 %. A polarimeter, installed just in front of the scattering chamber for the quadrupole-dipole-dipole (QDD) magnetic spectrograph, monitored protons scattered elastically by a  $^{12}\text{C}$  target using surface-barrier silicon detectors 2 mm in thickness and aluminum absorbers 2 mm and 5 mm in thickness for the 29.3 and 40.3 MeV experiment, respectively. The sign of polarization was changed at a beam amount of every 0.6  $\mu$  Coulomb. The absolute value of polarization was determined from the data of the double-scattering measurements,<sup>5),6)</sup> and its error was less than 10 %. Difference of the polarization between an up-spin beam and a down-spin one was less than 3 % throughout the experiment. Particles scattered by the  $^{24}\text{Mg}$  target were momentum analyzed by the QDD magnetic spectrograph and detected with a drift-type position-sensitive single wire proportional counter (80-III),<sup>7)</sup> placed on the focal plane of the spectrograph. The effective range of the detection of the counter is 80 cm long. Particle identification was made with two signals: energy losses from a  $\Delta E$  counter located behind the position-sensitive wires in the 80-III counter and energy signals from a plastic scintillator 10 mm thick and 100 cm long installed just behind the 80-III counter. The energy resolution was about 70 keV mainly due to a spread of the beam energy and the beam profile on the target. The experimental results of the  $\gamma$ -band are shown in Figs. 1 and 2 with the analyzing power data of  $E_p = 20.3$  MeV.<sup>8)</sup> The error of the absolute cross section is about 20 %.

The cross section data show normal behaviors for all the levels of the  $\gamma$ -band in the sense of kinematical understanding, and the analyzing power data of the  $2_2^+$  and  $4_2^+$  states are also normal, where the bottom and top peaks are getting smaller as the incident beam energy becomes higher. However, the energy correlation among 20.3, 29.3, and 40.3 MeV can be hardly found in the analyzing powers of the  $3_1^+$  state. This characteristic is not

\* Institute for Nuclear Study, University of Tokyo.

\*\* Department of Engineering, Hiroshima University.

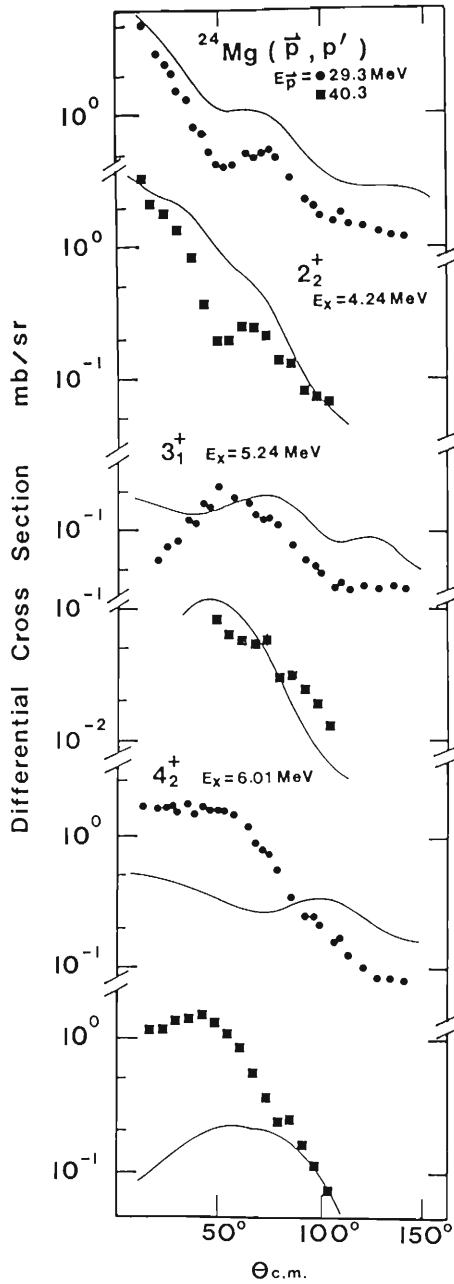


Fig. 1. The angular distributions of the differential cross sections of the  $\gamma$ -band in the  $^{24}\text{Mg}(\bar{p}, p')$  reaction at the incident proton energies of 29.3 and 40.3 MeV. The curves show the results of the second-order DWBA calculation including the  $(p-p''-p')$  processes via the  $2_1^+$  and  $2_2^+$  states and the  $(p-d-p')$  processes.

found in the cross section data.

In the analyses, the two-step processes as  $(p-p''-p')$  and  $(p-d-p')$ , are also calculated for the  $2_2^+$ ,  $3_1^+$ , and  $4_2^+$  states besides the direct one-step processes. Intermediate states, we choose for two-step processes, are the  $2_1^+$  and  $2^+$  states of  $^{24}\text{Mg}$  for the  $(p-p''-p')$  process and the  $3/2^+$  (ground state) and  $5/2^+$  ( $E_x = 0.47$  MeV) states of  $^{23}\text{Mg}$  for the  $(p-d-p')$  process, because effects of other states are quite small. The results of the calculation are shown in Figs. 1 and 2. The cross section of the  $3_1^+$  state is roughly reproduced by this calculation. The difference of

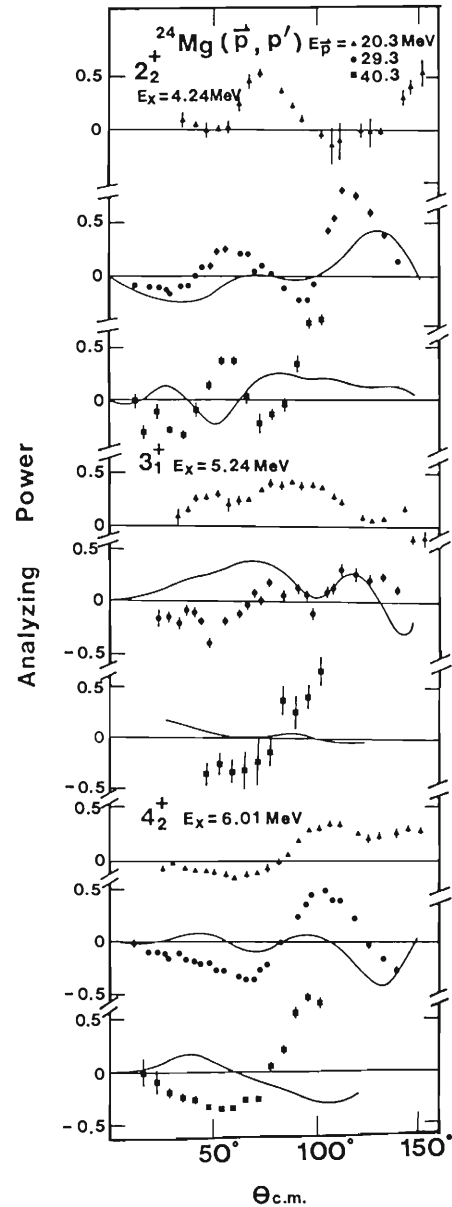


Fig. 2. The angular distributions of the analyzing powers of the  $\gamma$ -band at the energies of 20.3<sup>8)</sup>, 29.3, and 40.3 MeV. The curves are the same as those of Fig. 1 for analyzing powers.

analyzing powers of the  $3_1^+$  state between the data of  $E_p = 29.3$  and  $40.3$  MeV could be explained by energy dependence of the analyzing powers of the (p-d-p') processes. Although the failure of the CC calculation was attributed to the defects of the D-F model, the shell model description leads to proper cross sections. It is indicated that excitation of the  $3_1^+$  state would occur through ordinary couplings, because the coupling strengths between the  $3_1^+$  state and the two  $2^+$  states are quite large. The cross section of the  $4_2^+$  state was underestimated by a factor of about 5 in the forward angles, even when the second order DWBA was included. The direct excitation from the ground state might be most components of this transition due to a hexadecapole deformation of  $^{24}\text{Mg}$ ,<sup>2)</sup> although the shell model calculation provides small values for the E4 transitions.<sup>9)</sup> The remaining problem concerns this point and the inelastic excitation mechanisms of  $^{24}\text{Mg}$  would be brought up to light by further discussions on the data of the analyzing powers.

## References

- 1) J. Eenma, R. K. Cole, C. N. Waddell, H. S. Sandhu, and R. R. Ditman: Nucl. Phys., A218, 125 (1974); I. Lovas, M. Rogge, U. Schwinn, P. Turek, D. Ingham, and C. Mayer-Boerick: *ibid.*, A286, 12 (1977); R. M. Lombard, J. L. Escudie, and M. Soyeur: Phys. Rev. C, 18, 42 (1978); R. de Leo, G. d'Erasmus, E. M. Fiore, A. Pantaleo, M. Pignanelli, and H. V. Geramb: *ibid.*, 20, 13 (1979).
- 2) R. de Leo, G. d'Erasmus, A. Pantaleo, M. N. Harakeh, S. Micheletti, and M. Pignanelli: Phys. Rev. C, 23, 1355 (1981).
- 3) A. S. Davydov and G. F. Filipov: Nucl. Phys., 8, 237 (1958).
- 4) T. Fujisawa, S. Motonaga, N. Ueda, S. Yamada, and T. Hasegawa: AIP Conf. Proc. No. 69, p. 906 (1980).
- 5) R. M. Graig, J. C. Dore, G. W. Greenlee's, J. Love, and D. L. Watson: Nucl. Phys., 83, 493 (1966); *ibid.*, 79, 177 (1966).
- 6) L. N. Blumberg, E. E. Gross, A. van der Woude, A. Zucher, and R. H. Bassel: Phys. Rev., 147, 812 (1966).
- 7) M. H. Tanaka, S. Kubono, S. Kato: Nucl. Instr. Meth., 195, 509 (1982).
- 8) A. S. Blair, G. Glashauser, R. de Swiniarski, J. Goudergues, R. M. Lombard, B. Mayer, J. Thirion, and P. Vaganov: Phys. Rev. C, 1, 444 (1970).
- 9) B. A. Brown, W. Chung, and B. H. Wildenthal: *ibid.*, 21, 2600 (1980).

III-1-11. Multiple Coulomb Excitation of  $^{167}\text{Er}$ 

T. Inamura, A. Hashizume,  
M. Ohshima,\* E. Minehara,\* and M. Ishii\*

NUCLEAR REACTIONS  $^{167}\text{Er} (^{35}\text{Cl } ^{35}\text{Cl}', \gamma)$ ,  $E = 160$  MeV; measured  $E_\gamma$ ,  $I_\gamma(\theta)$ ,  $\gamma\gamma$  coin.,  $\gamma\gamma\text{DCO}$ , lifetimes; deduced levels,  $J$ ,  $\pi$ ,  $\gamma$  branching,  $\delta(E2/M1)$ ,  $B(M1)$ ,  $B(E2)$ .

It is well known that high- $j$  orbits such as  $i_{13/2}$  cause strong perturbation to the rotational bands of deformed odd-mass nuclei. However, interweaving of rotational and intrinsic motion is still to be studied quantitatively by measuring not only level energies but also transition moments of the band members. Recently, Hamamoto has made a cranking model calculation and demonstrated that even if the rotational frequency is relatively small, the perturbation effect of rotation on M1 and E2 transitions becomes quite large in the case of the odd-mass nuclei with the  $i_{13/2}$ -neutron orbit.<sup>1)</sup> It is of value to examine whether such a rotational perturbation is really appreciable.

We carried out multiple Coulomb-excitation experiment on  $^{167}\text{Er}$  whose ground-state rotational band is built on the  $i_{13/2}$ -neutron orbit, i.e.,  $7/2[633]$ . A self-supporting metallic target of  $^{167}\text{Er}$  (91.5 % enriched and about  $80 \text{ mg/cm}^2$  thick) was bombarded with a 160 MeV  $^{35}\text{Cl}$  beam from the 20 – UR tandem accelerator at Japan Atomic Energy Research Institute. We measured angular distributions of deexcitation  $\gamma$  rays,  $\gamma - \gamma$  coincidences,  $\gamma - \gamma$  directional correlations (DCO), and lifetimes of excited states in  $^{167}\text{Er}$ . The lifetimes were determined from Doppler broadened  $\gamma$ -ray lineshapes. The technique was the same as described in Ref. 2.

The ground-state rotational band of  $^{167}\text{Er}$  has been established up to the member with spin  $25/2$ . Higher spin states,  $19/2^+$  at  $772.75 \pm 0.03$  keV,  $21/2^+$  at  $954.95 \pm 0.05$  keV,  $23/2^+$  at  $1195.3 \pm 0.1$  keV, and  $25/2^+$  at  $1394 \pm 1$  keV, were newly identified. In Table 1 are summarized the observed properties of  $\gamma$  transitions in the ground-state rotational band.

As is shown in Fig. 1, the reduced transition probabilities of crossover E2 transitions  $B(E2; I \rightarrow I-2)$  have turned out to be very close to the rigid rotor predictions ( $Q_0 = 7.5 \text{ e b}$  was used, which was estimated from the  $B(E2; 7/2 \rightarrow 11/2)$  value adopted in Nuclear Data Sheets.<sup>3)</sup> It is, however, interesting to note that there seems to exist such a selection rule that  $B(E2)$  values between excited states labelled by the signature<sup>1),4)</sup>  $r = + i$  are reduced slightly as compared with those between neighbouring excited states with the signature  $r = - i$ , i.e.  $B(E2; (I, r = + i) \rightarrow (I-2, r = + i)) < B(E2; (I, r = - i) \rightarrow (I-2, r = - i))$ . This appears to coincide with the prediction made by Hamamoto.<sup>1)</sup>

In Fig. 2 the reduced M1-transition probabilities of stopover transitions  $B(M1; I \rightarrow I-1)$  are plotted as a function of initial spins  $I$  and compared to the rigid rotor predictions ( $g_k - g_R = -0.57$  was used, which is given in Ref. 5). Experimental  $B(M1)$  values are considerably smaller than the rigid rotor predictions, and they show that when the initial state has the signature  $r = + i$ , the M1-transition strength is reduced as compared with that of neighbouring excited states with the signature  $r = - i$ , i.e.  $B(M1; (I, r = + i) \rightarrow (I-1, r = - i)) < B(M1; (I, r = - i) \rightarrow (I-1, r = + i))$ . This signature dependence of M1-transition probability is also theoretically pointed out as the perturbation effect of rotation by Hamamoto.<sup>1)</sup>

It is of particular interest to study whether the observed transition probabilities are reproduced consistently in a framework that accounts for the attenuation of the Coriolis interaction which is introduced in making Coriolis band-mixing calculations to fit level energies.<sup>6)</sup>

\* Japan Atomic Energy Research Institute at Tokai.

Table 1. Summary of  $\gamma$  transitions in the  $7/2^+$  [633] ground-state rotational band of  $^{167}\text{Er}$ . Mixing ratios  $\delta(E2/M1)$  are the weighted averages of the values deduced from  $A_2$  and  $A_4$  and DCO ratios. Numbers in parentheses indicate the uncertainties in the least significant figure.

Initial spin $J^\pi$	Lifetime (ps)	Transition <sup>a)</sup> ( $\text{K}_{eV}$ )	Relative intensity		Ang. distr. coefficients		Mixing ratio $\delta(E2/M1)$
			$I_\gamma$	$I_T$	$A_2$	$A_4$	
$9/2^+$	119 (9) <sup>b)</sup>	79.33 (1)	563 (56)	3840 (380)	—	—	—
$11/2^+$	59 (6) <sup>b)</sup>	98.62 (1)	305 (31)	1240 (120)	-0.038 (12)	0.031 (54)	-0.45 (11)
		117.98 (1)	100 (5)	138 (7)	0.0176 (39)	-0.001 (6)	
$13/2^+$	42 (8)	116.99 (1)	88 (9)	250 (25)	-0.195 (22)	0.002 (30)	-0.23 (11)
		215.63 (1)	76 (4)	90 (5)	0.0776 (38)	0.012 (6)	
$15/2^+$	32 (4)	139.50 (1)	37 (4)	78 (8)	-0.245 (13)	0.028 (18)	-0.25 (6)
		256.47 (1)	60 (3)	66 (3)	0.110 (4)	0.015 (5)	
$17/2^+$	16 (2)	152.93 (1)	13 (1)	24 (2)	-0.303 (9)	-0.039 (12)	-0.31 (8)
		292.42 (1)	36 (18)	38 (2)	0.144 (4)	-0.017 (5)	
$19/2^+$	10 (2)	185.3 (2)	2.9 (5)	4.3 (7)	—	—	-0.35 (15)
		338.24 (1)	17 (1)	18 (2)	0.139 (4)	-0.013 (5)	
$21/2^+$	5 (1)	182.3 (2)	1.3 (2)	2.0 (3)	—	—	-0.15 (45)
		367.62 (4)	5.7 (6)	5.9 (6)	0.121 (15)	-0.010 (20)	
$23/2^+$	3.5 (7)	241.4 (5)	0.56 (6)	0.69 (7)	—	—	-0.20 (10)
		421.5 (1)	2.3 (3)	2.4 (3)	0.298 (37)	-0.009 (45)	
$25/2^+$	—	439 (1)	—	—	—	—	

a) Transitions whose mixing ratios are given in the last column are stopover (M1 + E2) transitions; otherwise they are crossover E2 transitions.

b) Cited from Nuclear Data Sheets.<sup>3)</sup>

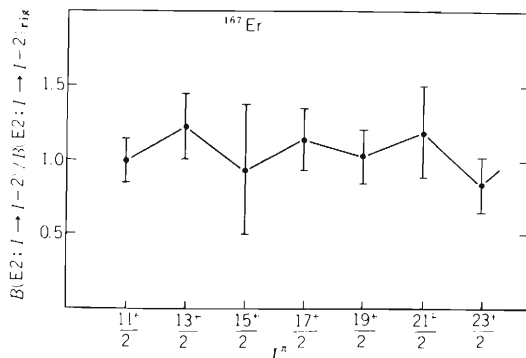


Fig. 1. Crossover E2-transition probabilities in the  $7/2^+$  [633] ground-state rotational band of  $^{167}\text{Er}$ . The  $B(E2)$  values are plotted in units of the rigid rotor estimates ( $Q_0 = 7.5 \text{ e b}$ ).

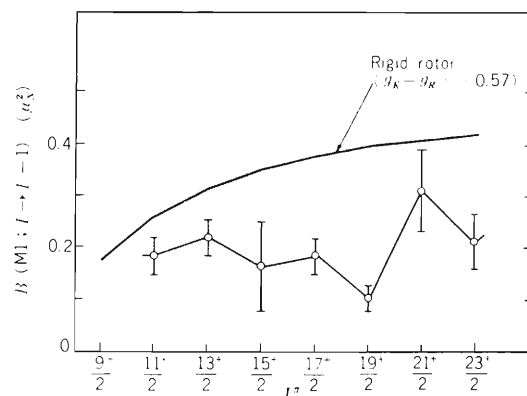


Fig. 2. M1-transition probabilities in the  $7/2^+$  [633] ground-state rotational band of  $^{167}\text{Er}$ . The  $B(M1)$  values are plotted in units of  $\mu_N^2$ . The solid line indicates the rigid rotor estimates ( $g_k - g_R = -0.57$ ).

## References

- 1) I. Hamamoto: Phys. Lett., 102B, 225 (1981); 106B, 281 (1981).
- 2) T. Inamura, F. Kearns, and J.C. Lisle: Nucl. Instr. and Meth., 123, 529 (1975).
- 3) B. Harmatz: Nuclear Data Sheets, 17, 143 (1976).
- 4) I. Hamamoto and H. Sagawa: Nucl. Phys., A327, 99 (1979).
- 5) A. Bohr and B.R. Mottelson: Nuclear Structure, 2, (W.A. Benjamin, Inc.), p. 303 (1975).
- 6) See, for example, S.A. Hjorth, A. Johnson, and G. Ehrling: Nucl. Phys., A184, 113 (1972).



transitions of 592, 453, and 782 keV between the states shown in Fig. 1. The experimental results of coincidences between  $\gamma$ -rays in the ground state band were also taken into accounts. Other levels in the side band are those based on the 2641 MeV level.

The energies of the levels in the ground state band up to  $10^+$  state of  $^{158}\text{Yb}$  were interpreted by IBM(Interacting Boson Model) employing 3 neutron pairs and 6 proton pairs. The main parts of wave function are composed of up to 6 d-bosons for  $10^+$  states.

Excited states in  $^{157}\text{Yb}$  have been investigated for the first time by measuring excitation functions,  $n\text{-}\gamma$  coincidences,  $\gamma\text{-}\gamma$  coincidences and angular distributions.<sup>2)</sup> We continued to analyze the experimental results and found that 674 keV E2  $\gamma$ -ray is also a member of yrast band transitions as shown in Fig. 1(b).

The level structures of nuclei of  $N = 87$  isotones in this region have been studied up to  $Z = 68$ . The level energy systematics between  $f_{7/2}$  and  $i_{13/2}$  states<sup>3)</sup> are shown in Fig. 2. As shown in the figure, energies of  $13/2^+$  states relative to those of  $7/2^-$  states decrease as  $Z$  numbers increase. It is expected that the  $7/2^-$  and  $13/2^+$  states lie very close in energy at  $Z = 70$ . For this reason the yrast band observed is supposed to be that built on  $13/2^+$  state. However, it is not clear if the  $13/2^+$  level is the ground state. To investigate this situation an experiment to observe conversion electrons from short lifetime states is in progress.

## References

- 1) A. Hashizume, T. Katou, Y. Tendow, and H. Kumagai: IPCR Cyclotron Progr. Rep., 14, 59 (1980).
- 2) A. Hashizume, T. Katou, Y. Tendow, and H. Kumagai: RIKEN Accel. Progr. Rep., 15, 54 (1981).
- 3) C.M. Lederer and V.S. Shirley: 'Table of Isotopes', John Wiley & Sons, Inc. (1978); J. Jansen, M. De Voigt, Z. Sujkowski, and D. Chmielewska: Nucl. Phys., A321, 365 (1979); P. Ager, G. Bastain, G.P. Tibeau, D. Barneau, G. Boute, and K. Fuan: Izv. Akad. Nauk SSSR Ser. Fiz., 41, 1992 (1977).

III-1-13. Analysis of Gamma-Ray Multiplicity Distributions for the  
 $^{159}\text{Tb}(^{14}\text{N}, \alpha xn)$  Reaction at 115 MeV\*

T. Inamura

$$\left[ \begin{array}{l} \text{NUCLEAR REACTIONS } ^{159}\text{Tb}(^{14}\text{N}, \alpha xn)^{169-X}\text{Yb}, \\ E = 115 \text{ MeV; massive transfer; } \gamma\text{-ray average} \\ \text{multiplicity, variance, skewness.} \end{array} \right]$$

Massive transfer is a type of heavy-ion reactions in which a massive fragment of the projectile is transferred to the target nucleus and energetic fragments such as protons or  $\alpha$  particles are emitted in the forward direction.<sup>1)</sup> Since the reaction is considered to occur for a narrow range of entrance-channel angular momenta ( $\ell$  window), it is interesting to study how the associated  $\gamma$ -ray multiplicity distribution reflects the existence of such an  $\ell$  window: the  $\gamma$ -ray multiplicity distribution is affected by the way of populating the entry states, i.e. the excited states prior to  $\gamma$  decay.

Table 1 summarizes the results of analyses of  $\gamma$ -ray multiplicity distributions for the  $^{159}\text{Tb}(^{14}\text{N}, \alpha xn)^{169-X}\text{Yb}$  reaction at 115 MeV. (Alpha particles of energies larger than 22 MeV in the laboratory system were recorded at  $12.3^\circ$  to the beam.) The  $\alpha 5n$  channel, which was the most intensive in those reactions, is one of typical examples of massive transfer.<sup>1)</sup> What are characteristic of this channel are as follows: (1) The average  $\gamma$ -ray multiplicity  $\langle M \rangle$  is independent of yrast spin values; (2) The sign of skewness  $s_M$  is likely to be positive.

The second feature supports the conclusion of a statistical calculation made for this reaction by assuming a spin localization in the entry state population.<sup>2)</sup> This calculation predicts the first feature as well. This feature has also been observed in other reactions that are probably considered as massive transfer.<sup>3)</sup>

As is seen from Table 1, these features are also remarkable in the cases of  $\alpha 3n$  and  $\alpha 4n$  channels, while the  $\alpha 6n$  channel is different. In the  $\alpha 6n$  channel  $\langle M \rangle$  increases with spin values, and the sign of skewness is likely to be negative. These properties are characteristic of complete fusion reactions.<sup>2),4)</sup>

It is interesting to note that even in the  $\alpha 5n$  channel  $\langle M \rangle$  increases with spin values  $I$  when it is measured by gating at low-energy  $\alpha$  particles (see Fig. 1). For  $\alpha$  particles of energies larger than 30 MeV,  $\langle M \rangle$  becomes independent of  $I$  as is seen in integrating over  $E_\alpha$  above 22 MeV. Therefore, it may be said that the fast component of  $\alpha$  particles which dominates the  $\alpha 5n$  channel originates from massive transfer, and the slow component is associated with complete fusion. The most probable  $\alpha$ -particle energy for the  $\alpha 5n$  channel in the present case is about 28 MeV.

As for the width (variance)  $\sigma_M$ , it is hard at present to extract something characteristic of massive transfer, compared with complete fusion.

\* Experiment was carried out in collaboration with A.C. Kahler, D.R. Zolnowski, U. Garg, and T.T. Sugihara at the Cyclotron Institute, Texas A & M University.

Table 1.  $\gamma$ -ray multiplicity distribution parameters for yrast transitions observed in the  $^{159}\text{Tb}(^{14}\text{N}, \alpha\text{xn})^{169-x}\text{Yb}$  reaction at 115 MeV. Numbers in parentheses indicate the statistical uncertainties in the least significant figure.

Final nucleus	Transition	$\langle M \rangle$	$\sigma_M$	$s_M$
$^{166}\text{Yb}$	$4^+ - 2^+$	10.2 (6)	5.0 (8)	—
	$6^+ - 4^+$	11.0 (5)	6.1 (10)	+1.0 (11)
	$8^+ - 6^+$	10.8 (5)	6.8 (9)	+2.0 (18)
	$10^+ - 8^+$	—	—	—
	$12^+ - 10^+$	10.8 (9)	5.1 (14)	—
	$14^+ - 12^+$	10.0 (20)	—	—
$^{165}\text{Yb}$	$17/2^+ - 13/2^+$	11.5 (6)	5.6 (10)	+1.8 (11)
	$21/2^+ - 17/2^+$	10.8 (6)	4.4 (14)	+2.0 (27)
	$25/2^+ - 21/2^+$	10.7 (5)	4.7 (11)	+2.8 (24)
	$29/2^+ - 25/2^+$	11.9 (9)	5.1 (16)	+0.9 (27)
$^{164}\text{Yb}$	$4^+ - 2^+$	13.9 (3)	6.2 (5)	+1.9 (7)
	$6^+ - 4^+$	13.9 (3)	6.8 (6)	+0.6 (5)
	$8^+ - 6^+$	13.9 (2)	5.1 (6)	+0.1 (12)
	$10^+ - 8^+$	14.5 (3)	4.5 (7)	+0.4 (15)
	$12^+ - 10^+$	14.3 (4)	5.1 (9)	+0.5 (17)
	$14^+ - 12^+$	13.6 (6)	4.2 (16)	+1.8 (39)
	$16^+ - 14^+$	13.5 (6)	4.6 (14)	—
$^{163}\text{Yb}$	$17/2^+ - 13/2^+$	11.4 (9)	8.0 (12)	—
	$21/2^+ - 17/2^+$	11.8 (6)	7.0 (13)	-0.3 (11)
	$25/2^+ - 21/2^+$	12.3 (3)	5.3 (9)	-0.4 (11)
	$29/2^+ - 25/2^+$	10.8 (16)	3.9 (28)	—
	$33/2^+ - 29/2^+$	13.6 (20)	4.3 (27)	—
	$37/2^+ - 33/2^+$	14.7 (42)	—	—

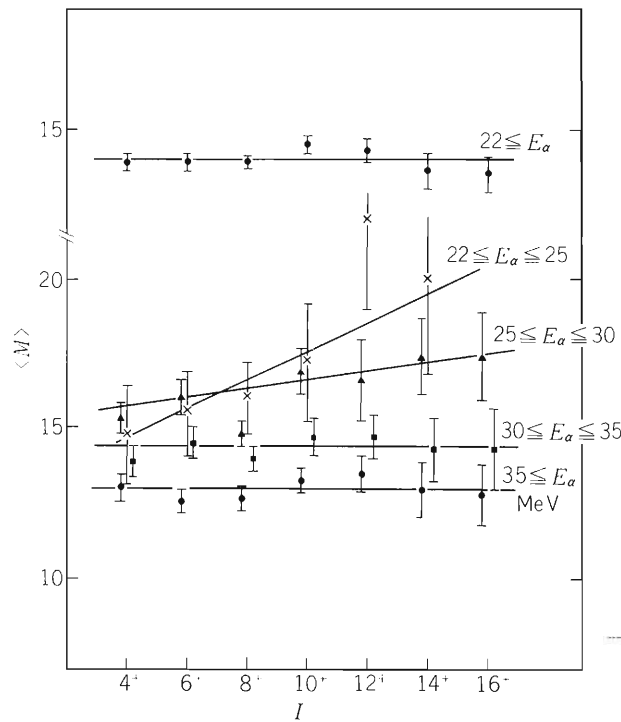


Fig. 1.  $\langle M \rangle$  vs. yrast state with spin  $I$  through which the  $\gamma$ -cascade has to go in the  $^{159}\text{Tb}(^{14}\text{N}, \alpha 5n)^{164}\text{Yb}$  reaction at 115 MeV. Alpha particle energy bin is indicated on the right.

## References

- 1) T.T. Sugihara: *Physica Scripta*, 24, 108 (1981), and references therein.
- 2) T. Inamura and M. Wakai: *J. Phys. Soc. Japan*, 51, 1 (1982).
- 3) H. Yamada, C.F. Maguire, J.H. Hamilton, A.V. Ramaya, D.C. Hensley, M.L. Halbert, R.L. Robinson, and F.E. Bertrand: *Phys. Rev. C*, 24, 2565 (1981).
- 4) G.B. Hagemann, R. Broda, B. Herskind, M. Ishihara, and S. Ogaza: *Nucl. Phys.*, A245, 166 (1975).

III-1-14. Level Scheme of  $^{217}\text{Ra}$ 

M. Sugawara, Y. Gono, Y. Itoh,  
T. Kubo, and T. Nomura

NUCLEAR REACTION  $^{208}\text{Pb}(^{13}\text{C}, 4n)$ ,  $E = 80$  MeV;  
 measured  $E_\gamma$ ,  $I_\gamma$ ,  $\gamma\gamma$ -coin,  $\alpha\gamma$ -coin;  $^{217}\text{Ra}$  deduced  
 levels,  $J$ ,  $\pi$ ,  $T_{1/2}$ .

Level scheme of  $^{217}\text{Ra}$  was studied by in-beam spectroscopic techniques. In this nucleus only two excited states are known from the  $\alpha$ -decay study of  $^{221}\text{Th}$ (Ref. 1). The  $\alpha$ -decay of the ground state in  $^{217}\text{Ra}$  is also known. The energy of the  $\alpha$ -decay is 8.990 MeV and the half-life is 1.6  $\mu\text{s}$  (Ref. 1).

Measurements of  $\alpha$ - $\gamma$  coincidence,  $\gamma$ - $\gamma$  coincidence,  $\gamma$ -ray angular distribution and  $\gamma$ -ray timing with respect to the beam bursts were performed using the  $^{208}\text{Pb}(^{13}\text{C}, 4n)^{217}\text{Ra}$  reaction at  $E = 80$  MeV. The  $\gamma$ -rays which belong to the  $^{217}\text{Ra}$  nucleus were identified in the coincidence  $\gamma$ -ray spectrum gated on the 8.990 MeV  $\alpha$ -line which is shown in Fig. 1. The  $\gamma$ - $\gamma$  coincidence spectra obtained by gating on 540 and 330 keV  $\gamma$ -rays which appear strongly in the above mentioned  $\alpha$ - $\gamma$  coincidence spectrum is shown in Fig. 2. Figure 3 shows a tentative level scheme of  $^{217}\text{Ra}$  which was constructed using the  $\gamma$ - $\gamma$  coincidence and  $\gamma$ -ray angular distribution data. Two parallel bands were observed. One band consists of the dipole cascade transitions with the quadrupole cross-over transitions between the 540 and 1455 keV levels. This band structure is somewhat similar to that in the  $^{218}\text{Ra}$  nucleus.<sup>2)</sup> An isomeric state with a half-life of 6.5 ns was found at the excitation energy of 2301 keV. The 330 and 737 keV levels seem to correspond to the previous<sup>1v</sup> known 331 and 756 keV levels.<sup>1)</sup> Further analysis is in progress.

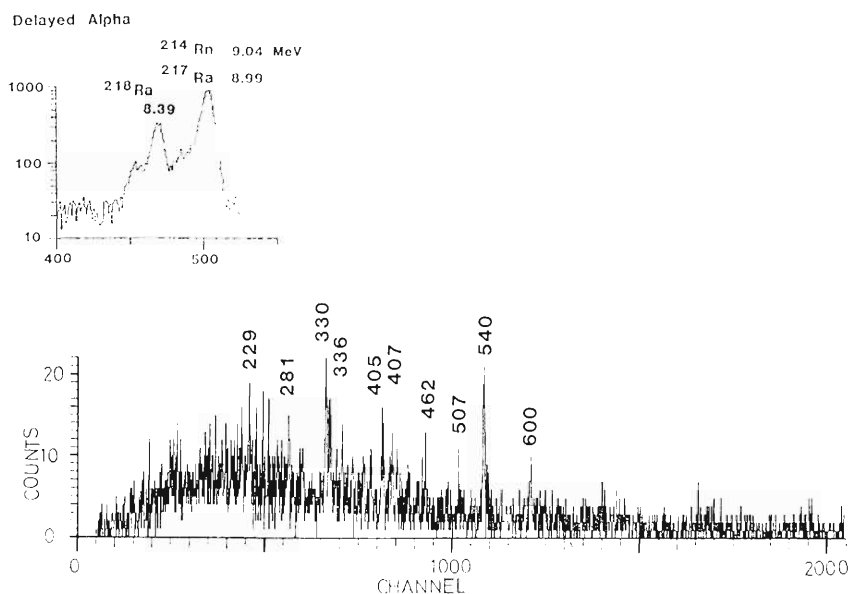


Fig. 1. Gamma-ray spectrum obtained by gating on 8.990 MeV  $\alpha$ -line of the ground state decay in  $^{217}\text{Ra}$ .

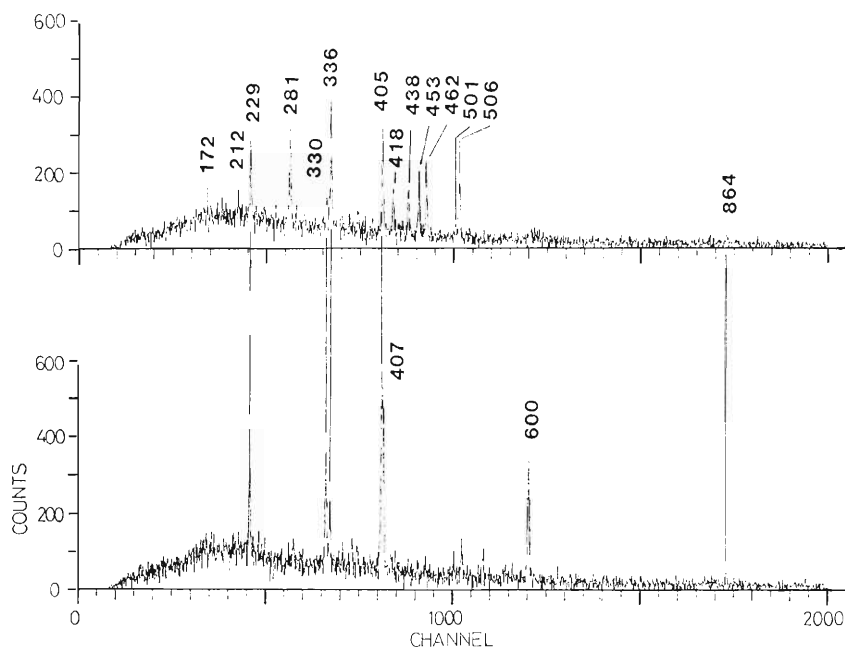


Fig. 2. Gamma-gamma coincidence spectra: the upper one is obtained by setting gate on 540 keV and the lower one on 330 keV gamma-rays.

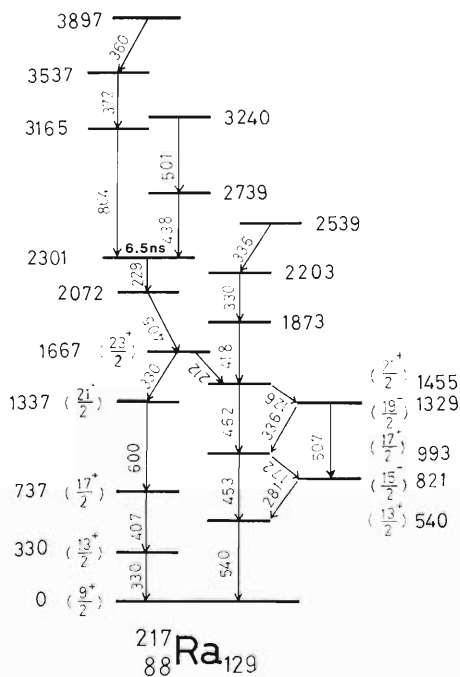


Fig. 3. A proposed level scheme of  $^{217}\text{Ra}$ .

## References

- 1) Table of Isotopes, 7th edition, (ed. C.M. Lederer and V.S. Shirley), John Wiley, New York (1978); and Nucl. Data Sheets, 28, No. 4 (1979).
- 2) Y. Itoh, Y. Gono, M. Sasagase, T. Kubo, M. Sugawara, S. Hayashibe, T. Kono, and T. Nomura: p. 48 in this report.

III-1-15. Level Schemes of  $^{216, 218}\text{Ra}$ 

Y. Itoh, Y. Gono, M. Sasagase,\* T. Kubo,  
M. Sugawara, S. Hayashibe, T. Kono,\*\* and T. Nomura

NUCLEAR REACTIONS  $^{208}\text{Pb}(^{12}\text{C}, 4n)$ ,  $E = 80$  MeV,  $^{208}\text{Pb}(^{13}\text{C}, 3n)$ ,  
 $(^{13}\text{C}, 5n)$ ,  $E = 65 - 95$  MeV; measured  $E_\gamma$ ,  $I_\gamma(\theta)$ ,  $I_\gamma(t)$ ,  $I_\gamma(E)$ , ICC,  
 $\gamma\text{-}\gamma$  coin.,  $\alpha\text{-}\gamma$  coin.,  $^{216, 218}\text{Ra}$  deduced levels. Ge(Li) and LEPS  
 detectors, enriched target.

We have studied excited states in  $^{216, 218}\text{Ra}$  by means of in-beam  $\alpha$ - and  $\gamma$ -ray spectroscopic techniques using  $^{12, 13}\text{C}$  beams provided by the cyclotron. The levels in  $^{216}\text{Ra}$  are extended to higher spin states than those in the previous report.<sup>1)</sup>

(1)  $^{216}\text{Ra}$ 

Levels in  $^{216}\text{Ra}$  were constructed up to the  $11^-$  state by Nomura et al.<sup>1)</sup> at first and extended recently up to the  $14^+$  level by Chevallier et al.<sup>2)</sup>

Adding to our previous work on  $^{216}\text{Ra}$ , we carried out an internal conversion electron and extended  $\gamma\text{-}\gamma$  coincidence measurements. The internal conversion electrons were measured with the  $^{208}\text{Pb}(^{12}\text{C}, 4n)$  reaction by using a mini-orange electron spectrometer with a cooled Si(Li) detector. The analysis of the conversion electron data confirmed that 399 keV and 557 keV transitions are both M1 + E2 type ones. In this analysis we used as calibration the internal conversion coefficients<sup>1)</sup> of the 344 keV, 476 keV, and 688 keV transitions which are of E2 character.<sup>1)</sup> The  $\gamma\text{-}\gamma$  coincidence measurement with two Ge(Li) detectors located at  $\theta = \pm 90^\circ$  was performed using the  $^{208}\text{Pb}(^{13}\text{C}, 5n)^{216}\text{Ra}$  reaction at  $E = 95$  MeV. This reaction was expected to populate higher spin states in  $^{216}\text{Ra}$  than the reactions used in our previous work.<sup>1)</sup> The delayed coincidence spectra among  $\gamma$ -rays in  $^{216}\text{Ra}$  suggested that at least two isomers exist.

Because of the existence of two isomers, the delayed  $\gamma$ -ray coincidence spectrum can be effectively used to construct the high spin states in  $^{216}\text{Ra}$ . The level scheme obtained is shown in Fig. 1. The level energies of two isomers were identified to be 3.76 MeV and 5.17 MeV, for which the half-lives were deduced to be  $6.0 \pm 0.4$  ns and  $6.7 \pm 0.6$  ns, respectively, from the  $\gamma$ -ray time spectra. Parallel cascade transitions of 199 keV – 221 keV and 290 keV – 130 keV were found as transitions below the first isomer. As previously reported,<sup>1)</sup> we also found a 51 keV transition of E1 character. On the basis of the  $\gamma$ -rays' time spectra of this transition, we put the 51 keV transition below the first isomer. These results confirmed the level scheme of  $^{216}\text{Ra}$  under the  $19^-$  state as shown in Fig. 1. We observed 110 keV and 120 keV  $\gamma$ -rays presumably between the  $14^+$  state and the  $19^-$  isomer. But we could not make them participate in the level scheme. Between the first and second isomers, four  $\gamma$ -rays were found to be in cascade. Their ordering was determined according to their transition intensities. Since the

\* Hitachi Computer Engineering.

\*\* Faculty of Science, Tokyo Institute of Technology.

multipolarity of 194 keV transition could not be determined, the spin-parity assignments of the 5.17 MeV state and states above it remain ambiguous.

The energy compression near the  $19^-$  isomer and the isomerism of the  $19^-$  and  $25^-$  states can be understood<sup>3)</sup> in terms of the couplings of two valence neutrons to the excited states in  $^{214}\text{Ra}$  (Ref. 4).

(2)  $^{218}\text{Ra}$

The level scheme of  $^{218}\text{Ra}$  was reported by two groups.<sup>5)</sup> In those reports the negative parity band as well as the ground state band were presented, and Fernández-Niello et al.<sup>5)</sup> concluded that the negative parity band is probably an octupole vibrational band.

In addition to the standard in-beam  $\gamma$ -ray spectroscopy,  $\alpha$ - $\gamma$  coincidence measurements on  $^{218}\text{Ra}$  were carried out using the  $^{208}\text{Pb}(^{13}\text{C}, 3n)^{218}\text{Ra}$  reaction at  $E = 70$  MeV. The  $\gamma$ -rays which belong to  $^{218}\text{Ra}$  were identified by the  $\alpha$ - $\gamma$  coincidence measurement setting a gate on the  $\alpha$ -line of the ground state decay of  $^{218}\text{Ra}$  ( $E_\alpha = 8.39$  MeV,  $T_{1/2} = 14$   $\mu\text{s}$  (Ref. 6)). Time spectra of  $\gamma$ -rays with respect to RF signals of the cyclotron which were taken by a 70 cm<sup>3</sup> Ge(Li) detector had no delayed component longer than  $T_{1/2} = 2$  ns. This limit of  $T_{1/2}$  is given by referring to the slope of the prompt spectrum which was obtained by irradiating  $^{12}\text{C}$  beam on an Al foil with the same set-up.

Figure 2 shows the level scheme of  $^{218}\text{Ra}$ . This level scheme is essentially the same as those

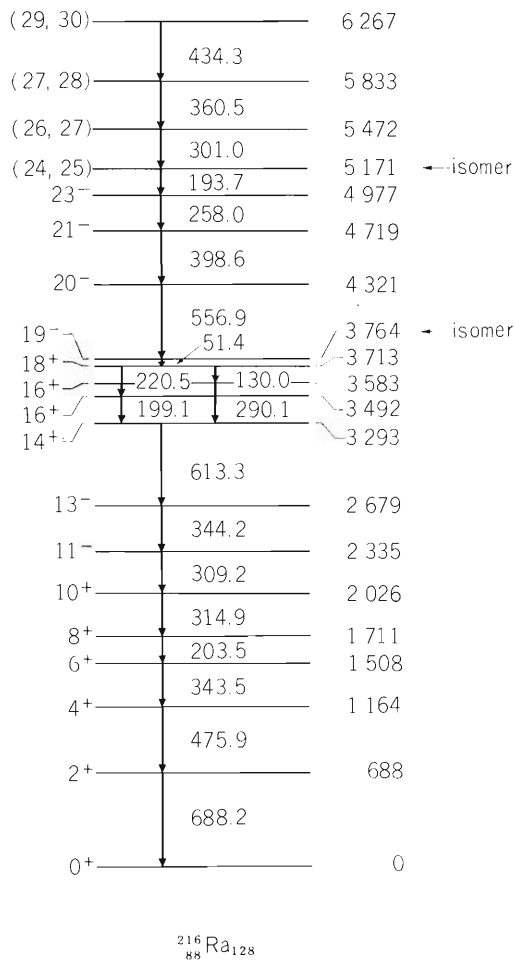


Fig. 1. A level scheme of  $^{216}\text{Ra}$ . Transition- and level-energies are in keV unit.

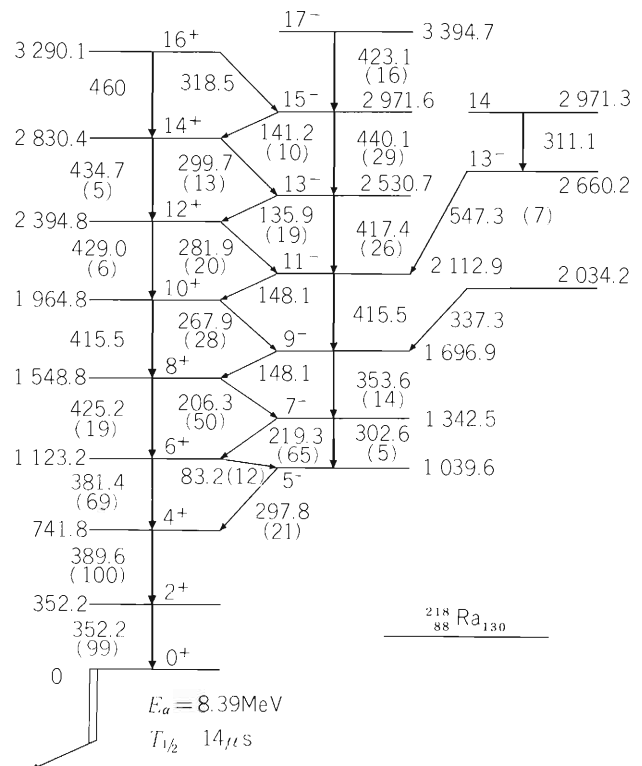


Fig. 2. A level scheme of  $^{218}\text{Ra}$ . Transition- and level-energies are in keV unit. The numbers in parentheses are relative transition intensities after corrections of the internal conversion coefficients.<sup>1)</sup> The arrow starting at the ground state indicates the ground state  $\alpha$ -decay.<sup>6)</sup>

reported by other groups.<sup>5)</sup> Ratios of the reduced transition probability,  $B(E1)/B(E2)$ , are of the order of  $10^{-6} \text{ fm}^{-2}$  for both transitions depopulating the ground state band and the negative parity band. It seems to be not probable that the negative parity band in  $^{218}\text{Ra}$  would be an octupole vibrational band as proposed by Fernández-Niello et al.<sup>5)</sup> since the model coupling an octupole vibration to a quadrupole core<sup>7)</sup> prohibits the E1 transitions from the ground state band to the negative parity band.

#### References

- 1) Y. Itoh, Y. Gono, M. Sasagase, T. Kubo, M. Sugawara, S. Hayashibe, K. Hiruta, and T. Nomura: RIKEN Accel. Progr. Rep., 15, 64 (1981), and references therein.
- 2) A. Chevallier, J. Chevallier, B. Haas, S. Khazrouni, and N. Schultz: Z. Phys., A308, 277 (1982).
- 3) Y. Itoh, Y. Gono, T. Kubo, M. Sugawara, and T. Nomura: to be published.
- 4) D. Horn, O. Häusser, B. Haas, T.K. Alexander, T. Faestermann, H.R. Andrews, and D. Ward: Nucl. Phys., A317, 520 (1979).
- 5) J. Fernández-Niello, H. Puchta, F. Riess, and W. Trautmann: *ibid.*, A391, 221 (1982); M. Gai, J.F. Ennis, A.C. Hayes, M. Ruscev, E.C. Schloemer, S.M. Sterbenz, N. Tsoupas, and D.A. Bromley: Proc. Int. Conf. on High Angular Momentum Properties of Nuclei at Oak Ridge, USA, (ed. N.R. Johnson), p. 118 (1982).
- 6) C.M. Lederer and V.S. Shirley, ed.: "Table of Isotopes, 7th ed.", John Wiley & Sons, Inc., New York (1978).
- 7) D.R. Zolnowski, T. Kishimoto, Y. Gono, and T.T. Sugihara: Phys. Lett., 55B, 453 (1975).

### III-1-16. In-Beam $\alpha$ - and $\gamma$ -Ray Study on $^{215}\text{Fr}$ and $^{217}\text{Ac}$

Y. Gono, Y. Itoh, M. Sasagase,\* M. Sugawara, T. Kubo,  
T. Nomura, S. Hayashibe, and K. Hiruta

$$\left[ \begin{array}{l} \text{NUCLEAR REACTION } ^{209}\text{Bi}(^{12}\text{C}, 4n), E = 80 \text{ MeV}; ^{205}\text{Tl}(^{13}\text{C}, 3n), E = 65 \text{ MeV}; \text{ measured} \\ E_{\gamma}, I_{\gamma}, \gamma(\theta), \gamma\gamma\text{-coin}, E_{\alpha}, I_{\alpha}, \alpha\gamma\text{-coin. } ^{217}\text{Ac}, ^{215}\text{Fr deduced levels, } J, \pi, T_{1/2}, \gamma_{\alpha}^2. \end{array} \right]$$

The  $\alpha$ -decays from the excited states in the  $N = 128$  isotones were studied using in-beam spectroscopic techniques. The nuclei  $^{215}\text{Fr}$  and  $^{217}\text{Ac}$  were produced by the  $^{205}\text{Tl}(^{13}\text{C}, 3n)^{215}\text{Fr}$  (at  $E = 65$  MeV) and  $^{209}\text{Bi}(^{12}\text{C}, 4n)^{217}\text{Ac}$  (at  $E = 80$  MeV) reactions, respectively. The  $\alpha$ -particle spectra were taken by a  $500 \mu\text{m}$  Si detector using a catcher-foil of  $30 \mu\text{m}$  carbon so that the energy resolution did not depend on the target thickness. The  $\gamma$ -rays were measured by standard in-beam spectroscopic techniques as well as  $\alpha$ - $\gamma$  coincidences.

#### (1) $^{217}\text{Ac}$

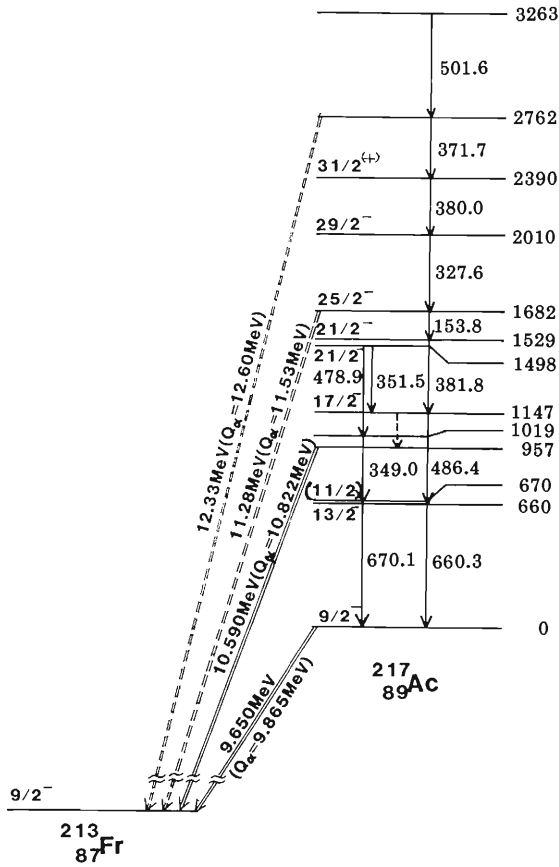
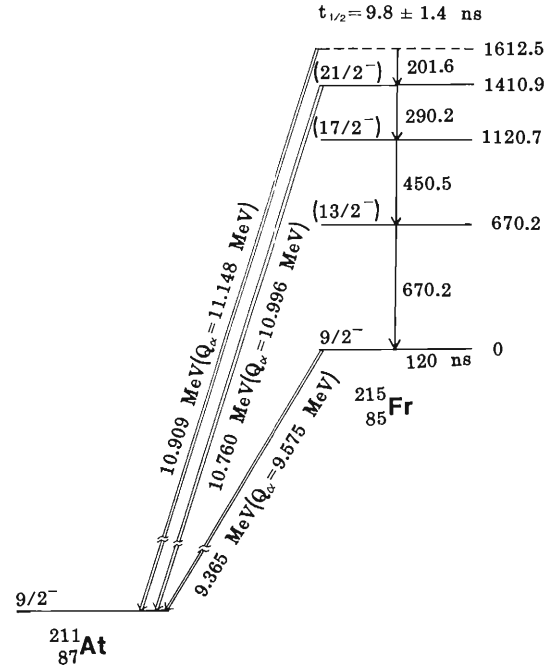
This nucleus was studied previously by the in-beam  $\alpha$ - and  $\gamma$ -ray spectroscopy.<sup>1,2)</sup> The  $\alpha$ -decays of 9.65, 10.54, and 11.13 MeV were identified as decays from the  $^{217}\text{Ac}$  nucleus.<sup>1)</sup> A level scheme of this nucleus was studied by Maier et al.<sup>2)</sup> However, the excitation energy of the state which deexcites by the 10.54 MeV  $\alpha$ -decay was quite ambiguous.

We have performed an  $\alpha$ - $\gamma$  coincidence as well as an extensive  $\gamma$ - $\gamma$  coincidence measurement on  $^{217}\text{Ac}$ . Several new  $\alpha$ -lines such as 9.74, 10.86, 11.03, 11.28, 11.40, 11.54, 12.15, and 12.33 MeV lines were observed. This resulted from the improvement of the energy resolution of the  $\alpha$ -spectrum. Relatively strong peaks at 10.590 and 9.650 MeV were used as gates in the  $\alpha$ - $\gamma$  coincidence measurement. The  $\gamma$ -rays of 327.6, 351.5, and 381.8 keV were observed in the  $\gamma$ -ray spectrum which was obtained by setting gate on the 10.590 MeV  $\alpha$ -line. The level scheme obtained is shown in Fig. 1.  $Q_{\alpha}$ -values of the other two  $\alpha$ -decays of 11.28 and 12.33 MeV fit to the energies of the deexcitations of the 1682 and 2762 keV states to the ground state in  $^{213}\text{Fr}$ , respectively, within the experimental accuracy. The proposed spins and parities are deduced from the  $\gamma$ -ray angular distribution measurements.

#### (2) $^{215}\text{Fr}$

This nucleus has been identified through the ground state  $\alpha$ -decay of 9.365 MeV (Ref.3). Nothing has been known on the excited states in this nucleus. A delayed  $\alpha$ -particle spectrum was taken after the  $^{205}\text{Tl}(^{13}\text{C}, 3n)^{215}\text{Fr}$  reaction. Two new  $\alpha$ -lines were observed at 10.760 and 10.909 MeV which decay with a half-life of  $9.8 \pm 1.4$  ns. The  $\gamma$ -ray spectrum was taken in coincidence with the 9.365 MeV  $\alpha$ -decay of the ground state in  $^{215}\text{Fr}$ . Strong  $\gamma$ -rays of 650, 450, 290, and 201 keV were assigned to the main cascade in this nucleus using the level systematics for the  $N = 128$  isotones.  $Q_{\alpha}$ -values of the two new  $\alpha$ -lines fit to the decay energies from the 1411 and 1613 keV levels in  $^{215}\text{Fr}$  to the ground state in  $^{211}\text{At}$ . A level scheme

\* Hitachi Computer Engineering.

Fig. 1. Level scheme of  $^{217}\text{Ac}$ .Fig. 2. Level scheme of  $^{215}\text{Fr}$ .

obtained is shown in Fig. 2.

We have so far studied  $\alpha$ -decays from the excited states in the  $N = 128$  isotones  $^{215}\text{Fr}$ ,  $^{217}\text{Ac}$ ,  $^{216}\text{Ra}$ (Ref. 4) and  $^{214}\text{Rn}$ (Ref. 5). Systematics of these  $\alpha$ -decays and the low-lying excited states is shown in Fig. 3 including nuclei  $^{212}\text{Po}$ (Ref. 6) and  $^{213}\text{At}$ (Ref. 7). The largest yield of the  $\alpha$ -decay from the excited states in each of  $^{212}\text{Po}$ ,  $^{214}\text{Rn}$ ,  $^{215}\text{Fr}$ , and  $^{216}\text{Ra}$  is observed as deexcitation of about 1.5 MeV level which corresponds to the excitation energies of the  $8^+$  states in the even-even nuclei in these isotones. About the same yield of the  $\alpha$ -decay as those mentioned above which is about 2.5 % of the intensity of the ground state  $\alpha$ -decay was obtained as deexcitation of the 957 keV state in  $^{217}\text{Ac}$ . This state is populated through the  $17/2^-$  state at 1147 keV promptly. The  $\gamma$ -ray which deexcites this state was not observed.

On the otherhand the half-life of the  $\alpha$ -decay from this state to the ground state in  $^{213}\text{Fr}$  whose spin and parity are  $9/2^-$  is shorter than 4 ns. The reduced  $\alpha$ -decay width,  $\gamma_{\alpha}^2$ , for this  $\alpha$ -decay is deduced to be less than 10 keV. This indicates that the angular momentum difference from  $9/2$  may not be larger than  $4\hbar$ . Hence the probable spin parity assignment to this states is  $17/2^-$ . The  $\gamma_{\alpha}^2$  value of 10 keV is about the same as those of ground state  $\alpha$ -decays in the  $N = 128$  isotones. However, the reduced  $\alpha$ -decay width of 10 keV is very large for the excited state of  $N = 128$  isotone. It may be worthwhile to point out that the  $\alpha$ -decay from the 957 keV state in  $^{217}\text{Ac}$  does not follow the systematic trend in  $N = 128$  isotones.

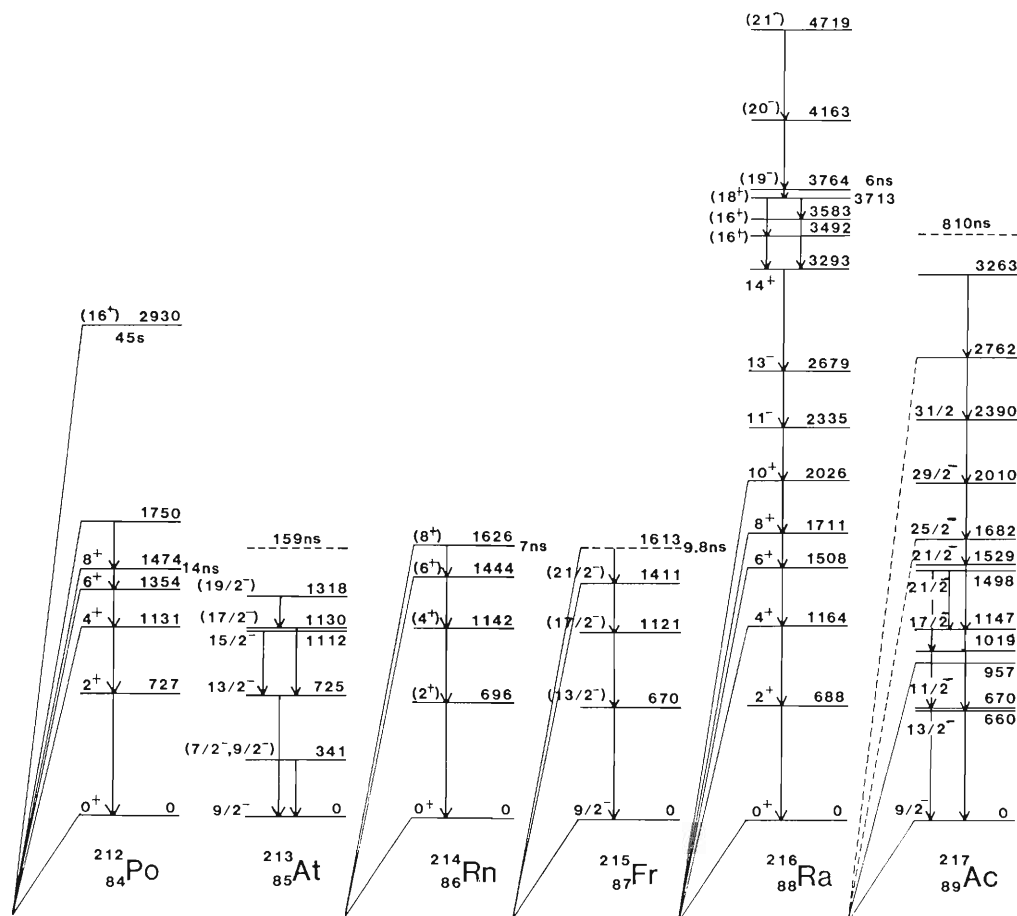


Fig. 3. Systematics of the low-lying excited states and the  $\alpha$ -decays from them in the  $N = 128$  isotones.

## References

- 1) T. Nomura, K. Hiruta, T. Inamura, and M. Odera: Nucl. Phys., **A217**, 253 (1973).
- 2) K.H. Maier, D.J. Decman, H. Growe, and H. Kluge: Proc. 4th Int. Conf. on Nuclei Far from Stability Line, Hersingor 1981, CERN 81-09, p. 183 (1981).
- 3) Table of Isotopes, 7th edition, (ed. C.M. Lederer and V.S. Shirley), John Wiley, New York (1978).
- 4) T. Nomura, K. Hiruta, M. Yoshie, H. Ikezoe, T. Fukuda, and O. Hashimoto: Phys. Lett., **58B**, 273 (1975).
- 5) Y. Gono, K. Hiruta, T. Nomura, M. Ishihara, H. Utsunomiya, T. Sugitate, and K. Ieki: J. Phys. Soc. Japan, **50**, 377 (1981).
- 6) R.M. Lieder, J.P. Didelez, H. Beuscher, D.R. Haenni, M. Muller-Veggian, A. Neskakis, and C. Mayer-Boricke: Phys. Rev. Lett., **41**, 742 (1978); P. Lemmertz, L.J. Alquist, R. Fass, H. Wolnik, D. Hirdes, H. Jungclas, R. Brandt, D. Schardt, and J. Zylicz: Z. Phys., **A298**, 311 (1980).
- 7) T.P. Sjoreen, U. Garg, and D.B. Fossan: Phys. Rev. C, **21**, 1838 (1980).

III-1-17. Numerical Analysis of 1280 MeV  $^{208}\text{Pb}$  Reactions  
on  $^{94}\text{Zr}$ ,  $^{110}\text{Pd}$ ,  $^{148}\text{Sm}$ , and  $^{170}\text{Er}$  Based  
on the Linear Response Theory

S. Yamaji, A. Iwamoto,\* K. Harada,\* and S. Yoshida

\left[ \begin{array}{l} \text{NUCLEAR REACTIONS Analysis for } ^{208}\text{Pb-induced reactions on } ^{94}\text{Zr}, ^{110}\text{Pd}, ^{148}\text{Sm}, \\ \text{and } ^{170}\text{Er}, E = 1280 \text{ MeV, linear response theory, two-center shell model.} \end{array} \right]

We have solved the equations of motion for 1280 MeV  $^{208}\text{Pb} + (^{94}\text{Zr}, ^{110}\text{Pd}, ^{148}\text{Sm}, ^{170}\text{Er})$  reactions<sup>1)</sup> in the framework of the linear response theory,<sup>2)</sup> taking the distance  $R$  between two colliding nuclei and deformation  $\delta$  of each nucleus as collective variables. The method is almost the same as in Ref. 3 except for the following four points taken into account.

- (1) The statistical fluctuations<sup>2)</sup> are included.
- (2) The time-dependent potential<sup>4)</sup>

$$V(\xi(t)) = V^{(S)}(1 - \xi(t)) + V^{(A)}\xi(t) \quad (1)$$

is used instead of the adiabatic potential  $V^{(A)}$  in Ref. 3. The order parameter  $\xi(t)$  in this expression is assumed to be

$$\xi(t) = \exp \left[ - \left\{ \int_{\infty}^t dt' / (1 + \exp(R(t') - (R_1 + R_2)/a)) \right\} / \tau_0 \right], \quad (2)$$

where  $R_1$  and  $R_2$  are radii of two nuclei. The parameter  $a$  is taken to be 0.9 fm and the relaxation time  $\tau_0$  is taken to be  $25 \times 10^{-23}$  sec. The potential obtained by folding the Yukawa-plus-exponential interaction by the density<sup>5)</sup> is used as the adiabatic potential  $V^{(A)}$  and the proximity potential<sup>6)</sup> is used as the sudden potential  $V^{(S)}$ . In Fig. 1, these potential  $V^{(A)}$  and  $V^{(S)}$  for the spherical shape are shown as a function of the distance  $R$  by the dashed and solid lines, respectively. The deformation effect is neglected in the calculation of  $V^{(S)}$ .

- (3) For the friction tensors, the following expression is assumed,

$$\gamma_{\mu\nu}(\xi(t)) = \gamma_{\mu\nu}^{(S)}(1 - \xi(t)) + \gamma_{\mu\nu}^{(A)}\xi(t) \quad \text{for } (\mu, \nu = R, \delta). \quad (3)$$

A microscopic calculation of friction tensors  $\gamma_{\mu\nu}^{(A)}$  has been performed using the two-center shell model on the basis of the linear response theory.<sup>7)</sup> For  $\gamma_{\mu\nu}^{(S)}$ , the following form is assumed,  $\gamma_{RR}^{(S)} = 0.0025 (\partial V^{(S)}/\partial R)^4$ ,  $\gamma_{R\delta}^{(S)} = \gamma_{\delta\delta}^{(S)} = 0.0$ .

- (4) The tangential and rolling frictional forces  $F_t$  and  $F_r$  written in the forms of  $F_t = -(R/(R_1 + R_2))^2 \gamma_{RR} (R_1(\dot{\theta}_1 - \dot{\theta}_0) + R_2(\dot{\theta}_2 - \dot{\theta}_0))$  and  $F_r = -1.2(R/(R_1 + R_2)) \gamma_{RR}(\dot{\theta}_1 - \dot{\theta}_2)$ , respectively, are included in the equations of motion, where  $\theta_0$  is the polar coordinate between the centers of two nuclei and  $\theta_1$  and  $\theta_2$  are the angles specifying the orientation of two nuclei. In the present calculation with this strong rolling frictional force, it is verified that the sticking condition has been achieved when the deforming motion starts. This satisfies the condition imposed on the present calculation that the system has to possess the symmetric axis throughout the collision.

\* Japan Atomic Energy Research Institute.

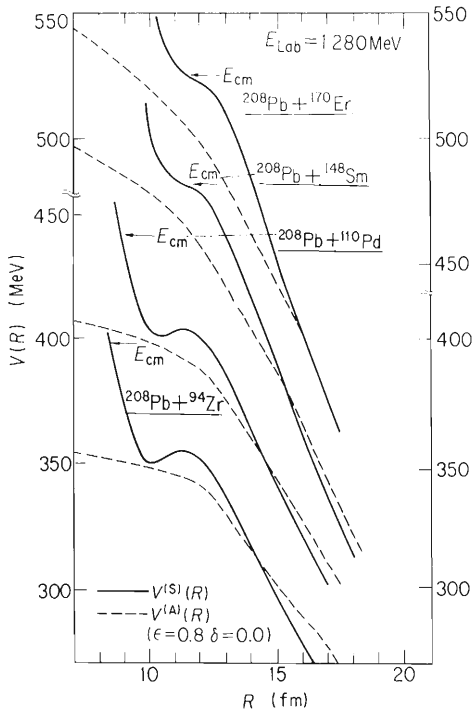


Fig. 1. The sudden potential  $V^{(S)}$  and adiabatic potential  $V^{(A)}$  for the spherical shape with the neck parameter  $\epsilon$  of 0.8 defined in Ref. 3 versus the relative distance  $R$ .

The difference between the solid and dashed lines in the asymptotic region comes from the fact that the adiabatic potential  $V^{(A)}$  is calculated under the assumption of the uniform charge distribution of the whole system. Horizontal arrows show the center of mass energies for four reactions.

The experimental results<sup>1)</sup> in Fig. 2 are compared with the calculated results in Fig. 3. Concerning the angular distributions  $d\sigma/d\theta$ , the relative peak positions for four reactions are well reproduced by the calculation, although the yields in the forward angles cannot be reproduced. The small pockets in the sudden potential for the reactions  $^{208}\text{Pb}+^{94}\text{Zr}$  and  $^{208}\text{Pb}+^{110}\text{Pd}$  keep the orbits which reach within the nuclear surface staying for a long time in the interaction region. These orbits contribute much to the cross sections near the peak position. For the reactions  $^{208}\text{Pb}+^{148}\text{Sm}$  and  $^{208}\text{Pb}+^{170}\text{Er}$ , there are no pockets in the sudden potentials, which explains the broader peaks at backward angles.

Concerning the total kinetic energy loss spectra  $d\sigma/dE$ , the maximum at the energy loss of 120 MeV in the experiment for the reaction  $^{208}\text{Pb}+^{94}\text{Zr}$  is well reproduced by the calculation, including a degree of freedom of deformation. In Fig. 4, the adiabatic potential  $V^{(A)}$  for the reactions  $^{208}\text{Pb}+^{94}\text{Zr}$  and  $^{208}\text{Pb}+^{170}\text{Er}$  are shown as a function of the deformation for several values of the distance  $R$ . The potentials for both cases have a minimum at  $\delta \sim 0.4$  in the surface region. This minimum disappears outside the nuclear surface. For the case of the reaction  $^{208}\text{Pb}+^{94}\text{Zr}$ , it is found that the deformation increases rapidly and reaches 0.4 during the collision for most partial waves contributing to the cross sections. In this case, the deforming motion is faster than the radial motion due to the attractive pocket of the sudden potential and also due to the gentle slope in the radial direction of the adiabatic potential. As the target nucleus becomes heavier, the attractive pocket in the sudden potential becomes shallower or even disappears and also the slope in the radial direction of the adiabatic potential becomes steeper, as can be seen in Fig. 1. Therefore, the maximum deformation obtained becomes smaller and the effect of deformation degree of freedom on the cross section becomes weaker.

As the conclusion, it can be said that the analysis based on the linear response theory for the Pb-induced reactions on  $^{94}\text{Zr}$ ,  $^{110}\text{Pd}$ ,  $^{148}\text{Sm}$ , and  $^{170}\text{Er}$  can explain the systematic feature of the angular distribution and kinetic energy loss spectra.

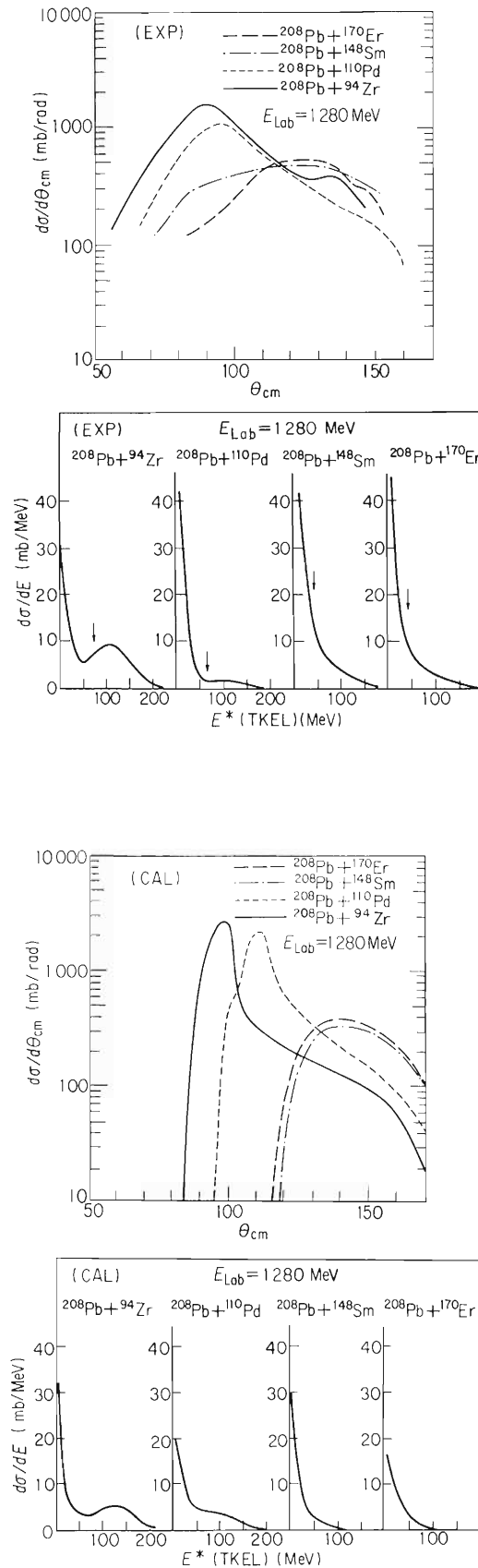


Fig. 2. Experimental results. The upper figure shows angular distributions for deep inelastic collision (DIC) events with energy losses exceeding 20 MeV. The lower figure shows total kinetic energy loss spectra. The arrows indicate the position of the Coulomb barrier calculated by assuming two spherical nuclei.

Fig. 3. Calculated results. The upper figure shows angular distributions for DIC events with energy losses exceeding 20 MeV. The lower figure shows total kinetic energy loss spectra.

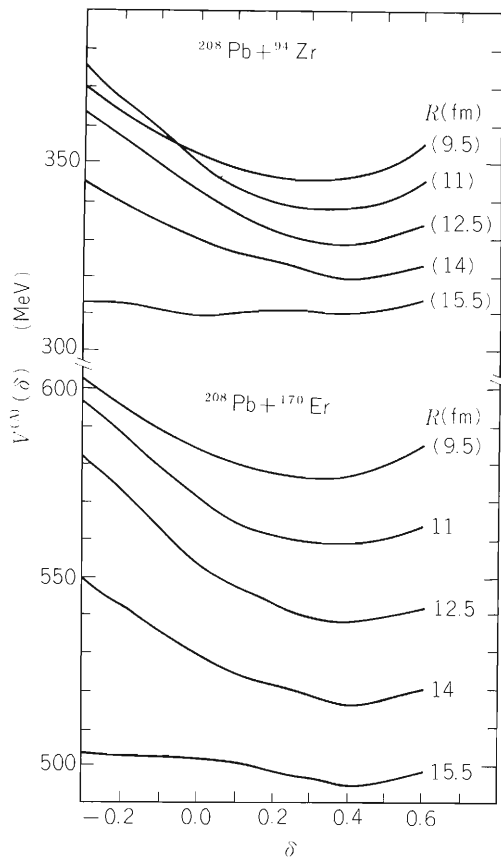


Fig. 4. The adiabatic potentials  $V^{(A)}$  for the reactions  $^{208}\text{Pb} + ^{94}\text{Zr}$  and  $^{208}\text{Pb} + ^{170}\text{Er}$  for several values of the distance  $R$  versus the deformation  $\delta$ .

#### References

- 1) K. E. Rehm, H. Essel, P. Sperr, K. Hartel, P. Kienle, H.J. Körner, R.E. Segel, and W. Wagner: Nucl. Phys., A366, 477 (1981).
- 2) H. Hofmann and P. J. Siemens: *ibid.*, A275, 464 (1977).
- 3) K. Sato, S. Yamaji, K. Harada, and S. Yoshida: Z. Physik, A290, 149 (1979).
- 4) W. Nörenberg and C. Riedel: *ibid.*, p. 335.
- 5) H. J. Krappe, J. R. Nix, and A. J. Sierk: Phys. Rev. C, 20, 992 (1979).
- 6) J. Blocki, J. Randrup, W. J. Swiatecki, and C. F. Tsang: Ann. Phys. (N.Y.), 105, 427 (1977).
- 7) A. Iwamoto, K. Harada, S. Yamaji, and S. Yoshida: Z. Physik, A302, 149 (1981).

### III-1-18. Effects of the Mass Fragmentation Potential on the Mass Diffusion Phenomena

S. Yamaji, A. Iwamoto,\* K. Harada,\* and S. Yoshida

$$\left[ \begin{array}{l} \text{NUCLEAR REACTIONS Analysis for } ^{208}\text{Pb} + ^{94}\text{Zr} \text{ reaction,} \\ \text{E} = 1280 \text{ MeV, linear response theory, two-center shell model.} \end{array} \right]$$

We report on the analysis of the relaxation phenomena in the mass exchange for the reaction  $1280 \text{ MeV } ^{208}\text{Pb} + ^{94}\text{Zr}$ <sup>1)</sup> based on the linear response theory.<sup>2)</sup> The relaxation phenomena in the mass exchange have been shown to be well reproduced by the theoretical values of mass diffusion coefficients  $D_A$  for various reactions.<sup>3),4)</sup> However, the value of  $D_A$  obtained by the same analysis as in Ref. 4 for the above mentioned reaction is  $0.25 \text{ T}/10^{-23} \text{ sec}$  and about ten times larger than that of Ref. 1, where T is the temperature of the intrinsic state in units of MeV.

We extend the study<sup>4)</sup> by solving coupled equations of motion with statistical fluctuations in the same way as in Ref. 5. The new point is that the projectile-like mass number  $A_1$  is taken into account as a collective variable in addition to the relative distance R and deformation  $\delta$ .

Figure 1 shows the total kinetic energy loss (TKEL) versus variance  $\sigma_A^2$ . The solid circles corresponding to the experimental data are well reproduced both by the solid line obtained by the present calculation and the dashed line obtained by Rehm's analysis.

It is worth mentioning the reason why both calculations have succeeded to reproduce the data in spite of using different values of  $D_A$ . For that purpose, the kinetic energy loss  $E^*$  and the variance  $\sigma_A^2$  as a function of collision time t are shown both for the present and Rehm's analyses in Fig. 2. We define the collision time t during which the mass exchange occurs by the time during which two colliding nuclei are staying within the distance  $C_1 + C_2$ , where  $C_i$  ( $i = 1 \text{ or } 2$ ) is the half-density radius calculated by  $C_i = a_i - 1.0/a_i$  using semi-major axis  $a_i$  of each deformed nucleus. One can obtain the results of Fig. 1 from those of Fig. 2 by removing the collision time. Rehm et al.<sup>1)</sup> obtained  $0.03/10^{-23}\text{sec}$ ,  $(0.15/10^{-23}\text{sec})^2$  and  $76 \times 10^{-23}\text{sec}$  for the values of the mass diffusion coefficient  $D_A$ , ensemble average of square of inertia mass transfer  $A_0^2$  and relaxation time  $\tau$  by the least square fitting of the expression

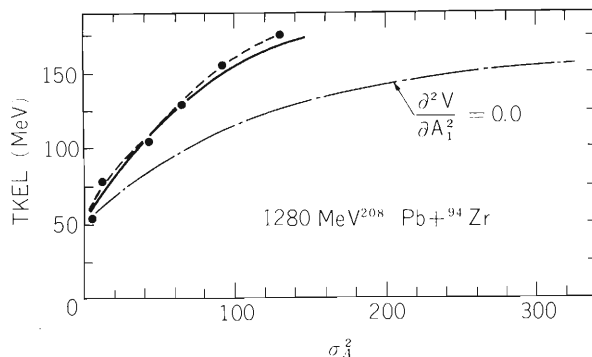


Fig. 1. TKEL versus  $\sigma_A^2$  for the reaction  $1280 \text{ MeV } ^{208}\text{Pb} + ^{94}\text{Zr}$ . The solid circles correspond to the experimental data. The solid and dashed lines show the present and Rehm's results, respectively. The dot-dashed line is calculated by setting  $\partial^2 V(A)/\partial A_1^2 = 0.0$ .

\* Japan Atomic Energy Research Institute, Tokai, Ibaragi, Japan.

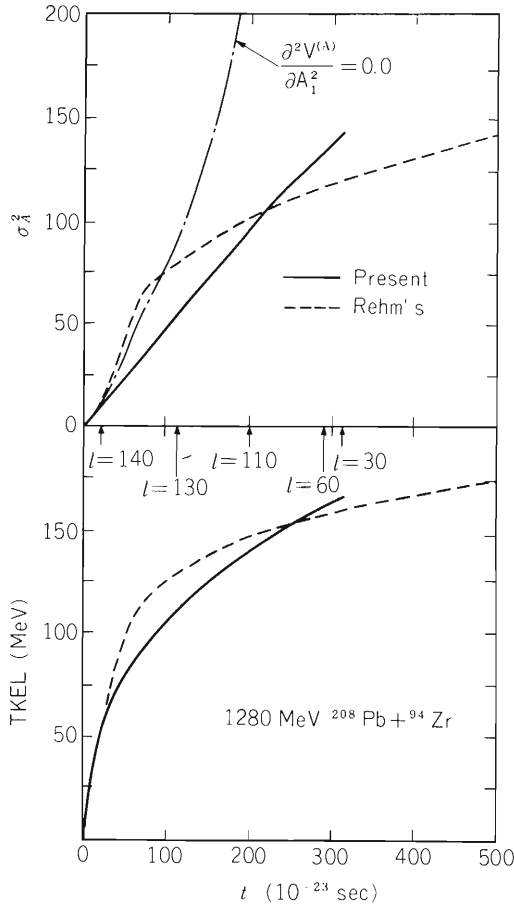


Fig. 2.  $\sigma_A^2$  and TKEL versus the collision time for the reaction 1280 MeV  $^{208}\text{Pb} + ^{94}\text{Zr}$ . The solid and dashed lines show the present and Rehm's results, respectively. The dot-dashed line shows  $\sigma_A^2$  calculated by setting  $\partial^2 V^{(A)} / \partial A_1^2 = 0.0$ . The arrows indicate the collision times obtained by the present calculation with given angular momenta  $\ell$ .

$$\sigma_A^2(t) = \dot{A}_0^2 \tau^2 (1 - \exp(-t/\tau))^2 + 2D_A t - D_A \tau (1 - \exp(-t/\tau)) \times (3 - \exp(-t/\tau)) \quad (1)$$

to the experimental values. The small value of  $D_A$ , that is,  $0.03/10^{-23}\text{sec}$  can be obtained from the slope of the dashed line of  $\sigma_A^2$  expressed by  $\sigma_A^2(t) \sim \dot{A}_0^2 \tau + D_A(2t - 3\tau)$  for  $t \gg \tau$ . It can be verified that the contribution from  $(\dot{A}_0 \tau)^2$  term to  $\sigma_A^2$  at  $t = 500 \times 10^{-23}\text{sec}$  is 120 and that from  $D_A(2t - 3\tau)$  is 20. Therefore, since the contribution of  $(\dot{A}_0 \tau)^2$  is rather large even at  $t \gg \tau$ ,  $\sigma_A^2(t)$  cannot be equal to  $2D_A t$  corresponding to the usual expression without the effect of the potential.

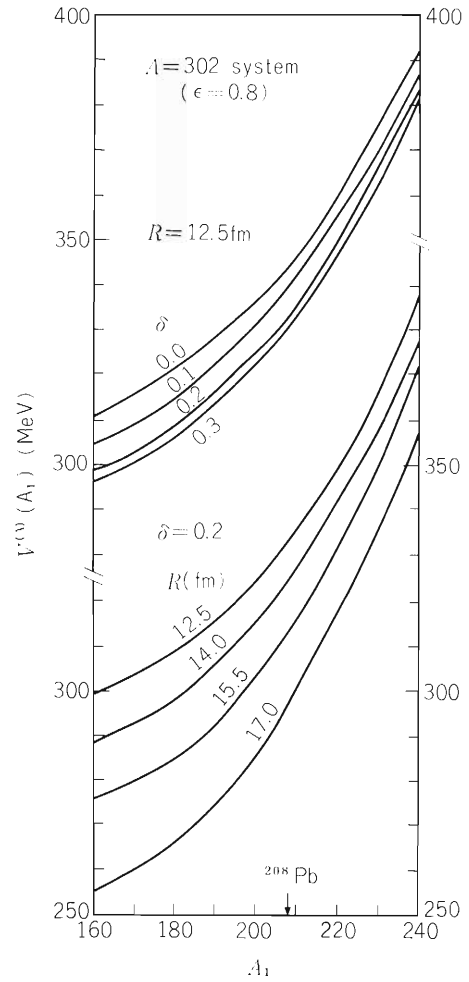


Fig. 3. The adiabatic potential  $V^{(A)}$  for the system of the total mass number of 302 versus the projectile-like mass number  $A_1$ . The upper lines show the adiabatic potentials for several values of  $\delta$ , fixing  $R = 12.5$  fm. The lower lines show the adiabatic potentials for several values of  $R$ , fixing  $\delta = 0.2$ . The neck parameter  $\epsilon$  defined by Ref. 4 is taken to be 0.8.

On the other hand, in the present case, the linear response theory<sup>2)</sup> gives the following expression to the variance  $\sigma_A^2(t)$ :

$$\sigma_A^2(t) = 2D_A/C \times (1 - e^{-Ct}) \sim 2D_A t (1 - Ct/2 + \dots) \quad (2)$$

under the assumption of the over-damped motion of mass exchange and of the constant values of  $D_A$  and  $C$ , where  $D_A$  and  $C$  are expressed in terms of the friction  $\gamma_{AA}$  corresponding to mass exchange, adiabatic potential  $V^{(A)}$  and nuclear temperature  $T$  in the forms of  $D_A = T/\gamma_{AA}$  and  $C = T/\gamma_{AA} \cdot \partial^2 V^{(A)}/\partial A_1^2$ . From the present numerical calculation,  $\gamma_{AA}$  is found to be  $(4\sim 5)\text{MeV} \cdot 10^{-23}\text{sec}$  in the region of  $0.0 \leq \delta \leq 0.4$  and  $12\text{fm} \leq R \leq 17\text{fm}$ , where mass exchange occurs. The potential curves  $V^{(A)}$  obtained by folding the Yukawa-plus-exponential interaction by the density<sup>6)</sup> which is also used in the coupled equations of motion are shown in Fig. 3. They can be approximated very well by the parabolic curves. The value of  $\partial^2 V^{(A)}/\partial A_1^2$  is found to be  $(2\sim 3) \times 10^{-2}\text{MeV}$ . The centrifugal potential is found to increase the above value by at most 10 percents for  $\ell = 130\hbar$ . The temperature  $T$  can be estimated by the relation  $T = 3.46 \sqrt{E^*/A}$ , in terms of TKEL  $E^*$ :  $T$  ranges from 1.5 MeV to 2.5 MeV in the present case. Then taking  $\gamma_{AA} \sim 4.5 \text{MeV} \cdot 10^{-23}\text{sec}$ ,  $\partial^2 V^{(A)}/\partial A_1^2 \sim 2.5 \times 10^{-2}\text{MeV}$  and  $T \sim 2 \text{MeV}$ , we obtain  $D_A \sim 0.5/10^{-23}\text{sec}$  and  $C \sim 0.01/10^{-23}\text{sec}$ . This approximate estimation by substituting these values into Eqn. (2) roughly reproduces solid line for  $\sigma_A^2$  which is obtained by solving three dimensional coupled equations of motion. If the effect of the fragmentation potential is neglected, that is,  $C = 0.0 \text{MeV}$ , the dot-dashed line for  $\sigma_A^2$  is roughly reproduced.

In conclusion, the reason why Rehm et al. got the small value of  $D_A$  is that the large contribution of  $(\dot{A}_0 \tau)^2$  to  $\sigma_A^2$  reduces  $D_A$  even at  $t \gg \tau$ . The large value of  $D_A$  obtained by the relation  $D_A = T/\gamma_{AA}$  in the present calculation can also reproduce the experimental  $\sigma_A^2$  for the reaction  $1280 \text{MeV } ^{208}\text{Pb} + ^{94}\text{Zr}$  as well as for other various reactions,<sup>4)</sup> if the effect of the fragmentation potential is included.

## References

- 1) K. E. Rehm, H. Essel, P. Sperr, K. Hartel, P. Kienle, H. J. Körner, R. E. Segel, and W. Wagner: Nucl. Phys., A366, 477 (1981).
- 2) H. Hofmann and P. J. Siemens: *ibid.*, A275, 464 (1977).
- 3) G. Wolschin and W. Nörenberg: Z. Phys., A284, 209 (1978).
- 4) S. Yamaji, A. Iwamoto, K. Harada, and S. Yoshida: Phys. Lett., 106B, 433 (1981).
- 5) S. Yamaji, A. Iwamoto, K. Harada, and S. Yoshida: p. 54 in this report.
- 6) H. J. Krappe, J. R. Nix, and A. J. Sierk: Phys. Rev.C, 20, 992 (1979).

### III-1-19. Exact Finite-range Coupled-channel Born Approximation Calculations with Spin-orbit Interactions

T. Takemasa

$\left( \begin{array}{l} \text{NUCLEAR REACTION Exact finite-range, zero-range, spin-orbit, CCBA,} \\ {}^{118}\text{Sn}(\vec{p}, t){}^{116}\text{Sn reaction, } 0^+ \text{ ground state, } 2^+ \text{ excited state, } E_p = 52 \text{ MeV.} \end{array} \right)$

The experimental data on  $(\vec{p}, t)$  reactions are now accumulating.<sup>1)</sup> Since there is evidence that multistep processes play an important role on  $(p, t)$  reactions,<sup>1)</sup> and the assumption of a zero-range (ZR) interaction responsible for the  $(p, t)$  transfer process has not received any physical justification, it is important to carry out exact finite-range (EFR) coupled-channel Born approximation (CCBA) calculations with spin-orbit coupling.

We have developed the EFR spin-orbit CCBA code SOCCBA by modifying the CCBA program without spin-orbit coupling which was used in Ref. 2. This code performs EFR-CCBA calculations with spin-orbit coupling very efficiently and quickly, because we have used an interpolation technique<sup>3)</sup> to construct finite-range form factors. SOCCBA can couple up to five states in both the entrance and the exit channel with a maximum of 200 partial waves. Twenty simultaneous transfer can be handled. Preliminary calculations are carried out for the  ${}^{118}\text{Sn}(\vec{p}, t){}^{116}\text{Sn}$  reaction at  $E_p = 52$  MeV leading to the  $0^+$  ground state (g.s.) and the  $2^+$  excited state, and are compared with the ZR-CCBA calculations, which are calculated by the computer program MARS.<sup>4)</sup>

The results for the differential cross sections and for the analyzing powers are shown in

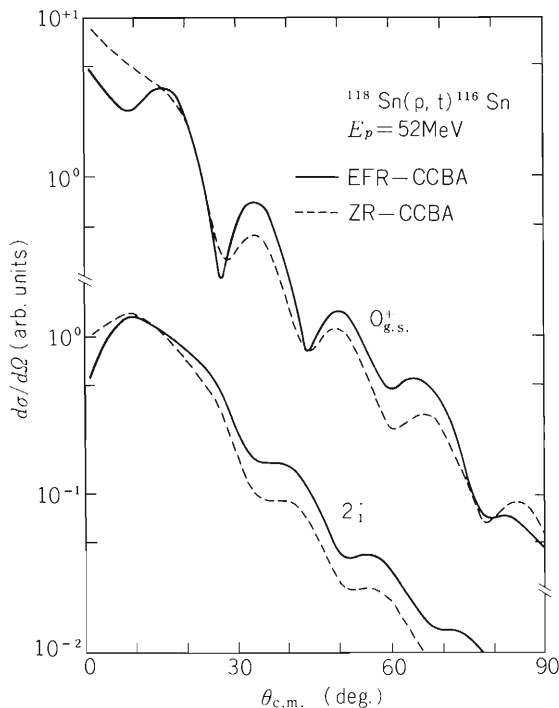


Fig. 1. Comparison of angular distributions calculated by ZR-CCBA (dashed-curve) and EFR-CCBA (full curve). The ZR-CCBA curves are normalized to the EFR-CCBA curves.

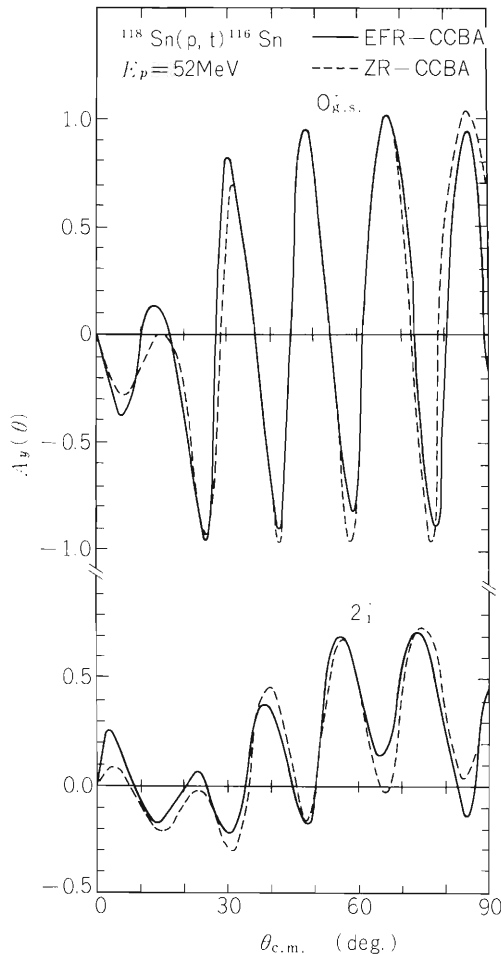


Fig. 2. Comparison of analyzing powers calculated by ZR-CCBA (dashed-curve) and EFR-CCBA (full curve).

Figs. 1 and 2, respectively. The nuclear model and parameters used are the same as those of Ref. 2. The ZR-CCBA calculations are carried out by using the same parameters used in the EFR-CCBA calculations. As is seen in the figures, there are rather large differences between the EFR and ZR calculations in both the angular distributions and the analyzing powers. It should be noted that the calculations are very sensitive to the radius parameter of the bound states and the choice of the optical parameters. This calculation, therefore, was only included to show the finite range effects. A comprehensive analysis of this reaction is currently underway.

#### References

- 1) G. G. Ohlsen, R. E. Brown, N. Jarmie, W. W. McNaughton, and G. M. Hale: Polarization Phenomena in Nuclear Physics – 1980 AIP Conf. Proc. No. 69, AIP, New York (1981).
- 2) T. Takemasa, T. Tamura, and T. Udagawa: Phys. Lett., 87B, 25 (1979).
- 3) T. Tamura: Phys. Rep., 14, 59 (1974).
- 4) T. Tamura and T. Udagawa: University of Texas, Center for Nuclear Studies Technical Report No. 3 (1972), unpublished.

### III-1-20. Effects of Two Particle-Two Hole Excitations on the Mass Distributions in Ion-Ion Collisions

M. Tohyama and S. Yamaji

NUCLEAR REACTION DIC one-dimensional calculation of mass  
distributions, time-dependent coupled-cluster approximation.

The time-dependent Hartree-Fock (TDHF) theory has been extensively used to describe the deep inelastic heavy-ion collisions. Although the TDHF calculation gives mean values of the mass distributions and total kinetic energy loss etc, it can not reproduce the widths of these observables.<sup>1)</sup> Here our concern is related to the widths of the mass distributions. In a microscopic theory, the number operator which counts probability in the right half plane is

$$\hat{N}_R = \sum \langle \alpha | \beta \rangle_R a_\alpha^\dagger a_\beta, \quad (1)$$

where  $\langle \alpha | \beta \rangle_R$  is the right-hand overlap integral of the single-particle wave functions. The mean number  $\bar{N}_R$  of particles and the standard deviation  $\sigma_R$  of the mass distribution in the right fragment are expressed as

$$\bar{N}_R = \langle \hat{N}_R \rangle \quad (2)$$

and

$$\sigma_R^2 = \langle \hat{N}_R^2 \rangle - (\langle \hat{N}_R \rangle)^2, \quad (3)$$

where  $\langle \hat{N}_R \rangle$  and  $\langle \hat{N}_R^2 \rangle$  denote the expectation values of  $\hat{N}_R$  and  $\hat{N}_R^2$ , respectively:

$$\langle \hat{N}_R \rangle = \frac{\langle \Psi | \hat{N}_R | \Psi \rangle}{\langle \Psi | \Psi \rangle} \quad \text{and} \quad \langle \hat{N}_R^2 \rangle = \frac{\langle \Psi | \hat{N}_R^2 | \Psi \rangle}{\langle \Psi | \Psi \rangle}. \quad (4)$$

If  $|\Psi\rangle$  is a single Slater determinant, the standard deviation becomes

$$\sigma_{R \text{ TDHF}}^2 = \sum_{\nu=1}^A \langle \nu | \nu \rangle_R - \sum_{\nu, \nu'}^A \langle \nu | \nu' \rangle_R \langle \nu' | \nu \rangle_R. \quad (5)$$

The widths of the mass distributions calculated with this formula are always an order of magnitude smaller than observed values.<sup>1)</sup> This comes from the fact that the TDHF theory does not give mean values of two-body operators correctly. To treat the widths of the mass distributions, we have to take into account higher configurations. It is an interesting problem to study how much the widths of the mass distributions are increased by improving the wave function.

We study the effect of two particle-two hole excitations on the widths of the mass distributions. We use the time-dependent coupled-cluster approximation (TDCCA). In this theory the wave function is written in the exp(S) form:<sup>2)</sup>

$$|\Psi\rangle = e^{\hat{S}} |\Phi\rangle, \quad (6)$$

where

$$\hat{S} = \sum_{n=1}^A \hat{S}_n, \quad (7)$$

and  $\hat{S}_n$  is represented by n particle-n hole operator referring to a Slater determinat  $|\Phi\rangle$ ,

$$\hat{S}_n = \frac{1}{(n!)^2} \sum \langle \rho_1 \rho_2 \dots \rho_n | S_n | \nu_1 \nu_2 \dots \nu_n \rangle_A a_{\rho_1}^+ \dots a_{\rho_n}^+ a_{\nu_n} \dots a_{\nu_1}. \quad (8)$$

The indices  $\nu_j(\mu_j)$  and  $\rho_j(\sigma_j)$  denote normally occupied states and normally unoccupied states, respectively. The suffix A means antisymmetrization of the labels  $\nu_1 \dots \nu_n$ . A set of coupled nonlinear equations for the amplitude  $\langle \rho_1 \dots \rho_n | S_n | \nu_1 \dots \nu_n \rangle$  is obtained by projecting the Schrödinger equation as follows:

$$\langle \Phi | a_{\nu_1}^+ \dots a_{\nu_n}^+ a_{\rho_n} \dots a_{\rho_1} e^{-\hat{S}} \left( i \frac{\partial}{\partial t} - \hat{H} \right) e^{\hat{S}} | \Phi \rangle = 0. \quad (9)$$

We take units such that  $\hbar = 1$ . Hoodbhoy and Negele<sup>3)</sup> have derived a couple of equations by truncating Eqn. (9) at the  $n = 2$  level. The first equation determines the time evolution of the single-particle basis, which involves the effects of two-body collisions on the single-particle potential via  $\langle \rho_1 \rho_2 | S_2 | \nu_1 \nu_2 \rangle$ . The second equation specifies the time evolution of  $\langle \rho_1 \rho_2 | S_2 | \nu_1 \nu_2 \rangle$ . It is a very hard numerical task to solve self-consistently these time-dependent coupled equations. We assume as a first step that the amplitude  $\langle \rho_1 \rho_2 | S_2 | \nu_1 \nu_2 \rangle$  is small and take the lowest-order terms in the coupled equations. As discussed later, this assumption is justified if incident energies are small. The equation for the single-particle basis then becomes the TDHF equation

$$i \frac{\partial}{\partial t} \varphi_\nu(t) = h(t) \varphi_\nu(t), \quad (10)$$

where  $h(t)$  is the Hartree-Fock (HF) Hamiltonian. The equation for  $\langle \rho_1 \rho_2 | S_2 | \nu_1 \nu_2 \rangle$  becomes

$$i \frac{d}{dt} \langle \rho_1 \rho_2 | S_2 | \nu_1 \nu_2 \rangle_A = \langle \rho_1 \rho_2 | V | \nu_1 \nu_2 \rangle_A, \quad (11)$$

where  $V$  is the two-body residual interaction. This equation can easily be integrated. The two-body density matrix is related to  $\langle \rho_1 \rho_2 | S_2 | \nu_1 \nu_2 \rangle$ .<sup>4)</sup> Using the two-body density matrix, we obtain the expression for the standard deviation  $\sigma_R$  of the mass distribution in the right-hand fragment.

We have performed calculations for one-dimensional collisions of two fragments  $A_1 = 4$  and  $A_2 = 8$ . In Fig. 1(a) we show the results of  $\sigma_R$  for various bombarding energies. The results of the TDHF calculation are also shown. The standard deviation  $\sigma_R$  are enhanced about three times as compared to the TDHF results. In Fig. 1(b) the mean numbers of particles on the right-hand side are compared with the TDHF results. As for the mean number of particles, the TDCCA calculation gives almost the same results as the TDHF calculation. We remark that two particle-two hole excitations affects much the observables related to the two-body operators. The decrease in  $\sigma_R$  at 2 MeV/A is due to a little change in the reaction mechanism. As seen from Fig. 1(b), at lower energies the light fragment gains mass. The situation is inverse at higher energies.

In Fig. 2 we show the density distributions in the initial and final states. The effect of two-body collisions is remarkable in the final stage of the collision as seen in one-dimensional calculations with a phenomenological collision term by Grangé et al.<sup>5)</sup> However, at these bombarding energies the difference between the TDCCA density and the TDHF one is rather small. We consider therefore that the assumption that the TDHF equation describes the time evolution of the single-particle states is valid.

In summary we have found that two-body collisions have a large effect on the widths of the mass distributions. It is an interesting problem to extend the present calculation to realistic three-dimensional collisions.

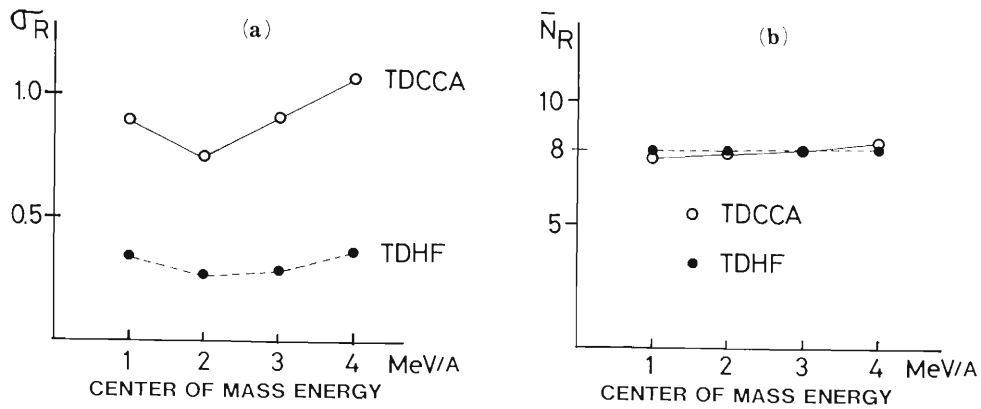


Fig. 1. Standard deviations  $\sigma_R$  (a) of the mass distributions and the mean numbers  $\bar{N}_R$  (b) of particles in the right fragment for  $A_1 = 4$  and  $A_2 = 8$  collisions. The solid line connects the TDCCA results (open circle) and the dotted line, the TDHF results (closed circle).

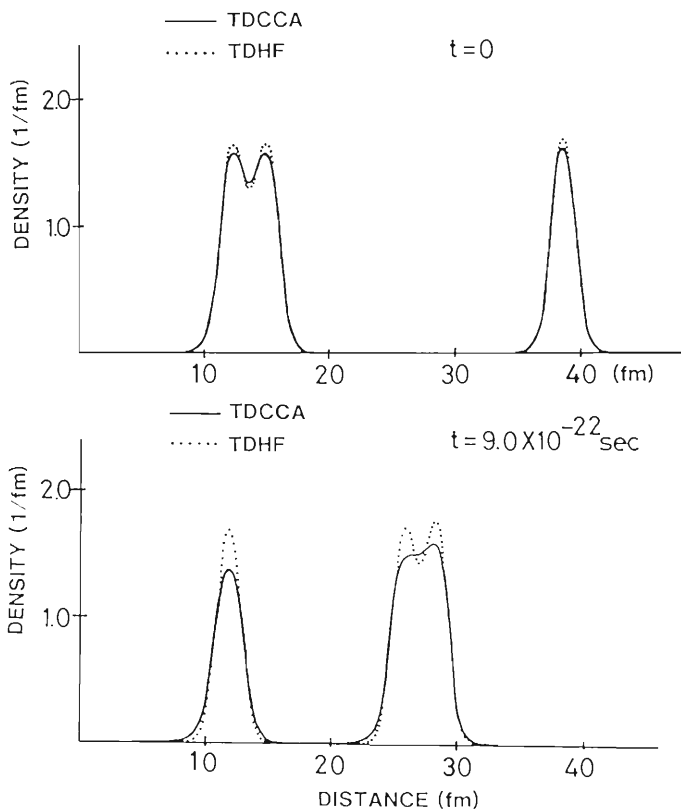


Fig. 2. The density distributions in the initial and final states for  $A_1 = 4$  and  $A_2 = 8$  collisions. The solid line denotes the TDCCA calculation and the dotted line, the TDHF calculation. The center-of-mass energy is 2 MeV/A.

#### References

- 1) K.T.R. Davies and S.E. Koonin: Phys. Rev. C, 23, 2042 (1981).
- 2) H. Kümmel, K.H. Lührmann, and J.G. Zabolitzky: Phys. Rep., 36C, 1 (1978).
- 3) P. Hoodbhoy and J.W. Negele: Phys. Rev. C, 19, 1971 (1979).
- 4) K. Emrich, J.G. Zabolitzky, and K.H. Lührmann: *ibid.*, 16, 1650 (1977).
- 5) J. Richert, D.M. Brink, and H.A. Weidenmüller: Phys. Lett., 87B, 6 (1979); P. Grangé, J. Richert, G. Wolschin, and H.A. Weidenmüller: Nucl. Phys., A356, 260 (1981).

## III-2. Atomic and Solid-State Physics

### 1. Target Gas Pressure Dependence of REC X-Rays from Ne-Ion Bombardment

T. Kambara, Y. Awaya, A. Hitachi\*, M. Kase,  
I. Kohno, and T. Tonuma

We have measured energy spectra of X-rays from radiative electron capture (REC) process by 5.5 MeV/amu Ne-ion bombardment on gaseous targets. In the process, an electron in a target atom is captured into a K-shell vacancy of an incident Ne-ion with emission of a photon.<sup>1),2)</sup> We reported on the analysis of the shape of the REC X-ray spectra as a function of the target atomic number.<sup>2)</sup>

In the present work, the REC X-ray spectra for H<sub>2</sub> gas target are analysed as a function of the target gas pressure which is proportional to the target thickness. The measurement system with a Si(Li) detector was described in the previous report.<sup>2)</sup> The pressure of the H<sub>2</sub> gas target contained in a gas cell was between 9 and 120 Torr and the distance between the entrance window (7  $\mu$ m thick Al foil) of the gas cell and the area viewed by the detector was about 70 mm.

The peak energy of the REC X-ray is shown in Fig. 1(a) and the REC X-ray yield divided by the gas pressure, referred to as relative yield hereafter, is shown in Fig. 1(b) as a function of the gas pressure. The REC peak shifts to higher energy and the X-ray relative yield increase when the gas pressure increases.

These effects are explained by the fact that the charge state distribution of the projectile

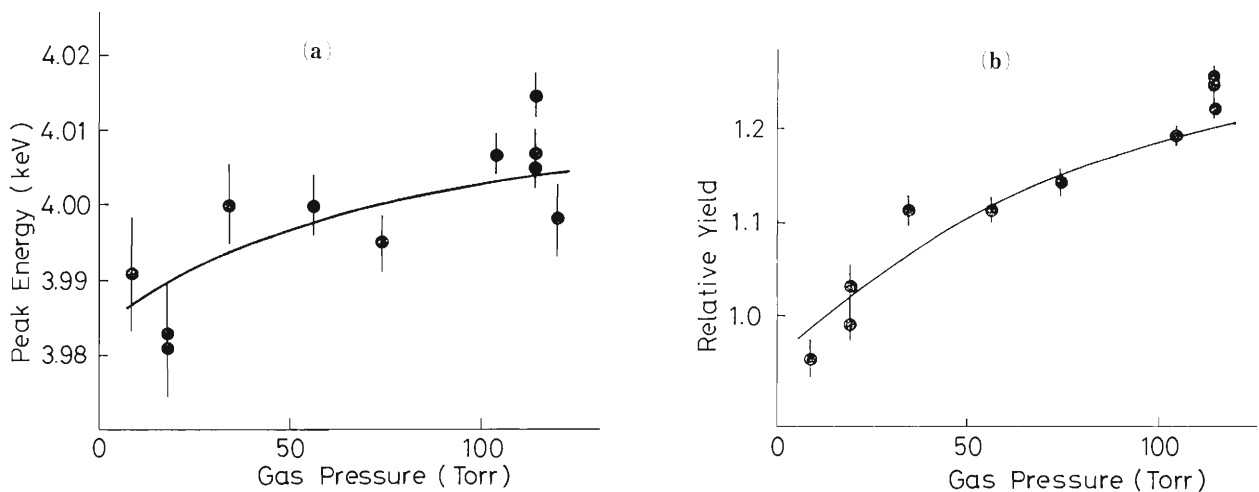


Fig. 1. Dependence of REC peak energy (a) and REC relative yield (b) on the gas pressure for H<sub>2</sub> gas target. The full curves show the calculation results based on the charge equilibration process of the ions in the gas. The calculated result of REC peak energy is lowered by 250 eV to fit the experimental data.

\* Radiation Laboratory, University of Notre Dame.

Ne-ions depends on the gas target thickness. The REC process to the K-shell of the incident ion in gas is possible for  $\text{Ne}^{9+}$ - and  $\text{Ne}^{10+}$ -ions, which have one and two K-shell vacancies respectively. The capture cross section and the emitted X-ray energy for the capture by a  $\text{Ne}^{9+}$ -ion are lower than those by a  $\text{Ne}^{10+}$ -ion, because a  $\text{Ne}^{9+}$ -ion has one electron in the K-shell. Therefore the X-ray energy and the relative yield increase when the fraction of the  $\text{Ne}^{10+}$ -ion increases.

The dependence of the charge state distribution on the target thickness is due to electron transfer processes between the ions and the gas atoms, which is described by rate equations.<sup>3)</sup> In the present experimental condition, most of the ions are at the charge states higher than 7+ after the ions pass through the entrance Al window. Then the charge state distribution of the ions at gas target thickness  $x$  (atoms/cm<sup>2</sup>) is as follows:

$$\begin{aligned} f_8 &= f_8^0 \exp(-\sigma_L^8 x) \\ f_9 &= f_9^0 \exp(-\sigma_L^9 x) \\ &\quad + f_8^0 \frac{\sigma_L^8}{\sigma_L^8 - \sigma_L^9} \left\{ \exp(-\sigma_L^9 x) - \exp(-\sigma_L^8 x) \right\} \\ f_{10} &= 1 - f_9 - f_8, \end{aligned}$$

where  $f_q$  is the fraction of ion with charge  $q$ ,  $f_q^0$  is that after the passage of the entrance window of the gas cell and  $\sigma_L^q$  is the electron loss cross section of ion with charge  $q$ . The electron capture cross section is much smaller than  $\sigma_L^q$  according to calculations based on OBK model<sup>4)</sup> and is neglected in these formula. The values of  $\sigma_L^9$  is taken from the calculation based on BEA model which gives about  $2.6 \times 10^{-20}$  cm<sup>2</sup> for the cross section of the process  $\text{Ne}^{9+} + \text{H} \rightarrow \text{Ne}^{10+} + \text{H} + e$ .<sup>5)</sup> The cross section  $\sigma_L^8$  is estimated by the same formula for the process  $\text{F}^{8+} + \text{H} \rightarrow \text{F}^{9+} + \text{H} + e$  and the result is multiplied by two, the number of electrons in the incident ion.

The values of  $f_q^0$  are taken from experimental data of charge state distribution of heavy ions in Al presented by Northcliffe,<sup>6)</sup> which gives 62 % for  $f_{10}^0$  and 35 % for  $f_9^0$ .

The charge state fractions ( $f_q$ ) at the area viewed by the detector, at 70 mm of flight path from the entrance window, are calculated for various gas pressures up to 120 Torr, which corresponds to  $5.6 \times 10^{19}$  atoms/cm<sup>2</sup>. The calculation predicts that the fraction of  $\text{Ne}^{10+}$  ions increases from 62 % to 91 % when the ion beam passes through the gas at 120 Torr from the entrance window to the area viewed by the detector.

The X-ray peak energy is calculated by assuming that the REC spectrum consists of two Gaussian peaks separated by 170 eV corresponding to transitions to  $\text{Ne}^{9+}$  and  $\text{Ne}^{10+}$  respectively. The REC relative yield is assumed to be proportional to  $2f_{10} + \alpha f_9$  where  $\alpha$  is the ratio of the REC cross section for a  $\text{Ne}^{9+}$  to that for a  $\text{Ne}^{10+}$ . It is estimated as the ratio of free electron capture cross section by a point charge with  $Z = 9$  to that with  $Z = 10$ , resulting in  $\alpha = 0.7$ .

The results are shown in Figs. 1(a) and 1(b) by full curves. The calculated peak energy in Fig. 1(a) must be lowered by about 250 eV to fit the experimental data. The agreement between the calculated results and the experimental data is good for the X-ray relative yield. The shift of the peak energy in its relative value is also well reproduced by the calculation.

A more detailed report will be given elsewhere.<sup>7)</sup>

## References

- 1) T. Tonuma, Y. Awaya, T. Kambara, H. Kumagai, and I. Kohno: IPCR Cyclotron Progr. Rep., 12, 86 (1978).
- 2) T. Kambara, Y. Awaya, A. Hitachi, M. Kase, I. Kohno, and T. Tonuma: *ibid.*, 14, 88 (1980).
- 3) H. D. Betz: "Method of Experimental Physics: Atomic Physics, Accelerators", (ed. P. Richard), Academic Press, New York, 17, 73 (1980).
- 4) J. Eichler and F. T. Chan: Phys. Rev. A, 20, 104 (1979).
- 5) T. Shirai, K. Iguchi, and T. Watanabe: J. Phys. Soc. Japan, 42, 238 (1977).
- 6) L. C. Northcliffe: Ann. Rev. Nucl. Sci., 13, 67 (1963).
- 7) T. Kambara, Y. Awaya, A. Hitachi, M. Kase, I. Kohno, and T. Tonuma: J. Phys. B: At. Mol. Phys., 15, 3759 (1982).

### III-2-2. Target Gas Pressure Dependence of K-X Rays from 110 MeV Ne Ions

T. Kambara, Y. Awaya, M. Kase, H. Kumagai, I. Kohno,  
A. Hitachi, and T. Tonuma

The K-X rays from 110 MeV  $\text{Ne}^{9+}$  ions (hydrogen-like) in gaseous targets with atomic number  $Z_t \leq 10$  have been studied at various gas pressures up to 300 Torr. Last year we reported on measurements using a Si(Li) detector with a resolution of 250 eV(FWHM).<sup>1)</sup> In the measurements, two peaks appeared in the energy spectrum of K-X rays: One from the transitions  $np - 1s$  with  $n > 2$  (1.21 – 1.36 keV) which were not resolved and the other due to the  $2p - 1s$  transition (1.0 keV).

For the targets with  $Z_t > 2$ , the former peak was found to shift to lower energy when the gas pressure increased. In order to find out the reason for the energy shift, we made measurements of the energy spectrum of the former peak to resolve it into peaks arising from  $np - 1s$  transitions of various values of  $n$ . The targets were  $\text{N}_2$  and Ne gases, each of which was contained in a gas cell with pressure between 20 and 300 Torr. We used a broad range crystal spectrometer with a plane crystal and a position sensitive proportional counter. The details of the spectrometer were reported elsewhere.<sup>2)</sup> We used an RAP crystal ( $2d = 26.12 \text{ \AA}$ ) for the analyser and a  $4 \mu\text{m}$  thick Mylar foil for the window of the position sensitive proportional counter. The foil was supported by an  $80 \mu\text{m}$  thick stainless steel mesh from the outside to hold the gas in the counter whose pressure was about 3.2 atm. The electronic circuit system to analyze the signals from the counter was modified a little to distinguish the low level signals due to K-X rays from backlash pulses of higher level noise signals. The range of the energy of X-rays observed by the spectrometer was between 1.1 and 1.44 keV where the  $np - 1s$  transitions with  $n$  greater than 2 could be observed. The resolution was about 10 eV (FWHM).

Examples of the observed spectra are shown in Fig. 1: Figure 1(a) is for  $\text{N}_2$  gas target at 300 Torr and Fig. 1(b) at 21 Torr. Peaks from the transitions  $np - 1s$  ( $n = 3, 4,$  and  $5$ ) are well resolved. As seen in the

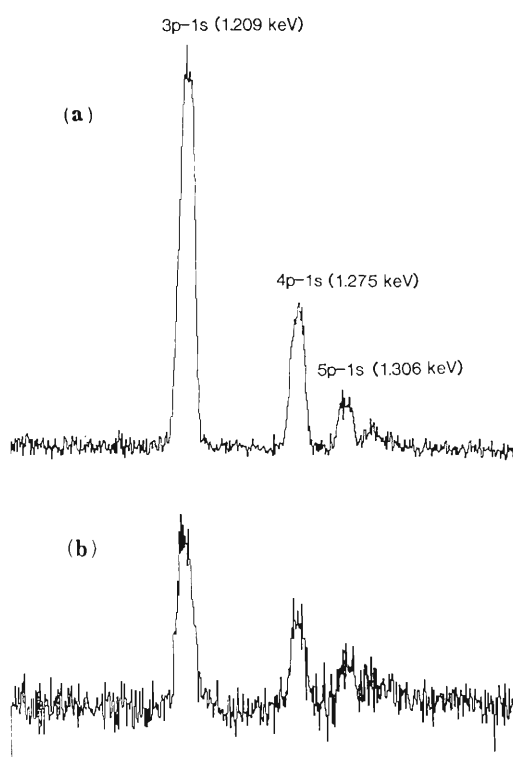


Fig. 1. X-ray energy spectra of K-X rays from  $\text{Ne}^{9+}$  ions in  $\text{N}_2$  gas at (a) 300 Torr and (b) 21 Torr.

spectra, the relative intensity between the transitions depends on the gas pressure. For example, the intensity of the  $4p - 1s$  transition is about 0.5 times as large as that of  $3p - 1s$  at 21 Torr and the ratio decreases to 0.3 at 300 Torr. In Fig. 2, the intensities of the  $4p - 1s$  and  $5p - 1s$  transitions relative to the  $3p - 1s$  transition are plotted against the gas pressure, where the dependence of the absorption of the X-ray photons on the target gas pressure is corrected. The result shows that the occurrence of the radiative transition from a higher level decreases faster than that from a lower level when the gas pressure increases. It is the reason for the shift of the peak energy observed in the low resolution measurements.

This effect is explained as a result of collisional quenching in which a  $\text{Ne}^{9+}$  ion in an excited state transfers to another state by a collision with a target atom before it decays with a radiative emission.<sup>3)</sup> The probability of the collisional quenching depends on the lifetime of the excited state  $\tau$ , the velocity of the ion  $v$ , the density of the target atoms  $N$  and the cross section of the quenching  $\sigma$ . According to Matthews,<sup>4)</sup> the intensity of the radiation from the decay of the excited state is proportional to  $Nv/(1 + Nv\tau\sigma)$ . Thus the relative intensity of the radiation from decay of a state  $i$  to that of a state  $j$  is proportional to  $(1 + Nv\tau_j\sigma_j)/(1 + Nv\tau_i\sigma_i)$  which causes the target gas pressure dependence of the relative intensities.

The experimental data are fitted by the least square calculation using the expression described above. For each value of the quenching cross section of the  $3p$  state  $\sigma_{3p}$ , the most probable values of the cross sections of the  $4p$  and  $5p$  states,  $\sigma_{4p}$  and  $\sigma_{5p}$ , are derived. The values of the lifetime for the states are obtained by multiplying the lifetime of the corresponding states of a hydrogen atom by  $10^{-4}$ . The values of  $\sigma_{4p}$  and  $\sigma_{5p}$  are plotted against the values of  $\sigma_{3p}$  in Fig. 3. The result is that the values of the quenching cross section for the  $4p$  and  $5p$  states are almost the same and larger than  $1 \times 10^{-17}\text{cm}^2$ . This is consistent with that obtained by Matthews for the quenching cross section of  $2^3P_1$  metastable state of 30 MeV  $\text{F}^{7+}$  ions.<sup>4)</sup>

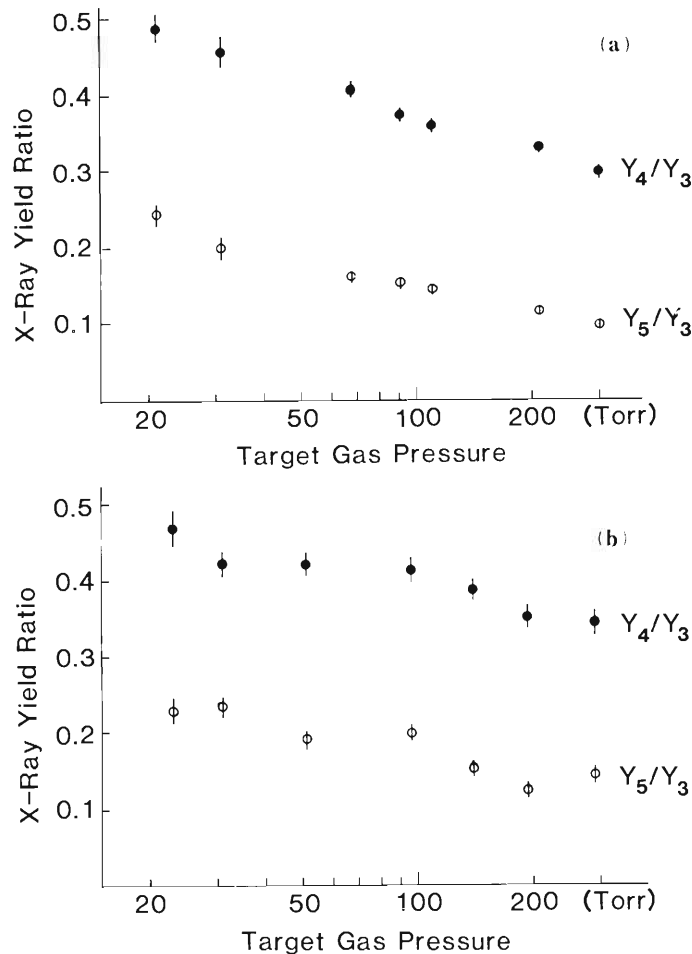


Fig. 2. Target gas pressure dependence of the ratio of intensities of  $5p - 1s$  transition ( $Y_5$ ) and  $4p - 1s$  transition ( $Y_4$ ) to that of  $3p - 1s$  transition ( $Y_3$ ) for (a)  $\text{N}_2$  target and (b)  $\text{Ne}$  target.

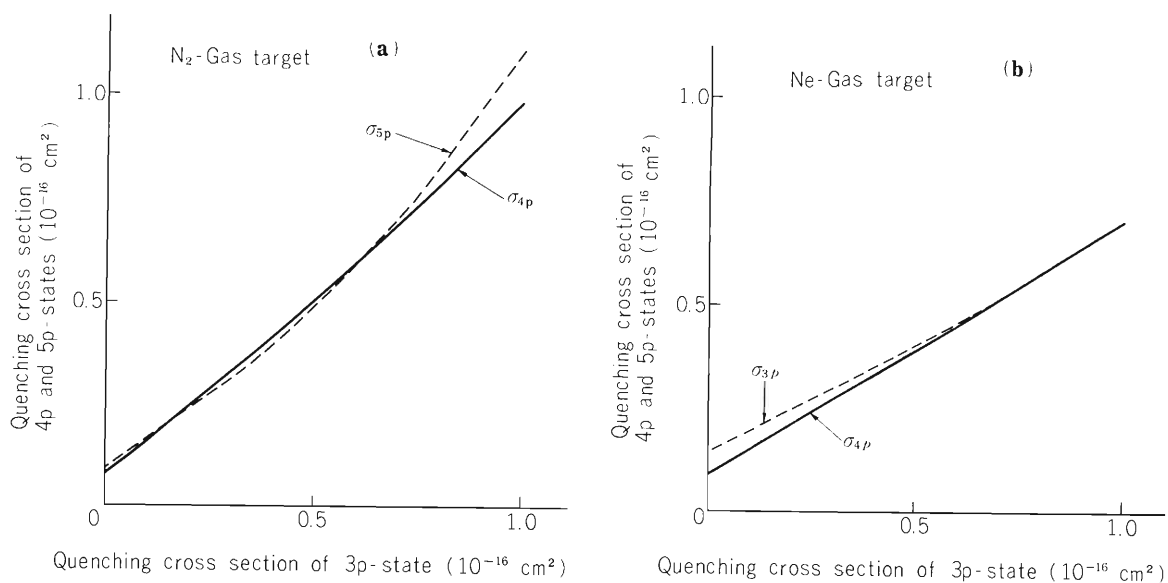


Fig. 3. Relation between values of quenching cross section for excited states 3p, 4p, and 5p ( $\sigma_{3p}$ ,  $\sigma_{4p}$ , and  $\sigma_{5p}$ ) for (a)  $N_2$  target and (b) Ne target.

#### References

- 1) T. Kambara, Y. Awaya, A. Hitachi, M. Kase, I. Kohno, H. Kumagai, and T. Tonuma: RIKEN Accel. Progr. Rep., 15, 71 (1981).
- 2) A. Hitachi, H. Kumagai, and Y. Awaya: Nucl. Instr. and Meth., 195, 631 (1982).
- 3) F. Hopkins: "Method of Experimental Physics, Vol. 17: Atomic Physics, Accelerators", (ed. by P. Richard), Academic Press, New York, p. 355 (1980).
- 4) D. L. Matthews, R. J. Fortner, and G. Bissinger: Phys. Rev. Lett., 36, 664 (1976).

### III-2-3. High Resolution Measurements of K X-Rays from Argon Ions Impinging on Foils

Y. Awaya, T. Kambara, M. Kase, H. Kumagai,  
J. Takahashi, J. Urakawa, T. Matsuo, and M. Namiki

The K X-ray spectra have been studied for Ar ions passing through various target foils in order to investigate the dependence of multiple inner-shell ionization of projectiles on the atomic number of target atom.

The Ar<sup>4+</sup> ions were accelerated by the linear accelerator and momentum analysed by a magnet. The incident energy of Ar ions was 33.6 MeV and target elements were C, Mg, Al, Ca, Ti, V, Cr, Fe, Co, Ni, Zn, Y, Mo, Sn, Ta, and Au. Targets were self-supporting foils but for Ca which was evaporated onto a 10  $\mu\text{g}/\text{cm}^2$  carbon foil. The thickness of the target was in the range of 0.5  $\text{mg}/\text{cm}^2$  to 1  $\text{mg}/\text{cm}^2$  except for C, V, Zn, Ta, and Au. The thickness of C foil was 80  $\mu\text{g}/\text{cm}^2$  and those of V, Zn, Ta, and Au foils were between 2  $\text{mg}/\text{cm}^2$  and 2.6  $\text{mg}/\text{cm}^2$ . The angle between direction of the beam and the target was 60°. The Ar K X-rays emitted from the beam-incident side of the target foil at right angle to the beam direction were measured by a broad range X-ray crystal spectrometer<sup>1)</sup> with a position sensitive proportional counter(PSPC) and a crystal of Ge(111).

Examples of K X-ray spectra from Ar ions are shown in Fig. 1. The target elements are Al, Ti, Fe, and Ta.  $\text{KL}^n$  ( $n = 0, 1, \dots$ ) denotes single K-shell and  $n$  L-shell vacancy configuration in the initial state. Relative intensities of  $\text{KL}^n$  lines vary according to the atomic number of target element,  $Z_2$ . The group of peaks at higher energies are  $\text{K}\alpha$  hypersatellites and  $\text{K}\beta$  satellites. These assignments are made by referring to the previous work on Ar K X-rays excited by N ions done by Tonuma et al.<sup>2)</sup> and by comparing the spectra obtained with and without a Rh-absorber, whose  $L_{\text{III}}$ -absorption edge is 3.004 keV, in front of the PSPC in the present work.

Assuming that the cross section of simultaneous single K-shell and  $n$  L-shell ionization,  $\sigma_{\text{K},n\text{L}}$ , is expressed by a binomial distribution<sup>3)</sup> as

$$\sigma_{\text{K},n\text{L}} = \binom{8}{n} P_{\text{L}}^n (1 - P_{\text{L}})^{8-n} \sigma_{\text{K}}, \quad (1)$$

we obtained the value of  $P_{\text{L}}$  for each target element. Here,  $P_{\text{L}}$  is the ionization probability of an L-shell electron at the impact parameter of zero and  $\sigma_{\text{K}}$  is the K-shell ionization cross section. In the analysis, the intensity of each  $\text{KL}^n$  line is obtained by the least square fitting of multiple Gaussian curves, and a constant value of the fluorescence yield is assumed for  $\text{KL}^n$  lines. The obtained  $P_{\text{L}}$  values are shown as a function of  $Z_2$  in Fig. 2.

When we discuss the  $P_{\text{L}}$  values, some considerations are required on the thickness of the target. It affects the charge state of the projectile, the energy loss of the projectile which causes the change of  $\sigma_{\text{K},n\text{L}}$ , the absorption of projectile X-rays in the target foil and the situation whether the projectile emits the X-rays in the foil or in vacuum and so forth.

According to the work by Baron,<sup>4)</sup> the 33.6 MeV Ar ion is considered to be in equilibrium charge state in C-foil after it passes the thickness of 5  $\mu\text{g}/\text{cm}^2$  and its value is about 11.<sup>5)</sup> Most of Ar K-holes produced near the surface of the target foils will, therefore, be filled in the foils

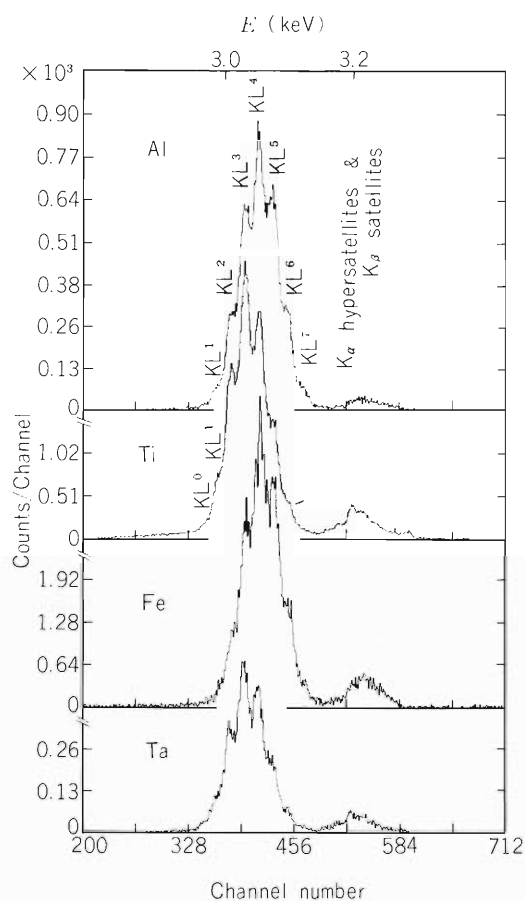


Fig. 1. The K X-rays from 33.6 MeV Ar ions impinging on Al, Ti, Fe, and Ta target foils.

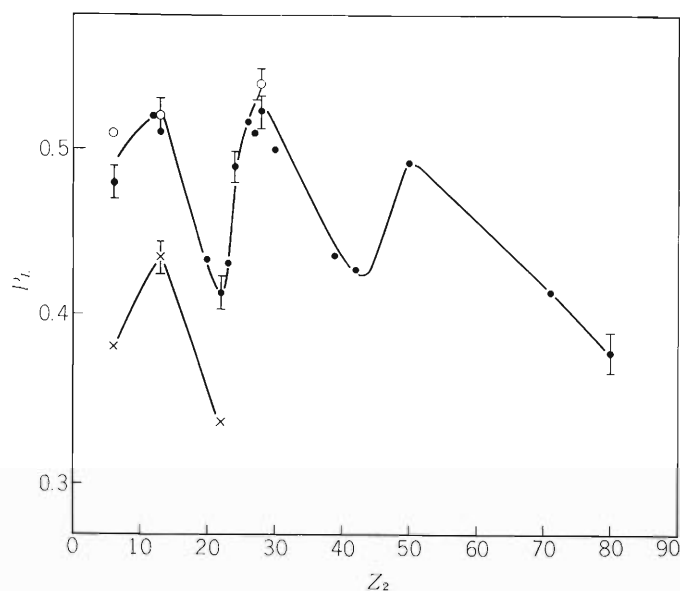


Fig. 2.  $P_L$  values for simultaneous single K-shell and multiple L-shell ionization of Ar ions vs. the atomic number of target elements.

●, ○ :  $P_L$  for 33.6 MeV Ar ions and ○ for thinner foils;

× :  $P_L$  for 21.1 MeV Ar ions.

Curves are only to guide the eye.

for the target thicknesses used and the velocity of the projectile, except in the case of the C target. The thickness of foil, which attenuates Ar K X-rays to a half of its initial intensity, is about  $2 \text{ mg/cm}^2$  for Ti and  $0.3 \text{ mg/cm}^2$  for Ta.

The effect of target thickness on  $P_L$  was examined for C, Al, and Ni targets by using two foils of different thicknesses: 20 and  $80 \text{ }\mu\text{g/cm}^2$  for C, 0.20 and  $1 \text{ mg/cm}^2$  for Al, and 0.45 and  $0.89 \text{ mg/cm}^2$  for Ni. The open circles in Fig. 2 show the  $P_L$  values for thinner foils. It is found when the thickness of the target increases, the  $P_L$  value decreases. Change of  $P_L$  with the incident energy was also studied for  $80 \text{ }\mu\text{g/cm}^2$  C,  $0.2 \text{ mg/cm}^2$  Al and  $0.9 \text{ mg/cm}^2$  Ti targets. The  $P_L$  values for  $E = 21.1 \text{ MeV}$  are shown by crosses in Fig. 2.

By taking into consideration these facts and also the decrease of Ar K-shell ionization cross section owing to the energy loss of Ar ions in the target, most of Ar K X-rays detected can be regarded to be emitted within first  $1 \text{ mg/cm}^2$  of the target and that the behaviour of  $P_L$  values vs.  $Z_2$  shown in Fig. 2 reflects the atomic structure of the target element in collision system.

As is seen in Fig. 2, the  $P_L$  value displays oscillatory behaviour against  $Z_2$ . It reaches the first minimum at around  $Z_2 = 22$  and probably the second one at around  $Z_2 = 45$ , where the L-shell binding energy of highly ionized Ar ions matches the L-shell and M-shell binding energy of the target atoms, respectively. This may suggest that the electron capture cross section to the

L-shell of the Ar ions from the target atoms varies according to  $Z_2$  and becomes large when the level matching occurs, even though the velocity of Ar ions is comparable to or a little higher than the velocity of bound electron concerned.

Further analysis is in progress.

#### References

- 1) A. Hitachi, H. Kumagai, and Y. Awaya: Nucl. Instr. Meth., 195, 631 (1982).
- 2) T. Tonuma, Y. Awaya, T. Kambara, H. Kumagai, I. Kohno, and S. Özkök: Phys. Rev. A, 20, 989 (1979).
- 3) J. M. Hansteen and O. P. Mosebekk: Phys. Rev. Lett., 29, 1361 (1972); J. H. McGuire and P. Richard: Phys. Rev. A, 8, 1374 (1973).
- 4) E. Baron: IEEE Trans. Nucl. Sci., NS-19, 256 (1972).
- 5) Y. Baudinet-Robinet: Phys. Rev. A, 26, 62 (1982).

### III-2-4. Argon L-MM Auger Spectra in $\text{Ar}^{n+} + \text{Ar}$ Collisions (I)

#### Identification of Auger Lines

A. Yagishita, T. Kambara, M. Kase, T. Tonuma,  
T. Matsuo, J. Urakawa, J. Takahashi,  
H. Kumagai, and Y. Awaya

Auger electrons are ejected from atoms or molecules when fast charged particles are incident on them. Much information on both atomic structures and excitation mechanisms can be obtained from the electron energy distributions. Consequently, a number of works concerning the ejected electrons in ion-atom collisions has been reported so far.<sup>1)</sup> But, measurements of the electrons originating from heavy-ion atom collisions are scarce in the energy range higher than a few MeV. In order to investigate heavy-ion atom collisions in this energy region, we have constructed a high-resolution electron spectrometer. Some measurements have been made for the Auger electrons produced in  $\text{Ar}^{n+} + \text{Ar}$  collisions, using the beams from the heavy-ion linear accelerator.

The electron spectrometer consists of electron optical lenses and a hemispherical electrostatic energy filter of mean radius of 50 mm. An electron gun is prepared for the alignment and calibration of the spectrometer. The energy resolution  $\Delta E/E$  is about  $10^{-4}$  at the best condition. The target Ar gas is effused from a multi-channel capillary positioned a few milli-meters below the collision region. The detail of the apparatus has been described in the previous report.<sup>2)</sup>

The result of the measurement is shown in Fig. 1. It was obtained with incident energy of 4.3 MeV and at emission angle of  $132^\circ$  with respect to the direction of the ion beam. The range of measured electron energy is from 80 to 330 eV, scanning with 0.52 eV step interval. The L-MM Auger peaks from the projectile Ar ions shift to the energy region below 80 eV in this condition according to the Doppler shift, so that the peaks which appeared are attributed to the

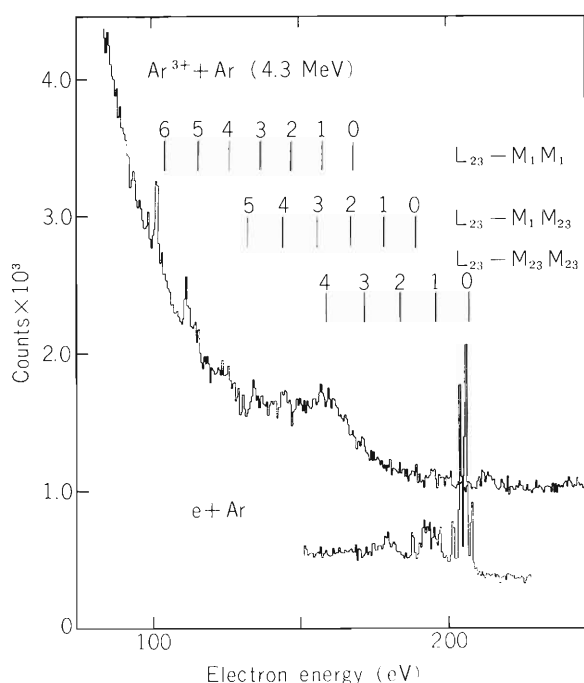


Fig. 1. An electron spectrum obtained for (4.3 MeV -  $\text{Ar}^{3+} + \text{Ar}$ ) system compared with that for (1 keV -  $e + \text{Ar}$ ) system, measured at  $132^\circ$  with respect to the direction of the incident beam. The lines above spectrum indicate the calculated energies for the corresponding transitions denoted at the right of them. The number on each line shows the number of the 3p-hole in the initial state.

electrons from the targets. The energy of the electrons was calibrated by the measurement of Ar L-MM Auger spectrum induced by 1.0 keV electron impact using the electron gun. The energy values of L-MM peaks were referred to the results by Werme et al.<sup>3)</sup> The present energy resolution is 0.7 eV FWHM. The uncertainty of the energy determined is estimated to be less than  $\pm 0.2$  eV.

The spectrum is characterized by two sharp peaks located at 101 and 112 eV, and by a broad peak extending through 120 to 200 eV. This structure is quite different from that obtained by electron impact. For the identification of the Auger peaks, we compared the spectrum with the theoretical calculation by Larkins, who have shown that the Auger lines shift to the lower energy as the degree of outer-shell ionization increases.<sup>4)</sup> The lines above spectrum in Fig. 1 indicate the energies calculated with the adiabatic model by Larkins. Two isolated peaks, at 101 and 112 eV, are considered to be due to the transitions  $L_{23}\text{-}M_1M_1(N = 6)$  and  $L_{23}\text{-}M_1M_1(N = 5)$ , respectively, where the number N indicates the degree of the  $M_{23}$ -shell ionization in the initial state. Stolterfoht et al.<sup>5)</sup> have also found Auger peaks corresponding to the transitions  $L_{23}\text{-}M_1M_1(N = 4)$  and  $L_{23}\text{-}M_1M_1(N = 5)$ . The isolated peak corresponding to the  $L_{23}\text{-}M_1M_1(N = 6)$  transition was observed for the first time in the present measurement. The broad peak may be ascribed to the superposition of many transitions, such as  $L_{23}\text{-}M_1M_{23}(N = 5, 4, 3, 2, 1, 0)$  and  $L_{23}\text{-}M_{23}M_{23}(N = 4, 3, 2, 1, 0)$ .

The present measurement shows that the high-resolution Auger spectroscopy for heavy-ion atom collisions is a powerful method to determine the energy levels for multiply-ionized atoms.

## References

- 1) M.E. Rudd and J.H. Macek: Case Studies in Atomic Collisions, North-Holland/American Elsevier, p. 46 (1974).
- 2) A. Yagishita and T. Nakamura: IPCR Cyclotron Progr. Rep., 14, 143 (1980).
- 3) L.O. Werme, T. Bergmark, and K. Siegbahn: Physica Scripta, 8, 149 (1973).
- 4) F.P. Larkins: J. Phys. B, 4, 1 (1971).
- 5) N. Stolterfoht, D. Schneider, and H. Gabber: Phys. Lett., 47A, 271 (1974).

### III-2-5. Argon L-MM Auger Spectra in $\text{Ar}^{n+} + \text{Ar}$ Collisions (II)

#### Energy Dependence of the Auger Spectra

T. Matsuo, J. Urakawa, A. Yagishita,  
Y. Awaya, T. Kambara, M. Kase,  
J. Takahashi, and H. Kumagai

The energy distributions of Ar L-MM Auger electrons produced in  $\text{Ar}^{3+} + \text{Ar}$  collisions have been measured at collision energies of 5.3, 11.5, and 14.3 MeV. The projectile ions were accelerated by the RILAC. The measurement was made in the energy range from 80 to 340 eV, scanning with 0.52 eV step interval. The Auger spectra obtained are shown in Fig. 1, where the continuous background underlying the Auger spectrum was subtracted. The lines above spectra indicate the Auger electron energies calculated by Larkins.<sup>1)</sup> The identification of the Auger peaks has been discussed in the preceding report.<sup>2)</sup> We discuss here about the energy dependence of the distribution of the Auger electron energy. They are characterized by isolated peaks, located at 101 and 112 eV, and by broadened structure extended through 120 to 250 eV. It is notable that the intensity of the  $L_{23}\text{-}M_1M_1$  ( $N = 6$ ) peak becomes weak as the collision energy is increased, while the broadened structure between 120 and 250 eV is enhanced. Besides, a remarkable structure can be seen in the energy range from 200 to 250 eV. This structure can not be identified as due to the  $L_{23}\text{-}MM$  transitions, because the multiple-ionization of the M-shell causes the  $L_{23}\text{-}MM$  Auger spectrum shift to the lower energy. They are considered to be due to the Auger electrons resulting from the  $L_1$ -shell vacancy. In the Auger electron spectrum by electron impact,

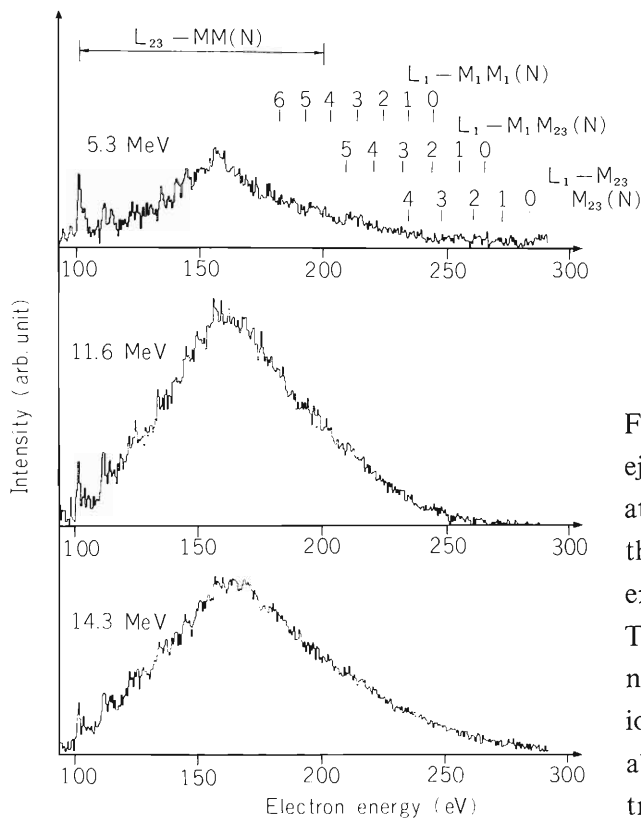


Fig. 1. Energy distribution of electrons ejected in  $\text{Ar}^{3+} + \text{Ar}$  collisions, measured at  $132^\circ$  with respect to the direction of the ion beam and with incident ion energies of 5.3, 11.5, and 14.3 eV. The intensities of the spectra are normalized with the number of incident ions and the target pressure. The lines above spectra indicate the  $L_1\text{-}MM(N)$  transition energies calculated by Larkins.

no significant peak has been observed in the energy range between 220 and 300 eV, corresponding to the transition energies of the Ar  $L_1$ -MM Auger electrons, because of the high Coster-Kronig transition probability for filling of a 2s-vacancy by a 2p electron. Here, it should be noted that as the degree of ionization (N) in the M-shell increases, the  $L_1$ - $L_{23}M$  Coster-Kronig transition process becomes energetically forbidden. Larkins have also predicted that the  $L_1$ - $L_{23}M_{23}$  Coster-Kronig process can not occur for  $N > 3$ , and the  $L_1$ - $L_{23}M_1$  process for  $N > 2$ . In the figure, the energies of the  $L_1$ -MM Auger electrons calculated by Larkins<sup>1)</sup> are also indicated. The spectrum between 200 eV and 250 eV is well explained by the Auger process resulting from the Ar  $L_1$ -shell vacancy production with simultaneous ionization of the M-shell.

#### References

- 1) F.P. Larkins: J. Phys. B, 4, 1 (1971).
- 2) A. Yagishita, T. Kambara, M. Kase, T. Tonuma, T. Matsuo, J. Urakawa, J. Takahashi, H. Kumagai, and Y. Awaya: p. 75 in this report.

### III-2-6. Argon L-MM Auger Spectra in $\text{Ar}^{n+} + \text{Ar}$ Collisions (III)

Structure of Argon L-MM Auger Spectra in 21 MeV  $\text{Ar}^{4+}$   
Impact on Ar

J. Urakawa, T. Matsuo, A. Yagishita, Y. Awaya,  
T. Kambara, M. Kase, J. Takahashi, and H. Kumagai

Some studies have been made for the L-Auger electrons in  $\text{Ar}^{3+} + \text{Ar}$  collisions with incident energies from 800 keV to 14 MeV, using the heavy-ion linear accelerator (RILAC).<sup>1),2)</sup> It has been shown that many satellite lines resulting from multi-vacancy states appear dominantly. This indicates that several electrons are ejected from  $M_{23}$ -shell, once L-shell electrons are ionized. When the outer shell is partly stripped, a large number of different vacancy states are created. But when the outer shell is more and more stripped, the number of states produced becomes limited. For example, two isolated peaks corresponding to the transition  $L_{23}-M_1M_1(N)$  were observed in  $\text{Ar}^{3+} + \text{Ar}$  collisions with the incident energy of 4.3 MeV (see Fig. 1 in Ref. 1), where N takes the values of 6 and 5, and indicates the degree of  $M_{23}$ -shell ionization. This result is consistent with that calculated by Larkins.<sup>3)</sup>

The strong Argon  $L_{23}$ -Auger yield is expected to be induced by the projectile with the same velocity as the orbital velocity of the  $L_{23}$  bound electrons; corresponding energy for Argon ion is 21 MeV. Furthermore, the strong electron stripping of the outer shell is expected to be produced by sufficiently heavy projectiles such as Argon ion. Since the target atom is set in motion by the recoil, Doppler broadening of target Auger line is induced. The Doppler broadening is also expected to become narrow as collision energy increases, because the recoil velocity of the target atom is calculated approximately as

$$v_t(b) = \frac{Z_t \cdot Z_p \cdot e^2}{m_t \cdot b} (2m_p/E_p)^{1/2},$$

where  $Z_t(m_t)$  and  $Z_p(m_p)$  are the atomic numbers(mass) of the target and projectile ions, respectively,  $b$  is the impact parameter and  $E_p$  is the projectile energy.<sup>4)</sup> Therefore, in order to obtain the detailed structure of the isolated Auger lines  $L_{23}-M_1M_1(N = 6, 5)$ , the spectrum in the 21 MeV  $\text{Ar}^{4+} + \text{Ar}$  collision was measured in the energy range from 90 to 156 eV at 0.13 eV step. The experimental apparatus, procedure and condition have been described previously.<sup>1),2)</sup> The measured spectrum is shown in Fig. 1. It is clearly seen that the  $L_{23}-M_1M_1(N = 6, 5, 4)$  peaks are divided either into a few sharp peaks or broad ones (compare Fig. 1 in Ref. 1).

Two sharp peaks of the  $L_{23}-M_1M_1(6)$  are positioned at 100.3 eV and 102.7 eV, and the intensity ratio between them is about 2:1. They are considered to correspond to the transitions toward the final state  $\text{Ar}^{8+}(1s^22s^22p^6)1S_0$  from the initial vacancy states  $\text{Ar}^{7+}(1s^22s^22p^53s^2)-L_3(^2P_{3/2})$  and  $L_2(^2P_{1/2})$ , respectively, because the ratio of the peak intensity is almost the same as that of the degeneracy( $2J + 1$ ) between the initial states, and the energy splitting of 2.4 eV is nearly equal to the difference between the  $L_2(^2P_{1/2})$  and  $L_3(^2P_{3/2})$  binding energies (2.1 eV for

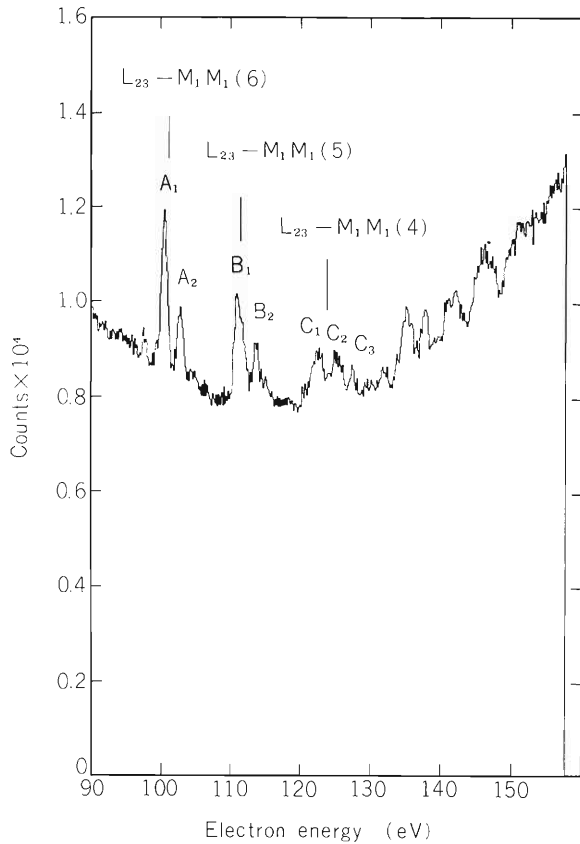


Fig. 1. Argon L-Auger electron spectra produced by 21 MeV  $\text{Ar}^{4+}$  bombardment on Argon. The notation  $L_{23}\text{-}M_1M_1(N)$  denotes single  $L_{23}$ -shell and  $N$ th degree  $M_{23}$ -shell vacancies in the initial state.

neutral Ar).

The structure of the  $L_{23}\text{-}M_1M_1(5)$  is complicated because of the superposition of many Auger transition lines stemming from various multiplets of the initial and final states in the  $L_{23}\text{-}M_1M_1(5)$ .

The structure of the  $L_{23}\text{-}M_1M_1(4)$  is more complicated than that of the  $L_{23}\text{-}M_1M_1(5)$ . This complexity is induced by superposition of many Auger transition lines stemming from double L-shell ionization and various multiplets of the initial and final states for the  $L_{23}\text{-}M_1M_1(4)$  transition (refer to Ref. 3). In the energy range between 128 and 156 eV, there is a broad "humps" in addition to the broad Auger peaks. It is tentatively attributed to a superposition of many weak Auger transition lines stemming from double L-shell ionization in addition to several Auger transition lines ( $L_{23}\text{-}M_1M_{23}(5)$ ,  $L_{23}\text{-}M_1M_{23}(4)$ ,  $L_{23}\text{-}M_{23}M_{23}(4)$ ).

Table 1 shows a partial list of measured line energies of designated Ar L-Auger electrons observed in the present work. The line energies of  $L_{23}\text{-}M_1M_1(N)$  ( $N = 6, 5$ ) transitions measured by us are smaller than those calculated by Larkins with the discrepancy of about 3 eV, but the line energy of  $L_{23}\text{-}M_1M_1(4)$  transition agrees well with that calculated by Larkins. Results of Larkins for the line energies of  $L_{23}\text{-}M_{23}M_{23}(N)$  transitions agree well with that of  $L_{23}\text{-}M_{23}M_{23}(0)$  transition measured in electron impact on Argon for  $N = 0$  and those of  $L_{23}\text{-}M_{23}M_{23}(N)$  transitions measured by Stolterfoht et al.<sup>5)</sup> for  $N = 4, 3$ , and 2. These Auger electron energies decrease linearly with an average shift of 11 eV per degree of  $M_{23}$ -ionization. But the line energy of  $L_{23}\text{-}M_1M_1(0)$  transition is larger than that calculated by Larkins with a discrepancy of about 10 eV. Using the experimental energy values of  $L_{23}\text{-}M_1M_1(0)$  transition and  $L_{23}\text{-}M_1M_1(N)$  ( $N = 4, 5$ , and 6) transitions, the average shift per degree of  $M_{23}$ -ionization for  $L_{23}\text{-}M_1M_1(N)$  transitions is derived to be 13 eV on the assumption that the Auger electron energies of  $L_{23}\text{-}M_1M_1(N)$  transitions decrease linearly with degree of  $M_{23}$ -ionization.

Table 1. A partial list of measured transition energies of designated Ar L-Auger electrons produced by bombardment of Ar with 21 MeV Ar<sup>4+</sup>. For comparison the transition energies calculated by Larkins<sup>3)</sup> are also included. The “peak label” refers to Fig. 1. Values on the left in line energy are weighted averages for peaks of L<sub>23</sub>M<sub>1</sub>M<sub>1</sub>(N) transitions.

Peak label	Line energy(eV)	Larkins(eV)	Tentative assignment
L <sub>23</sub> -M <sub>1</sub> M <sub>1</sub> (6)	A <sub>1</sub>	100.3	Ar <sup>7+</sup> (2p <sup>5</sup> ( <sup>2</sup> P <sub>3/2</sub> )3s <sup>2</sup> )
	A <sub>2</sub>	102.7	Ar <sup>7+</sup> (2p <sup>5</sup> ( <sup>2</sup> P <sub>1/2</sub> )3s <sup>2</sup> )
L <sub>23</sub> -M <sub>1</sub> M <sub>1</sub> (5)	B <sub>1</sub>	110.3	Ar <sup>6+</sup> (2p <sup>5</sup> ( <sup>2</sup> P <sub>3/2</sub> )3s <sup>2</sup> 3p)
	B <sub>2</sub>	113.2	Ar <sup>6+</sup> (2p <sup>5</sup> ( <sup>2</sup> P <sub>1/2</sub> )3s <sup>2</sup> 3p)
L <sub>23</sub> -M <sub>1</sub> M <sub>1</sub> (4)	C <sub>1</sub>	121.6	( <sup>2</sup> P <sub>3/2</sub> )
	C <sub>2</sub>	124.2	Ar <sup>5+</sup> (2p <sup>5</sup> 3s <sup>2</sup> 3p <sup>2</sup> )
	C <sub>3</sub>	126.3	( <sup>2</sup> P <sub>1/2</sub> )
			( <sup>1</sup> S)
			→ Ar <sup>8+</sup> ( <sup>1</sup> S)
			→ Ar <sup>7+</sup> (3p( <sup>2</sup> P))
			→ Ar <sup>6+</sup> (3p <sup>2</sup> ( <sup>1</sup> D))
			( <sup>3</sup> P)

The uncertainty of the electron energy is estimated to be less than ± 0.2 eV.

## References

- 1) A. Yagishita, T. Kambara, M. Kase, T. Tonuma, T. Matsuo, J. Urakawa, J. Takahashi, H. Kumagai, and Y. Awaya: p. 75 in this report.
- 2) T. Matsuo, J. Urakawa, A. Yagishita, Y. Awaya, T. Kambara, M. Kase, J. Takahashi, and H. Kumagai: p. 77 in this report.
- 3) F. P. Larkins: J. Phys. B, 4, 1 (1971).
- 4) R. Mann, F. Folkmann, R. S. Peterson, Gy. Szabo, and K - O. Groeneveld: *ibid.*, 11, 3045 (1978).
- 5) N. Stolterfoht, D. Schneider, and H. Gabler: Phys. Lett., 47A, 271 (1974).

## III-2-7. Angular Distribution of Sn L X-Rays

J. Takahashi, A. Hitachi,\* Y. Awaya, H. Kumagai,  
T. Kambara, M. Kase, T. Tonuma, and A. Yagishita

We have studied the multiple ionization of inner shell electrons by measuring emitted X-rays with high resolution, systematically.<sup>1)</sup> Ionization probabilities  $P_L$  and  $P_M$  were derived from these experiments, and the reduced parameters to fit the universal curve were obtained. In this analysis it was assumed that satellite X-rays were isotropic because Jamison and Richard<sup>2)</sup> had shown that the polarization of KL X-rays from Al target bombarded by He or Li ions was smaller when the incident energy was larger. In order to study this point, we measured the K X-rays from Ti target excited by 82 MeV  $N^{7+}$  (5.9 MeV/amu) with a broad range X-ray crystal spectrometer<sup>3)</sup> and found that the satellite X-rays were isotropic.<sup>4)</sup> There is no report on L X-rays emitted after the multiple ionization, therefore, L X-rays of Sn have been measured by the broad range X-ray crystal spectrometer and a Si(Li) detector. This report gives an analysis of the experimental results.

Target was a self-supporting metallic foil Sn(1  $\mu$ m). It was excited by 82 MeV  $N^{7+}$  ion beam from the cyclotron. Typical spectrum obtained by the Si(Li) detector for Sn L X-rays is shown in Fig. 1 with  $\chi^2$ -fitting by the FACOM M200 computer. The spectrum was divided into 5 peaks assuming a gaussian form. Main components of the peaks are  $L_\ell$ ,  $L_\alpha$ ,  $L_{\beta_1}$ ,  $L_{\beta_2+15}$ ,  $L_{2,3}$ , respectively, and peak positions are shifted to higher energy side owing to the multiple ionization of M shell electron. Weak lines are included in each peak. Arrows indicate energies of the lines

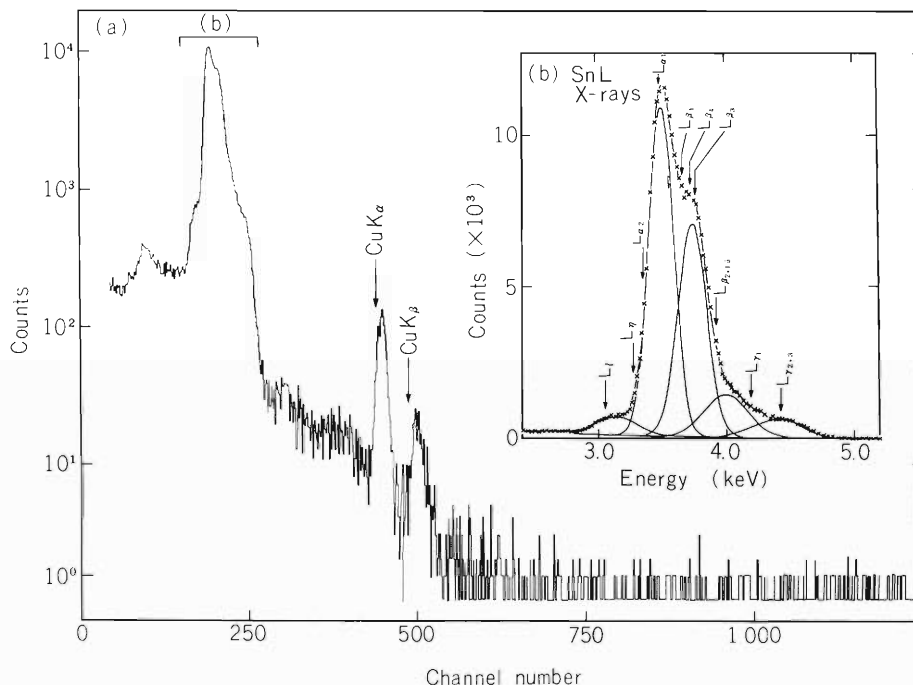


Fig. 1. (a) Sn L X-ray spectrum obtained by the Si(Li) detector at  $25^\circ$ . Incident beam was 82 MeV  $N^{7+}$ . Cu  $K_\alpha$  and  $K_\beta$  peaks may be due to the scattering from a copper part in the chamber. (b) Solid curves are  $\chi^2$ -fitting by the computer.

\* Present address: University of Notre Dame.

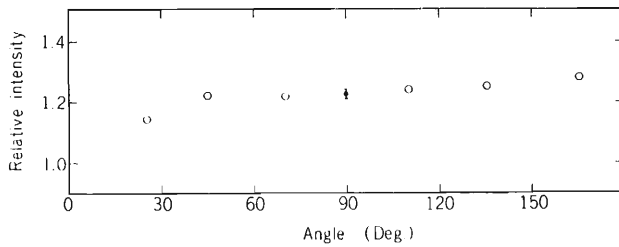


Fig. 2. Angular distribution of total intensity normalized by measurement of another Si(Li) detector at a fixed angle ( $90^\circ$ ) and corrected for self-absorption using the absorption coefficient of  $L_{\alpha 1}$ .

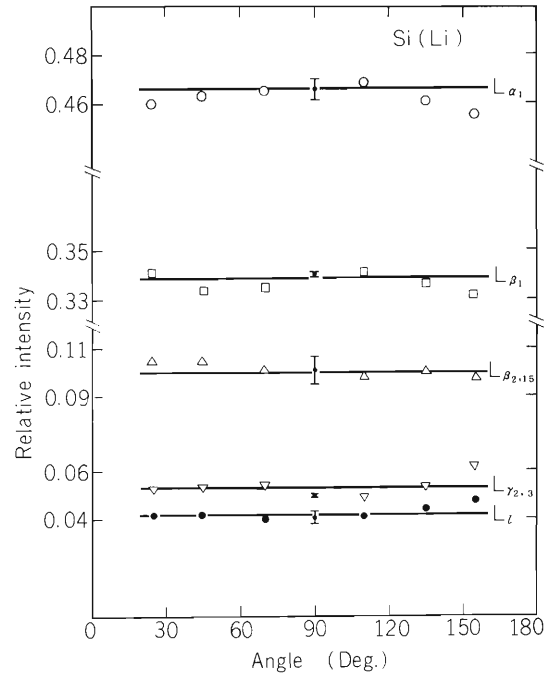


Fig. 3. Angular distribution of each peak in Fig. 1, relative to the total intensity.

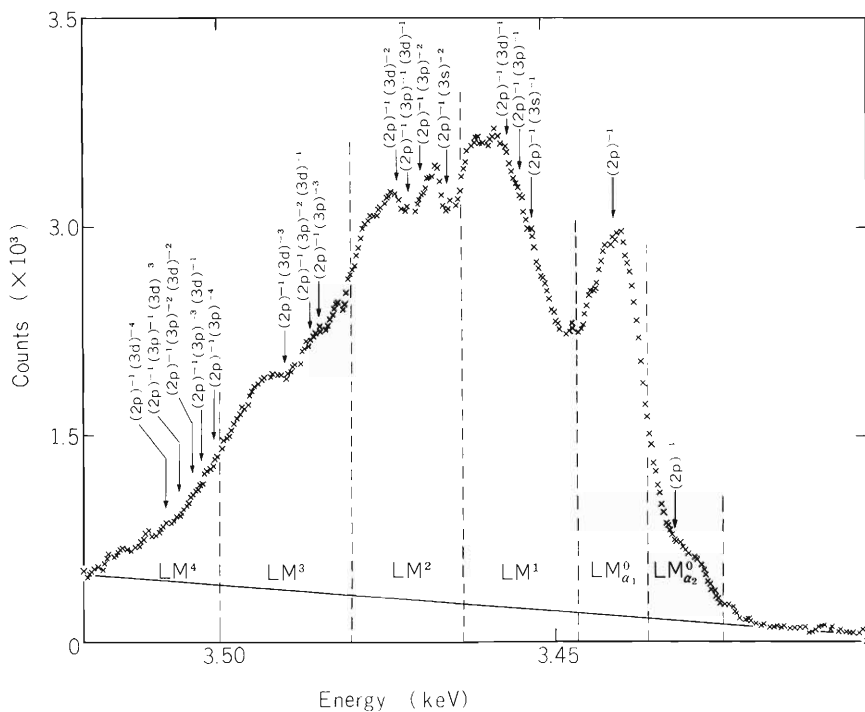


Fig. 4. Sn  $L_{\alpha}$  X-ray spectrum obtained by the broad range X-ray crystal spectrometer at  $70^\circ$ . Incident beam was 82 MeV  $N^{7+}$ . The spectrum is divided into 6 groups:  $LM^0_{\alpha 1}$ ,  $LM^1$ ,  $LM^2$ ,  $LM^3$ ,  $LM^4$ , and  $LM^0_{\alpha 2}$ , by dotted lines, where  $LM^x$  denotes the initial state which has a vacancy at  $L_3$  shell and  $x$  vacancies at M shell. The configuration  $(2p)^{-1} (3\ell)^{-x}$  denotes the initial state which has a vacancy at  $2p$  shell and  $x$  vacancies at  $3\ell$  shell ( $l = s, p, d$ ).

without multiple ionization.<sup>5),6)</sup> Figure 2 shows the angular dependence of the total intensity which is normalized by the measurement of another Si(Li) detector placed at a fixed angle ( $90^\circ$ ). It is seen that total intensity is high at  $155^\circ$  and low at  $25^\circ$ . A study on why intensity changes with the observed angle is in progress. The relative intensities of each peak to the total intensity are shown in Fig. 3. They do not change with angle within experimental errors.

Typical spectrum of  $L_\alpha$  X-rays obtained by the broad range X-ray crystal spectrometer is shown in Fig. 4 with transition energies calculated using the computer program of Herman and Skillman.<sup>7)</sup> Actually, the multiplet from an initial and final state configuration and presence of vacancies at N shell may broaden a peak. Since each transition is not resolved and does not always agree with rather broad peaks obtained experimentally, the spectrum is divided into 6 groups:  $LM_\alpha^0$ ,  $LM^1$ ,  $LM^2$ ,  $LM^3$ ,  $LM^4$ , and  $LM_{\alpha_2}^0$ , as shown by dotted lines. The integrated counts of each group relative to the total counts of  $L_\alpha$  X-rays are plotted as a function of emitted photon angle in Fig. 5. All intensity groups are constant within experimental errors.

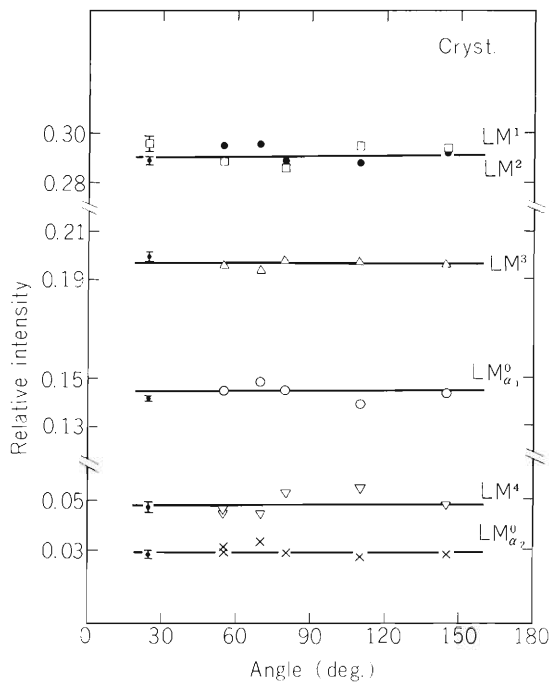


Fig. 5. Angular distribution of each intensity group in Fig. 4, relative to the total  $L_\alpha$  intensity.

## References

- 1) Y. Awaya: "Electronic and Atomic Collisions", (Ed. by N. Oda and K. Takayanagi), North-Holland Publishing Co., p. 325 (1980).
- 2) K. A. Jamison and P. Richard: *Phys. Rev.*, **17**, 1642 (1978).
- 3) A. Hitachi, H. Kumagai, and Y. Awaya: *Nucl. Instr. and Methods*, **165**, 631 (1982).
- 4) A. Hitachi, Y. Awaya, T. Kambara, M. Kase, H. Kumagai, T. Tonuma, and A. Yagishita: *RIKEN Accel. Progr. Rep.*, **15**, 69 (1981).
- 5) J. A. Bearden: *Phys. Rev.*, **39**, 78 (1967).
- 6) J. H. Scofield: *Atomic Data and Nucl. Data Tables*, **14**, 121 (1974).
- 7) F. Herman and S. Skillman: "Atomic Structure Calculations", Prentice-Hall Inc., Englewood Cliffs, New Jersey (1963).

### III-2-8. Production of Highly Charged Ions by Heavy-Ion Bombardment of Rare-Gas Targets

T. Tonuma, M. Kase, T. Matsuo, J. Urakawa, J. Takahashi,  
H. Kumagai, T. Kambara, I. Kohno,  
S. Özkök,\* and Suck Hee Be

An experimental apparatus to measure secondary ions produced in collision of heavy ions with gaseous targets has been reported.<sup>1)</sup> The apparatus was newly set up in order to carry out the experiment using the beam from the heavy-ion linac. The exhausting system and the analyzer magnet were improved. The apparatus is evacuated by a 5000  $\ell$ /sec cryo pump and a 220  $\ell$ /sec turbo molecular pump. The background and operating pressure were  $7 \times 10^{-8}$  Torr and  $1.3 \times 10^{-6}$  Torr, respectively.

A schematic diagram of the apparatus is shown in Fig. 1. A heavy-ion beam crosses a gaseous target emerging from a gas jet and ionizes gas atoms. Ionized atoms, namely secondary ions, are extracted perpendicularly to the beam direction by an electric field applied between the parallel plate electrodes and are focused on a detector by an Einzel lens and the analyzer magnet. The secondary ions are detected by a channeltron and the output signals are amplified and integrated by MCS(multi-channel scalar) through a SCA circuit. The charge states of the ions are analyzed by scanning the magnetic field.

Figure 2 shows a charge-state spectrum of secondary Ar ions produced by 37 MeV Ar<sup>4+</sup> ion-bombardment. The size of beam spot was 1 mm wide and 2 mm high on the target and the beam current was about 1 nA. The electric potential was kept at 2 kV throughout the measurement. The channel advances with 15 nC of integrated beam charge on the Faraday cup. The peaks corresponding to Ar<sup>1+</sup> and Ar<sup>2+</sup> have fine structures caused by the beam fluctuation, which will have to be improved.

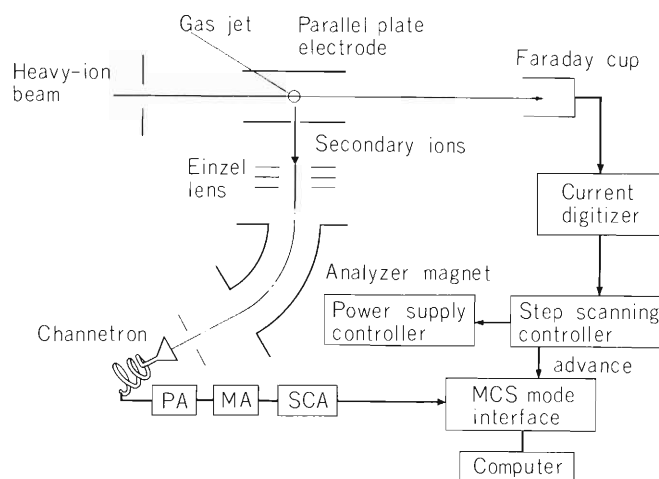


Fig. 1. Schematic diagram of the apparatus.

\* Permanent address: University of Istanbul Nuclear Physics Dept., Istanbul, Turkey.

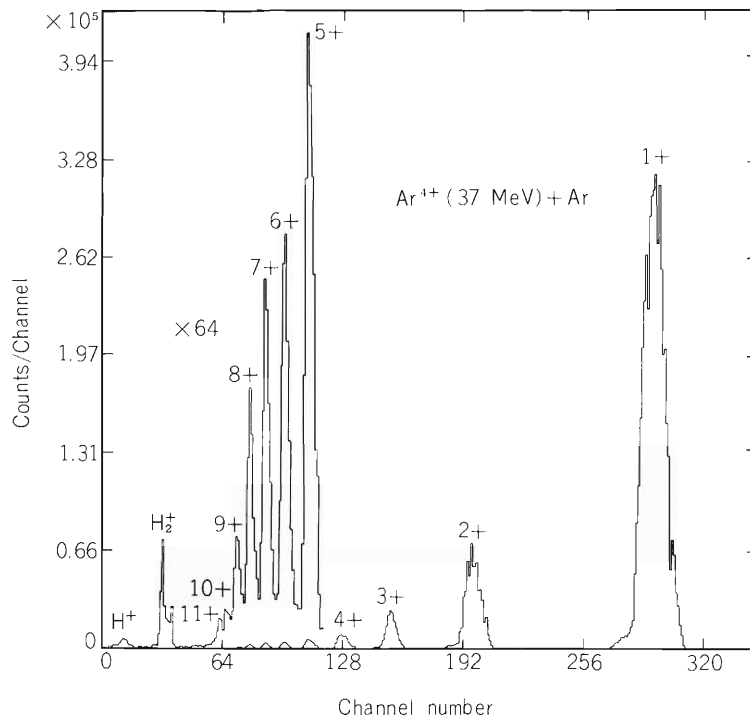


Fig. 2. Charge-state spectrum of the secondary Ar ions produced by 37 MeV Ar<sup>4+</sup> ion-bombardment.

#### Reference

- 1) T. Tonuma, A. Yagishita, M. Kase, T. Kambara, Y. Awaya, H. Kumagai, and I. Kohno: RIKEN Accel. Progr. Rep., 15, 72 (1981).

### III-2-9. Mechanical Design of Apparatus to Measure Secondary Ions

T. Tonuma, T. Chiba, and A. Yagishita

The apparatus was designed and constructed to have an experimental study of secondary ions produced by heavy ion bombardment on rare-gas targets. The mechanical layout of the apparatus is shown in Fig. 1. The apparatus consists mainly of a gas nozzle, parallel plate electrodes, an Einzel lens, an analyzer magnet and a detector part. The gas nozzle has multi-capillary jet whose inside diameter is 1 mm. It can be moved up and down to set the optimum condition. The parallel plate electrodes are arranged to have a distance of 2 cm between them and one electrode is provided with a slit 2 mm wide and 6 mm high for the extraction of ions. The gas nozzle is inserted between the electrodes. The Einzel lens consists of three plates which have slits of 12 mm  $\times$  12 mm and is used to focus the secondary ions on a detector. The chamber itself is made of stainless steel and the electrodes and the lens are made of molybdenum. The characteristics of the analyzer magnet are as follows: 3 cm of pole gap, 18 cm of effective radius, 60° of deflection angle and 16.1° of entrance and exit angles which focus the ions vertically and horizontally. Maximum magnetic field is about 6 kG. A quartz support is used to adjust the position and the size of the beam spot. The chamber is evacuated with 5000  $\ell$ /sec cryo pump and a 220  $\ell$ /sec turbo molecular pump.

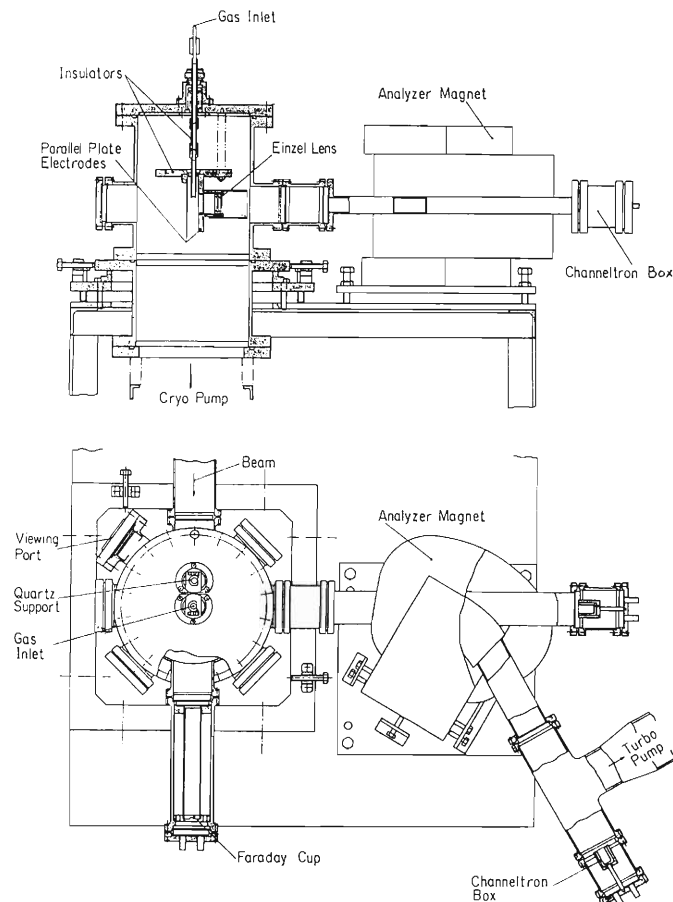


Fig. 1. Layout of the apparatus.

### III-2-10. Scan Controller for Secondary Ion Experiment

M. Kase, H. Kumagai, T. Tonuma, and K. Nishi

A scan control circuit for the secondary ion experiment has been developed. For the experiment, one has to change accurately the extraction voltage or the magnet current by fine steps remotely from the measurement room which is at a distance of about 70 m from the experimental area. In order to minimize the number of signal lines between the two places and to eliminate the noise disturbance on the signal lines, a pulse-counting method is employed. The principle is shown in Fig. 1. The scan controller sends a series of pulses (0.6 msec width, 400 Hz) to the power supply system via a 70 m signal line. The power supply system has a binary counter and a 16 bit digital-to-analog converter (DAC). The DAC provides the power supply with the reference dc voltage,  $V_{ref}$ , a magnitude of which is proportional to the total number of pulses stored in the counter. The output (a high voltage (up to 5 kV) in the case of the voltage scan or a constant current to the analysing magnet in the case of the field scan) is obtained according to  $V_{ref}$ . One can set the initial condition,  $N_i$ , the final one,  $N_f$ , and the step width,  $n_s$ . The measurement period,  $t_m$ , for each step is determined by the integration of the beam current on a target.

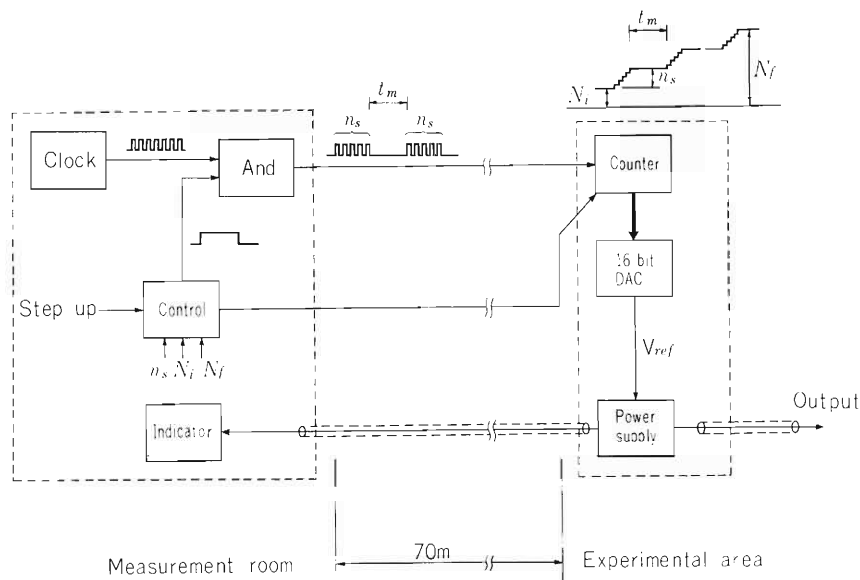


Fig. 1. A block diagram of the scan controller.  $n_s$ ,  $N_i$ , and  $N_f$  are presettable and step up signals come from a current integrator.

### III-2-11. Analysis of F $K\alpha$ -Emission Satellite Spectra from Fluorine Compounds by the DV- $X\alpha$ Method

K. Fujima, K. Fuwa, and M. Uda

The difference in valence electron nature of various fluorine compounds has been clearly observed in their F  $K\alpha$  emission satellite spectra. The energies of satellite peaks do not change with the change in the fluorides and agree well with the atomic values estimated by several computational methods.<sup>1),2),3)</sup> However, their satellite intensities change owing to the difference in valence structure. This fact can not be interpreted from the atomic nature.

Intending to analyse these features, the DV- $X\alpha$  cluster method has been applied to  $NiF_2$ ,  $CuF_2$ , and NaF clusters as the representatives for the fluorides.

The results obtained show that in the molecular orbital scheme, the valence orbitals of the F atom lower their energies and are localized by the strong attractive Coulomb potential caused by the K-hole. As a result, the F atom should have an atomic nature in the ionized state, even if it is buried in a solid. This is also true for the multi-ionized state and leads to the fact that the satellite peak positions do not change even when there exist the difference in chemical surroundings of the F atom.

Once this atomic nature is realized, the K-emission intensities, calculated by means of the dipole approximation, are the same for all the fluorides. This atomic state is thought not to have a chance of relaxation through radiative nor non-radiative process, which may alter the satellite intensities.

By the way, KVV-Auger probability has been reported to be sensitive to the valence relaxation immediately after the K-ionization.<sup>4)</sup> Since Auger process is the competitive process of K-emission, the intensity of satellite might be influenced through this first excitation process.

Our present calculation has been encouraging because it shows that the charge distribution soon after the K-ionization decreases the intensity of satellite peaks and enhances that of the main peak. The figures illustrated below show the charge distribution of  $NiF_2$  cluster in the ground state (a), soon (b), and long enough (c) after the K-ionization. The charge distribution (c) no more radiates the photon of satellite energies but radiates that of the main peak.

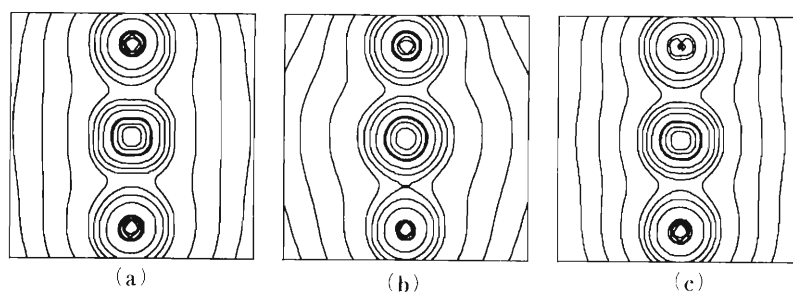


Fig. 1. The charge distribution of  $NiF_2$  cluster in the ground state (a), soon (b), and long enough (c) after the K-ionization.

## References

- 1) Z. Horak: Proc. Phys. Soc. London Sec., A77, 980 (1961).
- 2) E. H. Kennard and E. Ramberg: Phys. Rev., 46, 1040 (1936).
- 3) T. Åberg: Phys. Lett., 26A, 515 (1968).
- 4) O. Gunnarsson and K. Schöuhammer: Phys. Rev. B, 22, 3710 (1980).

### III-2-12. Determination of Electron Contact Densities for Outermost Electrons in Tin Compounds

H. Muramatsu, T. Miura, H. Nakahara,  
M. Fujioka, E. Tanaka,\* and A. Hashizume

The experimental evidence of the influence of chemical environment on outer-shell internal conversion in  $^{119}\text{Sn}$  was reported in the previous report.<sup>1)</sup> In the present report, we describe about electron contact densities for the outermost electrons in white tin and  $\text{CaSnO}_3$ .

Internal conversion sources were prepared by implantation of radioactive  $^{119}\text{Sb}$  ( $T_{1/2} = 38.0$  h) using the electromagnetic isotope separator at Cyclotron and Radioisotope Center, Tohoku University. Detailed descriptions on the preparation of two sources were given in the previous report.<sup>1)</sup>

In order to assign the final chemical state of the conversion sources, the Mössbauer effect in the 23.87 keV transition of  $^{119}\text{Sn}$  was measured with a  $\text{CaSnO}_3$  absorber. In Fig. 1 there are shown the emission Mössbauer spectra obtained from the implanted white tin and  $\text{CaSnO}_3$  samples together with the transmission spectra obtained from the measurements with a transmission geometry using a standard source  $\text{Ca}^{119\text{m}}\text{SnO}_3$ . In the case of white tin, the emission spectrum could be clearly fitted with a single line at  $\delta = -2.48$  mm/s which is in good agreement with that of the transmission spectrum (Fig. 1 (a)). This means that the implanted  $^{119}\text{Sb}$  atom occupies the normal lattice point of tin in the metal. On the other hand, in the case of  $\text{CaSnO}_3$ , a more complex spectrum

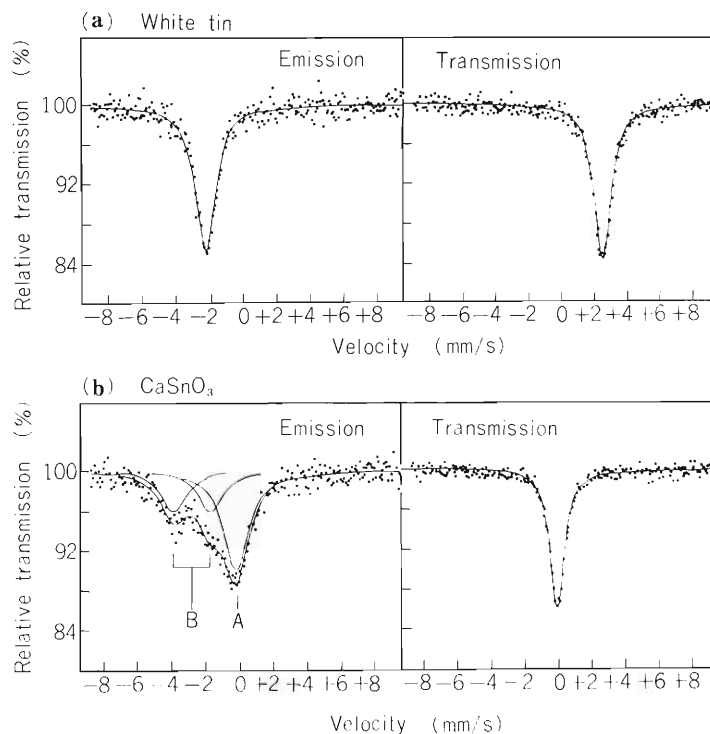


Fig. 1. Mössbauer spectra obtained from the sources of  $^{119}\text{Sb}$  implanted into white tin and  $\text{CaSnO}_3$  with a  $\text{CaSnO}_3$  absorber (emission). For comparison there are shown the 'transmission' spectra taken with a standard  $\text{Ca}^{119\text{m}}\text{SnO}_3$  source and absorbers of white tin or  $\text{CaSnO}_3$ .

\* Faculty of Science, Tohoku University.

was observed as shown in Fig. 1 (b). The emission spectrum of  $\text{CaSnO}_3$  sample could be decomposed to three absorption peaks. Line A corresponds to the normal substitutional site in  $\text{CaSnO}_3$  because a similar consideration as in the case of white tin mentioned above can be applied (see the transmission spectrum in Fig. 1 (b)). Line B may be attributed to the quadrupole doublet of Sn(II) on the basis of the fact that its isomer shift and quadrupole splitting are close to those reported by Boyle et al.<sup>2)</sup> for the tetragonal or orthorhombic SnO. The number of  $^{119}\text{Sb}$  atoms in the site A was estimated from the temperature dependence of Mössbauer spectrum as 47 %.

The conversion-electron spectra were measured with a 50 cm, double focusing, iron-free  $\beta$ -ray spectrometer at the IPCR. Detailed procedure for measurement of conversion electrons was described in the previous report.<sup>1)</sup> The analyses of the conversion spectra were carried out using the computer code ACSEMP.<sup>3)</sup> The internal conversions of O shells which correspond to the internal conversions of 5s and 5p electrons, could not be resolved at all into subshells ( $\text{O}_I$ ,  $\text{O}_{II}$ , and  $\text{O}_{III}$ ). However, since the contribution of  $\text{O}_{II,III}$  conversion to the total conversion of O shells was estimated to be less than 5 % for the M1 transition, it was neglected in the analysis. In order to deduce the accurate intensity of the O-lines, the contribution of the K-LM Auger lines of tin which superimposed on the N- and O-lines in the same momentum region was subtracted as an Auger-background obtained by an independent measurement using radioactive  $^{117m}\text{Sn}$ .

Results of the analyses for two different sources are listed in Table I and the conversion spectra are shown in Fig. 2. Here, since the Mössbauer spectrum indicated that only 47 % of the  $^{119}\text{Sb}$  implanted into the host material was in the form of  $\text{CaSnO}_3$  for the source of  $\text{CaSnO}_3$ , the  $\text{O}/\text{N}_I$  intensity ratio was corrected on the assumption that the conversion intensity of site B was equal to that of white tin from the equality of the isomer shift. The 5s electron density at the nucleus, that is, the so-called electron contact density can be deduced from the observed  $\text{O}/\text{N}_I$  ratio by using the formula

$$|\psi_{5s}(0)|^2 = |\psi_{4s}(0)|^2_{\text{theor.}} (\text{O}/\text{N}_I),$$

where  $|\psi_{4s}(0)|^2_{\text{theor.}}$  is the theoretical 4s electron density of the tin atom. The observed electron-density difference between white tin and  $\text{CaSnO}_3$  was larger than that observed by Bocquet et al. by a factor of 2.5 in

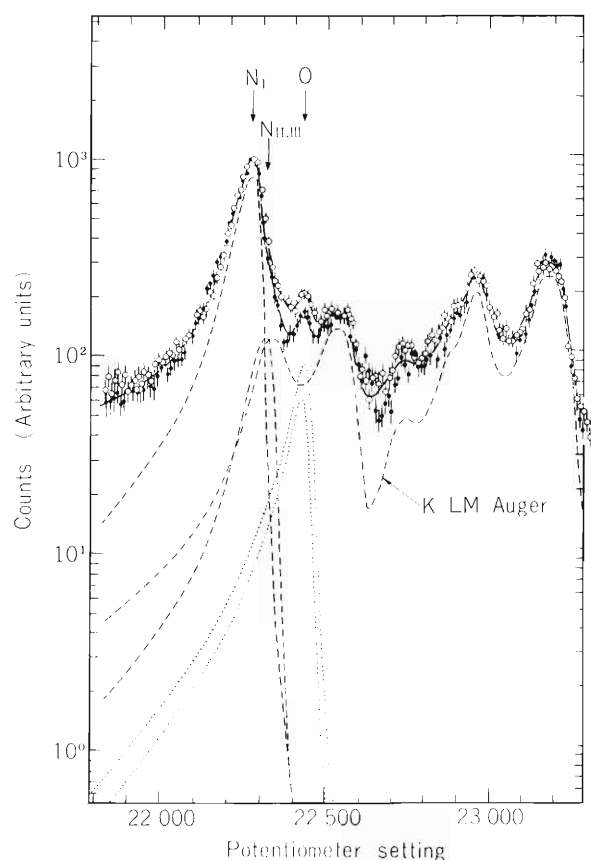


Fig. 2. Conversion electron spectra from two different  $^{119}\text{Sb}$  sources of white tin and  $\text{CaSnO}_3$ . The curves have been normalized to equal  $\text{N}_I$  line intensity.  
 ○ white tin, ●  $\text{CaSnO}_3$

Table 1. Relative intensities of  $N_I$  and O lines from the internal conversion of the 23.87 keV M1 transition in  $^{119}\text{Sn}$  for two well-defined chemical forms, the forms of white tin and  $\text{CaSnO}_3$ .

Chemical form	O/ $N_I$	$ \psi_{5s}(0) ^2$ <sup>a)</sup> (a.u.)	$\delta$ (mm/s)
$\text{CaSnO}_3$	$0.0197 \pm 0.0232$	$14.2 \pm 16.7$	0
White tin	$0.101 \pm 0.10$	$72.7 \pm 7.3$	2.48
	$\Delta  \psi_{5s}(0) ^2 = 58.5 \pm 18.2$ a.u.		

a)  $|\psi_{4s}(0)|^2 = 719.65$  a.u. is assumed.

its magnitude.<sup>4)</sup> It was found that the 5s electron density at the nucleus is about 80 % smaller in  $\text{CaSnO}_3$  than in white tin.

For the estimation of the occupation numbers of the electrons in the valence shell or of the electronic configuration of the valence electrons, it seems to be a simple and useful approach to renormalize the atomic wave functions within the Wigner-Seitz sphere, as described by Friedman et al.<sup>5)</sup> In this approach one utilizes the free-atom wave functions, truncates them at the radius  $r_{ws}$  of the Wigner-Seitz sphere, and renormalizes them within this sphere, thereby preserving charge neutrality. This approach makes it possible to take into account the problem of the charge compression or the size effect of atoms in solids, at least approximately. According to Friedman et al., the renormalization factor N is represented as

$$\begin{aligned} \psi_{\text{solid}}(r) &= N \psi_{\text{free atom}}(r), \quad r < r_{ws} \\ &= 0, \quad r > r_{ws}. \end{aligned}$$

The renormalized-atom ratio of the contact densities between 4s and 5s electrons for  $\text{Sn } 5s^2 5p^2$  is

$$\left[ |\psi_{5s}(0)|^2 / |\psi_{4s}(0)|^2 \right]_{\text{ren. atom}} = 0.120.$$

If this ratio is compared with the observed value of the O/ $N_I$  ratio for white tin in the present work,  $0.101 \pm 0.016$ , the occupation number of the 5s subshell of white tin is  $1.68 \pm 0.28$ . In the same fashion, the configuration for  $\text{CaSnO}_3$  is estimated to be  $5s^{0.39} 5p^{3.61}$  by using a free-atom ratio for Sn in the configuration  $5s5p^3$ , 0.047, and  $N = \sqrt{1.06}$ .

## References

- 1) H. Muramatsu, T. Miura, H. Nakahara, M. Fujioka, E. Tanaka, and A. Hashizume: RIKEN Accel. Progr. Rep., 15, 51 (1981).
- 2) A. J. F. Boyle, D. St. P. Bunbury, and C. Edwards: Proc. Phys. Soc. (London), 79, 416 (1962).
- 3) M. Fujioka, M. Takashima, and M. Kanbe: Z. Phys., A299, 283 (1981).
- 4) J. P. Bocquet, Y. Y. Chu, O. C. Kistner, M. L. Perlman, and G. T. Emery: Phys. Rev. Lett., 17, 809 (1966).
- 5) R. M. Friedman, R. E. Watson, J. Hudis, and M. L. Perlman: Phys. Rev. B, 8, 3569 (1973).

### III-2-13. Optical Detection of Atomic and Nuclear Spin Polarization Produced by Beam-Foil Interaction

S. Kohmoto, M. Ishihara, T. Nomura,  
Y. Gono, and Y. Itoh

A nuclear-polarized ion beam with a kinetic energy in MeV range was generated by the tilted foil method<sup>1),2)</sup> and the degree of nuclear polarization was determined.

In Fig. 1, an ion beam passes through a thin carbon foil (foil I) whose normal is tilted relative to the beam direction ( $\phi \neq 0^\circ$ ). The ions are not only excited but also polarized atomically at the exit of the surface of the foil due to the non-cylindrical symmetry. This polarization is transferred to the nucleus via the hyperfine interaction during the flight. The detection of light emitted from the ions after passage through the second thin foil (foil II) placed perpendicularly to the beam direction ( $\phi = 0^\circ$ ) is the proof of the transfer of the polarization: atom  $\rightarrow$  nucleus  $\rightarrow$  atom, because a cylindrical symmetry is kept at the foil II.

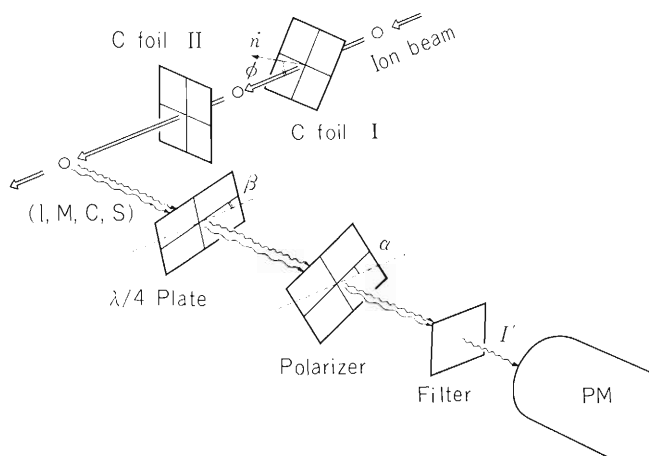


Fig. 1. Schematic experimental arrangement. Photons are observed in a direction perpendicular to the beam axis and to the normal of the tilted foil.

$^{14}\text{N}$  ion beam of 5 MeV kinetic energy was produced in the Linac Accelerator. The two carbon foils were of  $5 \mu\text{g}/\text{cm}^2$  thickness and the tilt angle  $\phi$  of the foil I was  $50^\circ$ . The polarization of light emitted from the ions downstream from the foil II was determined with a rotating  $\lambda/4$  plate followed by a fixed linear polarizer ( $\alpha = 0^\circ$ ), an interference filter and a single photon counting photo-multiplier (PM) with low dark counts. Another PM was set at the other side of the apparatus for the purpose of normalization. The atomic transition selected by the filter was  $1s^26f^2F - 1s^27g^2G$  494 nm. The relative Stokes parameter  $S/I$  averaged over the fine components of the transition which were not resolved in our experiment was obtained measuring the intensity  $I'$  for  $\beta = \pm 45^\circ$ , i.e.

$$\overline{S/I} = \left\{ I'(+45^\circ) - I'(-45^\circ) \right\} / \left\{ I'(+45^\circ) + I'(-45^\circ) \right\}.$$

The result was  $\overline{S/I} \simeq 0.7\%$ . From this value, we deduced the nuclear polarization  $P_{\text{I}} \simeq 3\%$ , using the relation<sup>3)</sup> between  $\overline{S/I}$  and  $P_{\text{I}}$ . Of course, we have verified that the Stokes parameter  $S/I$  simply changes the sign but not the absolute value when one changes the tilt angle  $\phi$  to  $-\phi$ . Although our  $P_{\text{I}}$  value should be taken to give only the rough magnitude because, for example, we have chosen the distance between two foils (1.5 cm) rather arbitrarily, we emphasize that it is the first observation of  $P_{\text{I}}$  in the MeV energy range.

#### References

- 1) B.I. Deutch, F. Q. Lu, and J. Y. Tang: *Hyp. Int.*, 9, 169 (1981).
- 2) S. Kohmoto, M. Ishihara, T. Nomura, Y. Gono, and M. Sasagase: *RIKEN Accel. Progr. Rep.*, 15, 86 (1981).
- 3) H. J. Andrä, H. J. Plöhn, A. Gaupp, and R. Fröhling: *Z. Phys.*, 281, 15 (1977).

### III-2-14. Effects of Chemical Bond on O $K\alpha$ Spectra from Multiply Ionized States

M. Uda, K. Maeda, Y. Sasa, A. Koyama,  
and S. Nakamura

For a wide range of target atomic numbers, effects of chemical bond on intensity distributions of X-ray satellites arising from multiply ionized states have extensively been investigated.<sup>1)</sup> Their intensity distributions have changed dramatically in X-ray emission related to transitions between inner shells and valence bands with the difference in the chemical bonds for most of the chemical compounds.<sup>2)-5)</sup> O  $K\alpha$  X-ray spectra are, therefore, also expected to show similar effects on their intensity distributions.

O  $K\alpha$  satellite spectra have been observed in a previous paper.<sup>6)</sup> Their intensity distributions should differ for different methods of ionization and species of chemical compounds. The former gives difference in the ionization cross sections for multiply ionized states. The latter gives rise to difference in the electronic rearrangement in the valence band prior to X-ray emission.

$C^{3+}$  ions were accelerated up to 2.8 MeV by the Tandetron (General Ionex Corp.). White X-rays generated from Rh anode were also used, for the comparison, to emit O  $K\alpha$  X-rays. Specimens used here were MgO,  $MgSO_4$ , CuO, and  $Cu_2O$ .

O  $K\alpha$  satellite spectra were energetically analyzed with a RAP flat single crystal (010). The results are shown in Figs. 1-4  $K^1L^n$  denotes the emitted X-rays from the initial state with one and n vacancies in K and L shells, respectively. From the comparison between the spectra induced by  $C^{3+}$  and those by white X-rays, change in the electronic rearrangement might be deduced. Analytical treatment for this is in progress.

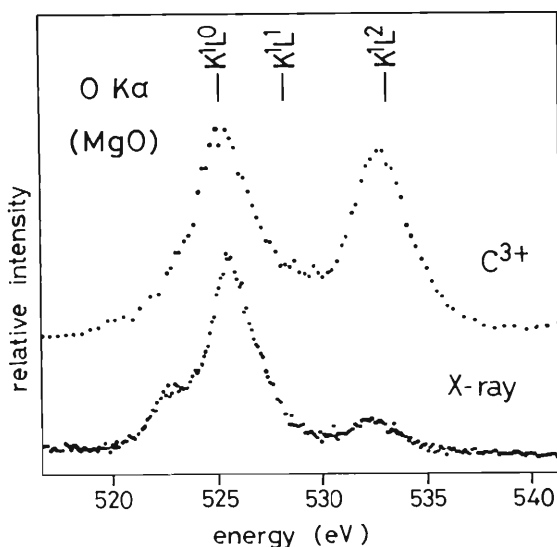


Fig. 1. O  $K\alpha$  satellite spectra of MgO.

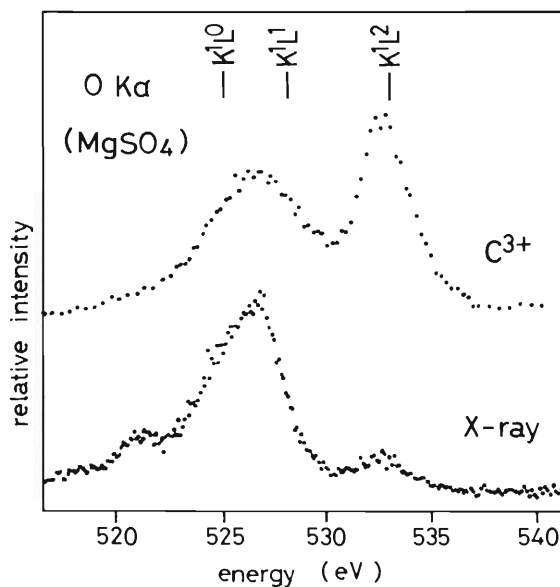


Fig. 2. O  $K\alpha$  satellite spectra of  $MgSO_4$ .

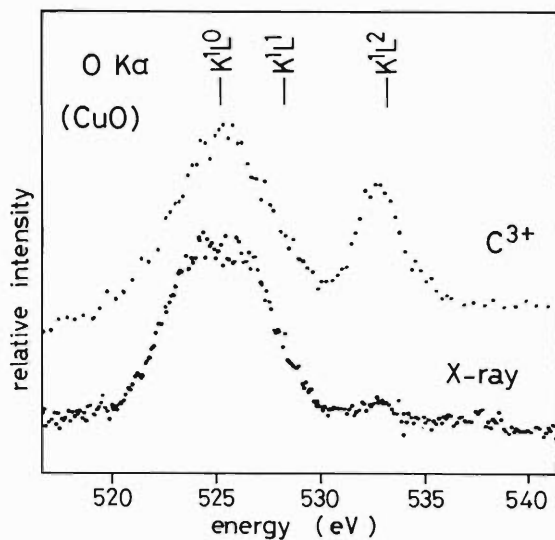


Fig. 3. O K $\alpha$  satellite spectra of CuO.

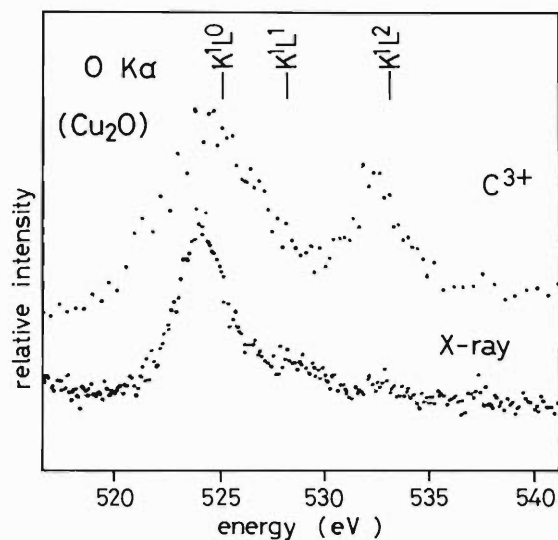


Fig. 4. O K $\alpha$  satellite spectra of Cu<sub>2</sub>O.

#### References

- 1) H. Endo and M. Uda: *Z. Phys. A*, **306**, 187 (1982).
- 2) M. Uda, H. Endo, K. Maeda, Y. Awaya, M. Kobayashi, Y. Sasa, H. Kumagai, and T. Tonuma: *Phys. Rev. Lett.*, **42**, 1257 (1979).
- 3) H. Endo, M. Uda, and K. Maeda: *Phys. Rev. A*, **22**, 1436 (1980).
- 4) M. Uda, H. Endo, K. Maeda, Y. Sasa, and M. Kobayashi: *Z. Phys. A*, **300**, 1 (1981).
- 5) K. Maeda and M. Uda: *Phys. Lett.*, **91A**, 223 (1982).
- 6) K. Maeda, Y. Sasa, K. Fuwa, and M. Uda: *RIKEN Accel. Progr. Rep.*, **15**, 75 (1981).

### III-2-15. Supertransferred Hyperfine Magnetic Field at $^{119}\text{Sn}^{4+}(\leftarrow^{119}\text{Sb}^{5+})$ on $\text{Cr}_2\text{O}_3$ Surfaces

T. Okada, S. Ambe, F. Ambe, and H. Sekizawa

In the preceding volume of this report, we presented an emission Mössbauer study on carrier-free  $^{119}\text{Sb}^{5+}$  ions adsorbed on  $\alpha\text{-Fe}_2\text{O}_3$  surfaces.<sup>1)</sup> From the observation of the supertransferred hyperfine (STHF) interaction between the ordered  $\text{Fe}^{3+}$  ions of the substrate and  $^{119}\text{Sn}^{4+}$  ions arising from  $^{119}\text{Sb}^{5+}$ , the adsorbed  $^{119}\text{Sb}^{5+}$  ions were found to form  $\text{Fe}^{3+}\text{-O}^{2-}\text{-}^{119}\text{Sb}^{5+}$  bonds on the surfaces. In this period, similar measurements were made on  $\text{Cr}_2\text{O}_3$  substrate.

$\text{Cr}_2\text{O}_3$  is an antiferromagnet with the same crystal structure as  $\alpha\text{-Fe}_2\text{O}_3$  (corundum-type). Its low Néel temperature (303 K) made it possible to study the effect of bulk magnetization of substrate upon the STHF field at  $^{119}\text{Sn}$  nuclei arising from  $^{119}\text{Sb}^{5+}$  on the surfaces.

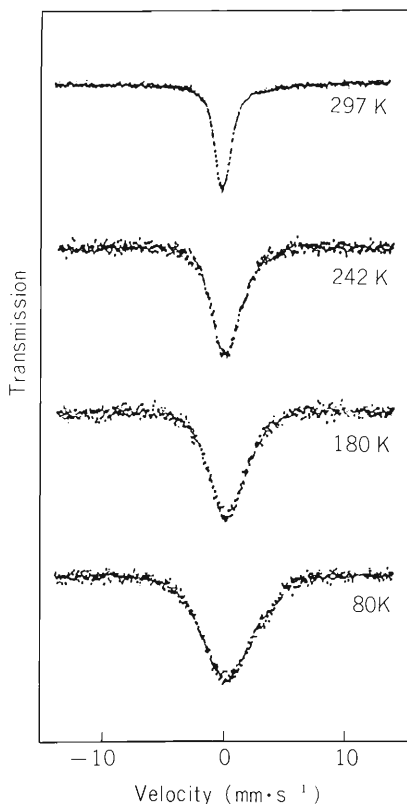


Fig. 1. Emission Mössbauer spectra of the "as adsorbed"  $\text{Cr}_2\text{O}_3\text{-}^{119}\text{Sb}^{5+}$  specimen measured at different temperatures. The isomer shift is given relative to  $\text{BaSnO}_3$ .

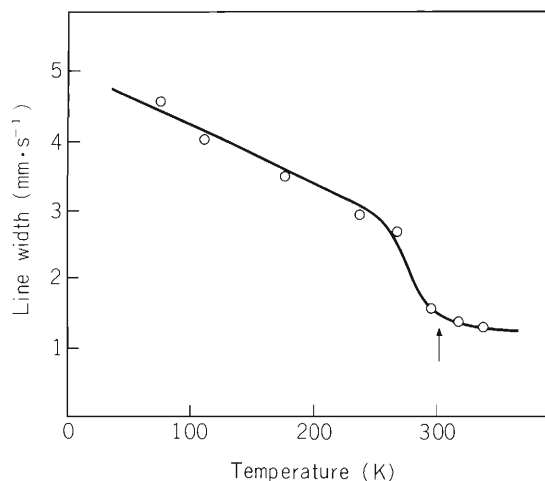


Fig. 2. Variation of the full width at half maximum of the emission line of the "as adsorbed"  $\text{Cr}_2\text{O}_3\text{-}^{119}\text{Sb}^{5+}$  specimen with the temperature of measurement. The arrow shows the Néel temperature of bulk  $\text{Cr}_2\text{O}_3$ .

Pentavalent  $^{119}\text{Sb}$  (half life: 38.0 h) produced by the Cyclotron<sup>2)</sup> was adsorbed onto  $\text{Cr}_2\text{O}_3$  powder at  $100^\circ\text{C}$  from a  $0.25 \text{ mol dm}^{-3}$   $\text{LiCl}$  solution of pH 3.0. The oxide was filtered, washed with distilled water, and dried at room temperature over  $\text{P}_2\text{O}_5$ . Emission Mössbauer spectra of  $^{119}\text{Sn}$  produced by the EC decay of  $^{119}\text{Sb}^{5+}$  on surfaces of the oxide specimens were recorded against a  $\text{BaSnO}_3$  absorber.

Typical emission spectra of the “as adsorbed”  $\text{Cr}_2\text{O}_3 - ^{119}\text{Sb}^{5+}$  specimen at different temperatures are shown in Fig. 1. The spectra consist of an unresolved emission line of  $^{119}\text{Sn}^{4+}$ , whose width depends remarkably on the temperature of measurement (Fig. 2). It can be seen from Fig. 2 that near and above the Néel temperature of bulk  $\text{Cr}_2\text{O}_3$  the emission line has a width corresponding to ordinary diamagnetic  $^{119}\text{Sn}^{4+}$  ions, but it is considerably broadened below that temperature. Namely, the broadening occurs in parallel with the magnetic ordering of  $\text{Cr}^{3+}$  ions of the substrate. This observation is a decisive evidence for our view that the observed broadening is caused by the STHF interaction of the  $^{119}\text{Sn}^{4+}$  ( $\leftarrow$  adsorbed  $^{119}\text{Sb}^{5+}$ ) ions with the magnetically ordered  $\text{Cr}^{3+}$  ions of the  $\text{Cr}_2\text{O}_3$  surfaces. Thus, we can conclude that the adsorbed  $^{119}\text{Sb}^{5+}$  ions form  $\text{Cr}^{3+} - \text{O}^{2-} - \text{Sb}^{5+}$  bonds on the surfaces as in the case of  $\alpha\text{-Fe}_2\text{O}_3 - ^{119}\text{Sb}^{5+}$ .

As shown in Fig. 3, the effect of heat treatments on the  $\text{Cr}_2\text{O}_3 - ^{119}\text{Sb}^{5+}$  specimens was similar to that on  $\alpha\text{-Fe}_2\text{O}_3 - ^{119}\text{Sb}^{5+}$  reported previously. In the present case of  $\text{Cr}_2\text{O}_3$ , however, decrease in hyperfine fields was observed at higher temperatures. This is ascribable to coagulation of  $^{119}\text{Sb}^{5+}$  ions with diamagnetic impurities on the surfaces.

Detailed description of the experimental procedures and results as well as discussion based on a simplified surface model has been published elsewhere.<sup>3)</sup> A similar study on ferrimagnetic  $\gamma\text{-Fe}_2\text{O}_3$  is also reported in this volume.<sup>4)</sup>

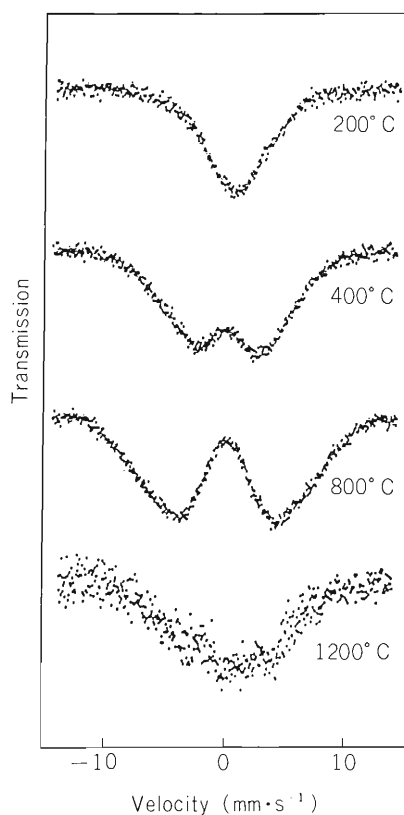


Fig. 3. Emission Mössbauer spectra of the 2h heat-treated  $\text{Cr}_2\text{O}_3 - ^{119}\text{Sb}^{5+}$  specimens measured at liquid nitrogen temperature. The isomer shift is given relative to  $\text{BaSnO}_3$ .

## References

- 1) T. Okada, H. Sekizawa, F. Ambe, and S. Ambe: RIKEN Accel. Progr. Rep., 15, 91 (1981).
- 2) S. Ambe, F. Ambe, and T. Okada: *ibid.*, p. 112.
- 3) T. Okada, S. Ambe, F. Ambe, and H. Sekizawa: J. Phys. Chem., 86, 4726 (1982).
- 4) T. Okada, F. Ambe, S. Ambe, and H. Sekizawa: p. 101 in this report.

### III-2-16. Emission Mössbauer Studies of Dilute $^{119}\text{Sb}$ Ions Adsorbed on Ferrimagnetic Spinel Oxide Surfaces

T. Okada, F. Ambe, S. Ambe,  
and H. Sekizawa

Previously, we reported results of emission Mössbauer measurement of  $^{119}\text{Sb}$  arising from carrier free pentavalent  $^{119}\text{Sb}$  ions hydrolytically adsorbed on surfaces of antiferromagnetic oxide,  $\alpha\text{-Fe}_2\text{O}_3$ .<sup>1,2)</sup> This work has been extended to a ferrimagnetic oxide with the spinel structure,  $\gamma\text{-Fe}_2\text{O}_3$ . The aim of these works is as follows. By observing the broadening and splitting of the emission spectra which are caused by the supertransferred hyperfine (hereafter abbreviated as STHF) magnetic fields coming from the ordered magnetic ions of the substrates, microscopic information on the physical and chemical states of the adsorbed ions is able to be investigated.

A Mössbauer analysis was made on the 23.8 keV  $\gamma$ -rays emitted by the first excited states of  $^{119}\text{Sn}$  ( $^{119}\text{Sn}^*$ , half life: 17.8 ns) arising from  $^{119}\text{Sb}$  (half life: 38.0 h) by the EC decay.

Experimental procedures have already been reported in previous reports.<sup>1,2)</sup> Carrier-free  $^{119}\text{Sb}$  ions were adsorbed on the surfaces of the ferrimagnetic oxide powders of  $\gamma\text{-Fe}_2\text{O}_3$ , the Néel temperature of which was about 590°C. The average particle size of these acicular powders was about 1  $\mu\text{m}$  as determined from electron micrographs. Adsorption of the pentavalent  $^{119}\text{Sb}$  ions was made hydrolytically at room temperature. Emission Mössbauer spectra of the “as adsorbed” and the heat-treated specimens were taken at liquid nitrogen temperature against  $\text{BaSnO}_3$  absorber. The temperatures of heat treatments were 200, 300, 400, 500, and 600°C. A few examples of the obtained spectra on  $\gamma\text{-Fe}_2\text{O}_3$  and  $\text{Cr}_2\text{O}_3$  are given in Fig. 1. The spectrum of adsorbed ions on  $\text{Cr}_2\text{O}_3$  above its Néel temperature is also shown as the reference spectrum in which the STHF magnetic fields are absent. Detailed report on  $\text{Cr}_2\text{O}_3$  has been given elsewhere.<sup>2,3)</sup>

Even in the “as adsorbed” specimen of  $\gamma\text{-Fe}_2\text{O}_3$ , there could be seen a remarkably broadened emission line. The line transformed into the more broadened magnetic hyperfine patterns with the elevation of the temperature of isochronal heat treatments. As the cubic  $\gamma\text{-Fe}_2\text{O}_3$  is gradually converted to the rhombohedral  $\alpha\text{-Fe}_2\text{O}_3$  on being heated to temperatures above 400°C, the emission patterns of the heat-treated specimens above 400°C become complex. The distribution of hyperfine magnetic fields ( $H_{\text{hf}}$ ) obtained by analyzing the spectra by means of the method of Hesse<sup>4)</sup> is shown in Fig. 2. The distribution of the hyperfine magnetic fields for the “as adsorbed” specimen of  $\gamma\text{-Fe}_2\text{O}_3$  is almost equal to that of  $\alpha\text{-Fe}_2\text{O}_3$  reported previously.<sup>2)</sup> With the elevation of the temperature of heat treatment, the high field components grew up rapidly accompanied by a slow decrease of the low field components. This makes a remarkable contrast to the case of  $\alpha\text{-Fe}_2\text{O}_3$ .

The chemical formula of  $\gamma\text{-Fe}_2\text{O}_3$  is also rewritten as  $(\text{Fe}^{3+}) [\text{Fe}^{3+}_{2/3} \square_{1/3}] \text{O}_4$ , where  $(\text{Fe}^{3+})$  denotes the  $\text{Fe}^{3+}$  ions in the tetrahedral A sites and  $[\text{Fe}^{3+}_{2/3} \square_{1/3}]$  denotes the  $\text{Fe}^{3+}$  ions and the cation vacancies in the octahedral B sites of the spinel structure. Some of the  $^{119}\text{Sb}^{5+}$  ions adsorbed on the surface of  $\gamma\text{-Fe}_2\text{O}_3$  are considered to be trapped near to the vacancies because of valence compensation. The hyperfine magnetic fields of the  $^{119}\text{Sb}^{5+}$  ions trapped to the vacancies are

expected to be very small. The remaining low field components at high temperature are ascribed to these trapped ions.

The detailed investigation is in progress.

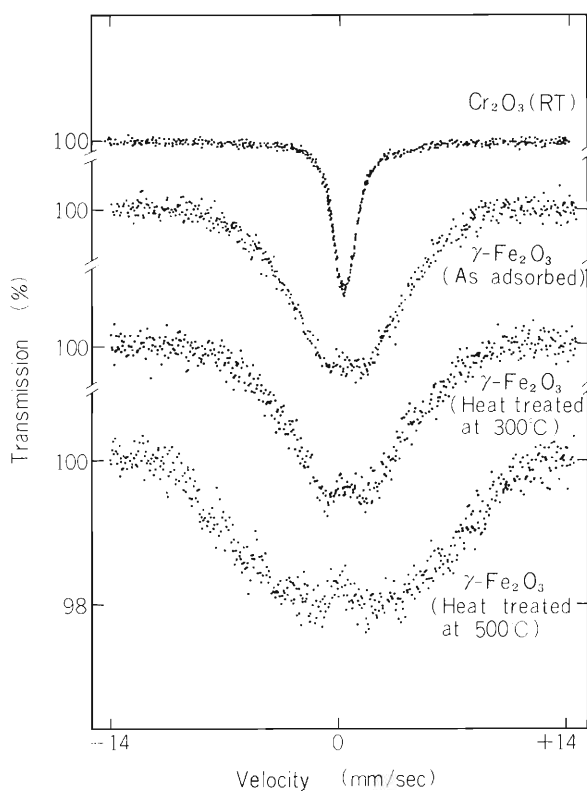


Fig. 1. Emission Mössbauer spectra of  $\gamma$ -Fe<sub>2</sub>O<sub>3</sub> and Cr<sub>2</sub>O<sub>3</sub> at liquid nitrogen temperature.

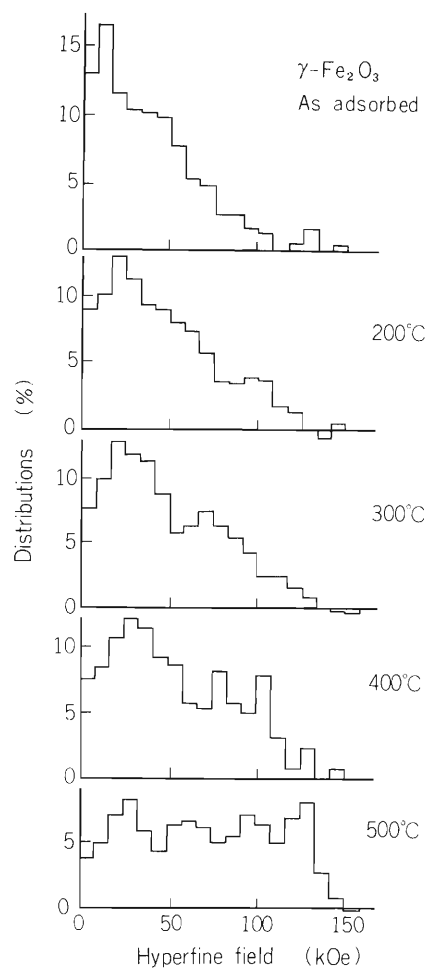


Fig. 2. The distribution of the hyperfine magnetic fields for the "as adsorbed" and heat-treated specimen of  $\gamma$ -Fe<sub>2</sub>O<sub>3</sub>.

#### References

- 1) T. Okada, H. Sekizawa, F. Ambe, and S. Ambe: RIKEN Accel. Progr. Rep., 15, 91 (1981).
- 2) T. Okada, S. Ambe, F. Ambe, and H. Sekizawa: J. Phys. Chem., 86, 4726 (1982).
- 3) T. Okada, S. Ambe, F. Ambe, and H. Sekizawa: p. 98 in this report.
- 4) J. Hesse and A. Rübartsch: J. Phys. E. Sci. Instrum., 7, 526 (1974).

### III-2-17. Perturbed Angular Correlation of $\gamma$ -Rays Emitted from $^{111}\text{Cd}(\leftarrow ^{111}\text{In})$ on $\alpha\text{-Fe}_2\text{O}_3$ , $\text{Cr}_2\text{O}_3$ , and $\alpha\text{-Al}_2\text{O}_3$ Surfaces

K. Asai, F. Ambe, S. Ambe, and H. Sekizawa

The present work aims to utilize perturbed angular correlation measurements in studying the chemical states of dilute metal ions adsorbed onto the surfaces of oxides. In this report, we present the results obtained on time differential perturbed angular correlation (TDPAC) of  $\gamma$ -rays emitted from  $^{111}\text{Cd}(\leftarrow ^{111}\text{In})$  on corundum-type antiferromagnets  $\alpha\text{-Fe}_2\text{O}_3$ ,  $\text{Cr}_2\text{O}_3$  and a diamagnet  $\alpha\text{-Al}_2\text{O}_3$ .

Samples were hydrolytically prepared. About 100 mg of  $\alpha\text{-Fe}_2\text{O}_3$ ,  $\text{Cr}_2\text{O}_3$ , or  $\alpha\text{-Al}_2\text{O}_3$  powder was added to a dilute HCl solution (pH 2 ~ 3) of "carrier-free"  $^{111}\text{In}$ . Then, the pH of the solution was adjusted to 7 – 8 with a dilute NaOH solution, and the suspension was stirred to let the  $^{111}\text{In}$  ions be adsorbed onto the oxide surfaces. The oxide was separated by centrifugation and washed with distilled water several times to remove  $\text{Cl}^-$  ions, and then dried over  $\text{P}_2\text{O}_5$  in vacuum at room temperature. A portion of the oxide containing about 60  $\mu\text{Ci}$  of  $^{111}\text{In}$  was subjected to TDPAC measurement.

The time spectra of 173 – 247 keV  $\gamma$ - $\gamma$  cascade emitted from  $^{111}\text{Cd}$  were taken with a conventional fast-slow coincidence set up with two NaI(Tl) detectors at room temperature and also at 77 K. For a polycrystalline specimen, the TDPAC spectrum is expressed in the form

$$W(\theta, t) = \sum_{k=\text{even}} A_{kk}(t) P_k(\cos \theta),$$

where  $\theta$  is the angle between the cascade  $\gamma$ -rays,  $t$  the interval between them, and  $P_k$  the Legendre polynomials.<sup>1)</sup> Therefore, the perturbation factor  $A_{22}(t)$  is derived from  $W(180^\circ, t)$  and  $W(90^\circ, t)$  in the form

$$A_{22}(t) = \frac{2}{3} \{ W(180^\circ, t) - W(90^\circ, t) \}$$

by neglecting the higher terms  $A_{kk}(t)$  with  $k \geq 4$ .

Figure 1 shows the perturbation factor  $A_{22}(t)$  for  $\alpha\text{-Al}_2\text{O}_3$  at room temperature. As can be seen, the factor decreases to become almost zero in a comparatively short time ( $\sim 10$  ns), then recovers a little, and thereafter exhibits no visible structure but keeps nonzero value in average. This apparently non-periodic behavior, which is common to all  $A_{22}(t)$  observed in this work, suggests that intensities of the hyperfine interactions have a wide distribution, and/or that they are time-dependent. Figure 2 shows the smoothed data of  $A_{22}(t)$  in the vicinity of  $t = 0$ . It is found for all the specimens that  $A_{22}(t)$  decreases and recovers in a shorter time at 77 K than at room temperature. This finding means that the hyperfine interactions at 77 K are stronger in average, and/or have a longer correlation time than those at room temperature.

It is considered that the dominant hyperfine interactions are associated with the unstable excited ionic states created by the preceding electron capture decay ( $^{111}\text{In} \rightarrow ^{111}\text{Cd}$ ). After the

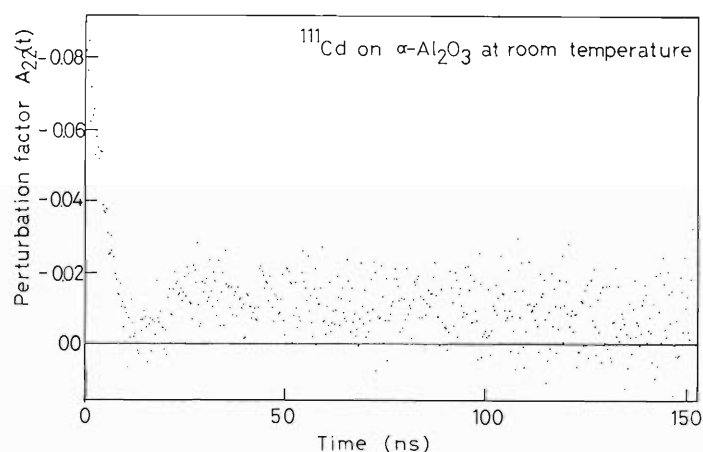


Fig. 1. Perturbation factor  $A_{22}(t)$  of the  $^{111}\text{Cd}$   $\gamma$ - $\gamma$  correlation on  $\alpha\text{-Al}_2\text{O}_3$  at room temperature.

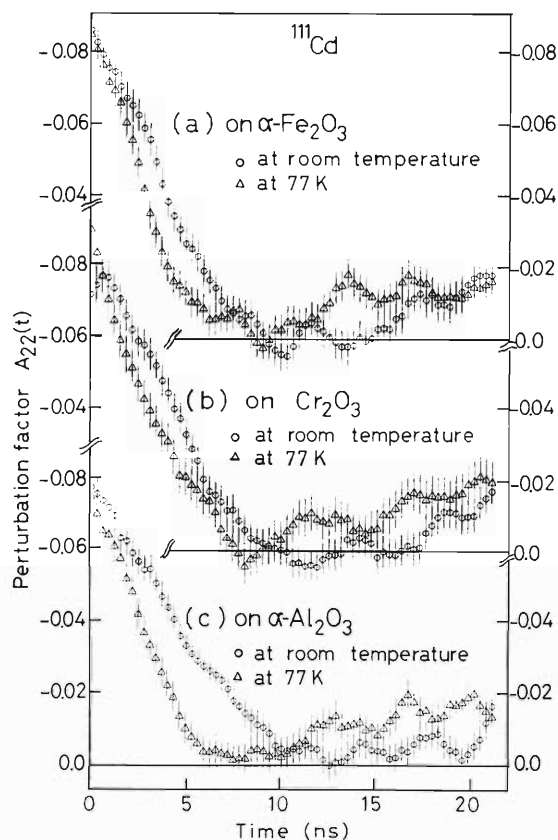


Fig. 2. Perturbation factors  $A_{22}(t)$  of  $^{111}\text{Cd}$   $\gamma$ - $\gamma$  correlations at room temperature and at 77 K: (a) on  $\alpha\text{-Fe}_2\text{O}_3$ , (b) on  $\text{Cr}_2\text{O}_3$ , and (c) on  $\alpha\text{-Al}_2\text{O}_3$ .

Auger process following the electron capture, the ion is left in one of the various unstable charge states, and relaxes to the stable state in a certain time duration.<sup>2)</sup> On the unstable ions, intensities of the hyperfine interactions have a wide distribution and also change with time.<sup>2)</sup> The more rapid attenuation at 77 K means that the electronic relaxation becomes slow at low temperature.

The relaxation process reflects the character of the chemical bonds between the adsorbed ions and the substrate oxides. Though precise analysis is now in progress, it can be said that the TDPAC measurement is a useful tool for these studies.

## References

- 1) H. Frauenfelder and R. M. Steffen: "α-, β-, and γ-Ray Spectroscopy", 2, (ed. by K. Siegbahn), North-Holland, Amsterdam (1964).
- 2) H. Haas and D. A. Shirley: J. Chem. Phys., 58, 3339 (1973).

### III-2-18. Dependence of Secondary Electron Emission Coefficients on Metal Targets under Bombardment with Bare Projectiles

A. Koyama, T. Shikata,  
H. Sakairi, and E. Yagi

There is still a shortage of measurements of the secondary electron emission coefficients  $\gamma$  under heavy ion bombardment in the high-energy region of several MeV/amu.

According to Oda and Lyman,<sup>1)</sup> the energy dependence of  $\gamma$  is different from that of  $S$ , the energy loss per unit path length of projectiles, and the dependence of  $\gamma$  on the projectile atomic number  $z_1$  is the same with that of  $S$ . On the contrary, according to Clerc et al.,<sup>2)</sup> the energy dependence of  $\gamma$  agrees with that of  $S$ , and the  $z_1$ -dependence of  $\gamma$  does not. In the previous paper<sup>3)</sup> we revealed that the energy dependence of  $\gamma$  was different from that of  $S$ . This result agreed with those by Oda and Lyman.

In the present paper we examine the  $z_1$ -dependence of  $\gamma$ . Figure 1 shows both  $\gamma_{\text{back}}$  (the backward secondary electron emission coefficients) for thick Al and Ag targets and for an Au foil target, and  $\gamma_{\text{for}}$  (the forward secondary electron emission coefficients) for the Au foil target. Incident ions were  $\text{He}^{2+}$ ,  $\text{C}^{6+}$ ,  $\text{N}^{7+}$ , and  $\text{O}^{8+}$ , and their energy was 6.2 MeV/amu. The experimental apparatus and conditions are given in detail elsewhere.<sup>4)</sup> This figure shows the clear deviation from proportionality to  $z_1^2$  for  $\gamma_{\text{back}}$  and  $z_1^{*2}$  for  $\gamma_{\text{for}}$ , where  $z_1^*$  is the effective charge number of projectiles. The deviation can be given by

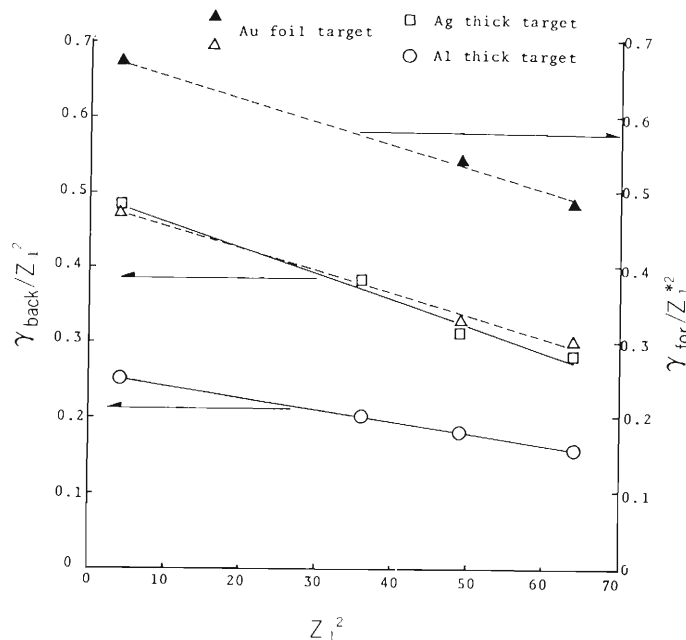


Fig. 1. Dependence of  $\gamma_{\text{back}}/z_1^2$  on  $z_1$  for Al and Ag thick targets, and those of  $\gamma_{\text{back}}/z_1^2$  and  $\gamma_{\text{for}}/z_1^{*2}$  for an Au foil target. Incident energy is 6.2 MeV/amu.

$$\gamma_{\text{back}}/z_1^2 \propto 1 - 0.006z_1^2, \text{ for all three targets,}$$

$$\gamma_{\text{for}}/z_1^{*2} \propto 1 - 0.004z_1^2, \text{ for the Au foil target.} \quad (1)$$

The decreasing trend with increasing atomic number is consistent with the experimental results by Clerc et al.,<sup>2)</sup> and is not with those by Oda and Lyman.<sup>1)</sup>

According to the theory by Schou,<sup>5)</sup>  $\gamma$  can be written as,

$$\gamma = \beta \cdot S \cdot \Lambda, \quad (2)$$

where  $\beta$  is the dimensionless factor and  $\beta \cdot S$  gives the energy dissipated per unit path length to electrons in the surface region of a target, and  $\Lambda$  is the factor which gives the fraction of secondary electrons (SE's) that can escape from the surface and is dependent on the surface barrier height  $U$ . Then with respect to the foil target, it can be written that

$$\gamma_{\text{back}} = \beta_0 \cdot S_0 \cdot \Lambda_0, \quad (3)$$

$$\gamma_{\text{for}} = \beta_d \cdot S_d \cdot \Lambda_d,$$

where subscripts 0 and d mean the positions of the inlet and outlet surfaces, respectively.

Under the reasonable assumptions that for the film target which is thin enough, the summation of the energies dissipated to target electrons in the inlet and outlet surface regions is equal to  $S$ , that is,  $\beta_0 + \beta_d = 1$ , and that the factor  $\Lambda$  is the same both on the inlet and outlet surfaces, that is,  $\Lambda_0 = \Lambda_d$ , values of  $\beta_0$ ,  $\beta_d$ , and  $\Lambda_0 (= \Lambda_d)$  can be obtained from experimental values of  $\gamma_{\text{back}}$  and  $\gamma_{\text{for}}$ . Figure 2 shows the  $z_1$ -dependence of  $\beta_0$ ,  $\beta_d$ , and  $\Lambda_0 (= \Lambda_d)$  for the Au foil target. The factors  $\beta_0$  and  $\beta_d$  do not depend on  $z_1$ , but the factor  $\Lambda$  does depend on it. It suggests that the surface barrier height  $U$  changes dynamically with  $S$ .

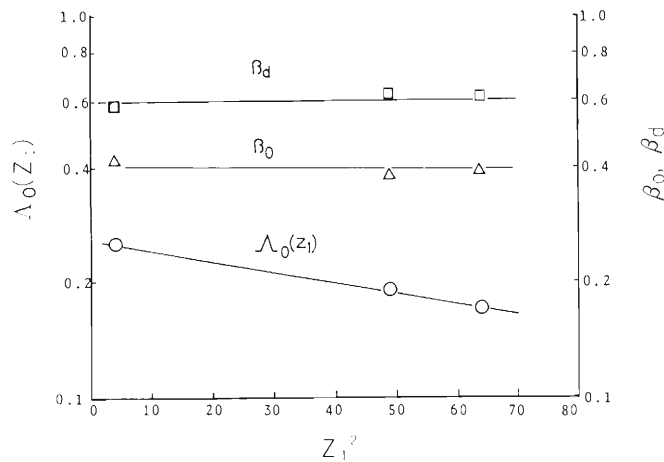


Fig. 2. Dependences of  $\beta_0$ ,  $\beta_d$ , and  $\Lambda_0(= \Lambda_d)$  on  $z_1$ . Both  $\beta_0$  and  $\beta_d$  are independent of  $z_1$  within data scattering of  $\pm 5\%$ , but  $\Lambda_0(= \Lambda_d)$  depends on  $z_1$ .

## References

- 1) N. Oda and J. T. Lyman: *Radiat. Res.*, 7, Suppl., p. 20 (1965).
- 2) H. G. Clerc, H. J. Gehrhardt, L. Richter, and K. H. Schmidt: *Nucl. Instr. and Meth.*, 113, 325 (1973).
- 3) A. Koyama, T. Shikata, H. Sakairi, and E. Yagi: *RIKEN Accel. Progr. Rep.*, 15, 88 (1981).
- 4) A. Koyama, T. Shikata, H. Sakairi, and E. Yagi: *Jpn. J. Appl. Phys.*, 21, 1216 (1982).
- 5) J. Schou: *Phys. Rev. B*, 22, 2141 (1980).

### III-2-19. Lattice Location of Sn Atoms Implanted into Al Crystals as Investigated by Means of Channeling Method

E. Yagi, A. Koyama, H. Sakairi, and  
R. R. Hasiguti\*

The investigation on the lattice location of implanted impurity atoms provides the information on the interaction of impurities with defects, both of which are introduced by the ion implantation. From the point of view of technology, it is also important for the understanding of the mechanism of material modification made by the ion implantation method. It has been considered that there is a difference in the impurity-defect interaction between oversized impurities and undersized ones. In the present study, the lattice location of oversized impurity Sn atoms implanted into Al crystals is investigated by means of channeling method.

The implantation was carried out at room temperature and at 150 kV with the dose of  $10^{14}$  Sn/cm<sup>2</sup>. The axial channeling effect was investigated with respect to  $\langle 100 \rangle$ ,  $\langle 110 \rangle$ , and  $\langle 111 \rangle$  axes by means of backscattering with 1 MeV He<sup>+</sup> ions. Figure 1 shows the normalized backscattering yields from Al and Sn atoms as a function of the angle between the incident beam direction and the concerned crystallographic axis. The backscattering yields from Sn atoms give a shallower dip than the Al-dip in each of three cases. In the  $\langle 111 \rangle$  angular scan, a very narrow dip was observed for Sn yields. The location of Sn atoms was determined from the analysis of the results of angular scan by using the multistring potential. About 35% of Sn atoms occupy the substitutional lattice sites and 20% occupy the interstitial sites which are displaced from the lattice points in the  $\langle 100 \rangle$  direction by about 0.72 Å. The remaining 45% of Sn atoms are at random sites.

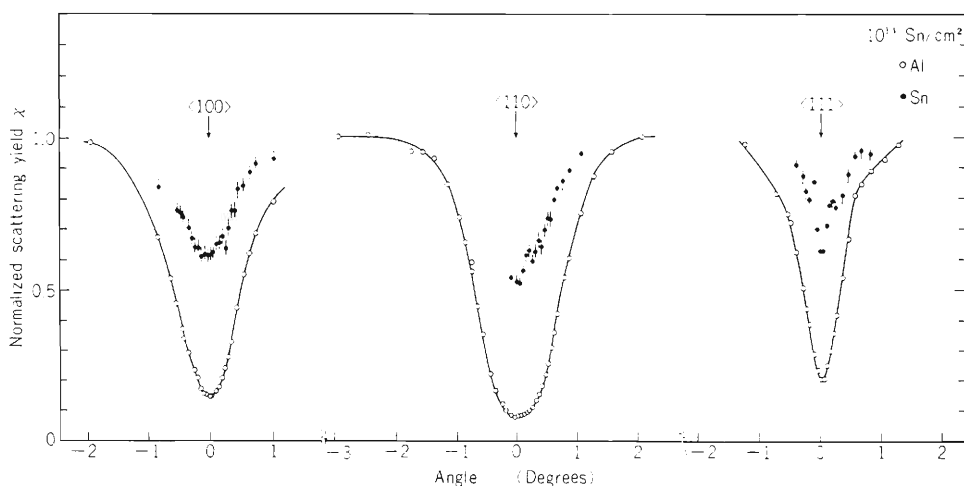


Fig. 1. The  $\langle 100 \rangle$ ,  $\langle 110 \rangle$ , and  $\langle 111 \rangle$  angular scans of the backscattering yields of He<sup>+</sup> ions in Sn-implanted Al crystals.

\* The Science University of Tokyo.

### III-2-20. Amorphization of Diamond Surface Layer by Zn-implantation

S. Sato, M. Iwaki, and H. Sakairi

In our previous report, radiation damage and depth profile of Ar-implanted diamond have been investigated by means of 1 MeV  $^4\text{He}$  channeling technique with the use of the TANDETRON.<sup>1)</sup> The results show that the average projected range and standard deviation of Ar implanted in diamond are in good agreement with these predicted by the range theory and Ar-implantation results in producing an amorphous layer with high conductivity. In the present report, a study has been made of radiation damage and depth profile of Zn-implanted diamond by means of channeling technique.

Substrates used were natural and colorless diamonds with the surface nearly parallel to the (111) plane. Ion implantation was performed with the dose of  $1 \times 10^{16}$  Zn/cm<sup>2</sup> at the energy of 150 keV. The ion beam was sent in a direction deviating by a few degrees from the  $\langle 111 \rangle$  crystal axis in order to reduce the deep penetration of implanted zinc by channeling.

Channeling measurements (Rutherford backscattering) were done by using 1 MeV  $^4\text{He}^+$  with the fluence of  $5 \mu\text{C}$ . Backscattered particles at an angle of  $150^\circ$  were detected and analyzed by a solid state detector and conventional electronics.

Figures 1 and 2 show the  $\langle 111 \rangle$  aligned and random spectra observed for zinc implanted diamond. The leading edge of the diamond target is at channel number 438 (located at half-height) and the energy edge of zinc at the diamond surface at channel number 1274. The energies at channel numbers 438 and 1274 are 0.273 and 0.795 MeV, respectively. The spectra obtained for backscattered particles from zinc implanted in diamond do not exhibit any difference between random and channeling spectra as shown in Fig. 1. Moreover, as shown in Fig. 2, the

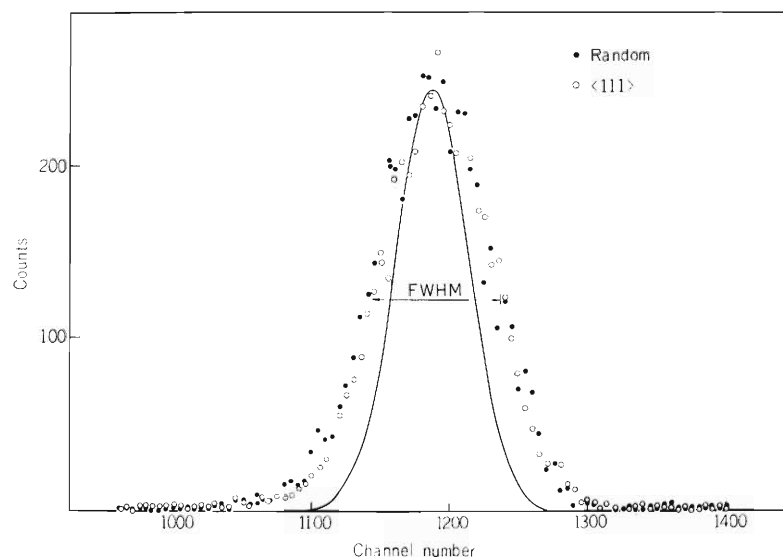


Fig. 1. Random (●) and  $\langle 111 \rangle$  aligned (○) spectra of zinc implanted in diamond.

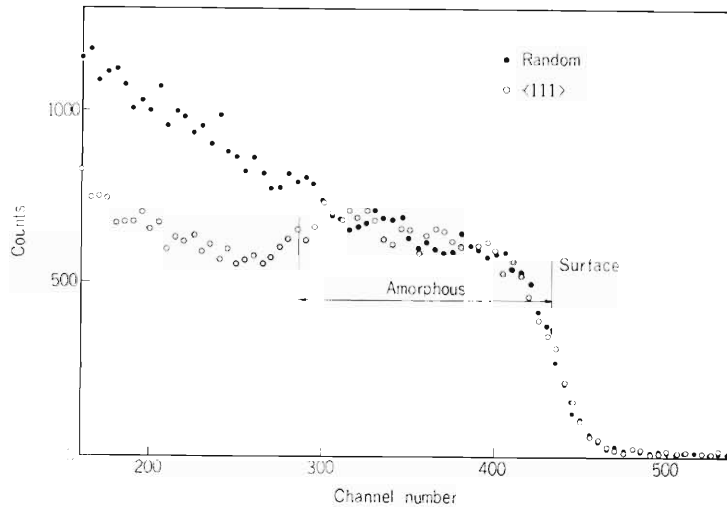


Fig. 2 Random (●) and  $\langle 111 \rangle$  aligned (○) spectra of diamond implanted with zinc.

channeling spectrum overlaps with the random spectrum at channel number above 304. These results display that zinc implantation in diamond produces the amorphous layer near its surface, where implanted zinc atoms are located at random sites.

The depth profile of implanted zinc and the thickness of the amorphous layer can be obtained from Figs. 1 and 2 by using a zero-order analysis. The solid line Fig. 1 indicates the depth distribution predicted by the range theory. The depth corresponding to the peak obtained from the spectra is about 50.6 nm, which is in good agreement with the predicted range of 50.7 nm. The standard deviation calculated from the FWHM of the spectra is about 22.3 nm, which is a little larger than the predicted value of 15.4 nm.

The thickness of the amorphous layer is, if it is assumed to be the region from channel 286 to 433 as indicated in the figure, about 97.9 nm, which is 1.9 times as large as the average projected range. The amorphous layer of the diamond surface produced by Zn-implantation exhibited electrical conductivity, which was measured by means of a four point probe method. The sheet resistivity of the specimen was about  $130 \Omega/\text{cm}^2$ . If the conductivity is assumed to be attributed to amorphous layer, the resistivity is  $130 \times 97.9 \times 10^{-9} = 1.3 \times 10^{-3} \Omega \cdot \text{cm}$ , which is one half as large as that of Ar-implanted diamond or the glassy carbon (produced by Tokai Carbon Company Ltd.). The results show that the conductivity enhancement for zinc implantation may be due not only to the amorphous phase but also to implanted metallic elements themselves.

It is concluded that the average predicted range of zinc implanted in diamond is in fairly good agreement with that predicted by the range theory. By zinc implantation of  $1 \times 10^{16}$  ions/ $\text{cm}^2$  at 150 keV, the conductivity induced by zinc implantation is larger than that of the glassy carbon on the market.

#### Reference

- 1) M. Iwaki and H. Sakairi: RIKEN Accel. Progr. Rep., 15, 98 (1981).

### III-2-21. Pulsed Laser Annealing of Cd-implanted GaP

K. Aono, M. Iwaki, and S. Namba

Laser annealing of disordered semiconductors is a relatively new field of semiconductor physics. The laser beam used for annealing has an energy large enough for rapid recrystallization in heavily damaged regions near water surface, such as ion-implanted layers which range from the surface to a few hundred nanometers. In the present work, the effect of laser irradiation on the profiles of Cd and radiation damage in Cd-implanted GaP was investigated by means of a  $^4\text{He}^+$  channeling technique.

Substrates used were n-GaP with the surface parallel to the (111) plane. Surfaces of all wafers were mirror-polished and chemically etched. Cadmium-implantations were carried out at ion energies of 50, 100, and 150 keV with doses from  $1 \times 10^{12}$  to  $1 \times 10^{16}$  ions  $\text{cm}^{-2}$  at  $2 \times 10^{-6}$  Torr. Target temperature during implantation was held at room temperature or at about  $350^\circ\text{C}$ . The Cd ion beam was sent in a direction deviating by a few degrees from the  $\langle 111 \rangle$  crystal axis. Annealing was carried out with nanosecond pulsed lasers. The surface was swept by the laser spot,  $100 \mu\text{m}$  in diameter, to heat the implanted area. The samples mounted on a 3 axis goniometer in a target chamber, which was kept at a pressure below  $\sim 5 \times 10^{-6}$  Torr, were

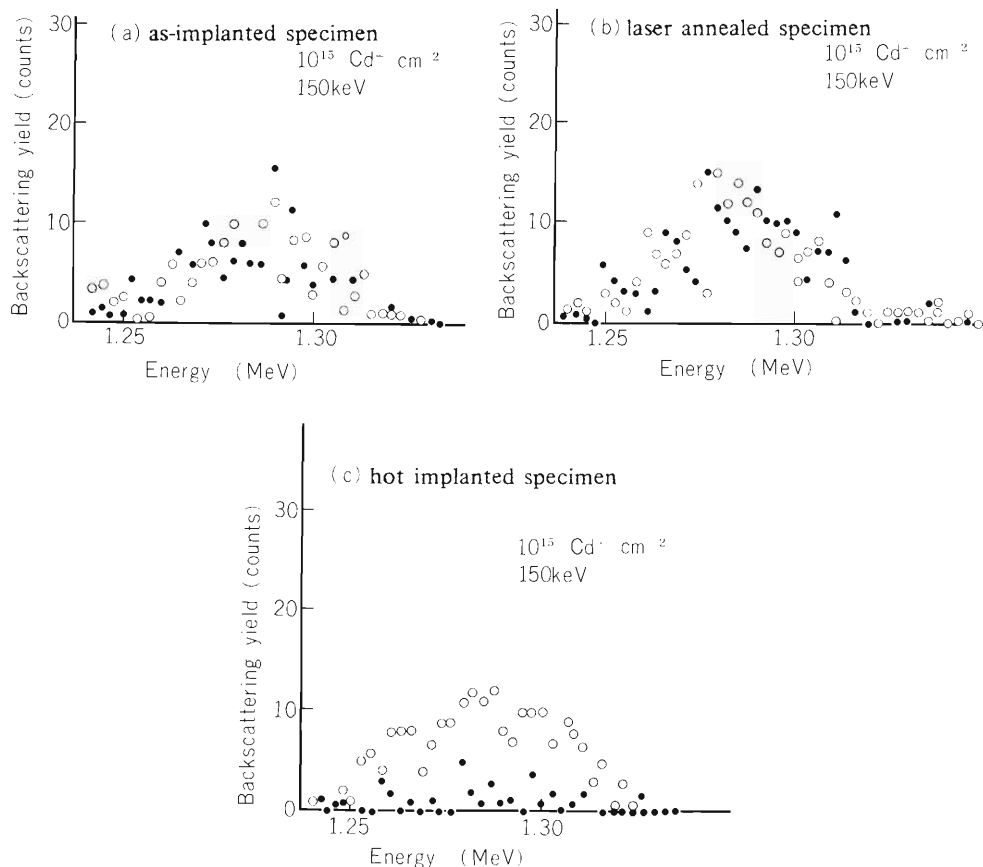


Fig. 1. Random (○) and  $\langle 111 \rangle$  aligned (●) spectra of Cd implanted in GaP.

analyzed with 1.5 MeV  $^4\text{He}^+$  beam using the Rutherford backscattering and channeling technique. Backscattered particles at an angle of  $150^\circ$  were detected and analyzed by a conventional electronics.

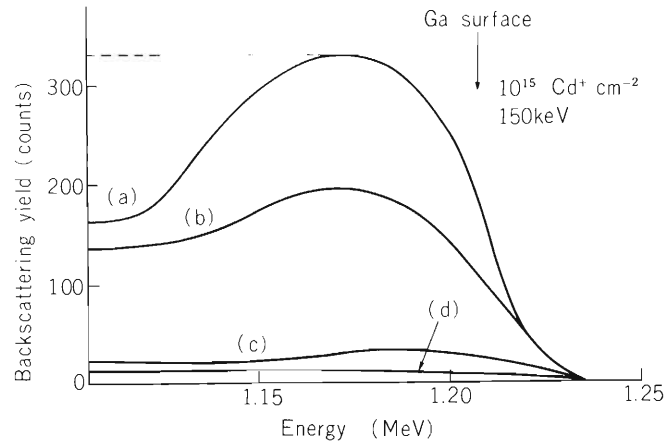


Fig. 2. Random (---) and  $\langle 111 \rangle$  aligned (—) spectra of GaP implanted with Cd.

- (a) the as-implanted specimen,
- (b) the laser annealed specimen,
- (c) the hot implanted specimen,
- (d) the un-implanted specimen.

Figures 1 and 2 shows the random and  $\langle 111 \rangle$  aligned spectra observed for Cd-implanted GaP with  $15^{15}$  ions  $\text{cm}^{-2}$  at 150 keV. The Cd depth profiles in the random spectra of as-implanted, laser annealed and hot implanted specimens have similar distributions which are gaussian as shown in Fig. 1. No difference is exhibited between the random and the aligned spectra of the as-implanted specimen and the laser annealed specimens. However, in the scattering yield from the hot implanted specimen, the aligned spectrum shows a strong reduction. This result shows that most of Cd atoms occupy substitutional lattice sites in the case of hot implantation.

Radiation damages in Cd-implanted layers were investigated from the spectra obtained from Ga in GaP. The result is shown in Fig. 2. Backscattering yields of the aligned spectra decrease after laser irradiation, and for hot implantation they are almost the same as those of an un-implanted specimen.

From channeling measurements we can conclude that radiation damage in the hot implanted specimen was smaller than that of the laser annealed specimen.

### III-2-22. Radiation Damages in Amorphous Alloys Irradiated with $C^{4+}$ and $N^{4+}$ Ions

S. Nanao,\* Y. Watanabe,\* K. Oda,\* and N. Shiotani

Recent studies suggest that amorphous alloys have large resistance against radiation damages. This originates mainly in the characteristics of amorphous alloys, that is, random atomic arrangement. At the present stage, however, very few information has been obtained on the structures and recovery behaviors of the radiation damages produced in amorphous alloys.

The aim of the present study is to investigate the recovery stages of the radiation damages induced in an amorphous alloy  $Fe_{80}B_{20}$  by irradiation with  $C^{4+}$  and  $N^{4+}$  ions at low temperatures using the cyclotron and to identify the defects and/or relaxation of the amorphous structure relevant to each recovery-stage.

As the first step, we have measured the changes in electrical resistivity due to isochronal annealing of 30 min. after irradiation with 80 MeV  $C^{4+}$  ions at 77 K. The irradiation was performed with mean current of 90 nA in a vacuum. The total dose was about  $10^{21}$  ions/m<sup>2</sup>. The resistivity measurements were done at 77 K.

The results are shown in Fig. 1. Two or three stages are observed in the change of electrical resistivity as a function of the annealing temperature. Above 0 °C, no appreciable difference in the electrical resistivity are observed up to 160 °C, which indicates that nearly all the damages have recovered below 0 °C.

Further measurements and analyses are now in progress.

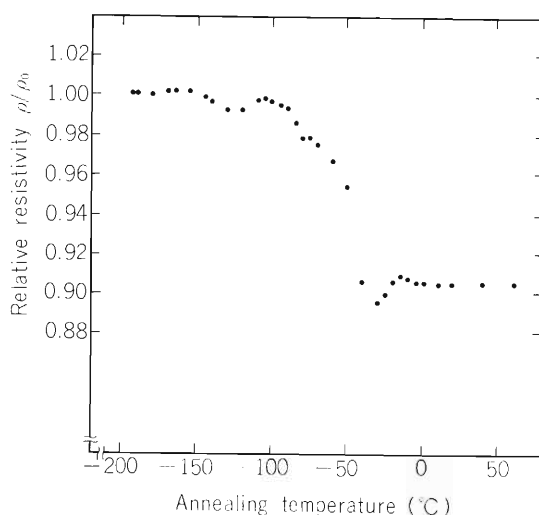


Fig. 1. Relative resistivity ( $\rho/\rho_0$ ) measured at 77 K as a function of isochronal annealing temperature in a  $C^{4+}$  irradiated  $Fe_{80}B_{20}$  amorphous alloy.

\* Institute of Industrial Science, University of Tokyo.

### III-2-23. Positron Angular Correlation Measurements on Oxygen Implanted Molybdenum Containing Voids

M. Hasegawa,\* E. Kuramoto,\*\* and N. Shiotani

Recently it has been discovered that positroniums are formed in niobium and vanadium metals which contain voids and small amount of impurity atoms such as oxygen and carbon atoms. The positrons are considered to be trapped at the inner surface of the voids. However, by the presence of the oxygen and carbon atoms the trapping potential for the positrons at the surface is changed so as to convert the trapped positrons into positroniums which can move in the voids. In the present study an attempt is made to see the positronium formation in molybdenum.

The specimen containing almost no oxygen nor carbon impurities was first irradiated by neutrons in order to produce the voids. At this stage the positronium formation was not detected. Then the oxygen beam  $O^{5+}$  was accelerated to 90 MeV by the cyclotron and implanted into the specimen up to  $6.24 \times 10^{14} O^{5+}/cm^2$  at room temperature. According to the calculation by modified E-DEP-1 code the implanted oxygen distribution should spread from the surface to about  $40 \mu m$  in depth and has a sharp peak at about  $30 \mu m$ . However, the actual distribution spreads more due to beam heating and migration of lattice defects produced during implantation.

Positron angular correlation measurements were made on this specimen. The results are shown in Figs. 1 and 2. The oxygen implantation made the half width of the angular correlation curve narrower than that of as-neutron-irradiated one. However, the width is still much broader than those observed in niobium and vanadium, the half width of which is about 2 mrad. Therefore, the positronium formation in the voids in molybdenum could not be concluded, but some tendency for it is thought to be taking place. Probably the amount of oxygen implanted was not large enough to modify the surface of all the voids in the specimen.

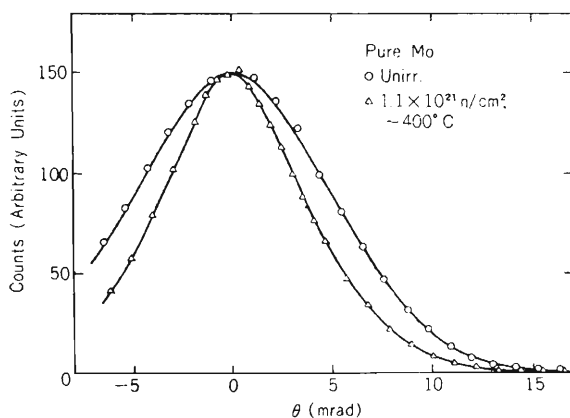


Fig. 1. Positron angular correlation curve for unirradiated and neutron-irradiated molybdenum.

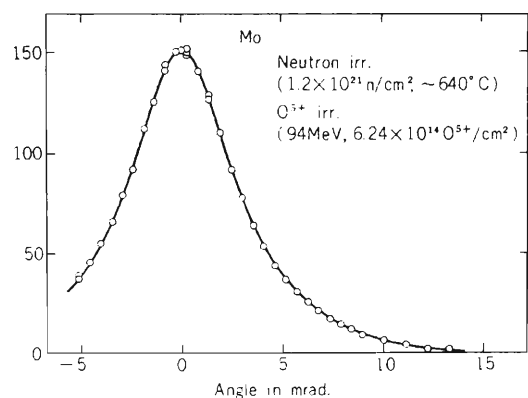


Fig. 2. Positron angular correlation curve for neutron-irradiated and oxygen implanted molybdenum.

\* The Research Institute for Iron, Steel and Other Metals, Tohoku University.

\*\* Research Institute for Applied Mechanics, Kyushu University.

### III-2-24. Effect of an Injected Helium Layer near Surface on the Tensile Properties of Fe-Ni-Cr Alloys

N. Yamamoto,\* H. Shiraishi, H. Yoshida,\*  
H. Kamitsubo, I. Kohno, and T. Shikata

It is well known that helium generated by  $(n,\alpha)$  reactions causes a loss of ductility in alloys used for fast breeder and magnetic fusion reactor structural components, because it accumulates at grain boundaries where it has a strong positive influence on intergranular fracture. Among the experimental methods to study this phenomenon, helium injection by using an accelerator is a convenient way of introducing large amount of helium into the specimen in a short time. Therefore, we took this method, and have investigated effect of helium on the high temperature tensile properties of various Fe–Ni–Cr alloys, using sheet specimens into which helium was uniformly injected all over their thickness by  $\alpha$  particle irradiation of the cyclotron.<sup>1)</sup>

On account of experimental restriction, however, the helium concentration in this “uniform helium injection mode” is low (only up to 10 at.ppm) compared to that produced in fast breeder or fusion reactor environment. On the other hand, “local helium injection mode” in which helium is locally injected into a thin layer near the surface of the specimen can form a portion of much higher helium concentration (up to 100 at.ppm) at the same  $\alpha$  particle irradiation dose. And it seems likely that some indication of premature intergranular fracture of the helium injected layer during the high temperature tensile test after local helium injection would be observed on the stress-strain curve and thereby some of the information could be obtained on the effect of highly concentrated helium on the high temperature tensile properties of the alloy. In the present work, therefore, helium was injected with local helium injection mode, and effect of highly concentrated helium on the high temperature tensile properties was studied for several Fe–Ni–Cr alloys.

Result of chemical analysis of the alloys used are presented in Table 1. SUS 316 is a typical fast breeder structural material. Alloys 7817 and 7818 are  $\gamma'$ -Ni<sub>3</sub>(Ti, Al) and  $\gamma'$ -Ni<sub>3</sub>Nb precipitation strengthened alloys, respectively. Tensile test specimens were die-stamped out from 0.2 mm thick sheets. The dimension of gauge section was 10 mm long, 4 mm wide, and 0.2 mm thick. The specimens were solution treated for 30 min. at certain temperature : 1050 °C for SUS 316, 1000 °C for 7817, and 1100 °C for 7818. This treatment resulted in the mean grain sizes of

Table 1. Chemical composition of the samples. (wt%)

Alloy	C	Ni	Cr	Mo	Ti	Al	Nb	Si	Mn	B	Fe
SUS 316	0.043	13.9	16.1	2.50	—	—	—	0.44	1.42	0.0006	balance
7817	0.021	40.2	14.6	3.19	2.01	0.87	—	0.47	0.19	0.0049	balance
7818	0.024	39.2	14.7	3.03	0.31	—	2.96	0.48	0.19	0.0048	balance

\* National Research Institute of Metals.

46  $\mu\text{m}$ , 20  $\mu\text{m}$ , and 69  $\mu\text{m}$ , respectively. Finally, the specimens received various pre-injection thermomechanical treatments. Helium was injected at constant high temperature (650  $^{\circ}\text{C}$ ), by using the cyclotron. The helium concentration and thickness of the helium injected layer were about 5 – 100 at. ppm and 10 – 20  $\mu\text{m}$ . The tensile tests were carried out at 650  $^{\circ}\text{C}$  or 750  $^{\circ}\text{C}$  in vacuum below  $5 \times 10^{-6}$  Torr. The fracture surface of the specimens was examined by a scanning electron microscope.

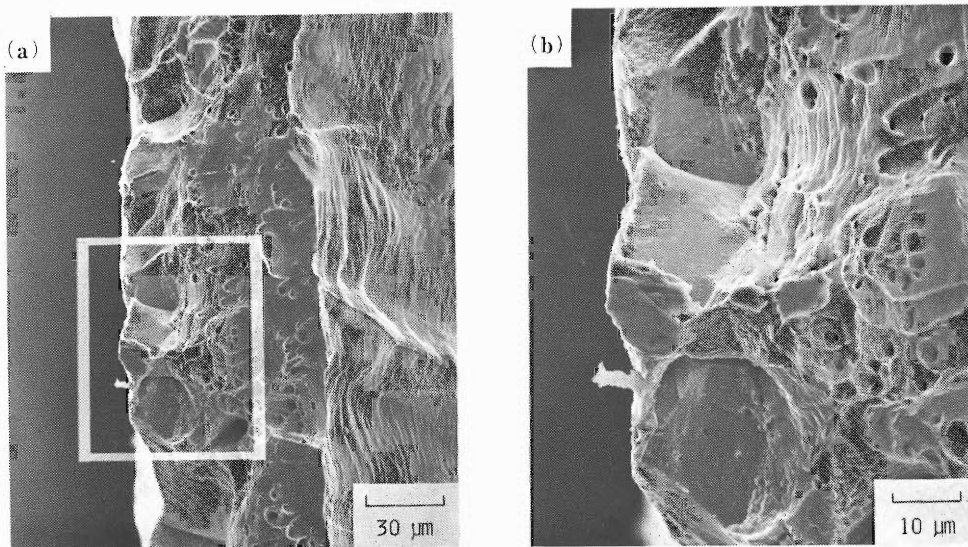


Fig. 1. Electron fractographs of the fracture surface of tensile tested SUS 316 which contained a helium injected layer (100 at. ppm He, 10  $\mu\text{m}$  thick). Pre-injection treatment: ST (1050  $^{\circ}\text{C}$ , 30 min.), test temperature: 650  $^{\circ}\text{C}$ , strain rate:  $5 \times 10^{-4}$   $\text{s}^{-1}$ . Figure (b) is a magnified picture of the rectangular area shown in figure (a).

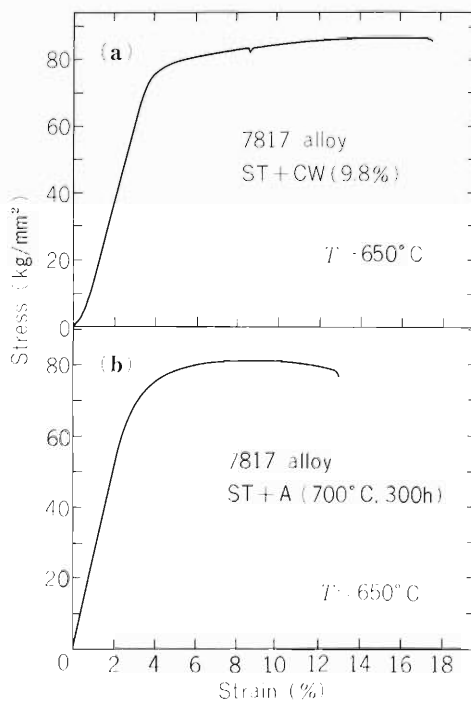


Fig. 2. Stress-strain curves for locally helium injected 7817 alloy. Test temperature: 650  $^{\circ}\text{C}$ , strain rate:  $5 \times 10^{-4}$   $\text{s}^{-1}$ . Figure (a) pre-injection treatment: ST (1000  $^{\circ}\text{C}$ , 30 min) + CW (9.8 %), helium injected layer: 100 at.ppm He, 10  $\mu\text{m}$  thick. Figure (b) pre-injection treatment: ST (1000  $^{\circ}\text{C}$ , 30 min) + A (700  $^{\circ}\text{C}$ , 300 h), helium injected layer: 50 at.ppm He, 20  $\mu\text{m}$  thick.

As shown in Fig. 1, fractographs by SEM revealed that in almost all cases, fracture occurred, at least partially, in intergranular brittle mode in the helium injected layer and its adjacent region, while the other portion of the specimen showed a transgranular ductile fashion. This observation implies that intergranular fracture mentioned above should be caused by injected helium. On the other hand, as illustrated in Fig. 2, the load drop which should result from premature fracture of the helium injected layer was observed on some of the high temperature stress-strain curves of locally helium injected specimens (Fig. 2a), while there were some others on which any indication of premature fracture was hardly observed (Fig. 2b). Thus, the results of the tensile tests are still difficult to explain at the present time, and more systematic experiments changing the helium concentration, thickness of the helium injected layer, the strength of the alloys, and so on, will be needed to obtain information on the effect of highly concentrated helium on high temperature tensile properties of alloys.

### III-2-25. Effects of Fast Neutron Irradiation on Insulating Materials

H. Kamitsubo, I. Kohno, S. Motonaga, M. Yanokura,  
T. Shikata, M. Yatsunami,\* T. Suematsu,\* and H. Kobayashi\*

Needs for use of plastics and elastomers in areas of high-radiation levels are increasing and detailed information on radiation-induced effects in polymers is required to determine their stability in their applications and the service life that can be expected.

The radiation effects in the plastics and elastomers have been investigated mainly by irradiating with gamma rays from  $^{60}\text{Co}$  sources or electron linacs and also slow neutrons from reactors. However it becomes more important to get the information on the effects of fast neutron irradiations in these materials, because development of fast breeder reactors and thermonuclear fusion reactors, which will generate much higher flux of fast neutrons than the existing reactors, is hurried on.

We have studied the effects induced by fast neutrons in polymers which are used as insulating material for electric wires. Change of resistivity, dielectric constant, dielectric loss, tensile strength and elongation under the influence of its fast neutron irradiation is to be measured for these materials. Size of the samples was determined to be 5 cm by 5 cm in area and 1 mm in thickness from the minimum size needed for the measurement of mechanical properties. Taking into account the results of gamma ray irradiation,<sup>1)</sup> the maximum dose should be as high as  $5 \times 10^8$  rad. and total neutron fluence must be higher than  $10^{16}$  neutrons/cm<sup>2</sup>. Figure 1 shows the irradiation system. Fast neutrons were generated by bombarding a thick beryllium target with 20 MeV deuterons from the cyclotron. Two beryllium plates of 2 mm in thickness were tightly fixed to a water-cooled flange, which is insulated from the earth and beam current on the target could be measured by the current integrator.

Neutrons from the thick target have broad energy spectra and their intensity distribution depends strongly on the emission angles.<sup>2)</sup> Neutron fluence as well as total dose was estimated using data in Ref. 2 and conversion rate of 1 rad =  $2 \times 10^8$  neutrons. We tried to determine the neutron fluence by the activation method as described below. In order to get as high neutron flux as possible at the samples, the samples were placed very close to the target. As shown in Fig. 1, a sample holder which can contain three samples at the same time was attached directly

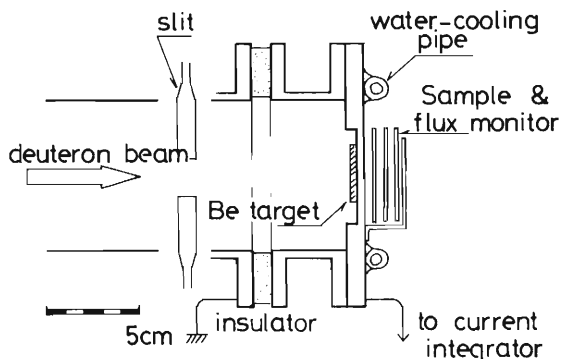


Fig. 1. The irradiation system.

\* Fujikura Cable Works Ltd.

to the outer side of the target flange. The distance between the target and the samples was small so that the neutron fluence was not uniform on the samples. Foils of aluminum, iron and nickel of the same size as the sample were put together with samples and irradiated at the same time. After the irradiation, each foil was cut into 25 pieces of  $1\text{ cm} \times 1\text{ cm}$  and the induced radio-activities were measured for them. Thresholds of neutron activation are different for three kinds of foils so that we can get the fluence of neutrons whose energy is higher than 2 MeV.

The irradiation was done with the average deuteron current of  $10\ \mu\text{A}$ . Five samples of polyvinylchloride were irradiated for 1, 5, 7, 11, and 12 h, respectively. Figure 2 shows the fluence distribution at the sample which was irradiated for 12 h. Mechanical and electric measurements are in progress and the irradiation at higher fluence is scheduled.

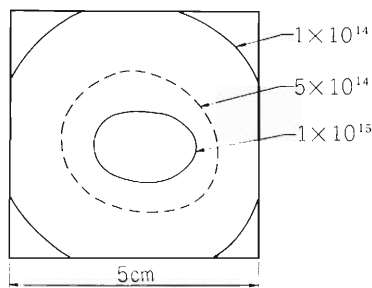


Fig. 2. Measured total neutron flux distribution at the target position using the activation method.

## References

- 1) M. Asaka, S. Yamamoto, M. Yatsunami, G. Hara, and S. Sakai: Fujikura Densen Giho, 48, 61 (1973).
- 2) M.A. Lone, C. B. Bigham, J. S. Fraser, H. R. Schneider, T. K. Alexander, A. J. Ferguson, and A. B. McDonald: Nucl. Instr. and Methods, 143, 331 (1977).

### III-3. Radiochemistry and Nuclear Chemistry

#### 1. Radioisotope Production and Labelled Compound Synthesis

Y. Minai, T. Nozaki, S. Ambe, and M. Iwamoto

In this period, the production of  $^{29}\text{Al}$  and the synthesis of radiobromine-labelled 6-bromopurine and 6-bromo-9-benzylpurine have been studied.

Aluminium is abundant in nature, but its behaviour and role in the biosphere have remained obscure. This is due to the absence of any radiotracer nuclide as well as of stable tracer nuclide. We intended to produce  $^{29}\text{Al}$  (6.7 min,  $\beta^-$ , 1.27 MeV  $\gamma$ -ray) and to use it as a tracer in life sciences, in spite of its limited life. The  $^{26}\text{Mg}(\alpha, p)^{29}\text{Al}$  reaction is regarded as the only useful reaction for the production of  $^{29}\text{Al}$  in high specific activity. The excitation function and thick target yield for this reaction were measured together with those for some relevant reactions. The results for the main reaction are shown in Fig. 1.

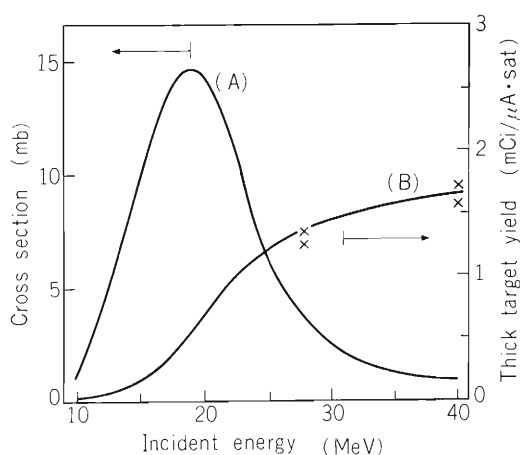


Fig. 1. Excitation function (A) and thick target yield (B) for the  $^{26}\text{Mg}(\alpha, p)^{29}\text{Al}$  reaction.

Target: Magnesium metal of natural isotopic composition. Star plots: Experimental result of the thick target yield; Full line for the thick target yield: Result obtained by calculation from the excitation function.

Two methods were examined for the chemical separation of the no-carrier-added  $^{29}\text{Al}$  from the magnesium target: (1) adsorption of the  $^{29}\text{Al}$  in a cellulose powder column from its neutral solution, followed by elution with a dilute acid, and (2) extraction of the  $^{29}\text{Al}$  as acetylacetonate into benzene from a faintly acid solution, followed by evaporation of the organic solvent and sublimation of the  $^{29}\text{Al}$  acetylacetonate. In Method 1, the procedure can be completed within 20 min with an  $^{29}\text{Al}$  yield of about 60%. The separated  $^{29}\text{Al}$ , however, is inevitably contaminated with a small fraction of by-product radioactivities, such as  $^{27}\text{Mg}$ ,  $^{18}\text{F}$ , and  $^{24}\text{Na}$ , and of target magnesium. In Method 2, the  $^{29}\text{Al}$  can be separated in excellent radiochemical and chemical purity. The separation, however, requires 20 to 30 min with a yield of about 30%. Method 1 is preferred in the preparation of  $^{29}\text{Al}$  tracer for agricultural study, but Method 2 should be used when the  $^{29}\text{Al}$  is injected to animals. About 1 mCi of  $^{29}\text{Al}$  ready for injection is now prepared. Efforts are being made for the shortening of the separation time and the elevation of the yield in Method 2.

A preliminary study of  $^{29}\text{Al}$  uptake by plants has been undertaken. Some plants were found to take up  $^{29}\text{Al}$  fairly rapidly from an aqueous solution.

In 1975, we prepared  $^{18}\text{F}$ -labelled 2- and 6-fluoro-9-benzylpurine and measured their animal distribution.<sup>1)</sup> The  $^{18}\text{F}$  activity injected as 6-fluoro-9-benzylpurine showed a notable concentration in the brain as well as in the skeleton. Since then physiological behaviour of this compound has been investigated, and its suitable preparation method was found in the National Institute of Radiological Sciences.<sup>2)</sup> Now in collaboration with this institute, we intend to prepare  $^{77}\text{Br}$ - and  $^{75}\text{Br}$ -labelled 6-bromo-9-benzylpurine and to study its *in vivo* behaviour, expecting some possibility for the radiobromine to show a high brain concentration without any notable accumulation in the skeleton.

This compound and 6-bromopurine were found to be labelled successfully by isotopic exchange in dehydrated dimethylformamide at 130 °C. The radiobromine was produced by the  $^{75}\text{As}(\alpha, 2n)^{77}\text{Br}$  or  $^{75}\text{As}(^3\text{He}, 3n)^{75}\text{Br}$  reaction in a gallium arsenide target, and was separated by sublimation under radio-frequency fusion of the target. Several materials were tested as the flux in the target fusion, and copper grains were found to give the best sublimation efficiency. In the fusion for a few minutes the radiobromine came out from the melt almost quantitatively, and, after being carried for a short distance by a slow helium stream, deposited on the inside wall of the sublimation apparatus with a small amount of metallic arsenic. The radiobromine was then washed out in dehydrated dimethylformamide. About half of the radiobromine remained on the wall, though nearly quantitative washing out by water was possible.

The isotopic exchange was effected at 130 °C in 1 ml of the solvent containing the radiobromine and a few milligrammes of the substrate compound. The labelled organic compound was separated from the inorganic bromine by a small silica gel column with the eluent of AcOEt – EtOH (9 vol : 1 vol). About 80 % of the radiobromine was found to be incorporated into the bromopurines in 2 h. Their animal distribution will be studied very soon.

## References

- 1) T. Nozaki, S. Ambe, M. Iwamoto, T. Ohsawa, T. Karasawa, M. Okano, Y. Kasida, T. Ido, K. Suzuki, K. Fukushi, L. Iwata, T. Irie, T. Hara, and K. Taki: *IPCR Cyclotron Progr. Rep.*, 9, 101 (1975).
- 2) T. Irie, K. Fukushi, O. Inoue, T. Yamasaki, T. Ido, and T. Nozaki: *Int. J. appl. Radiat. Isotopes*, 33, 633 (1982).

### III-3-2. Charged Particle Activation Analysis of Semiconductor Materials

T. Nozaki, Y. Itoh, and M. Iwamoto

Application of charged particle activation analysis to the study of semiconductor materials has been continued in collaboration with various outside researchers. Main works in this period are (1) determination of highly reliable calibration curve for the IR spectrophotometry of oxygen in semiconductor silicon, (2) analysis of nitrogen, oxygen and phosphorus in epitaxial films on semiconductor silicon wafers, (3) more accurate determination of the solubility and diffusion coefficient of oxygen in solid silicon at various temperatures, (4) more systematic study on surface oxygen, and (5) some other studies concerning oxygen profiles and behaviour in silicon of various histories. Two bombardment devices have been completed: one for successive bombardment of 4 samples in a vacuum, and the other for homogeneous bombardment of a sample along its length.

Oxygen in semiconductor silicon is routinely measured by IR spectrophotometry in semiconductor factories. Several different calibration curves have been reported for this spectrophotometry and used.<sup>1)</sup> It has thus been of ultimate importance, especially in commercial transaction of semiconductor silicon, to establish highly reliable calibration curve for this measurement together with corresponding practical procedure and to use them commonly all over the world. It is still better to prepare a sufficient number of silicon wafers of exactly known oxygen concentrations and distribute a set of the wafers with various oxygen contents to anyone who want to use it as the standard in this measurement.

In Japan a committee was set up for these purposes. Under its supervision, silicon wafers with various oxygen contents and thicknesses were carefully prepared at several places and submitted to the IR spectrophotometry in companies and research institutes. About 70 wafers in all were measured in about 15 laboratories. After the IR measurement, 22 wafers, all 1 mm thick, were analyzed by charged particle activation analysis with the  $^{16}\text{O}(^3\text{He}, \text{p})^{18}\text{F}$  reaction in our institute. Researchers from several companies and a research institute joined with us for this oxygen analysis.

The wafer was bombarded with  $^3\text{He}$  particles (18 MeV, about 2  $\mu\text{A}$ ) for 20 min behind an aluminium foil (80  $\mu\text{m}$  thick), and then its surface layer ( $23 \pm 2 \mu\text{m}$ ) was removed by etching with HF-HNO<sub>3</sub>. The wafer was placed after 1 h from the end of bombardment, directly on a Ge(Li) detector and the annihilation radiation was measured. The measurement was repeated to give the decay curve, which indicated the absence of any other notable positron activity than  $^{18}\text{F}$ . As for the activation standard, a quartz plate was used with an aluminium cover of 20  $\mu\text{m}$  thick, in which the incident  $^3\text{He}$  particle energy was degraded equally as in the silicon surface layer removed by the etching. Within a period of each cyclotron machine time, usually 8 such plates were bombarded for the ascertainment of reproducibility. The analysis of each silicon sample was repeated at least twice. Samples, for which the results of the first two analyses deviate more than 4 % from each other, were subjected to third analysis. When the three analyses gave no satisfactory results, fourth analysis was undertaken. Also, one common sample

was always analyzed in all machine times to indicate good reproducibility of the analysis.

The calibration curve thus obtained is shown in Fig. 1. This agrees well with the curve we reported previously,<sup>1,2)</sup> and can be believed to be the most reliable of all the curves ever reported for this purpose. Silicon wafers for use as the standard samples are now under preparation in some factories.

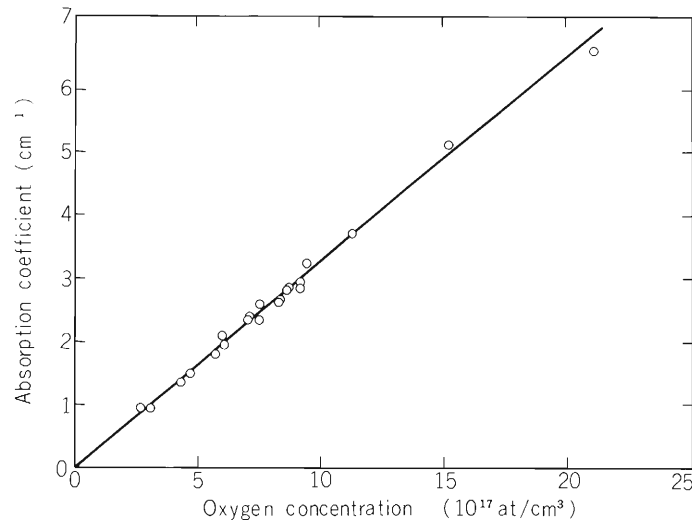


Fig. 1. Calibration curve for IR spectrophotometry of oxygen in silicon.

By being covered with a suitable epitaxial film, semiconductor silicon is known to be provided with profitable characteristics in use as high-voltage rectifier. The film is composed of nitrogen, oxygen, hydrogen, silicon, and sometimes phosphorus. In collaboration with Hitachi Ltd., nitrogen, oxygen, and phosphorus in the film made under various conditions were analyzed by charged particle activation with the reactions  $^{14}\text{N}(p, \alpha)^{11}\text{C}$ ,  $^{16}\text{O}(^3\text{He}, p)^{18}\text{F}$ , and  $^{31}\text{P}(\alpha, 2n)^{34\text{m}}\text{Cl}$ , respectively. The sample was covered with a thin wafer of semiconductor silicon and bombarded with the incident particles of such an energy as to be degraded approximately to the energy corresponding to the maximum of the excitation function for the given reaction at the epitaxial film. The induced activity was then measured nondestructively by a Ge(Li) detector, and the decay was followed. Hydrogen was measured by Rutherford forward scattering; details about this method is shown in a separate report of this volume. Some systematic dependence was already found between contents of these elements and preparation condition of the film. This work is still in progress, and more detailed results will be reported in the next volume.

The measurement of oxygen solubility and diffusion coefficient in solid silicon has been continued. The solubility curve is shown in Fig. 2 after slight modification of the previous curve.<sup>3)</sup> Both the solubility and diffusion coefficient curves show noticeable tailings in the logarithm- $1/T$  expression, indicating the existence of some diffusion faster than the usual diffusion into a perfect crystal. From thermochemical considerations, the faster diffusion can be assumed to be a rapid penetration of oxygen through a lineage fault formed in the heat treatment of the sample. Efforts are made by various techniques to verify this assumption.

The work of surface oxygen analysis also has been continued.<sup>4)</sup> More varieties of samples were analyzed under various atmospheric conditions. Detailed results of this study will be reported in the next volume.

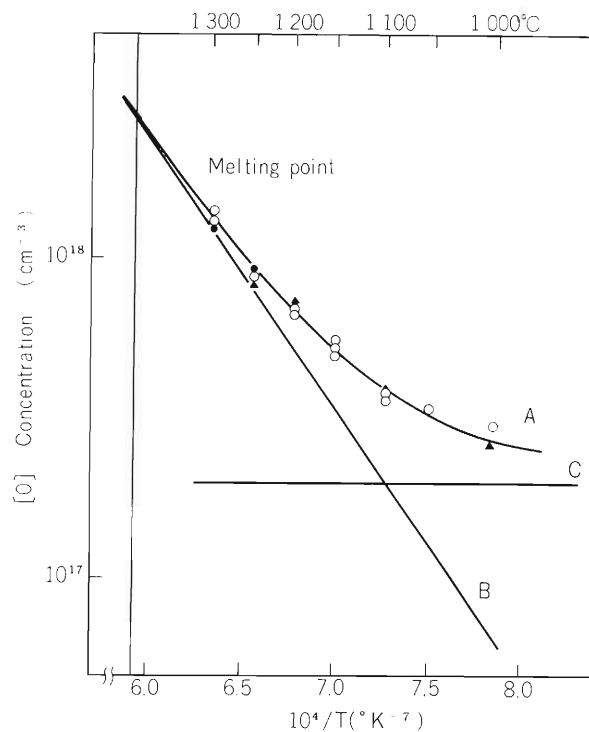


Fig. 2. Solubility of oxygen in solid silicon.  
 A: Experimental result; B: Presumably, real oxygen solubility; C: Presumably, oxygen in lineage faults. Initial oxygen concentration of the sample: ●  $> 1 \times 10^{18}$  at/cm<sup>3</sup>,  
 ▲  $1 \times 10^{17} \sim 1 \times 10^{18}$  at/cm<sup>3</sup>,  
 ○  $< 5 \times 10^{16}$  at/cm<sup>3</sup>.

## References

- 1) e.g., Landolt-Bernstein Zahlenwerte und Funktionen aus Naturwissenschaften und Technik, Neue Ser., III/17, p. 368, Springer, Berlin (1982).
- 2) Y. Yatsurugi, N. Akiyama, Y. Endo, and T. Nozaki: J. Electrochem. Soc., 120, 975 (1973).
- 3) Y. Itoh and T. Nozaki: RIKEN Accel. Progr. Rep., 15, 107 (1981).
- 4) T. Nozaki and M. Iwamoto: *ibid.*, p. 105.

### III-3-3. Rutherford Forward Scattering Applied to the Study of Hydrogen in Amorphous Silicon for Solar Cell

H. Nagai, M. Aratani, T. Nozaki, M. Yanokura,  
I. Kohno, O. Kuboi, and Y. Yatsurugi

Measurements of hydrogen concentration and depth profile in solids and thin layers are often of vital importance, especially in the study of amorphous silicon for solar cells. Rutherford forward scattering measurement can be regarded as particularly useful for this purpose. Using this method with accelerated argon ions as incident particles, we have obtained hopeful results.<sup>1),2)</sup>

Rutherford scattering is nuclear elastic scattering. By the measurement of the intensity and energy-angle relationship for scattered or recoiled ions, the concentration and depth profile of the element in question can be known.

Samples were prepared in the Komatsu Electronic Metals Co. by the glow-discharge decomposition of monosilane. Amorphous silicon films were deposited on substrate silicon wafers. Several pieces of samples (19 mm X 9 mm) were mounted on an aluminium holder. The arrangement of experimental apparatus is shown in Fig. 1. The scattered and recoiled ions were measured with a silicon detector behind a slit (3 mm in diameter) in a scattering chamber (100 cm in diameter). Incident angle  $\theta_1$  and detector angle  $\theta_2$  in Fig. 1 can be changed by remote-controlled movement of the sample holder and the detector, the former being also movable vertically for the change of the sample. As the incident particle beam, argon ions were accelerated to 43 MeV (at maximum) by Riken Linear Accelerator. Several tens nA of this beam was focussed (2 mm X 2 mm) and impinged on the sample. Output pulses of the detector were amplified and assorted by a pulse-height analyzer to give the energy spectrum of the recoiled hydrogen and silicon ions and the scattered argon ions. Optimum measurement condition under the given accelerator operation was looked for by the change of  $\theta_1$  and  $\theta_2$ . Similar measurements were

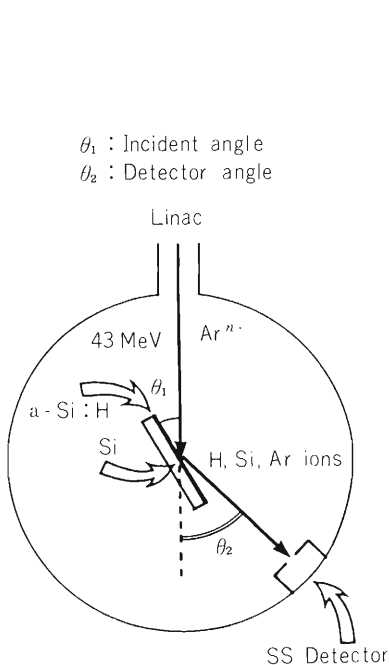


Fig. 1. Experimental arrangement.

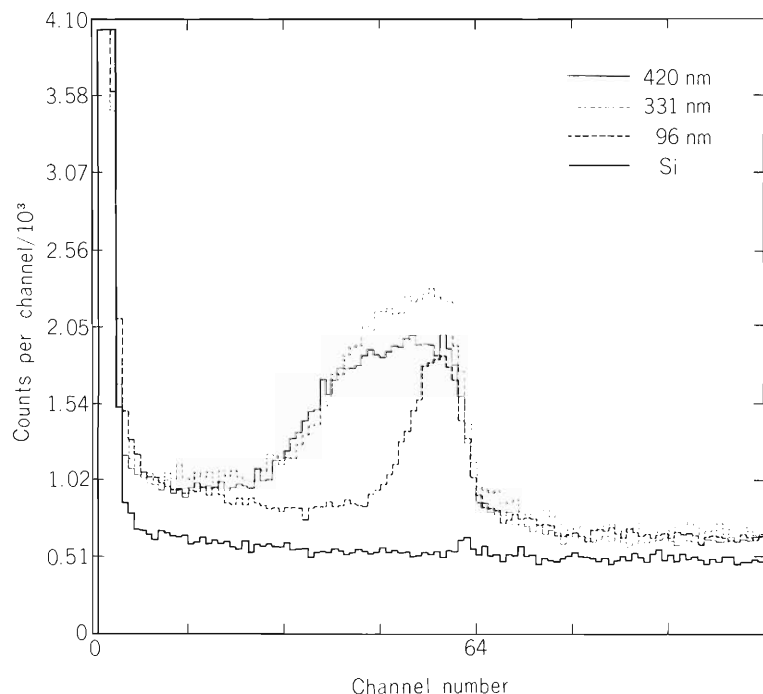


Fig. 2. Rutherford forward spectra for hydrogen depth profiling obtained by 22 MeV argon ions.

performed for a high-purity silicon crystal as a reference sample without hydrogen, PIQ (polyiminoquinone) films as a standard sample for hydrogen, and thin films of silicon nitride, silicon oxide and SIPOS (semiinsulating polycrystalline silicon) on silicon plates.

Some of the spectra are shown in Fig. 2. Clear peaks due to hydrogen are observed. During 70 minutes irradiation, no notable change was seen in the spectrum. The PIQ film gave somewhat complicated spectrum, and was not used as a standard for quantitative hydrogen determination up to present. The hydrogen quantity was calculated from the hydrogen peak area and silicon continuum area in the spectrum in Fig. 2 by the use of the theoretical recoiling cross sections for hydrogen and silicon ions and their energy losses in the given matrix.<sup>3,4)</sup> The results are shown in Fig. 3. As is understood from Fig. 2, this method can also be used for hydrogen depth profiling. Remarkably improved spectrum for hydrogen depth profiling was obtained by the increase of the incident argon energy. The results are shown in Fig. 4. Amorphous silicon films prepared from deuterated monosilane was also examined. Depth profile of both H and D can be known simultaneously (Fig. 5).

Studies on the reaction mechanism for the formation of amorphous silicon is now under way by the use of this technique. Further improvement in the spectrum for depth profiling is expected by the decrease of the incident angle  $\theta_1$  at a higher argon energy. Rutherford forward scattering method is thus highly effective in the

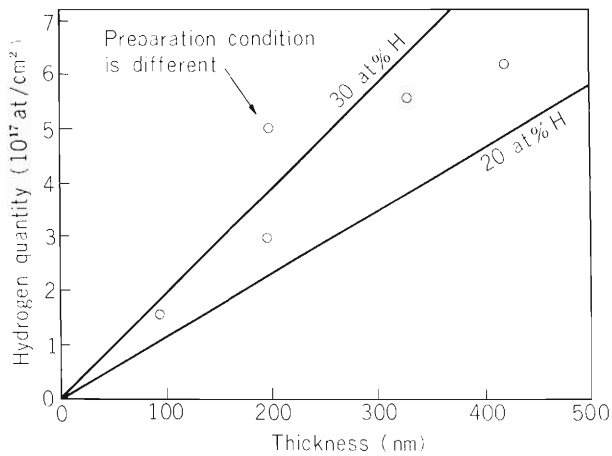


Fig. 3. Hydrogen quantity calculated from the hydrogen peak area and the silicon continuum area.

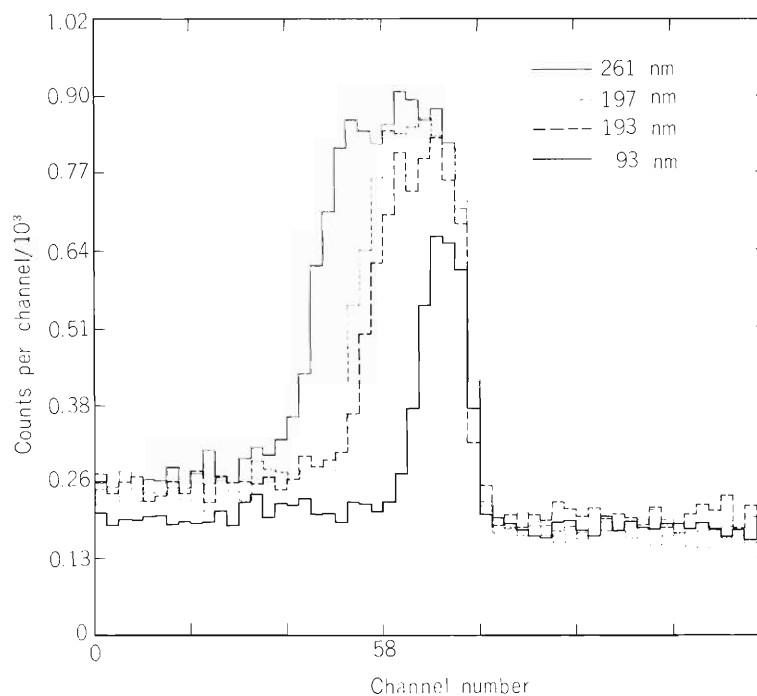


Fig. 4. Hydrogen depth profile obtained by 34 MeV argon ions.

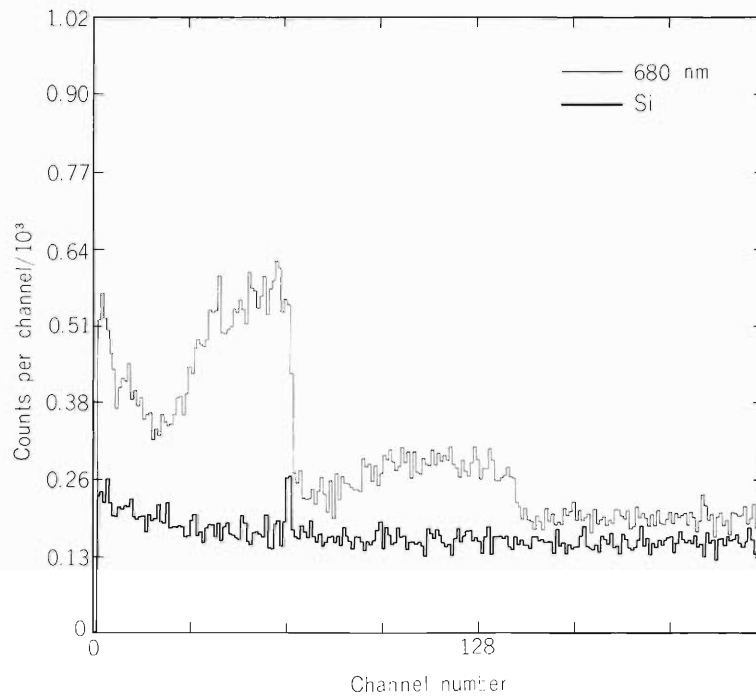


Fig. 5. Depth profile of H and D.

study of amorphous silicon films. Since heavy ions suffer large energy losses, they can be used profitably for fine depth profiling. The scheduled characteristics of Riken Linear Accelerator is quite suitable for the present study. Since hydrogen in other matrices can be measured similarly, this method is applicable to the study of hydrogen uptake and storage by various materials. From some of our results, this method is shown to be applicable also to the determination and depth profiling of nitrogen and oxygen.

#### References

- 1) H. Nagai, M. Aratani, T. Nozaki, M. Yanokura, and I. Kohno: Proc. of the 6th Symp. on Ion Sources and Ion-Assisted Technol., p. 221 (1982).
- 2) H. Nagai, M. Aratani, T. Nozaki, M. Yanokura, I Kohno, O. Kuboi, and Y. Yatsurugi: Proc. of 26th Ann. Meet. of Radiochem., p. 46 (1982).
- 3) J. F. Ziegler: The Stopping and Ranges of Ions in Matter, Vol. 5, Handbook of Stopping Cross-Sections for Energetic Ions in All Elements, Pergamon Press, New York (1980).
- 4) U. Littmark and J. F. Ziegler: *ibid.*, Vol. 6, Handbook of Range Distributions for Energetic Ions in All Elements, Pergamon Press, New York (1980).

### III-3-4. Separation of $^{119}\text{Sb(V)}$ , $^{119\text{m}}\text{Te(IV)}$ and $\text{Sn(IV)}$ by Adsorption on Activated Carbon

S. Ambe

We have been studying separation and purification of cyclotron-produced trace elements by adsorption on activated carbon. Previously, we reported batch-method purification of carrier-free  $^{119}\text{Sb(V)}$  by adsorption of impurity  $\text{Sn(IV)}$  on activated carbon.<sup>1)</sup> This year, purification of  $^{119}\text{Sb}$  by means of column method was studied, since column method is much more convenient in routine separation. Adsorption behavior of  $^{119\text{m}}\text{Te(IV)}$  and milking of  $^{119}\text{Sb(V)}$  from  $^{119\text{m}}\text{Te(IV)}$  adsorbed on activated carbon were also studied.  $^{113}\text{Sn}$  was used as the tracer for  $\text{Sn(IV)}$ . Shirasagi and No. 2186 (Merck) were used as activated carbons.

One  $\text{cm}^3$  of  $0.25 \text{ mol dm}^{-3} \text{ LiCl}$  solution of pH 6.0 containing  $^{119}\text{Sb(V)}$  was put in a column filled with 200 mg of activated carbon. On eluting with distilled water about 95 % of  $^{119}\text{Sb(V)}$  was collected in the first 3  $\text{cm}^3$ .  $^{113}\text{Sn(IV)}$  in  $0.25 \text{ mol dm}^{-3} \text{ LiCl}$  solution of pH 6 – 7 was passed through a carbon column of the same size and the column was washed with 40  $\text{cm}^3$  of  $0.25 \text{ mol dm}^{-3} \text{ LiCl}$  of pH 6.0. The radioactivities in the eluate were less than 1 %, and most of it turned out to be  $^{125}\text{Sb}$  impurity.

These results indicate that  $\text{Sn(IV)}$  impurity can be removed by passing the  $^{119}\text{Sb(V)}$  solution through a column of activated carbon. In practice, the neutralized  $^{119}\text{Sb(V)}$  solution obtained by the chemical separation procedure described in the previous report<sup>1)</sup> is passed through a column of activated carbon to remove impurity  $\text{Sn(IV)}$ . The carrier-free  $^{119}\text{Sb}$  solution thus obtained are now used for various tracer and Mössbauer studies.<sup>2)</sup>

In the adsorption study of  $^{119\text{m}}\text{Te(IV)}$  by batch method, 100 mg of activated carbon was added to 20  $\text{cm}^3$  of  $\text{LiCl}$  solutions containing  $^{119\text{m}}\text{Te(IV)}$ . After the adjustment of pH, the suspension was shaken for 1 h at room temperature. The carbon was separated by centrifugation. The radioactivities in the solutions before and after the adsorption were measured with an  $\text{NaI}$  scintillation counter. Effect of pH on the adsorption of carrier-free  $^{119\text{m}}\text{Te(IV)}$  is shown in Fig. 1.

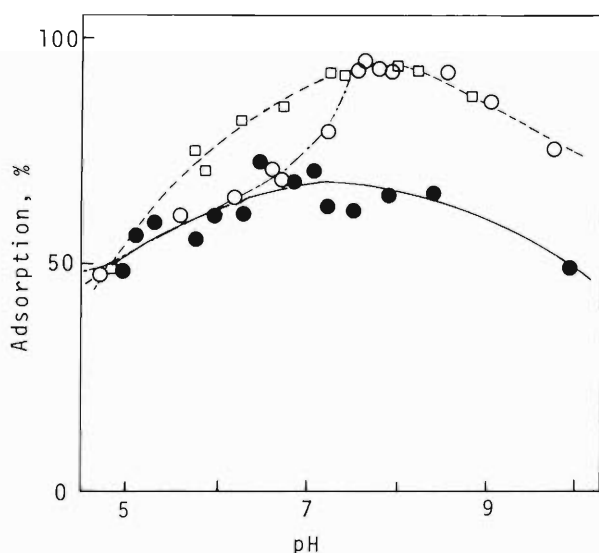


Fig. 1. Effect of pH on the adsorption of carrier-free  $^{119\text{m}}\text{Te(IV)}$  by 100 mg of activated carbon. Adsorption from 20  $\text{cm}^3$  of  $0.25 \text{ mol dm}^{-3} \text{ LiCl}$  solution by Shirasagi (●), from  $0.25 \text{ mol dm}^{-3} \text{ LiCl}$  solution by No. 2186 (○), and from  $0.01 \text{ mol dm}^{-3} \text{ LiCl}$  solution by No. 2186(□).

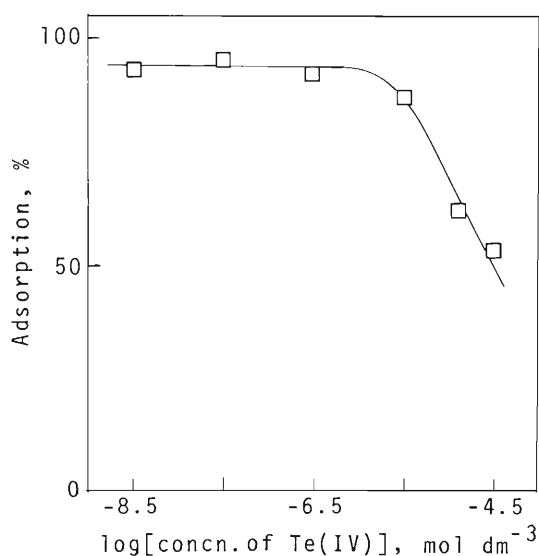


Fig. 2. Effect of concentration on the adsorption of Te(IV) from 20 cm<sup>3</sup> of 0.01 mol dm<sup>-3</sup> LiCl solution by No. 2186 (100 mg).

The adsorption of <sup>119m</sup>Te(IV) from 0.01 mol dm<sup>-3</sup> LiCl solution was found to be more efficient in a wider pH range than that from 0.25 mol dm<sup>-3</sup> LiCl. Figure 2 shows the effect of concentration of Te(IV) on its adsorption from 0.01 mol dm<sup>-3</sup> LiCl solutions of pH 7. In Te(IV) solutions with concentrations less than 10<sup>-6</sup> mol dm<sup>-3</sup>, about 95 % of Te(IV) was adsorbed. Increase in the concentration of Te(IV) above 10<sup>-6</sup> mol dm<sup>-3</sup> resulted in remarkable decrease in the adsorption of Te(IV). Hence, in adsorption of Te(IV), it is advisable to use a solution containing small amount of Te(IV) and salts, and sufficient quantity of activated carbon.

The chemical procedure to milk <sup>119</sup>Sb from <sup>119m</sup>Te described in the previous report<sup>1)</sup> consists of several steps and therefore takes much time. Difference in the adsorption characteristics between <sup>119</sup>Sb(V) and <sup>119m</sup>Te(IV) suggests a possibility of milking of <sup>119</sup>Sb from <sup>119m</sup>Te on activated carbon. Carrier-free <sup>119m</sup>Te(IV) in a neutral solution was adsorbed on the top of a column filled with 200 mg of activated carbon and then the column was washed with distilled water. <sup>119</sup>Sb(V) was milked by eluting with distilled water every two or three days. The yield of <sup>119</sup>Sb eluted from the <sup>119m</sup>Te-column was about 4 % of that of the precipitation method.<sup>1)</sup> This rather low yield is ascribed to the adsorptions of <sup>119</sup>Sb(III) produced by the EC decay of <sup>119m</sup>Te(IV). It was experimentally ascertained that carrier-free <sup>119</sup>Sb(III) is adsorbed by activated carbon in contrast with <sup>119</sup>Sb(V). About 1 % of <sup>119m</sup>Te came out in the first milking solution but the breakthrough decreased with repetition of milking. The breakthrough was reduced to 0.1 % by using columns filled with 400 mg of activated carbon.

The significant point of this method is that <sup>119</sup>Sb(V) is milked from <sup>119m</sup>Te(IV)-column by passing distilled water, to yield <sup>119</sup>Sb(V) solutions in a carrier-free and salt-free state.

Further studies are in progress in order to diminish the breakthrough of <sup>119m</sup>Te and to raise the yield of <sup>119</sup>Sb.

## References

- 1) S. Ambe, F. Ambe, and T. Okada: RIKEN Accel. Progr. Rep., 15, 112 (1981).
- 2) T. Okada, F. Ambe, S. Ambe, and H. Sekizawa: p.101 in this report.

### III-3-5. Mössbauer Emission Study of Defect $^{119}\text{Sn}$ Atoms in Solids

F. Ambe and S. Ambe

Mössbauer emission spectroscopy of  $^{119}\text{Sn}$  using cyclotron-produced  $^{119\text{m}}\text{Te}$  and  $^{119}\text{Sb}$  as source nuclides<sup>1)-3)</sup> has been applied in this period to a variety of systems. Here, a study on defect  $^{119}\text{Sn}$  atoms in non-magnetic solids is reported. Surface studies on magnetic oxides are described in separate papers.<sup>4),5)</sup> A study on chemical separation of the source nuclides is also reported elsewhere.<sup>6)</sup>

Previously, we reported a systematic concerning the isomer shifts of defect and normal  $^{119}\text{Sn}$  atoms in binary compounds of antimony and tellurium with elements from indium to iodine.<sup>7)</sup> It has now been extended to defect  $^{119}\text{Sn}$  arising from  $^{119}\text{Sb}$  and  $^{119\text{m}}\text{Te}$  in compounds with silver and cadmium, that is,  $\text{Ag}_2\text{Te}$  and  $\text{CdSb}$ .

$\text{Ag}_2^{119\text{m}}\text{Te}$  and  $\text{Cd}^{119}\text{Sb}$  were prepared by fusing a stoichiometric mixture of each metal in argon. Their Mössbauer emission spectra were measured against a  $\text{BaSnO}_3$  absorber at liquid nitrogen temperature. Details of the measurement were the same as described in a previous paper.<sup>1)</sup>  $\text{Ag}_2^{119\text{m}}\text{Te}$  gave two emission lines with essentially the same intensity, as shown in Fig. 1. The EC decay of  $^{119\text{m}}\text{Te}$  to  $^{119}\text{Sb}$  can bring about displacement of the decaying atoms in part. However, the  $^{119}\text{Sb}$  atoms are considered to be finally stabilized in the site of Te on the basis of an electronegativity consideration.<sup>1)</sup> We assign, therefore, the two lines to a quadrupolar doublet with an isomer shift of  $2.27 \text{ mm s}^{-1}$ .  $\text{Cd}^{119}\text{Sb}$  gave a slightly asymmetric doublet with an isomer shift of  $2.10 \text{ mm s}^{-1}$ . Combining these results with the data reported previously,<sup>7)</sup> we obtain Fig. 2 which shows the relation between the isomer shifts of defect and normal  $^{119}\text{Sn}$  and the atomic number of their nearest neighbor atoms.

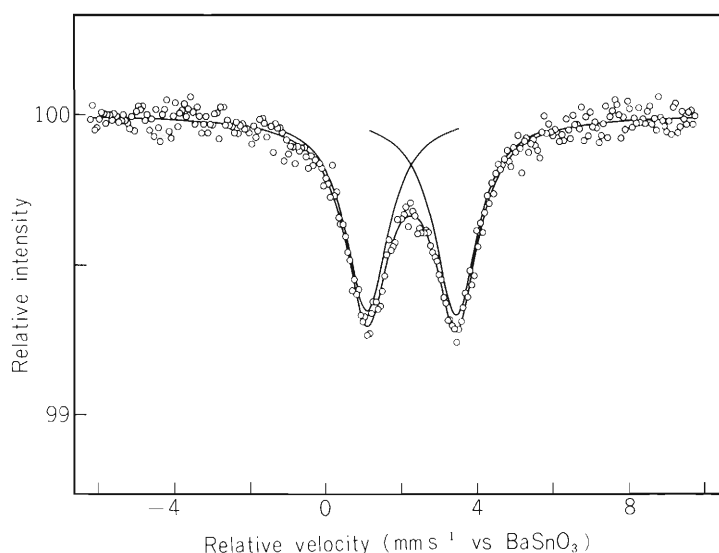


Fig. 1. Emission Mössbauer spectrum of  $\text{Ag}_2^{119\text{m}}\text{Te}$  at liquid nitrogen temperature.

Starting from the compounds with the most electronegative iodine, the isomer shift is seen from Fig. 2 to decrease with the decrease in electronegativity of the nearest neighbor atoms irrespective of the different crystal structures and types of bonding. However, it can be concluded from the present results on  $\text{Ag}_2^{119\text{m}}\text{Te}$  and  $\text{Cd}^{119}\text{Sb}$  that the decrease in isomer shift saturates for nearest neighbor atoms with atomic numbers smaller than that of tin. Namely,  $^{119}\text{Sn}$  atoms with ligands more electropositive than tin show an isomer shift value around  $2.1 \text{ mm s}^{-1}$ . The exceptionally low isomer shift for  $^{119}\text{Sn}$  in the Te site of  $\text{In}_2^{119\text{m}}\text{Te}_3$  can be ascribed to the structure of the compound with vacancies.

In this way, Mössbauer emission spectroscopy is a useful technique for studying the electronic state of atoms in unusual chemical environments. Further studies on various other solids, such as the Sn-S system, are now in progress.

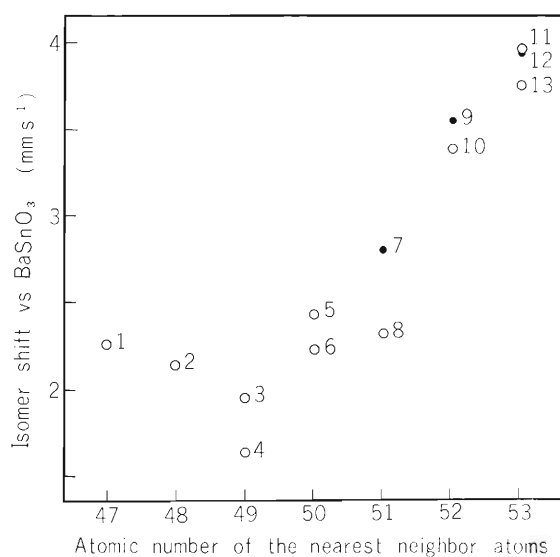


Fig. 2. Isomer shifts of defect and normal  $^{119}\text{Sn}$  in binary compounds of antimony and tellurium with elements from silver to iodine. Open circles refer to defect  $^{119}\text{Sn}$  in emission measurements and close ones to normal  $^{119}\text{Sn}$  in absorption measurements.

1.  $\text{Ag}_2^{119\text{m}}\text{Te}$ , 2.  $\text{Cd}^{119}\text{Sb}$ , 3.  $\text{In}^{119}\text{Sb}$ ,
4.  $\text{In}_2^{119\text{m}}\text{Te}_3$ , 5.  $\text{Sn}^{119}\text{Sb}$ , 6.  $\text{Sn}^{119\text{m}}\text{Te}$ ,
7.  $\text{SnSb}$ , 8.  $\text{Sb}_2^{119\text{m}}\text{Te}_3$ , 9.  $\text{SnTe}$ ,
10.  $^{119}\text{Sb}_2\text{Te}_3$ , 11.  $^{119}\text{SbI}_3$ , 12.  $\text{SnI}_2$ ,
13.  $^{119\text{m}}\text{TeI}_4$ .

## References

- 1) F. Ambe and S. Ambe: *J. Chem. Phys.*, **73**, 2029 (1980).
- 2) F. Ambe and S. Ambe: *ibid.*, **75**, 2463 (1981).
- 3) T. Okada, S. Ambe, F. Ambe, and H. Sekizawa: *J. Phys. Chem.*, **86**, 4726 (1982).
- 4) T. Okada, S. Ambe, F. Ambe, and H. Sekizawa: p. 98 in this report.
- 5) T. Okada, F. Ambe, S. Ambe, and H. Sekizawa: p.101 in this report.
- 6) S. Ambe: p.128 in this report.
- 7) F. Ambe and S. Ambe: *IPCR Cyclotron Progr. Rep.*, **14**, 96 (1980).

### III-3-6. Research Project on Coulomb-Excitation Mössbauer Spectroscopy Using Heavy Ions Accelerated by RILAC

F. Ambe, K. Asai, N. Sakai, and A. Hashizume

We have been studying application of Mössbauer spectroscopy to solid state physics and chemistry making use of short-lived radio-isotopes produced by the cyclotron.<sup>1)-3)</sup> Now that heavy-ion beams are available from RILAC, a variety of on-line Mössbauer spectroscopic investigations utilizing Coulomb excitation are planned in the following fields:

- (1) Study of the physical and chemical behavior of energetic atoms in alloys and semi-conductors;
- (2) Study of the structure and electronic state of inorganic, organic and biological compounds;
- (3) Study of magnetic materials.

For the time being,  $^{57}\text{Fe}$ ,  $^{61}\text{Ni}$ , and  $^{73}\text{Ge}$  are listed as the candidates for Mössbauer nuclides to be investigated. Search for a new Mössbauer nuclide will be also made.

Preparatory experiments have been already started. A few examples of Coulomb-excitation induced  $\gamma$ -ray spectra observed with a 37 MeV  $\text{Ar}^{4+}$  beam are shown in Fig. 1.

A design for a thin-window chamber equipped with a heavy-duty Mössbauer spectrometer is now being worked out.

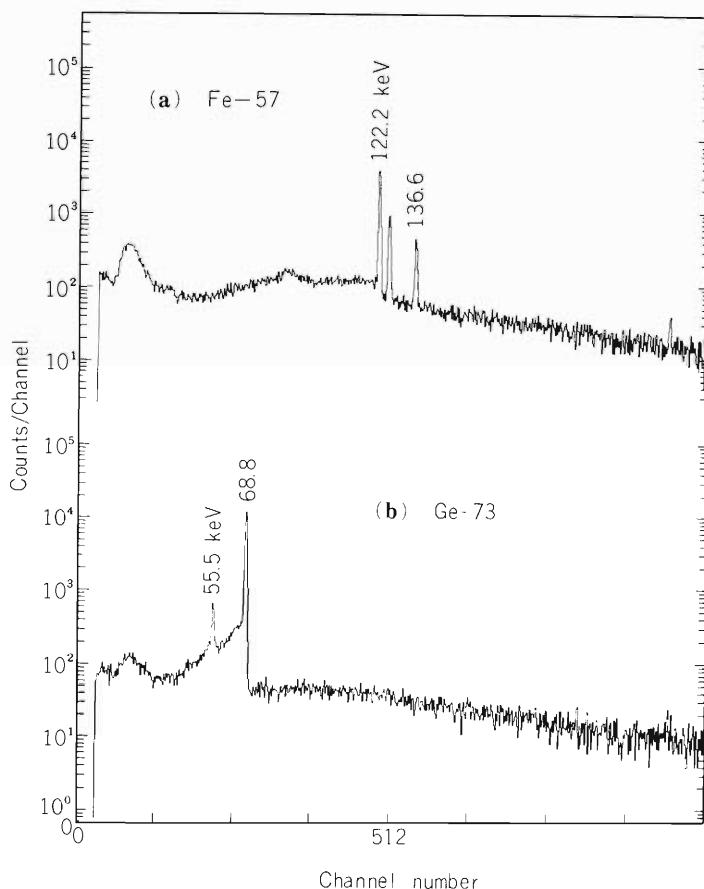


Fig. 1. Coulomb-excitation induced  $\gamma$ -ray spectra of (a) iron (the 14.4 keV Mössbauer  $\gamma$ -ray is not recorded because of absorption by the window of the chamber, and the 126.0 keV  $\gamma$ -ray is ascribed to impurity manganese in the target) and (b) germanium targets observed with a 37 MeV  $\text{Ar}^{4+}$  beam. An intrinsic germanium detector was employed.

## References

- 1) F. Ambe and S. Ambe: J. Chem. Phys., 73, 2029 (1980).
- 2) F. Ambe and S. Ambe: *ibid.*, 75, 2463 (1981).
- 3) T. Okada, S. Ambe, F. Ambe, and H. Sekizawa: J. Phys. Chem., 86, 4726 (1982).

### III-4. Radiation Chemistry and Radiation Biology

#### 1. Spectroscopic Studies on the Electronic Excited States Formed at High Density in Heavy-Ion Track

K. Kimura, Y. Toda, and M. Imamura

##### (1) Decay and time resolved spectra of $\sigma$ -excitons in alkali halides

We have previously found that the emission-intensity ratio of  $\sigma$ - to  $\pi$ -excitons in C-ion irradiated KBr single crystal is 5 times larger than that in VUV-light or x-irradiation. This enhanced ratio was ascertained not due to enhanced radiationless relaxation of the  $\pi$ -excitons because of the invariant lifetime of  $\pi$ -excitons with LET change.<sup>1)</sup> Therefore, this enhanced ratio may be attributed to an increase in yield of  $\sigma$ -excitons or acceleration of their radiative second-order decay in dense heavy-ion tracks.

To ascertain that, the decay of the  $\sigma$ -excitons was measured by a single-ion hitting and single-photon counting method which has ns time-resolution. The decay rate was found to be of the first order and not shortened with increasing LET. It was, therefore, concluded that the enhanced emission-intensity ratio by high-LET irradiation is attributable to the increase in yield of  $\sigma$ -excitons.<sup>2)</sup> This fact suggests that the present LET effect is interpreted as the effect on the formation processes of  $\sigma$ -excitons, i.e., the relaxation process of free excitons which are shortlived ( $< 10^{-12}$  s) precursors of the  $\sigma$ -excitons. The free excitons formed at high density along heavy ion-tracks may produce more  $\sigma$ -excitons by interaction than in photo-irradiation where  $\sigma$ -excitons is produced only by spontaneous relaxation of free excitons.

The conclusion mentioned above was further confirmed by measurement with RbBr and KI single crystals. The decay times of  $\sigma$ -excitons,  $\tau_1$ , in C-ion and photo-irradiation are listed in Table 1, in which unidentified longer lifetimes,  $\tau_2$ , which were found simultaneously at the same wavelength as did for  $\sigma$ -excitons, are also given. Time-resolved emission spectra have no indication of new band due to  $\tau_2$ . Typical emission spectra for RbBr are shown in Fig. 1.

A new detector system with 100-ps resolution will be completed soon and used for more detailed studies on this problem.

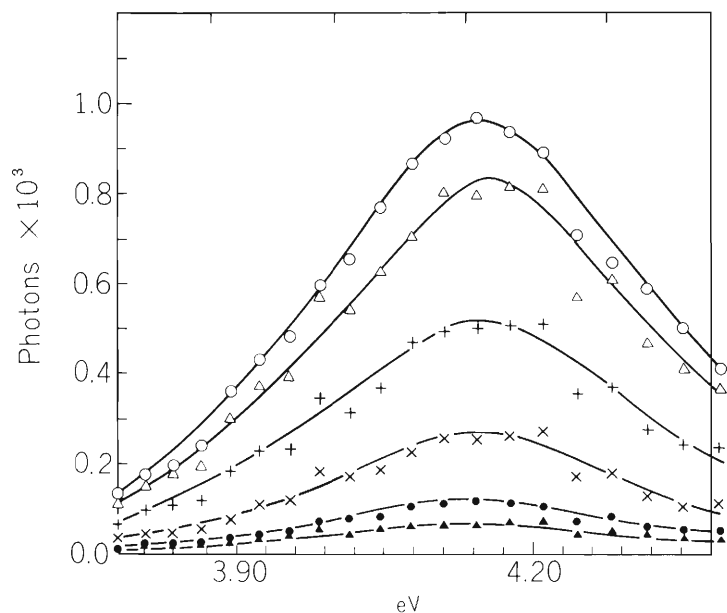


Fig. 1. Time-resolved emission spectra for C-ion irradiated RbBr single crystal at 4.5 K.  $\circ$ (0),  $\triangle$ (2),  $+$ (5),  $\times$ (9),  $\bullet$ (13), and  $\blacktriangle$ (17) s after ion-hitting.

Table 1. Lifetimes of  $\sigma$ -excitons.

Ions	Samples	Temp.(K)	Wavelength	$\tau_1$ (ns)	$\tau_2$ (ns)	Intensity ratio
C <sup>6+</sup>	KBr	4.5	285	3.7	16.9	10.0
H <sup>+</sup>	KBr	5	280	3.3	17.0	10.0
C <sup>6+</sup>	RbBr	4.5	304	2.7	16.9	27.5
H <sup>+</sup>	RbBr	5	300	3.0	13.0	4.0
C <sup>6+</sup>	KI	4.5	306	3.1	23.3	13.6
H <sup>+</sup>	KI	5.	300	2.3	—	—

Data for H<sup>+</sup>: I.M. Blair et al., AERE – R6906.

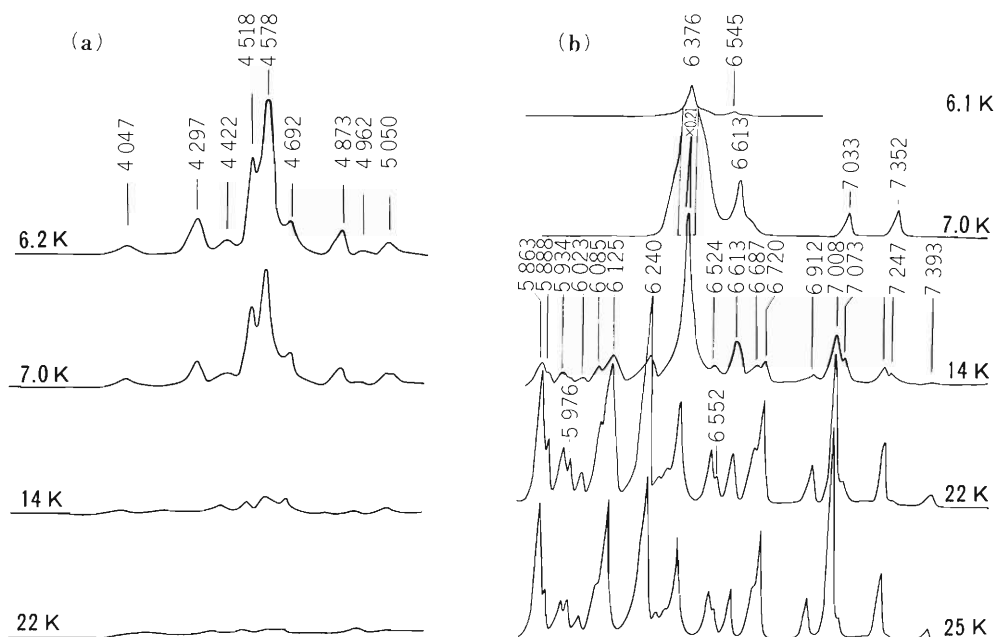


Fig. 2. Temperature dependent emission spectra of helium irradiated by 95 MeV N-ions. Spectral intensities are normalized to the irradiation dose of 5.9 nC (or  $2.7 \times 10^9$  ions).

## (2) Emission spectra from Helium irradiated with 95 MeV N-ions near critical temperature

The emission spectra of He gas irradiated by N-ion near critical temperature were found to show different features in some respects compared with results reported for microwave-discharged helium at room temperature:<sup>3)</sup> (i) temperature effect on the spectra, (ii) pressure effect on the emission intensities, and (iii) surface effect.

The emission spectrum obtained by 95 MeV N-ion irradiation at 6 K is well resolved as shown in Fig. 2, although their peaks were not so sharp as atomic spectra. Most of the peaks can be identified with those of helium excimers. The spectrum shows marked variations with temperature. The peaks in the short wavelength region at 6.2 K shown in Fig. 2(a) mostly disappear at 22 K, whereas the peaks in the long wavelength region in Fig. 2(b) change in a drastic and complex manner. The peak at 6376 Å strengthens rapidly on going from 6.1 to 7.0 K, but then decreases with wavelength shifts with further increasing temperature accompanying growth of new peaks.

Marked pressure dependence of the emission intensity was also observed. The peak intensity at 6376 Å becomes 250 times when the volume of He gas increased 16 times in a cryostat, as shown in Fig. 3. This volume change corresponds to the pressure change from 200 to 3000 Torr at room temperature. Our result is

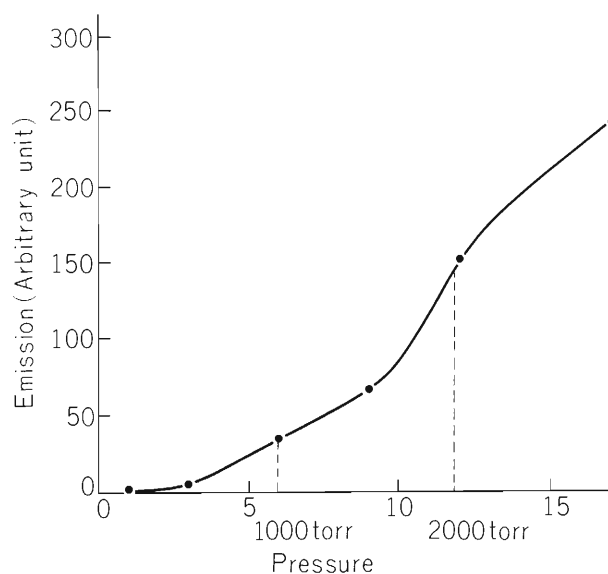


Fig. 3. Pressure dependence of emission intensity of 6376-Å peak.

far different from Collins and Robertson's result obtained by microwave discharge at room temperature; they reported that the maximum intensity is observed at 30 Torr.

The emission was observed to be intensified whenever some surface is present in the beam trajectory area. These unexpected features of the emission spectra are supposedly related with the phase conditions near critical temperature and with the exciting source. Further studies are being carried out bearing these points in mind.

#### References

- 1) K. Kimura and M. Imamura: *Phys. Letters*, **67A**, 159 (1978).
- 2) K. Kimura, M. Mochizuki, T. Fujisawa, and M. Imamura: *ibid.*, **78A**, 108 (1980).
- 3) C. B. Collins and W. W. Robertson: *J. Chem. Phys.*, **40**, 2202 (1964).

### III-4-2. Application of Thermoluminescence Dosimeter for Dose Measurement of High-LET Radiation

F. Yatagai and K. Nakano

Both an accurate dosimetry and a uniform irradiation are required for investigating various effects of high-LET radiation on biological materials. For the purpose of uniform irradiation, elastically scattered beam at a certain angle with respect to a beam axis has been used in the biological-irradiation system of IPCR cyclotron (Fig. 1).

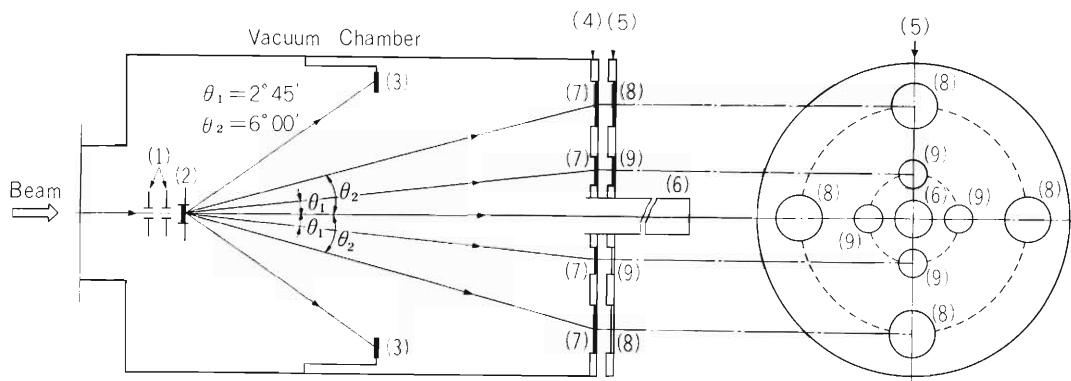


Fig. 1. Scheme of the apparatus for biological irradiation.

- (1) Slits, (2) Scattering foil, (3) Solid state detectors,  
 (4) End of vacuum window, (5) Sample wheel, (6) Faraday cup,  
 (7) Vacuum window, (8) and (9) Sample holders for low- or  
 high-dose irradiation, respectively, (10) TLD ribbon (LiF700).

Thermoluminescence dosimeter (TLD, Harshow Model 2000) was employed to examine whether or not this irradiation system provide a uniform irradiation. A fairly good uniformity ( $\pm 10\%$ ) was obtained in the area of surface of sample holder when TLD ribbons (LiF700), 0.25 mm in thickness, mounted on the holders were rotated during irradiation with N ions (4.7 MeV/amu) (data, not shown). A small fluctuation in TL response was also observed among the TLD ribbons mounted on different holders, which were located on the circle of scattering angle  $\theta = 6^\circ 00'$  (Fig. 2). Although the data was not shown, similar fluctuation was observed for the case of  $\theta = 2^\circ 45'$ . These fluctuations seem to be caused by the small difference between the beam axis and the center of apparatus.

Determinations of dose-response curves for biological samples are usually carried out by eliminating such fluctuations with either of the two methods as follows. One of them is to assay the biological activity for each dose after mixing all the samples irradiated at the four different windows. The other is to circulate the sample holders from window to window during irradiation so that total dose for each sample will be given by fractionated irradiation at the four different windows (Fig. 3).

As can be seen from the dose response curves of TLD ribbons in Fig. 3, TLD is available to monitor the dose of high LET radiation.

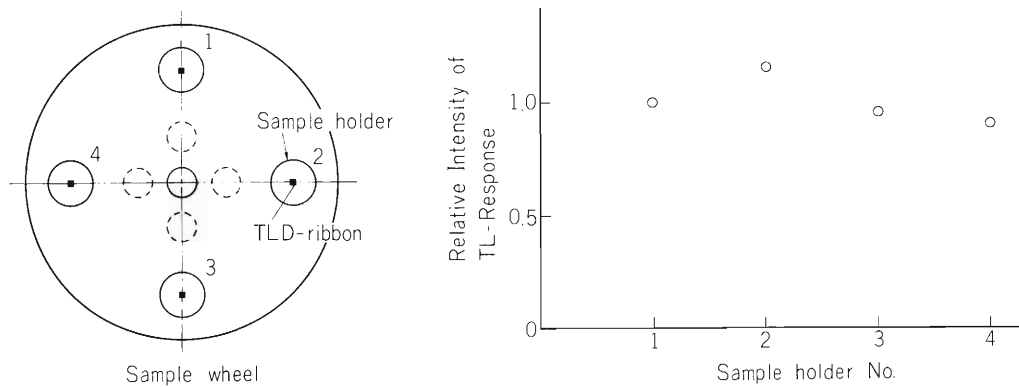


Fig. 2. Fluctuations in TL response among the TLD ribbons mounted on different holders (scattering angle  $\theta = 6^{\circ}00'$ ). TL response for each TLD ribbon irradiated with N ions (4.7 MeV/amu) is expressed in the relative value.

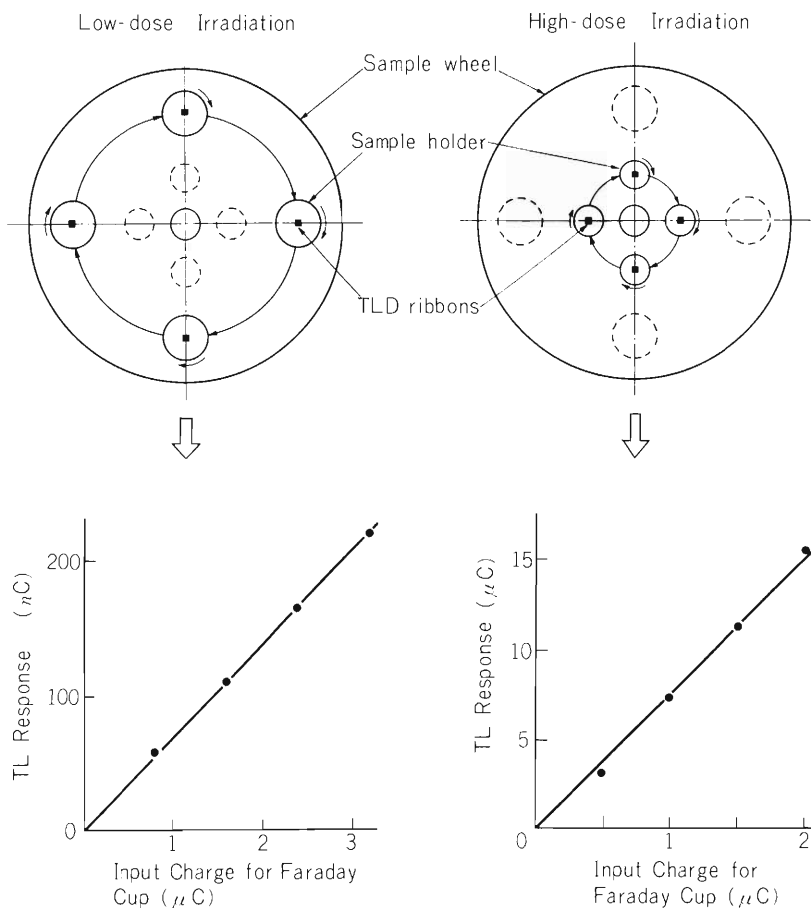


Fig. 3. Dose-response curves of TLD ribbons (LiF700). TLD ribbons on the sample holders for low- or high-dose irradiation, corresponding to (8) or (9) in Fig. 1, respectively, were exposed to N ions (4.7 MeV/amu). Total dose for each TLD ribbon was given by fractionated irradiation at the four different windows (see text).

### III-4-3. Track Structure Theories and Inactivation Cross Sections of Bacterial Spores for Heavy Ions

T. Takahashi and F. Yatagai

Precise evaluation of the dose around the path of an ion is prerequisite for a better understanding of inactivation of bacterial spores. We have calculated Katz's close-collision dose, Ahlen's distant-collision dose and Chatterjee-Schaefer's dose in water. We have also examined whether they are consistent with the stopping power.<sup>1)</sup> In Fig. 1 are shown Katz's dose and Ahlen's dose and in Fig. 2 are shown Katz's dose and Chatterjee-Schaefer's dose for comparison. The energy dependence of the inactivation cross sections of *B. subtilis* spores for ions carbon through neon is only slight and the mean cross sections for C ions (0.6 – 4.1 MeV/amu), O ions (0.8 – 1.1 MeV/amu) and Ne ions (2.2 – 3.7 MeV/amu) were found to be 0.22, 0.23, 0.26, and 0.33  $\mu\text{m}^2$ , respectively (Fig. 3).

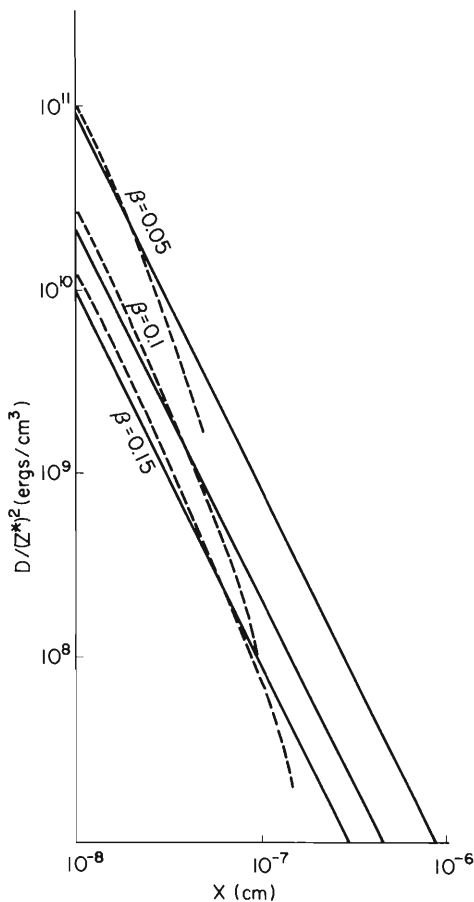


Fig. 1. Solid lines are Katz's close-collision dose and dotted lines are Ahlen's distant-collision dose.  $Z^*$  is the effective charge of heavy ion.

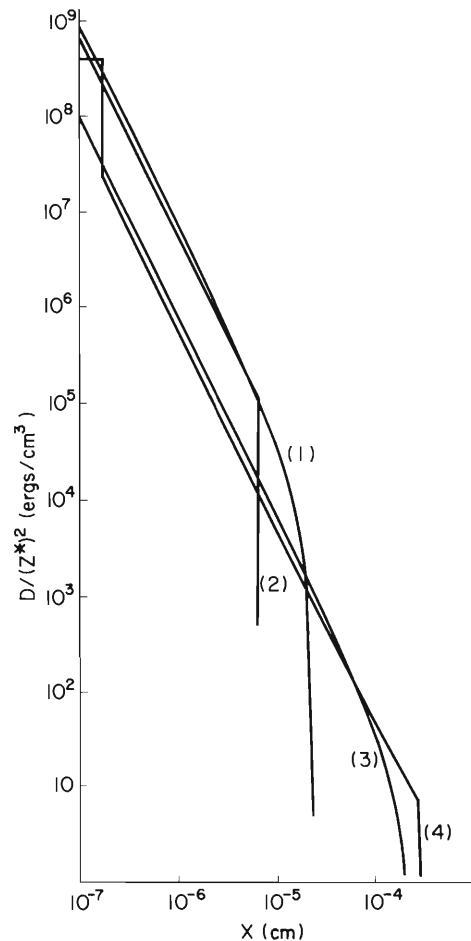


Fig. 2. (1) Katz's dose for  $\beta = 0.05$ ; (2) Chatterjee-Schaefer's dose for  $\beta = 0.05$ ; (3) Katz's dose for  $\beta = 0.15$ ; (4) Chatterjee-Schaefer's dose for  $\beta = 0.15$ .

To interpret these results, analysis was carried out along lines similar to Katz's target theory but the parameters were chosen so that they have an experimental basis and are different from those used by Katz, since Katz's original parameters could not account for the survival curve of the spore for gamma-rays.<sup>2)</sup> The area of "sensitive element"  $\pi a^2$  in Katz's target theory was chosen so that it corresponds to the spore core area ( $0.22 \mu\text{m}^2$ ), and we assumed that one target has one sensitive element in case of the spore, in contrast to Katz's original paper. Furthermore, we introduced a new idea to separate out the effect of delta-rays, as will be described below.

If we assume the whole spore core is a target and is a short cylinder of radius  $a$  whose axis is parallel to and at distance  $r$  from the path of an ion, the inactivation cross section is expressed as

$$S = \int_0^a 2\pi r P_{\text{in}} dr + \int_a^\infty 2\pi r P_\delta dr,$$

where

$$P_{\text{in}} = 1 - \exp(-\bar{D}(r)/E_{\text{in}}), \quad r < a$$

and

$$P_\delta = 1 - \exp(-\bar{D}(r)/E_\delta). \quad r > a$$

Here,  $P_{\text{in}}$  is the probability that the spore is inactivated when the ion impinges upon and goes through the spore core.  $E_{\text{in}}$  corresponds to the dose at which there is an average of one hit per target when the nucleus of the ion hit the spore core.  $P_\delta$  is the probability of inactivation when the ion passes by the spore core and the trajectories of its delta-rays come into the spore core and  $E_\delta$  is the 37% survival dose for delta-rays.  $\bar{D}(r)$  is the mean absorbed dose by the target which is given in an analytical form in Ref. 1.

Experimental inactivation cross sections are in fairly good agreement with the theoretical estimates for N ions, if we assume Chatterjee-Schaefer's dose and appropriate values are chosen for  $E_{\text{in}}$  and  $E_\delta$ . These values are found to be  $E_{\text{in}} = 10$  krad and  $E_\delta = 40$  krad as shown in Fig. 3 and discussions on them are given in Ref. 1. For U ions,<sup>3)</sup> experimental cross sections are larger

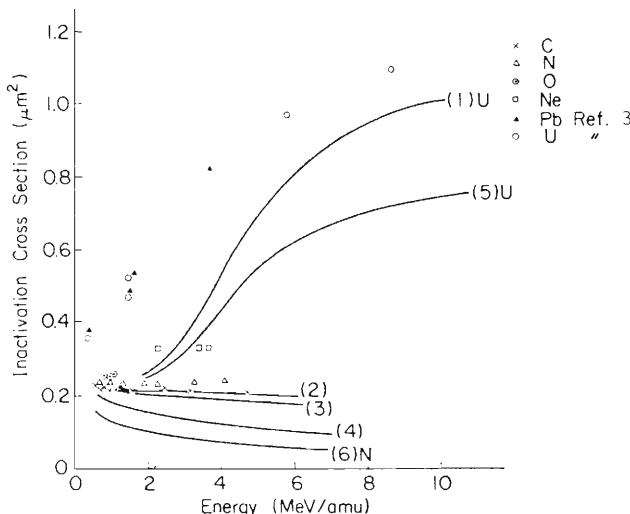


Fig. 3. Experimental and theoretical inactivation cross sections for *Bacillus subtilis*. (1) – (7): Calculated by using Chatterjee-Schaefer's dose. (1) U ion,  $E_\delta = 40$  krad,  $E_{\text{in}} = 10 - 40$  krad; (2) N ion,  $E_\delta = 40$  krad,  $E_{\text{in}} = 10$  krad; (3) N ion,  $E_\delta = 40$  krad,  $E_{\text{in}} = 15$  krad; (4) N ion,  $E_\delta = E_{\text{in}} = 40$  krad; (5) U ion,  $E_\delta = 63.5$  krad,  $E_{\text{in}} = 10 - 63.5$  krad; (6) N ion,  $E_\delta = E_{\text{in}} = 63.5$  krad. (Experimental 37% survival dose for gamma-rays was found to be 63.5 krad.)

than the theoretical values as seen in Fig. 3. The discrepancy may be ascribed to “long range effect” as previously pointed out. In the course of analysis, we used the dose of Katz and Ahlen as well as that of Chatterjee and Schaefer. For U ions, calculations based on Katz’s dose or combination of Katz and Ahlen’s dose yielded slightly larger inactivation cross sections than those based on Chatterjee-Schaefer’s dose, but the difference is not so large as to draw different conclusions.<sup>1)</sup>

#### References

- 1) T. Takahashi, F. Yatagai, and S. Kitayama: Life Sciences and Space Research, Pergamon Press, London (1982); T. Takahashi, F. Yatagai, K. Aoki, and S. Yamanaka: Hoshasen (Ionizing Radiation), 9, 24 (1982).
- 2) T. Takahashi, F. Yatagai, and A. Matsuyama: Sci. Papers I. P. C. R., 74, 51 (1980).
- 3) M. Schaefer, R. Facius, K. Baltschukat, and H. Bucker: 7th Symp. on Microdosimetry (1980).

### III-4-4. Mutagenesis of Chinese Hamster V79 Cells by Nitrogen Ion Beam

I. Kaneko, G. Okada, K. Nakano, and T. Nishimura

Mutagenesis is one of the most important biological effects of the ionizing radiations and is considered to be the first step for carcinogenesis. Although one of the potential medical application of heavy ions is its use in cancer therapy through effective killing of cancer cells, irradiation of normal tissue near the site of cancer might result in new carcinogenesis in later years after irradiation of the primary cancer. The purpose of the present study is to establish a method of detection of mutagenesis and to obtain a dose-effect relationship for assessment of mutagenic potential of heavy ions beams.

Most of previous studies of mutagenesis on mammalian cells have been carried out mostly with low LET radiations (X and gamma rays) and only a few work has been available with heavy ion beams. In the present study, a 6-thioguanine resistant marker (considered to be deficiency in hypoxanthine phosphoribosyltransferase), the most frequently used one among several markers, was used for comparison with the work of others.

Chinese hamster V79 cells in exponentially growing phase were used. The cells attached to Petri dishes were irradiated with nitrogen ions (65.8 MeV/nucleon,  $N^{4+}$ ,  $LET_{\infty} \sim 392$  keV/um) at a dose rate of approximately 1.8 Gy/min or with gamma rays from a Cobalt 60 source at a dose rate of 1.4 Gy/min both in air. Immediately after irradiations, the cells were trypsinized and divided into two portions. One was plated for colony formation to estimate its surviving fraction. The second portion was plated and incubated for five days. Then, they were trypsinized and plated for mutant colony formation in the 6-thioguanine containing medium. Figure 1 shows that a dose-effect relationship of mutagenesis for 6-thioguanine resistant marker by nitrogen beams was of curve-linear type, similar to that of gamma rays. However, induced mutation frequency per unit dose for nitrogen beam seems to be much higher than that for gamma rays. When a gamma ray dose of 6.5 Gy to give 10 percent survival is used for a reference point for RBE estimation, RBE of cell killing for nitrogen beam vs. gamma rays was 1.3, while RBE of

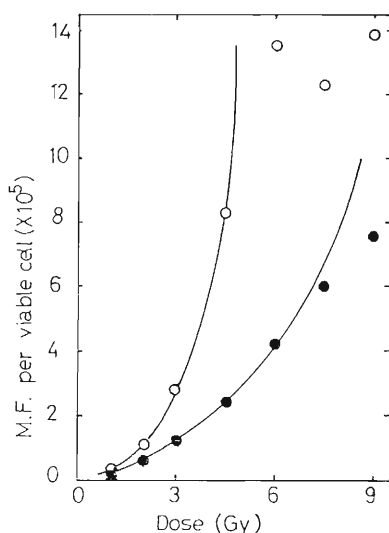


Fig. 1. The effect of nitrogen ion (65.8 MeV/n) (o—o) on mutation in Chinese hamster V79 cells, as compared to  $\gamma$ -rays (●—●).

mutagenesis was 1.9 (Table 1). This indicates that nitrogen beam of 392 keV/um induced mutation more effectively than cell killing.

Table 1. RBE value for cell killing and mutation induction for nitrogen ions.

Cell	R B E		
	Inactivation (10 % survival)	Mutation induction ( $6 \sim 7 \times 10^{-5}$ )	
H F 19	1.7	2.8	Cox et al. <sup>1)</sup> (1977)
V 79	2.5	5.3	
V 79	1.3	1.9	

#### Reference

- 1) R. Cox, J. Thacker, D.T. Goodhead, and R. J. Munson: Nature, 267, 426 (1977).

### III-4-5. Recovery from Potentially Lethal Damage of Human Cultured Cells after Irradiation of Nitrogen Ion Beams

I. Kaneko, T. Ohno, K. Eguchi, T. Inada,  
G. Okada, and K. Nakano

Irradiation with high-LET charged particles may be an effective therapy for solid malignant tumors. Many investigations have been done on tumor cell inactivation after irradiation with high-LET radiation, however, there is no concrete evidence regarding the extent of recovery from potentially lethal damage (PLD) in human normal and tumor cells after irradiation with high-LET particles.

Because of discrepancies in the results hitherto obtained regarding the recovery from PLD in tumor cells after irradiation with neutrons and charged particles, recovery from PLD in normal human lung fibroblasts and radiation resistant human melanoma cells after irradiation with nitrogen ions accelerated in the cyclotron and  $^{60}\text{Co}$   $\gamma$ -rays was examined.

Cultured human normal fibroblast IMR 90 cells and HMV-1 cells from human melanoma were grown up to their saturation density. The recovery from PLD was observed after the nitrogen ion irradiation, but the extent was less than that after  $\gamma$ -irradiation. Ratios between  $D_0$ 's (the dose required to reduce the number of clonogenic cells to 37 % of their former value) before and after the 6 h incubation at the saturation density of IMR 90 cells were 1.1 and 1.8 for nitrogen ion beams and  $\gamma$ -rays, respectively. The half maximum time in IMR 90 cells was 3.1 h after nitrogen ion irradiation while it was 1.3 h after  $\gamma$ -irradiation (Fig. 1). The half maximum recovery time in HMV-1 cells was 7 h and 5 h for nitrogen ion beams and  $\gamma$ -rays, respectively. For nitrogen ion beams, dose dependency of the recovery from PLD was not observed although it was observed for  $\gamma$ -rays. These results suggest that the recovery from PLD in human normal and tumor cells may be virtually identical between low- and high-LET irradiation but practically appear with a large difference in the mean recovery time and the recovery ratio of initial damage after irradiation.

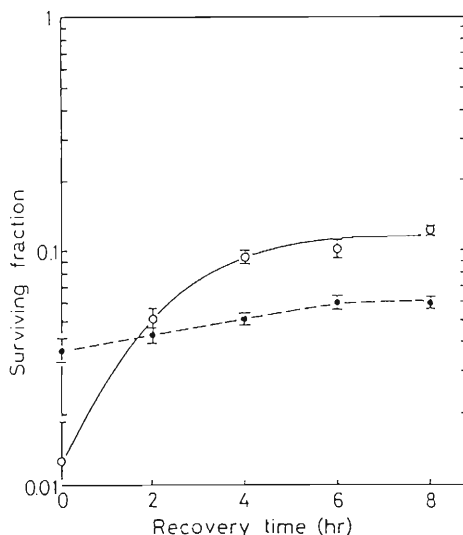


Fig. 1. Time course of recovery from potentially lethal damage after irradiation with nitrogen ion beams and  $^{60}\text{Co}$   $\gamma$ -rays in normal human fibroblasts, IMR 90. Plateau-phase culture of IMR 90 cells were irradiated with nitrogen ion beams and  $^{60}\text{Co}$   $\gamma$ -rays. Division ages of the cells and dose of the irradiation used were 36 PDL and 3.6 Gy for nitrogen ion beam irradiation (●) and 39 PDL and 5.2 Gy for  $\gamma$ -irradiation (○), respectively. Vertical bars are standard deviation of mean 4 dishes.

### III-5. Miscellaneous

#### 1. Quantitative Trace Analysis by Particle Induced X-Ray Emission

K. Maeda, Y. Sasa, S. Nakamura, and M. Uda

In order to establish a rapid and reliable method for quantitative trace analysis by particle induced X-ray emission (PIXE), preliminary experiments were performed and computer programs to analyze the PIXE spectra were made.

Samples supported by thin Mylar films were irradiated with 3 or 5 MeV/amu  $H^+$  and  $N^{4+}$  ions accelerated by the cyclotron. X-ray signals detected by a Si(Li) detector were processed by a multichannel analyzer and recorded on a paper tape or a floppy disk. The acquired PIXE spectra were treated off-line by FACOM M-200 computer to obtain the element concentrations in the samples. The experimental set-up and the detailed descriptions of the computer programs are reported in Ref. 1.

Samples used here were 25 specimens of blood serum collected from various diseased persons, 12 specimens of healthy human whole blood and two standard materials (bovine liver-NBS biological reference material and a mixture of chemical compounds of known concentrations). The elements observed in blood serum and whole blood were P, S, Cl, K, Ca, Fe, Cu, Zn, and Br. Minimum detection limit for each of these elements is around  $10^{-8}$  g under the experimental conditions (sample amount:  $1 \mu\ell$ , incident beam: 5 MeV  $H^+$ , beam current: 5nA, distance between the target and the detector: 80 mm, detector: ORTEC 7866S). While any significant differences in the element concentrations could not be detected among the healthy whole blood samples, the element concentrations in some diseased blood serum samples showed marked changes. For example, an increase in copper content was observed in a blood serum sample taken from a patient with parathyroid disease (Cu in normal human blood serum:  $1 \mu\text{g}/\text{ml}$ ). Figure 1 shows the PIXE spectrum of this case.

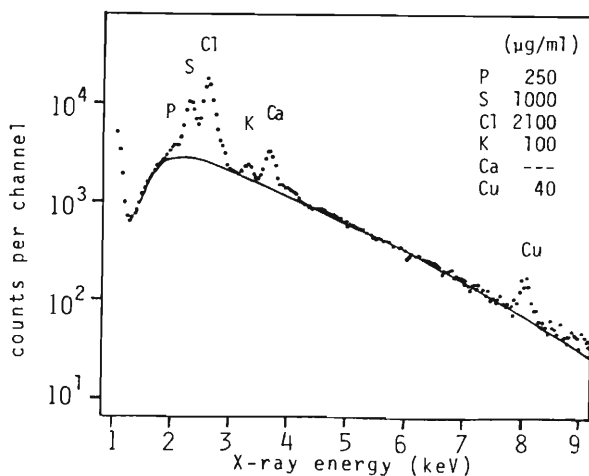


Fig. 1. 5 MeV  $H^+$  induced X-ray spectrum of a blood serum sample taken from a patient with parathyroid disease. The solid line shows the continuum background radiation.

Statistical treatment of the data obtained from a great many samples is necessary to find the correlations between diseases and elemental contents in biological tissues. Now we are constructing a target chamber for PIXE, which is equipped with an automatically changeable multiple sample assembly and is to be connected to Linac. PIXE spectra induced by heavy ions accelerated by Linac were also measured by using the target chamber for X-ray angular distribution measurement.<sup>2)</sup> One of these spectra is shown in Fig. 2. The preliminary measurements proved that Linac can be used for PIXE analysis.

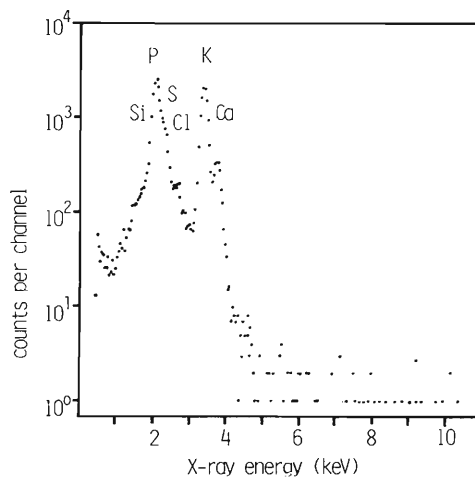


Fig. 2. X-ray spectrum of bovine liver induced by 10 MeV C<sup>2+</sup> ions accelerated by Linac.

#### References

- 1) K. Maeda and M. Uda: Reports I.P.C.R., (in Japanese), 58, 96 (1982).
- 2) Y. Awaya, I. Takeshita, Y. Tendow, and T. Katou: IPCR Cyclotron Progr. Rep., 14, 70 (1980).

## IV. ACCELERATOR DEVELOPMENT

### 1. Beam Attenuation Method Using Charge Transfer Reactions

M. Kase and T. Kambara

When one wants to know the energy spectrum of a beam or the time information of a particle in the beam, at the RILAC, a simple and accurate way is to measure them with a surface-barrier-type semiconductor detector (SSD) which is set in the beam line. During the measurement, however, one has to weaken the beam current down to a level as low as  $10^{-16} \sim 10^{-17}$  particle amperes in order to prevent the radiation damage on the detector. To get such a weak beam, the beam attenuation by a factor of  $10^{-6}$  is required.

For the accurate measurement of energy, one needs to keep the beam quality the same as before the beam is attenuated. If one reduces the beam intensity by changing the beam transport, there is a possibility that a stray beam, such as scattered beam, is led to the detector. Therefore, one has to maintain the settings of magnetic devices (Q-magnet, steering magnet, etc.) unchanged. At the ion source, limiting the arc power, one can attenuate the beam by  $10^{-1} \sim 10^{-2}$ . On the other hand, the beam attenuation of  $10^{-3}$  can be obtained by inserting, into the beam line, the thin copper plates with many small apertures ( $0.3 \text{ mm}\phi$ ). Anyway, an additional device is needed for the further beam attenuation.

The method using two sequential charge transfer reactions in the injector beam line is very easy to do and needs no special instrument, providing a stable and controllable attenuation by a factor of  $10^{-5}$  or less. All one has to do is change of the setting of the bending magnet (BM1). Figure 1 (a) shows the normal beam trajectory of ions represented as  $X^{n+}$ , when a couple of dipole magnets (BM1 and BM2) are adjusted at the same field  $B_0$ . The charge changed components which are produced through collisions with the residual gas in the beam pipe, are removed by BM1 and BM2. When the magnetic field of BM1 is changed from  $B_0$  to  $(\frac{n}{n-1}) B_0$ , the situation becomes as shown in Fig. 1(b). First, the main beam  $X^{n+}$  is removed by BM1, and instead,  $X^{(n-1)+}$  ions, which are produced as the result of single electron capture in the section from A to B, are introduced to the next stage of beam line. Next,  $X^{n+}$  ions, which are produced as the result of electron loss in the section from C to D, are introduced by BM2 to the cavity # 1 of the linac. Consequently, the  $X^{n+}$  beam at the entrance of the cavity # 1 is decreased extremely through the two sequential inverse charge transfers.

The attenuation ratio,  $\zeta$ , depends on the kind of ion (X and n), the beam energy, the contents of residual gas, and their densities (or pressure, p) in the beam pipe. In the case when  $\text{Ar}^{4+}$  beam (1.1 MeV) is used and the average vacuum pressure,  $p_0$ , in the beam pipe is  $5 \times 10^{-7}$  Torr ( $\text{N}_2$  equivalent),  $\zeta$  becomes  $6 \times 10^{-5}$ . Since  $\zeta$  is roughly proportional to  $p_0^2$ , one can adjust  $\zeta$  by changing  $p_0$ .

The beam quality is changed slightly through the attenuation process. A beam emittance is

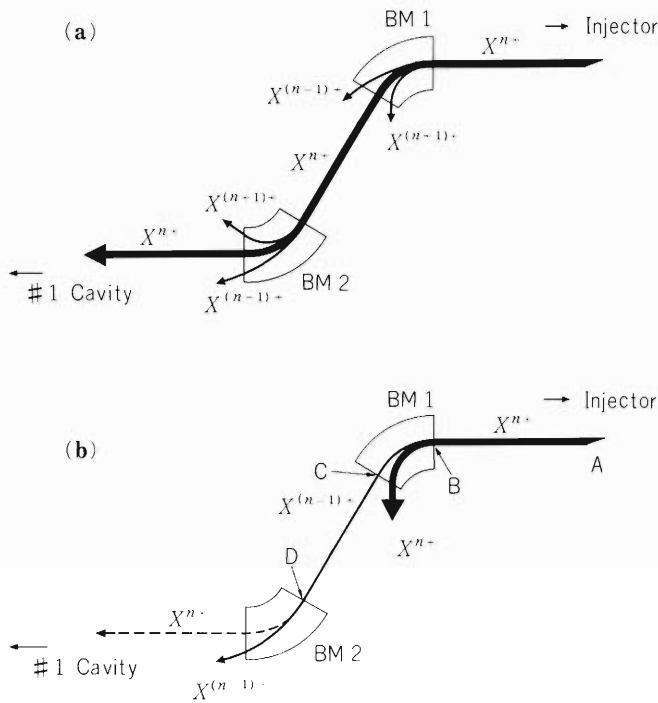


Fig. 1(a) The beam trajectory of ions,  $X^{n+}$ , in the normal operation. Magnetic fields of both bending magnets, BM1 and BM2, are  $B_0$ . (b) The beam trajectory when the field of BM1 is changed to  $\left(\frac{n}{n-1}\right) B_0$ .

increased due to momentum transfers by the two sequential reactions. But it causes no effect on the energy spectrum of the linac output beam, because the slit system of the injector beam line limits the emittance of beam injected to the cavity # 1.

One can use other charge transfer processes for the beam attenuation. For example, the process,  $X^{n+} \rightarrow X^{(n+1)+} \rightarrow X^{n+}$ , or  $X^{n+} \rightarrow X^{(n-2)+} \rightarrow X^{n+}$ , etc. can also be used. Though they can provide a smaller value for  $\zeta$ , the beam quality becomes worse.

## IV-2. Design of Axial Extraction PIG-Source

K. Hoshino

## (1) Construction of ion source

An ion source of linear accelerator to produce multiply charged metal ions from non-corrosive organometallic compounds which have relatively high vapour pressures has been constructed. The ion source was designed considering the following requirements: the gas pressure in the beam path should be maintained sufficiently low to prevent loss of multiply charged ions by charge exchange collisions with residual gas molecules; potential distribution in the ionizing region should be such that the impinging ions on the filament are reduced to minimize consumption of the filament.

The central part of the ion source is shown in Fig. 1 and overall construction in Fig. 2. The ion source housing is set in a solenoid. The central part is constructed with electrodes A, B, C, D, E, and F. The central part a of electrode A has a hole of dia. 3 mm. The construction of B is such that part b can be replaced easily, because b is eroded by sputtering by the beam. The potential of electrode E is kept higher than the potential of electrode D to repel the positive ions back to the ionization region C. Electrode D has a channel h through which gases are introduced from gas supply. Gases are blown out from the circular slit of h into the cavity of D. The construction of the slit is designed to form a gas jet and send most of the gas to the outside region of C through the gap between C and D. Ions produced in the cavity are accelerated by the electric field between the electrodes C and D. The strength of the electric field is adjustable.

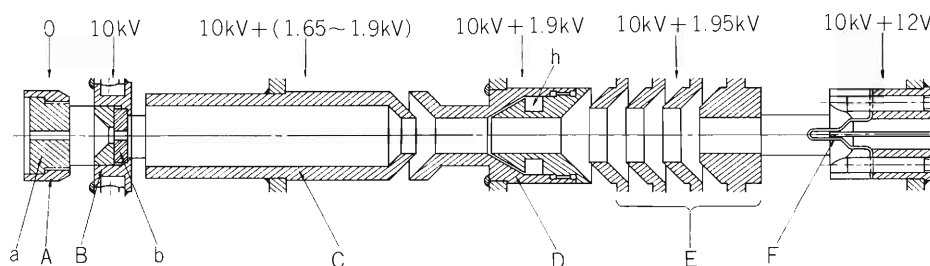


Fig. 1. Schematic diagram of the main part of axial extraction PIG-source and potential distribution.

F is the filament. The potential of B is kept lower by 12 V than that of F, so that all of the electrons emitted from F are sent back without hitting the surface of B.

It is necessary to prevent ions from impinging on the surface of the filament. Potential of the electrode E is set higher by 50 V than that of D. The gas flowing through the slit of h forms a jet stream and most of gas is sent to the gap between C and D, but a part of it moves toward F. It is intended to reduce the gas pressure between E and F by providing evacuation slots in E. As the distance between the electrodes E and F is small, it is expected that not much ions are produced between E and F. Therefore the number of ions impinging on F is not large. Potential difference between electrodes C and D can be set at a value between 0 and 250 V. It is hoped to increase the multiply charged ions by making transit time of ions, hence confinement time in the region C, moderate by use of small potential difference between C and D. When the organometallic compound has not enough vapor pressure to produce the ions of metal of concern, the elemental metal may be used applying sputtering scheme. For that purpose, a target b made of the metal can be inserted in the central part of B. It is necessary to drill a hole of dia. 3 mm at the center of B to provide the passage for the ions. Inert gas will be used to help sputtering of metal from b.

Figure 3 shows the construction of the ion source. The ion source is cooled by deionized water. The cooling water is circulated through holes of supports. The supports between electrodes are steatite pipes.

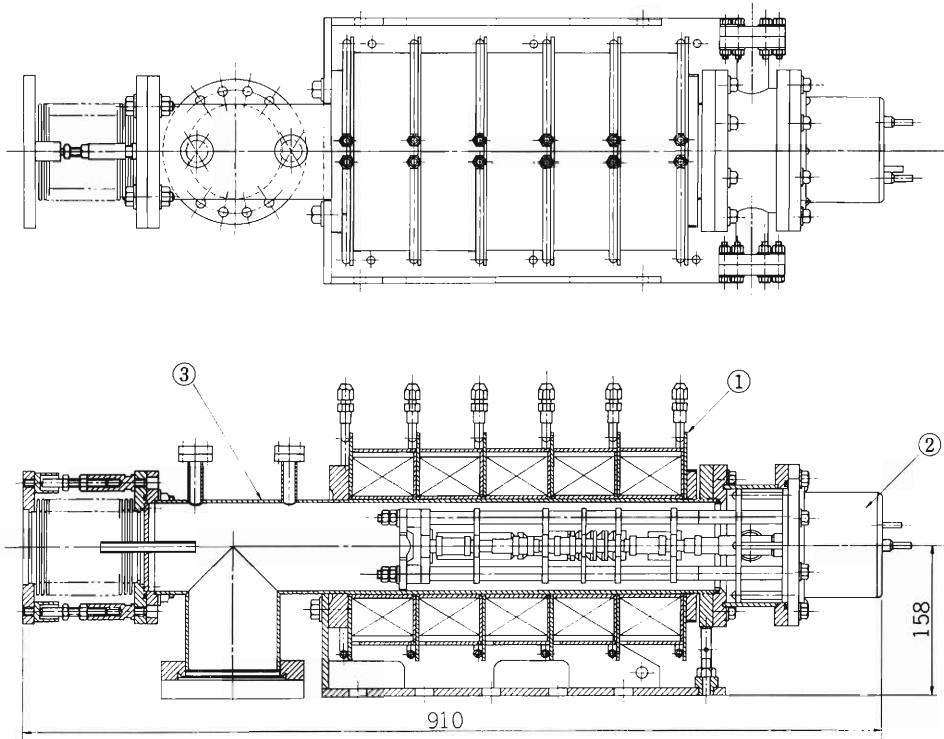


Fig. 2. Ion source vessel and solenoid.

- ① Solenoid, ② Ion source, ③ Ion source housing.

Each section of solenoid has a winding of 304 turns of 2.4 mm × 2.8 mm PVF coated wire, and they are connected in parallel. The resistance of the solenoid is 0.076 Ω. Magnetic flux density at the center of the solenoid is 1000 G for the solenoid current 100 A, and the wattage consumed by the solenoid is 760 W.

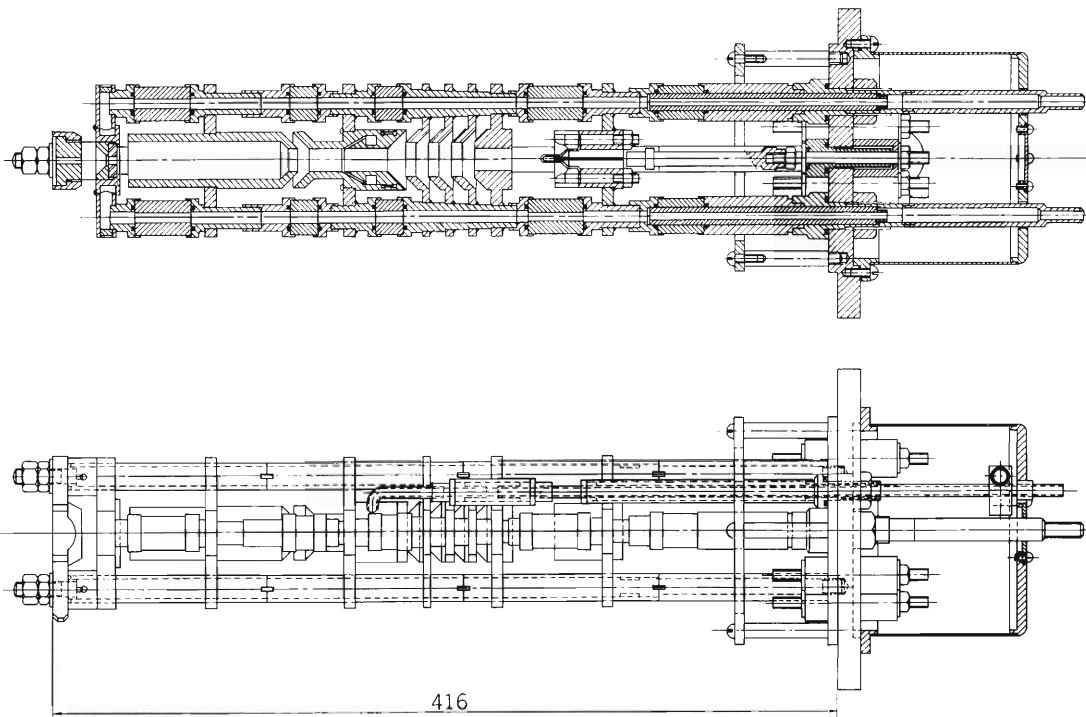


Fig. 3. Construction of axial extraction PIG-source.

On the other hand, gas passage is heated up by electric current to prevent the condensation of the organometallic compound.

Figure 2 shows the construction composed of solenoid, ion source, and ion source housing.

(2) Detection of ions

It is impossible to eliminate the large distribution of velocity of ions produced in the axial extraction IIG

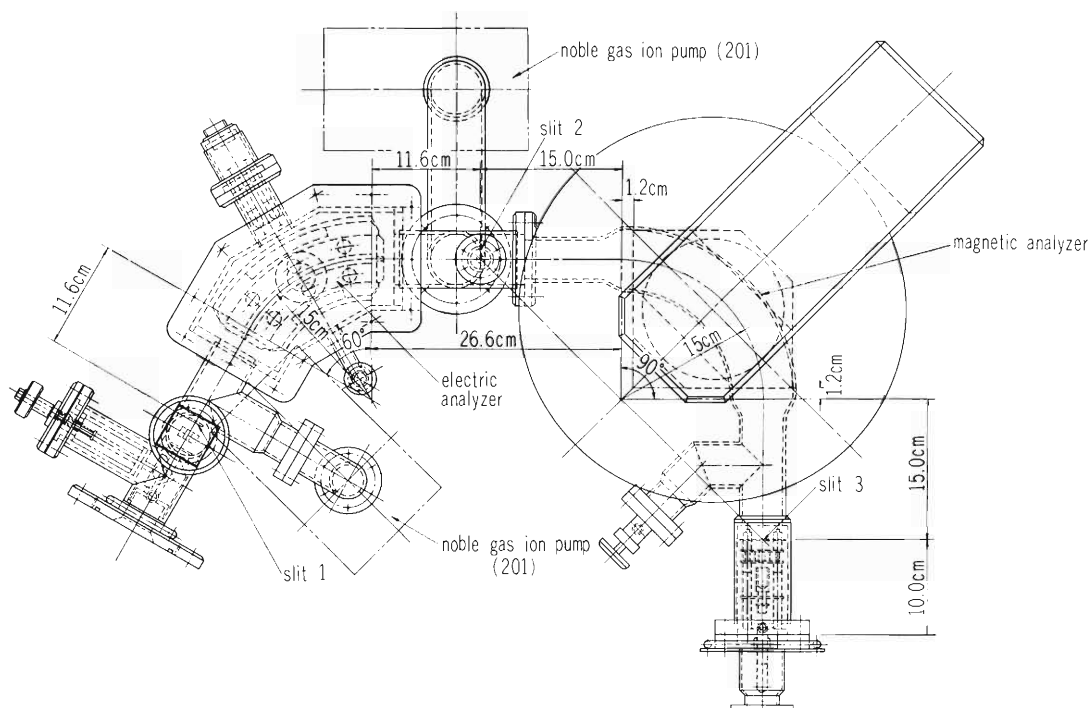


Fig. 4. Plan view of double focussing mass spectrometer.

Table 1. Specification of double focussing mass spectrometer.

Electrostatic analyzer	Radius of the orbit	15 cm
	Deflection angle	60°
	Gap between the electrodes	1 cm
	Max. potential difference between the electrodes	1670 V
Magnetic analyzer	Radius of the orbit	15 cm
	Deflection angle	90°
	Max. flux density	10.7 kG
	Max. power	150 W
Arrangement	The position of the two images of the electrostatic analyzer	Symmetrical
	The position of the two images of the magnetic analyzer	Symmetrical
Width of slit	Slit 1	0.2 mm
	Slit 2	1 mm
	Slit 3	0.8 mm
Mass range	$M/e_{\max.} = 100$	at ion accel. voltage of 12.5 kV
	$M/e_{\max.} = 125$	at ion accel. voltage of 10 kV

ion source. Most of the ejected ions are produced in the narrow region between C and D where potential variation is relatively small. As the potential difference between electrodes A and E is about 12 kV and the maximum potential difference between C and E is 300 V, the resolving power for the distinct peaks of the mass spectra of ions can be made larger than 40 by the use of a mass spectrometer composed of magnetic analyzer alone. For the smaller peaks, however, sufficient resolving power can not be obtained by the same arrangement because the ions produced in the region between the electrodes B and C are added to the ions produced in the region between the electrodes B and E. Small peaks will be buried under the neighbouring larger peaks. Use of electrostatic analyzer in conjunction with the magnetic field is necessary for this type of the ion spectrum analysis. Double focussing mass spectrometer as shown in Fig. 4 was designed for the detection of the ions extracted from this source. As the instrument has not only magnetic analyzer but also electric analyzer, it is expensive and more complex than a single focussing machine, but has an advantage that it can analyze ions having distribution in energy and in charge states at a time. Its specifications are shown in Table 1.

## IV-3. ECR Ion Source

M. Yanokura and M. Odera

An electron cyclotron resonance (ECR) type ion source for RIKEN Linac has been constructed<sup>1)</sup> and tested using Ar gas. The layout of the ECR test stand was already reported.<sup>2)</sup> In Fig. 1, we show its photograph.

In this ion source, a 2.45 GHz magnetron is used as the UHF power source. Resonant magnetic field is about 880 gauss for this frequency. Sufficient magnetic field can be obtained by use of a pair of solenoid coil. The coil is made of hollow copper conductor and its electrical resistance is 25 m $\Omega$ . The mirror ratio of the magnetic field is determined by the distance between the coils. In our source, the ratio is 1.8.

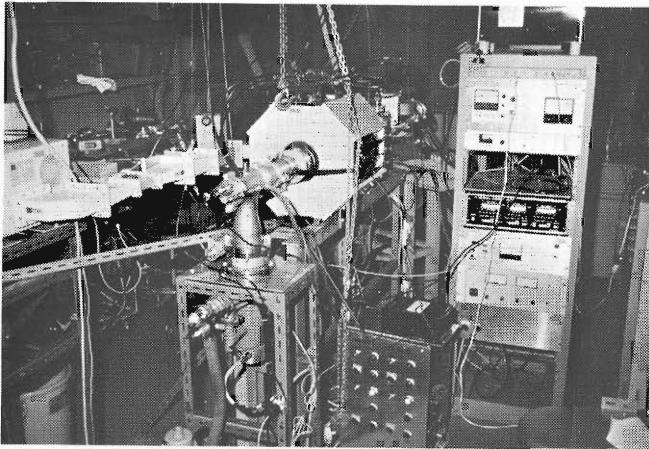


Fig. 1. Photograph of ECR ion source test stand.

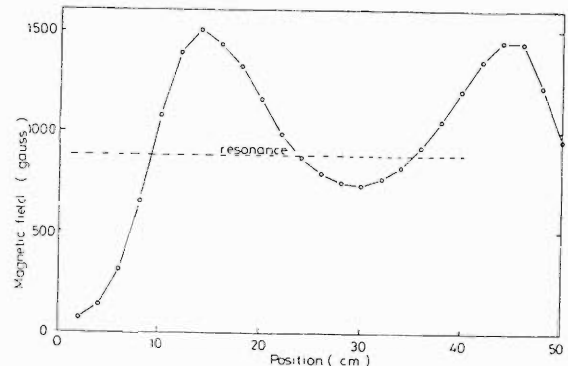


Fig. 2. Axial magnetic field of ECR cavity at main coil current of 190 A.

The UHF power is supplied to the ECR cavity through isolator, power monitor, EH tuner and RF window. Glass ceramic called Macor is used as material of RF window. In order to extract an ion beam, only the ECR cavity is kept at a positive high voltage. The other components such as pumps, solenoid coils and their power supplies are kept at ground potential. Power consumption of the coils is saved by use of a soft iron return yoke.<sup>1)</sup> When the coil current is 190 A (42000 AT), sufficient magnetic field is formed as shown in Fig. 2. At this condition, strength of the magnetic field at the center of the cavity is smaller than the resonance field.

This test stand has three diffusion pumps, and its total pumping speed is 3600  $\ell$ /sec. When Ar gas is introduced into the cavity at a flow rate of 0.1 sccm, the pressure inside the cavity is around  $10^{-4}$  Torr. After Ar gas was supplied, UHF power is fed into the cavity, and plasma is formed easily at the same time. It is observed by the microwave power monitor that the greater part of the power supplied from the magnetron is fed into the cavity.

Extracted beam current increased with increase of extracting voltage. This relation is shown in Fig. 3. In the following test, the extracting voltage was fixed at 7.5 kV. An extracted beam was analyzed using a bending magnet with maximum B of 108 kgauss-cm, and the ion current

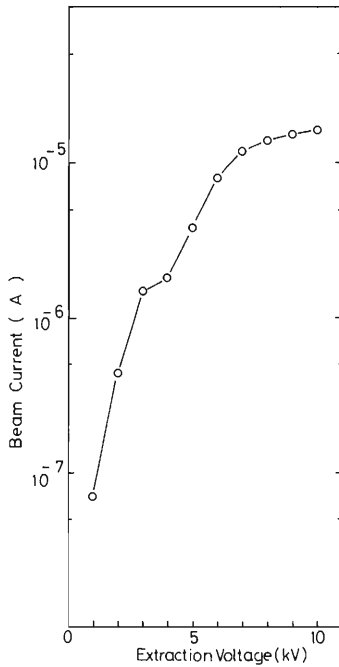


Fig. 3. Extracted beam current vs. extraction voltage. Pressure of the cavity is  $2 \times 10^{-4}$  Torr and UHF power is about 1.3 kW.

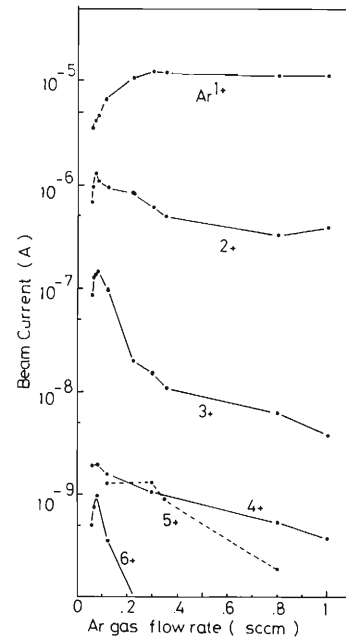


Fig. 4. Extracted beam current of each charge state vs. Ar gas flow rate. Ar<sup>5+</sup> ion current includes O<sup>2+</sup> ion current. Extraction voltage is 7.5 kV.

was measured by a Faraday-cup. The ion current of each charge state vs Ar gas flow rate is shown in Fig. 4. Ar<sup>5+</sup> ion current, shown in the figure, includes that of O<sup>2+</sup> ions, possibly. When the gas flow rate decreases, Ar<sup>1+</sup> ion current decreases, and for the gas flow rate larger than 0.4 sccm, its ion current is nearly constant. For the ions of the other charge states, a maximum ion current is obtained when Ar gas flow rate is around 0.1 sccm.

In this experiment, multiply charged ion current was very small; for example, Ar<sup>6+</sup> ion current was only 1 nA. Therefore we are trying to get more beam current by modification of the extracting geometry, the microwave window and gas injection nozzle. Furthermore, we intend to use the permanent magnets for forming multipole field to stabilize plasma and to prevent heating the cavity by plasma.

## References

- 1) M. Yanokura and M. Odera: IPCR Cyclotron Progr. Rep., 14, 113 (1980).
- 2) M. Yanokura and M. Odera: RIKEN Accel. Progr. Rep., 15, 136 (1981).

#### IV-4. Identification Method of Ions in the Beam from the RILAC Injector

M. Kase and T. Kambara

The RILAC can accept a variety of ions, from proton to uranium ions, with a mass-to-charge ratio,  $M/q$ , smaller than 24. When multiply-charged heavy ions are produced with the PIG source,<sup>1),2)</sup> the  $M/q$  spectra of ions at the source are sometimes so complex that it is troublesome to search for the desired ions. There are, in the spectra, some peaks of contaminating ions such as  $O^+$ ,  $O^{2+}$ ,  $N^+$ ,  $N^{2+}$ ,  $H_2O^+$ ,  $OH^+$  etc. and also peaks due to the supporting gas when the metal ion source<sup>3)</sup> is used. Moreover, a heavy element has, in general, several isotopes, and there are also peaks due to charge transfers of ions with the residual gas in the beam duct in the acceleration stages. To prevent the acceleration of unwanted ions, it is necessary to identify the ions in the beam from the source, occasionally.

For this purpose, a procedure to know the charge state of ions by use of charge transfer in the RILAC injection system has been developed. In Fig. 1 is shown the beam line from the source to the first cavity. The beam from the injector, which is roughly analysed with an ion source magnet, is bent twice by an angle of  $60^\circ$  with a couple of dipole magnets (BM1 and BM2). The procedure to know the charge state of ions is as follows: First, every parameters of the equipments in the injector system are set according to the acceleration conditions and the beam is optimized at the Faraday cup (FC-014) by further tuning. Next, the pressure in the beam

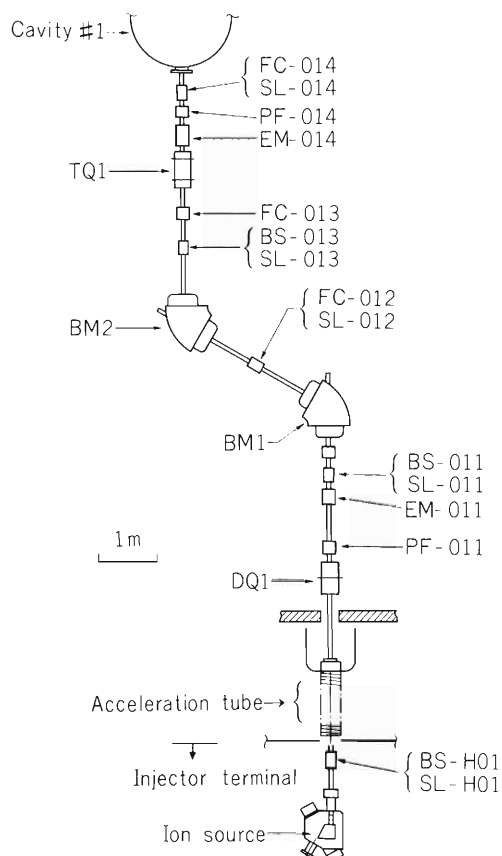


Fig. 1. The beam line from the ion source to the first cavity in the RILAC. Notations are as follows: FC, Faraday cup; BM, bending magnet; EM, emittance monitor; BS, beam stopper; PF, profile monitor; DQ, doublet quadrupole magnet; TQ, triplet quadrupole magnet; SL, slits.

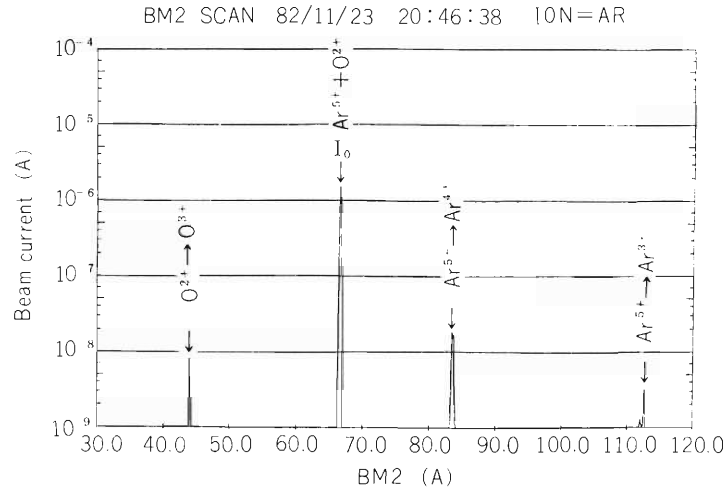


Fig. 2. The beam current at FC-013 vs. the BM2 magnet current which has approximately a linear relation to the magnetic field in the range in concern.  $I_0$  ( $= 67$  A) is the magnet current when the beam is optimized. The peak at  $84$  A ( $= (5/4)I_0$ ) is due to the one electron capture of  $\text{Ar}^{5+}$ , the peak at  $112$  A ( $= (5/3)I_0$ ) due to the two electron capture of  $\text{Ar}^{5+}$ , and the peak at  $44$  A ( $= (2/3)I_0$ ) due to the one electron loss of  $\text{O}^{2+}$ .

duct between BM1 and BM2 is raised up from the normal value ( $\sim 2 \times 10^{-7}$  Torr) to several  $10^{-6}$  Torr. Then, the beam current at the Faraday cup (FC-013) is monitored, as the field in BM2 is scanned. A current spectrum thus obtained for  $\text{Ar}^{5+}$  beam is shown in Fig. 2. The spectrum shows some peaks due to the charge transfer collisions of ions in the beam with the gas in the beam duct between BM1 and BM2. Since the momentum of the ions changes very little through the charge transfer, the magnetic rigidity of ions is inversely proportional to their charges. If the charge number before and after the collision are represented by “i” and “f”, respectively, the field in BM2 which provides a current peak at FC-013 for the f-component is given by  $(i/f)B_0$ , where  $B_0$  is the field when the beam is optimized. In the velocity range of the RILAC injector ( $0.006 < V/C < 0.016$ ), electron loss processes occur mainly for low i. On the other hand, for higher i, electron capture processes occur more frequently. As shown in Fig. 2, there are peaks due to charge exchange processes ( $i \rightarrow f$ ) such as  $(5 \rightarrow 4)$ ,  $(5 \rightarrow 3)$ , and  $(2 \rightarrow 3)$ . The spectrum shows that the beam consists of two kinds of ions,  $\text{Ar}^{5+}$  and  $\text{O}^{2+}$ . One can also estimate the fraction of  $\text{Ar}^{5+}$  in the beam if the electron capture cross section and the target thickness are given.

Molecular ions such as  $\text{H}_2\text{O}^+$  can be identified by use of a dissociation process like  $\text{H}_2\text{O}^+ \rightarrow \text{OH}^+ + \text{H}$ . In this case, the field which gives a peak for the dissociative component ( $\text{OH}^+$ ) is given by  $(m_f/m_i)^{1/2} B_0$ , where  $m_i$  is the mass of the molecular ion and  $m_f$  the mass of the dissociated fragment with the same charge state as the incident ion.

These ion identification methods are very simple but reliable. All parameters of magnetic devices can be fixed after the beam optimization except for BM2 which is less important as the

beam analyser than BM1 which selects practically the ions to be accelerated by the linac.

#### References

- 1) Y. Miyazawa, M. Yanokura, M. Hemmi, F. Yoshida, M. Kase, and M. Odera: IPCR Cyclotron Progr. Rep., 13, 151 (1979).
- 2) M. Kase and Y. Miyazawa: *ibid.*, 14, 132 (1980).
- 3) M. Kase, Y. Miyazawa, and T. Chiba: RIKEN Accel. Progr. Rep., 15, 133 (1981).

#### IV-5. Bunch Signal Sensitization by Use of Secondary Electron Emission

M. Kase

When a beam bunch is monitored at the early acceleration stage of heavy ion linacs where the beam velocity is relatively small ( $\beta \sim 0.01$ ), a bunch signal induced by the slow beam has a slow response to the bunch shape. Therefore it is difficult to know accurately the longitudinal distribution of charges in a bunch from the signal shape. In order to eliminate this signal distortion, a shield plate with small apertures is placed just in front of the detection plate in the case of a coaxial Faraday cup (Ref. 1). But the plate stops a part of beam and the bunch signals are weakened. As the result, the measurement should be made with a bad SN ratio. This difficulty can be reduced easily using the secondary electron effect which is usually suppressed in the coaxial Faraday cup scheme.

A secondary electron effect bunch probe was developed and is being used to monitor the bunch structure at the RILAC (RIKEN linac). A schematic diagram of the probe head is shown in Fig. 1. The probe is plunged into the beam line remotely with a pneumatic cylinder during the measurement. The structure is similar to that of the coaxial Faraday cup except that an electron collector is set to absorb efficiently the electrons emitted from the stopping plate by the ion bombardment.

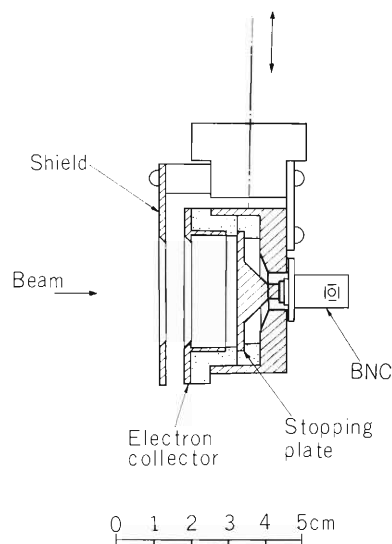


Fig. 1. Schematic view of the secondary electron effect bunch probe.

Two kinds of currents appear in the signal coaxial cable. One is the current ( $I_i$ ) induced by the ions which approach the stopping plate and collide with it. The other is the current ( $I_e$ ) due to the secondary electrons which are emitted from the stopping plate and absorbed by the electron collector. The signal shapes of these currents were calculated on the assumption that the beam bunch has a triangular shape distribution with the spread of 2 nsec(fwhm) as shown in Fig. 2 by dashed lines, and that no electric charge is induced on the stopping plate until the ion goes through the entrance aperture of the electron collector. The results of calculation are shown in Fig. 2(a) and (b) by solid lines. The signal of  $I_i$  occurs before the bunch reaches the stopping plate and its shape is broadened. The signal of  $I_e$  is delayed a little bit but its shape is similar to

the bunch shape. When the electron collector is biased at a negative voltage as in normal use of a coaxial Faraday cup, only  $I_i$  can be observed since  $I_e$  is suppressed. On the other hand, when the electron collector is biased at a positive voltage, the signal of  $I_i + I_e$  is obtained. But  $I_e$  is, in general, much larger than  $I_i$ , i.e.  $\zeta \gg 1$ , and therefore, the signal shape is given almost entirely by  $I_e$ . The output signals on a 350 MHz oscilloscope are shown in Fig. 3(a) and (b): (a) is with a negative bias on the electron collector, while (b) is with a positive bias. The signals have the same tendency as those of the calculations in Fig. 2(a) and (b). The factor of signal enhancement,  $\zeta$ , which depends on the beam energy, the ion species and the material of stopping plate, is around 15 for a 2.3 MeV  $\text{Ar}^{4+}$  beam with a copper plate for the stopping plate.

Using the secondary electron effect bunch probe, the beam bunch measurement for a low intensity beam can be made with a better SN ratio as well as an accurate response to the beam bunch.

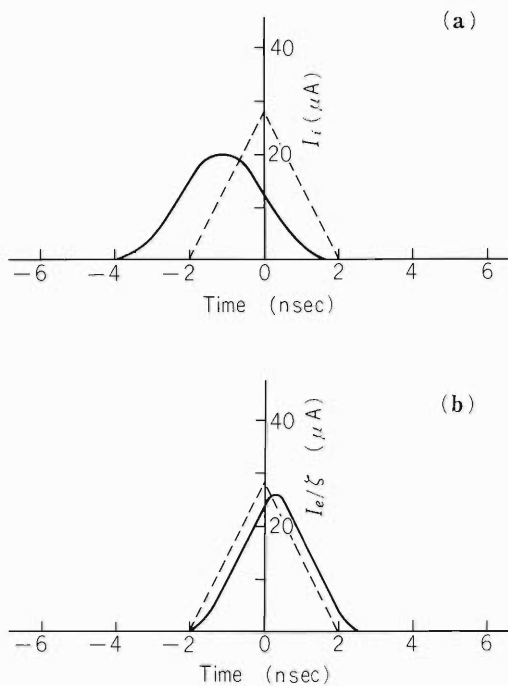


Fig. 2. Calculation of bunch signals. A solid line in (a) is for  $I_i$  and that in (b) is for  $I_e$  when  $\beta = 0.015$  and the beam current is  $1 \mu\text{A}$ . The bunch shape is assumed as shown by dashed lines. The peak of the bunch reaches the stopping plate at  $t = 0$ .  $\zeta$  is the factor of signal enhancement by secondary electrons.

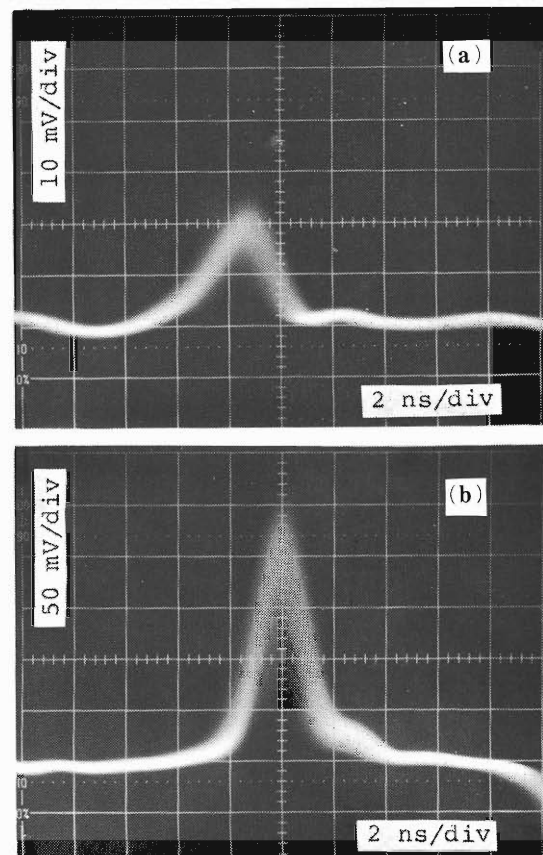


Fig. 3. Bunch signals for  $I_i$  (a), for  $I_i + I_e$  (b). The beam is of 2.3 MeV  $\text{N}^+$  ( $\beta = 0.019$ ). The electron collector is biased at  $-500 \text{ V}$  in (a),  $+1.5 \text{ kV}$  in (b). The trigger conditions of the both cases are the same.

#### Reference

- 1) J. Klabunde, V. Schaa, E. Schaffner, P. Strehl, H. Vilhjalmsson, and D. Wilms: Proc. of 1979 Linear Acc. Conf., p. 297.

IV-6. Bunch Phase Monitor

I. Yokoyama, M. Kase, S. Kohara, and Y. Yano

To know the beam phase relative to rf voltage is very helpful for the fine tuning of rf accelerators such as the RILAC and the RIKEN SSC (under construction). Sometimes, however, bunch signals have bad SN ratios when the beam currents are weak (during the tuning process, for example) or when the measurements with probes set inside the SSC are made in the presence of severe rf noises. It is necessary to develop a device which makes it possible to measure the beam phase under such bad conditions and is suitable for use in the variable-frequency scheme.

A bunch phase monitor using the mixing (heterodyne) scheme has been developed. The basic principle is the same as that in Ref. 1: the information on the beam phase is transferred to the signal with a fixed intermediate frequency,  $f_{if}$ . This system involves an automatic tuning circuit for the frequency range of 17 ~ 45 MHz. No additional adjustment is necessary when the acceleration frequency is changed.

A block diagram of this system is shown in Fig. 1. Two kinds of signals (one is a reference signal from an rf cavity and the other is a bunch signal from a probe) are fed to the two inputs, respectively. The reference signal, after its frequency is doubled ( $f \rightarrow 2f$ ), is mixed with the output signal of a voltage controlled oscillator (VCO) in a double balanced mixer (MIX1). Being filtered (QF1), the mixer output is sent back to the phase lock loop. When the circuit is in tune, the VCO generates the signal of  $2f + f_{if}$  and, as the result, the reference signal in the intermediate-frequency stage is phase-locked with regard to the oscillator (OS1) output. Being filtered again by

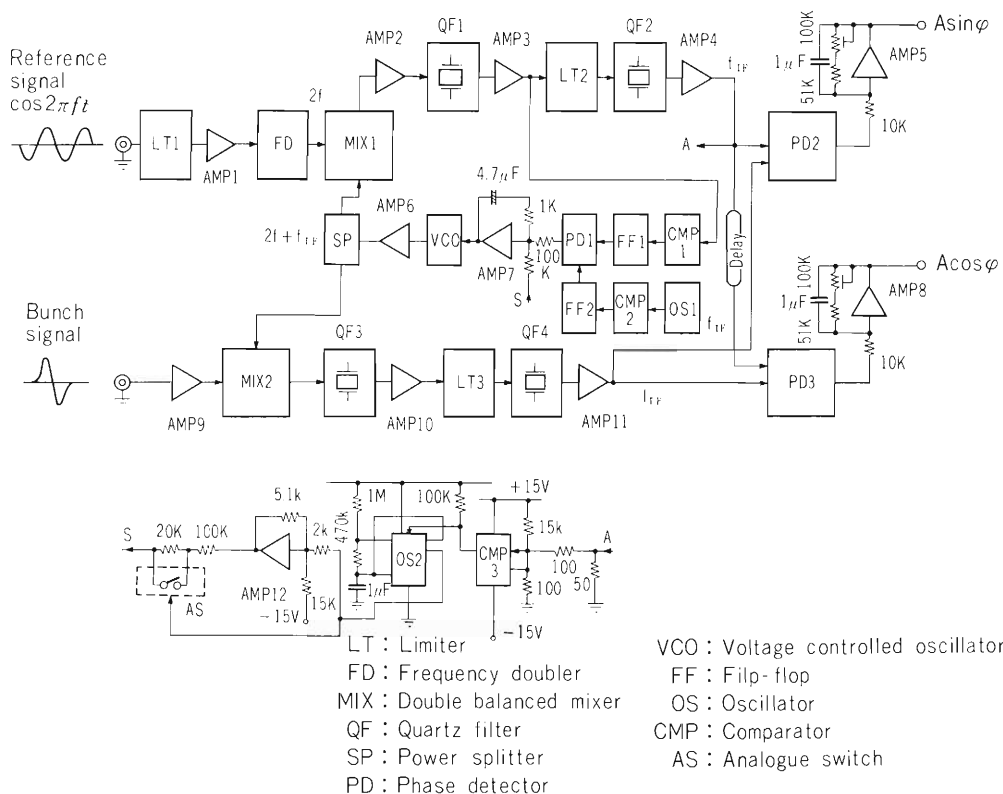


Fig. 1. A block diagram of the bunch phase monitor.

a narrow band filter (QF2), the reference signal is fed to a phase detector (PD2) and also to another phase detector (PD3) after being phase-shifted by  $90^\circ$  with a coaxial delay line. When the circuit is out of the tunable range of the phase lock loop, it is automatically tuned with the other loop including an oscillator (OS2) by scanning the frequency of the VCO output ( $2f_{\min} + f_{\text{if}} \sim 2f_{\max} + f_{\text{if}}$ , where  $f_{\min} = 17$  MHz,  $f_{\max} = 45$  MHz and  $f_{\text{if}} = 10.7$  MHz).

The bunch signal, which is generally bipolar, is also mixed with the VCO output at MIX2 in the same way as the reference signal. The mixer output is filtered with a couple of narrow band filters (QF3 and QF4) which remove the effects of frequency components in the bunch signal other than that of the second harmonics of the fundamental frequency (that is,  $2f$  component). The bunch signal in the intermediate frequency stage is fed to the other inputs of the phase detectors PD2 and PD3.

The two dc outputs are obtained: one is  $A \sin \phi$  and the other is  $A \cos \phi$ , where  $A$  is a factor related to the beam intensity. If  $\theta$  is the beam phase to be obtained, then  $\theta = 1/2 \phi + C$ , where  $C$  is a constant inherent in the system.

#### Reference

- 1) W. Bräutigam, M. Herschbach, K. Kennepohl, and J. Reich: IEEE Trans. on Nucl. Sci., NS-26, 2375 (1979).

#### IV-7. Linac Energy Tuning by Phase Control

M. Kase, T. Kambara, T. Tonuma, and M. Odera

The RILAC (RIKEN linac) is a heavy-ion linac with six tunable cavities. To meet the request of applications for different energies, the beam energy can be varied by changing the following factors:

- (1) the number of the cavities in use (from 1 to 6);
- (2) the acceleration frequency (17 ~ 45 MHz);
- (3) the input phase of beam bunch to the last cavity.

The first scheme is very simple and normally used in multi-tank linacs. It provides six discrete energies for a given acceleration frequency. When the second scheme is used together with the first one, the energy can be continuously changed over a wide range (0.01 ~ 4.1 MeV/n). However, to operate the linac with the change of the frequency, most of the parameters of the linac including its injector have to be readjusted and it takes much time to do this. For the frequent change of energy by fine steps, the third scheme (that is, the phase control) is more useful than the above, and by combining it with the first scheme the energy can be varied over a wide range.

The method of the phase control is shown in Fig. 1. Let #N denote the cavity used for the control. Turning off the later cavities, #(N + 1), #(N + 2) ....., and keeping the former cavities, #(N - 1), #(N - 2) ....., in the normal operation, the input phase of the beam relative to the radio frequency at the first acceleration gap of the cavity #N is shifted from the normal phase ( $-25^\circ$ ). Figure 2 shows the variation of energy with the change of the input beam phase,  $\phi$ . The solid lines in the figure show the results of the calculation (for N = 3, 4, 5, and 6) which were made using the impulse approximation.<sup>1)</sup> The experimental results are also shown in Fig. 2. The energy was measured with a dipole magnet (SW magnet) placed behind the cavity #6, while the input beam phase was estimated using the phase shift of the rf voltage of the cavity #N from the normal condition which gives the synchronous beam phase of  $-25^\circ$ . Fairly good agreement between the calculations and the measurements is obtained.

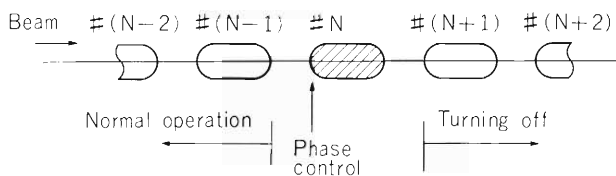


Fig. 1. The phase control method for multi-cavity linacs.

Using the phase control scheme, the output beam energy of the cavity in concern can be decreased smoothly down to the level lower than that of the input one. It implies that the use of the phase control together with the first scheme provides the continuous energy change in the wide range without varying the frequency. In the range of  $\phi$  between  $-180^\circ$  and  $0^\circ$ , no remarkable growth of beam emittance was observed. The energy spread of the output beam has a minimum value (0.7 % fwhm) at  $\phi = 0$  and increases gradually as  $\phi$  decreases, being around 2 %

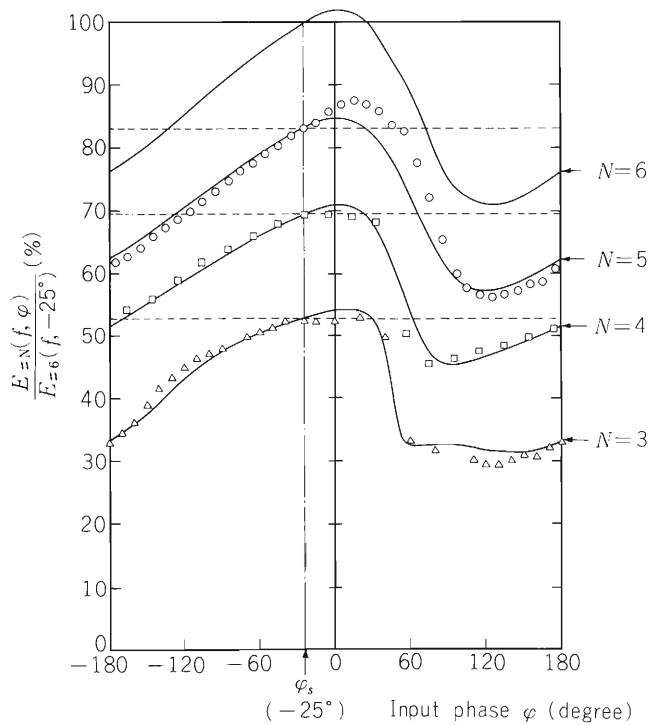


Fig. 2. The variations of beam energy vs. the input beam phase of the “last” cavity (#N) of those being in use. Energy is normalized to the designed value at the cavity #6,  $E_{\#6}(f, -25^\circ) = 0.00202 \times f^2$  (MeV/n) where  $f$  is the frequency in MHz. Triangles, squares and circles are the experimental values obtained at  $f = 22.3$  MHz for  $N = 3, 4,$  and  $5,$  respectively.

(fwhm) at  $\phi = -120^\circ$ . The procedure to change the energy in this way is much simpler than those including the change of acceleration frequency, because the operator has to adjust no parameters in the portion from the injector to the cavity  $\#(N - 1)$ , but only the rf phase of the “last” cavity (#N) and parameters of magnetic devices in the later portion of the linac.

In this mode of operation, it is possible that the acceleration frequency is chosen, independently of the energy in concern, only by taking account of the  $M/q$  value of ions to be accelerated. In any case, there is no need of the exact frequency setting for each energy.

## Reference

- 1) T. Tonuma, F. Yoshida, and M. Odera: Reports I.P.C.R., (in Japanese), 51, 53 (1975).

#### IV-8. Suppression of Secondary Electron from Beam Stopper

M. Hemmi

Many slit boxes are used in the beam handling and transport system.<sup>1)</sup> Each box contains a beam stopper plate downstream to the four slit blades. It is made of copper, cooled by water and is thrown in and out by use of an air cylinder. A large rate of emission of the secondary electrons is inevitable by bombardment with heavy-ion beams and current reading is enhanced by a factor of between two and ten for a simple planar stopper plate. The phenomenon makes beam diagnosis difficult.

Usually, a Faraday cup having a large depth compared to its aperture is used to minimize the secondary electron effect. However there is no space to accept such a long cup in the slit box. Therefore, in the initial phase of test operation of the linac, we used method of self-biasing of stopper by zener diodes. The scheme was simple and seemed to work well. It was, however, soon found that the positive potential developed by self-biasing gives rise to collection of nearby electrons in the box leading to the current reading lower than that of the correct value. We have adopted another method. A shallow cup is fixed on the stopper plate and a pair of rare-earth cobalt magnet forms magnetic field across volume of the Faraday cup composed of the cup and the plate. Figure 1 is its photograph. The cup is insulated. There is no need of power supply for electron suppression, and this makes its structure simple and compact. Stronger magnetic field might be desirable for suppression of the secondary electrons. However the stray field in

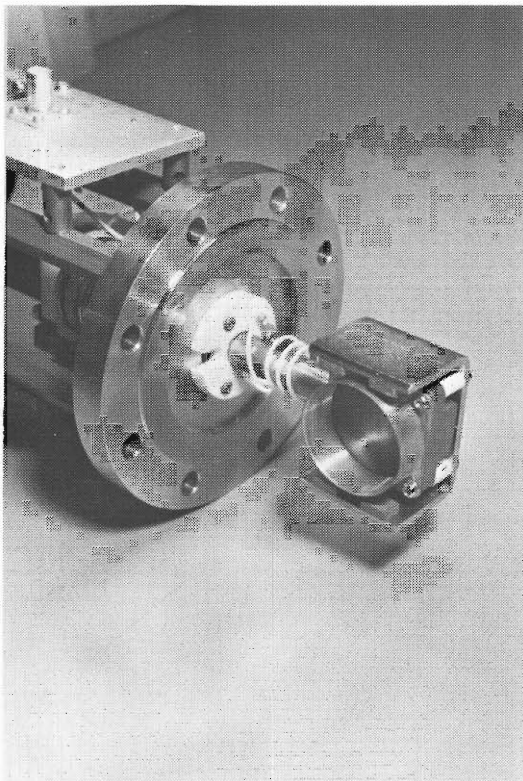


Fig. 1. Photograph of the beam stopper equipped with secondary electron suppresser which uses rare-earth cobalt permanent magnets.

the beam path, when the stopper is extracted out of the path, may affect the beam and give undesirable effect in the beam trajectory downstream when the stray field is too large. Therefore, assuming almost all the secondary electrons are of energy less than 300 eV we have concluded that the field strength of around 100 G is sufficient for electron suppression. By adjusting the number and relative positions of the permanent magnet pieces, we have succeeded in producing necessary field strength and its distribution in the Faraday cup. In Fig. 2 are shown results of measurement of the leakage field along the straight paths at various distance from the replaced beam stopper. The curve tagged 0 is measured on the beam axis and 10 corresponds to the line displaced 10 mm from the axis to the stopper. Integrated field strengths are shown in the inset of Fig. 2. This field gives only negligible deviation of the beam. Comparison of current readings by this magnet-equipped shallow cup and by a normal long cup was made with an Ar beam. Any systematic difference between two readings was not found assuring effective suppression of the secondary electrons by the magnetic field given by the permanent magnets. We are preparing for further measurements using heavier projectiles.

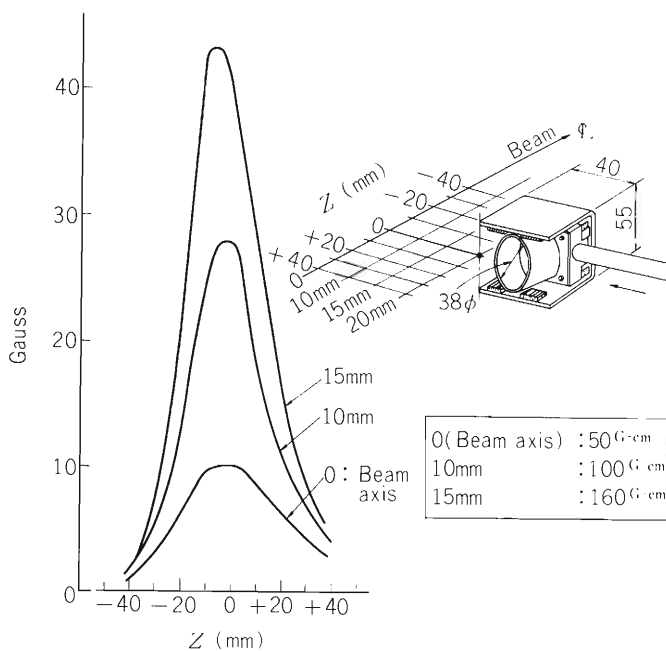


Fig. 2. Leakage field distribution along the beam path. Number on each curve means distance in mm of path from the center line of the beam pipe. Distance of the edge of the stopper from the beam axis is 20 mm. Inset gives integrated field strength.

#### Reference

- 1) M. Hemmi, Y. Miyzawa, M. Odera, and T. Tonuma: IPCR Cyclotron Progr. Rep., 12, 138 (1978); M. Kase, I. Yokoyama, and M. Hemmi: *ibid.*, 14 115 (1980).

## IV-9. Status of RILAC RF System

T. Kubo

In this period, several improvements were made in the RILAC radio-frequency(RF) system.<sup>1)</sup> The control circuit<sup>2)</sup> fabricated temporarily for each main resonator was improved to simplify and stabilize the operation further. This circuit has been used to provide beams since last year. A similar control circuit was applied to an RF buncher<sup>3)</sup> which had been used in the injection beam line to improve acceleration efficiency.

## (1) RF system of six main resonators

Figure 1 schematically shows the present control circuit equipped for the RF system of each main resonator.

This control circuit includes four feed back loops as follow:

- (i) Loop for stabilizing the amplitude of the accelerating voltage generated in the resonator,
- (ii) Loop for maintaining the tuning of the resonator,
- (iii) Loop for restoring the accelerating voltage,
- (iv) Loop for stabilizing the accelerating phase.

The last two loops were newly added to the control circuit described in Ref. 2.

The third loop is designed to restore automatically the accelerating voltage lost by a discharge which occurred in the resonator. When the voltage is lost by the discharge, it cannot usually be recovered again of itself because multipactoring phenomena rapidly grow in the resonator and its vacuum becomes worse. To regenerate the voltage, the multipactoring phenomena have to be extinguished by once turning off the excitation of the resonator. The auto-restoration circuit in this loop performs this procedure automatically referring to a feed back signal of the accelerating voltage. The excitation signal is instantly turned off when the voltage is lost, and the excitation mode is changed from continuous wave(CW) mode to pulse mode( $\sim 1.5$  Hz, duty factor  $\sim 5\%$ ). The small duty factor allows ions and electrons generated by the discharge and the multipactoring

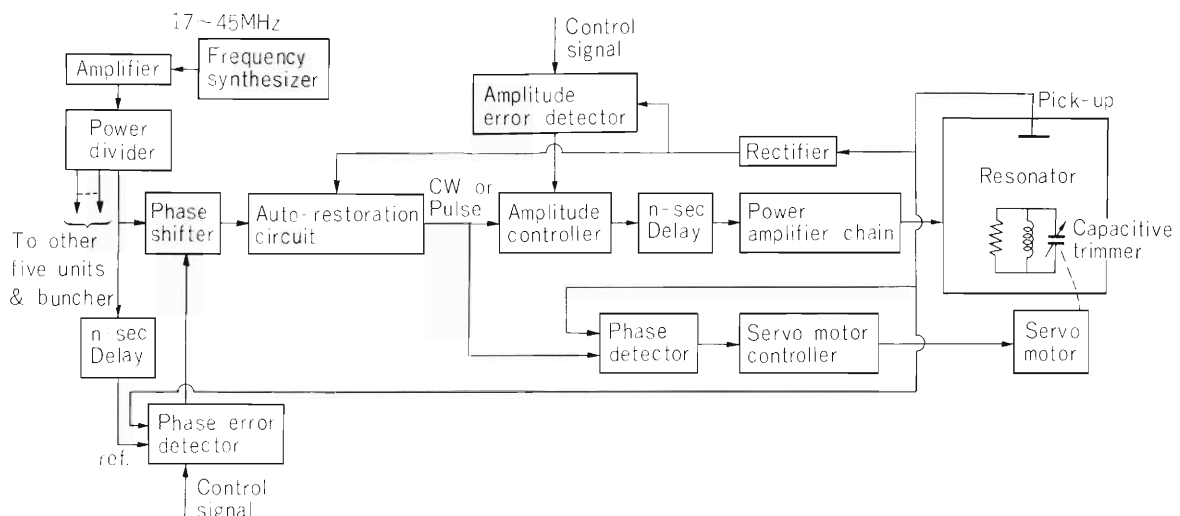


Fig. 1. A schematic diagram of the control circuit for the main resonator.

phenomena to recombine or drift to the resonator wall during the time between pulse excitations, so that probabilities to fall into the multipactoring decrease. As soon as the voltage is generated during the pulse mode, the excitation mode is again switched back to the CW mode. Thus the voltage can be quickly restored, and the CW excitation in such an abnormal state can be avoided that the final tube<sup>1)</sup> has a very different load impedance from regular one because of the occurrence of the multipactoring. When the RF power is continued to be fed in such a mismatched state, some troubles are frequently induced.

This loop is also found useful to search a resonance of the resonator. The accelerating voltage can be generated only when the resonator is almost on the resonance. The resonator is excited by the pulse mode if it is far off the resonance. Thus the search can be made by moving a capacitive trimmer manually in such direction that the excitation mode automatically turns to the CW mode.

The fourth loop can suppress phase noise and phase drift of the accelerating voltage. These phase errors are detected by a phase detector and are fed back to a phase shifter so that they can be compensated.

Part of the control circuit is connected to the control computer(HP1000)<sup>4)</sup> in the control room. So far, the generation of the accelerating voltage, the adjustment of the reference signal for it and the activation of the first two feed back loops are controlled by the computer.

## (2) RF system of buncher

A schematic diagram of the RF system for the buncher is shown in Fig. 2. The resonator of the buncher is of a quarter wave length coaxial type, and its frequency tuning is made by a variable vacuum capacitor (VVC). A wide band amplifier is used to excite the resonator.

The control circuit for the buncher includes two feed back loops to stabilize the amplitude and phase of the bunching voltage. They consist of a phase error detector, an amplitude error detector and an amplitude and phase controller.

The feed back loop to maintain the tuning is not included in the circuit because the Q-value of the resonator is low(1000 ~1500) and the necessary RF power is small(less than ~150W). The feed back loop to restore the bunching voltage is also not included because the multipactoring phenomena have not occurred as yet.

Operation frequencies used in this period for the beam acceleration are between 18 and 30 MHz.

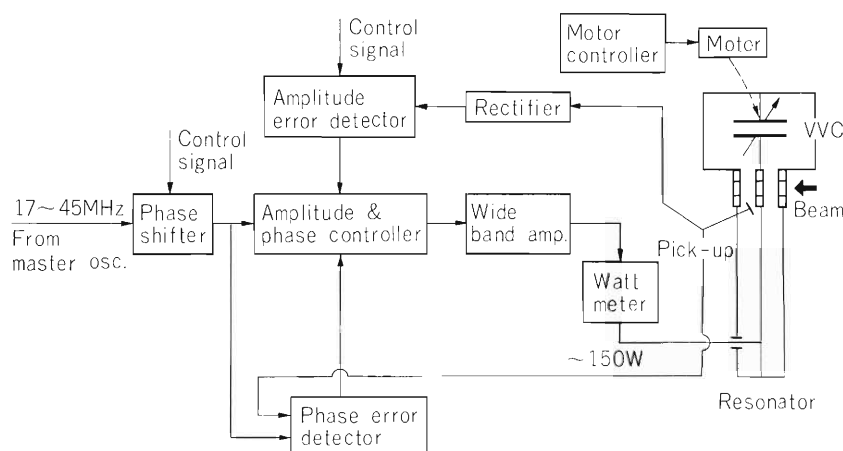


Fig. 2. A schematic diagram of the RF system for the buncher.

## References

- 1) T. Kubo and Y. Chiba: IPCR Cyclotron Progr. Rep., 14, 123 (1980).
- 2) T. Kubo, M. Hemmi, and Y. Chiba: RIKEN Accel. Progr. Rep., 15, 137 (1981).
- 3) M. Yanokura and M. Odera: IPCR Cyclotron Progr. Rep., 13, 149 (1979).
- 4) T. Kambara, M. Odera, and S. Takeda: *ibid.*, p. 134.

#### IV-10. Investigation of Frequency Characteristics of the Screen Grid Bypass Capacitor at the Final Stage of RF Power Amplifier for RILAC

T. Fujisawa and Y. Chiba

The RIKEN linear accelerator (RILAC) has been constructed and operated well in the frequency range of 17 to 30 MHz. In order to extend the frequency range up to 45 MHz, the performance of the screen grid bypass capacitor at the final stage of the RF power amplifier was investigated. In Fig. 1 the schematic diagram of the amplifier is shown. The investigation was carried out as follows: The amplifier was disconnected from the feeder line, and the plate and grid circuits were tuned in the frequencies to be measured. The plate circuit was excited by a signal generator, and the screen and control grid voltages induced from the plate were measured with oscilloscopes. In Fig. 2, the schematic view of the bypass capacitor is shown. The screen grid voltages were measured at position A, B, and C. The plate and control grid voltages were measured with the voltage pick-ups shown in Fig. 1.

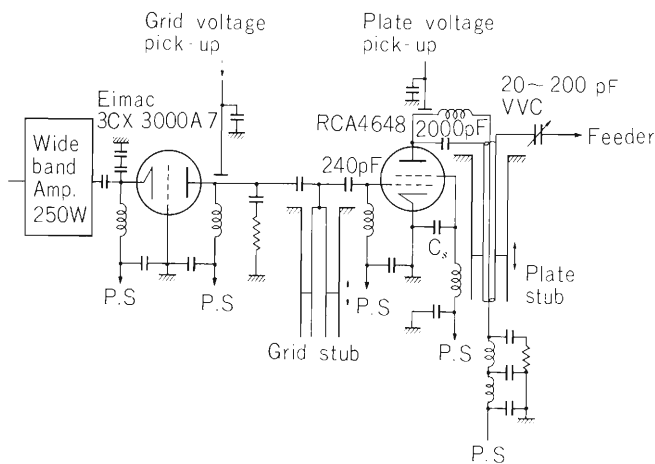


Fig. 1. Simplified diagram of the RF power amplifier of RILAC, P.S: Power supply.  $C_s$ : Screen grid bypass capacitor.

In Fig. 3, the ratios of control and screen grid voltages to the plate voltage are shown (closed circles). The frequency dependence of the ratio is complicated in the range of 33 to 45 MHz, which is not desirable for the stable operation of the amplifier.

This resonance-like frequency dependence is caused by the ceramic capacitors at the outer ends of the sheet capacitor using KAPTON film. The subsequent measurements were carried out without the ceramic capacitors. The results are also shown in Fig. 3 (open circles). The frequency dependence of the ratio becomes simple except the resonance at 34 MHz. This resonance is caused by the choke coil in the plate circuit of the preceding amplifier. After the improvement of the choke coil the flat frequency dependences was obtained.

The measured ratios of the screen and control grid voltages to the plate voltage are about 0.006 and 0.08, respectively, in the frequency range of 17 to 45 MHz. Much smaller ratios are desired for the stable operation of the amplifier. Improvements of the KAPTON sheet capacitor were carried out. The performance of the improved capacitor is presented by the authors in this progress report.<sup>1)</sup>

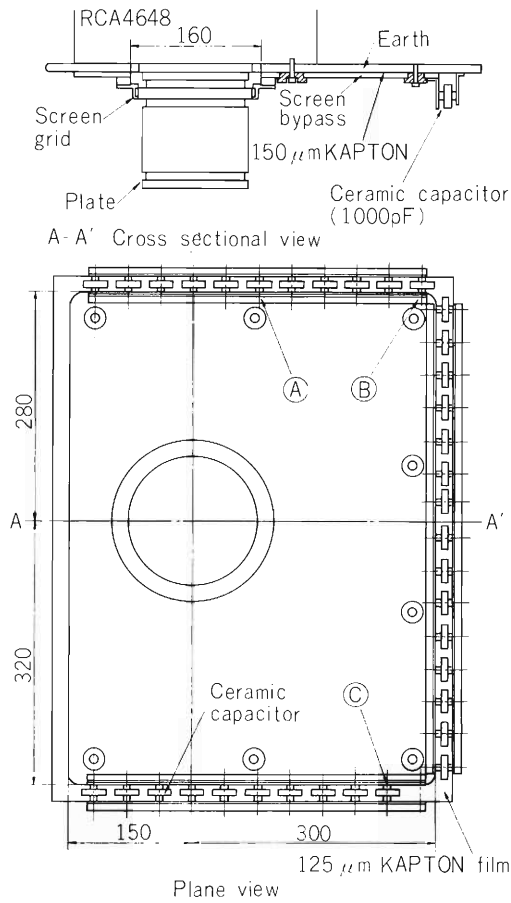


Fig. 2. Schematic view of the screen grid bypass capacitor. The screen voltages are measured at positions A, B, and C. The capacitance of the KAPTON sheet capacitor is  $0.03 \mu\text{F}$ .

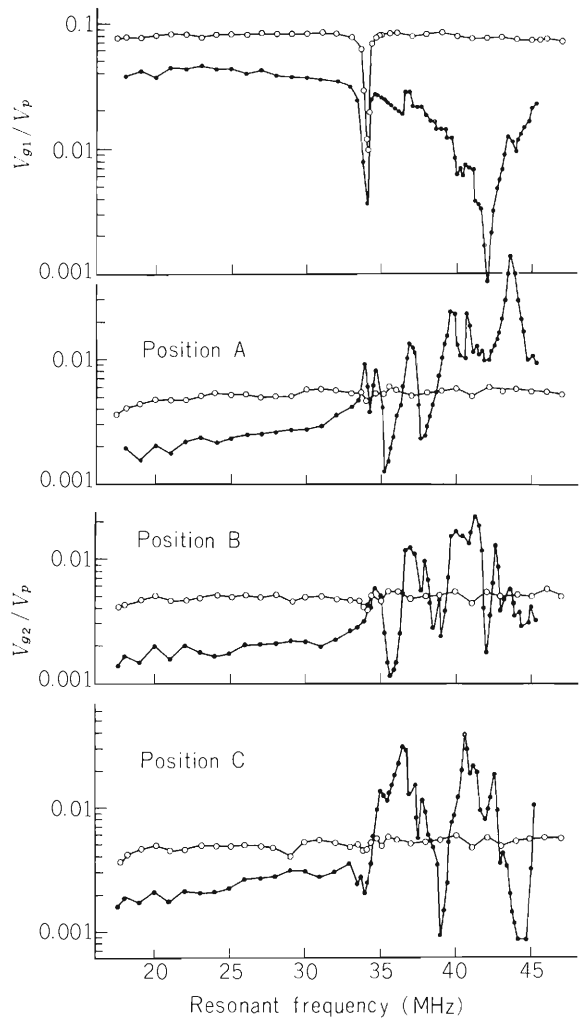


Fig. 3. Ratios of the control and screen grid voltages to the plate voltage. The lines are only to guide the eye. The closed and open circles are the data with and without the ceramic capacitors, respectively. See the text and Fig. 2.

Reference

- 1) S. Kohara, T. Fujisawa, and Y. Chiba: p. 171 in this report.

### IV-11. Basic Study on the RF High Power Amplifier for RIKEN SSC

#### Study of the Screen Bypass Capacitor for the Final Stage

S. Kohara, T. Fujisawa, and Y. Chiba

Screen bypass capacitors for RCA 4648 tetrode were manufactured by way of trial, which will be used for the high power amplifiers of RIKEN SSC. The performance of capacitors was studied.

The power amplifier for the resonators of RIKEN SSC is required to supply the maximum RF power of 300 kW in the frequency range of 17 to 45 MHz. RCA 4648 tetrode is to be used as a grounded cathode amplifier. In Fig. 1, the schematic diagram of the amplifier is shown. The plate tuning circuit is a  $\lambda/4$  type stub and tuned by changing the length of the stub. The grid tuning circuit is a  $\lambda$  type stub and tuned by a variable capacitor. In Fig. 2(a), the simplified circuit diagram of the amplifier is shown. The symbols  $C_0 \sim C_4$  show the capacitances between electrodes of the tetrode and  $C_5$  shows the capacitance of the screen bypass. For the stable

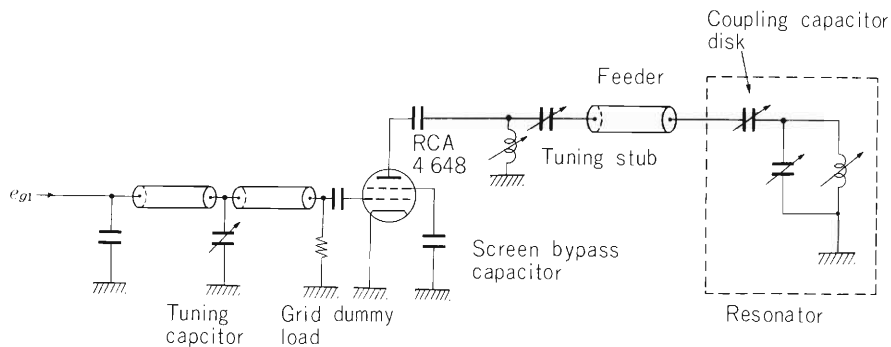


Fig. 1. Schematic diagram of the high power amplifier of RIKEN SSC.

Capacitances given in the catalogue (measured)

- |                               |                      |
|-------------------------------|----------------------|
| $C_0 = 0.6\text{pF}$ (1.5pF)  | $P$ : Plate          |
| $C_2 \leq 85\text{pF}$ (75pF) | $G_1$ : Control grid |
| $C_3 = 775\text{pF}$ (737pF)  | $G_2$ : Screen grid  |
| $C_4 = 425\text{pF}$ (357pF)  | $K$ : Cathode        |
| $C_1 = (4.5\text{pF})$        |                      |

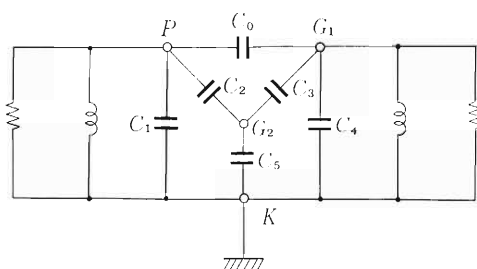


Fig. 2(a) Simplified diagram of the circuit of amplifier.

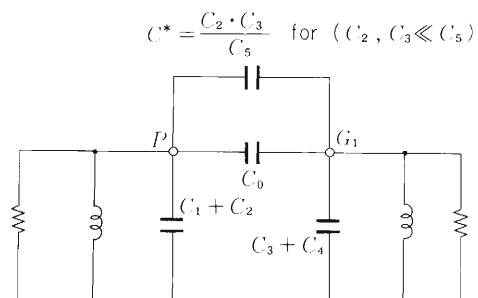


Fig. 2(b) Equivalent circuit for the circuit in Fig. 2 (a).

operation of the amplifier, it is necessary to reduce the coupling between the plate and control grid to a value as small as possible. A part of the coupling is due to the direct interelectrode capacitance  $C_0$ . The other part is attributed to the screen bypass  $C_5$  which takes a finite value. The latter effect can be replaced equivalently by an additional capacitance  $C_0^*$  to  $C_0$  as shown in Fig. 2(b). It can be seen that the capacitance of screen bypass has to be as large as possible in order to reduce the coupling.

In Fig. 3, the screen bypass capacitor manufactured is shown. The insulator is made of  $50\ \mu\text{m}$  KAPTON film (prepared by Du Pont). The calculated and measured capacitances are  $0.28\ \mu\text{F}$  and  $0.11\ \mu\text{F}$ , respectively. This discrepancy was supposed to be due to poor flatness of the electrode of the capacitor. Therefore the KAPTON film coated by conductive silver paint was examined. The capacitance became  $0.26\ \mu\text{F}$ .

The  $50\ \mu\text{m}$  KAPTON film could endure a voltage as high as 5 kV DC for a long time (30 h) in a preliminary test.

The capacitor was mounted on RCA 4648 tetrode without the plate and grid tuning circuits. The plate was excited by a signal generator, and the voltages of screen and control grids induced from the plate were measured. In Fig. 4, the ratios of screen and control grid voltages to the plate voltage are shown as a function of radiofrequency. The ratios, when the screen grid was grounded, are also shown. The flat frequency responses seen in Fig. 4, show that these capacitors operate well in this frequency range. The value of  $C_0$  deduced from the ratios is 1.5 pF and those of  $C_0^*$  for  $C_5 = 0.11\ \mu\text{F}$  and  $0.26\ \mu\text{F}$  are 0.5 and 0.2 pF, respectively. The measured value of  $C_0$  is 2.5 times the value given in the catalogue. The capacitance  $C_0^*$  for  $C_5 = 0.11\ \mu\text{F}$  is one third of  $C_0$ . In stability consideration of the amplifier it is indispensable to take account of the coupling effect of this order of magnitude.

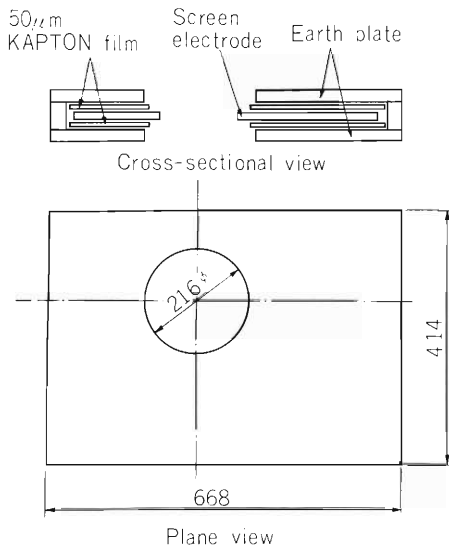


Fig. 3. The capacitor manufactured.

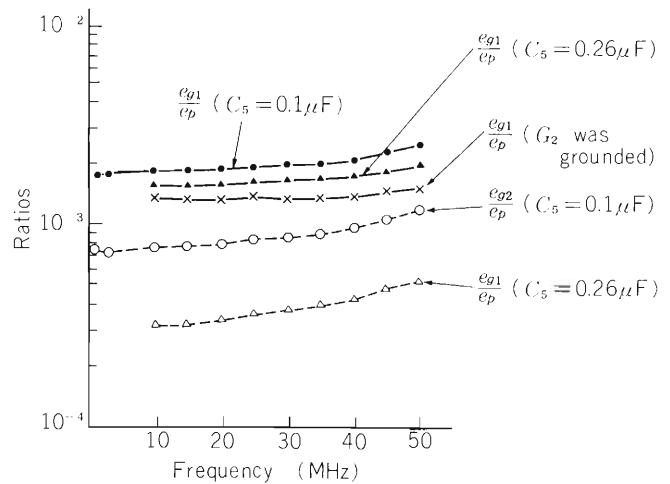


Fig. 4. Ratios of the screen and control grid voltages to the plate voltage.

### IV-12. Grid Tuning Circuit of $\lambda$ Type for the RF Power Amplifier for RIKEN SSC

S. Kohara and T. Fujisawa

The amplifier of RIKEN SSC is required to work in the frequency range of 17 to 45 MHz. An RCA 4648 tetrode is to be used for the final stage of the amplifier. The capacitance of the control grid to the screen grid and cathode is 1200 pF (in the catalogue). The necessary grid RF voltage is estimated to be 300 V to drive the 4648. The capacitance as a load for this voltage at the highest frequency drains a large current which is difficult to be supplied directly by any reasonably sized amplifier. Therefore it is desirable to drive with a grid tuning circuit. A  $\lambda$  type grid tuning circuit is designed which is tuned by a variable capacitor. Figure 1 shows the schematic diagram of the circuit. The capacitance ( $C_{in}$ ) is determined to equal the grid capacitance (1200 pF). In Fig. 2, the capacitance of the variable capacitor required to tune the circuit is shown as a function of radio frequency. This circuit has following merits:

- (1) The grid voltage is equivalent to the input voltage.
- (2) The tuning and impedance matching are simultaneously done by one variable capacitor.

Frequency dependence of grid input impedance of the 4648 is studied in order to design the tuning circuit in detail. In Fig. 3, the simplified circuit of the 4648 is shown. The symbols  $C_0$  to  $C_4$  are the interelectrode capacitances and  $C_5$  is the capacitance of the screen bypass. The grid input impedances are measured in the frequency range of 1 to 80 MHz using the device shown in Fig. 4. In Fig. 5, the results are shown together with the calculated impedances. The impedances calculated with the interelectrode capacitances (broken line) are not in agreement with

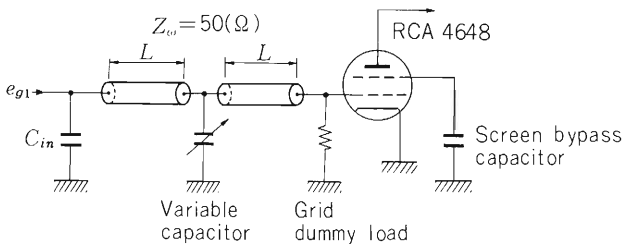


Fig. 1. Grid tuning circuit of the amplifier which uses an RCA 4648 tetrode.

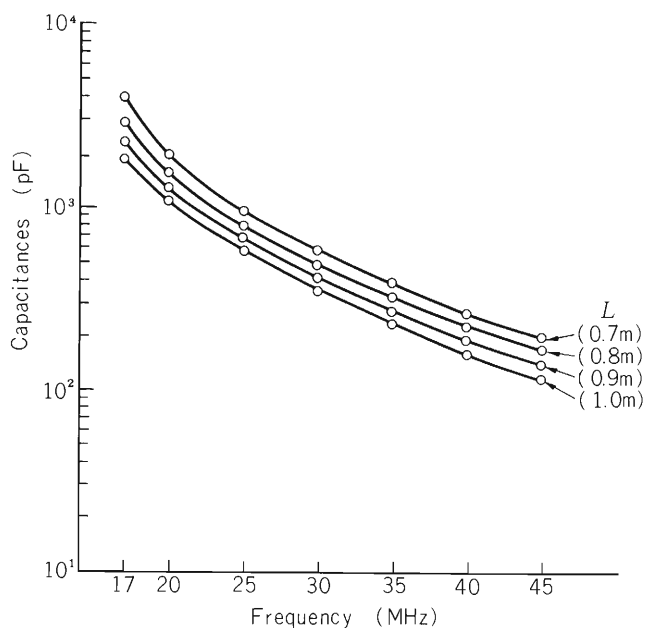


Fig. 2. Capacitances of the variable capacitor for tuning the grid circuit. The parameters are the length of the coaxial line. See Fig. 1.

the measured impedances in the frequency range of 30 to 80 MHz. The circuit of 4648 cannot be represented by the calculation with only direct interelectrode capacitances in this frequency range.

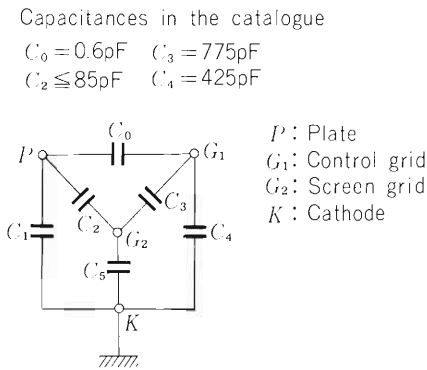


Fig. 3. Simplified circuit diagram of the 4648 tetrode and screen bypass capacitor.

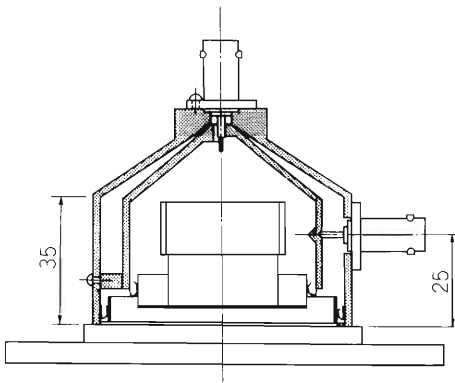


Fig. 4. Cross sectional view of the device for measurement of the control grid impedance.

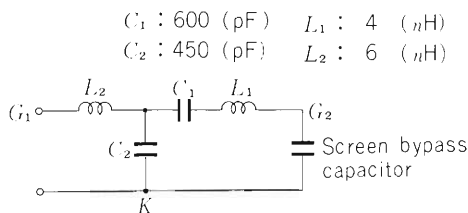


Fig. 6. Equivalent circuit of the grid of RCA 4648 tetrode given by Yingst et al. with screen bypass capacitor.

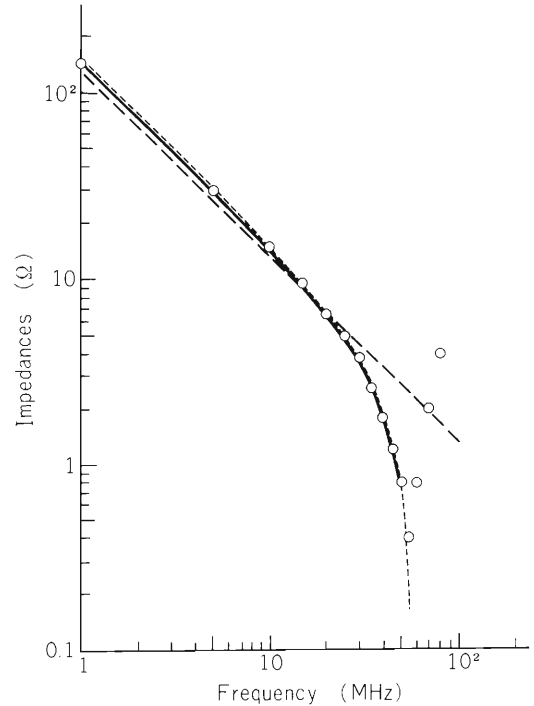


Fig. 5. Frequency characteristics of the grid input impedance of RCA 4648 tetrode. The open circles show the measured data. The solid, broken and dotted lines show the impedances calculated for the circuits in Figs. 7, 3, and 6, respectively.

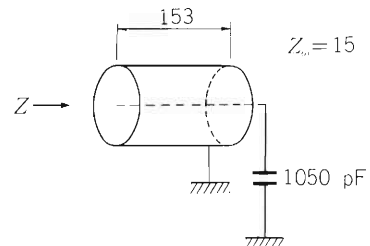


Fig. 7. Circuit constructed with transmission line and capacitor, of which impedances are equivalent to the grid input impedances of RCA 4648 tetrode.

In Fig. 6, the equivalent circuit of the 4648 given by Yingst et al.<sup>1)</sup> is shown. The grid input impedances calculated for this circuit (dotted line) are also shown in Fig. 5. The measured impedances are well reproduced by the calculation. Therefore the capacitance (1200 pF) at the input of the tuning circuit has to be replaced by the equivalent circuit. The equivalent circuit can be approximately transformed to a circuit which consists of a transmission line and a capacitor (see Fig. 7). The impedances calculated for this circuit are also shown in Fig. 5. The impedances calculated for these circuits agree with each other. If the circuit shown in Fig. 7 is installed at the input of the tuning circuit and the circuit is tuned, the input impedance becomes equal to the resistance of the grid dummy load.

#### Reference

- 1) T.E. Yingst, D.R. Carter, J.A. Eshleman, and J.M. Pawlikowski: Proc. of the IEEE, Mar. p. 357 (1973).

#### IV-13. Control System of the Linac

T. Kambara, M. Kase, and T. Kubo

The control system of the linac with an HP-1000 computer system<sup>1)</sup> has been working stably since November 1979. Major troubles of the computer system occurred three times during the period from October 1981 to October 1982: one was due to the failure of the memory controller and the others were due to the parity error of the memory. The time spent for the recovery was one day for the former case and a few hours for the latter cases which caused little trouble on the linac operation.

The communication line between the computer and devices in the accelerator vault was replaced from a serial data link with a twisted pair cable to HP-IB extenders (HP 37203A) with optical fibers. It increased the data transfer rate from 180 characters/sec to 40 kbyte/sec and allowed quicker response from those devices to operators' commands. The serial link is now available as a back-up communication line in case of break-down of the optical fiber systems. It can also be used for a portable terminal (HP-3070A) with a keyboard to communicate with the computer from places in the accelerator vault.

An HP-IB interface card was added to the computer system, resulting in two cards. The communication with nearby devices connected by HP-IB cables and that with distant devices connected by the optical fiber systems were separated among the two interfaces.

The auto-tuning circuits of the radio-frequency system<sup>2)</sup> were connected to the computer. Thus the amplitude of the acceleration voltage in the cavities is controlled and monitored at the CRT terminals on the control console. The RF signals of the cavities and the beam bunch signals which are picked up between the cavities are sent to the control room with dedicated coaxial cables and are displayed on an oscilloscope. Therefore the adjustment of the RF phase has become much easier. These improvements contributed to the speed-up of the tuning of the RF system.

The vacuum pressure values measured at the beam injection line, the cavities and the beam switching magnet are monitored in the control room at both the control console and a monitoring panel for the vacuum system. The meters on the monitoring panel were replaced by a 12-point dot printing recorder to take continuous long-term records. At the same time, the values of the vacuum pressure at the cavities are sent to the computer to give information on the condition of the RF system. The parameters of the PIG ion source are also sent to the computer for the monitoring and recording.

The values of the magnet currents can be recorded on a magnetic tape at any time during the linac operation. The recorded data are used to reproduce the past setting at the start-up of the linac and also used for later analysis of the parameters.

A block diagram of the control system in October 1982 is shown in Fig. 1.

We intend to improve the display and key-in systems on the control console by introducing new devices like a color graphic CRT display and a touch panel. We also intend to gather, process and display the data from beam diagnostic devices by the computer.

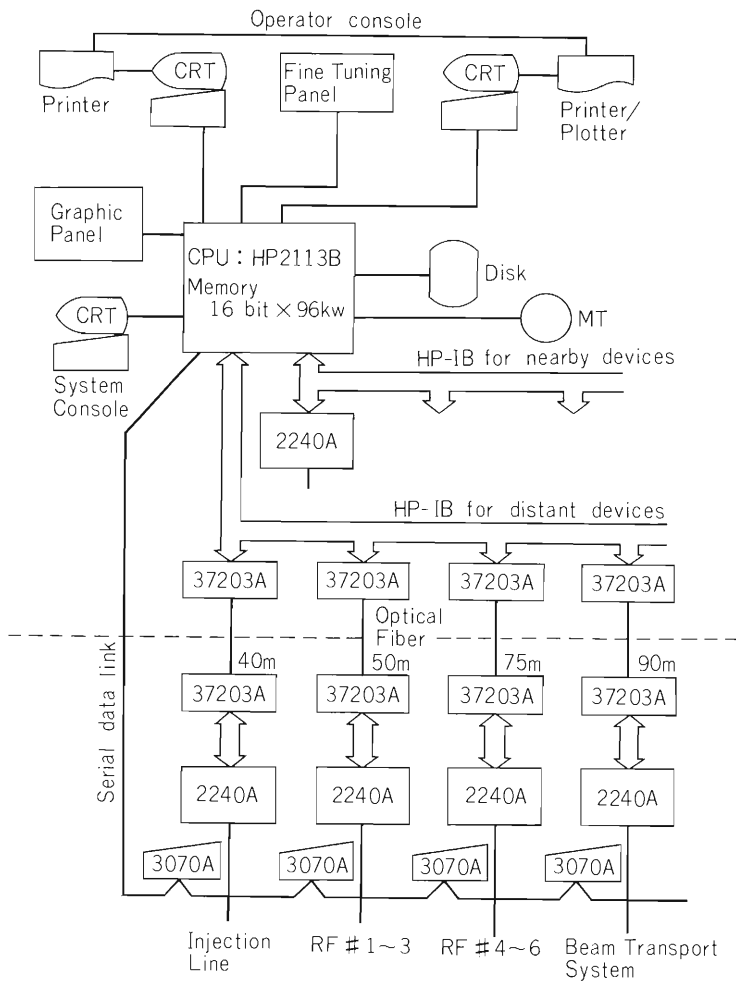


Fig. 1. A block diagram of the control system in October 1982. 2240A denotes a measurement and control processor, 37203A denotes a HP-IB extender by optical fibers, and 3070A denotes a local terminal connected to the serial data link.

## References

- 1) T. Kambara, S. Takeda, and M. Odera: IPCR Cyclotron Progr. Rep., 14, 110 (1980).
- 2) T. Kubo, M. Hemmi, and Y. Chiba: RIKEN Accel. Progr. Rep., 15, 137 (1981).

IV-14. On a Possible Medium- $\beta$  RFQ Structure

M. Odera, T. Chiba, and M. Hemmi

The RFQ, or radiofrequency quadrupole structure of linac has been devised to provide transversal focusing force as well as accelerating field at a time by controlling the radiofrequency field. The scheme was originally proposed by V.V. Vladimirsky.<sup>1)</sup> Initial trial to apply the principle for a heavy-ion accelerator was not successful,<sup>2)</sup> and received little attention until it was rediscovered at LANL in summer of 1978 in a Russian paper written by I.M. Kapchinsky and V.A. Teplyakov.<sup>3)</sup> D.A. Swenson and his accelerator division, AT-DO of LANL, achieved rapid progress in formulation of the method of analysis of the orbit and made the detailed model study, culminating in realization of the acceleration of protons up to 640 keV in early spring 1980.<sup>4)</sup> The very attractive characteristics of the RFQ demonstrated are large capture efficiency of injected beam to the acceleration regime and a very low voltage required for injection. Efficiency of more than 90 % has been reported. The high efficiency is useful for acceleration of heavy ions since yield of the multiply charged ions from ion source is far from being copious. Also the small beam spill will make problem of activation less for deuteron acceleration than the usual linac schemes. Injector voltage around 30 to 50 kV is enough for proton allowing elimination of the expensive and voluminous high voltage equipments.

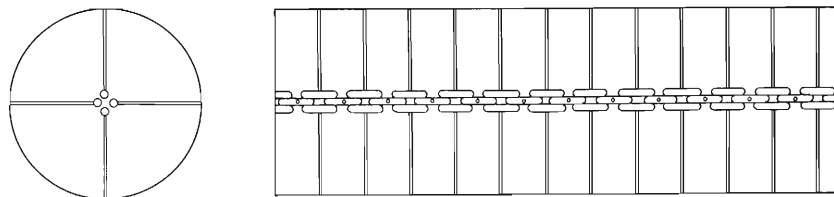


Fig. 1. Sketch showing a general idea of a medium- $\beta$  Alvarez-type RFQ structure.

Although feasibility of acceleration of very heavy ions by this scheme remains still to be demonstrated, INS, University of Tokyo, has succeeded in operation of an RFQ for Li acceleration,<sup>5)</sup> showing validity of principle of the structure. However, it is also believed to be effective only in the low- $\beta$  region of less than a few %. The structures developed in the United States or Germany lose power efficiency rapidly with increase of particle energy. We have tried to find other structures effective in the higher energy region. Figure 1 shows one such structure examined. It resembles the “drift tube structure with horn” studied by Boussard.<sup>2)</sup> Unlike the predecessor, ours has no metallic cylinder to protect ions from deceleration field. It is composed of horizontal and vertical pairs of rods supported by separate stems. Axial distance between stems for the different pairs is  $\beta\lambda$  and between neighboring stems of the rods in the same azimuthal position is  $2\beta\lambda$ . Accelerating field exists around the gaps of the rods and its period is  $\beta\lambda$ , since the gaps of different pairs alternate with each other.

In order to investigate this structure, a high frequency model and a magnetic analogue model have been fabricated as shown in Fig. 2 and Fig. 3. The high frequency model has two cells and is being used to study effect of capacitive loading of the resonator by the quadrupolar rod

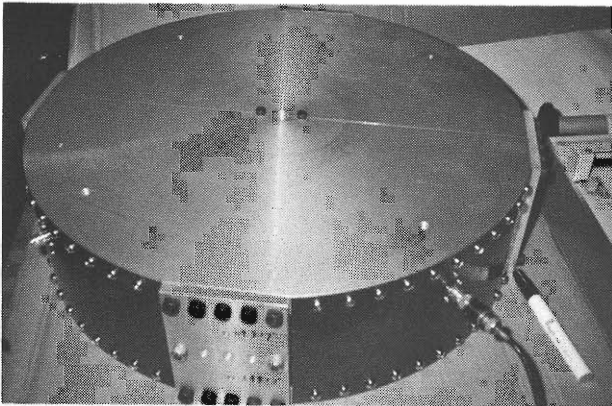


Fig. 2. Photograph of the two-cell high frequency model.

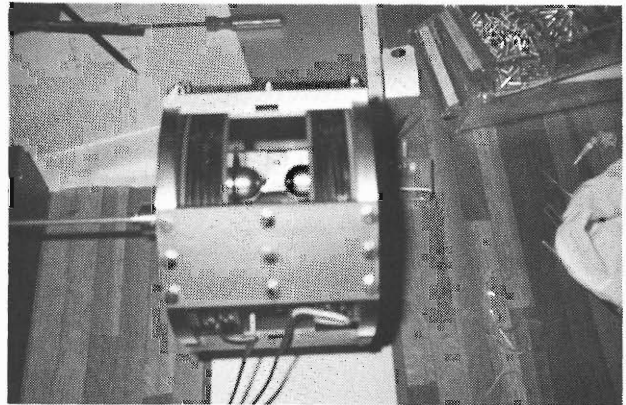


Fig. 3. Photograph of the magnetic analogue of the center region of the RFQ for study of the three dimensional field pattern.

configuration. Its resonant frequency was found to be 351.98 MHz and its cell length of 48.9 mm corresponds to  $\beta = 5.7\%$ , or roughly 1.5 MeV/n which can be expected for particles accelerated by our heavy ion linac, RILAC or a low- $\beta$  RFQ structure. The magnetic analogue model made of iron is used to measure the three dimensional field distribution in this configuration. Near the beam axis, the pattern of the magnetic field closely reproduce that of electric field, if permeability of the iron is sufficiently large. Result of measurement of axial field is shown in Fig. 4. Considerable axial component exists even in the midway of distance between the accelerating gaps. This field pattern makes transit time factor less than 0.5. The numerical value may be improved somewhat by adjusting rod size and aperture. However, such an open electrode structure seems not suited for getting a good acceleration efficiency. We are investigating other characteristics of this structure and trying to find better RFQ configuration suitable to be used in the medium- $\beta$  region.

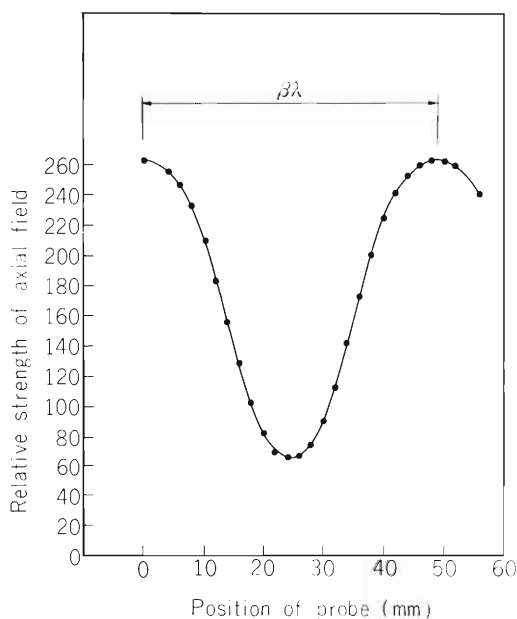


Fig. 4. Distribution of accelerating field measured along the axis of the magnetic analogue model.

## References

- 1) V. V. Vladimirsky: *Pribory i Tekhn. Eksp.*, 3, 35 (1956).
- 2) D. Boussard: *IEEE*, NS-12, 640 (1965); *Comp. Rend. Ac. Sci.*, 265, 4665 (1965).
- 3) I. M. Kapchinsky and V. A. Teplyakov: *Pribory i Tekhn. Eksp.*, 17, 19 (1970).
- 4) R. W. Hamm, K. R. Crandall, L. D. Hansborough, J. M. Potter, G. W. Rodentz, P. H. Stokes, J. E. Stovall, D. A. Swenson, T. P. Wangler, C. W. Fuller, M. D. Machalek, R. A. Jameson, E. A. Knapp, and S. W. Williams: *Proc. Intern. Conf. on Low Energy Ion Beams*, Bath, England, Apr. 1980; T. P. Wangler and R. H. Stokes: *IEEE*, NS-28, 1494 (1981).
- 5) Y. Hirao: Private communication.

## IV-15. Present Status of the RIKEN SSC Project

H. Kamitsubo

The RIKEN Separated Sector Cyclotron (SSC) Project started in 1980. It aims at construction of a  $K = 540$  SSC for the purpose to extend research activities in nuclear science at the Institute of Physical and Chemical Research. The SSC will be a post accelerator of the present variable-frequency heavy-ion linac (RILAC). In addition to the RILAC, an AVF cyclotron will be constructed at the final stage of the project as the second injector for the SSC.<sup>1)</sup>

The sector magnets with trim coils and their power supplies were ordered to Sumitomo Heavy Industries Ltd. in 1981 and construction of them is now under way. Two among four sector magnets were completed in June, 1982. After installing them at the factory, excitation characteristics and field distributions were measured. In order to measure the field distributions correctly in the valley region between two sector magnets, alignment of two magnets was carefully done so that their median planes exactly coincided with each other and the center radii of the poles made a right angle to each other. Figure 1 shows a photograph of two sector magnets installed at the factory.

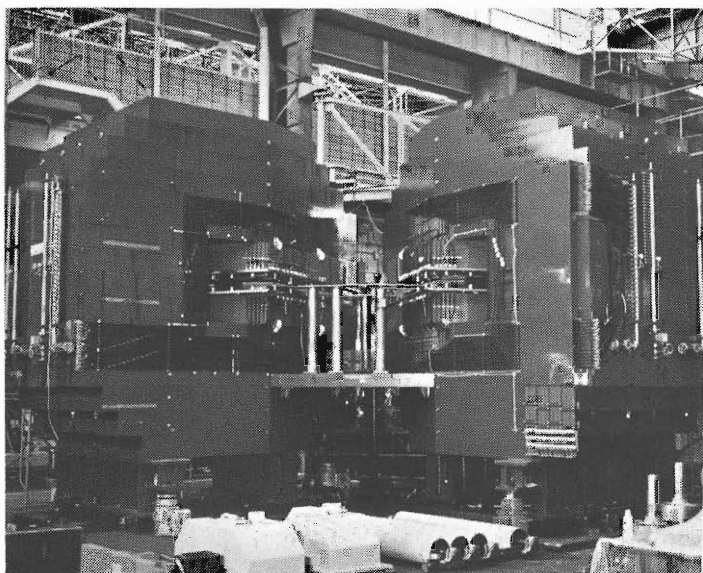


Fig. 1. Photograph of two sector magnets installed at the factory of Sumitomo Heavy Industries, Ltd.

The field measuring device was designed by us and was made by Sumitomo Heavy Industries, too. It is made of aluminum and can be equipped with twenty Hall elements. The holder of the Hall elements can be moved radially as well as azimuthally by a driving system with air pistons.<sup>2)</sup>

Results of the measurements were quite satisfactory.<sup>3)</sup> Very good agreement was obtained between the results of the measurements and the calculations with TRIM code on the excitation characteristics of the magnets. The magnetic field of 1.55 T, which is the maximum base-field strength required for operation at the highest magnetic rigidity, was achieved with a magnetomotive force of  $1.28 \times 10^5$  AT. Distributions of the base field in the valley and hill (gap) regions were measured at the field strength of 0.7, 1.1, 1.5, and 1.57 T. Effective field boundaries and effective sector angles were determined from the measured field distributions as a function of radial coordinate,  $R$ . Variation of the effective sector angles with  $R$  is small except in the region of small  $R$ .

Distributions of the field produced by the trim coils were also measured along the center radius of the pole. Method of the optimization of the trim coil currents were developed.<sup>4)</sup> Orbit calculations were made by taking the actual field distributions into account.

Conceptual design of the RF system has been performed. Two types of the resonator cavities were investigated from electrical and mechanical points of view and finally the resonator having a movable box as a frequency-changing device was adopted,<sup>5)</sup> since total height of the system and the current density at the contact

fingers can be reduced considerably as compared with that having a moving short. The one-fifth scale model resonator was made and the resonant frequency, Q-values and radial distributions of RF electric field were measured for it. Results of the measurements were very satisfactory<sup>5)</sup> and a larger scale model will be made to get more precise data.

The vacuum chamber of the SSC is divided into eight sections, that is, four magnet chambers, two RF resonator chambers and two valley chambers. The reason is that the RF resonators should be withdrawn backwards for adjustment and repair. Because of limited space in the central region of the SSC, it seems to be impossible to apply usual vacuum sealing method. A sealing method with pneumatic expansion seals is considered to save space and to simplify connecting and disconnecting procedure of the RF resonators.

Three different types of one-third model of the seal were made and tested to investigate their performance.<sup>6)</sup> Numerical analysis of the elastic and plastic deformation of the seal using the finite element method is now in progress. Design of the evacuation system has been performed. Total pumping speed of  $16 \times 10^4$   $\ell$ /sec is needed to keep the vacuum in the chamber better than  $1 \times 10^{-7}$  Torr. Cryogenic pumps as well as turbomolecular pumps will be used. In order to save time for pumping possibility to apply the discharge cleaning technique has been investigated.<sup>7)</sup>

Beam from the injectors is to be injected along a line tilted to the median plane of the SSC.<sup>1)</sup> Design of the beam transport line between the RILAC and the SSC and the section for beam matching to the acceptance of the SSC was almost finished. Detailed design of the injection elements such as bending magnets, magnetic inflection channels and electric inflection channel and also the extraction elements is in progress.

Conceptual design of the control system has been continued. It consists of a network of several minicomputers and CAMAC system. To decrease the number of CAMAC crates and signal cables, new CAMAC modules named CIM (Communication Interface Module) and DIM (Device Interface Module) are being developed. They have microprocessors inside them and are connected to CAMAC data-way. Sixteen DIMs will be connected to one CIM through serial lines of optical fibre cables. The CIM has a random access memory to store the data sent from the DIMs at a proper time interval.

We have a plan to optimize the operation of the SSC by using the computer. In order to realize this successfully it is necessary to equip various types of beam diagnostic devices for measurement of current distributions, emittance and phases of the beam inside the SSC and also along the beam transport lines. Theoretical study of adjusting and optimizing procedure is in progress. Detailed design of the beam diagnostic devices is continued.

The beam transport lines to the experimental areas can be operated in the following modes: (1) Achromatic, double telescopic transport to every target area, (2) double dispersive, double telescopic transport with momentum resolution up to 25000 and (3) isochronous, non-dispersive, double telescopic transport.<sup>8)</sup> Beam dynamical calculations were almost finished and final design of each magnet is in progress.

Basic design of the SSC building was finished last year and radiation protection problems were examined. Construction of the building will start soon.

## References

- 1) H. Kamitsubo: Proc. of 9th Intern. Conf. on Cyclotrons and their Applications, Caen, p. 13 (1981).
- 2) H. Takebe, I. Takeshita, J. Fujita, I. Yokoyama, T. Wada, and S. Motonaga: Proc. 4th Symp. on Accel. Sci. and Technol., Wako, p. 301 (1982).
- 3) S. Motonaga: *ibid.*, p. 293.
- 4) A. Goto, H. Takebe, S. Motonaga, and T. Wada: *ibid.*, p. 295.
- 5) K. Ogiwara, T. Fujisawa, and Y. Oikawa: *ibid.*, p. 247.
- 6) K. Ikegami, S. Nakajima, and Y. Oikawa: *ibid.*, p. 207.
- 7) Y. Ishibe, H. Ohyama, Y. Sakamoto, K. Ikegami, S. Nakajima, Y. Oikawa, and S. Motonaga: *ibid.*, p. 221; K. Ikegami, S. Nakajima, Y. Oikawa, S. Motonaga, Y. Ishibe, H. Ohyama, and Y. Sakamoto: *ibid.*, p. 223.
- 8) T. Inamura, N. Kishida, H. Saito, and M. Watanabe: Sci. Papers I.P.C.R., 75, 236 (1981).

#### IV-16. Construction of the Sector Magnets for the RIKEN SSC

S. Motonaga, H. Takebe, A. Goto, T. Wada,  
Y. Oikawa, I. Takeshita, Y. Ikegami, J. Abe,\*  
T. Tsukumo,\* H. Saito,\* and T. Sato\*

Fabrication of the sector magnets started in 1981 at the factory of Sumitomo Heavy Industries. The first and the second magnets of the four sectors were completed in March and July 1982, respectively. In April we made measurement on the basic characteristics of the magnetic fields, machining accuracies of the fabrication and other operational properties with one sector magnet excited. Measurement of fields for use in the orbit calculations was carried out with the two sector magnets. Results of the field measurements are presented elsewhere in this report.<sup>1)</sup>

The detailed design study and technical problems on the construction are described in the previous report.<sup>2)</sup> Table 1 lists the characteristics of the sector magnet. The magnetic field of 15.8 kG was achieved with the magneto-motive force of  $1.35 \times 10^5$  ampere-turns and the effective angle of sector magnet obtained from the measurements was found to agree with the designed value of  $50^\circ$  to  $51^\circ$ . Because the magnetic field strength and field profile for the sector magnet depend on the quality of its material, very high homogeneously forged and rolled steel with low carbon content was used for the poles and yokes. Table 2 tabulates the measured characteristics of the steel used. The ratio of cross sectional area of the yoke to that of the pole base is 0.94.

Table 1. Characteristics of SSC Magnet.

Number of sector magnets	4	Maximum magnetic field	15.8 kG
Sector angle	$50^\circ$	Maximum magnetomotive force	$1.38 \times 10^5$ A·T
Gap width	8 cm	Maximum current	1050 A
Height of magnet	5.24 m	Maximum power	480 kW
Total weight	2105 ton	Number of trim coils	29 pairs $\times$ 4
	(526 ton/one sector)	Maximum current	590 A
		Total trim coil power	216 kW

Table 2. Measured characteristics of the low carbon steel (weight percent).

	C	Si	Mn	P	S	Cu	Al
Pole	0.01	0.001	0.08	0.013	0.002	0.01	0.018
	0.01	0.001	0.09	0.011	0.003	0.01	0.036
	0.01	0.001	0.10	0.011	0.002	0.01	0.031
Yoke	0.04	< 0.01	0.31	0.14			
	0.04	< 0.01	0.30	0.10			

\* Sumitomo Heavy Industries, Ltd.

Table 3. Operational characteristics of the coils for sector magnet.

Supplied current (A)	Power consumption (kW)	Temperature of coil ( $^{\circ}\text{C}$ )	Temperature increase of water ( $\Delta^{\circ}\text{C}$ )	Resistance of coil ( $\Omega$ )
500	26.5	26	7	0.105
700	52	33	13	0.107
900	88.5	42	21	0.109
1000	112.5	48	27	0.113
1100	138	55	33	0.114

Pressure drop of the cooling water:  $5 \text{ kg/cm}^2$

Flow rate of the cooling water:  $54 \text{ l/min}$

Specification of the power supplies of coils for SSC Magnets.

	Max. current (A)	Max. Voltage (V)	By pass current (A)	Power (kW)
PS-1	1050	352	—	370
PS-2	1050	133	70	140

Measurement of the fabrication accuracies of the two sector magnets was done by the manufacturer. The obtained accuracies of their fabrication and assembly are as follows:

Gap distance	0.04 mm
Sector angle	0.006 deg
Profile of pole edge	0.13 mm
Parallel setting of trim-coil assembly	1 mm
Flatness of pole face	0.02 mm

The power consumption in the main coils, the flow rate and pressure drop of cooling water, temperature increase of the water, and resistance increase of the coils were found to be of almost the expected values in the design. In Table 3 are listed the operational characteristics of the main coils and specifications of their power supplies. Two types of power supplies (PS-1 and PS-2) will be used. The difference of the magnetic field between the four sector magnets will be adjusted by a bypass control circuit equipped in the PS-2 power supply.

Fabrication and assembly of the trim coils were also successfully completed. Specifications of power supplies for the trim coils were decided on the basis of the measured data of the trim coil fields. Four types of power supplies (types A, B, C, D) totally having 61 control units are required to optimize the field. Total power of all the trim coils' power supplies is estimated 216 kW.<sup>3)</sup>

Structural analysis of the sector magnet was performed with a computer code SAP-V.<sup>4)</sup> Preliminary measurement of the vertical displacement and decrease of the gap width between the magnet poles due to magnetic force was made at several positions along the pole's side edge by the manufacturer.<sup>5)</sup> The result is shown in Fig. 1. Because the difference between values for the two magnets amounts to about  $50 \mu\text{m}$  at most, it will pose no problem on the junction of the magnets with other parts such as the vacuum chamber or the RF resonators. Detailed measurement of these values will be performed when the four sectors will be delivered to our institute.

It was found that the completed sector magnets have good performance in accordance with the design and that they do not require a serious modification. The remaining two sector magnets are currently being manufactured by SHI. The whole sector magnets will be delivered at the end of 1983. The construction of the whole magnet system is scheduled to start at the beginning of 1984.

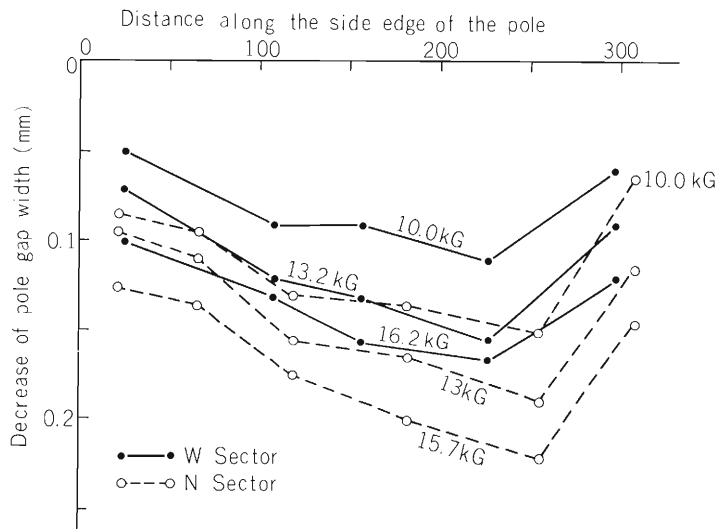


Fig. 1. Decrease ( $\delta$ ) of the pole gap width for the two sector magnets (named by N and W sectors) due to magnetic force measured at several positions along the pole's side edge. Values are given as a difference between the values measured with and without magnetic field. (taken from Ref. 5).

#### References

- 1) S. Motonaga, H. Takebe, A. Goto, T. Wada, J. Fujita, N. Nakanishi, Y. Yano, N. Kishida, I. Yokoyama, I. Takeshita, H. Saito, and T. Sato: p. 186 in this report.
- 2) S. Motonaga, H. Takebe, A. Goto, J. Fujita, T. Wada, Y. Oikawa, I. Takeshita, and Y. Ikegami: RIKEN Accel. Progr. Rep., 15, 162 (1981); Reports I.P.C.R. (in Japanese), 57, 156 (1981).
- 3) A. Goto, H. Takebe, S. Motonaga, Y. Yano, N. Nakanishi, and T. Wada: p. 197 in this report.
- 4) M. Deto, M. Hara, and T. Wada: p. 193 in this report.
- 5) H. Saito, T. Sato, and J. Abe: Proc. 4th Symp. on Accel. Sci. and Tech., p. 299 (1982).

## IV-17. Measurement of the Magnetic Fields of the RIKEN SSC

S. Motonaga, H. Takebe, A. Goto, T. Wada, J. Fujita,  
N. Nakanishi, Y. Yano, N. Kishida, I. Yokoyama,  
I. Takeshita, H. Saito,\* and T. Sato\*

Excitation characteristics and detailed field distributions obtained with the two sector magnets, and the magnetic fields produced by some trim coils were measured at the factory of Sumitomo Heavy Industries (SHI) in April and August 1982.

The magnetic field of 15.5 kG, which is the maximum base field required for the RIKEN SSC, was achieved with the magneto-motive force of  $1.28 \times 10^5$  ampere turns. The excitation characteristics of the sector magnet are shown in Fig. 1. The magnetic field of 15.8 kG was obtained at the magneto-motive force of  $1.35 \times 10^5$  Ampere turns, which is the maximum in the design. The measured values were found to agree well with the calculation.

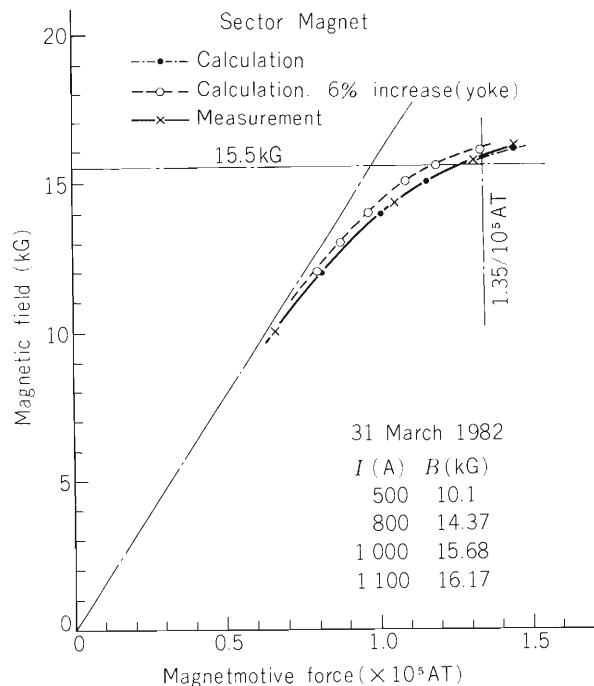


Fig. 1. Excitation characteristics of the sector magnet.

Measurement of map fields for use in the orbit calculations was carried out with the two sector magnets set perpendicular to each other. The measurement was made at base field of 7, 11, 14, 15, and 15.7 kG over the region from  $0^\circ$  to  $45^\circ$  using the computer-controlled magnetic field measuring system.<sup>1)</sup> Typical results of the base field profile along the hill center line are shown in Fig. 2. Figure 3 shows changes of the effective sector angles obtained by the effective boundaries of the magnetic field with one or two magnets. The angle of effective boundary decreases by about  $1^\circ$  in the injection region. This decrease is due to the shape of the sector in

\* Sumitomo Heavy Industries Ltd.

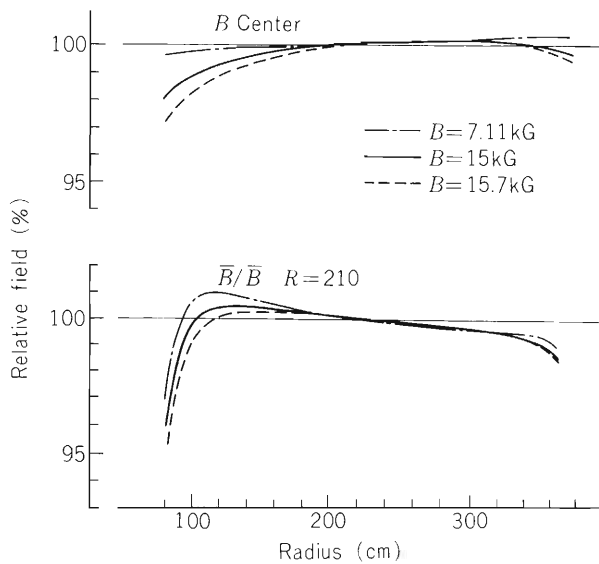


Fig. 2. Radial distributions of the magnetic field normalized to the field value at the radius of 210 cm.

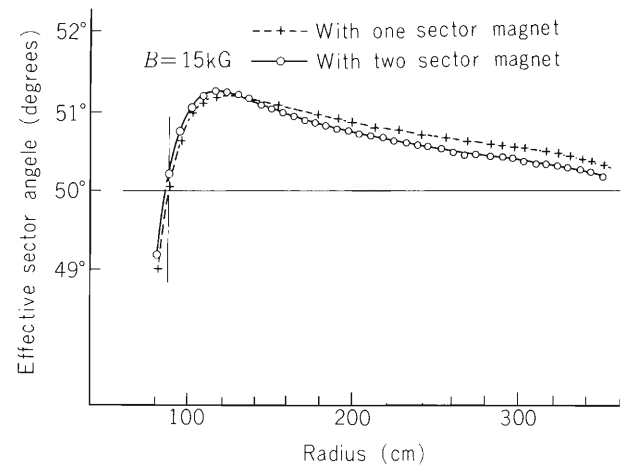


Fig. 3. Change of the sector angles obtained by effective field boundaries along the radius.

this region. These edge fields could be adjusted to correct for such a decrease in the angle of effective boundary with iron shims or central region trim coils. At this stage, however, we decided not to use these iron shims because it was found that the trim-coil currents required in the central region can be kept below a reasonable value (less than about 500 Amps.) if no iron shim are used. Trim coils' fields were measured along the hill center line at the base fields of 7, 11, 14, 15, and 16 kG for appropriately chosen eight trim coils. Optimization of the trim coils' currents for the isochronous field was performed using these fields together with the base fields.<sup>2)</sup>

In order to check the accuracies of the approximations for  $B_r$ ,  $B_\theta$ , and  $B_z$  which are used in the orbit calculation programs, we made measurement on map fields of  $B_r$ ,  $B_\theta$ , and  $B_z$  off the median plane at the base field of 7 and 15 kG. Analysis of these data is now in progress.

The field measurement with the whole magnet system are scheduled to start in the spring of 1984 after the four sector magnets will be delivered to our institute.

## References

- 1) H. Takebe, I. Takeshita, J. Fujita, I. Yokoyama, T. Wada, S. Motonaga, and T. Sato: p. 188 in this report.
- 2) A. Goto, H. Takebe, S. Motonaga, Y. Yano, N. Nakanishi, and T. Wada: p. 197 in this report.

## IV-18. Magnetic Field Measuring System for the RIKEN SSC Sector Magnet

H. Takebe, I. Takeshita, J. Fujita, I. Yokoyama,  
T. Wada, S. Motonaga, and T. Sato\*

A pneumatically driven magnetic field measuring system was designed and constructed. It can cover the area over  $180^\circ$  of the beam orbit plane in the SSC. The magnetic field of the two sector magnets, constructed this summer, was measured by this system.<sup>1)</sup>

Field mapping area necessary for the orbit calculations has different radial range in each azimuthal zone as seen in Fig. 1. Table 1 shows the radial range and steps in each azimuthal zone of  $45^\circ$  mapping area measured in

Table 1. Step and range of measuring area of 'MAP1' program for an orbit calculation. ( $\theta = 0$  means magnet centre line,  $\theta_i$  initial angle,  $R_i$  initial radius, and  $R_f$  final radius.)

Zone	$\theta_i$	$\theta_f$	$\Delta\theta$	Step	$N_\theta$	$R_i$ (mm)	$R_f$ (mm)	$\Delta R$ (mm)	Step (mm)	$N_r$
#6	$0^\circ$	$10^\circ$	$10^\circ$	$1^\circ$	11	810	3810	3000	20	151
#5	$10^\circ$	$18^\circ$	$8^\circ$	$1^\circ$	8	810	3770	2960	20	149
#4	$18^\circ$	$22^\circ$	$4^\circ$	$1^\circ$	4	770	3770	3000	20	151
#3	$22^\circ$	$26^\circ$	$4^\circ$	$.25^\circ$	16	690	3690	3000	20	151
#2	$26^\circ$	$29^\circ$	$3^\circ$	$.5^\circ$	6	690	3690	3000	20	151
#1	$29^\circ$	$45^\circ$	$16^\circ$	$1^\circ$	16	690	3690	3000	20	151

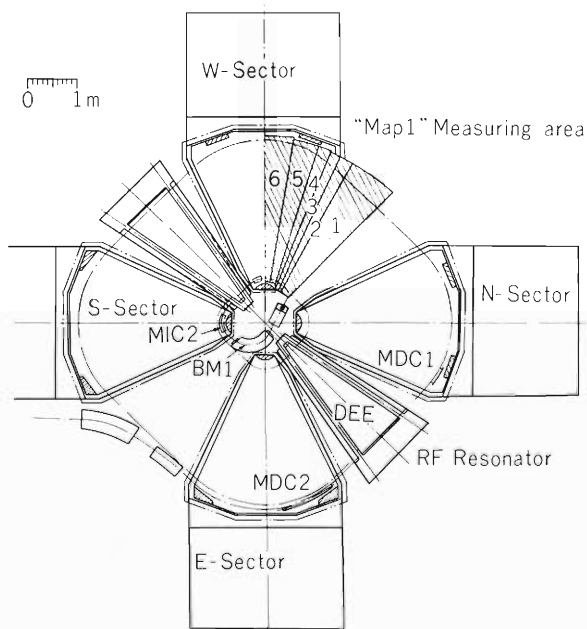


Fig. 1. Sector magnets and the area which were used in the measurement in the summer of 1982 by 'MAP1' program.

Table 2. Actual moving time of the Hall assembly for one step cycle.

Direction	Step	Time
R	5 mm	1 sec
	20 mm	1.6 sec
$\theta$	$0.25^\circ$	2 sec (Hill & Valley)
	$0.25^\circ$	4 sec (Magnet edge)
	$1.0^\circ$	2.5 sec (Hill & Valley)

\* Sumitomo Heavy Industries, Ltd.

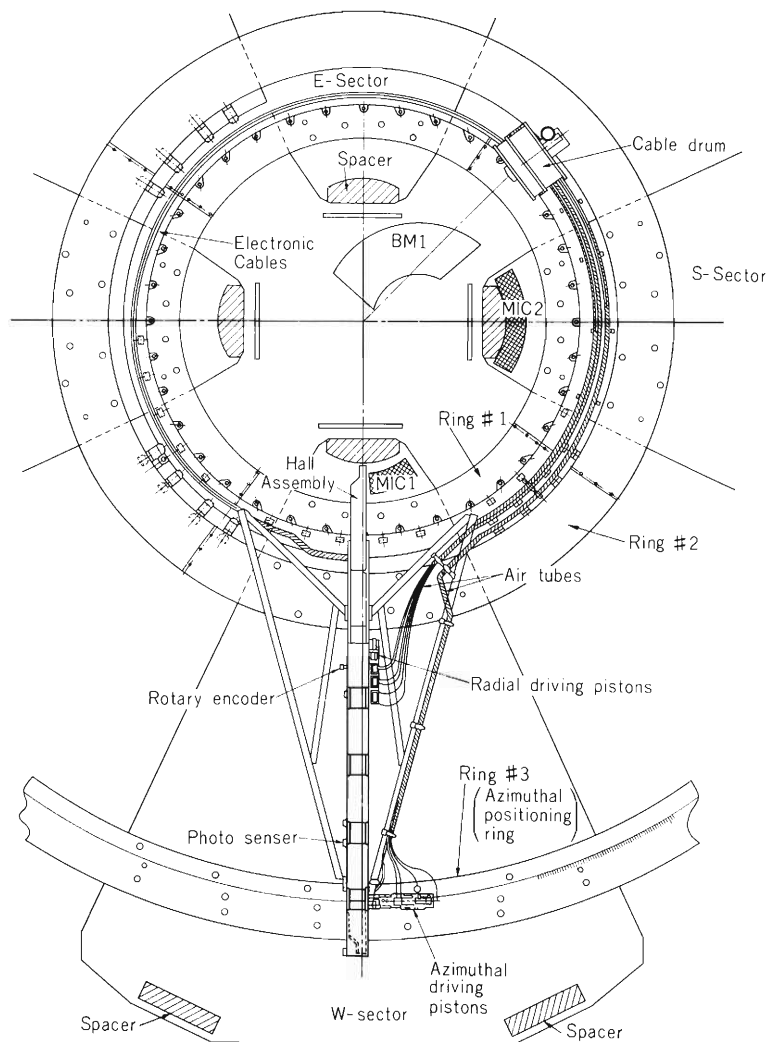


Fig. 2. Plan view of mechanical part of the magnetic field measuring system.

this summer. Hall assembly, which contains magnetic field detectors, has a radial length of 2660 mm. It has to clear gap spacers, and injection and extraction elements. In order to get an accurate positioning of the Hall assembly and to make tension of the rotating assembly small, three pneumatic pistons are equipped to the rotating assembly for each direction (Fig. 2). Two pistons moving 5 mm and 20 mm in the radial direction, and the other two for  $0.25^\circ$  and  $1.0^\circ$  in azimuth are connected in tandem, respectively. The third piston for each direction is used for locking the assembly. Figure 3 shows the radial driving pistons in detail. Moving time of the Hall assembly in the azimuthal direction is different at each position because of the eddy current by a fringing field. Accordingly, in order to determine the timing for the locking piston, the actual position of the driving piston is detected by a potentiometer in each direction. Table 2 shows the actual moving time of the assembly for one step cycle. Two rotary encoders (COPAL: RE-20A) and up-down counters indicate the coarse position of the Hall assembly in order to check the piston error.

The system is controlled by LSI-11 micro computer<sup>2)</sup> (Fig. 4). Twenty sets of Hall probes (SBV-601-s1) are mounted radially in line with pitch of 140 mm on the Hall assembly. Their twenty outputs and other analog signals (current monitors etc.) are led to a relay scanner (FLUKE: 2204A) through thirty pairs of twisted cables (20 m long) and measured by a DVM (8502A). Sampling time of the DVM had to be longer than 250ms/channel because of noisy environment in the big factory.\* Reading error of the DVM was less than  $2 \mu\text{V}$  which corresponds to 0.6 Gauss of field. Hall control currents (200 mA) are connected in series and stabilized with an accuracy better than  $5 \times 10^{-5}$ .

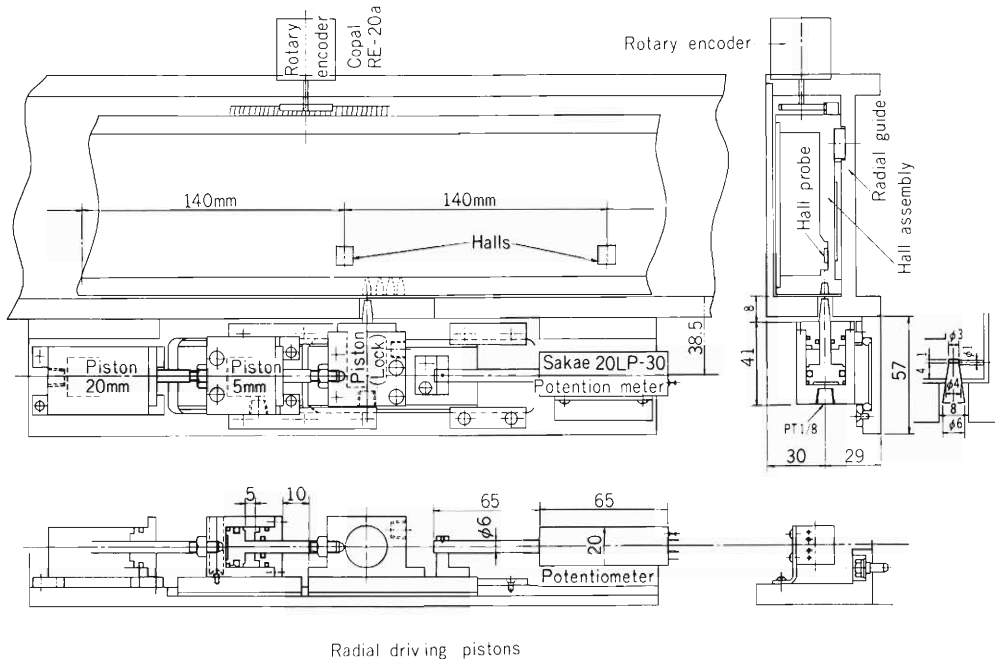


Fig. 3. Details of the piston driving system for radial direction.

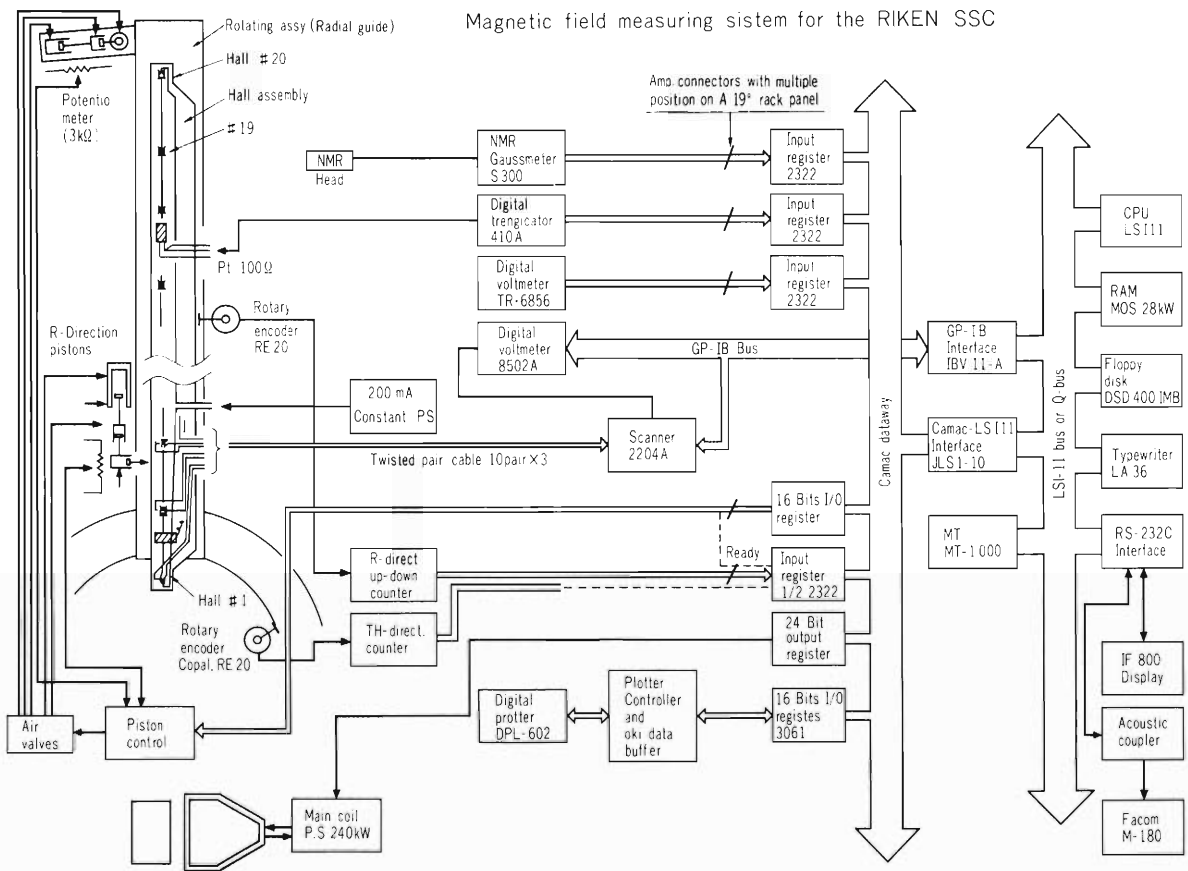


Fig. 4. Schematic diagram of the electrical system.

Most of programs are written in FORTRAN. The subroutines for CAMAC control and colour graphic control are written in MACRO-assembly language. These programs are developed not only in LSI-11 but also in FACOM M-200 large computer.

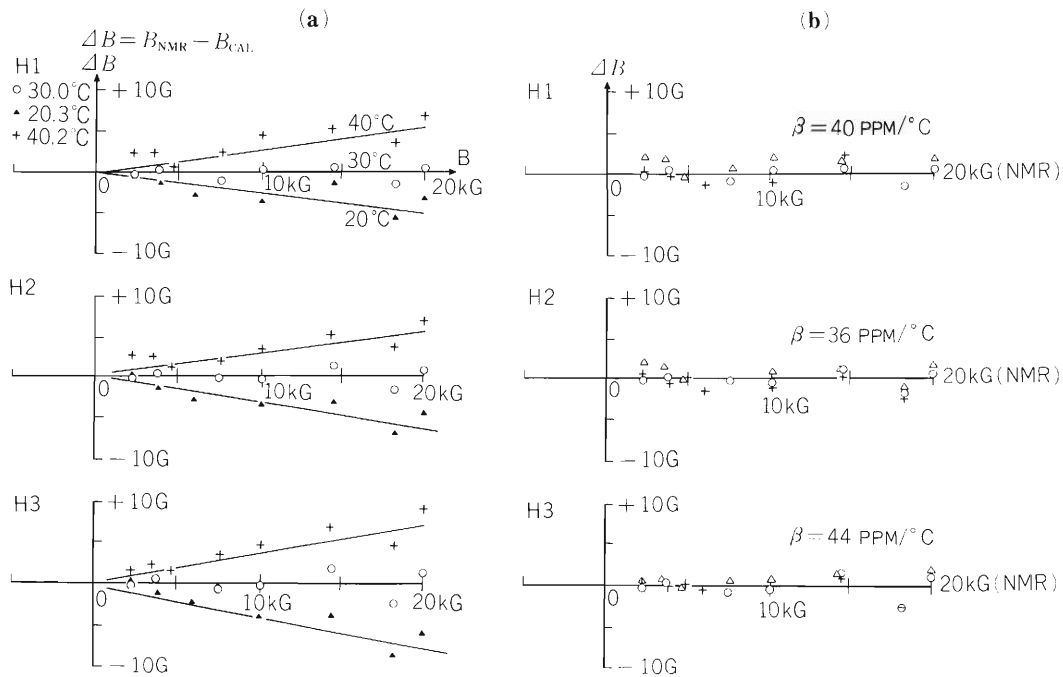


Fig. 5. Fitting errors and temperature dependence of the Hall characteristics by 5th order polynomials for 30° C's data.

Hall calibration polynomials (5th order and one temperature coefficient) were determined for 24 sets of Hall probes previously. Figure 5 (a) shows fitting errors of calculated field in 20° C and 40° C data from the 30° C data's polynomials. Figure 5 (b) shows similar errors but compensated with a temperature coefficient as given by the following equation:

$$B_{\text{cal}} = (A_0 + A_1V + A_2V^2 + A_3V^3 + A_4V^4 + A_5V^5) \times (1 + \beta \times t) ,$$

where  $t$  is the temperature,  $\beta$  the temperature coefficient and  $V$  the Hall output voltage.  $A_0$  was small enough to be neglected (about  $\pm 0.5G$ ).

Figure 6 shows an example of contour lines of the magnetic field obtained from the "MAP1" data. In order to reduce systematic errors caused by a change of the Hall characteristics or by some unknown reasons, each neighbouring Hall probe can measure the same point by moving the assembly 140 mm radially. Figure 7 shows the difference between the calculated fields of the above neighbouring Hall probes at the same point, which are obtained from the "MAP1" data. The difference,  $\Delta B_n$ , is given by

$$\Delta B_n = B_{n+1} - B_n ,$$

where  $B_n$  is the calculated field for the Hall number  $n$ . Field strength at the magnet hill is about 15.7 kG. Large difference ( $\Delta B$ ) can be seen in the fringe field of 10 k – 13 kG, which are caused by a setting error ( $\pm 0.2$  mm) of the probe in the azimuthal direction. These setting errors can be reduced by adjustment of the probes position, instead of the measurement for the center of the Hall probe active area.

Small difference in a flat field of the magnet hill (about 15.7 kG) are used for actual Hall re-calibration factors.<sup>3)</sup>

At the measurement, the magnetic field is calculated using the calibration polynomials and displayed on a digital plotter or a colour graphic unit (OKI: IF-800). The data are recorded in an 8 inch floppy disk, and copied to the magnetic tape to be processed in M-200 large computer.

Total measuring time for 'MAP1's 45° mapping area as that for the Table 1 was two hours and a half. This measuring time will become short in the accelerator room, because of more quiet environment.

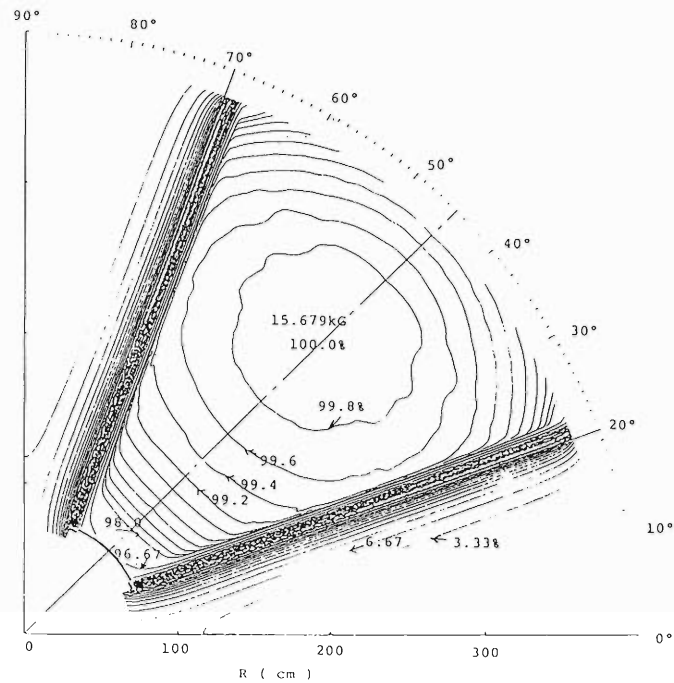


Fig. 6. Contour lines of the magnetic field of 'MAP1' data.

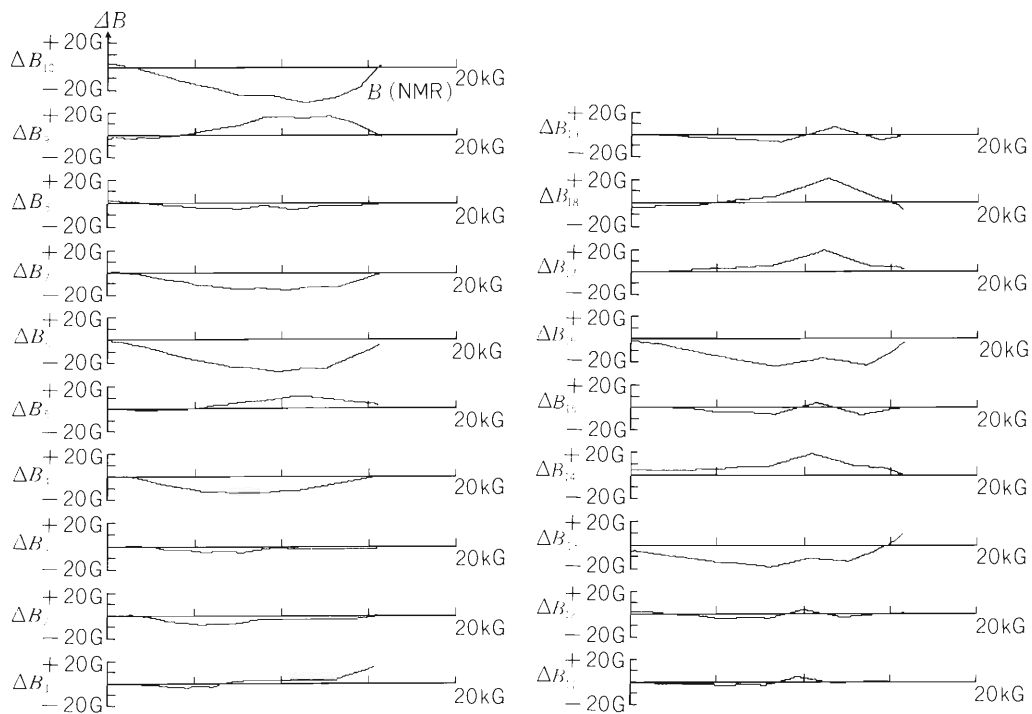


Fig. 7. Differences of the calculated field of two Hall probe outputs measured at the same points. This is obtained by processing of the 'MAP1' data.

#### References

- 1) S. Motonaga, H. Takebe, A. Goto, T. Wada, Y. Oikawa, I. Takeshita, Y. Ikegami, J. Abe, T. Tsukumo, H. Saito, and T. Sato: p. 183 in this report.
- 2) J. Fujita, T. Wada, and H. Takebe: *RIKEN Accel. Progr. Rep.*, **123**, 15 (1981).
- 3) H. Takebe, I. Takeshita, J. Fujita, I. Yokoyama, T. Wada, S. Motonaga, and T. Sato: *Sci. Papers I.P.C.R.*, **77**, 20 (1983).

## IV-19. Structural Analysis of Sector Magnet by Finite Element Method

M. Deto,\* M. Hara, and T. Wada

Results of two dimensional analysis have been reported in previous reports.<sup>1),2)</sup> The analysis by three dimensional code SAP-V<sup>3)</sup> has been done this year. In this analysis we investigated three kinds of structure which are the same as those of the previous reports. To this structure, two supporting feet made of soft iron are installed under the magnet. The nodal points on the floor are fixed in x, y, and z directions. Eight node brick and truss elements are used and total number of elements is now 2656. The magnetic and vacuum forces loaded on the pole face elements are  $9.75 \text{ kg/cm}^2$  and  $1.033 \text{ kg/cm}^2$ , respectively. Figure 1 shows the subdivisions for the three dimensional analysis.

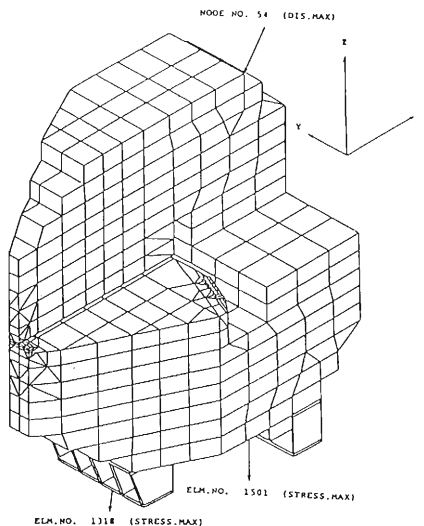


Fig. 1. Subdivisions for three dimensional analysis.

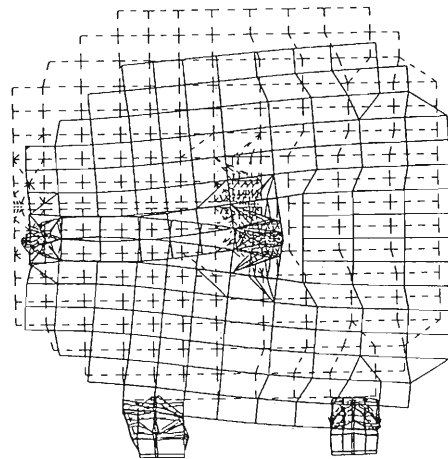


Fig. 2. The calculated deformation of the whole magnet. The solid and broken lines show the shapes before and after deformation. Deformation is exaggerated.

### (1) Static analysis

Figure 2 shows the calculated deformation of the whole magnet seen from y direction. Figure 3 shows the azimuthal and radial distributions of vertical deflections of the upper and lower pole faces. It can be seen that the deflections of the nodal points along the magnet center decrease by about 23 % for both upper and lower poles, if small gaps of 1 mm are provided in the pole bases. From the azimuthal distributions for the upper pole, it can be seen that the deflections decrease by about 10 ~ 64 % by the effect of small gaps, although for the lower pole the effect is not so large.

Comparing these results with those of FEM-II code,<sup>4)</sup> it is found that the deflections are 2 times and 3 times as large as those of the two dimensional analysis for the structures without gaps and with gaps, respectively. The maximum deformation of the supporting feet is  $120 \mu\text{m}$  and the stress is much smaller than the allowed one. The maximum compressive stress of the gap spacer is larger than that of the feet. It is  $13.4 \text{ kg/mm}^2$  but still much smaller than the allowed compressive stress ( $52 \text{ kg/mm}^2$ ) and yield strength ( $21 \text{ kg/mm}^2$ ) of the stainless steel. The value  $13.4 \text{ kg/mm}^2$  agrees quite well with the value  $13.84 \text{ kg/mm}^2$  of FEM-II code.

\* Colleged of Humanities and Science, Nihon University.

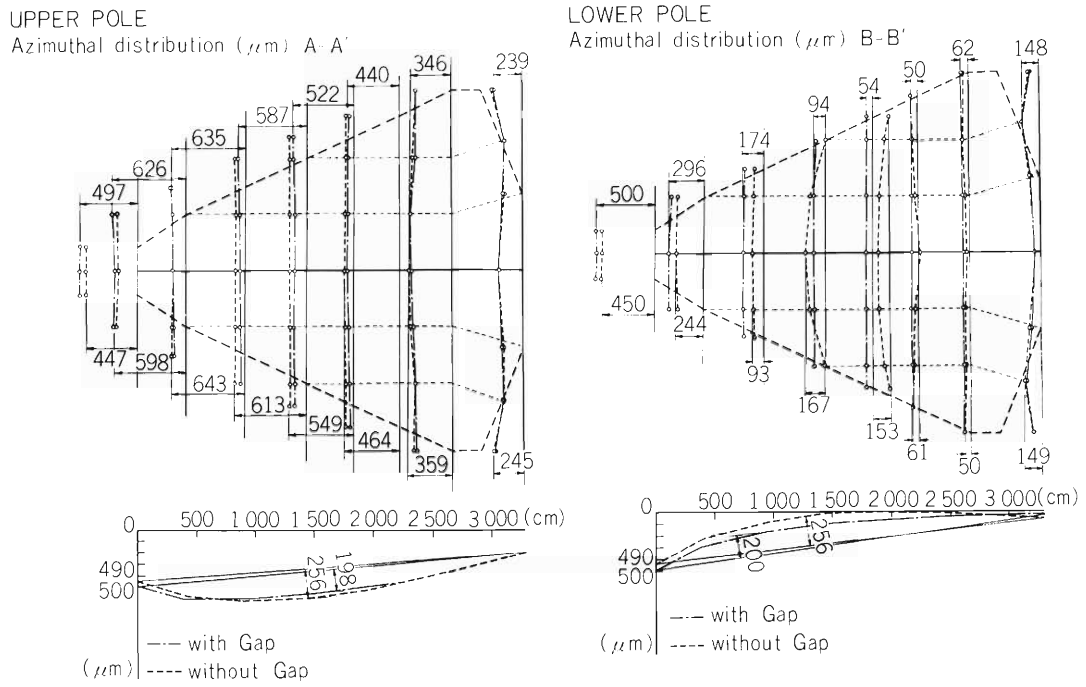


Fig. 3. The azimuthal and radial distributions of vertical deflections of the upper and lower pole faces.

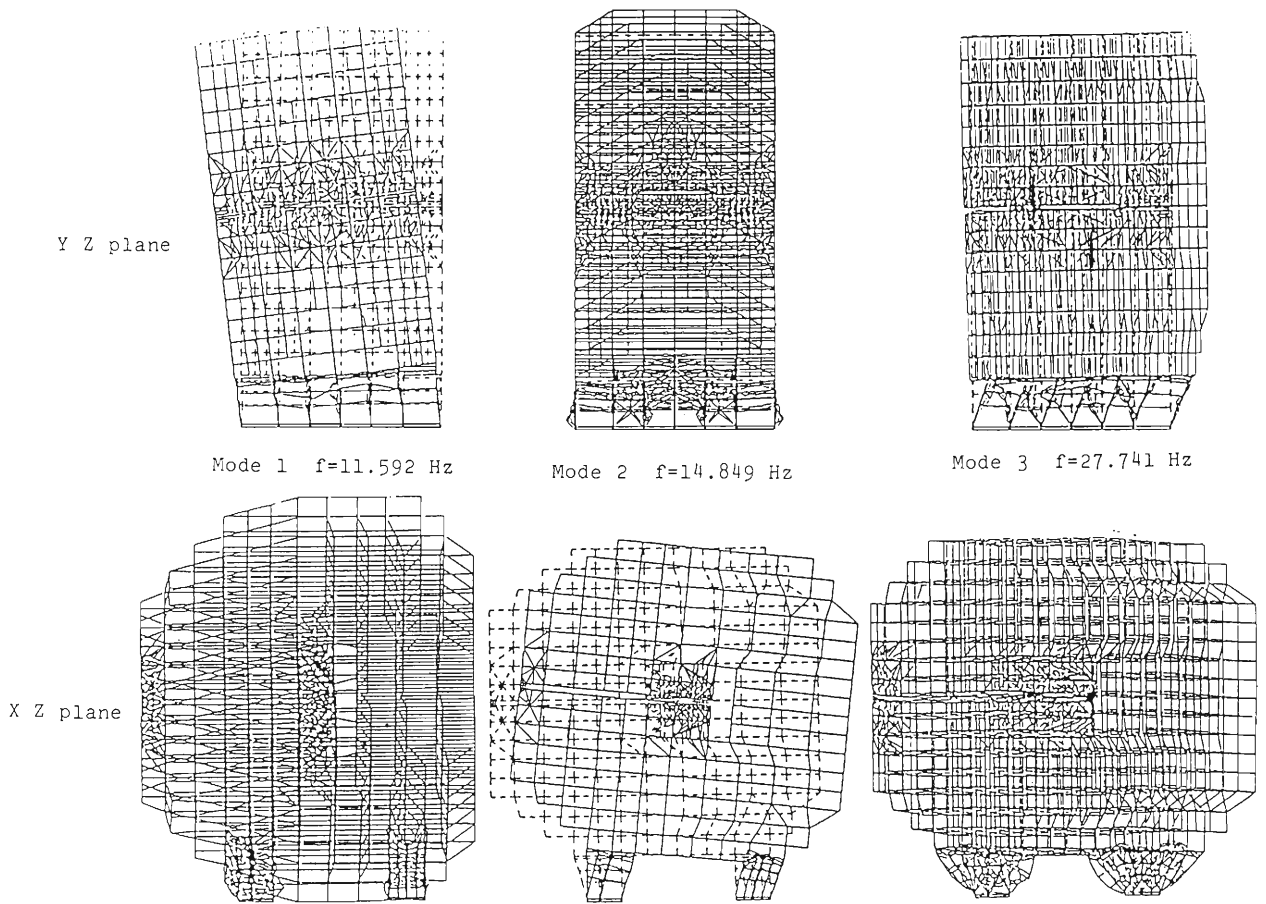


Fig. 4. The oscillations of mode 1 to 3.

## (2) Eigenvalue/eigenvector solution

In dynamic analysis, only solid type elements are used. The number of nodal points and elements are 2407 and 1656, respectively. Table 1 lists the calculated characteristic frequencies of lower 10 modes. Figure 4 shows the oscillations of mode 1 to 3.

## (3) Forced dynamic response by mode superposition

In order to investigate the strength of supporting feet, a forced dynamic response analysis was done using mode superposition method by SAP-V code. The frequencies of lower 5 modes are used. For the input data, used are the numerical data of earthquake in the offing of Miyagi prefecture on 12th of June in 1978.\* The NS and EW components of the earthquake waves are forced in x and y directions, respectively. A damping factor of 0.02 is applied for the magnet. The response histories are calculated for 25 seconds at the time step of 0.002 second. It is found that the displacement is largest at the top of magnet while the stress is largest at the supporting feet. Table 2 shows the histories of displacement for the top of magnet, and Table 3 shows those of stress for each supporting foot. Figure 5 shows the NS component of earthquake waves and response histories of displacement and stress. It can be seen that the supporting feet can withstand the earthquake of this strength. It should be noted that in this dynamic analysis the displacement and stress by static forces are not included.

Table 1. Characteristic frequencies.

Mode	Frequency (Hz)
1	10.2078
2	18.3596
3	24.5187
4	52.3578
5	70.5038
6	70.9365
7	82.1998
8	110.356
9	119.129
10	144.263

Table 2. Displacement maxima.

Mode No.	Displacement component	Maximum value ( $\mu\text{m}$ )	Time at max. (s)
54	x	42.640	13.96
54	y	55.506	14.02

Table 3. Stress maxima.

Elm. No.	Stress component	Maximum value ( $\mu\text{m}$ )	Time at max. (s)
1318	$\sigma_{xx}$	5.289	13.96
	$\sigma_{yy}$	0.838	13.96
	$\sigma_{zz}$	33.331	13.96
	$\sigma_{xy}$	0.029	13.98
	$\sigma_{yz}$	0.367	13.98
	$\sigma_{zx}$	9.473	13.96
1501	$\sigma_{xx}$	3.959	13.96
	$\sigma_{yy}$	0.104	13.96
	$\sigma_{zz}$	2.718	13.96
	$\sigma_{xy}$	0.014	13.96
	$\sigma_{yz}$	0.059	13.96
	$\sigma_{zx}$	1.314	13.96

\* Strong Earthquake Motion Observation Center, Earthquake Research Institute of Tokyo University.

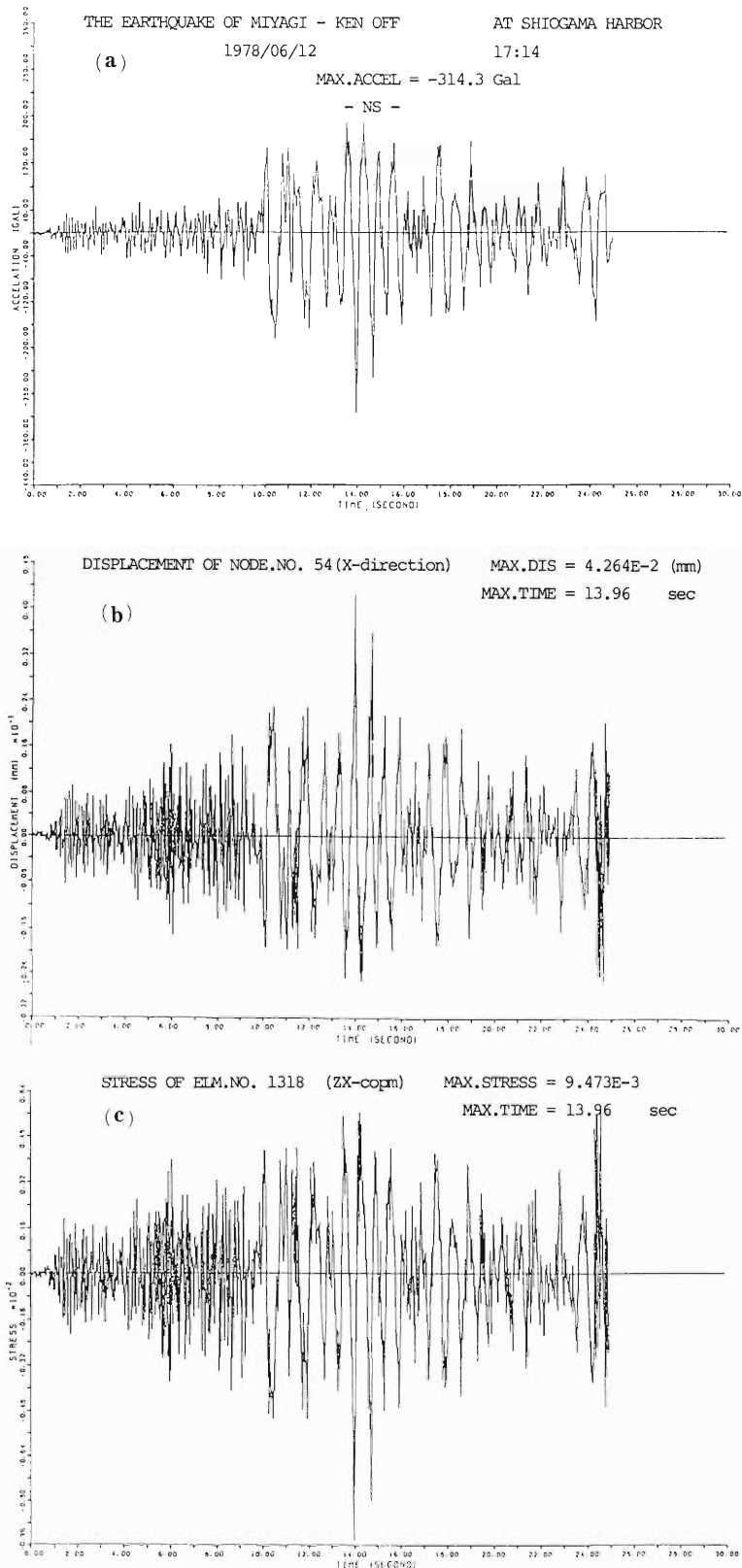


Fig. 5. The time histories of displacement and stress. (a) The NS component of input earthquake wave, (b) The time history of displacement of nodal point number 54, (c) The time history of stress of element number 1318.

#### References

- 1) Y. Ikegami, T. Wada, and M. Hara: RIKEN Accel. Progr. Rep., 15, 166 (1981).
- 2) Y. Ikegami, T. Wada, and M. Hara: Reports I.P.C.R., (in Japanese), 57, 177 (1981).
- 3) K. Bathe, E. L. Wilson, and F. E. Peterson: SAP-V User's Manual, UC Rep. No. EERC, 73-11 (1974).
- 4) H. Togawa: "A Guide to Finite Element Method", (in Japanese), Science Co. Ltd., Tokyo (1979).

## IV-20. Measurement of the Trim Coil Fields and Determination of Trim Coils Power Supplies for the RIKEN SSC

A. Goto, H. Takebe, S. Motonaga, Y. Yano,  
N. Nakanishi, and T. Wada

On the sector magnets of the RIKEN SSC are set 29 pairs of trim coils, the radial positions and widths of which were designed on the basis of model measurements and field calculations.<sup>1)</sup> To determine these parameters, a computer code was used that can optimize currents of the coils with the least-squares fitting method.<sup>1)</sup>

We measured last summer the field distributions of trim coils along the hill center-line of one of the two sector magnets which had been completed by then.<sup>2)</sup> The measurements were made for trim coils No. 3, No. 7, No. 9, No. 14 – 15, No. 18 – 19 (hyphen means that these coils are connected in series), No. 22, No. 26, and No. 28 at five base fields of 7, 11, 14, 15, and 16 kG. A current of each trim coil was set to be 150 and 300 Amps. We did not make measurements in the case of current higher than 300 Amps because of the limitation of the capacity of the present power supply. With respect to the measuring system, see Ref. 3. Figures 1 and 2 show the magnetic field distribution of each trim coil at the base fields of 7 and 16 kG, respectively. The field distribution presents a step-wise profile. It can be seen that the radial field distributions are flat in the case of

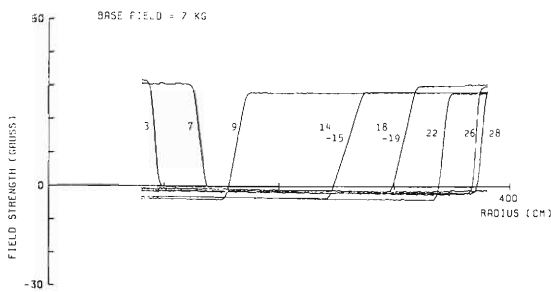


Fig. 1. Magnetic field distribution of each trim coil at a base field of 7 kG. Each trim coil's current is 100 Amps. Note that the returns of trim coils from No. 1 to No. 7 are wound around the nose of the pole.

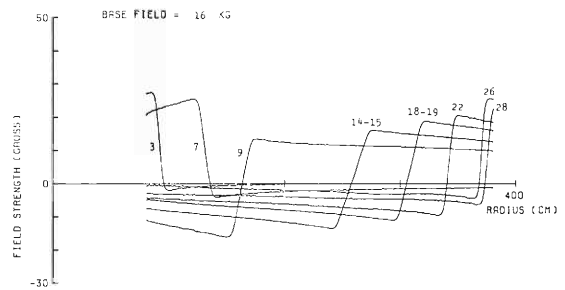


Fig. 2. Magnetic field distribution of each trim coil at a base field of 16 kG. Each trim coil's current is 100 Amps. It can be seen that the distributions of undershoot and overshoot fields decrease radially because of saturation of the yoke.

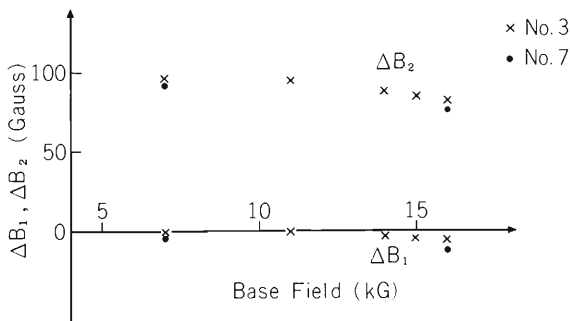


Fig. 3. Variation of the undershoot field ( $\Delta B_1$ ) and overshoot field ( $\Delta B_2$ ) with respect to the strength of base field for the trim coils No. 3 and No. 7. Each trim coil's current is 300 Amps.

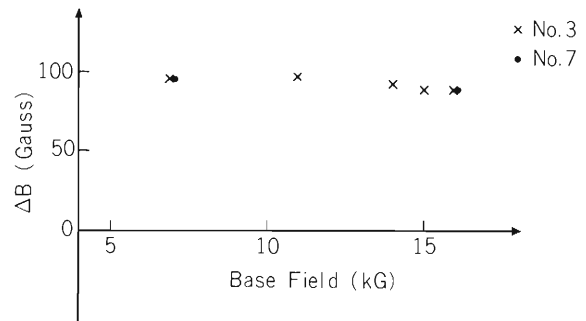


Fig. 4. Variation of the field step height ( $\Delta B = \Delta B_1 + |\Delta B_2|$ ) with respect to the strength of base field for the trim coils No. 3 and No. 7. Each trim coil's current is 300 Amps.

7 kG, but that the field strengths decrease with radius in the case of 16 kG. This difference results from the effect of finite permeability of the return yoke.<sup>4)</sup> The saturation effect can also be seen in the magnitudes of the undershoot and overshoot fields, Figure 3 shows the variation of the maxima of undershoot field ( $\Delta B_1$ ) and overshoot field ( $\Delta B_2$ ) with respect to the base field for trim coils No. 3 and No. 7 whose returns are wound around the nose of the pole. The variation of field step height ( $\Delta B = \Delta B_1 + |\Delta B_2|$ ) is given in Fig. 4. Figures 5 and 6 show the same quantities as in Figs. 3 and 4, respectively, for trim coils whose returns are wound around the back of the pole. Values of  $\Delta B_1$  and  $\Delta B_2$  change beyond the base field of about 11 kG. As can be seen especially in Fig. 5, the larger the area of the pole surface which is surrounded by the trim coil and its return, the more drastically they change. In all cases we have obtained a very good linearity of the field step height to the current. Furthermore, we measured trim coil fields for two cases: in one case all the trim coils were excited at 150 or 300 Amps and in the other all trim coils except one were excited. The trim coil field distributions obtained as the differences of these two measurements were found not to show such a large change from the before-mentioned distributions as was seen on the cyclotron at IUCF.<sup>5)</sup>

The magnetic field distributions of coils other than the eight coils were obtained by interpolating the measured data. We have calculated the optimal trim coils' currents for isochronizations in cases of seventeen typical ions using the above-mentioned program code. In Fig. 7 is shown, as an example, the comparison of the calculated magnetic field distribution formed by the trim coils with the isochronous field for the 135 MeV/u  $C^{6+}$  ion.

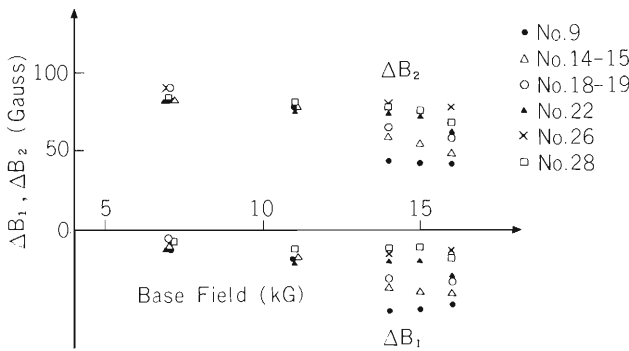


Fig. 5. Variation of the undershoot field ( $\Delta B_1$ ) and overshoot field ( $\Delta B_2$ ) with respect to the strength of base field for the trim coils No. 9, No. 14 - 15, No. 18 - 19, No. 22, No. 26, and No. 28. The values change drastically beyond the base field of about 11 kG.

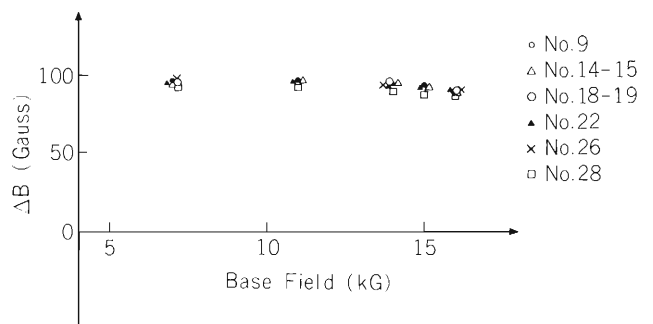


Fig. 6. Variation of the field step height ( $\Delta B = \Delta B_1 + |\Delta B_2|$ ) with respect to the strength of base field for the trim coils No. 9, No. 14 - 15, No. 18 - 19, No. 22, No. 26, and No. 28.

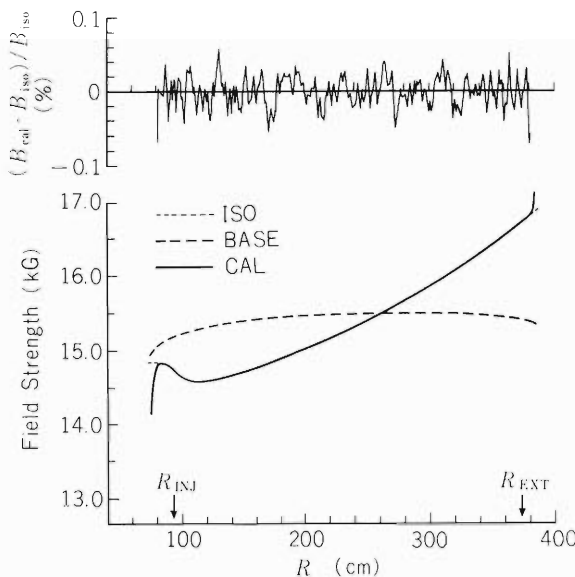


Fig. 7. Comparison of the calculated magnetic field distribution formed by the trim coils with the isochronous field for acceleration of the  $C^{6+}$  ion to 135 MeV/u.

Table I. Maximum and minimum currents of each trim coil for isochronization and resistances of the coils and cables. Coils No. 4, 5, 6, 26, 27, and 28 are also used for harmonic fields.

Coil No.	Power Sup. No.	Resistance of coil (m $\Omega$ )	Current		Sector			
			Min. (A)	Max. (A)	S	W	N	E
					Type Resistance of coil and cables (m $\Omega$ )			
1		7.8	0	0				
2		7.5	0	0				
3	1	7.89	47	399	C2 12.5	C2 9.8	C1 21.4	
4 -H	2	7.6	144	476	D3 12.3	D3 9.6	D3 10.5	D3 13.4
5 H (74A)	3	7.9	-17	404	D3 12.6	D3 9.9	D3 10.8	D3 13.7
6 H (74A)	4	7.8	-82	223	D2 12.5	D2 9.8	D2 10.7	D2 13.6
7	5	7.5	-203	29	B1	B1 41.6	B1	B1
8	6	9.4	-48	297		A1 43.4		
9	7	10.2	50	370		A2 46.6		
10-11	8	15.2	47	471	B3	B3 66.6	B3	B3
12-13	9	14.5	29	481		A4 63.8		
14-15	10	13.9	40	504	B4	B4 61.4	B4	B4
16-17-20-21	11	12.4 + 11.9	9	440		A3 103.0		
18-19	12	12.1	19	486	B3	B3 54.2	B3	B3
22	13	6.4	22	541	B5	B5 31.4	B5	B5
23-24	14	6.7 + 6.6	12	515		A5 58.2		
25	15	6.6	9	380	B2	B2 32.2	B2	B2
26H (400A)	16	7.5	5	176	D2 12.2	D2 9.5	D3 10.4	D3 13.3
27H (400A)	17	7.5	5	176	D2 12.2	D2 9.5	D3 10.4	D3 13.3
28 -H	18	5.9	0	0	D1 15.2	D1 9.9	D2 8.8	D2 11.7
29		5.8	0	0				

In Table 1 are tabulated the maximum and minimum currents for each trim coil obtained by calculations for the seventeen typical ions (6.5 MeV and 9.3 MeV Protons, 9.2 MeV  $H_2^+$ , 28 MeV  $^3He^+$ , 7 MeV  $C^{3+}$ , 48 MeV  $C^{6+}$ , 84 MeV  $C^{6+}$ , 23 MeV  $Ar^{11+}$ , 152 MeV  $Ar^{15+}$ , 49 MeV  $Kr^{17+}$ , 180 MeV  $Kr^{24+}$ , 77 MeV  $Xe^{23+}$ , 115 MeV  $Xe^{30+}$ , 121 MeV  $Pb^{30+}$ , 181 MeV  $Pb^{36+}$ , 138 MeV  $U^{33+}$ , and 200 MeV  $U^{40+}$ ). Trim coils No. 1, 2, 28, and 29 are not used for the isochronization but for compensation of fields around the injection or extraction elements. Trim coils No. 4, 5, and 6 and trim coils No. 26, 27, and 28 are used for harmonic field excitations or compensation of their undershoots in the injection and extraction region, respectively. Field deviation from the isochronous field was found not to become larger in spite of serial connections of the coils No. 10 - 11, 12 - 13, 14 - 15, 16 - 17 - 20 - 21, 18 - 19, 23 - 24. Trim coils No. 8, 9, 12 - 13, 16 - 17 - 20 - 21, and 23 - 24 are respectively

connected in series through four sectors. These coils are excited with power supplies named type A. Currents of trim coils No. 7, 10–11, 14–15, 18–19, 22, and 25 are adjusted for each sector magnet by a bypass control circuit<sup>1)</sup> with power supplies of type B. Each of the coils other than these is excited independently for each sector magnet using power supplies of types C and D. Total resistance of each trim coil and its connection cables are also listed in this table.

Voltage and current specifications of the trim coil power supplies were thus decided and are listed in Table 2. Each of power supplies of types A<sub>1</sub>, B<sub>1</sub>, and D has a polarity switch. The total power of all the trim coil power supplies is estimated to be about 216 kW.

Table 2. Voltage and current specifications and types of the trim coil power supplies. The '+-' sign means that the power supply has a polarity switch.

Type	I(Max.) (A)	I(Max.) (A)	Pol.	V(Max.) (V)	R(Coil + Cables) (mΩ)	Branch I(Bypass)		Sets	Total power (kW)
A1	330	0.25	+ -	14.3	43.4			1	4.7
A2	410	40.0		19.1	46.6			1	7.8
A3	490	1.0		50.5	103.0			1	24.7
A4	530	15.0		33.8	63.8			1	17.9
A5	560	1.0		32.6	58.2			1	18.3
B1	230	5.0	+ -	9.6	41.6	4	+--15	1	2.2
B2	420	50.0		13.5	32.2	4	-50	1	5.7
B3	530	50.0		61.0	115.0	8	-50	1	32.3
B4	550	40.0		33.8	61.4	4	-40	1	18.6
B5	590	50.0		18.5	31.4	4	-50	1	10.9
C1	450	1.0		9.63	21.4			1	4.3
C2-1	500	1.0		4.9	9.8			1	5.6
C2-2	500	1.0		6.3	12.5			1	
D1-1	250	0.5	+ -	2.5	9.9			1	1.6
D1-2	250	0.5	+ -	3.8	15.2			1	
D2-1	400	0.5	+ -	3.92	9.5, 9.5, 8.8, 9.8			4	18.6
D2-2	400	0.5	+ -	4.68	10.7, 11.7			2	
D2-3	400	0.5	+ -	5.0	12.2, 12.2, 12.5			3	
D2-4	400	0.5	+ -	5.44	13.6			1	
D3-1	550	0.5	+ -	5.45	9.6, 9.9			2	42.7
D3-2	550	0.5	+ -	5.94	10.4 × 2, 10.5, 10.8			4	
D3-3	550	0.5	+ -	7.54	12.6, 12.3 13.3 × 2, 13.4, 13.7			6	
Total									215.9 kW

## References

- 1) H. Takebe, A. Goto, S. Motonaga, T. Wada, Y. Oikawa, and I. Takeshita: RIKEN Accel. Progr. Rep., 15, 173 (1981).
- 2) S. Motonaga, H. Takebe, A. Goto, T. Wada, J. Fujita, N. Nakanishi, Y. Yano, N. Kishida, I. Yokoyama, I. Takeshita, H. Saito, and T. Sato: p. 186 in this report.
- 3) H. Takebe, I. Takeshita, J. Fujita, I. Yokoyama, T. Wada, S. Motonaga, and T. Sato: p. 188 in this report.
- 4) E.D. Hudson, J.A. Martin, M.L. Mallory, F.E. McDaniel, and F. Irwin: Proc. 7th Int. Conf. on Cyclotrons and their Applications, p. 201 (1975).
- 5) D.L. Friesel and R.E. Pollock: IEEE Trans. on Nucl. Sci., NS-22, 1981 (1975).

## IV-21. Beam Extraction System for the RIKEN SSC (II)

### Design Calculation of Magnetic Deflection Channel

N. Kishida and Y. Yano

The beam extraction system for the RIKEN SSC was previously reported.<sup>1)-3)</sup> This system consists of an electrostatic deflection channel, two magnetic deflection channels (MDC1 and MDC2) and two uniform-field bending magnets. Required characteristics of each element are tabulated in Ref. 1. The present report describes the calculated results of the magnetic field distribution by the designed MDC systems.

Requirements for the magnetic channels are quite severe:

- (1) MDC1 and MDC2 must reduce the magnetic field of sector magnets by 0.05 T and 0.17 T, respectively, for the case of extracting  $^{12}\text{C}^{6+}$  ions at 135 MeV/u (this corresponds to the extreme case);
- (2) While reducing the field for the deflected beam, the channels must not unduly disturb the circulating beam about 5 cm away from the deflected beam, that is, harmonic fields in this region must be small;
- (3) As for our variable energy SSC, the channels must be capable of producing a wide range of magnetic field reduction;
- (4) Because of space limitations the current density of coils is usually very high. On the other hand, from the point of view of the cooling problems, it is required to hold the density below 50 A/mm<sup>2</sup>.

We have three possible ways to construct the channels that satisfy the above requirements:

- (1) by a septum coil inserted in the magnet;
- (2) by iron plates inserted in the pole gap of the magnet;
- (3) by a combination of coils and iron plates.

A pure iron-plate channel is more attractive than a current septum channel from the economical point of view. But it is impossible to adjust the field reduction without changing the thickness of iron plate. We cannot, therefore, adopt this type of MDC system, so that we have studied the magnetic field distributions of the other two channels by model calculations using the magnetostatic field calculation program TRIM.<sup>4)</sup>

Design of the MDC systems was performed using the least-squares method similar to Ref. 5 in such a way as to minimize field disturbance outside the channel and make the field distribution uniform inside under some constrained conditions (eg. upper and lower limits of current density and series connection between some coils). For this purpose, we developed a computer program MDCFIT which was coded using a sequential unconstrained minimization technique. We assumed in this calculation that the finally obtained field will be produced by superposing the magnetic field of current cells upon the magnetic field by the sector magnet (the base field). The base field was obtained by the calculation using the sector magnet with the cross sectional form which we require so as to reproduce the excitation curve and the radial field distribution of the 1/3 scale model magnet. The magnetic field generated by each current cell (output field) was obtained by subtracting the base field from the magnetic field which was calculated with a current cell inserted in a pole gap of the sector magnet.

The actual field calculation was carried out only for the case of extracting  $^{12}\text{C}^{6+}$  ions at 135 MeV/u with the base field of 1.675 T. The output field strength was found to be completely proportional to the current value up to 2500 A. Figure 1 shows a typical example of the output field of a pair of current cell and proves the correctness of the above statement. By means of a combination of the current cells, we compensate the overshoot output field outside the channel as much as possible within the distance of 6 cm from the deflected orbit (D.O.) without affecting the last accelerating orbit (L.A.O.) and not to make harmonic fields.

Figure 2 shows a cross section of designed MDC1. We placed the current cells not on the median plane but shifted it in order to increase the field uniformity inside MDC1, so that the required current became large in comparison with that for the configuration in which the cell installed in contact with the median plane. Figure 3 shows the field distribution near MDC1 for the best fit to optimize the field uniformity and disturbance. The undershoot field is found to be almost zero (0.01 mT). This combination of the coil currents requires four power

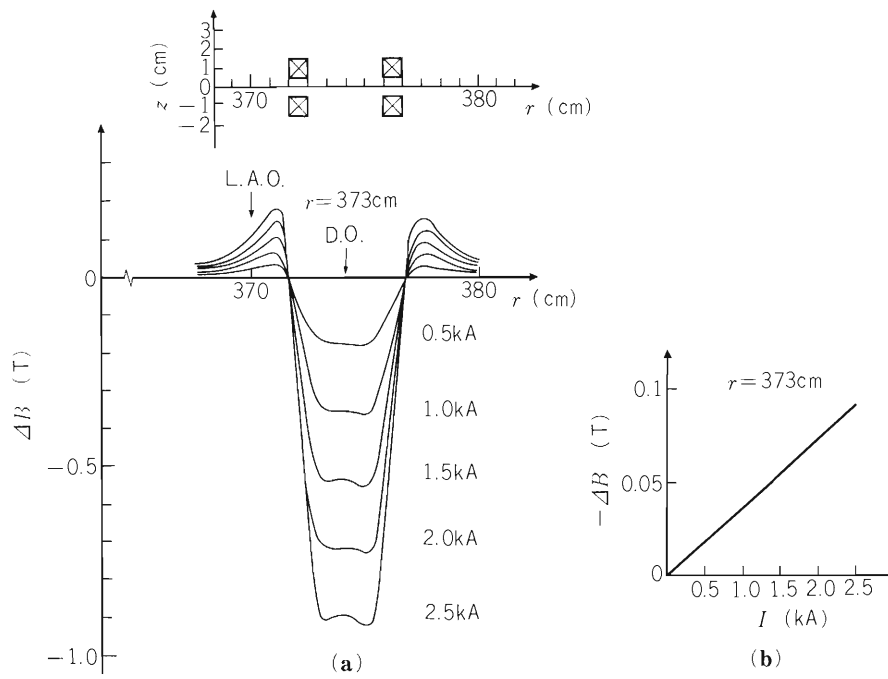


Fig. 1 (a) Typical field distributions produced by current cells with the configuration which is shown in the upper part of this figure.  
 (b) Relation between the current and the output field.

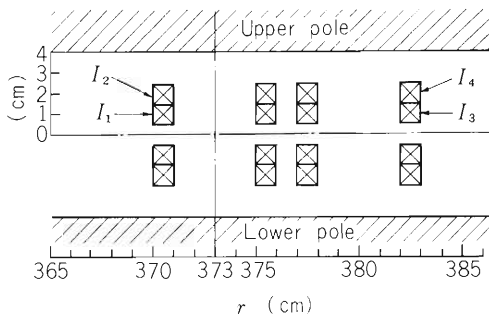


Fig. 2. Schematic drawing of MDC1.  $r$  denotes the radial distance from the center of the SSC.  $I_3$  and  $I_4$  indicate the currents that flow through respective compensation coils.

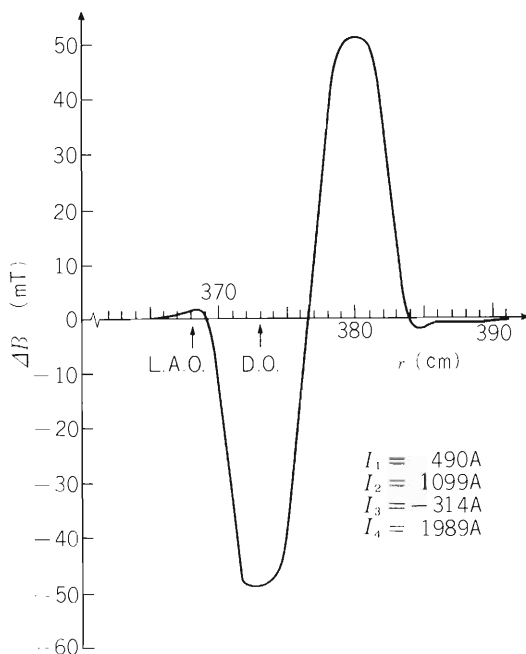


Fig. 3. Magnetic field distribution produced by MDC1 at  $B_{base} = 1.675$  T.

supplies, which leads to a rise in production cost. In order to avoid it, we, therefore, searched another solutions that generate almost the same field distribution as that of the best combination using only two independent current. Those were found to be  $I_1 = I_3 = 471$  A and  $I_2 = I_4 = 1104$  A. We will adopt the latter combination in practical operation.

If we insert a channel with two sheets of iron plate in the pole gap of the magnet which is installed perpendicularly to the magnet pole face in such a way that the deflected beam is surrounded by the plates on both sides, the magnetic field inside the channel is reduced to some extent in proportion to the thickness. If the field reduction required by MDC2 must be realized by the same cross sectional structure as MDC1, the current density exceeds the upper limit ( $50$  A/mm<sup>2</sup>). Consequently we decided to adopt MDC2 that consists of current cells and iron plates. The thickness of iron plates was selected so that the reduced field may take the value which lies nearly at the middle of the variable range of MDC2.

Figure 4 shows a cross section of designed MDC2. The thickness of the plate is  $0.25$  cm. The plate decreases the base field by about  $0.06$  T inside the channel and produces an undershoot field of about  $0.003$  T outside. This undershoot cancels out the overshoot field generated by the current cell in this case, so that any compensation coil is not needed. But we adopt it to eliminate an undershoot field that may be produced in the case of extracting other ions. The current cells were installed in contact with the median plane for the purpose of decreasing the power consumption. Figure 5 shows the field distribution generated by MDC2 in its neighborhood. The field inhomogeneity is a little larger than that of MDC1.

We tried to calculate the influence on phase-space ellipses for the beam caused by the field inhomogeneity due to the MDC systems. We expanded the magnetic field inside MDC on the median plane along the central ray as follows:

$$B(x) = B(O) \left\{ 1 + \epsilon(1)x + \epsilon(2)x^2 \right\} ,$$

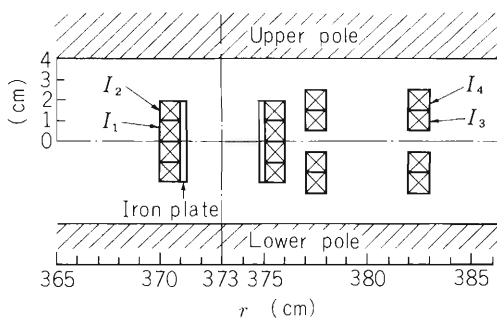


Fig. 4. Schematic drawing of MDC2. The width of iron plate is  $0.25$  cm.

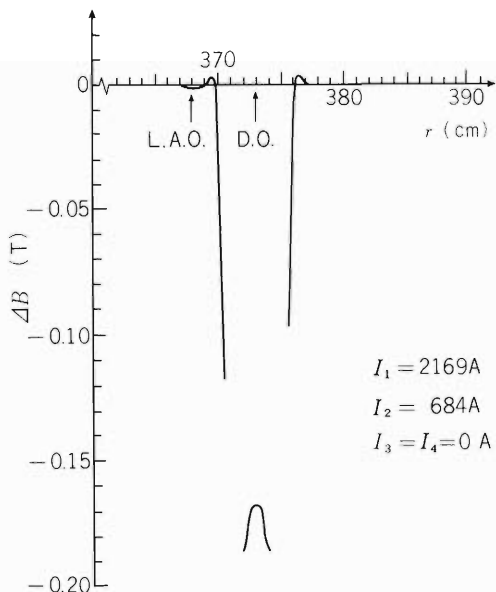


Fig. 5. Magnetic field distribution produced by MDC2 at  $B_{base} = 1.675$  T. The cut-off parts of field distribution correspond to the position at which the iron plates are installed.

Table 1. Field expansion coefficient of MDC1 and MDC2.

	$\epsilon(1) (\text{cm}^{-1})$	$\epsilon(2) (\text{cm}^{-2})$
MDC1	$-4.84 \times 10^{-4}$	$4.59 \times 10^{-4}$
MDC2	$-2.06 \times 10^{-4}$	$-1.26 \times 10^{-2}$

where  $x$  denotes the horizontal displacement from the central ray and  $\epsilon(1)$  and  $\epsilon(2)$  denote field expansion coefficients of quadrupole and sextupole terms, respectively. The expansion coefficients of MDC are listed on Table 1. The increase of phase-space area after passing through the beam extraction system was calculated using these values with the aid of a program TRANSPORT.<sup>6)</sup> As the result, it was found that the area of phase-space ellipses increased by about 20 % in both horizontal and vertical phase spaces. This comes from large value of  $\epsilon(2)$  of MDC2. As we cannot allow it, we have now to design another type of MDC2.

#### References

- 1) Y. Yano, N. Kishida, H. Takebe, A. Goto, T. Wada, and S. Motonaga: Proc. 9th Int. Conf. on Cyclotrons and Applications, Caen, France, p. 473 (1981).
- 2) A. Goto, Y. Yano, N. Kishida, and T. Wada: *ibid.*, p. 439.
- 3) N. Kishida, A. Goto, and Y. Yano: RIKEN Accel. Progr. Rep., 15, 183 (1981)
- 4) J. S. Colonias and J. H. Porst: Magnet Design Applications of the Magnetostatic Problem called, TRIM, UCRL-16382 (1965).
- 5) H. Braun: Proc. Int. Conf. on Magnet Technology, Hanburg, Germany, p. 1620 (1970).
- 6) K. L. Brawn, F. Rothacker, D.C. Carey, and Ch. Iselin: SLAC Report, No. 91, Rev. 1 (1974).

## IV -22. Vacuum System of the SSC

S. Nakajima, K. Ikegami, Y. Oikawa, and I. Takeshita

The vacuum chamber of the RIKEN SSC is divided into eight parts, namely, four magnet chambers, two valley chambers and two RF resonators. Details of the vacuum chamber as well as pumping system are described in a previous report.<sup>1)</sup>

Recently a decision was made to adopt a new type of RF resonator with a movable box to change the frequency<sup>2)</sup> and accordingly the design of the resonator chambers was modified.

The vacuum enclosure of the RF resonator is made of stainless steel and its inner surface is clad by copper plate of about 7 mm in thickness. The RF resonators are anticipated to have large gas load and cannot be evacuated by the pumps equipped at the valley chambers, because the magnet chambers form low-conductance passages of gas between the RF resonators and the valley vacuum chambers. It is necessary to add pumps for the RF resonators. A turbo-molecular pump having a pumping speed of 5000  $\ell$ /sec for air and cryo-genic pumps having a total pumping speed of 30000  $\ell$ /sec for air are mounted on the back side of each RF resonator.

A partition wall having 20 rectangular holes each of 20 mm in width and 1000 mm in height is fixed in front of the cryo-genic pumps in order to shield them from the thermal radiation caused by the strayed RF electric field. The partition is 30 mm in thickness, about 2700 mm in

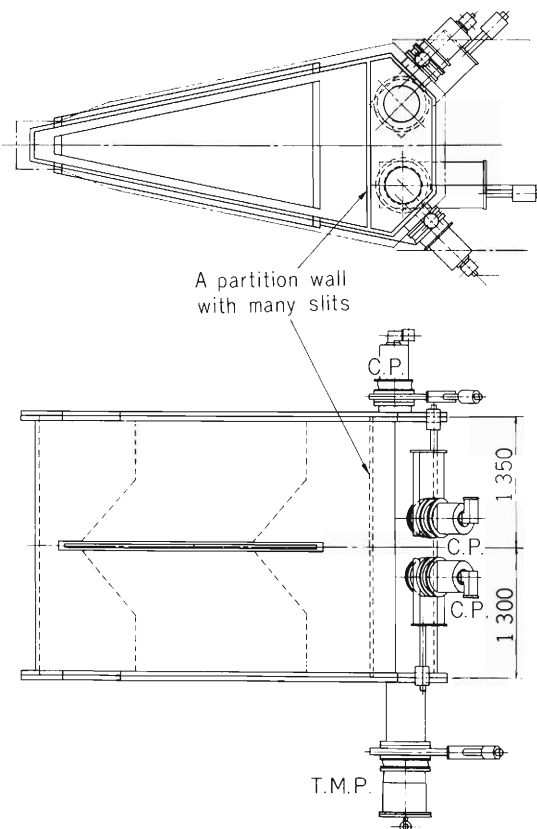


Fig. 1. Schematic view of the resonator enclosure.

height, and about 1720 mm in width. It is made of stainless steel clad by copper. The space where the RF electric field is generated is evacuated through the rectangular holes in the partition wall with the pumps located on the back side of the resonator.

The total height of the resonator is 2700 mm. The valley vacuum chambers were enlarged in height from 600 mm to 900 mm. Figure 1 shows the revised RF resonator with vacuum pumps. The moving boxes are not drawn in the figure. Figure 2 shows the plan view of the whole vacuum chamber. Volume and surface area of the chamber are as follows:

Volume:

Magnet vacuum chambers	~ 1.8 m <sup>3</sup>
Valley vacuum chambers	~ 5.4
Resonator vacuum chambers	~ 22.8
Total	~ 30 m <sup>3</sup> ;

Surface area exposed to vacuum:

Magnet vacuum chambers	~ 80 m <sup>2</sup>
Valley vacuum chambers	~ 26
Resonator vacuum chambers	~ 236
Elastomer O rings	~ 3
Total	~ 350 m <sup>2</sup>

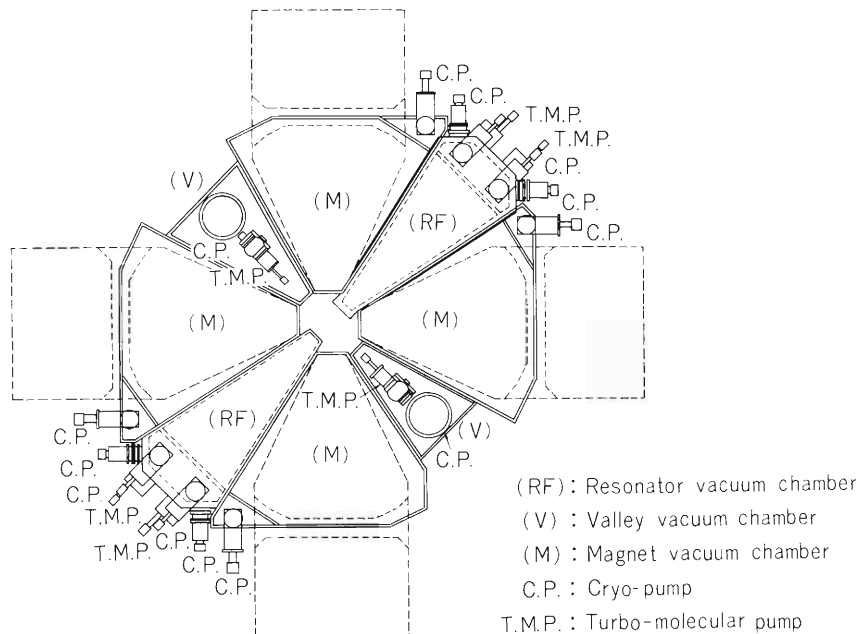


Fig. 2. Plan view of the whole acceleration chamber.

## References

- 1) K. Ikegami, S. Nakajima, Y. Oikawa, and I. Takeshita: RIKEN Accel. Progr. Rep., 15, 200 (1981).
- 2) T. Fujisawa: *ibid.*, p. 196.

IV -23. Test of Model Pneumatic Expansion Seal

K. Ikegami, S. Nakajima, Y. Oikawa, and M. Hara

A pneumatic expansion seal is to be used between each vacuum chamber section of the SSC. Three 1/3 scale models of the seal were constructed and tested to investigate the performance. Using a finite element method, the structural analysis of the seal was done.

In the previous test, a single O-ring of diameter 10 mm was put between two flanges, and the compression force of about 11 kg/cm was applied to the O-ring by the pneumatic seal.<sup>1)</sup> The deformation ratio of the O-ring was 15 %. No leakage was detected in the expansion of about 20 mm. We consider that squeezing force on O-ring of more than 10 kg/cm is needed to keep vacuum-tightness.

In order to investigate the optimum applying pressure, relation between expansion length and applied pressure to the seal was measured. The stress of the seal was measured with a strain gauge. The gap between the two flanges was fixed to be about 14 mm between each vacuum chamber. Pressure sensors whose thickness and diameter are 0.6 mm and 6 mm, respectively, were put between the O-ring and the flanges. Forces squeezing the O-ring were measured with them. Figure 1 shows the distributions of seal expansion and the squeezing force, in the case where the width and the thickness of seal are 100 mm and 1.0 mm, respectively. When the pressure of 1.0 kg/cm<sup>2</sup> was applied to the seal, the squeezing force at the straight section was about 10 kg/cm in the case of A type seal (W = 100, T = 1.0), and 12 kg/cm in the case of B type seal (W = 120, T = 1.0). The squeezing force at the circular section was, in both cases, half compared with that of the straight section. Figure 2 shows the relation between the squeezing force and applied pressure.

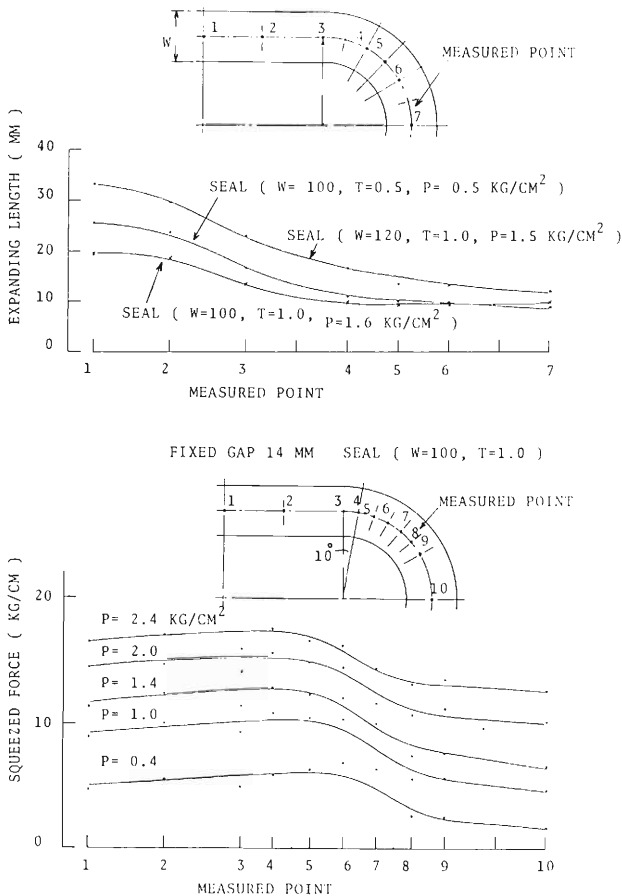


Fig. 1. Expansion distribution and squeezing force distribution for A type (W = 100, T = 1.0) seals.

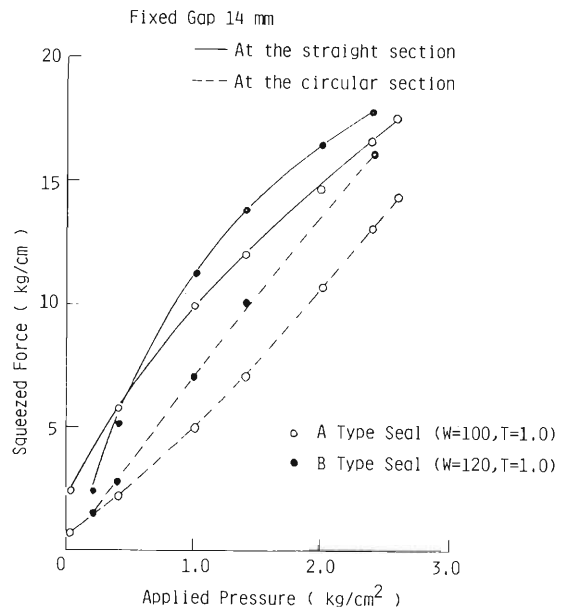


Fig. 2. Relation between the force squeezing O-ring and applied pressure.

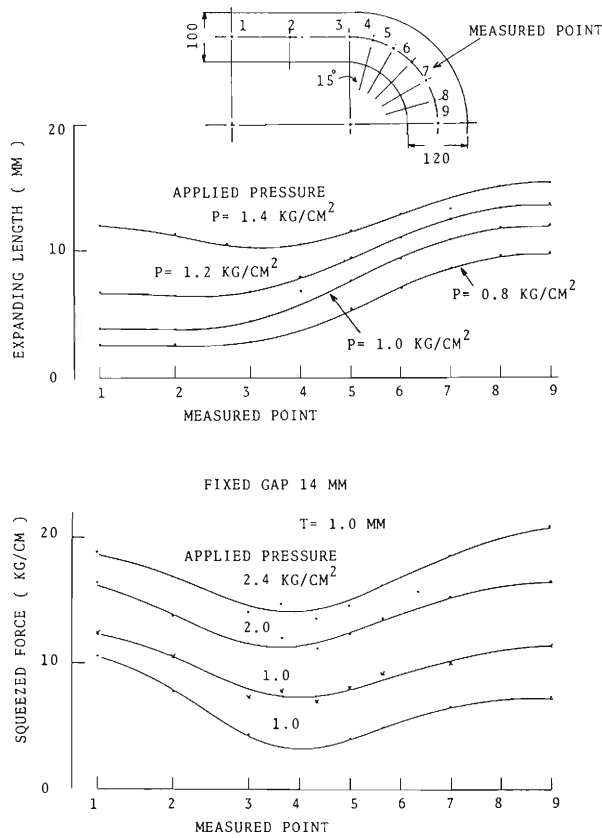


Fig. 3. Distributions of the expansion and the force squeezing O-ring for the improved pneumatic expansion seal. Filled circles: the measured value while applied pressure increased gradually. Crosses: the measured value while applied pressure decreased gradually till 1 kg/cm<sup>2</sup>.

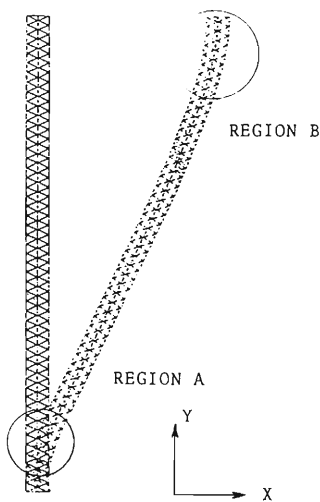


Fig. 4. Calculated deformation of the A type seal ( $W = 100, T = 1.0$ ). A quarter of the cross-section is shown. The length in X direction only is exaggerated by scale factor 2.5.

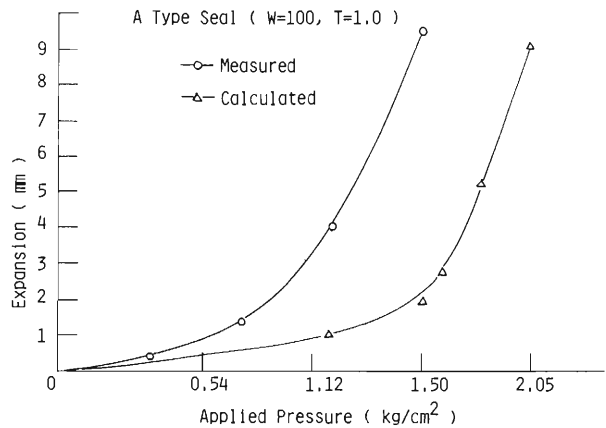


Fig. 5. Comparison of the calculated and the measured expansion of the seal.

A model which has different widths in straight and circular sections was constructed and tested. This seal has improved characteristics of the expansion distribution. Figure 3 shows distribution of the expansion and squeezing force of the improved pneumatic expansion seal.

When the pressure was applied to the seal, the seal was deformed non-elastically if the force is stronger than the substance's elasticity limit. Using the finite element method, the elastic and plastic analysis (EPIC) of the seal was done two dimensionally. Figure 4 shows a quarter of the cross-section of the seal whose deformation was calculated using the finite element method. When the pressure applied to the seal was increased gradually, only the region A of the seal was deformed beyond the yielding point of the stainless-steel at first, and then the region B also was deformed beyond the yielding point. A relation between the expansion of the seal and the applied pressure was measured for a seal whose width and thickness are 100 mm and 1.0 mm, respectively. Figure 5 shows the results together with that calculated by EPIC code. The magnitude of expansion calculated by EPIC is small compared with the measured value. The reason seems that the force generated by the applied pressure to the seal exceeds the yielding point stress of the welding region. The detailed analysis of the seal is in progress with the finite element method.

#### Reference

- 1) C. J. van Lamp: NAC/AR/80-01 Annual Rep., p. 105 (1978).

#### IV-24. Preliminary Experiment on the Surface Cleaning of the Vacuum Chamber for the RIKEN SSC

Y. Ishibe, H. Oyama, Y. Sakamoto, K. Ikegami,  
S. Nakajima, Y. Oikawa, and S. Motonaga

The inner surface area of designed SSC vacuum chamber is approximately 350 m<sup>2</sup>. In order to achieve the final pressure of 10<sup>-8</sup>Torr in the chamber without baking, the rate of desorption from wall must be decreased to the order of 10<sup>-10</sup>Torr ℓ/sec cm<sup>2</sup>. Eliminating the contamination on the surface, we can achieve the above value. The most common contaminants are hydrocarbons, water molecules and dust.

We are studying the methods which make clean the inner surface of the large vacuum chamber. The degree of cleanliness is evaluated by the electron spectroscopy for chemical analysis (ESCA). Material of the samples used in this experiment was stainless-steel AISI 304. To eliminate the gross contamination, the surfaces were pretreated by means of glass beads blast; the size of beads was 150 mesh. After such treatment, it was attempted to clean the surface by various cleaning methods.

The wide range energy spectrum of electron from the surface was measured by the ESCA. Three typical cases are shown in Fig. 1. It is seen that the height of carbon peak is decreased drastically in the cases (B) and (C) compared to that of case (A). The results obtained for surfaces treated by various cleaning methods are arranged in order of the height of carbon peak and are shown in Fig. 2. With the decrease in the peak height of carbon from hydrocarbons, that of iron increased remarkably. This fact shows that the surface became clean. The height and

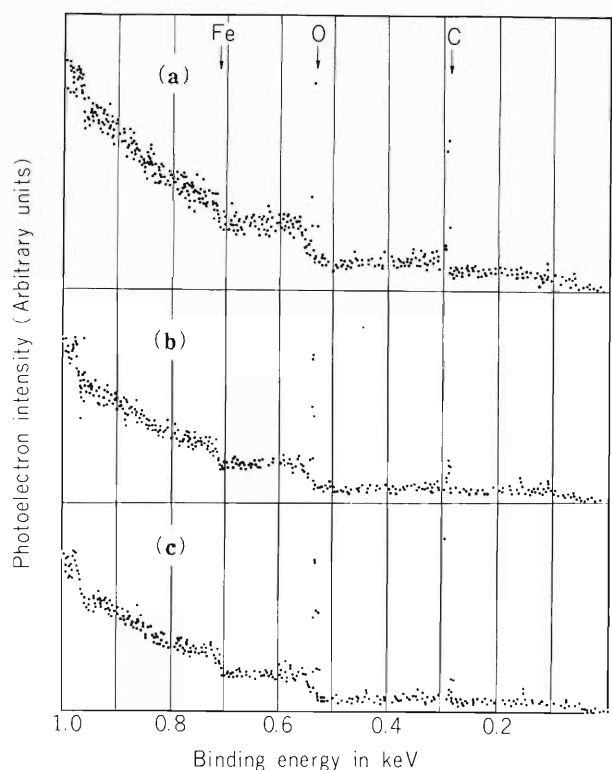


Fig. 1. Photoelectron spectrum of the surface made clean by following methods:

- (a) glass beads blast,
- (b) rinse with distilled water after cleaning with synthetic detergent,
- (c) supersonic cleaning in the trichloroethylene.

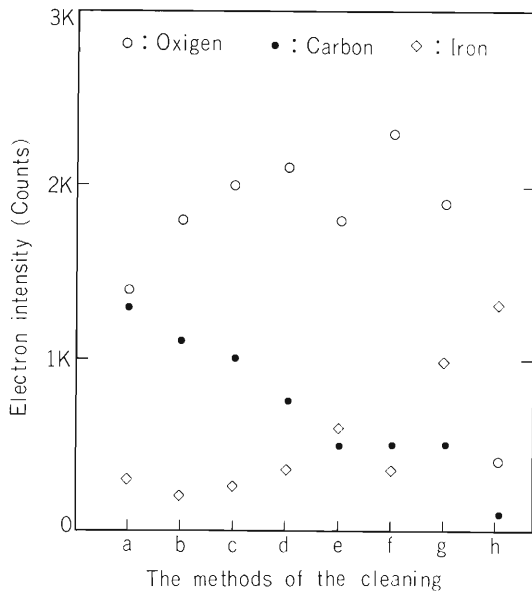


Fig. 2. The cleaning effect by various cleaning methods as follows:

- (a) glass beads blusting,
- (b) rinsing with distilled water,
- (c) immerse in solvent of trichloroethylene,
- (d) rinse with distilled water after washing with synthetic detergent,
- (e) rinse with tap water after washing with synthetic detergent,
- (f) supersonic cleaning in solvent of trichloroethylene,
- (g) baking ( $200^{\circ}\text{C}$ , 2 h) after the treatment of (f),
- (h) Ar ionetching for 40 min after the treatment of (g).

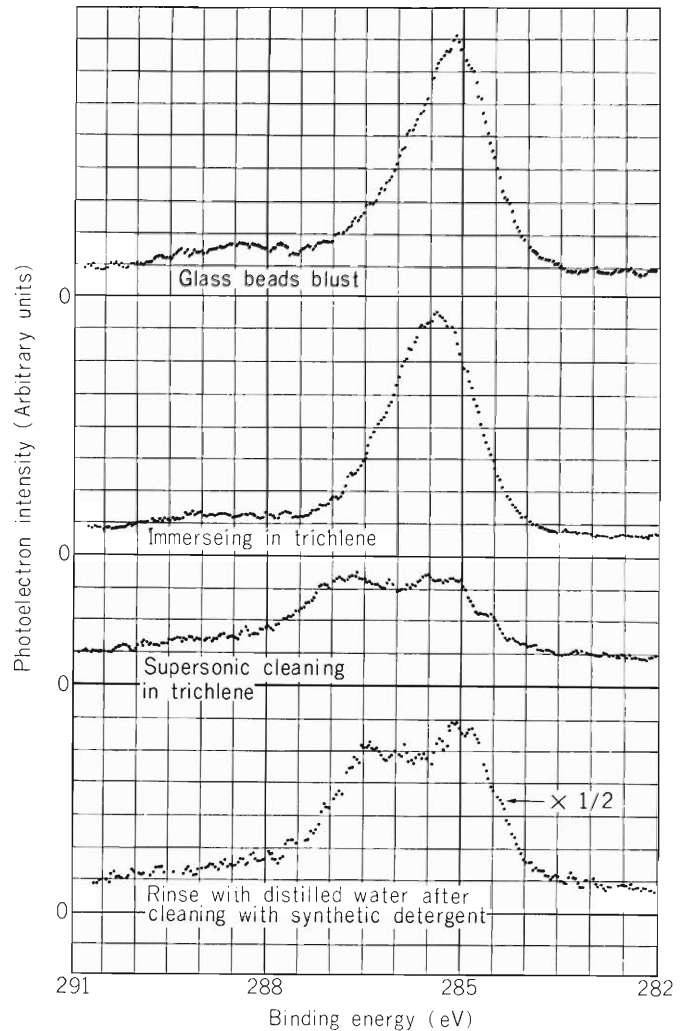


Fig. 3. Comparison of the height and shapes of carbon peaks from the surface cleaned by different methods.

shape of the carbon peak originating from hydrocarbons on the surfaces are varied by miscellaneous cleaning methods except by immersing samples in solvent as is shown in Fig. 3.

The height and shape of peaks after synthetic detergent solution cleaning is similar to those of supersonic cleaning. However, the sort of hydrocarbons remaining on the surface are not yet identified.

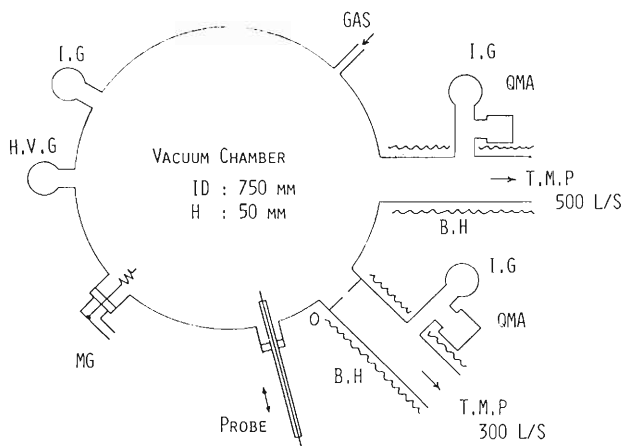
As mentioned above, the effects of the cleaning are confirmed by the surface analysis. However, it is recognized that cleaning agent used always remained slightly. In order to solve the problem, we are thinking of applying composite procedures for surface cleaning.

#### IV-25. Preliminary Experiment on Discharge Cleaning of a Sector Magnet Vacuum Chamber for the SSC

K. Ikegami, S. Nakajima, Y. Oikawa, Y. Ishibe,  
H. Oyama, Y. Sakamoto, and S. Motonaga

A sector magnet of the SSC has a narrow gap. The vacuum chamber inserted into the gap has low conductance compared with pumping speed at the valley. It is difficult to obtain the aimed pressure of  $3 \sim 4 \times 10^{-6}$  Pa on the median plane because baking of the surfaces of the magnet vacuum chamber is practically impossible. High speed evacuation owing to degassing by discharge cleaning becomes attractive. Because the magnetic field is produced inside the chamber, ECR (electron cyclotron resonance) discharge cleaning method can be applied for this purpose. We investigated the ECR discharge cleaning by the use of a model which has the conductance of 180  $\ell$ /sec, the surface area of  $1 \times 10^4$  cm<sup>2</sup> and the pumping speed of 500  $\ell$ /sec.

The experimental apparatus is schematically shown in Fig. 1. A vacuum chamber with 5 cm height and 75 cm diameter made of stainless steel 304L is inserted between magnet poles the diameter of which is 72 cm. The cross section of the magnet as well as the field distribution is shown in Fig. 2. Microwave whose frequency and maximum power are 2.45 GHz and 800 W (CW) respectively is supplied via helix launcher. A double probe is used to measure the electron temperature and the ion density of plasma produced for cleaning. A quadrupole mass analyser (QMA) is set near the pump head of a turbomolecular pump (500  $\ell$ /sec) to observe the residual gases, and another QMA is set after an orifice (conductance = 0.6  $\ell$ /sec) to allow observation of



M.G : MICROWAVE GENERATOR  
FREQUENCY : 2.45 GHz, POWER : 800 W CW MAX  
I.G : ION GAUGE  
H.V.G : HIGH VACUUM GAUGE  
QMA : QUADRUPOLE MASS ANALYSER  
B.H : BAKING HEATER  
O : ORIFICE ( CONDUCTANCE : 0.6 L/S )

Fig. 1. Schematic diagram of experimental arrangement.

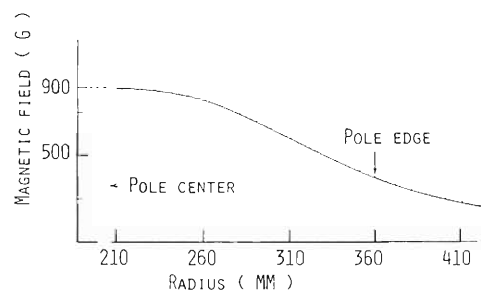
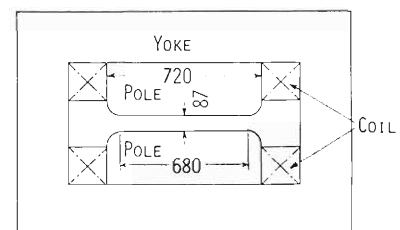


Fig. 2. Electromagnet used and the radial distribution of axial magnetic field.

produced gases during discharge cleaning. Baking heaters are wound around the pumping ports to prevent adsorption of gases produced during discharge cleaning.

The cleaning plasma was produced at a hydrogen pressure of  $3.7 \times 10^{-2}$  Pa. The vacuum wall temperature increased from  $25^\circ$  to  $80^\circ$  C during about 6.5 h. The microwave power was typically about 600 W. The plasma was not uniform in the chamber and the spatial distribution depended upon the pressure and the magnetic field. Nevertheless the electron temperature of  $10 < T_e < 20$  eV and the ion density of  $3 \times 10^9 < N_i < 1 \times 10^{10}$  cm $^{-3}$  were measured at the radius of 280 mm. Produced gases during cleaning were H<sub>2</sub>O, CO, CH<sub>4</sub>, and CO<sub>2</sub> for virgin surface. Temporal variation of the total pressure and the QMA signals are shown in Fig. 3 and Fig. 4, respectively.

The ECR discharge cleaning is accomplished by wall surface impact of hydrogen atoms and chemical reaction between the wall surface impurities (oxygen and carbon) and hydrogen ions

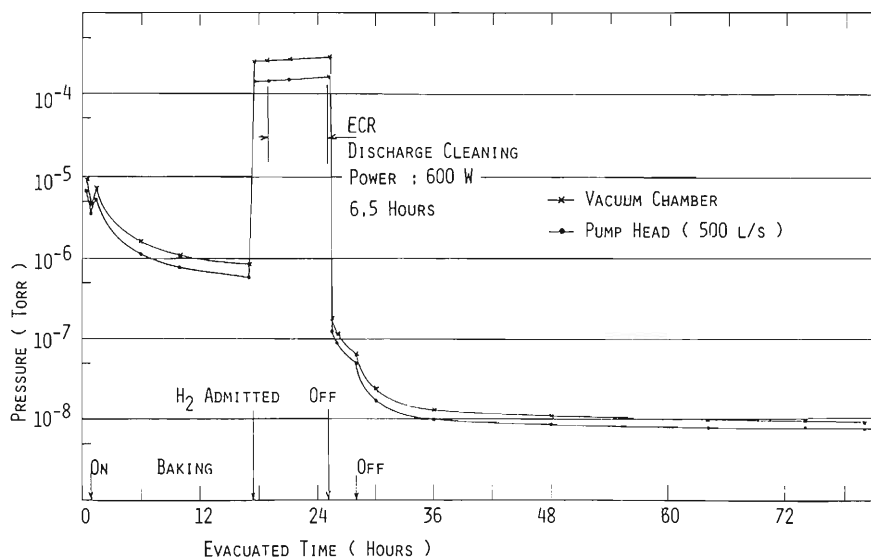


Fig. 3. Temporal variation of total pressure.

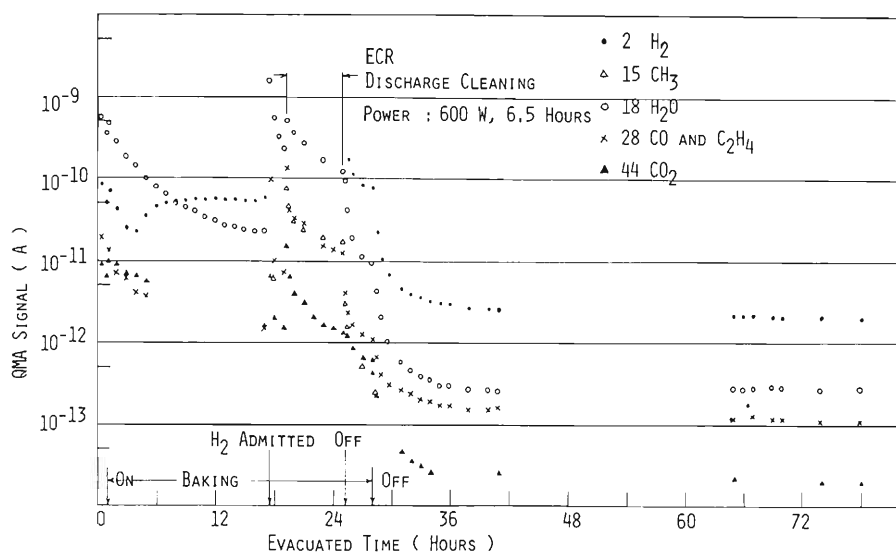


Fig. 4. Temporal variation of partial pressures.

and Franck-Condon neutrals from the plasma.<sup>1)</sup> We give here very rough estimation of the fluxes by assuming that (1) ions hit the wall surfaces along the magnetic line of force (top and bottom surface), (2) the neutrals hit uniformly all surfaces, (3) the plasma exists uniformly in the domain  $r \leq 68/2 = 34$  cm with the density and the electron temperature of  $3 \times 10^9 \text{ cm}^{-3}$  and 10 eV, respectively and (4) ions have the thermal speed ( $2.5 \times 10^5 \text{ cm} \cdot \text{sec}^{-1}$  for proton at 300 K). The calculation gives

$$\text{ion flux } \phi_1 \simeq 7.5 \times 10^{14} \text{ cm}^{-2} \cdot \text{sec}^{-1}$$

$$\text{and neutral flux } \phi_0 \simeq 6 \times 10^{14} \text{ cm}^{-2} \cdot \text{sec}^{-1} .$$

On the other hand the pressure increases on the average by  $\Delta p = 6.7 \times 10^{-3}$  Pa due to the production of  $\text{H}_2\text{O}$  and so on. The amount  $Q$  of gas produced is given by  $Q = \int_0^T S p \Delta p$ , where  $S$  is the pumping speed (500  $\ell/\text{sec}$ ) and  $T$  is the total cleaning time (6.5 h). The value of  $Q$  obtained is  $7.8 \times 10^4 \text{ Pa} \cdot \ell \sim 7.2 \times 10^{22}$  molecules. This means we transformed the surface impurities of  $7.2 \times 10^{18}$  molecules/ $\text{cm}^2$ , into gases, that is to say, about  $10^3$  monolayers are treated by assuming the surface roughness factor of unity. The final pressure obtained was  $1.2 \times 10^{-6}$  Pa after evacuating 78 h.

Model study on ECR discharge cleaning of the vacuum chamber inserted in the magnet was carried out by using  $\text{H}_2$  gas pressure of  $3.7 \times 10^{-2}$  Pa and 2.45 GHz microwave of 600 W. A hydrogen plasma, whose density and electron temperature were  $3 \times 10^9 < n_i < 1 \times 10^{10} \text{ cm}^{-3}$  and  $10 < T_e < 20$  eV respectively, transformed the impurities (C and O) into  $\text{H}_2\text{O}$ , CO,  $\text{CH}_4$ , and  $\text{CO}_2$ . About  $10^3$  monolayers near the surface were cleaned down. We obtained the final pressure of  $1.2 \times 10^{-6}$  Pa after evacuating 78 h.

## Reference

- 1) Y. Sakamoto, Y. Ishibe, K. Yano, H. Ohyama, Y. Tanaka, N. Fujisawa, Y. Matsuzaki, N. Suzuki, K. Maeno, T. Yamamoto, and K. Yokokura: J. Nucl. Mater., 93-94, 333 (1980).

## IV-26. Beam Diagnostic System for the RIKEN SSC

Y. Yano, N. Kishida, A. Goto, and N. Nakanishi

In the RIKEN accelerator complex system, a beam preaccelerated by the injector is transported to the SSC through the injection beam transport system and then is accelerated by the SSC. The high-energy beam extracted from the SSC is transported to an experimental setup through the beam handling system. In such beam transportation and acceleration, parameters for the relevant beam handling elements should be optimized on the basis of beam properties observed at strategic locations with various kinds of beam diagnostic apparatus. We have determined the arrangement of these apparatus, considering necessary procedures for adjusting the beam handling devices.

Figure 1 shows the beam diagnostic system for the SSC. With the aid of this system, each element of the SSC is tuned up as follows: We optimize the parameters (position, current and voltage) for the beam injection elements (BM1, MIC2, MIC1 and EIC), measuring the beam trajectory with the slit system (SI0 – SI3) as well as the main differential probes (MDP1 and MDP2). The MDP1 is equipped with the Fork probe (FK) by which beam bunch length is measured. This type of probe has been developed at GANIL and is successfully used. From the bunch length measured with the FK, the voltage for the buncher on the injection beam transport line is adjusted so as to give the minimum bunch length at injection point. By means of the FK, we can also observe the variation of bunch length of accelerated beam inside the SSC. One of the features of our beam diagnostic system is that the emittance measuring device (EM1) is installed at the injection point. Because the fringe magnetic field from the sector magnets (SM) exists at this area, the emittance is calculated on the basis of the magnetic field data as well as the beam

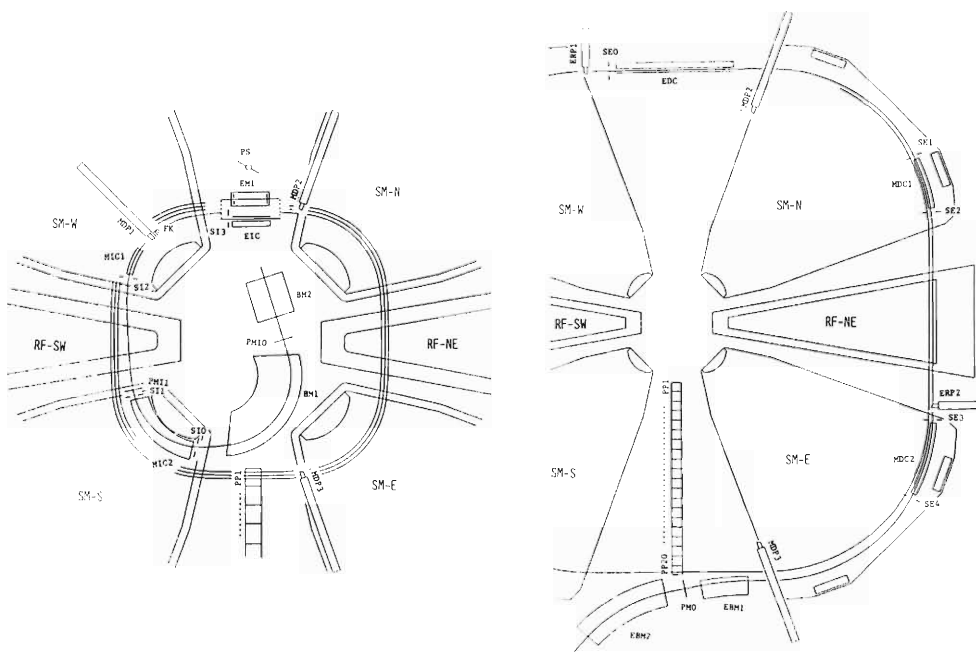


Fig. 1. The arrangement of beam diagnostic devices in the SSC.

current data from the EM1. It can easily be done by using the above emittance measuring device to match the beam emittance in six-dimensional phase space with the desired one. In one of the vacuum chambers, twenty pairs of phase probes (PP) of capacitive pickup type are arranged radially. These probes observe the phase history of accelerated beam in a non-destructive manner. From the measured phase history, the currents of main coils and trim coils of the sector magnets are optimized so as to produce the isochronous magnetic field. The orbit center of acceleration orbit is measured by three main differential probes (MDP1 – MDP3). We can obtain the two-dimensional position of the orbit center. By observing the behavior of movement of the orbit center in the injection region, the voltage of the EIC and the currents of injection harmonic coils are adjusted so that the orbit center may move to the machine center. The harmonic field is also applied in the extraction region to increase the turn separation and accordingly improve the extraction efficiency. The movement of the orbit center in the extraction region is observed again by the MDP system and the currents of extraction harmonic coils are adjusted. The parameters for the beam extraction elements (EDC, MDC1, MDC2, EBM1, and EBM2) are optimized in the same manner as in the injection case by measuring the beam trajectory with the slit system (SE0 – SE4), the MDP system and the extraction radial probe (ERP).

The theoretical study of the adjusting procedures mentioned above is now in progress.

#### IV-27. Model Test of 1/5 Scale Movable Box Type RF Resonator for the RIKEN SSC

K. Ogiwara, T. Fujisawa, and Y. Oikawa

A resonator whose resonant frequency is varied from 17 to 45 MHz with the use of movable box in the resonator is designed for the RIKEN SSC.<sup>1)</sup> The transmission line approximation is used in the calculation for the resonator shown in Fig. 1. Based on the calculation, a 1/5 model resonator was constructed and the resonant frequencies, Q-values and radial distributions of RF electric field at the accelerating gap were measured. The resonant frequencies and Q-values measured are shown in Fig. 2 together with the calculated values. The resonant frequencies measured are fairly well reproduced by the calculation. However, the measured Q-values are about those of 0.4 times the calculated ones. The poor agreement between the measured and calculated Q-values may be due to poor contact between the movable box and the outer wall and to the complex structure of this resonator.

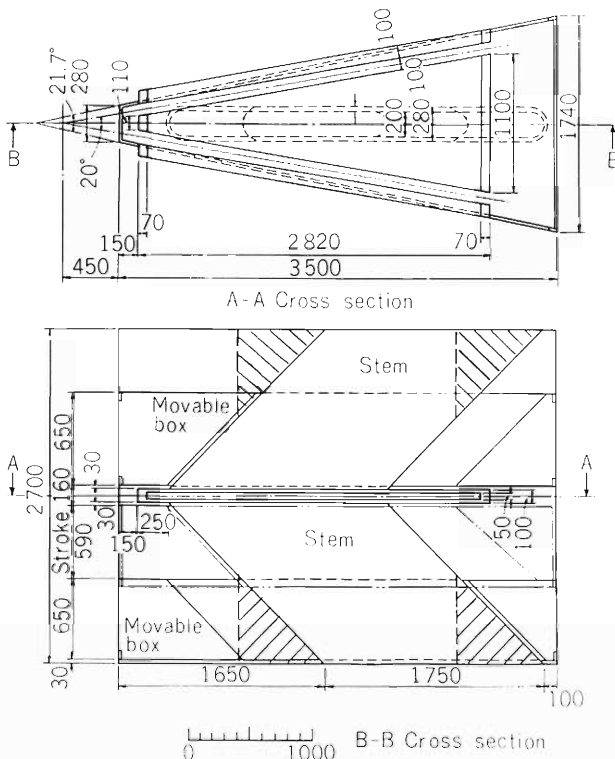


Fig. 1. Schematic view of the movable box type resonator.

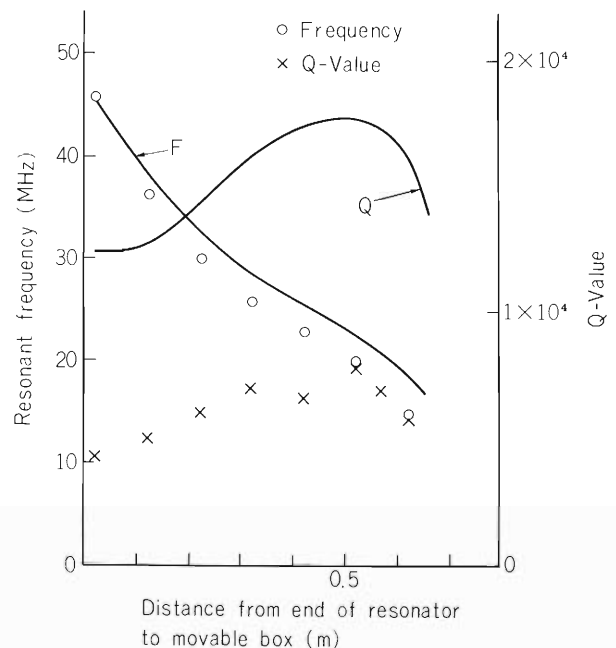


Fig. 2. Resonant frequencies( $f$ ) and Q-values measured( $\circ$  and  $\times$ ) and calculated( $-$ ) by the transmission line approximation.

Relative distributions of RF electric field along the dee edge of the model resonator were measured by perturbation method.<sup>2)</sup> The measured distributions are shown in Fig. 3, where the dee voltages are normalized at injection radius. The strength of the field at middle radius is 75 % of that at the injection radius for 45.9 MHz. This is not desirable for beam acceleration. In order

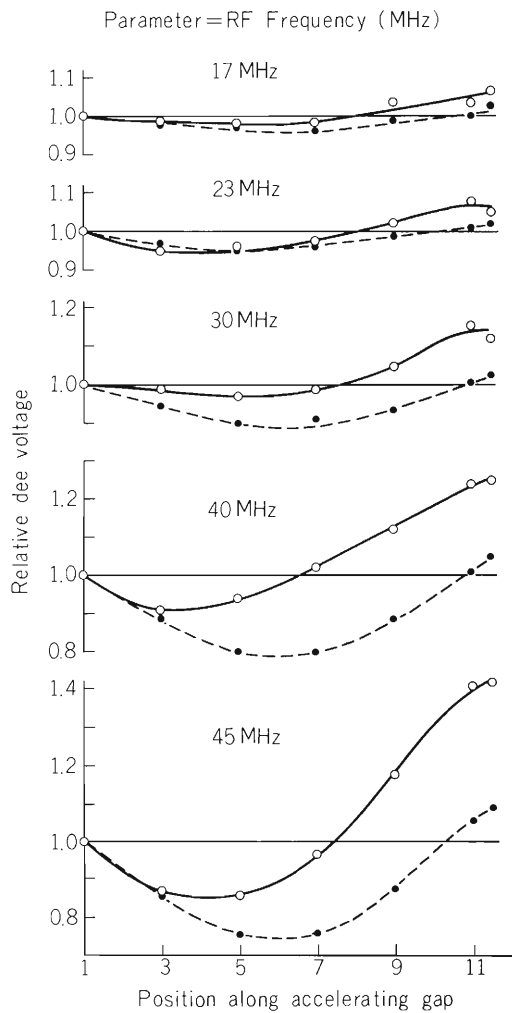


Fig. 3. Relative distributions of RF electric field along the accelerating gap for the 1/5 model resonator. Solid lines show the values after the modification.

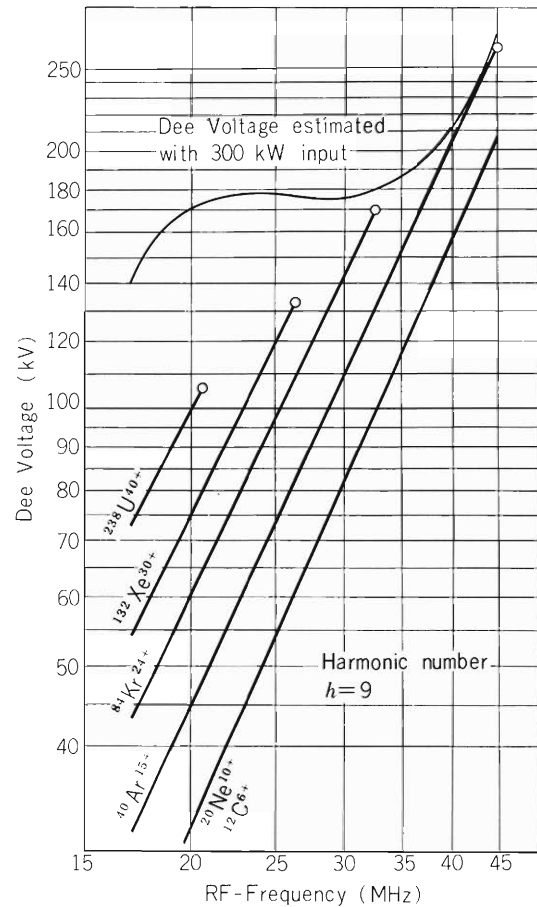


Fig. 4. Dee voltage required for beam acceleration.

to improve the distributions, the stem were modified as shown in Fig. 1 (hatched). The electric field distributions are improved by the modifications as shown in Fig. 3. The dee voltages required for beam acceleration have been calculated for several particles,<sup>3)</sup> which are shown in Fig. 4 as function of RF-frequency. The maximum output power of the amplifier for the resonator is to be 300 kW. The dee voltages generated by the present amplifier are estimated using the measured and calculated Q-values. The results are also shown in Fig. 4. The estimated dee voltages are sufficient for the beam acceleration.

## References

- 1) T. Fujisawa: RIKEN Accel. Progr. Rep., 15, 196 (1981).
- 2) L.C. Maier, Jr. and J.C. Slater: J. Appl. Phys., 23, 68 (1952).
- 3) A. Goto: RIKEN SSC Engineering Note, OA-10 (1982).

## IV-28. Effect of Resonance on the Beam in the RIKEN SSC

N. Nakanishi, Y. Yano, and A. Goto

Recently, measurement was carried out for magnetic fields in the system of two full-scale sector magnets, and beam dynamical properties of the RIKEN separated sector cyclotron have been recalculated by using the measured data. As one of properties, focusing frequencies for typical particles and energies were examined, and it was confirmed that the results are not so different from those which had been obtained using magnetic fields in model magnets.

According to the calculation, a 9 MeV proton beam crosses the resonance line  $\nu_r - 2\nu_z = 0$  in a  $(\nu_r, \nu_z)$  space during acceleration. The focusing frequency is shown in Fig. 1. This resonance is known to be a quadratic non-linear coupling resonance and arises from the existence of the second-order derivatives of the magnetic field distribution. It is seen that the beam encounters the resonance at the betatron frequencies of  $\nu_r = 1.3$  and  $\nu_z = 0.65$  ( $E = 144$  MeV,  $R = 295$  cm).

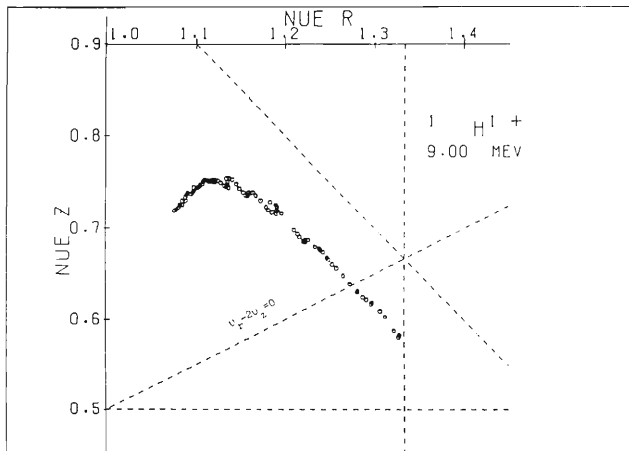


Fig. 1 Focusing frequency of a 9 MeV proton beam.

We have only the data of the axial component of magnetic induction  $B_z(r, \theta)$  on the median plane, that is of  $B(r, \theta, z = 0) = B_z(r, \theta)$ . The field  $B(r, \theta, z)$  off the median plane is obtained in a power expansion in  $z$  using symmetry with respect to the median plane:<sup>1)</sup>

$$B_z = B + \frac{1}{2} z^2 \cdot f_2,$$

where

$$f_2 = - \left\{ \frac{\partial^2 B}{\partial r^2} + \frac{1}{r} \frac{\partial B}{\partial r} + \frac{1}{r^2} \frac{\partial^2 B}{\partial \theta^2} \right\} z = 0.$$

From  $\text{rot } B = 0$ , radial and azimuthal components of the magnetic field are given as

$$B_r = z \frac{\partial B}{\partial r} + \frac{1}{6} z^3 \cdot f_3$$

$$r \cdot B_\theta = z \frac{\partial B}{\partial \theta} + \frac{1}{6} z^3 \cdot g_3,$$

where

$$f_3 = \frac{\partial}{\partial r} f_2 = - \left\{ \frac{\partial^3 B}{\partial r^3} + \frac{1}{r} \frac{\partial^2 B}{\partial r^2} - \frac{1}{r^2} \frac{\partial B}{\partial r} + \frac{1}{r^2} \frac{\partial^3 B}{\partial r \partial \theta^2} - \frac{2}{r^3} \frac{\partial^2 B}{\partial \theta^2} \right\} z = 0$$

and

$$g_3 = \frac{\partial}{\partial \theta} f_2 = - \left\{ \frac{\partial^3 B}{\partial r^2 \partial \theta} + \frac{1}{r} \frac{\partial^2 B}{\partial r \partial \theta} + \frac{1}{r^2} \frac{\partial^3 B}{\partial \theta^3} \right\} z = 0.$$

Calculation has been done by modifying the program ACCELP.<sup>2)</sup> Figures 2(a) and (b) show the radial and axial oscillations of particles around the central orbit during acceleration. In order to examine the effect of the higher-order terms on amplitudes, two particles of initial amplitude 5 mm in each direction were traced using equations without (case a) and with (case b) the higher order terms. The accelerating voltage was assumed to be 250 kV. We could not find any remarkable difference in amplitude between them. These initial amplitudes correspond to the emittances of around 30 and 20 mm·mrad, respectively, and these are probable values in practice. Thus the influence of the resonance on amplitudes is practically negligibly small.

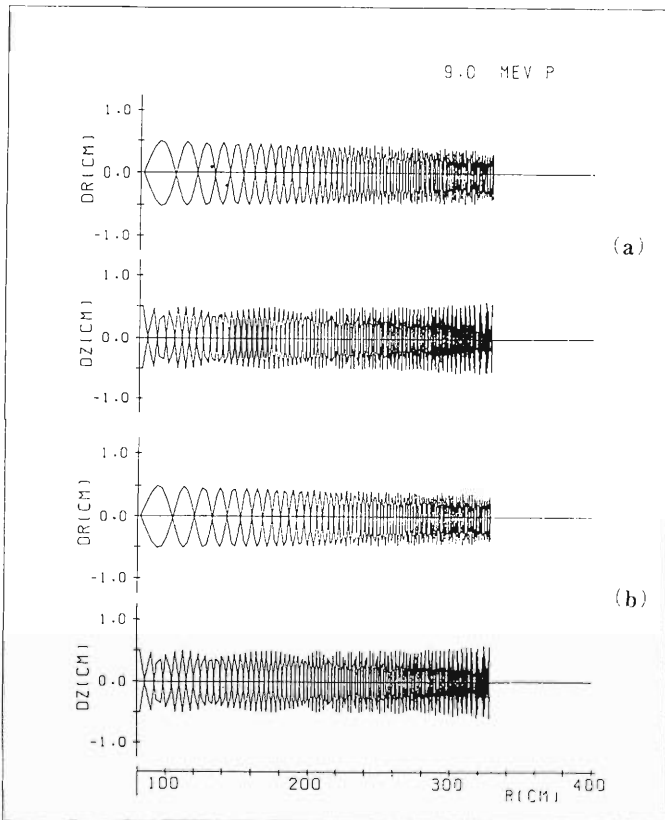


Fig. 2. Calculated oscillation patterns around the central orbit during acceleration. Calculation was done without (a) and with (b) the higher-order terms.

In order to observe clearly the effect of the higher-order terms, calculation has been done for a beam with a large axial amplitude in the accelerating voltage of 60 kV. The axial oscillations are shown in Fig. 3. As seen in the lower drawing in Fig. 3, it is observed that amplitude grows up in the case b.

In order to make the resonance effect small it may be required that the injected beam is of good quality and that the energy gain per turn is made as large as possible.

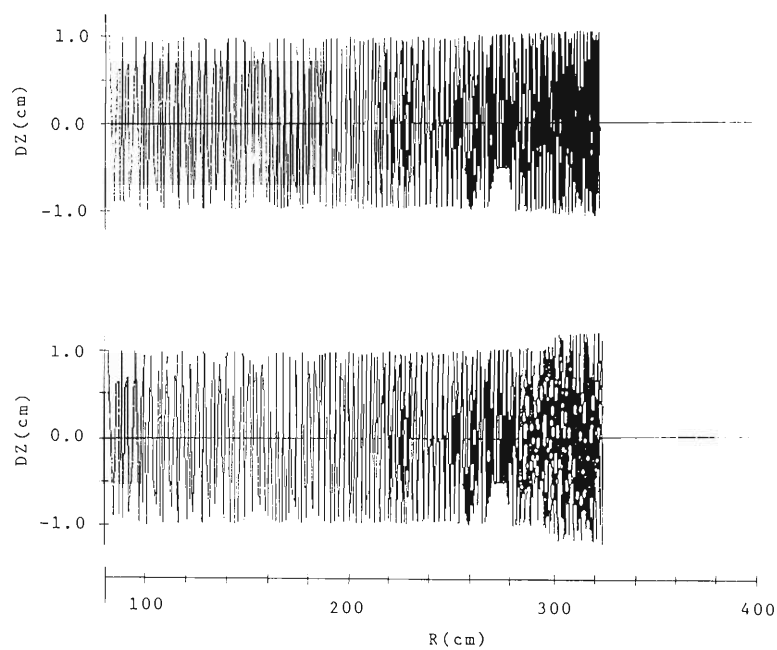


Fig. 3. Axial oscillation patterns in the case of a large initial amplitude. Calculations were done without(upper) and with(lower) the higher-order terms.

#### References

- 1) J. P. Blaser and H. A. Willax: IEEE Trans., NS-13, 194 (1966).
- 2) N. Nakanishi: Reports I.P.C.R., (in Japanese), 57, 189 (1981).

## IV-29. SSC Beam Handling System

T. Inamura and N. Kishida

The revised plan view of the SSC beam handling system is shown in Fig. 1. The previously reported design<sup>1)</sup> has been modified to provide more target areas. The revised system transports the beam from the SSC to eight main target areas. The beam reaches six target areas after passing two standardized 90°-bending magnets, which are placed in mirror or antimirror symmetry. The target area  $T_7$  is arranged so that a crossed-beam experiment could be made using the beams from an AVF injector cyclotron and from the SSC.

Numerical calculations of the ion optics have been carried out to second order using the computer code "TRANSPORT".<sup>2)</sup>

The present system provides the following beam preparation modes:

- (1) Achromatic, double-telescopic transport to every target area;
- (2) Double-dispersive, double-telescopic transport with a momentum resolution up to 20000 in lab. 2, 3, and 6;
- (3) Isochronous, nondispersive, double-telescopic transport with a time resolution less than 500 ps in lab. 4 and 6.

It should also be stated that even in mode (1) or (3) the momentum resolution becomes about 10000. By taking into account the second-order aberration, the momentum resolution was estimated for a beam whose maximum divergence is 2.432 mrad at the object point  $S_0$ ; the slit

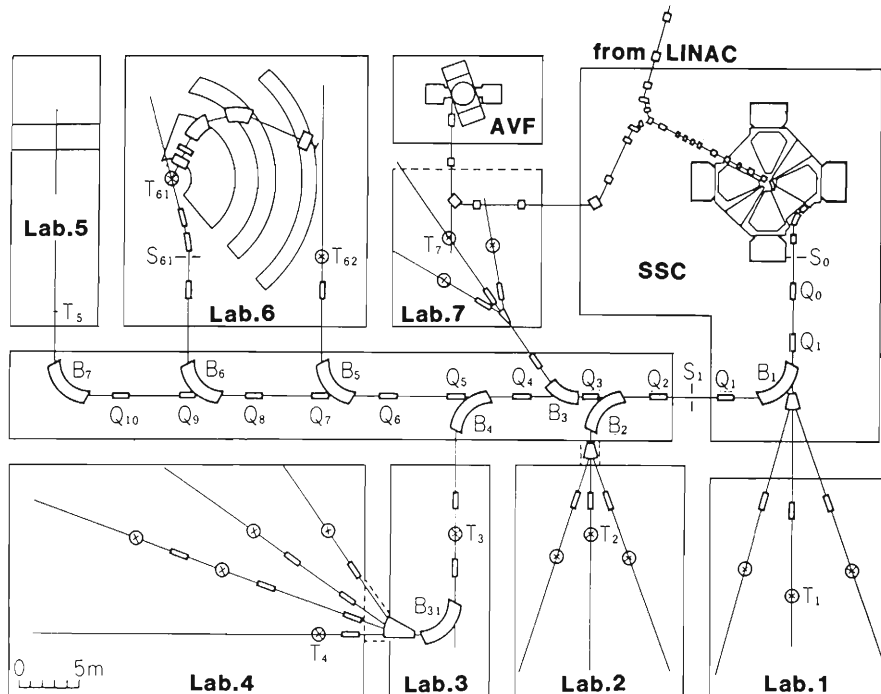


Fig. 1. Plan view of the beam handling system for the RIKEN SSC.  $S_0$  is the object point of the system.

width at  $S_0$  is 1.0 mm. In this connection, the first-order momentum resolution is 23000.

We assumed at the moment that the entrance and exit pole faces of the bending magnets are flat and the fringing field boundaries are given by an unclamped Rogowski field. If the curved pole faces are adopted, the principal second-order aberration can be minimized to result in much higher momentum resolution.

#### References

- 1) T. Inamura, N. Kishida, H. Saito, and M. Watanabe: Sci. Papers I.P.C.R., 75, 236 (1981);  
T. Inamura, N. Kishida, and H. Saito: RIKEN Accel. Progr. Rep., 15, 203 (1981).
- 2) K.L. Brown, F. Rothacker, D.C. Carey, and Ch. Iselin: SLAC Report, p. 91 (1974).

## IV 30. Biological and Physical Irradiation Beam Channel for the RIKEN SSC

N. Kishida, S. Kohmoto, A. Goto,  
E. Takenaka,\* and H. Kamitsubo

Biological and physical irradiation at the RIKEN SSC facility aims at development of heavy-ion irradiation technique, basic study of biological effect induced by heavy-ion irradiation, and preliminary study of physical irradiation by heavy-ions. Transportation of various kinds of heavy-ions to irradiation areas and easy adjustment of irradiation conditions are required for the biological and physical irradiation channel.

It is desired that the irradiation spot size is continuously variable from 1 ~ 2 mm squares for a spot scanning irradiation to 20 cm squares for an overall irradiation. It is also desired that the irradiation channel has both horizontal and vertical irradiation beam-channels which are shielded from each other by thick concrete walls.

The biological and physical irradiation room is to be located in the eastern end of the SSC experimental halls, and the area inside the shielding walls is 7.5 m × 22 m square (Fig. 1). Figure 2 shows a cross sectional view of the beam transport system to each irradiation room. Figure 3 shows a plan view of radioactive isotope (RI) beam production channel which is installed on the same level as the horizontal irradiation beam-channel.

The beam extracted from the SSC is transported to point T<sub>5</sub> so as to become an achromatic beam which is used as an initial beam in ion-optical calculation of the irradiation beam transport system.

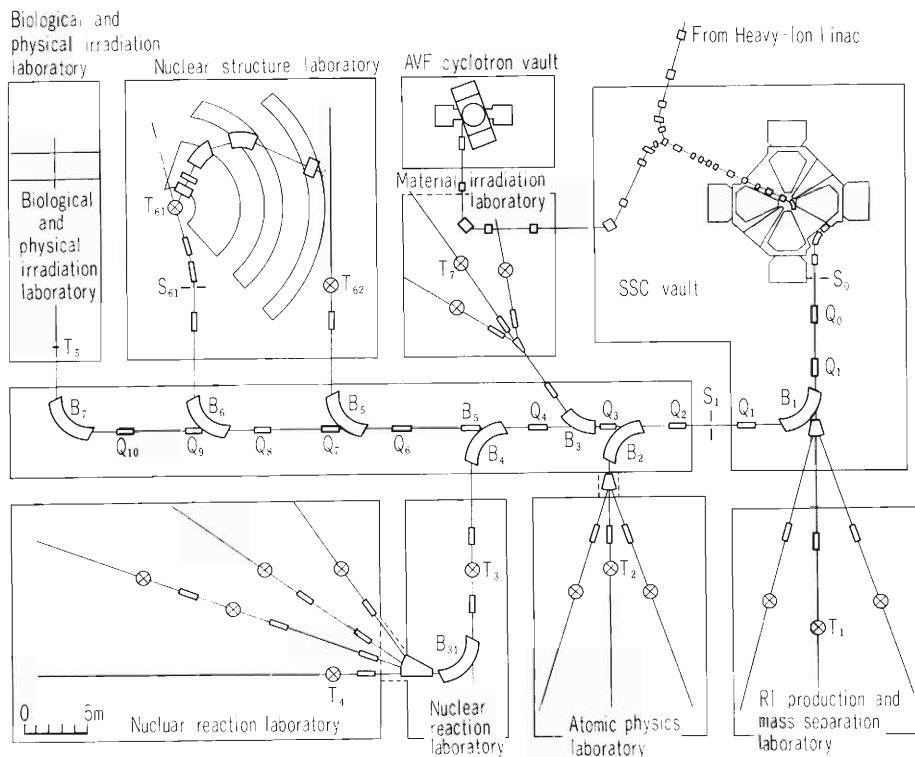


Fig. 1. Beam transport system and layout of experimental and irradiation areas with the SSC. The biological and physical irradiation laboratory is located in the target area T<sub>5</sub> which is at the eastern end of the SSC experimental halls.

\* Faculty of Medicine, University of Tokyo.

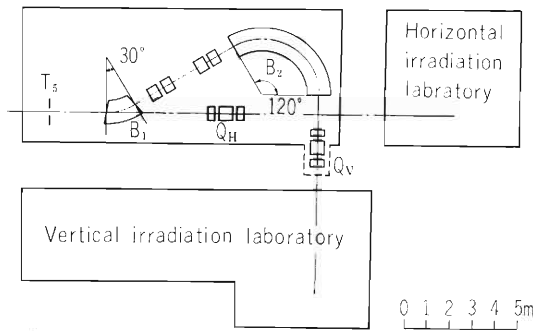


Fig. 2. Cross sectional view of the beam transport system in the biological and physical irradiation laboratory.

Table 1. Positron emitting nucleides produced by the SSC beam.

Nucleide	Reaction	Half life	Energy
$^{11}\text{C}$	$(^{12}\text{C}, ^{11}\text{C})$	20.34 m	Larger than 100 MeV/u
$^{13}\text{N}$	$(^{14}\text{N}, ^{13}\text{N})$	9.96 m	
$^{15}\text{O}$	$(^{16}\text{O}, ^{15}\text{O})$	123 s	
$^{18}\text{F}$	$(^{19}\text{F}, ^{18}\text{F})$	109.7 m	
$^{19}\text{Ne}$	$(^{20}\text{Ne}, ^{19}\text{Ne})$	17.4 s	
$^{23}\text{Mg}$	$(^{24}\text{Mg}, ^{23}\text{Mg})$	12.1 s	Less than 100 MeV/u
$^{27}\text{Si}$	$(^{28}\text{Si}, ^{27}\text{Si})$	4.14 s	
$^{30}\text{P}$	$(^{31}\text{P}, ^{30}\text{P})$	2.50 m	
$^{31}\text{S}$	$(^{32}\text{S}, ^{31}\text{S})$	2.72 s	

In the horizontal irradiation target area the beam spot size is variable by a triple quadrupole magnet ( $Q_H$ ) from  $2\text{ mm} \times 2\text{ mm}$  to  $20\text{ cm} \times 20\text{ cm}$ . The achromatic beam is transported to the vertical irradiation room using two bending magnets, four single quadrupole magnets and one triple quadrupole magnet. The quadrupole magnet  $Q_V$  controls the beam size from  $1\text{ mm} \times 1\text{ mm}$  to  $10\text{ cm} \times 10\text{ cm}$ .

It is required to know the accurate position irradiated, especially in the case of irradiating deep internal organs using heavy-ion beams. High energy heavy-ions induce nuclear reactions in the organs and produce radioisotopes which emit positrons. If necessary the accurate stopping position of the radioisotopes which are produced by the nuclear reactions can be determined by positron computed tomography (PCT). If secondly RI beams can be utilized, those will be very valuable not only for the biological and physical irradiation but also for the study in many other fields. For these purposes a production and transport system of RI beams is designed.

Positron emitting nuclides with a short half-life time which can be produced by the SSC beam and used for the irradiation are listed in Table 1.

Target for producing a secondly RI beam is installed at point  $T_s$ , and the slit S excludes background beams which are dispersing by the bending magnet BE2 (Fig. 3). The primary beam passing through the target without a nuclear reaction is introduced into a beam dump.

We will, as an example, try to estimate beam strength of  $^{11}\text{C}$  ions which are generated by the  $^{12}\text{C}(^{12}\text{C}, ^{11}\text{C})^{13}\text{C}$  reaction at an incident energy of 130 MeV/u using this system. The required RI beam transport system is such that it will collect the ions which are emitted from the target within  $5.0^\circ \pm 0.5^\circ$  and  $0.0^\circ \pm 0.5^\circ$  in horizontal and vertical directions, respectively, and  $\pm 1\%$  in momentum spread. The target thickness  $1\text{ g/cm}^2$  is thus determined: the energy loss difference between the ions in the target may not exceed the momentum acceptance of the transport system. If  $^{12}\text{C}^{6+}$  ions of  $1\text{ }\mu\text{A}$  (one particle micro ampere) impinge on the target and if the differential cross section of the reaction is estimated at  $454.1\text{ mrad/sr}$ ,  $4 \times 10^7$  ions of  $^{11}\text{C}^{6+}$  will be

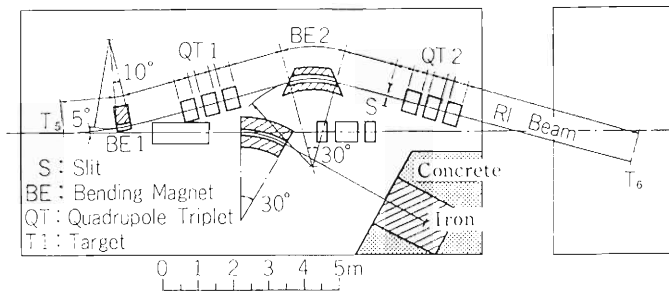


Fig. 3. Plan view of RI beam production and transport channel (All of the magnets but B1 belonging to the vertical irradiation system are omitted in this figure.). The target for producing secondly beam is installed at T<sub>5</sub>. S is a beam slit for excluding background beams.

**RADIOACTIVE BEAM COURSE**

SINGLE RAY X=2.00 MM, DX=8.73 MR, Y=0.00 MM, DY=0.00 MR, DP=4.00%

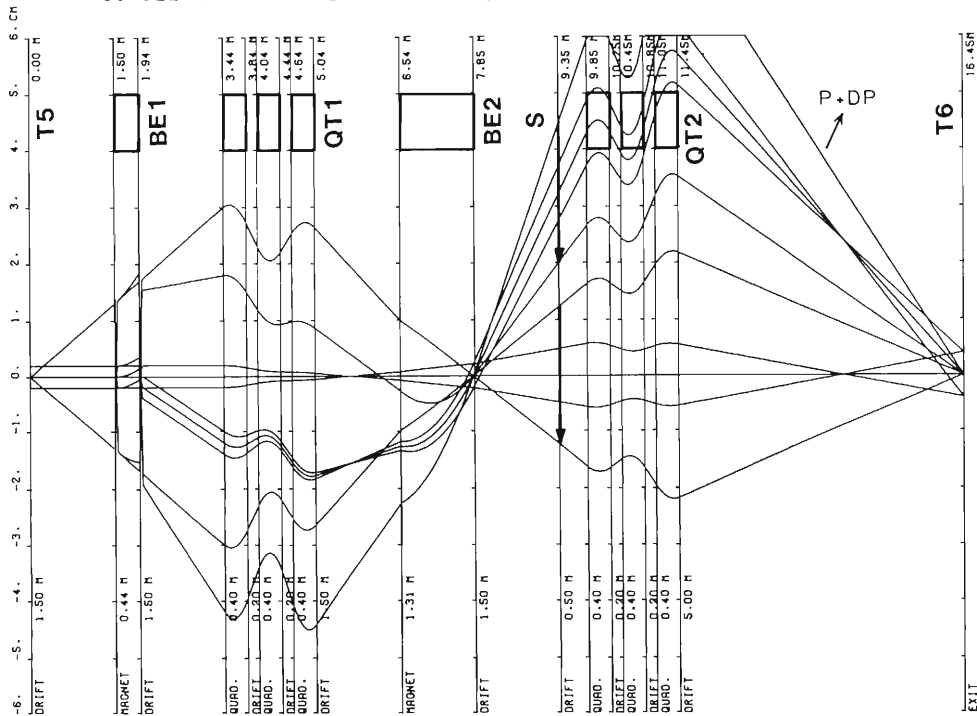


Fig. 4. Ray trace of five ions with a central momentum and other five ions with momentum larger by 4 % than the former in the RI beam transport system. Two arrows at S denote each beam size.

obtained every second.

Traces of a single ray are shown in Fig. 4. It is found that the ions dispersed by the bending magnet BE2 can be analyzed by slit S, where the ions do not focus.

More detailed discussion of this work has been published in Ref. 1.

**Reference**

- 1) N. Kishida, S. Kohmoto, A. Goto, E. Takenaka, and H. Kamitsubo: Reports I.P.C.R., (in Japanese), 58, 77 (1982).

## IV-31. Calculation of RF Electromagnetic Field by Finite Element Method ( II )

M. Hara, T. Wada, T. Fukasawa, and F. Kikuchi

Efforts are continued to develop computer codes to calculate electromagnetic fields in the cavities based on finite element method. We have already developed two computer codes H2DB and HAX<sup>1)</sup> which are used for a resonator with constant cross section and for an axisymmetric resonator. We improved these and related codes. At the same time we developed arbitrary three dimensional calculation program to solve Maxwell's equations using penalty method.

### (1) Improvement

We have added new functions to H2DB and HAX codes. One of them is a restart function. The calculation which is terminated by time limit can be restarted any number of times using the previous results from disk file. We have developed a bandwidth minimization code in order to save memory size and computing time, introducing a connection table.<sup>2)</sup> Minimization procedure is useful especially for complicated shape of cavity. The code MESH2D is also improved in numbering the nodal points to minimize the bandwidth. It is necessary to find boundary for field plotting and power loss calculation. We use also connection table to find it, which extremely reduces computing time.

### (2) Three dimensional calculation code (MAX3D)

In the case of a resonator with constant cross section or an axisymmetric field, many works have been done with satisfactory results.<sup>1),3)</sup> But actually we have many problems that are hard to treat with two dimensional calculations, and true three dimensional calculations are strongly required. In general three dimensional case, only a few papers have been published.<sup>4)</sup> It is no more useful to use only one unknown variable such as a scalar potential. It is convenient to take electric field  $E = (E_x, E_y, E_z)$  as unknown variables because of the easy treatment of boundary conditions and easy understanding of physical meaning. In this case, we must take care of the condition  $\text{div } E = 0$ .

We deal with the time-harmonic propagation of electromagnetic waves in a vacuum of bounded space  $\Omega$  surrounded by perfect conductor. Eliminating H, Maxwell's equations are written as

$$\text{rot rot} E - \lambda E = 0, \quad \text{div} E = 0 \quad (\text{in } \Omega), \quad (1)$$

where  $\lambda = \omega^2 \epsilon \mu$ ,  $\epsilon$  and  $\mu$  are dielectric constant and magnetic permeability in a vacuum. Boundary conditions are

$$n \times E = 0 \quad (\text{on } \Gamma), \quad (2)$$

where  $n$  denotes the outward normal on the boundary  $\Gamma$ . This is an eigenvalue problem for three components of electric field  $E$ . Restriction of  $\text{div } E = 0$  is to be imposed in order to exclude undesired solutions. Penalty method is a convenient way to impose such a restriction.<sup>4)</sup> We take a weak formulation:

$$\int_{\Omega} (\text{rot} E, \text{rot} \delta E) dV + s \int_{\Omega} (\text{div} E, \text{div} \delta E) dV = \lambda \int_{\Omega} (E, \delta E) dV, \quad (3)$$

where  $s$  is a penalty parameter. Euler's equation is obtained from Eqn. (3) as

$$\text{rot rot} E - s \text{grad div} E = \lambda E. \quad (4)$$

In this case,  $\text{div } E = 0$  and  $\text{rot } E = 0$  are satisfied when  $\lambda = 0$ . For positive  $\lambda$ , the solutions of Eqn. (1) are always those of Eqn. (4). Equations (4) may have other solutions than those of Eqn. (1). So far as the

the parameter  $s$  is set to be large in some degree, such a mixture can be avoided for lower modes. Divergence-free condition can be checked by evaluating the following equations:

$$\text{div} \equiv \frac{s \int_{\Omega} (\text{div}E)^2 dV}{\int_{\Omega} (\text{rot}E)^2 dV + s \int_{\Omega} (\text{div}E)^2 dV} \quad (5)$$

In the present study, four noded tetrahedral elements are used and  $E_x$ ,  $E_y$ , and  $E_z$  are approximated with the first-order test functions. In order to impose boundary conditions, Euler's angles are used, if necessary, to determine the normal direction and to rotate the axes at each surface point. Jennings method is used to solve the generalized eigenvalue problem  $Ax = \lambda Bx$  for real symmetric band matrices.<sup>5)</sup> First we made calculation for a rectangular cavity resonator. Parameter  $s$  is set to 1 and the smallest five eigenvalues are calculated. In this case, unphysical solutions are not found below the fifth mode. Next we made calculation for a cylinder cavity and the example is shown in Fig. 1. In this case, unphysical solutions are mixed for certain region of  $s$  values. It is found that these solutions do not satisfy the condition of  $\text{div} E = 0$ . Parameter  $s$ -dependence of eigenvalues are shown in Fig. 2. It can be seen that the  $s$ -dependence is small for physical solutions.

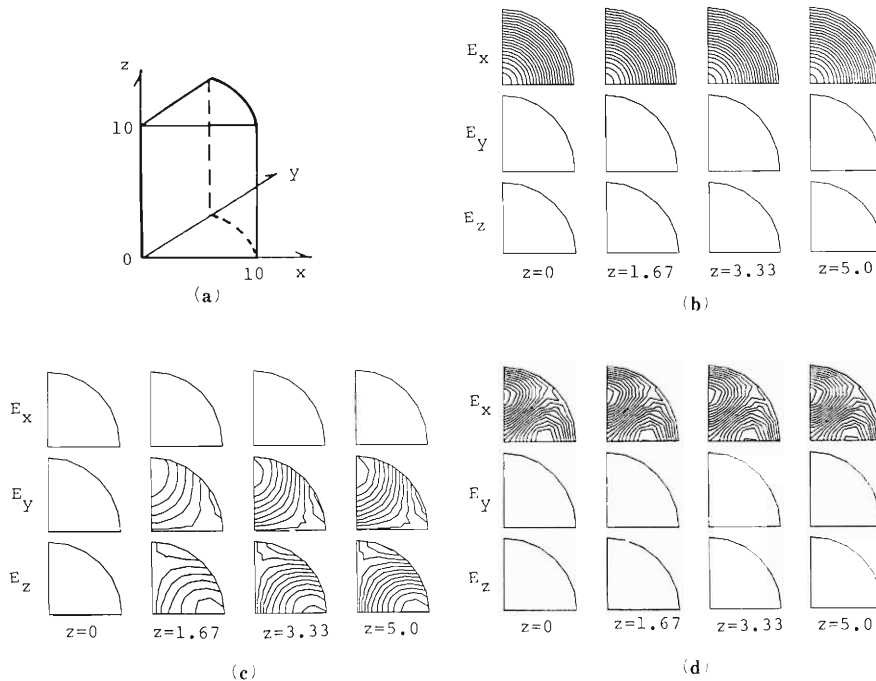


Fig. 1. Calculations for 1/4 cylinder of 10 in height and 10 in radial length. At two planes of  $x = 0$  and  $y = 0$ , mirror symmetry boundary conditions are imposed. Penalty parameter  $s$  is set to 1. Results are shown by contour plots of  $E_x$ ,  $E_y$ , and  $E_z$  at  $z = \text{constant}$  planes.

- (a) Schematic view of 1/4 cylindrical cavity,
- (b) Contour plot for  $TM_{010}$  mode.
- (c) Contour plot for  $TE_{211}$  mode.
- (d) Contour plot for  $TM_{210}$  mode.

Furthermore, we made some calculation deforming these rectangular and cylindrical cavities slightly and smoothly. Obtained results are consistent with the perturbation theory as far as the deformation is small. When the deformation is large, however, the condition  $\text{div} E = 0$  does not become fully satisfied because of the roughness of mesh size and the slow convergence of solution. In the present calculation, number of the nodal points is limited to be less than 1000 because of the memory size of the computer, which means about ten nodes in each direction. For very complicated boundary shape, errors become large because mesh size is coarse and therefore the condition  $\text{div} E = 0$  is not fully satisfied. But this difficulty will be overcome with increasing available memory size.

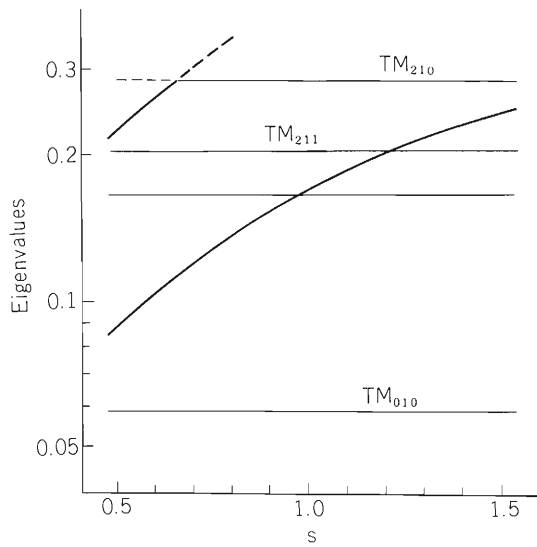


Fig. 2. Penalty parameter dependence of eigenvalues for 1/4 cylindrical cavity. Varying  $s$ -parameter from 0.5 to 1.5, we calculated five modes for each  $s$ . Among these solutions, only three modes are physically allowed. Physically allowed modes have little  $s$ -dependence and satisfy the condition  $\text{div } \mathbf{E} = 0$ .

#### References

- 1) M. Hara, T. Wada, A. Toyama, and F. Kikuchi: *Sci. Papers I.P.C.R.*, 75, 143 (1981).
- 2) E. Cuthill and J. Mckee: *Proc. 24th Nat. Conf. Assoc. Comput. Math.*, ACM Publ., p. 69, 1122 Ave. of the Americas, New York, N.Y. (1969).
- 3) K. Halbach and R. Holsinger: *Particle Accelerators*, 7, 213 (1976).
- 4) R. Leis: *Math. Zeitschr.*, 106, 213 (1968); R. Hoppe: *Numer. Math.*, 36, 389 (1981).
- 5) FACOM FORTRAN Scientific Subroutine Library SSL-II User's Guide.

## IV-32. Status Report of the Prototype Baby Cyclotron

T. Karasawa, N. Hayashi,\* and T. Nozaki

Early in the year,  $^3\text{He}^{++}$  ions were accelerated to 13 MeV with the dee voltage below 20 kV and the frequency of 38 MHz by second harmonic mode. We applied this experience to  $^3\text{He}$  acceleration at the 168-type Baby Cyclotron at the Muroran Plant of JSW, which will be used for activation analysis of semiconductors.

In this year, over three hundred cases were submitted to diagnosis by the brain imaging with positron ECT (emission computed tomography) after respiratory injection of  $^{11}\text{CO}_2$  gas and/or oral injection of  $^{11}\text{C}$ -labeled glucose produced by photo-synthesis.

Some troubles of the cyclotron happened: (1) in February, a small amount of oil for the deflector cooling rushed out into the vacuum chamber; (2) electric insulation of the magnet coil was damaged because of miss operation done without water cooling; (3) about 30  $\ell$  of water leaked out into the vacuum chamber from a tube for ion source cooling in December.

ECT imaging of positron emitters utilizes the annihilation coincidence detection, the annihilation occurring at the end of the positron range. Thus, the positron range is naturally smaller than the spatial resolution of ECT instrument itself. The range of positrons emitted from  $^{11}\text{C}$ ,  $^{13}\text{N}$ ,  $^{15}\text{O}$ , and  $^{18}\text{F}$  in Mylar and Al foils have been measured by a  $2\pi$  gas flow counter (Geiger-Müller region). The results are shown in Fig. 1, and the 1/10 thicknesses are tabulated with the maximum positron energies.

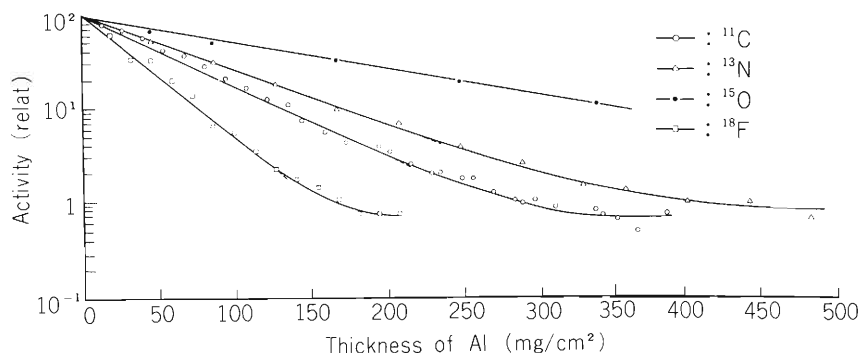


Fig. 1. Absorption curve of positron in Al.

Table 1. 1/10 thickness of positrons.

Nuclide	Mylar (g/cm <sup>2</sup> )	Al (g/cm <sup>2</sup> )	E (MeV)
$^{11}\text{C}$	0.120	0.131	0.97
$^{13}\text{N}$	0.169	0.170	1.19
$^{15}\text{O}$	—	0.346	1.74
$^{18}\text{F}$	0.073	0.077	0.635

\* Takeda Chemical Industries, Ltd.

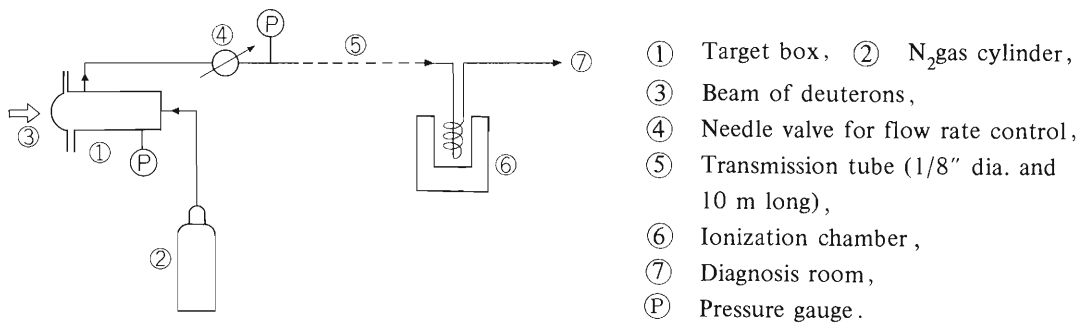


Fig. 2 Flow diagram of continuous gas flow system for <sup>15</sup>O production.

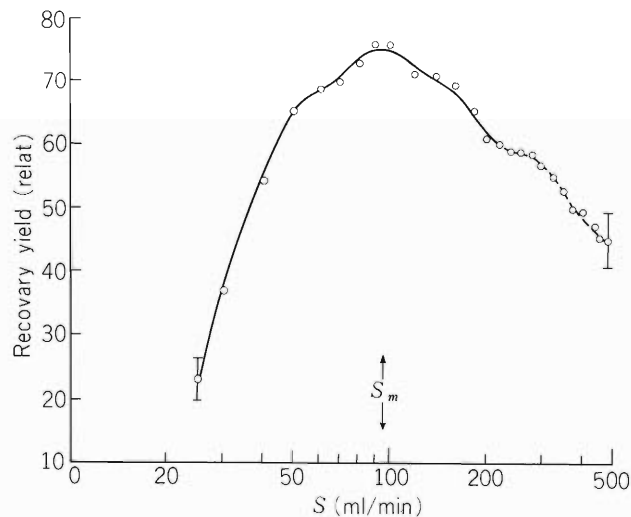


Fig. 3. Recovery yield vs. flow rate <sup>15</sup>O production at continuous flow.

At present, the spatial resolution of the positron ECT is about 10 mm, while the 1/10 thicknesses of positrons emitted from <sup>11</sup>C, <sup>13</sup>N, <sup>15</sup>O, and <sup>18</sup>F are below 4 mm in water as shown in the Table 1. We may conclude that the spatial resolution of the positron ECT is not degraded by the positron range for positrons emitted from those nuclei.

The target gas of nitrogen under bombardment by deuterons is continuously swept out of the target box and transported to diagnosis room. The flow diagram is shown in Fig. 2. Target volume and pressure, and sweep gas flow rate affect recovery yield at the diagnosis room. An example of the yield vs. the flow rate is shown in Fig. 3.

In Fig. 3, the yield has a maximum at the flow rate of  $s_m$ . In the region of  $s < s_m$ , the yield increases exponentially with the flow rate due to the decrease of the decay in transit from the target box to the diagnosis room. In the region of  $s > s_m$ , the yield decreases gradually with the flow rate. It is caused by the shortening of irradiation time. For a closed target irradiation, the yield  $C$ (mCi) during the time  $t$ (sec.) is expressed by the following equation,<sup>2)</sup>

$$C = C_0 I \left\{ 1 - \exp(-\lambda t) \right\}, \quad (1)$$

where  $C_0$ (mCi/ $\mu$ A) is the saturation activity per beam current,  $I$ ( $\mu$ A) is the beam current and  $\lambda$  is the decay constant. When  $\lambda t$  is small, Eqn.(1) is approximately equal to  $C = C_0 I \lambda t$ .

For a continuous flow, the equation for the recovery yield is as follows:

$$C_f = C_0 \lambda \exp(-\lambda V_a/s)/(1 + \lambda V_t P_t/s), \quad (2)$$

where  $V_a$  is the nominal volume of the transmission tube from the target box to the diagnosis room,  $s$  is the flow rate and  $V_a/s$  is the transit time.  $V_t$  and  $P_t$  are the volume and pressure of the target box, respectively. We are going to check Eqn.(2) experimentally.

An apparatus for automatic synthesis of methionine  $^{11}\text{C}$  from homocystein thiolactone and  $^{11}\text{CH}_3\text{I}$  has been set up. A schematic diagram of its main part is shown in Fig. 4. There, Block A is a source of distilled water and organic solvents, Block B is the portion for the introduction of the product into a syringe through a millipore-filter, and Block C consists of a waste reservoir and a source of reduced pressure. Beside these, a box is attached with tubes for supplying liquids of desired temperatures and for pressure addition and evacuation.

Methionine- $^{11}\text{C}$  is synthesized in Reaction Flask in Fig. 4 and separated by liquid chromatography to give final product ready for intravenous injection. The entire process is completed in 15 min. The yield is 80 %, when  $^{11}\text{CH}_3\text{I}$  is introduced into the apparatus with less than 3 ml of an inert gas. Some efforts are needed to concentrate  $^{11}\text{CH}_3\text{I}$  in such a small amount of gas.

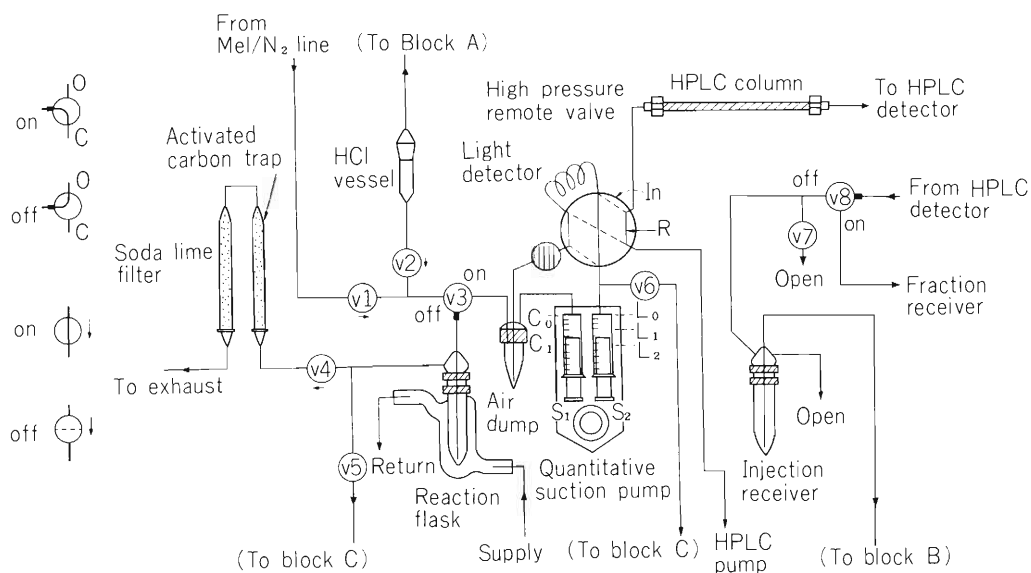


Fig. 4. Automatic methylation apparatus.

## References

- 1) N. Feather: Proc. Cambridge Phil. Soc., 34, 599 (1938); L.E. Glendenin: Nucleonics, Jan., p. 12 (1948).
- 2) J.C. Clark, and P.D. Buckingham: "Short-lived Radioactive Gases for Clinical Use", Butterworth, London, p. 323 (1975).

## V. RADIATION MONITORING

### 1. Routine Monitoring of the Cyclotron

M. Koyama, K. Igarashi, I. Usuba  
S. Fujita, and I. Sakamoto

Results of routine radiation monitoring carried out on the cyclotron from April 1981 to March 1982 are described.

No remarkable change in leakage radiation and residual activities was observed during this period. Some aspects of the leakage radiation are described in the following report.

#### (1) Surface and air contamination

The surface contamination has been kept below  $10^{-5}$   $\mu\text{Ci}/\text{cm}^2$  on the floor of cyclotron room, the underground passage and hot laboratory, and below  $10^{-6}$   $\mu\text{Ci}/\text{cm}^2$  in the experimental areas and chemical laboratories. The radioactive nuclides found by the  $\gamma$ -ray spectrometry were  $^{22}\text{Na}$ ,  $^{58}\text{Co}$ ,  $^{60}\text{Co}$ ,  $^{65}\text{Zn}$ ,  $^{75}\text{Se}$ ,  $^{183}\text{Re}$ ,  $^{185}\text{Os}$ , and  $^{137}\text{Cs}$ . The contamination was wiped off twice a year, and immediately after this decontamination, the contamination on the floor of the above places had been reduced to a value below  $10^{-7}$   $\mu\text{Ci}/\text{cm}^2$ .

When radioactive substances were handled in the hot laboratory and chemical laboratories, slight contamination of the air in the draft chamber was observed. The air in the draft chamber was discharged through the exhaust, and the value of radioactivity concentration in the exit was

Table 1. Annual exposure dose received by the cyclotron workers from April 1981 to March 1982.

Workers	Number of persons			Total	Collective dose (man-mrem)
	Dose undetectable	10 – 100 (mrem)	> 100 (mrem)		
Operators	3	5		8	180
Nuclear physicists	6	3		9	30
Accelerator physicists	15	3		18	40
Physicists in other fields	25	3		28	90
Nuclear chemists	3	6	2	11	700
Radiation chemists	2			2	
Biological chemists	8			8	
Health physicists	5			5	
Total	67	20	2	89	1040

Average annual dose per person: 11.7 mrem

Maximum individual annual dose: 180 mrem

below  $10^{-12}$   $\mu\text{Ci}/\text{cm}^3$ . The quantity of activities on the glass fiber filter in the exhaust was  $10^{-2} - 10^{-4}$   $\mu\text{Ci}/100 \text{ cm}^2$ , and the radioactive nuclides were  $^{76}\text{Br}$  and  $^{117\text{m}}\text{Sn}$ .

(2) Drainage

The radioactive concentration of the drain water from the cyclotron building was found to be of the order of  $10^{-7}$   $\mu\text{Ci}/\text{cm}^3$ . The total quantity of activities in the aqueous effluents in this period was about 3  $\mu\text{Ci}$ , and the radioactive nuclide found by the  $\gamma$ -ray spectrometry was mainly  $^{60}\text{Co}$ .

(3) Personnel monitoring

The external exposure dose to personnel was measured with  $\gamma$ -ray and neutron film badges. The dose received during the present period by all the cyclotron workers is shown in Table 1. The collective  $\gamma$ -ray dose to all workers was 1040 man-mrem, while the collective dose owing to thermal and fast neutron exposures were too small to be detected. The collective dose to the cyclotron workers is about 55 % of the value in the preceding period.

In this period the average annual dose per person was 11.7 mrem, and the maximum individual annual dose was 180 mrem.

## V-2. Leakage-Radiation Measurement at the Underground Passage of the Cyclotron Building

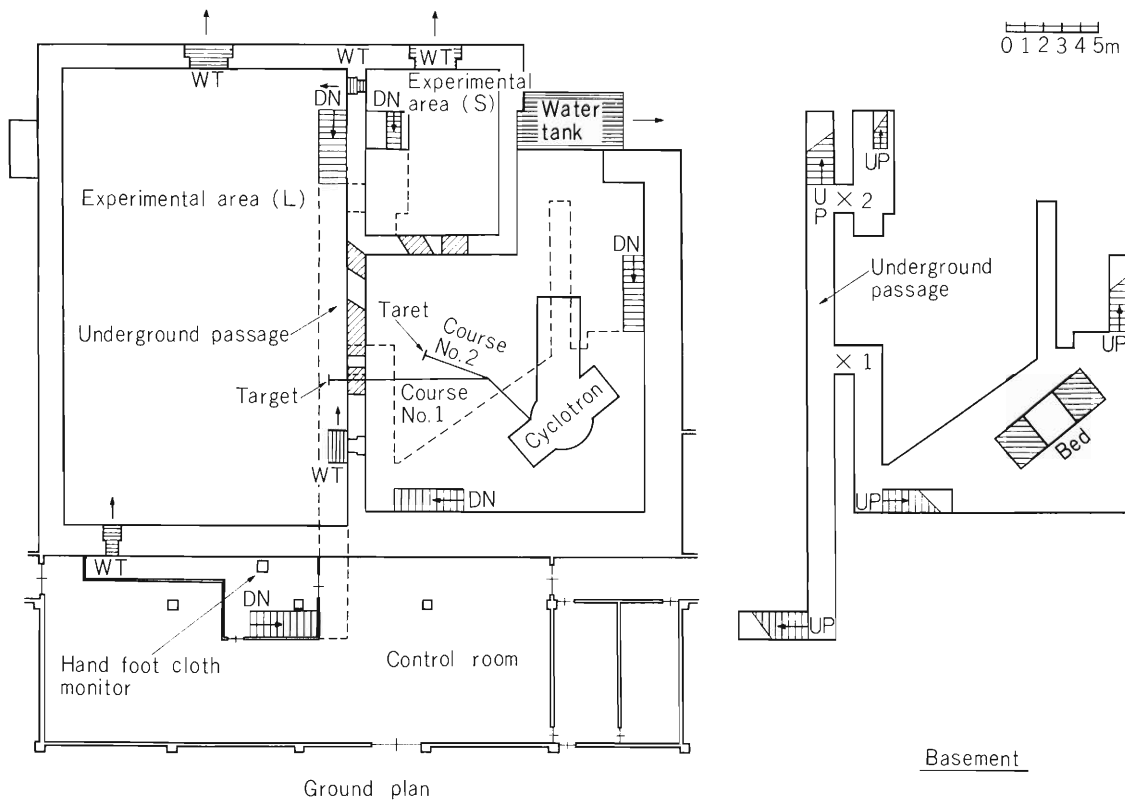
I. Sakamoto and S. Fujita

Leakage radiation during operation of the cyclotron at the underground passage of the cyclotron building was measured. Leakage dose received from April 1981 to March 1982 by  $\gamma$ -ray and neutron film badges which were left at the underground passage, are shown in Table 1. No machine time was allotted for deuteron acceleration in this period.

Table 1. Leakage radiation dose (in mrem) at the underground passage of the cyclotron building from April 1981 to March 1982.

Point of observation*	1	2
Radiation		
$\gamma$ -rays (mrem)	1340	0
Thermal neutrons (mrem)	380	0
Fast neutrons (mrem)	90	40
Total (mrem)	1810	40

\* See the figure shown below.



As to the dose values at point No. 1 measured every month, the maximum total dose of 430 mrem was observed in July. In this case, the values of gamma dose and thermal neutron dose were 340 mrem and 90 mrem, respectively.

The fast neutron dose observed at point No. 1 in October was larger than those in other months. The values of thermal neutron dose and fast neutron dose were 40 mrem and 70 mrem. As a result of investigation, it was concluded that the increase of the neutron dose was mainly due to  $^3\text{He}$ -particle activation analysis for surface oxygen on silicon, aluminum, tin and zinc in the beam course No. 2 carried out in October. Moreover, in this month, about 2 mCi of radioisotopes were produced by  $^{59}\text{Co}(^3\text{He}, n)^{61}\text{Cu}$  and  $^{75}\text{As}(\alpha, 2n)^{77}\text{Br}$  reactions in the beam course No. 1 and No. 2.

### V -3. Leakage X-Ray Measurement on TANDETRON

I. Usuba, Y. Sasa, M. Uda, and H. Sakairi

X-ray monitoring was carried out on TANDETRON for the acceleration of Si and Au ions. Areal intensity distributions of leakage X-rays at 1 m above the ground were measured with an ionization chamber survey meter for X-rays and  $\gamma$ -rays (27 keV  $\sim$  2 MeV).

#### (1) Acceleration of Si ions

Si ions were accelerated on the operation condition that current intensity of injected  $\text{Si}^-$  ions is  $9 \mu\text{A}$  and terminal voltage is 0.5 MV. In this case energies of accelerated  $\text{Si}^{2+}$ ,  $\text{Si}^{3+}$ , and  $\text{Si}^{4+}$  ions were 2.4 MeV, 3.2 MeV, and 4.0 MeV, respectively and the currents were  $2 \mu\text{A}$ ,  $0.8 \mu\text{A}$ , and  $0.25 \mu\text{A}$ , respectively. Current of  $\text{Si}^+$  ions could not be measured because of a power limit of the analyzing magnet and those of ions with valence higher than 4 were negligibly small.

In the monitoring experiment,  $\text{Si}^{4+}$  ions were selected and transported to a thick Cu target. The leakage of X-rays was not detected. By removing part of shielding Pb plate of thickness 2 mm, surrounding the tank of  $\text{SF}_6$  gas, leakage of X-rays became slightly detectable. Results of the intensity distribution of measured X-rays are shown in Fig. 1.

The leakage X-rays could not be detected around the target chamber.

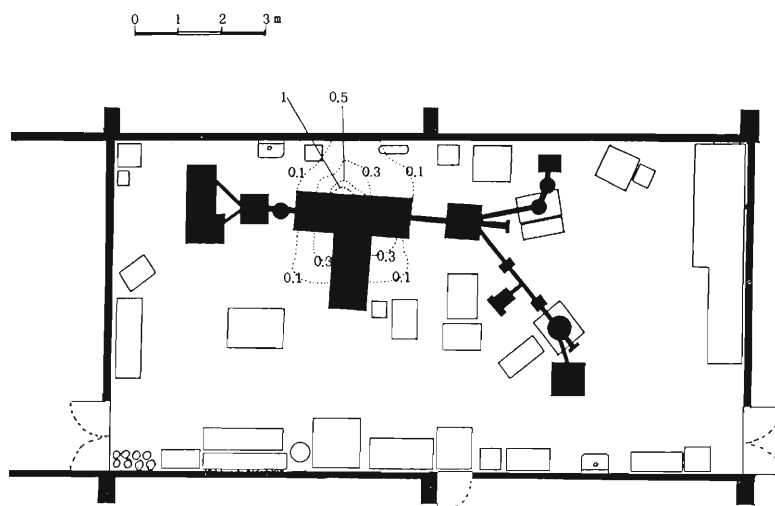


Fig. 1. Distribution of leakage X-ray intensities (mR/h) at 1 m above the ground for Si ion acceleration (4 MeV,  $0.25 \mu\text{A}$ ).

#### (2) Acceleration of Au ions

Acceleration of Au ions were carried out on the condition that current intensity of injected  $\text{Au}^-$  ions is  $4 \mu\text{A}$  and terminal voltage is 0.7 MV. In this operation, energies of accelerated  $\text{Au}^{3+}$  and  $\text{Au}^{4+}$  ions were 2.8 MeV and 3.5 MeV, respectively and the currents were  $1.2 \mu\text{A}$  and  $2.0 \mu\text{A}$ , respectively. Currents of  $\text{Au}^+$  and  $\text{Au}^{2+}$  ions could not be measured and those of ions with valence higher than 4 were negligibly small. In the monitoring measurement,  $\text{Au}^{4+}$  ions were selected and transported to a thick brass target. The leakage of X-rays was not detected as for the Si ions. By

removing the shielding Pb plate in the same way as for the Si ions, the intensity distribution of leakage X-rays was measured as shown in Fig. 2.

No leakage X-rays was observed in this case too around the target chamber.

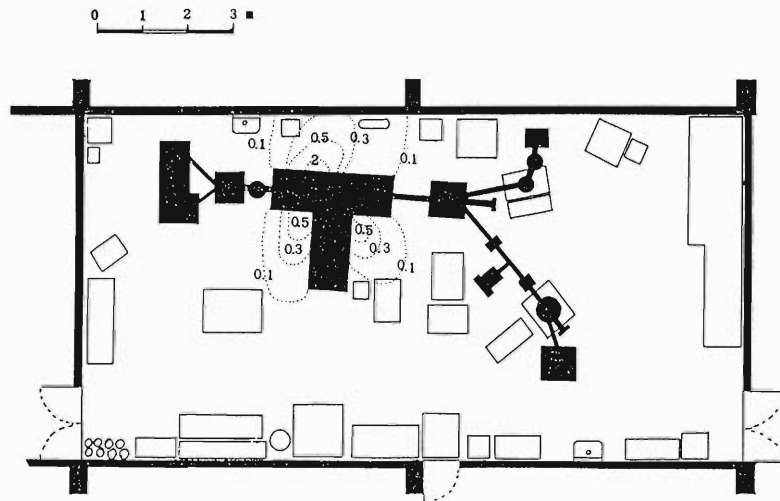


Fig. 2. Distribution of leakage X-ray intensities (mR/h) at 1 m above the ground for Au acceleration (3.5 MeV,  $4\mu\text{A}$ ).

#### V-4. Radiation Levels Due to Neutrons from the Cyclotron outside the Cyclotron Building

T. Shikata, S. Fujita, I. Kohno, H. Kamitsubo, M. Okano,  
T. Nakamura, T. Kosako, A. Hara,\* and S. Iwai\*

Contribution of neutrons generated at the cyclotron to the environmental radiation level was investigated in 1968, using a large  $\text{BF}_3$  counter covered with 2 cm polyethylene moderator. It was found that leakage flux from the cyclotron building gave an average increment of only several percent of cosmic-ray level at the cyclotron monitoring post.<sup>1)</sup>

Recently an experiment to study the effects of fast neutron irradiation in the plastics and elastomers started at our laboratory and high intensity neutrons were generated for many hours in the cyclotron vault. Taking this opportunity, distribution of leakage neutron flux or dose rates were measured at several points around the cyclotron.

As we did not know precise neutron spectra, we measured neutrons with three kinds of detectors having different sensitivity to high energy neutrons, to get as accurate data as possible. A neutron rem counter, a  $\text{BF}_3$  counter (Bonner cylinder) and two helium-3 counters of different gas pressures were used. The rem counter was calibrated in the neutron reference field at the Electrotechnical Laboratory. A conversion factor from the counting rate (counts/sec.) to dose rate ( $\mu\text{rem/h}$ ) was obtained as  $0.21 \mu\text{rem/cps}$  taking into account the energy dependence of intensity in the neutron energy spectra. The  $\text{BF}_3$  counter was used with and without the moderator. Four polyethylene moderators of 1, 3, 6, and 10 cm in thickness covered with 0.5 mm cadmium plate were prepared for it. The helium-3 counters which were developed by M. Okano et al. were also used with and without polyethylene moderators, the effective thickness of which was 3, 6, and 15 cm. The bare helium-3 counter is very sensitive to thermal neutrons and its sensitivity to the fast neutrons (for example,  $E_n > 1 \text{ MeV}$ ) is 0.1 % or less compared with that to the thermal neutrons<sup>2)</sup> so that we can assume that it detect only slow neutrons.

Fast neutrons were generated in the cyclotron vault by bombarding a thick beryllium target with 20 MeV deuterons. The average beam current was  $10 \mu\text{A}$ . Neutrons were measured at various positions inside the campus of the institute, on the roof of the cyclotron building and in the large experimental hall. Figure 1 shows the positions of the measurements. At the cyclotron monitoring post (indicated as CMP in Fig. 1) neutrons were measured with all counters mentioned above. The counting rates (cps) were tabulated in Table 1. Using conversion factor of neutron rem counter the dose rate due to neutrons was estimated as  $0.35 \mu\text{rem/h}$  at the cyclotron monitoring post. The conversion factor of the high pressure helium-3 counter with a moderator of 15 cm thick was estimated to be  $1.38 \mu\text{rem/cps}$ . From the data of this counter the dose rate was obtained as  $0.33 \mu\text{rem/h}$ . Dose rate due to cosmic-ray neutrons, which is estimated as about  $0.16 \mu\text{rem/h}$  at the ground level in Japan, is included in these data.

The dose rates at the linac monitoring posts (indicated as LMP I and LMP II in Fig. 1) were measured with helium-3 counters and obtained as  $0.23$  and  $0.47 \mu\text{rem/h}$ , respectively. Analysis of the data taken with other counters is in progress. From the present measurements it is

\* Institute for Nuclear Study, University of Tokyo.

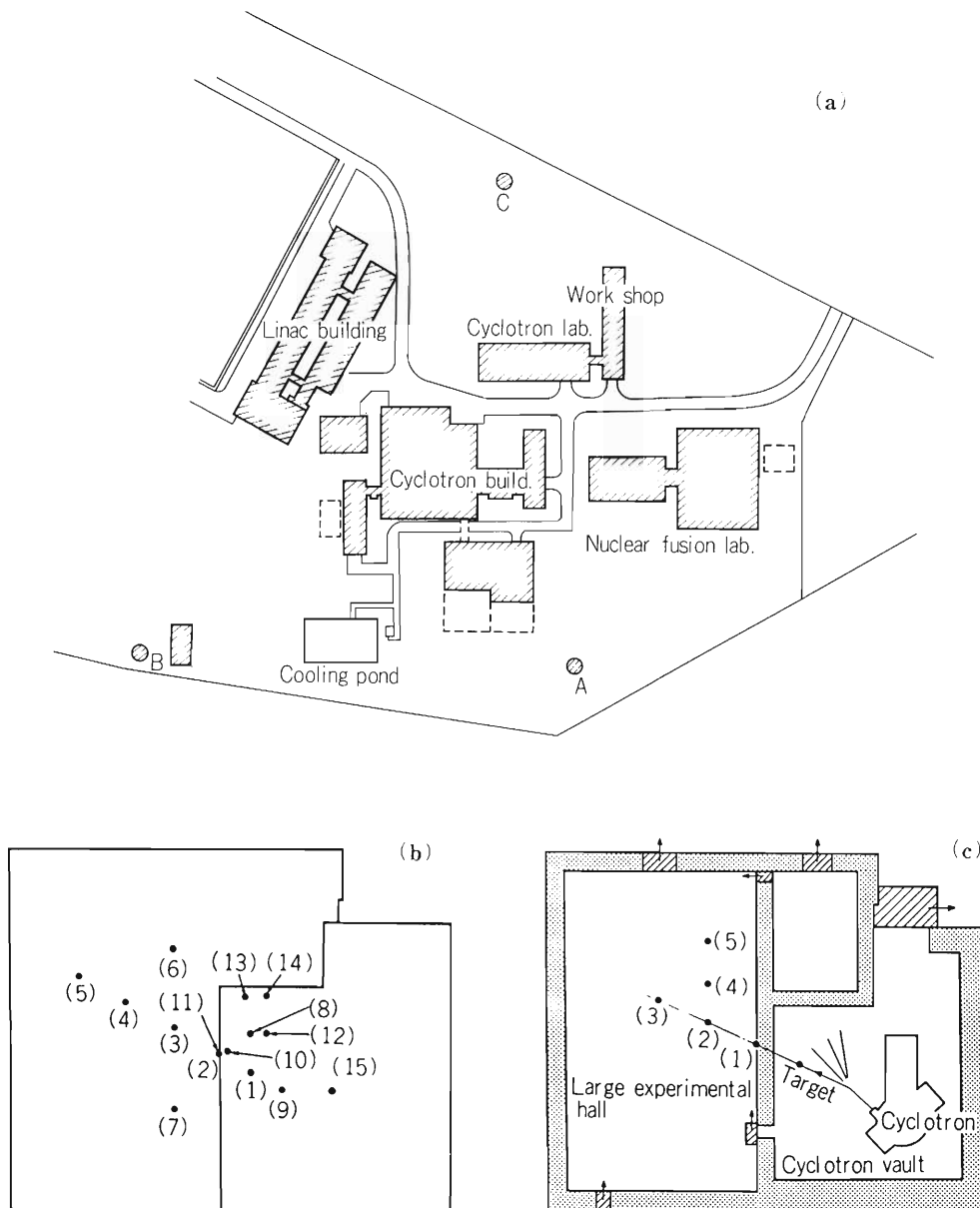


Fig. 1. Positions of the measurements.

(a) Plan of an environment around the cyclotron,

(b) Positions of measurements of the neutron dose on the roof of the cyclotron building,

(c) Positions of measurements of the neutron dose in the experimental hall.

confirmed that the radiation levels due to neutrons from the cyclotron are less than 1 mrem/year even if we assume the cyclotron accelerates deuterons at highest energy for three thousands hours which corresponds to two thirds of total beam time.

In order to compare these data with calculations of sky-shine, we measured neutron fluxes on the roof of the cyclotron building. The results are given in Table 2. Dose rates in the large experimental hall were also measured and listed in Table 3.

Table 1. Counting rates of neutron at the cyclotron monitoring post (CMP), linac monitoring post I (LMP I) and II (LMP II).

Counters	Counting rates (counts per second)		
	CMP	LMP I	LMP II
Rem counter	1.67 (E - 03) <sup>c)</sup>		
BF <sub>3</sub> (bare)	4.30 (E - 02)		
(M-10) <sup>a)</sup>	1.47 (E - 02)		
(M-6)	3.91 (E - 02)		
(M-3)	4.26 (E - 02)		
(M-1)	1.46 (E - 02)		
<sup>3</sup> He-I (bare) <sup>b)</sup>	3.83 (E - 01)	4.16 (E - 01)	9.4 (E - 01)
(M-3)	6.5 (E - 01)	3.22 (E - 01)	
(M-6)	5.3 (E - 01)	4.37 (E - 01)	
(M-15)	2.4 (E - 01)	1.68 (E - 01)	3.4 (E - 01)
<sup>3</sup> H-II (bare) <sup>b)</sup>	1.15		1.22
(M-3)	1.15		
(M-15)	1.27		1.2

a) (M-10) indicates that the detector is covered with a polyethylene moderator of 10 cm thick.

b) <sup>3</sup>He-I and <sup>3</sup>He-II are helium-3 counters, the gas pressure of which are 9.5 atm. and 2.8 kg/cm<sup>2</sup>, respectively.

c) Read as  $1.67 \times 10^{-3}$ .

Table 2. Dose rates on the roof of the cyclotron building.

Measuring points <sup>a)</sup>	Counting rates (cps)	Dose rates (mrem/h)
(1)	4.92 (E - 01)	1.0 (E - 01)
(2)	1.53 (E - 01)	3.2 (E - 02)
(3)	4.6 (E - 02)	9.7 (E - 03)
(4)	2.41 (E - 02)	5.7 (E - 03)
(5)	2.37 (E - 02)	5.0 (E - 03)
(6)	3.41 (E - 02)	7.2 (E - 03)
(7)	3.06 (E - 02)	6.4 (E - 03)
(8)	6.49	1.37
(9)	2.54 (E - 01)	5.3 (E - 02)
(10)	1.35 (E + 01)	2.8
(11)	2.97	6.2 (E - 01)
(12)	8.35 (E + 01)	1.76 (E + 01)
(13)	7.17 (E - 01)	1.5 (E - 01)
(14)	3.42	7.2 (E - 01)
(15)	1.73 (E - 01)	3.6 (E - 02)

a) Refer to Fig. 1(b)

Table 3. Dose rates in the large experimental hall.

Measuring points <sup>a)</sup>	Counting rates (cps)	Dose rates (mrem/h)
(1)	1432.6	301.6
(2)	118.8	25.0
(3)	29.8	6.3
(4)	21.0	4.4
(5)	7.0	1.5

a) Refer to Fig. 1(c)

#### References

- 1) M. Wada, M. Okano, I. Sakamoto, and T. Hamada: IPCR Cyclotron Progr. Rep., 2, 163 (1968).
- 2) T. Hamada, M. Okano, K. Izumo, T. Katou, H. Kumagai, and M. Nishida: Kankyo Hoshano Chosa Kenkyu Seika Rombun Shorokushu, 22, 147 (1979); *ibid.*, 23, 155 (1980).

## V-5. Radiation Shielding for the RIKEN SSC Facility

T. Shikata, T. Kosako,\* S. Fujita,  
S. Yamaji, and H. Kamitsubo

On the basis of the calculated results of Alsmiller et al.<sup>1)</sup> and of Roussin et al.<sup>2)</sup> a diagram which gives the neutron dose rate multiplied by  $r^2$  as a function of depth in the concrete shield was obtained previously.<sup>3)</sup> To see if there are any differences between the attenuation characteristics of parallel neutron beams incident on a slab<sup>2)</sup> and those of neutrons incident on a covering enclosing a point source, calculation was carried out with the ANISN code for the case of a spherical shell, at the center of which a monoenergetic neutron source was located. The spherical shell has inner radius of 6 m and thickness of 3 m. Results compared with those of Roussin et al. are shown in Fig. 1. There are no significant differences between these two calculations. Therefore, our previous estimation<sup>3)</sup> based on the results of Alsmiller et al. and of Roussin et al. can be supposed to be justified.

The thickness of walls around the target area was decided to be 2 or 3 m from the point of view of materials costs, but this thickness is inadequate to attenuate neutron dose beneath the proposed levels<sup>4)</sup> without beam dumps. Double layer beam dumps which incorporates a combination of iron and concrete were designed, as the use of ordinary concrete alone would result in the sacrifice of floor space.

Besides the estimation using a rough dose-geometry contours reported in a previous report,<sup>3)</sup> other calculations\*\*

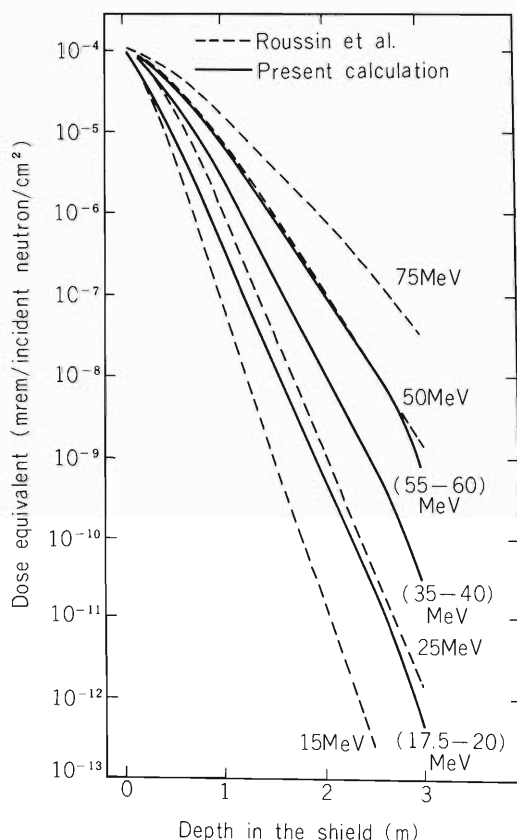


Fig. 1. Dose equivalent vs. depth in shield.  
Dashed line: slab.  
Solid line: spherical shell.

\* University of Tokyo, Institute for Nuclear Study. (Present Address: Research Center for Nuclear Science and Technology, University of Tokyo.)

\*\* S. Ban calculated the attenuations of neutron flux in concrete and iron slabs with the HET and the ARIES codes for monoenergetic neutrons incident on slabs. He offered us the calculated results kindly for the sake of our shielding design for RIKEN SSC. On the basis of this, we obtained a diagram showing the dose equivalent as a function of depth in iron and concrete shields, for the given source<sup>4)</sup> with their emitting angles as parameters.

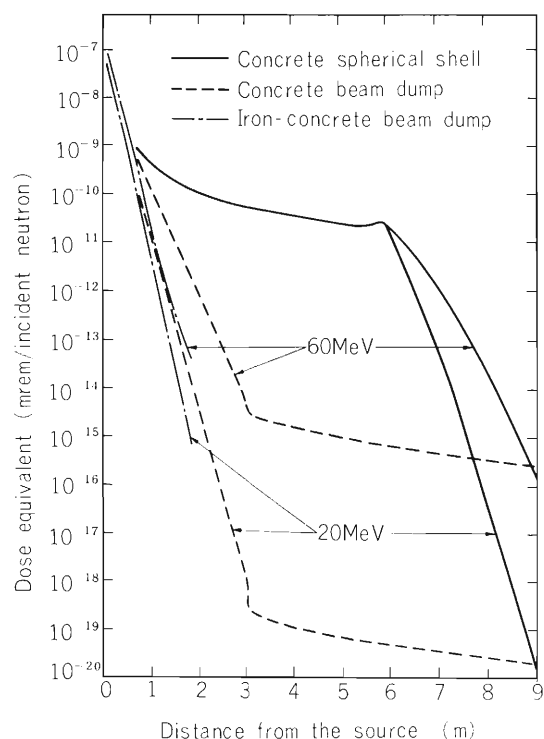


Fig. 2. Dose equivalent as a function of radial distance from a point source for three kind of shieldings.

- : Concrete spherical shell which has inner radius of 6 m and thickness of 3 m.
- - - : Concrete beam dump which has thickness of 3 m in radial direction and a spherical vacant space 0.1 m in radius at the center.
- · - · : Iron-concrete beam dump which has thickness of 0.8 m(iron) and 1 m (concrete) in radial direction, respectively, and has a spherical vacant space 0.1 m in radius at the center.

illustrate that the iron shielding of 0.8 m in thickness attenuates the neutron dose to nearly the same levels as does the concrete shielding of 2 m in thickness for a given neutron source.<sup>4)</sup> Dose attenuations for monoenergetic neutrons in a spherical concrete beam dump, in a iron-concrete beam dump, and in a large spherical concrete shell mentioned above were calculated also with the ANISN code. Here, the thickness of the concrete beam dump in radial direction is 3 m, and that of iron-concrete beam dump is the sum of 0.8 m (iron) and 1 m (concrete). Both beam dumps have, respectively, a spherical vacant space 0.1 m in radius at the center. Results of calculation are shown in Fig. 2. This shows that the spherical concrete beam dump and the large concrete spherical shell attenuate the neutron dose to nearly the same level at 9 m. Thus, our diagram<sup>3)</sup> mentioned at the beginning of this report seems to be appropriate for the shielding design of both wall and beam dump.

In designing the shield for high-energy accelerators, it is necessary to consider also the skyshine effect. In the previous report,<sup>3)</sup> Thomas' empirical equation was applied for the designing purpose. But Thomas' equation cannot be relied upon at a close distance such as the border of the campus which lies along the south side of the building for the SSC facility. Alsmiller et al.<sup>5)</sup> obtained the neutron importance functions, numerically, which may be used to estimate the dose equivalent from skyshine at radial distances of 11, 108, 495, and 1005 m for a monoenergetic point source with energies  $\leq 400$  MeV located 15 m above the ground and emitting neutrons into the upper hemisphere. On the other hand, Nakamura and Kosako<sup>6)</sup> showed a simple formula correlating the neutron dose equivalent (and/or flux) from skyshine as a function of the radial distance for the neutrons with energies  $\leq 15$  MeV emitted upwards isotropically within cones having several different apex angles from a point on the ground. In our situation, the roof above a target area lies nearly on the same level as the ground and the energies of neutrons passing through it will be in 175 MeV range. A simple application of Alsmiller et al.'s method to our situation would lead to some underestimation of the dose equivalent from skyshine, because the effects of the vertical location of the point source on the dose, especially at a close distance, are to be considered. The energy dependence of the ratio of the dose equivalent from skyshine due to one neutron, calculated using Nakamura and Kosako's formula compared to that calculated by Alsmiller et al., at radial distance of 11 m, is shown in Fig. 3. Here, as it is desirable that the shielding design should be performed somewhat with overestimation, the emitting direction and emitting half apex angle of neutrons were selected to be  $80 \sim 90^\circ$  (Alsmiller et al.) and  $85^\circ$  (Nakamura and Kosako), which give the largest dose equivalents at a close distance, respectively. Then, we assume the ratio of the dose from skyshine above mentioned to be 3 for neutrons of energies  $> 15$  MeV. Thus, a rough correction to our results estimated using Alsmiller et al.'s importance functions for 11 m was performed

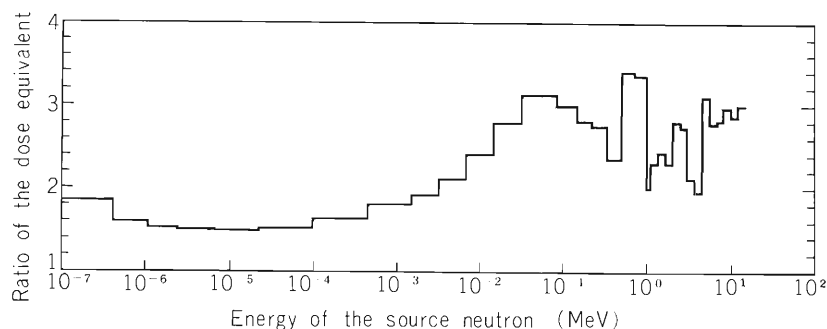


Fig. 3. Energy dependence of the ratio of the dose equivalent due to one neutron emitted from the source calculated using Nakamura and Kosako's formula to that calculated using Alsmiller et al.'s importance functions at radial distance of 11 m. Emitting direction and emitting half apex angle of neutrons were selected to be  $80^\circ \sim 90^\circ$  (Alsmiller et al.) and  $85^\circ$  (Nakamura and Kosako), respectively.

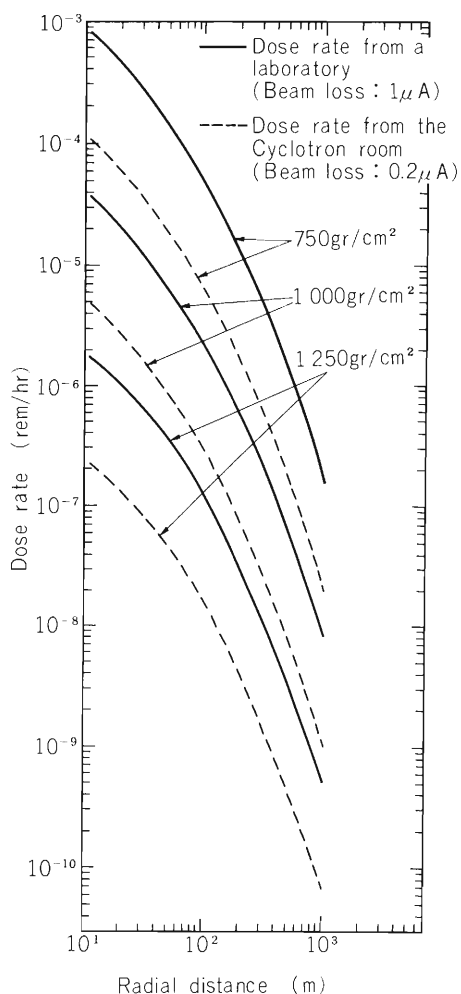


Fig. 4. Corrected dose rate from skyshine.

in the following way: the dose equivalent due to the neutrons with energy bin  $15 \sim 175$  MeV was multiplied by the factor 3, and this quantity was added to the dose equivalent due to neutrons of energies  $\leq 15$  MeV calculated using Nakamura and Kosako's formula. The dose equivalents at other distances (108, 495, 1005 m) were not corrected, because they were not necessary for our shielding design explicitly. The resultant diagram is shown in Fig. 4.

Using Fig. 2 in Ref. 3 and Fig. 4 the radiation level at any place can be estimated easily. Shielding by means

of the concrete covering of 2 or 3 m in thickness around the target area with the typical iron-concrete beam dumps (radial thickness in iron is 0.8 m and that in concrete is 1 ~ 2 m) will be adequate to reduce radiation intensity beneath the allowable levels.

#### References

- 1) R. G. Alsmiller, Jr., F. R. Mynatt, J. Barish, and W. W. Engle, Jr.: Nucl. Instr., 72, 213 (1969).
- 2) R. W. Roussin, R. G. Alsmiller, Jr., and J. Barish: Nucl. Eng. Design, 24, 250 (1973).
- 3) S. Fujita, S. Yamaji, and T. Shikata: Reports I.P.C.R. (in Japanese), 57, 239 (1981).
- 4) S. Fujita, S. Yamaji, and T. Shikata: IPCR Cyclotron Progr. Rep., 14, 203 (1980).
- 5) R. G. Alsmiller, Jr., J. Barish, and R. L. Childs: ORNL/TM-7512.
- 6) T. Nakamura and T. Kosako: Nucl. Sci. Eng., 77, 168 (1981).

## VI. LIST OF PUBLICATIONS

1. Accelerator development and accelerator physics
  - 1) N. Kishida, S. Kohmoto, A. Goto, E. Takenaka, and H. Kamitsubo: "Biological and Physical Irradiation Beam Channel for the RIKEN SSC", Reports I.P.C.R., (in Japanese), 58, 77 (1982).
2. Nuclear physics and nuclear instrumentation
  - 1) H. Kudo, Y. Nagame, H. Nakahara, K. Miyano, and I. Kohno: "Correlation between Angular Anisotropy and Fragment Mass in 15 MeV Proton-Induced Fission of  $^{232}\text{Th}$ ", Phys. Rev. C, 25, 909 (1982).
  - 2) H. Kudo, H. Muramatsu, H. Nakahara, K. Miyano, and I. Kohno: "Fission Fragment Yields in the Fission of  $^{232}\text{Th}$  by Protons of Energies 8 to 22 MeV", Phys. Rev. C, 25, 3011 (1982).
  - 3) S. Kohmoto, M. Ishihara, H. Kamitsubo, T. Nomura, Y. Gono, H. Utsunomiya, T. Sugitate, and K. Ieki: "Final-State Interaction and Time Information in  $^{14}\text{N}$ -induced Reactions Studied by  $\alpha$ - $\alpha$  Correlations", Phys. Lett., 114B, 107 (1982).
  - 4) T. Inamura and M. Wakai: "Calculation of Gamma-Ray Multiplicity Moments Associated with Massive-Transfer Reactions", J. Phys. Soc. Japan, 51, 1 (1982).
  - 5) M. Tohyama: "Proton Particle – Neutron Quasiparticle Calculations of the Isobaric Analog Resonances of the Tin Isotopes", Prog. Theor. Phys., 68, L317 (1982).
  - 6) T. Sugitate, T. Nomura, M. Ishihara, Y. Gono, H. Utsunomiya, K. Ieki, and S. Kohmoto: "Polarization of Preequilibrium Proton Emission in the  $^{93}\text{Nb} + ^{14}\text{N}$  Reaction", Nucl. Phys., A388, 402 (1982).
3. Atomic and solid-state physics
  - 1) T. Tonuma, Y. Awaya, T. Kambara, H. Kumagai, M. Kase, A. Yagishita., and I. Kohno: "Krypton  $K\beta/K\alpha$  Intensity Ratios for 6 MeV/amu Ion Bombardment", Inner-Shell and X-Ray Physics of Atoms and Solids, Plenum Press, New York and London, p. 153 (1981).
  - 2) T. Tonuma, M. Kase, T. Matsuo, J. Urakawa, J. Takahashi, H. Kumagai, T. Kambara, and I. Kohno: "Production of Highly-Charged Ions by Heavy-Ion Bombardment of Rare-Gas Targets", Atomic Collision Res. in Japan Progr. Rep., No. 8, p. 96 (1982).
  - 3) Y. Awaya, A. Hitachi, T. Kambara, M. Kase, H. Kumagai, T. Tonuma, and A. Yagishita: "A Broad Range X-Ray Crystal Spectrometer and Angular Distributions of X-Rays Following Multiple Inner-Shell Ionization", Atomic Collision Res. in Japan Progr. Rep., No. 8, p. 99 (1982).
  - 4) A. Yagishita, T. Kambara, M. Kase, T. Tonuma, T. Matsuo, J. Urakawa, M. Namiki, and Y. Awaya: "Argon LMM-Auger Electron Spectra in  $\text{Ar}^{3+} + \text{Ar}$  Collisions", Atomic Collision Res. in Japan Progr. Rep., No. 8, p. 307 (1982).
  - 5) T. Kambara, Y. Awaya, M. Kase, A. Hitachi, T. Tonuma, and I. Kohno: "Target Gas Pressure Dependence of K X-Rays from 110 MeV Ne Ions", Atomic Collision Res. in Japan Progr. Rep., No. 8, 321 (1982).

- 6) A. Koyama, T. Shikata, H. Sakairi, and E. Yagi: "Secondary Electron Emission from Metal Targets under Heavy Ion Bombardment", *Jpn. J. Appl. Phys.*, 21, 586 (1982).
  - 7) A. Koyama, T. Shikata, H. Sakairi, and E. Yagi: "Dependence of Secondary Electron Emission Coefficients on  $Z_1$  in Metal Targets under Bombardment with Bare Projectiles", *Jpn. J. Appl. Phys.*, 21, 1216 (1982).
  - 8) K. Maeda and M. Uda: "Computer Programs for Quantitative Analysis by PIXE(I)", *Reports I.P.C.R.*, (in Japanese), 58, 96 (1982).
  - 9) T. Kambara, Y. Awaya, A. Hitachi, M. Kase, I. Kohno, and T. Tonuma: "X-Rays from Radiative Electron Capture Induced by 110 MeV Ne Ions", *J. Phys. B: At. Mol. Phys.*, 15, 3759 (1982).
  - 10) A. Hitachi, H. Kumagai, and Y. Awaya: "Broad Range X-Ray Crystal Spectrometer", *Nucl. Instr. Methods*, 195, 631 (1982).
  - 11) T. Okada, S. Ambe, F. Ambe, and H. Sekizawa: "Emission Mössbauer Studies of Carrier-Free Pentavalent Antimony-119 Ions Adsorbed on  $\alpha$ -Fe<sub>2</sub>O<sub>3</sub> and Cr<sub>2</sub>O<sub>3</sub>", *J. Phys. Chem.*, 86, 4726 (1982).
  - 12) K. Kaeda and M. Uda: "Radiative Auger Emission from KL Double Hole States", *Phys. Lett.*, 91A, 223 (1982).
  - 13) H. Endo and M. Uda: "Atomic Number Dependence of L-Shell Vacancy Rearrangement Probabilities on  $K\alpha$  X-Ray Satellites Induced by 6 MeV/amu N<sup>4+</sup> Impacts", *Z. Phys. A*, 306, 187 (1982).
  - 14) Y. Awaya, H. Kumagai, and A. Hitachi: "Position Sensitive Proportional Counter for X-ray Measurements", *The Handbook of Atomic Collisions -Techniques-*, Study Group of Fundamental Atomic Process, (in Japanese), p. 74 (1982).
  - 15) K. Ishii, M. Sebata, M. Kamiya, A. Kuwako, S. Morita, Y. Awaya, and T. Tonuma: "K-Shell Vacant Production in Light-Element with  $\alpha$  Particles and N<sup>7+</sup> Ions of 5, 6, and 7 MeV/amu", *J. Phys. Soc. Japan*, 51, 4021 (1982).
  - 16) H. Sakairi, E. Yagi, A. Koyama, and R.R. Hasiguti: "The Damage Function Based on the Focusing Model", *Point Defects and Defect Interactions in Metals*, Univ. of Tokyo Press, Tokyo, p. 818 (1982).
4. Radiochemistry, radiation chemistry and radiation biology
- 1) K. Kimura, K. Mochizuki, T. Fujisawa, and M. Imamura: "Measurement of the Decay and Time-Resolved Spectra of the Emission from  $\sigma$ -Excitons in KBr in the Nano Second Range, Produced by Heavy-Ion Irradiation", *Phys. Letters*, 78A, 108 (1980).
  - 2) Y. Itoh and T. Nozaki: "Oxygen Depth Profiling by Activation with the  $^{16}\text{O}(^3\text{He}, p)^{18}\text{F}$  Reaction", *J. Radioanal. Chem.*, 70, 329 (1982).
  - 3) T. Nozaki: "Chemical Separation of  $^{18}\text{F}$  as  $\text{KBF}_4$  in Oxygen Analysis by the  $^{16}\text{O}(^3\text{He}, p)^{18}\text{F}$  Reaction", *J. Radioanal. Chem.*, 72, 527 (1982).
  - 4) H. Emori, M. Umehara, M. Takeya, K. Nomura, Y. Terai, and T. Nozaki: "Determination of Oxygen in GaAs by  $^3\text{He}$  Activation Analysis", *Gallium Arsenide and Related Compounds 1981*, *Inst. Phys.*, Bristol, p. 47 (1982).
  - 5) M. Iwamoto, T. Nozaki, Y. Takahashi, and K. Usami: "Distribution of Forward Recoil Range of  $^{18}\text{F}$  Formed by Various Nuclear Reactions", *Radiochim. Acta*, 30, 73 (1982).

- 6) T. Takahashi, F. Yatagai, K. Aoki, and S. Yamanaka: "Track Structure Theories and Inactivation Cross Sections of Bacterial Spores for Heavy Ions", *Ionizing Radiat.*, 9, 24 (1982).
- 7) T. Irie, K. Fukushi, O. Inoue, T. Yamasaki, T. Ido, and T. Nozaki: "Preparation of  $^{18}\text{F}$ -labeled 6- and 2-fluoro-9-benzylpurine as a Potential Brain-scanning Agent", *Int. J. appl. Radiat. Isotopes*, 33, 633 (1982).
- 8) Y. Itoh and T. Nozaki: "Oxygen Depth Profiling in Heat-treated Silicon as Measured by Charged Particle Activation Analysis", TG SSD 81-115~130 IECE of Japan (1982).

**(Papers Presented at Meetings)**

1. Accelerator development and accelerator physics
  - 1) T. Fujisawa, K. Ogiwara, M. Hara, and S. Kohara: "Model Study of the Resonator for the RIKEN SSC", 1982 Spring Meeting of the Phys. Soc. Japan, Tokyo, Mar. (1982).
  - 2) M. Hara, T. Wada, A. Toyama, and F. Kikuchi: "Calculation of RF Electromagnetic Field by Finite Element Method (II)", 1982 Spring Meeting of the Phys. Soc. Japan, Tokyo, Apr. (1982).
  - 3) N. Kishida, S. Kohmoto, A. Goto, E. Takenaka, and H. Kamitsubo: "Biological and Physical Irradiation Beam Channel for the RIKEN SSC", 1982 Spring Meeting of the Phys. Soc. Japan, Tokyo, Apr. (1982).
  - 4) K. Ikegami, K. Ogiwara, I. Kohno, and T. Kageyama: "New Gas Feed System and Acceleration Test of Heavy Ions with Gas Mixing", 6th Symp. on Ion Source and Ion-Assisted Technology, Tokyo, June (1982).
  - 5) M. Kase and Y. Miyazawa: "Heavy Ion Source for RIKEN Linac", 6th Symp. on Ion Source and Ion-Assisted Technology, Tokyo, June (1982).
  - 6) M. Kase: "Beam Bunch Probes of RIKEN Heavy Ion Linac", 7th Symp. on Linear Accelerator, Tsukuba, Aug. (1982).
  - 7) M. Kase, Y. Miyazawa, M. Hemmi, and T. Chiba: "Production of Various Ions with PIG type Ion Source", 7th Symp. on Linear Accelerator, Tsukuba, Aug. (1982).
  - 8) M. Yanokura: "ECR Heavy Ion Source for Linac (1)", 7th Symp. on Linear Accelerator, Tsukuba, Aug. (1982).
  - 9) M. Hara, T. Wada, T. Fukasawa, and F. Kikuchi: "Calculation of RF Electromagnetic Field by Finite Element Method", Meeting of the Japan Soc. for Simulation Technology, Tokyo, Sept. (1982).
  - 10) M. Hara, T. Wada, T. Fukasawa, and F. Kikuchi: "Calculation of RF Electromagnetic Field by Finite Element Method (III)", 37th Ann. Meeting of the Phys. Soc. Japan, Sapporo, Oct. (1982).
  - 11) M. Kase and T. Kubo: "Beam Bunch Probes at the RILAC", 37th Ann. Meeting of the Phys. Soc. Japan, Sapporo, Oct. (1982).
  - 12) M. Yanokura: "ECR Type Heavy Ion Source (1)", 37th Ann. Meeting of the Phys. Soc. Japan, Sapporo, Oct. (1982).
  - 13) H. Kamitsubo: "Status of RIKEN SSC", Proc. 4th Symp. on Accelerator Science and Technology, Wako, Nov., p. 19 (1982).

- 14) M. Odera and RILAC group: "Status of Operation of the Variable Frequency Heavy-Ion Linac, RILAC", Proc. 4th Symp. on Accelerator Science and Technology, Wako, Nov., p. 53 (1982).
- 15) T. Shikata, S. Fujita, S. Yamaji, H. Kamitsubo, and T. Kosako: "Design of Radiation Shielding for the RIKEN SSC", Proc. 4th Symp. on Accelerator Science and Technology, Wako, Nov., p. 63 (1982).
- 16) N. Nakanishi, Y. Yano, and A. Goto: "The Effect of a Resonance on the Beam in the RIKEN SSC", Proc. 4th Symp. on Accelerator Science and Technology, Wako, Nov., p. 99 (1982).
- 17) M. Kase: "Bunch Signal Sensitization by Use of Secondary Electron Emission", Proc. 4th Symp. on Accelerator Science and Technology, Wako, Nov., p. 111 (1982).
- 18) I. Yokoyama, M. Kase, S. Kohara, and Y. Yano: "Bunch Phase Monitor", Proc. 4th Symp. on Accelerator Science and Technology, Wako, Nov., p. 113 (1982).
- 19) M. Kase, M. Odera, T. Tonuma, and T. Kambara: "Linac Energy Tuning by Phase Control of Last Cavity", Proc. 4th Symp. on Accelerator Science and Technology, Wako, Nov., p. 115 (1982).
- 20) Y. Yano, N. Kishida, A. Goto, and N. Nakanishi: "Beam Diagnostic System for the RIKEN SSC", Proc. 4th Symp. on Accelerator Science and Technology, Wako, Nov., p. 149 (1982).
- 21) S. Nakajima, K. Ikegami, Y. Oikawa, and I. Takeshita: "Design of the Acceleration Chamber and the Evacuation System of the RIKEN SSC", Proc. 4th Symp. on Accelerator Science and Technology, Wako, Nov., p. 203 (1982).
- 22) K. Ikegami, S. Nakajima, and Y. Oikawa: "Test of the Model Pneumatic Expansion Seal", Proc. 4th Symp. on Accelerator Science and Technology, Wako, Nov., p. 207 (1982).
- 23) Y. Ishibe, H. Ohyama, Y. Sakamoto, K. Ikegami, S. Nakajima, Y. Oikawa, and S. Motonaga: "Preliminary Experiment on Discharge Cleaning of a Sector Magnet Vacuum Chamber for the RIKEN SSC (1)", Proc. 4th Symp. on Accelerator Science and Technology, Wako, Nov., p. 221 (1982).
- 24) K. Ikegami, S. Nakajima, Y. Oikawa, S. Motonaga, Y. Ishibe, H. Ohyama, and Y. Sakamoto: "Preliminary Experiment on Discharge Cleaning of a Sector Magnet Vacuum Chamber for the RIKEN SSC (2)", Proc. 4th Symp. on Accelerator Science and Technology, Wako, Nov., p. 223 (1982).
- 25) T. Kageyama, K. Ikegami, K. Ogiwara, S. Kohara, and I. Kohno: "Heavy Ion Source for IPCR Cyclotron", Proc. 4th Symp. on Accelerator Science and Technology, Wako, Nov., p. 237 (1982).
- 26) M. Kase, Y. Miyazawa, T. Chiba, M. Hemmi, and T. Inoue: "Multiply Charged Ion Production by the RILAC PIG Source", Proc. 4th Symp. on Accelerator Science and Technology, Wako, Nov., p. 239 (1982).
- 27) K. Ogiwara, T. Fujisawa, and Y. Oikawa: "Model Test of 1/5 Scale Movable Box Type RF Resonator for the RIKEN SSC", Proc. 4th Symp. on Accelerator Science and Technology, Wako, Nov., p. 247 (1982).
- 28) S. Kohara, T. Fujisawa, and Y. Chiba: "Basic Study of the RF High Power Amplifier for the RIKEN SSC (Study of the Screen Bypass Capacitor for the Final Stage)", Proc.

- 4th Symp. on Accelerator Science and Technology, Wako, Nov., p. 249 (1982).
- 29) M. Hara, T. Wada, T. Fukasawa, and F. Kikuchi: "Three Dimensional Analysis of RF Electromagnetic Field by Finite Element Method", Proc. 4th Symp. on Accelerator Science and Technology, Wako, Nov., p. 265 (1982).
  - 30) M. Hara, T. Wada, T. Fukasawa, and F. Kikuchi: "Two Dimensional Analysis of RF Electromagnetic Field by Finite Element Method", Proc. 4th Symp. on Accelerator Science and Technology, Wako, Nov., p. 271 (1982).
  - 31) S. Motonaga: "Present Status of the Sector Magnets of the RIKEN SSC", Proc. 4th Symp. on Accelerator Science and Technology, Wako, Nov., p. 293 (1982).
  - 32) A. Goto, H. Takebe, S. Motonaga, and T. Wada: "Measurements on the Trim Coil Fields and Optimization of the Trim Coil Currents for the RIKEN SSC", Proc. 4th Symp. on Accelerator Science and Technology, Wako, Nov., p. 295 (1982).
  - 33) H. Takebe, I. Takeshita, J. Fujita, I. Yokoyama, T. Wada, and S. Motonaga: "Magnetic Field Measuring System for the RIKEN SSC Sector Magnets", Proc. 4th Symp. on Accelerator Science and Technology, Wako, Nov., p. 301 (1982).
  - 34) N. Kishida and Y. Yano: "Design Study of Magnetic Deflection Channels for the RIKEN SSC", Proc. 4th Symp. on Accelerator Science and Technology, Wako, Nov., p. 309 (1982).
  - 35) M. Hara, T. Wada, and M. Deto: "Dynamic Structural Analysis of the Sector Magnet of the RIKEN SSC", Proc. 4th Symp. on Accelerator Science and Technology, Wako, Nov., p. 323 (1982).
  - 36) T. Inamura, N. Kishida, and Y. Hata: "The RIKEN SSC Beam Handling System", Proc. 4th Symp. on Accelerator Science and Technology, Wako, Nov., p. 345 (1982).
  - 37) J. Fujita, T. Kambara, K. Simizu, T. Wada, Y. Yano, and I. Yokoyama: "Design of Control System of the RIKEN SSC", Proc. 4th Symp. on Accelerator Science and Technology, Wako, Nov., p. 365 (1982).
  - 38) F. Kikuchi: "Three Dimensional Finite Element Program for Electromagnetic Waves", Theoretical Research on Diagnostic Methods in Fusion Plasma, Hakone, Nov. (1982).

## 2. Nuclear physics and nuclear instrumentation

- 1) T. Inamura: "Massive Transfer", Symp. on Mechanism of Heavy Ion Reactions, Tokyo, Feb. (1982).
- 2) T. Hasegawa, S. Kubono, N. Ueda, K. Iwatani, C. Tohei, K. Murakami, T. Fujisawa, and M. Sugitani: "Measurement of the Vector Analyzing Power of ( $\vec{d}$ ,  ${}^6\text{Li}$ ) Reaction", 1982 Spring Meeting of the Phys. Soc. Japan, Tokyo, Mar. (1982).
- 3) M. Sugitani, T. Hasegawa, Y. Ishizaki, S. Kubono, N. Ueda, K. Iwatani, T. Fujisawa, K. Murakami, and H. Nakamura: "Study of the Excited States of  ${}^{24}\text{Mg}(\vec{p}, p'){}^{24}\text{Mg}$  Reaction", 1982 Spring Meeting of the Phys. Soc. Japan, Tokyo, Mar. (1982).
- 4) Y. Gono: "High Spin States in Pb Region", 1982 Spring Meeting of the Phys. Soc. Japan, Tokyo, Mar. (1982).
- 5) Y. Itoh, Y. Gono, M. Sasagase, T. Kubo, and M. Sugawara: "In-beam  $\gamma$ -Ray Spectroscopy of  ${}^{216}\text{Ra}$ ", 1982 Spring Meeting of the Phys. Soc. Japan, Tokyo, Mar. (1982).
- 6) T. Inamura, M. Ishihara, K. Ieki, and S. Kohmoto: "In-plane/Out-of-plane Anisotropy of Gamma Rays from the  ${}^{159}\text{Tb}({}^{14}\text{N}, \alpha n)$  Reactions at  $E = 115$  MeV", 1982 Spring Meeting of the Phys. Soc. Japan, Tokyo, Apr. (1982).

- 7) A. Hashizume and T. Inamura: "Analysis of Deexcitation Gamma Rays from Multiply Coulomb-Excited  $^{167}\text{Er}$ ", 1982 Spring Meeting of the Phys. Soc. Japan, Tokyo, Apr. (1982).
- 8) K. Ieki and M. Ishihara: " $\gamma$ -Ray Circular Polarimeter", 1982 Spring Meeting of the Phys. Soc. Japan, Tokyo, Apr. (1982).
- 9) S. Yamaji, A. Iwamoto, K. Harada, and S. Yoshida: "A Numerical Analysis of 1280 MeV  $^{208}\text{Pb}$ -induced Reactions on  $^{94}\text{Zr}$ ,  $^{110}\text{Pd}$ ,  $^{148}\text{Sm}$  and  $^{170}\text{Er}$ ", 1982 Spring Meeting of the Phys. Soc. Japan, Tokyo, Apr. (1982).
- 10) T. Kubo, H. Ohnuma, T. Kishimoto, M. Sugitani, and T. Suehiro: "Deuteron D-state Effects on (d, p) Reaction at 55 MeV", 1982 Spring Meeting of the Phys. Soc. Japan, Tokyo, Apr. (1982).
- 11) I. Kohno: "Fission-like Heavy Fragments on Heavy Ion Nuclear Reaction", 1982 Spring Meeting of the Phys. Soc. Japan, Tokyo, Apr. (1982).
- 12) M. Ohshima, E. Minehara, M. Ishii, T. Inamura, and A. Hashizume: "Multiple Coulomb Excitation of  $^{167}\text{Er}$ ", INS Intern. Symp. on Dynamics of Nuclear Collective Motion, Fuji-Yoshida, July (1982).
- 13) Y. Gono: "In-Beam  $\alpha$ - and  $\gamma$ -Ray Study on  $^{215}\text{Fr}$  and  $^{217}\text{Ac}$ ", INS Intern. Symp. on Dynamics of Nuclear Collective Motion, Fuji-Yoshida, July (1982).
- 14) S. Yamaji, A. Iwamoto, K. Harada, and S. Yoshida: "Effect of the Mass Fragmentation Potential on the Width of the Mass Distribution in the Deep Inelastic Heavy Ion Collision", Intern. Conf. on Nucleus-Nucleus Collisions, Michigan, Sept. (1982).
- 15) M. Tohyama and S. Yamaji: "Two Particle- Two Hole Effects on the Mass Distributions in Deep Inelastic Heavy Ion Collisions", Intern. Conf. on Nucleus-Nucleus Collisions, Michigan, Sept. (1982).
- 16) M. Tohyama and S. Yamaji: "A Treatment of the Mass Distributions in Deep Inelastic Heavy Ion Collisions in the Time-dependent Coupled-Cluster Approximation", 37th Ann. Meeting of the Phys. Soc. Japan, Sapporo, Sept. (1982).
- 17) Y. Itoh, Y. Gono, T. Kubo, M. Sugawara, S. Hayashibe, M. Sasagase, T. Kono, and T. Nomura: "Levels in  $^{218}\text{Ra}$  and Dipole Transitions", 37th Ann. Meeting of the Phys. Soc. Japan, Sapporo, Sept. (1982).
- 18) I. Kohno, Y. Nagame, K. Sueki, and H. Nakahara: "Heavy Particle Emitting Reactions from 146 MeV  $^{20}\text{Ne} + ^{92,100}\text{Mo}$  Systems", 37th Ann. Meeting of the Phys. Soc. Japan, Sapporo, Oct. (1982).
- 19) K. Ieki, M. Ishihara, T. Inamura, S. Kohmoto, and H. Utsunomiya: "Circular Polarization of  $\gamma$ -rays Emitted in Heavy Ion Reactions", 37th Ann. Meeting of the Phys. Soc. Japan, Sapporo, Oct. (1982).
- 20) M. Ohshima, E. Minehara, M. Ishii, T. Inamura, and A. Hashizume: "Transition Probabilities in the Ground-State Rotational Band of  $^{167}\text{Er}$ ", 37th Ann. Meeting of the Phys. Soc. Japan, Sapporo, Oct. (1982).
- 21) T. Kubo, H. Ohnuma, T. Kishimoto, M. Sugitani, and T. Suehiro: " $(\vec{d}, p)$  and  $(\vec{p}, d)$  Reactions on Sn Isotopes", 37th Ann. Meeting of the Phys. Soc. Japan, Sapporo, Oct. (1982).
- 22) M. Takahashi, Y. Nagame, K. Sueki, and H. Nakahara: " $(^3\text{He}, n)$  Reactions", 26th Symp. on Radiochemistry, Niigata, Oct. (1982).

- 23) K. Sueki, H. Nakahara, Y. Nagame, M. Takahashi, and I. Kohno: "Heavy-Ion Reaction between  $^{14}\text{N}$  and  $^{62}\text{Ni}$ , the Excitation Functions Evaporation-like Products", 26th Symp. on Radiochemistry, Niigata, Oct. (1982).
- 24) H. Sakairi, E. Yagi, T. Kobayashi, and T. Urai: "RIKEN TANDETRON", Proc. 4th Symp. on Accelerator Science and Technology, Wako, Nov., p. 335 (1982).

### 3. Atomic and solid-state physics

- 1) T. Doke and T. Takahashi: "Stopping Powers of Ni, Ag, Au, and Pb for 7 MeV/n  $\alpha$ -Particles and Carbon Ions ( $Z_1^3$  Proportional Deviations from the Bethe Formula)", Japan – U.S. Seminar, Honolulu, Jan. (1982).
- 2) S. Sato, A. Masuyama, M. Iwaki, and H. Sakairi: "Ion Implantation in Diamond (II)", 29th Spring Meeting of the Japan Soc. Appl. Phys., Tokyo, Apr. (1982).
- 3) K. Aono and S. Namba: "Pulsed Laser Annealing of Ion Implanted GaP (V1)", 29th Spring Meeting of the Japan Soc. Appl. Phys., Tokyo, Apr. (1982).
- 4) A. Yagishita, T. Kambara, M. Kase, T. Tonuma, Y. Awaya, and Y. Miyazawa: "Ar L-MM Auger Spectra in  $\text{Ar}^{n+} + \text{Ar}$  ( $n = 2, 3, 4$ ) Collisions", 1982 Spring Meeting of the Phys. Soc. Japan, Yokohama, Apr. (1982).
- 5) T. Tonuma, A. Yagishita, M. Kase, T. Kambara, Y. Awaya, and I. Kohno: "Secondary Ion Production in Heavy-ion Atom Collisions", 1982 Spring Meeting of the Phys. Soc. Japan, Yokohama, Apr. (1982).
- 6) T. Takahashi, Y. Awaya, T. Tonuma, K. Izumo, A. Hashizume, A. Hitachi, S. Uchiyama, and T. Doke: "Stopping Powers for 7 MeV/n Carbon Ions and  $\alpha$ -Particles", 1982 Spring Meeting of the Japan Soc. Appl. Phys., Tokyo, Apr. (1982).
- 7) Y. Awaya, A. Hitachi, H. Kumagai, T. Kambara, T. Tonuma, M. Kase, A. Yagishita, T. Matsuo, J. Urakawa, and J. Takahashi: "Studies of Multiple-Innershell Ionizations by X-Ray Measurements", 6th Meeting of the Soc. for Atomic Collision Research, Tokyo, July (1982).
- 8) T. Matsuo, J. Urakawa, A. Yagishita, T. Kambara, M. Kase, Y. Awaya, and J. Takahashi: "Ar L-MM Auger Spectra in  $\text{Ar}^{3+} + \text{Ar}$  Collisions", 6th Meeting of the Soc. for Atomic Collision Research, Tokyo, July (1982).
- 9) K. Maeda and M. Uda: "RAE Satellite from KL Double Hole State", Intern. Conf. on X-Ray and Atomic Inner-Shell Physic, Eugene, Aug. (1982).
- 10) K. Fujima, K. Fuwa, and M. Uda: "Intensity Analysis of F  $K\alpha$ -Emission Satellite Spectra for Fluorine Compounds by the DV-X $\alpha$  Method", Intern. Conf. on X-Ray and Atomic Inner-Shell Physics, Eugene, Aug. (1982).
- 11) H. Endo and M. Uda: " $Z_2$  Dependence of L-Shell Vacancy Rearrangement Probability on  $K\alpha$  X-Ray Satellite", Intern. Conf. on X-Ray and Atomic Inner-Shell Physics, Eugene, Aug. (1982).
- 12) K. Aono, M. Iwaki, and S. Namba: "Annealing of Ion Implanted Gap", 43th Fall Meeting of the Japan Soc. Appl. Phys., Fukuoka, Sept. (1982).
- 13) S. Sato, A. Masuyama, M. Iwaki, and H. Sakairi: "Ion Implantation in Diamond (III)", 43th Fall Meeting of the Japan Soc. Appl. Phys., Fukuoka, Sept. (1982).
- 14) K. Oda, Y. Watanabe, S. Nanao, and N. Shiotani: "Radiation Damage in an Amorphous  $\text{Fe}_{80}\text{B}_{20}$  Alloy Bombarded with  $\text{C}^{4+}$  Ions", 91st Meeting of the Japan Inst. Metals, Sapporo, Sept. (1982).

- 15) Y. Higashiguchi, M. Narui, Y. Suzuki, H. Kayano, and E. Yagi: "Helium Embrittlement of Ti-Al Alloys", 91st Meeting of the Japan Inst. Metals, Sapporo, Sept. (1982).
  - 16) N. Nishiyama, K. Nagamine, T. Natsui, S. Nakajima, K. Ishida, Y. Kuno, J. Imazato, H. Nakayama, T. Yamazaki, and E. Yagi: "Critical Phenomena in Ni Studied with Pulsed  $\mu$ SR", Intern. Conf. Magnetism, Kyoto, Sept. (1982).
  - 17) K. Nishiyama, E. Yagi, K. Ishida, and K. Nagamine: "Muon Spin Rotation and Resonance in Ni Crystal", 37th Ann. Meeting of the Phys. Soc. Japan, Sapporo, Oct. (1982).
  - 18) Y. Awaya, T. Kambara, M. Kase, H. Kumagai, T. Matsuo, J. Urakawa, J. Takahashi, and M. Namiki: "Projectile Ar K X-Rays following Multiple Inner-Shell Ionization in Ar-ion-foil collisions at 30 MeV", 37th Ann. Meeting of the Phys. Soc. Japan, Sapporo, Oct. (1982).
  - 19) T. Kambara, Y. Awaya, M. Kase, I. Kohno, T. Tonuma, and A. Hitachi: "Target Gas Pressure Dependence of K-X Rays from 110 MeV Ne Ions", 37th Ann. Meeting of the Phys. Soc. Japan, Sapporo, Oct. (1982).
  - 20) T. Matsuo, J. Urakawa, A. Yagishita, T. Kambara, M. Kase, J. Takahashi, and Y. Awaya: "Ar L-MM Auger Electron Spectra in Ar<sup>3+</sup> + Ar Collisions", 37th Ann. Meeting of the Phys. Soc. Japan, Sapporo, Oct. (1982).
  - 21) T. Akioka, M. Kase, J. Kikuchi, and T. Doke: "Fano Factor of Xe Gas", 37th Ann. Meeting of the Phys. Soc. Japan, Sapporo, Oct. (1982).
  - 22) A. Hitachi, Y. Awaya, J. Takahashi, H. Kumagai, T. Kambara, M. Kase, T. Tonuma, and A. Yagishita: "Angular Distributions of X-rays Following Multiple Inner-Shell Ionizations", 37th Ann. Meeting of the Phys. Soc. Japan, Sapporo, Oct. (1982).
  - 23) T. Tonuma, M. Kase, T. Matsuo, J. Urakawa, J. Takahashi, H. Kumagai, T. Kambara, and I. Kohno: "Production of Highly-Charged Ions by Heavy-Ion Bombardment of Rare-Gas Targets", 37th Meeting of the Phys. Soc. Japan, Sapporo, Oct. (1982).
  - 24) K. Fujima, K. Fuwa, and M. Uda.: "The Intensity Analysis of X-Ray Emission from the Compounds in Multi-Ionized States-I", 37th Ann. Meeting of the Phys. Soc. Japan, Sapporo, Oct. (1982).
  - 25) K. Fuwa, K. Fujima, and M. Uda: "The Intensity Analysis of X-Ray Emission from the Compounds in Multi-Ionized States-II", 37th Ann. Meeting of the Phys. Soc. Japan, Sapporo, Oct. (1982).
  - 26) M. Uda, K. Maeda, Y. Sasa, A. Koyama, and S. Nakamura: "Chemical Effects on O K $\alpha$  Spectra Emitted from Multiply Ionized States", 37th Ann. Meeting of the Phys. Soc. Japan, Sapporo, Oct. (1982).
  - 27) K. Maeda, Y. Sasa, and M. Uda: "Data Processing for Quantitative Analysis by PIXE", 18th Oyo Spectrometry Tokyo Toronkai (18th Tokyo Symp. on Applied Spectrometry), Tokyo, Nov. (1982).
  - 28) H. Sakairi: "Electron Microscopic Observation on Heavy Ion Irradiation Damage", 12th Symp. on Fusion Reactor Materials, Nagoya, Dec. (1982).
4. Radiochemistry, radiation chemistry and radiation biology
- 1) Y. Itoh and T. Nozaki: "Oxygen Depth Profilin in Heat-treated Silicon as measured by Charged Particle Activation Analysis", Meeting of Technical Group on Semiconductors

- and Semiconductor Devices, Osaka, Feb. (1982).
- 2) T. Takahashi and F. Yatagai: "Recent Development of Plastic Track Detectors, Application for Biology and Medicine, Spring Meeting of Japan Soc. Appl. Phys., Tokyo, Apr. (1982).
  - 3) T. Takahashi, F. Yatagai, and S. Kitayama: "Effect of Heavy Ions on Bacterial Spores and Phages", 24th Committee on Space Research, Ottawa, May (1982).
  - 4) H. Nagai, M. Aratani, T. Nozaki, M. Yanokura, and I. Kohno: "Rutherford Scattering Applied to the Study of Hydrogen in Amorphous Silicon", 6th Symp. on Ion Sources and Ion-Assisted Technology, Tokyo, June (1982).
  - 5) K. Niisawa, J. Saito, K. Taki, T. Karasawa, and T. Nozaki: "The Reaction of  $^{11}\text{CO}_2$  in a Microwave Discharge", 5th Intern Symp. Radiopharm. Chem., Jülich, Aug. (1982).
  - 6) K. Ogawa, K. Taki, and T. Nozaki: "Synthesis of  $^{73}\text{Se}$ - or  $^{75}\text{Se}$ -Labeled Compounds by the Isotopic Exchange with Elemental Selenium-73 or -75", 5th Intern Symp. Radiopharm. Chem., Jülich, Aug. (1982).
  - 7) T. Hara and T. Nozaki: "Radioactivity Labeling of C-1 Position of Glucose and Mannose", 5th Intern. Symp. Radiopharm. Chem., Jülich, Aug. (1982).
  - 8) T. Irie, K. Fukushi, O. Inoue, T. Yamasaki, Y. Kasida, T. Ido, and T. Nozaki: " $^{18}\text{F}$ -Labeled 6-Fluoro-Purine Derivatives as a New Brain Scanning Agent", 5th Intern. Symp. Radiopharm. Chem., Jülich, Aug. (1982).
  - 9) M. Yanokura, H. Nagai, M. Aratani, T. Nozaki, and I. Kohno: "Rutherford Scattering Applied to the Study of Hydrogen in Amorphous Silicon", 7th Meeting on Linear Accelerator in Japan Ibaragi, Aug. (1982).
  - 10) Y. Itoh and T. Nozaki: "Heat Treatment Effect of Carbon and Oxygen to Gold Diffusion in Silicon", Fall Meeting of the Appl. Phys. Soc. Japan, Fukuoka, Sept. (1982).
  - 11) G. Okada, K. Kurita, K. Nakano, and I. Kaneko: "Mutagenesis of Chinese Hamster V79 Cells by Nitrogen Particles", 24th Ann. Meeting of the Japan Radiat. Res. Soc., Akita, Oct. (1982).
  - 12) T. Ohno, T. Nishimura, G. Okada, K. Nakano, and I. Kaneko: "Recovery from Potentially Lethal Damage of Human Normal Fibroblast Cells after Irradiation of Nitrogen Ion Beams", 24th Ann. Meeting of the Japan Radiat. Res. Soc., Akita, Oct. (1982).
  - 13) K. Eguchi, S. Satoh, M. Yaguchi, T. Inada, and I. Kaneko: "LET Dependency of the PLD of HMV-1 Cells", 24th Ann. Meeting of the Japan Radiat. Res. Soc., Akita, Oct. (1982).
  - 14) K. Eguchi, S. Satoh, M. Yaguchi, T. Inada, and I. Kaneko: "Effect of Nitrogen Ion Radiation on the DNA damage and Its Rejoining", 24th Ann. Meeting of the Japan Radiat. Res. Soc., Akita, Oct. (1982).
  - 15) S. Ambe: "Separation of Trace Elements, In(III), Sn(IV), Sb(V), and Te(IV) by Adsorption on Activated Carbon and Graphite", 26th Symp. on Radiochem., Niigata, Oct. (1982).
  - 16) T. Nozaki and Y. Itoh: "Measurement of Oxygen Solubility and Diffusion Coefficient of Oxygen in Silicon", 26th Symp. on Radiochem., Niigata, Oct. (1982).
  - 17) F. Ambe, S. Ambe, T. Okada, and H. Sekizawa: "Emission Mössbauer Studies of

- Carrier-Free  $^{119}\text{Sb}^{5+}$  and  $^{57}\text{Co}^{2+}$  Adsorbed on Magnetic Oxide Surfaces”, 26th Symp. on Radiochem., Niigata, Oct. (1982).
- 18) H. Nagai, M. Aratani, T. Nozaki, M. Yanokura, and I. Kohno, O. Kuboi, and Y. Yatsurugi: “Rutherford Forward Scattering Applied to the Analysis of Hydrogen”, 26th Ann. Meeting of Radiochem., Niigata, Oct. (1982).
  - 19) K. Kimura, Y. Toda, and M. Imamura: “Extraordinary Emission of He-gas near Critical Temperature Irradiated by  $\text{N}^{7+}$ -Ions”, 25th Conf. on Radiat. Chem., Sendai, Oct. (1982).
  - 20) F. Yatagai and K. Nakano: “Application of Thermoluminescence Dosimeter for Dose Measurement of High LET Radiation”, Proc. 4th Symp. on Accelerator Science and Technology, Wako, Nov., p. 185 (1982).
  - 21) G. Okada, K. Kurita, T. Nishimura, K. Nakano, and I. Kaneko: “Mutation Induction of Chinese Hamster V79 Cells by Nitrogen Ion Beams”, Proc. 4th Symp. on Accelerator Science and Technology, Wako, Nov., p. 189 (1982).
  - 22) I. Kaneko, T. Ohno, T. Nishimura, G. Okada, and K. Nakano: “Recovery from Potentially Lethal Damage of Human Normal Fibroblast IMR 90 Cells after Irradiation of Nitrogen Ion Beams”, Proc. 4th Symp. on Accelerator Science and Technology, Wako, Nov., p. 191 (1982).
  - 23) K. Eguchi, S. Sato, M. Yaguchi, T. Inada, K. Kobayashi, and I. Kaneko: “Recovery from Potentially Lethal Damage of Human Melanoma Cells after Irradiation of Proton and Nitrogen Ion Beam”, Proc. 4th Symp. on Accelerator Science and Technology, Wako, Nov., p. 193 (1982).
  - 24) I. Kaneko, K. Eguchi, T. Ohno, S. Satoh, T. Inada, and K. Nakano: “Recovery from Potentially Lethal Damage of Human Cells after Irradiation of Proton and Nitrogen Ion Beams”, 5th Radiation Biology Center Intern. Symp. on DNA Repair and Chemical Damage, Moriyama, Nov. (1982).

## VII. LIST OF OUTSIDE USERS AND THEIR THEMES

(Jan. – Dec. 1982)

- |    |   |   |
|----|---|---|
| 1) | S. Yoshida and K. Mitsui<br>“Study of Effect by Bombarding High Energy Proton on a GaAs Solar Cell” | LSI R & D Lab.<br>Mitsubishi Electric Co., Ltd.   |
| 2) | H. Nakahara and T. Miura<br>“Production of $^{77}\text{Br}$ and $^{58}\text{Co}$ ”                  | Faculty of Science, Tokyo<br>Metropolitan Univ.   |
| 3) | K. Yuita<br>“Production of $^{77}\text{Br}$ and $^{43}\text{K}$ ”                                   | National Inst. of Agricultural<br>Sciences  |
| 4) | T. Abe<br>“Radiochemical Analysis of $^{16}\text{O}$ in Si Crystal”                                 | Shinetsu Semiconductor Co., Ltd.  |
| 5) | K. Usami<br>“Radiochemical Analysis of $^{14}\text{N}$ in Si Crystal”                               | Central Res. Lab., Hitachi Ltd.   |
| 6) | H. Shinyashiki<br>“Radiochemical Analysis of $^{16}\text{O}$ in GaAs”                               | Central Res. Lab., Mitsubishi<br>Metal Co., Ltd.  |
| 7) | H. Muraoka<br>“Radiochemical Analysis of $^{14}\text{N}$ in Si Crystal”                             | Semiconductor Div., Toshiba<br>Electric Co., Ltd.   |
| 8) | T. Iizuka<br>“Radiochemical Analysis of $^{16}\text{O}$ in Si Crystal”                              | Japan Electric Industry<br>Developing Association (JEIDA)   |
| 9) | Y. Higashiguchi<br>“Study of Effect by Bombarding High Energy Helium on a Reactor Material”         | Research Inst. for Iron, Steel and<br>Other Metals, Tohoku Univ.<br>Irradiation Research Lab. in JMTR |

- 10) M. Koitabashi  
“Study of Effect by Bombarding High Energy Proton on a Teflon Plate Coated by a Silver”  
Central Res. Lab., Mitsubishi Electric Co., Ltd.
- 11) S. Suzuki  
“Study of Effect by Bombarding High Energy Proton on a Solid Fuel for a Rocket”  
Space Development Div., Nissan Automobile Co., Ltd.
- 12) M. Yatsunami and T. Suematsu  
“Study of Effect by Irradiating Fast Neutron on a Insulator Covering a Cable”  
Fujikura Cable Works, Ltd.
- 13) A. Morio and M. Harada  
“Study of Single Event Upset in Microprocessors by Bombarding  $^{20}\text{Ne}$  Particles”  
Japan Trust Center for Electronic Parts

## VIII. LIST OF SEMINARS

(Jan. – Dec. 1982)

- 1) A. van der Woude, KVI (Holland), 26 January  
“Barrier Properties of  $^{232}\text{Th}$  and  $^{238}\text{U}$  Deduced from Fission by Charged Particle Reactions”
- 2) K. Niita, Tohoku Univ. (Sendai), 28 January  
“Double Differential Cross Sections Based on the Quasi-Linear Response Theory”
- 3) F. Fukuzawa, Kyoto Univ. (Kyoto), 16 March  
“Experiment of Atomic Collisions in Denmark”
- 4) T. Kurihara, INS (Tokyo), 23 March  
“Study of  $^{208}\text{Pb}(\alpha, ^6\text{He})^{206}\text{Pb}$  Reaction and Systematic Studies of Neutron Pick-up Reactions”
- 5) M. Morinaga, Tech. Univ. München (West Germany), 30 April  
“Experiments using 250 MeV Nickel Beam; i) Spectroscopy of  $N = 82$  Proton-Rich Nuclei, and ii) Super Multi-Nucleon Transfer”
- 6) J. Kasagi, Tokyo Inst. Tech. (Tokyo), 9 June  
“Comparison of Non-Compound Neutron and Proton Emission in  $^{16}\text{O}$ -induced Reaction on  $^{238}\text{U}$ ”
- 7) M. Sakai, INS (Tokyo), 16 June  
“Study of Nuclear Physics after the Second World War”
- 8) T. Izumoto, Texas A & M Univ. (USA), 29 June  
“Pionic Modes of Excitation in Continuum from (p, n) Reaction”
- 9) T. Tamura, Univ. Texas at Austin (USA), 21 July  
“Boson Expansion”
- 10) U. Mosel, Giessen Univ. (West Germany), 22 July  
“Molecular Resonance in Inelastic Scattering of Light-Heavy Ion”
- 11) I. Hamamoto, Nordita (Denmark), 23 July  
“Residual Interactions in High Spin States”
- 12) K. Hara, Tech. Univ. München (West Germany), 27 July  
“Random Coupled Channel; A Model for DIC”

- 13) H. Yamada, Vanderbilt Univ. Tennessee (USA), 12 August  
“Massive-Transfer Reaction”
- 14) H. Morinaga, Tech. Univ. München (West Germany), 8 September  
“Cyclotron vs. Linac”
- 15) I. Hofmann, Max-Planck-Institute (West Germany), 21 September  
“Calculation of Orbits for Heavy Ion Accelerators”
- 16) J.Y. Park, North Carolina State Univ. (USA), 2 November  
“Theory of Nuclear Molecular States in Heavy Ion Collisions”
- 17) S. Iwasaki, Chiba Univ. (Chiba), 15 November  
“Treatment of Band Crossion using Angular Momentum Projection Method”
- 18) A. Ikeda, Tokyo Inst. Tech. (Tokyo), 30 November  
“Attenuation of Zero-Sound Wave at  $T = 0^\circ$ ”
- 19) S. Morinobu, RCNP (Osaka), 15 December  
“On On-Line Mass Separator”
- 20) S. Hayakawa, Ashikaga Inst. of Tech., 21 December  
“M1 Strength in  $^{208}\text{Pb}$ ”

## IX. LIST OF PERSONNEL

## Members of the Board

HAMADA Tatsuji 浜田達二	HASHIZUME Akira 橋爪朗
IMAMURA Masashi 今村昌	KAMITSUBO Hiromichi 上坪宏道
KOHNO Isao 河野功	MORI Kazuo 森一夫
NOZAKI Tadashi 野崎正 (Chairman)	ODERA Masatoshi 小寺正俊
SAKAIRI Hideo 坂入英雄	SEKIZAWA Hisashi 関沢尚
SHIMA Makoto 島誠	UDA Masayuki 宇田応之

## Cyclotron Operation and Maintenance Group

FUJITA Shin 藤田新	IKEGAMI Kumio 池上九三男
KAGEYAMA Tadashi 影山正	KOHARA Shigeo 小原重夫
KOHNO Isao 河野功	OGIWARA Kiyoshi 荻原清
TAKEBE Hideki 武部英樹	

## Linac Operation and Maintenance Group

CHIBA Yoshiaki 千葉好昭	GONO Yasuyuki 郷農靖之
HEMMI Masatake 逸見政武	IKEZAWA Eiji 池沢英二
INOUE Toshihiko 井上敏彦	KAMBARA Tadashi 神原正
KASE Masayuki 加瀬昌之	KUBO Toshiyuki 久保敏幸
MIYAZAWA Yoshitoshi 宮沢佳敏	TONUMA Tadao 戸沼正雄
YANOKURA Minoru 矢野倉実	

## Scientific and Engineering Personnel

## Cyclotron Laboratory

FUJISAWA Takashi 藤沢高志	FUJITA Jiro 藤田二郎
GOTO Akira 後藤彰	HARA Masahiro 原雅弘
ICHIMURA Atsushi 市村淳	IKEGAMI Yuji 池上祐司
INAMURA Takashi 稲村卓	ISHIHARA Masayasu 石原正泰
KAMITSUBO Hiromichi 上坪宏道	KARASAWA Takashi 唐沢孝
KISHIDA Norio 岸田則生	KOHMOTO Susumu 河本進
KOHNO Isao 河野功	KUDO Hisaaki 工藤久昭
MOTONAGA Shoshichi 元永昭七	NAKAJIMA Shunji 中島諄二
NAKANISHI Noriyoshi 中西紀喜	NOMURA Toru 野村亨
OIKAWA Yoshifumi 老川嘉郁	SHIKATA Takashi 四方隆史
SHIMIZU Kazuo 清水和男	TAKESHITA Isao 竹下勇夫
TOYAMA Mitsuru 遠山満	UTSUNOMIYA Hiroaki 宇都宮弘章
WADA Takeshi 和田雄	YAMAJI Shuhei 山路修平
YANO Yasushige 矢野安重	YOKOYAMA Ichiro 横山一郎

## (Visitors)

HIRUTA Kotaro 蛭田幸太郎 (Dept. Phys., Tokyo Gakugei Univ.)

ICHIMURA Munetake 市村宗武 (Inst. Phys., College General Education, Univ. of Tokyo)

KIKUCHI Fumio 菊地文男 (Dept. Math., College of General Education, Univ. of Tokyo)

KOSAKO Toshiso 小佐古敏莊 (Inst. Nucl. Phys., Univ. of Tokyo)

MORINAGA Haruhiko 森永晴彦 (Dept. Phys., Technische Universität München)

NAKAHARA Hiromichi 中原弘道 (Dept. Chem., Tokyo Metropolitan Univ.)

NAKAMURA Takashi 中村尚司 (Inst. Nucl. Phys., Univ. of Tokyo)

ÖZKÖK Seuket (Dept. Phys., Istanbul Univ.)

SATO Kenichi 佐藤憲一 (Dept. Phys., Tohoku College of Pharmacy)

SHIRAIISHI Haruki 白石春樹 (Nat. Res. Inst. for Metals)

TAKEMASA Tadashi 武政尹士 (Dept. Phys., Saga Univ.)

TAKIGAWA Noboru 滝川昇 (Dept. Phys., Tohoku Univ.)

YOSHIDA Shiro 吉田思郎 (Dept. Phys., Tohoku Univ.)

ZHANG Zhenkang 張振康 (Inst. Mod. Phys., Academia Sinica)

ZHOU Sixin 周嗣信 (Inst. Mod. Phys., Academia Sinica)

(Students)

AMANO Koichi 天野光一 (Facul. Sci. and Eng., Chuo Univ.)

DETO Masuo 出戸益男 (College of Hum. and Sci., Nihon Univ.)

FUKASAWA Tsutomu 深沢勉 (College of Hum. and Sci., Nihon Univ.)

HATA Yoshihiro 秦芳広 (College of Hum. and Sci., Nihon Univ.)

IEKI Kazuo 家城和夫 (Dept. Phys., Kyoto Univ.)

NAGAME Yuichiro 永目諭一郎 (Dept. Chem., Tokyo Metropolitan Univ.)

SUEKI Keisuke 末木啓介 (Dept. Chem., Tokyo Metropolitan Univ.)

YOSHIZAWA Shinzi 吉沢信治 (College of Hum. and Sci., Nihon Univ.)

Linac Laboratory

CHIBA Yoshiaki 千葉好明

GONO Yasuyuki 郷農靖之

HOSHINO Kiichi 星野紀一

ITOH Yoshinori 伊東芳紀

KASE Masayuki 加瀬昌之

MIYAZAWA Yoshitoshi 宮沢佳敏

SHIBATA Hiromi 柴田裕実

YANOKURA Minoru 矢野倉実

CHIBA Toshiya 千葉利哉

HEMMI Masatake 逸見政武

INOUE Toshihiko 井上敏彦

KAMBARA Tadashi 神原正

KUBO Toshiyuki 久保敏幸

ODERA Masatoshi 小寺正俊

TONUMA Tadao 戸沼正雄

(Visitors)

HAYASHIBE Shogo 林部昭吾 (Dept. Phys., Tohoku Univ.)

ISHII Keishi 石井慶之 (Dept. Nucl. Eng., Kyoto Univ.)

ITO Noriaki 伊藤憲昭 (Dept. Crystalline Materials, Nagoya Univ.)

MATSUO Takashi 松尾崇 (Tokyo Univ. of Agric. Technol.)

MORITA Susumu 森田右 (College of Eng., Hosei Univ.)

ODA Nobuo 織田暢夫 (Res. Lab. for Nucl. Reactors, Tokyo Inst. Tech.)

OTANI Shunsuke 大谷俊介 (Inst. Plasma Phys., Nagoya Univ.)

SUGAWARA Masahiko 菅原昌彦 (Fund. Sci., Chiba Inst. Tech.)

SUZUKI Hiroshi 鈴木洋 (Dept. Phys., Sophia Univ.)

TAKEDA Shigeru 竹田繁 (Nat. Lab. High Energy Phys.)

TAWARA Hiroyuki 俵 博 之 (Inst. Plasma Phys., Nagoya Univ.)  
 TSURUBUCHI Seiji 鶴 淵 誠 二 (Dept. Eng., Tokyo Univ. Agric. Tech.)  
 URAKAWA Junji 浦 川 順 治 (Res. Lab. for Nucl. Reactors, Tokyo Inst. Tech.)  
 YAGISHITA Akira 柳 下 明 (Nat. Lab. High Energy Phys.)

#### Radiation Laboratory

AWAYA Yohko 粟 屋 容 子	HAMADA Tatsuji 浜 田 達 二
HASHIZUME Akira 橋 爪 朗	IZUMO Koichi 出 雲 光 一
KATOU Takeo 加 藤 武 雄	KONNO Satoshi 金 野 智
KUMAGAI Hidekazu 熊 谷 秀 和	OKANO Masaharu 岡 野 真 治
TAKAHASHI Junzo 高 橋 純 三	TAKAHASHI Tan 高 橋 旦
TENDOW Yoshihiko 天 道 芳 彦	

#### (Visitors)

DOKE Tadayoshi 道 家 忠 義 (Sci. and Eng. Res. Lab., Waseda Univ.)  
 FUJIOKA Manabu 藤 岡 学 (Dept. Phys., Tohoku Univ.)  
 ISHII Keizo 石 井 慶 造 (Cyclotron, Tohoku Univ.)  
 MIURA Taichi 三 浦 太 一 (Dept. Chem., Tokyo Metropolitan Univ.)  
 MURAMATSU Hisakazu 村 松 久 和 (Nat. Lab. High Energy Phys.)  
 MORITA Susumu 森 田 右 (College of Eng., Hosei Univ.)  
 NAGAHARA Teruaki 永 原 照 明 (Inst. Atomic Energy, Rikkyo Univ.)  
 NAMIKI Masatoshi 並 木 雅 俊 (Div. General Education, Takachiho College)  
 TAWARA Hiroyuki 俵 博 之 (Inst. Plasma Phys., Nagoya Univ.)  
 URAKAWA Junji 浦 川 順 治 (Res. Lab. Nucl. Reactors, Tokyo Inst. Tech.)

#### (Student)

HATSUKAWA Yuji 初 川 雄 二 (Dept. Chem., Tokyo Metropolitan Univ.)

#### Thermonuclear Fusion Laboratory

ANDO Kozo 安 藤 剛 三	BE Such Hee 裴 碩 喜
-------------------	-------------------

#### Plasma Physics Laboratory

ISHIBE Yukio 石 部 行 雄	OYAMA Hitoshi 大 山 等
SAKAMOTO Yuichi 坂 本 雄 一	

#### Metal Physics Laboratory

KOYAMA Akio 小 山 昭 雄	SHIOTANI Nobuhiro 塩 谷 亘 弘
YAGI Eiichi 八 木 栄 一	

#### Magnetic Materials Laboratory

ASAI Kichizo 浅 井 吉 藏	OKADA Takuya 岡 田 卓 也
SAKAI Nobuhiko 坂 井 信 彦	SEKIZAWA Hisashi 関 沢 尚

## Semiconductors Laboratory

(Visitor)

AONO Keiko 青野桂子 (College of Liberal Arts, Kitazato Univ.)

## Solid-State Chemistry Laboratory

FUJIMA Kazumi 藤間一美

SASA Yoshihiko 佐々嘉彦

MAEDA Kuniko 前田邦子

UDA Masayuki 宇田応之

(Students)

FUWA Koh 不破耕 (School of Sci. Eng., Waseda Univ.)

NAKAMURA Shiho 中村志保 (School of Sci. Eng., Waseda Univ.)

## Radiochemistry Laboratory

AMBE Fumitoshi 安部文敏

ARATANI Michi 荒谷美智

IWAMOTO Masako 岩本正子

NAGAI Hisao 永井尚生

TERAI Yoshiro 寺井善郎

AMBE Shizuko 安部静子

ITOH Yoshiko 伊東芳子

MINAI Yoshitaka 薬袋佳孝

NOZAKI Tadashi 野崎正

(Visitors)

KUBOI Osamu 久保井 収 (Komatsu Electric Metals Co. Ltd.)

TAKI Ko 滝 幸 (Dept. Hygen., Kitazato Univ.)

USAMI Katsuhisa 宇佐美 勝久 (Hitachi Res. Lab., Hitachi Ltd.)

YATSURUGI Yoshifumi 八 劍 吉 文 (Komatsu Electric Metals Co. Ltd.)

## Radiation Chemistry Laboratory

IMAMURA Masashi 今村 昌

TODA Yutaka 戸田 豊

KIMURA Kazuie 木村 一 宇

## Radiobiology Laboratory

KANEKO Ichiro 金子 一 郎

NAKANO Kazushiro 中野和城

YATAGAI Fumio 谷田貝 文 夫

KITAYAMA Shigeru 北山 滋

OKADA Gensaku 岡田源作

(Visitors)

INADA Tetsuo 稲田哲雄 (Dept. Medicine, Tsukuba Univ.)

NISHIMURA Tetsuji 西村哲治 (Facul. Pharm. Sci., Univ. of Tokyo)

OHNO Tadao 大野忠夫 (National Inst. Radiological Sciences)

(Student)

EGUCHI Kiyomi 江口清美 (Dept. Medicine, Tsukuba Univ.)

**Safety Control Affairs Office**

IGARASHI Kazui 五十嵐 一 成  
MIYAGAWA Makoto 宮川 真 言  
USUBA Isao 薄 葉 勲

KOYAMA Masashi 小 山 政 史  
SAKAMOTO Ichiro 坂 本 一 郎

**Beam Analysis Center**

IWAKI Masaya 岩 木 正 哉  
SAKAIRI Hideo 坂 入 英 雄

KOBAYASHI Takane 小 林 峰  
URAI Teruo 浦 井 輝 夫

(Student)

SATO Susumu 佐 藤 進 (Facul. Eng., Toyo Univ.)



## AUTHOR INDEX

- ABE Junya 阿部 準也 183  
 AMBE Fumitoshi 安部 文敏 98, 101, 103, 130, 132  
 AMBE Shizuko 安部 静子 98, 101, 103, 120, 128, 130  
 AONO Keiko 青野 桂子 111  
 ARATANI Michi 荒谷 美智 125  
 ASAI Kichizo 浅井 吉蔵 103, 132  
 AWAYA Yohko 粟屋 容子 66, 69, 72, 75, 77, 79, 82  
 BE Suck Hee 裴 碩喜 85  
 CHIBA Toshiya 千葉 利哉 87, 178  
 CHIBA Yoshiaki 千葉 好明 5, 169, 171  
 DETO Masuo 出戸 益男 193  
 EGUCHI Kiyomi 江口 清美 144  
 FUJIMA Kazumi 藤間 一美 89  
 FUJIOKA Manabu 藤岡 学 91  
 FUJISAWA Takashi 藤沢 高志 35, 169, 171, 173, 217  
 FUJITA Jiro 藤田 二郎 186, 188  
 FUJITA Shin 藤田 新 2, 239, 243, 233, 235  
 FUKASAWA Tsutomu 深沢 勉 227  
 FUKUDA Tomokazu 福田 共和 26  
 FUWA Koh 不破 耕 89  
 GONO Yasuyuki 郷農 靖之 5, 46, 48, 51, 94  
 GOTO Akira 後藤 彰 183, 186, 197, 215, 219, 224  
 HAMAJIMA Yasunori 浜島 靖典 9, 22  
 HARA Akihisa 原 明久 239  
 HARA Masahiro 原 雅弘 193, 207, 227  
 HARADA Kichinosuke 原田 吉之助 54, 58  
 HASEGAWA Masayuki 長谷川 雅幸 114  
 HASEGAWA Takeo 長谷川 武夫 35  
 HASHIZUME Akira 橋爪 朗 38, 41, 91, 132  
 HASIGUTI R. Ryukiti 橋口 隆吉 108  
 HAYASHI Nobuyoshi 林 宣好 230  
 HAYASHIBE Shogo 林部 昭吾 48, 51  
 HEMMI Masatake 逸見 政武 5, 164, 178  
 HIRUTA Kotaro 蛭田 幸太郎 51  
 HITACHI Akira 月出 章 66, 69, 82  
 HOSHINO Kūichi 星野 紀一 149  
 IEKI Kazuo 家城 和夫 28  
 IGARASHI Kazui 五十嵐 一茂 233  
 IKEGAMI Kumio 池上 九三男 205, 207, 210, 212  
 IKEGAMI Yuji 池上 祐司 183  
 IKEZAWA Eiji 池沢 英二 2, 5  
 IMAMURA Masashi 今村 昌 134  
 INADA Tetsuo 稲田 哲雄 144  
 INAMURA Takashi 稲村 卓 28, 38, 43, 222  
 INOUE Toshihiko 井上 敏彦 5  
 ISHIBE Yukio 石部 行雄 210, 212  
 ISHIHARA Masayasu 石原 正泰 15, 28, 94  
 ISHII Mitsuhiko 石井 三彦 38  
 ISHIZAKI Yoshihide 石崎 可秀 35  
 ITOH Yoshiko 伊東 芳子 122  
 ITOH Yoshinori 伊東 芳紀 46, 48, 51, 94  
 IWAI Satoshi 岩井 敏 239  
 IWAKI Masaya 岩木 正哉 109, 111  
 IWAMOTO Akira 岩本 昭 54, 58  
 IWAMOTO Masako 岩本 正子 120, 122  
 IWATANI Kazuo 岩谷 和夫 35  
 KAGEYAMA Tadashi 影山 正 2  
 KAMBARA Tadashi 神原 正 5, 66, 69, 72, 75, 77, 79, 82, 85, 147, 155, 162, 176  
 KAMITSUBO Hiromichi 上坪 宏道 1, 115, 118, 181, 224, 239, 243  
 KANEKO Ichiro 金子 一郎 142, 144  
 KARASAWA Takashi 唐沢 孝 230  
 KASE Masayuki 加瀬 昌之 5, 66, 69, 72, 75, 77, 79, 82, 85, 88, 147, 155, 158, 160, 162, 176  
 KATORI Kenji 鹿取 謙二 26  
 KATOU Takeo 加藤 武雄 41  
 KIKUCHI Fumio 菊地 文雄 227  
 KIMURA Kazuie 木村 一字 134  
 KISHIDA Norio 岸田 則生 186, 201, 215, 222, 224  
 KISHIMOTO Tadafumi 岸本 忠史 31  
 KOBAYASHI Hirotada 小林 弘忠 118  
 KOBAYASHI Takane 小林 峰 8  
 KOHARA Shigeo 小原 重夫 2, 160, 171, 173  
 KOHMOTO Susumu 河本 進 18, 19, 28, 94, 224  
 KOHNO Isao 河野 功 2, 9, 12, 66, 69, 85, 115, 118, 125, 239  
 KONO Toshiyuki 河野 俊之 48  
 KOSAKO Toshiso 小佐古 敏莊 239, 243  
 KOYAMA Akio 小山 昭雄 96, 105, 108  
 KOYAMA Masashi 小山 政史 233  
 KUBO Toshiyuki 久保 敏幸 5, 18, 31, 46, 48, 51, 166, 176  
 KUBOI Osamu 久保井 収 125  
 KUBONO Shigeru 久保野 茂 22, 35  
 KUDO Hisaaki 工藤 久昭 18, 28  
 KUMAGAI Hidekazu 熊谷 秀和 41, 69, 72, 75, 77, 79, 82, 85, 88

- KURAMOTO Eiichi 蔵元英一 114
- LUI Y.-W. 15
- MAEDA Kuniko 前田邦子 96, 145
- MATSUO Takashi 松尾 崇 72, 75, 77, 79, 85
- MIHARA Yasuo 三原康雄 15
- MINAI Yoshitaka 薬袋佳孝 120
- MINEHARA Eisuke 峰原英介 38
- MIURA Iwao 三浦 岩 26
- MIURA Taichi 三浦太一 91
- MIYAZAWA Yoshitoshi 宮沢佳敏 5
- MOTONAGA Shoshichi 元永昭七 118, 183, 186, 188, 197, 210, 212
- MORITA Kohsuke 森田浩介 22
- MURAKAMI Tetsuya 村上哲也 15
- MURAMATSU Hisakazu 村松久和 91
- NAGAI Hisao 永井尚生 125
- NAGAME Yuichiro 永目諭一郎 9, 12
- NAKAHARA Hiromichi 中原弘道 9, 12, 91
- NAKAJIMA Shunji 中島諄二 205, 207, 210, 212
- NAKAMURA Shiho 中村志保 96, 145
- NAKAMURA Takashi 中村尚司 239
- NAKANISHI Noriyoshi 中西紀喜 186, 197, 215, 219
- NAKANO Kazushiro 中野和城 137, 142, 144
- NAMBA Susumu 難波 進 111
- NAMIKI Masatoshi 並木雅俊 72
- NANAO Susumu 七尾 進 113
- NISHI Katsuo 西 克夫 88
- NISHIMURA Tetsuji 西村哲治 142
- NOMURA Toru 野村 亨 18, 19, 22, 26, 46, 48, 51, 94
- NOZAKI Tadashi 野崎 正 120, 122, 125, 230
- ODA Katsuro 小田克郎 113
- ODERA Masatoshi 小寺正俊 153, 162, 178
- OGATA Hiroshi 小方 寛 26
- OGIWARA Kiyoshi 荻原 清 2, 217
- OHNO Tadao 大野忠夫 144
- OHNUMA Hajime 大沼 甫 31
- OHSHIMA Masumi 大島真澄 38
- OIKAWA Yoshifumi 老川嘉郁 183, 205, 207, 210, 212, 217
- OKADA Gensaku 岡田源作 142, 144
- OKADA Takuya 岡田卓也 98, 101
- OKANO Masaharu 岡野真治 239
- OYAMA Hitoshi 大山 等 210, 212
- ÖZKÖK. S. 85
- SAITO Hajime 斉藤 肇 183, 186
- SAKAI Nobuhiko 坂井信彦 132
- SAKAIRI Hideo 坂入英雄 8, 105, 108, 109, 237
- SAKAMOTO Ichiro 坂本一郎 233, 235
- SAKAMOTO Yuichi 坂本雄一 210, 212
- SASA Yoshihiko 佐々嘉彦 96, 145, 237
- SASAGASE Masaji 笹ヶ瀬正二 19, 48, 51
- SATO Susumu 佐藤 進 109
- SATO Takemi 佐藤岳実 183, 186, 188
- SEKIZAWA Hisashi 関沢 尚 98, 101, 103
- SHIKATA Takashi 四方隆史 105, 115, 118, 239, 243
- SHIMODA Tadashi 下田 正 26
- SHIMOURA Susumu 下浦 享 26
- SHIOTANI Nobuhiro 塩谷亘弘 113, 114
- SHIRAIISHI Haruki 白石春樹 115
- SUEHIRO Teruo 末広輝男 31
- SUEKI Keisuke 末木啓介 9, 12, 18, 28
- SUEMATSU Tatsuya 末松達也 118
- SUGAWARA Masahiko 菅原昌彦 46, 48, 51
- SUGITANI Michio 杉谷道朗 22, 31, 35
- TAKADA Eiichi 高田英一 15
- TAKAHASHI Junzo 高橋純三 72, 75, 77, 79, 82, 85
- TAKAHASHI Masato 高橋正人 9, 12
- TAKAHASHI Tan 高橋 且 139
- TAKEBE Hideki 武部英樹 2, 183, 186, 188, 197
- TAKEMASA Tadashi 武政尹士 61
- TAKENAKA Eiichi 竹中栄一 224
- TAKESHITA Isao 竹下勇夫 183, 186, 188, 205
- TANAKA Eiji 田中英二 91
- TANAKA Masahiko 田中雅彦 22
- TENDOW Yoshihiko 天道芳彦 41
- TOBA Yoshiyuki 外羽吉幸 15
- TODA Yutaka 戸田 豊 134
- TOHYAMA Mitsuru 遠山 満 63
- TONUMA Tadao 戸沼正雄 5, 66, 69, 75, 82, 85, 87, 88, 162
- TSUKUMO Takaaki 九十九高秋 183
- TRIBBLE R. 15
- UDA Masayuki 宇田応之 89, 96, 145, 237
- UNGRICHT E. 15
- URAI Teruo 浦井輝夫 8
- URAKAWA Junji 浦川順治 72, 75, 77, 79, 85
- USUBA Isao 薄葉 勲 233, 237
- UTSUNOMIYA Hiroaki 宇都宮弘章 18, 19, 22, 28
- WADA Takeshi 和田 雄 183, 186, 188, 193, 197, 227
- WATANABE Yasuhiro 渡辺康裕 113
- YAGI Eiichi 八木栄一 8, 105, 108

YAGISHITA Akira 柳下 明 75, 77, 79, 82, 87  
YAMAJI Shuhei 山路 修平 54, 58, 63, 243  
YAMAMOTO Norikazu 山本 徳和 115  
YANO Yasushige 矢野 安重 160, 186, 197,  
201, 215, 219  
YANOKURA Minoru 矢野倉 実 5, 118, 125, 153  
YATAGAI Fumio 谷田貝 文夫 137, 139

YATSUHASHI Motoharu 八橋 元治 118  
YATSURUGI Yoshifumi 八劍 吉文 125  
YOKOYAMA Ichiro 横山 一郎 160, 186, 188  
YOSHIDA Heitaro 吉田 平太郎 115  
YOSHIDA Shiro 吉田 思郎 54, 58

## **RIKEN Accelerator Progress Report**

理化学研究所加速器年次報告 第16卷(1982)

---

印刷 昭和58年(1983)5月25日

発行 昭和58年(1983)5月31日

発行者 理化学研究所

代表者 宮 島 龍 興

〒351 埼玉県和光市広沢2番1号

電話(0484)62-1111

編集者 理化学研究所加速器運営委員会

印刷所 丸星印刷株式会社

〒130 東京都墨田区亀沢1丁目3番3号

---

定価 5,000円

理化学研究所

埼玉県 和光市 広沢